$$h_o A_o = \frac{Q_{TS}}{T_{wall,avg} - T_{w,avg}} \tag{15}$$

where A_o is the outside test tube surface, $T_{wall,avg}$ is the average wall temperature, and $T_{w,avg}$ is the average cooling water temperature flowing inside the annulus.

3.5. The Nusselt number (Nu)

The Nusselt number is calculated as follows:

$$Nu = \frac{h_i D_i}{k_l} \tag{16}$$

where k_l is thermal conductivity of liquid refrigerant.

3.6. The frictional pressure drop (ΔP_f)

The total pressure drop, ΔP_{total}, is expressed as the sum of two important components, as follows:

$$\Delta P_{total} = \Delta P_f + \Delta P_a \tag{17}$$

The two terms on the right-hand side represent the frictional pressure drop (ΔP_f) and accelerational pressure drop (ΔP_a). The accelerational pressure drop, ΔP_a, was proposed by Tran [18] as follows:

$$\Delta P_a = G^2 \left(\left(\frac{x_{out}^2}{\rho_v \alpha_{out}} + \frac{(1-x_{out})^2}{\rho_l (1-\alpha_{out})} \right) - \left(\frac{x_{in}^2}{\rho_v \alpha_{in}} + \frac{(1-x_{in})^2}{\rho_l (1-\alpha_{in})} \right) \right) \tag{18}$$

where α is the void fraction and is presented by Zivi's correlation [19] as follows:

$$\alpha = \left(1 + \frac{(1-x)}{x} \left(\frac{\rho_v}{\rho_l} \right)^{\frac{2}{3}} \right)^{-1} \tag{19}$$

So far, the frictional pressure drop, ΔP_f, can be obtained by subtracting the accelerational pressure drop from the total measured pressure drop.

3.7. Two-phase friction factor (f_{tp})

The two-phase friction factor is calculated as follows:

$$f_{tp} = \frac{D_i \Delta P_f \rho_l}{2 G_{eq}^2} \tag{20}$$

where the equivalent mass flux, G_{eq}, is presented by Akers [21] as shown below:

$$G_{eq} = G \left[(1-x) + x \left(\frac{\rho_l}{\rho_v} \right)^{0.5} \right] \tag{21}$$

4. Results and discussion

In this study, the effects of corrugation pitch and corrugation depth on the Nusselt number and two-phase friction factor were experimentally investigated as a function of saturation temperature, heat flux, average quality, mass flux, and equivalent Reynolds number. The physical properties of the refrigerants were obtained by REFPROP, Version 6.01 [20]. The data cover five corrugated tubes and a smooth tube. The analysis of the data reported in Table 2 focuses on the effects of corrugation pitch and depth on the Nusselt number and two-phase friction factor.

4.1. Nusselt number

The experimental data for the smooth tube were validated by comparing the present heat transfer coefficient in terms of the Nusselt number with those taken from existing correlations such as those obtained by Akers et al. [21], Traviss et al. [22], Nualboonrueng et al. [23], Chen et al. [24], Cavallini and Zechin [25], Dobson and Chato [26], and Bassi and Bansal [27], as demonstrated in Fig. 4. It is found that around 90% of the data are correlated within the deviation of ±30%.

4.1.1. Effect of pitch on the Nusselt number

Fig. 5 illustrates the Nusselt number with average quality at various corrugation pitches (p = 5.08, 6.35, and 8.46 mm) with a constant corrugation depth of 1.5 mm at G = 400 kg/m^2 s, q'' = 10 kW/m^2, and T_{sat} = 40 °C. The results show that the Nusselt number increases with increasing average quality. At the same average quality, the Nusselt number obtained from the corrugated tubes is evidently higher than that from the smooth tube across the range of the average quality. Moreover, this figure shows that the Nusselt number at a lower corrugation pitch is higher than that at a higher one. This is because the corrugation pitch has a significant effect on mixing of the condensate film in the boundary layer

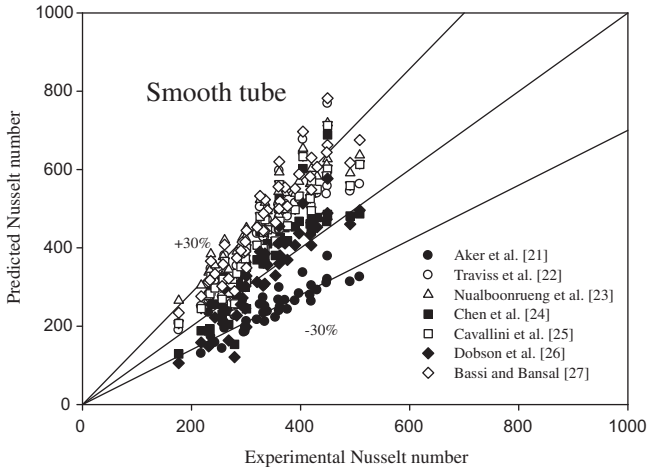

Fig. 4. Comparison of present R-134a Nusselt number data with existing correlation.

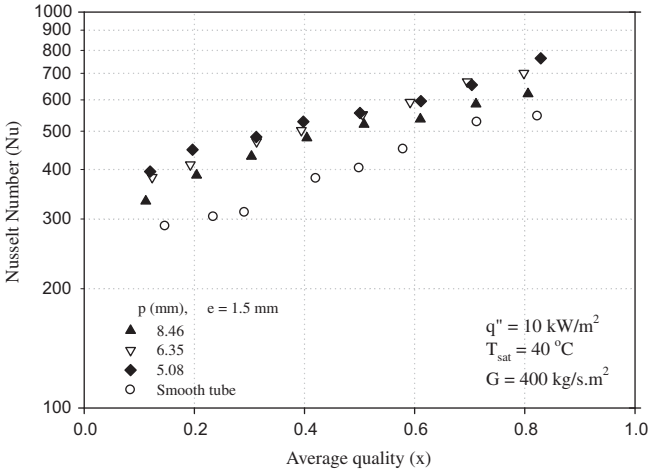

Fig. 5. Nusselt number vs average quality at T_{sat} = 40 °C, G = 400 kg/m^{2}s and q'' = 10 kW/m^2 for different pitches.

at the tube wall which causes the turbulence to increase. Therefore, the Nusselt number increases with decreasing corrugation pitch.

4.1.2. Effect of depth on the Nusselt number

Figs. 6 and 7 illustrate the Nusselt number with average quality and equivalent Reynolds number for different corrugation depths of 1, 1.25 and 1.5 mm, respectively with a constant corrugation pitch of 5.08 mm. As shown, the Nusselt number increases with increasing average quality and equivalent Reynolds number. At the same quality, the Nusselt number obtained from corrugation depth of 1.25 and 1.5 mm is obviously higher than that obtained from smooth tube. This is due to (1) drag forces exerted on the flow field by the corrugation, (2) flow blockage due to area reduction, (3) turbulence augmentation, and (4) rotational flow produced by the corrugation depth [11–12]. However, the Nusselt number obtained from corrugation depth of 1 mm is nearly same as the Nusselt number obtained from the smooth tube. This is because the axial momentum dominates the rotational flow produced by the corrugation depth of 1 mm.

4.1.3. Comparison of experimental data with proposed correlations

Fig. 8 shows a comparison of the experimental data for the corrugated tube with the proposed correlations. The proposed correlation is established from the Buckingham's Pi theorem in terms of Nusselt number, equivalent Reynolds number, Prandtl number, corrugation pitch and depth, and inside diameter. The proposed correlation is shown as follows:

$$Nu = 0.007\ Re_{eq}^{0.557} Pr^{3.8} \left(\frac{ep}{D_i^2}\right)^{0.02} \quad (22)$$

As illustrated in Fig. 8, the results show that approximately 90% of data fall within a deviation of ±10%.

4.2. Two-phase friction factor

The total condensation pressure drop was directly measured by the differential pressure transducer mounted on the header at the inlet and outlet of the test section. In our apparatus, the length between headers is 2.5 m while the length of the test section is 2 m. The frictional pressure drop can be obtained by subtracting the accelerational pressure drop from the total measured pressure drop. The results show the frictional pressure drop obtained from smooth and corrugated tubes in term of the Fanning two-phase friction factor.

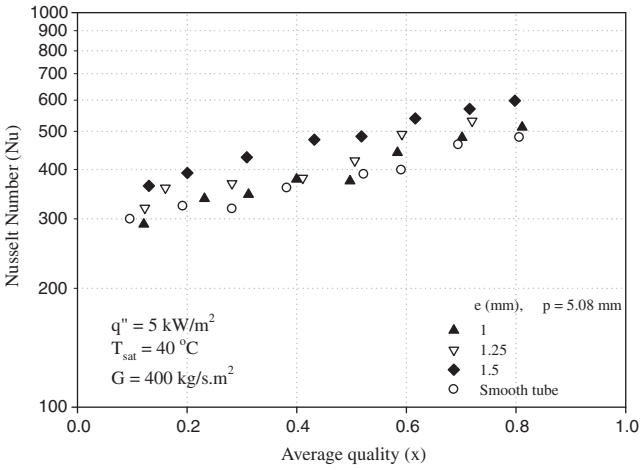

Fig. 6. Nusselt number vs average quality at T_{sat} = 40 °C, G = 400 kg/m^{2}s and q'' = 5 kW/m^2 for different depths.

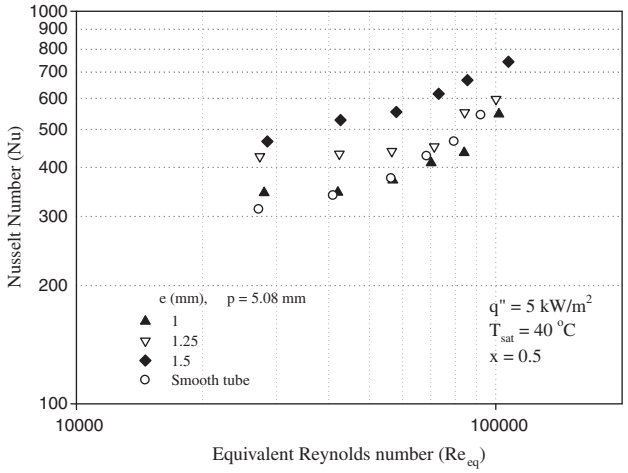

Fig. 7. Nusselt number vs equivalent Reynolds number at T_{sat} = 40 °C, q'' = 5 kW/m^2 and x = 0.5 for different depths.

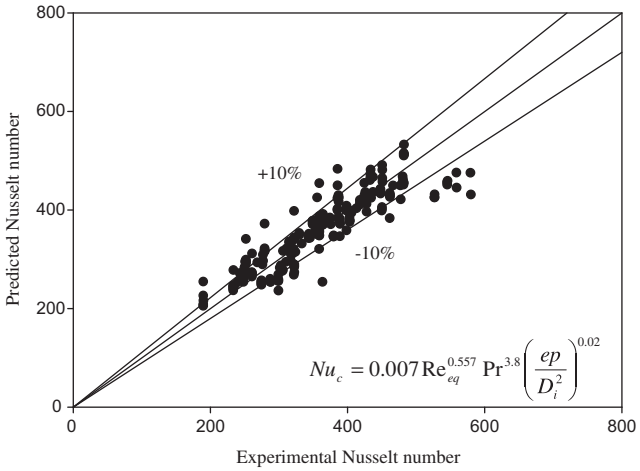

Fig. 8. Predicted Nusselt number using the proposed correlation vs the experimental data.

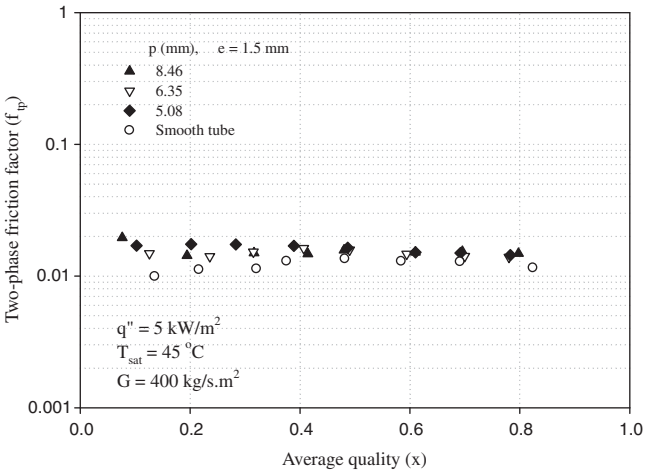

Fig. 9. Two-phase friction factor vs average quality at T_{sat} = 45 °C, G = 400 kg/m^{2}s and q'' = 5 kW/m^2 for different pitches.

4.2.1. Effect of pitch on two-phase friction factor

Fig. 9 illustrates the frictional pressure drop obtained from smooth and corrugated tubes in term of the Fanning two-phase friction factor. This plot shows that the two-phase friction factor slightly decreases with increasing average quality. The reason for this can be given in two aspects. Firstly, the frictional pressure drop increases with increasing average quality. This is because at higher average quality, the higher velocity of vapor flow causes more shear stress at the interface of the vapor and liquid film. Moreover, the secondary flow that becomes stronger at higher vapor velocity will produce more entrainment and redeposition of droplets, causing more flow turbulence. Secondly, the equivalent mass flux increases with increasing average quality. This is because the increasing in average quality increases the equivalent mass flux, according to Eq. (21). As the equivalent mass flux increase, the two-phase friction factor also decreases, according to Eq. (20). Therefore, the increase in average quality causes the two-phase friction factor to decrease. In addition, from the comparison of smooth and corrugated tubes, the two-phase friction factors obtained from corrugated tubes are higher than those obtained from smooth tube, under the same experimental condition. However, the effect of pitch on the two-phase friction factor is very small for all average quality.

4.2.2. Effect of depth on two-phase friction factor

Figs. 10 and 11 show the variations of the two-phase friction factor with average quality and the two-phase friction factor with equivalent Reynolds number, respectively. The experimental results show that the two-phase friction factor of the corrugated tube is greater than that of the smooth tube. The reason for this is similar to the reason given for Fig. 9. As shown in Figs. 10 and 11, the difference between two-phase friction factor obtained from corrugated tubes and smooth tube is reduced with increasing average quality and equivalent Reynolds number, respectively. This is because the secondary motion in refrigerant decreases as the axial momentum increases. However, from the present data, the effect of depth on the two-phase friction factor is insignificant.

4.2.3. The two-phase frictional multiplier (ϕ_l^2)

The two-phase frictional multiplier (ϕ_l^2) for the smooth tube is proposed by Chisholm [28] as follows:

$$\phi_l^2 = 1 + \frac{C}{X} + \frac{1}{X^2} \tag{23}$$

where X is the Martinelli parameter, which is given by

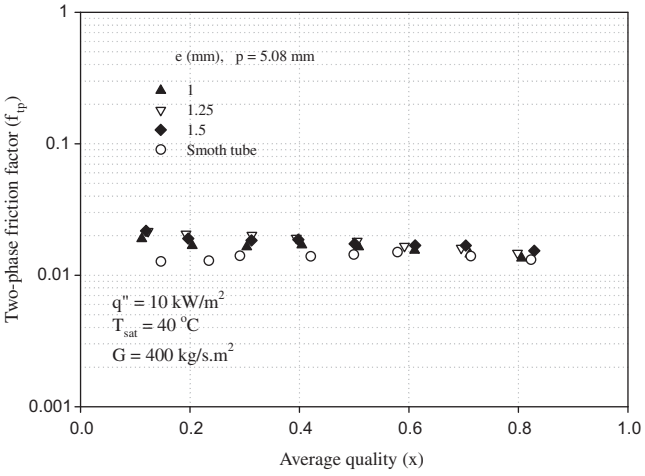

Fig. 10. Two-phase friction factor vs average quality at T_{sat} = 40 °C, G = 400 kg/m^{2}s and q'' = 10 kW/m^2 for different depths.

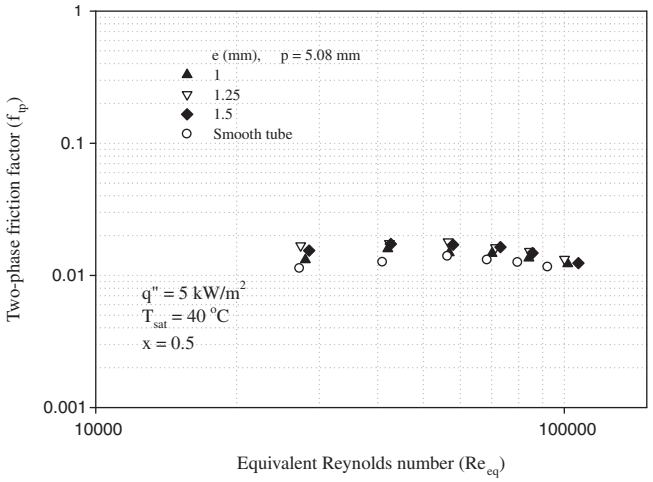

Fig. 11. Two-phase friction factor vs equivalent Reynolds number at T_{sat} = 40 °C, x = 0.5 and q'' = 5 kW/m^2 for different depths.

$$X^2 = \frac{\left(\frac{dp}{dz}\right)_l}{\left(\frac{dp}{dz}\right)_g} \tag{24}$$

The constant C in Eq. (23) is the parameter which indicates the two-phase flow condition.

Fig. 12 shows the comparison of the two-phase friction multiplier with the Martinelli parameter for different tubes. The predicted lines at values of constant C of 5, 10, and 20 are calculated by the Chisholm method. The constant value of C varies from 5 to 20 depending on the flow condition of the vapour and liquid. For instance, the constant C = 20 when the vapour and liquid flow is in the turbulent region. C = 10 when the vapour and liquid are laminar and turbulent, respectively. The value of C = 5 when the two-phase flow is in the laminar region. This figure shows that a smooth tube has a two-phase friction multiplier lower than that of the corrugated tube at the same Martinelli parameter. As shown in Fig. 13, almost all values of constant C obtained from the smooth tube are lower than those obtained from the corrugated tube at the same Martinelli parameter. However, the constant C depends not only on the Martinelli parameter but also on the Reynolds number and tube configurations. Therefore, constant C values can be correlated as follows:

$$\text{For smooth tube}: \quad C_s = 15.75\, X^{-0.5} Re_l^{-0.1} \tag{25}$$

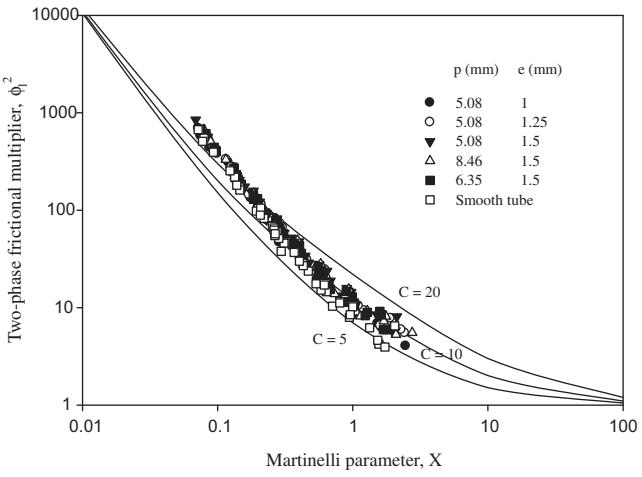

Fig. 12. Two-phase frictional multiplier vs Martinelli parameter.

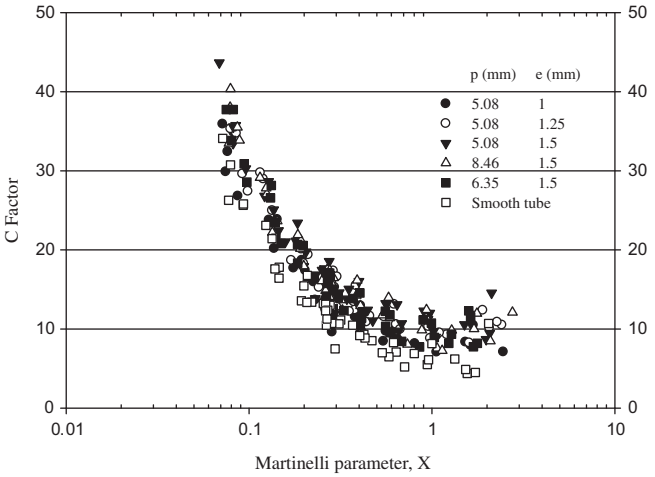

Fig. 13. Experimentally calculated *C* factors.

$$\text{For corrugated tube}: \quad C_c = 304.73X^{-0.254}Re_l^{-0.33}\left(\frac{ep}{D_i^2}\right)^{0.117} \tag{26}$$

The frictional pressure drops using the proposed *C* correlation are plotted with the experimental frictional pressure drop as shown in Fig. 14. It is found that about 95% of the data fall within a deviation of ±20%.

Fig. 15 shows the variation of the two-phase friction factor with equivalent Reynolds number for smooth tube and corrugated tubes. The experimental two-phase friction factor obtained from smooth tube is around 0.012. Moreover, Fig. 15 also shows that the two-phase friction factor obtained from corrugated tubes depends on the equivalent Reynolds number and tube geometry. The two-phase friction factor for corrugated tube is presented as follows:

$$\text{For corrugated tube}: \quad f_{tp,c} = 0.172Re_{eq}^{-0.2}\left(\frac{ep}{D_i^2}\right)^{0.09} \tag{27}$$

Fig. 16 shows the predicted frictional pressure drop of corrugated tubes using the proposed two-phase friction factor correlation versus the experimental data. However, the two-phase frictional pressure drop can be determined from Eqs. (27). Moreover, it is found that more than 90% of the data fall within a deviation of ±10%.

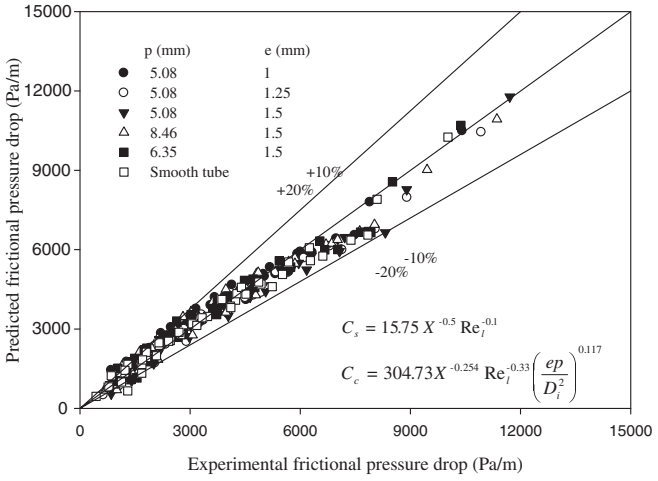

Fig. 14. Predicted frictional pressure drop using the proposed *C* factor correlation vs the experimental data.

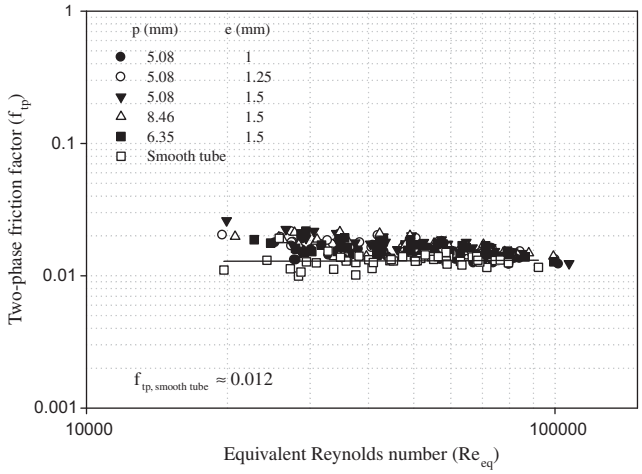

Fig. 15. Two-phase flow friction factor vs equivalent Reynolds number for smooth and corrugated tubes.

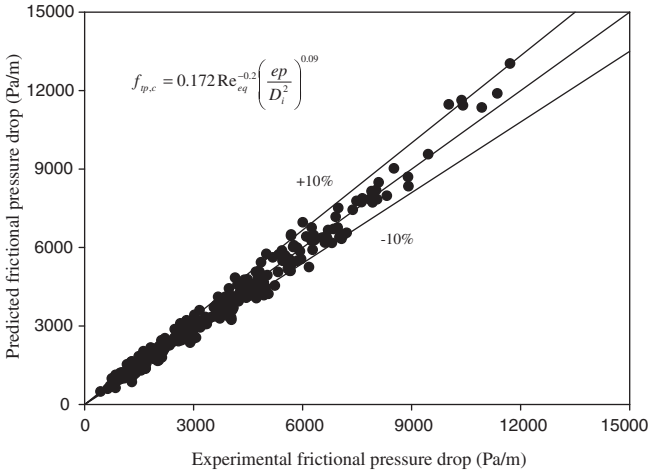

Fig. 16. Predicted frictional pressure drop using the proposed two-phase friction factor correlation vs the experimental data.

5. Conclusion

The experimental apparatus is designed to determine the Nusselt number and two-phase friction factor of R-134a using copper smooth and corrugated tubes. The test section is a counter-flow concentric tube-in-tube heat exchanger 2000 mm in length. A smooth tube and corrugated tubes having inner diameters of 8.7 mm are used as the inner tube. The corrugation pitches are 5.08, 6.35, and 8.46 mm. The corrugation depths are 1, 1.25, and 1.5 mm, respectively. The results obtained from the corrugated tubes are compared with those obtained from the smooth tube. Since the corrugation at the surface promotes turbulence of the refrigerant flow and mixing of the condensate film, it is evident that the Nusselt number and two-phase friction factor obtained from the corrugated tubes are significantly higher than those obtained from the smooth tube. The effect of pitch and depth on Nusselt number is significant. The Nusselt number increases with decreasing corrugation pitch and increases with increasing corrugation depth. On the other hand, the effect of pitch and depth on two-phase friction factor is insignificant. The new correlations are developed based on the present experimental data for predicting the Nusselt number and two-phase friction factor for corrugated tubes.

Acknowledgements

The present study was supported financially by King Mongkut's University of Technology Thonburi, the Thailand Research Fund, the Office of the Higher Education Commission and the National Research University Project, whose guidance and assistance are gratefully acknowledged.

References

[1] L.M. Schlager, M.P. Pate, A.E. Bergles, Evaporation and condensation heat transfer and pressure drop in horizontal 12.7-mm micro-fin tubes with refrigerant 22, J. Heat Transfer 112 (1989) 1041–1047.
[2] C.S. Kuo, C.C. Wang, In-tube evaporation of HCFC-22 in a 9.52 mm micro-fin/smooth tube, Int. J. Heat Mass Transfer 39 (1996) 2559–2569.
[3] Y. Kim, K. Seo, J.T. Chung, Evaporation heat transfer characteristics of R-410A in 7 and 9.52 mm smooth/micro-fin tubes., Int. J. Refrig. 25 (2002) 716–730.
[4] Y. Dong, L. Huixiong, C. Tingkuan, Pressure drop heat transfer and performance of single-phase turbulent flow in spirally corrugated tubes, Exp. Therm. Fluid Sci. 24 (2001) 131–138.
[5] A. Barba, S. Rainieri, M. Spiga, Heat transfer enhancement in a corrugated tube, Int. Commun. Heat Mass Transfer 29 (2002) 313–322.
[6] S. Rainieri, G. Pagliarini, Convective heat transfer to temperature dependent property fluids in the entry region of corrugated tubes, Int. J. Heat Mass Transfer 45 (2002) 4525–4536.
[7] V. Zimparov, Enhancement of heat transfer by a combination of three-start spirally corrugated tubes with a twisted tape, Int. J. Heat Mass Transfer 44 (2001) 551–574.
[8] V. Zimparov, Enhancement of heat transfer by a combination of a single-start spirally corrugated tubes with a twisted tape, Exp. Therm. Fluid Sci. 25 (2002) 535–546.
[9] V. Zimparov, Prediction of friction factors and heat transfer coefficients for turbulent flow in corrugated tubes combined with twisted tape inserts. Part 1: friction factors, Int. J. Heat Mass Transfer 47 (2004) 589–599.
[10] V. Zimparov, Prediction of friction factors and heat transfer coefficients for turbulent flow in corrugated tubes combined with twisted tape inserts. Part 2: heat transfer coefficients, Int. J. Heat Mass Transfer 47 (2004) 385–393.
[11] P.G. Vicente, A. Garcia, A. Viedma, Experimental investigation on heat transfer and friction factor characteristics of spirally corrugated tubes in turbulent flow at different Prandtl number, Int. J. Heat Mass Transfer 47 (2004) 671–681.
[12] P.G. Vicente, A. Garcia, A. Viedma, Mixed convection heat transfer and isothermal pressure drop in corrugated tubes for laminar and transition flow, Int. Commun. Heat Mass Transfer 31 (2004) 651–662.
[13] P. Naphon, M. Nuchjapo, J. Kurujareon, Tube side heat transfer coefficient and friction factor characteristics of horizontal tubes with helical rib, Energ. Convers. Manage. 47 (2006) 3031–3044.
[14] T. Targanski, J.T. Cieslinski, Evaporation of R407C/oil mixtures inside corrugated and micro-fin tubes, Appl. Therm. Eng. 27 (2007) 2226–2232.
[15] K. Bilen, M. Cetin, H. Gul, T. Balta, The investigation of groove geometry effect on heat transfer for internally grooved tubes, Appl. Therm. Eng. 29 (2009) 753–761.
[16] S. Laohalertdecha, S. Wongwises, The effects of corrugation pitch on the condensation heat transfer coefficient and pressure drop of R-134a inside horizontal corrugated tube, Int. J. Heat Mass Transfer 53 (2010) 2924–2931.
[17] S. Laohalertdecha, S. Wongwises, An experimental study into the evaporation heat transfer and flow characteristics of R-134a refrigerant flowing through corrugated tubes, Int. J. Refrig. 34 (2011) 280–291.
[18] T.N. Tran, Pressure drop and heat transfer study of two-phase flow in small channels, Ph.D. Dissertation, Texas Tech University, Lubbock, Texas, 1998.
[19] S.M. Zivi, Estimation of steady-state steam void-fraction by mean of the principle of minimum entropy production, J. Heat Transfer – Trans. ASME 86 (1964) 247–252.
[20] REFPROP, Refrigerant Properties Database, Version 6.01, NIST, Gaithersburg, MD, 1998.
[21] W.W. Akers, H.A. Beans, O.K. Crosser, Condensation heat transfer within horizontal tubes, Chem. Eng. Prog. Symp. 55 (1959) 29.
[22] D.P. Traviss, W.M. Rohsenow, A.B. Baron, Forced-convection condensation inside tubes: a heat transfer equation for condenser design, ASHRAE Trans. 79 (1973) 157–165.
[23] T. Nualboonrueng, J. Kaew-on, S. Wongwises, Two-phase condensation heat transfer coefficients of HFC-134a at high mass flux in smooth and micro-tubes, Int. Commun. Heat Mass Transfer 30 (2003) 577–590.
[24] S.L. Chen, F.M. Gerner, C.L. Tien, General film condensation correlation, Exp. Heat Transfer 1 (1987) 93–107.
[25] A. Cavallini, R. Zechin, A dimensionless correlation for heat transfer coefficient in forced-convection condensation, in: Proceedings of the 5th International Heat Transfer Conference, Japan, vol. 3, 1974, pp. 309–313.
[26] M.K. Dobson, J.C. Chato, Condensation in smooth horizontal tubes, J. Heat Transfer 120 (1998) 193–213.
[27] R. Bassi, P.K. Bansal, In-tube condensation of mixture of R134a and ester oil: empirical correlations, Int. J. Refrig. 26 (2003) 402–409.
[28] D. Chisholm, Pressure gradients due to friction during the flow of evaporating two-phase mixtures in smooth tubes and channels, Int. J. Heat Mass Transfer 16 (1973) 347–358.

Journal of Electronics Cooling and Thermal Control, 2011, 1, 38-44
doi:10.4236/jectc.2011.13005 Published Online December 2011 (http://www.SciRP.org/journal/jectc)

Experimental Study of Jet Nanofluids Impingement System for Cooling Computer Processing Unit

Paisarn Naphon[1*], Somchai Wongwises[2]
[1]*Thermo-Fluids and Heat Transfer Enhancement Lab, Department of Mechanical Engineering, Faculty of Engineering, Srinakharinwirot University, Ongkharak, Thailand*
[2]*Fluid Mechanics, Thermal Engineering and Multiphase Flow Research Lab, Department of Mechanical Engineering, King Mongkut's University of Technology Thonburi, Suksawas, Bangkok, Thailand*
E-mail: [*]*paisarnn@swu.ac.th*
Received September 20, 2011; *revised November* 15, 2011; *accepted November* 25, 2011

Abstract

An experimental investigation of the jet nanofluids impingement heat transfer characteristics of mini-channel heat sink for cooling computer processing unit of personal computer is performed. The experiments are tested under the real personal computer operating conditions: no load and full load conditions. The experiments are performed for the following ranges of the parameters: coolant flow rate varies from 0.008 to 0.020 kg/s, the nozzle diameter is set to 1.00, 1.40, 1.80 mm, the distance nozzle-to-fins tip is 2.00 mm, the channel width of the mini-channel heat sink is 1.00 mm. The nanofluids with suspending of TiO_2 particles in base fluid are used as a working fluids. It was observed that the average CPU temperatures obtained from the jet nanofluids impingement cooling system are 3.0%, 6.25% lower than those from the jet liquid impingement and from the conventional liquid cooling systems, respectively. However, this cooling system requires higher energy consumption.

Keywords: Jet Impingement, Nanofluids Cooling, Cooling CPU, Mini-Rectangular Fin Heat Sink

1. Introduction

In order to ensure reliable operation, the PCs or electronics devices must be operated in the specific temperature ranges which the exceeding maximum allowable temperature is the serious problem of these devices. There are many techniques to dissipate the generated heat. The development of the miniaturized technology, mini and micro-components has been introduced as one of heat transfer enhancement techniques. The study of a single phase heat transfer of the various geometrical heat sinks for cooling electronic devices are reported by Zhange *et al*.,[1]; Yu [2]; Peles [3]; Kosar and Peles [4]; Yakut *et al*. [5]; Mohamed [6]. Didarul [7] investigated the heat transfer and fluid flow characteristics of finned surfaces. Chein and Chuang [8] applied the thermoelectric with microchannel heat sink by using nanofluids as coolant for cooling electric components. Jeng and Tzeng [9] experimentally studied the pressure drop and heat transfer of a square pin-fin array. These studies indicated that the various geometrical heat sinks are possible for cooling electronics devices.

The most frequently used coolants in the heat transfer devices study are air, water, and fluoro-chemicals. However, the heat transfer capability is limited by the working fluid transport properties. One of the methods for the heat transfer enhancement is the application of additives to the working fluids to change the fluid transport properties and flow features. Therefore, in order to further enhance thermal performance of heat transfer devices, the use of nanofluids is proposed. The numerous papers presented on the single phase convective heat transfer of nanofluids, boiling heat transfer of nanofluids and heat transfer enhancement using nanofluids are continuously reviewed by Duangtongsuk and Wongwises [10]; Trisaksri and Wonwises [11]; Godson *et al*. [12]. However, improving the cooling performance had been continuously performed by using the jet liquid impingement technique. Thermal performance of a pin-fin heat sink with various geometrical with impingement cooling was considered by Kobus and Oshio [13]; Li *et al*. [14]. Geedipalli *et al*. [15] simulated the combination heating of food using microwave and jet impingement by coupling Maxwell's equation. Sung and Mudawar [16,17] studied the jet impingement single-phase and two-phase heat transfer characteristics. Reasonable

agreement was obtained between the predicted results and the measured data. Koseoglu and Baskaya [18] used a Laser Doppler Anemometry to observe the jet flow field and turbulence on heat transfer characteristics. The jet heat transfer enhancement from a flat surface was simulated by Katti and Prabhu [19]; Kanna and Das [20]; Cirillo and Isopi [21]. Goodro *et al*. [22] considered effects of the hole spacing on the spatially-resolved jet array impingement heat transfer. Jeng *et al*. [23] and Hewakandamby [24] investigated the jet air flow and heat transfer behaviors of the rotating heat sink and oscillation impinging jet. Nguyen *et al.* [25] studied the enhanced heat transfer with of nanofluids in a confined and submerged impinging jet on a flat, horizontal and circular heated surface. Koseoglu and Baskaya [26] experimentally and numerically investigated the impinging jet heat transfer. Chang *et al*. [27] studied the jet-array impingement heat transfer in a concentric annular channel with rotating inner cylinder. Sharif and Banerjee [28] applied the k-ε turbulence model to analyze the heat transfer of the confined slot-jet impingement on a moving plate. Whelan and Robinson [29] used the jet liquid impingement for cooling the electronics devices. Several studies showed that thermal conductivity of the nanofluids is higher than that of the base fluids and therefore great potential for the enhancement of heat transfer.

As mentioned above, the numerous papers presented the study on the heat transfer and pressure drop in the mini- and micro-channel, nanofluids heat transfer enhancement, jet impingement heat transfer characteristics. However, only one work [25] reported the passive and active heat transfer enhancement techniques by using the jet nanofluids impingement heat transfer characteristics of the heat sinks. Therefore, the present work focus on the experimental study of the jet nanofluids impingement heat transfer characteristics of the mini-rectangular fin heat sink for cooling computer processing unit (CPU) of personal computer (PC) based on the real operating conditions of PC. This is because it has an excellent chemical and physical stability, a safe material for human, produced commercially available products, and cheap. The TiO_2 nanoparticles are used in the present experiments. The results obtained from the jet nanofluids impingement cooling system are compared with those from the jet liquid impingement and the conventional liquid cooling systems.

2. Experimental Apparatus and Method

2.1. Test Loop

This paper primary tries to investigate the jet nanofluids impingement heat transfer of the mini-rectangular channel heat sinks for CPU of PC. A schematic diagram of the experimental apparatus is shown in **Figure 1**. The test loop consists of a set of ultrasonic system, cooling nanofluids loop and data acquisition system. The close-loop

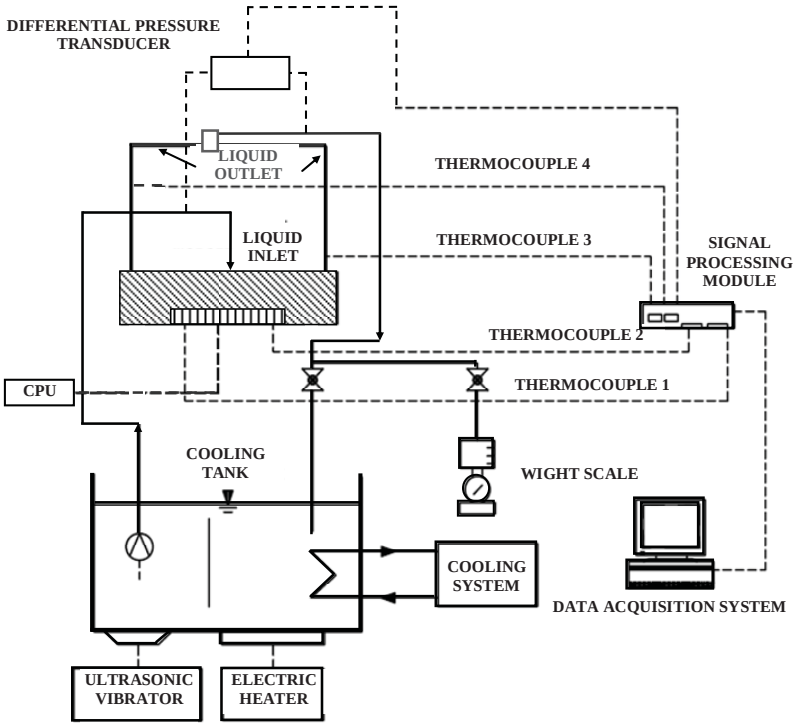

Figure 1. Schematic diagram of experimental apparatus.

of nanofluids consists of a 10^{-3} m^3 storage tank, pump, and the flow rate measurement system. After the temperatures of the nanofluids are cooled to achieve the desired level, the nanofluids is pumped out of the storage tank, passed through the mini-rectangular fin heat sink, and returned to the storage tank. The flow rates are varied during a set of experiments with the help of a dimmerstat connected to the pump. The flow rates of the cooling nanofluids are controlled by adjusting the valve and measured by collecting the nanofluids with the precise cylinder for a period of time during 15 min and the nanofluids mass is measured by an electronic weight scale. The maximum variation of the mass flow rate of nanofluids as determined by such simple technique has been estimated to be ±3.5%. The nanofluids with suspending TiO_2 nanoparticles in base fluids are used as working fluids. An average spherical particle size of TiO_2 nanoparticles is about 21 nm. In the present study, the base fluids are the deionized water. The nanofluids are prepared by ultrasonic method with the constant nanoparticles concentration of 0.4% by volume without using surfactant. The heat sink is fabricated from the block of copper by the wire electrical discharge machine (WEDM) with the channel width of 1.00 mm. In order to minimize thermal resistance between the CPU-cooling block, cooling block-heat sink, a thin film of high thermal conductivity grease is applied at their junction interface. In **Figure 1**, the type T copper-constantan thermocouples with an accuracy of 0.1% of full scale are employed to measure the temperatures at various positions. The CPU temperature is measured by two type-T copper-constantan thermocouples. All thermocouples are pre-calibrated with dry box temperature calibrator.

2.2. Experimental Method

Nanofluids were used as coolant in the present experiments. The nanofluids were pumped into the mini-rectangular fin heat sink which installed on the CPU of PC in the normal direction with the base bottom as shown on **Figure 2** and then returned to the storage tank. Experiments were conducted with various cooling nanofluids flow rates and operating condition of PC. The supplied load into the CPU was adjusted to achieve the desired level by setting the operating conditions of PC: no load and full load conditions. The energy consumption of the PC was measured by the watt-hour meter. The temperatures at each position and energy consumption were recorded in the period time of 200 minutes. Data collection was carried out using a data acquisition system (Data Taker).

3. Data Reduction

The heat transfer into the nanofluids is calculated from:

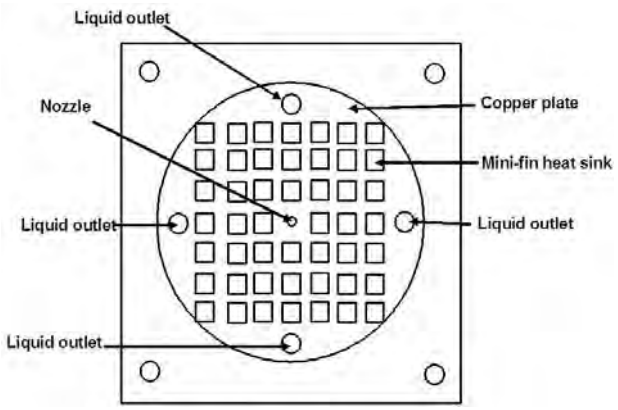

Figure 2. Schematic diagram of the inlet and outlet positions of the coolant.

$$Q_{nf} = \dot{m}_{nf} \times C_{p_{nf}} \times \left(T_{in,nf} - T_{out,nf}\right) \tag{1}$$

where Q_{nf} is the heat transfer by the nanofluids, $\dot{m}_{nf}$ is the mass flow rate of the nanofluids and $T_{in,nf}$, $T_{out,nf}$ are the inlet and outlet temperatures of the nanofluids.

The heat transfer coefficient is calculated from the following equation:

$$\bar{h} = \frac{Q_{nf}}{A_s\left(\Delta T_{LMTD}\right)} \tag{2}$$

where h is the average heat transfer coefficient, A_s is the total heat transfer surface area of the heat sink and ΔT_{LMTD} is the logarithm mean temperature difference which is given by:

$$\Delta T_{LMTD} = \frac{\left(T_b - T_{in,nf}\right) - \left(T_b - T_{out,nf}\right)}{\ln\left(\dfrac{\left(T_b - T_{in,nf}\right)}{\left(T_b - T_{out,nf}\right)}\right)} \tag{3}$$

where T_b is the temperature of the heat sink.

The average base temperature of the heat sink can be calculated from:

$$T_b = \bar{T}_{CPU} - \left(\frac{q_{in}L}{k_{hs}}\right) \tag{4}$$

where T_b is the base temperature of the heat sink, $\bar{T}_{CPU}$ is the CPU temperature, q_{in} is the heat flux, L is the base thickness of the heat sink and k_{hs} is the thermal conductivity of the heat sink.

The Nusselt number based on the nozzle diameter is calculated from the following equation:

$$\bar{N}u = \frac{\bar{h}D_{nozzle}}{k_{nf}} \tag{5}$$

where $\bar{N}u$ is the Nusselt number and D_{nozzle} is the diameter of the nozzle.

The thermal conductivity of the nanofluids is calculated

from Yu and Choi [30] using the following equation:

$$k_{nf} = \left[\frac{k_p + 2k_w - 2\phi\left(k_w - k_p\right)}{k_p + 2k_w + \phi\left(k_w - k_p\right)} \right] k_w \quad (6)$$

where k_{nf} is the thermal conductivity of the nanofluids, k_w is the thermal conductivity of the base fluid and k_p is the thermal conductivity of the nanoparticles.

The density of the nanofluids is calculated from Pak and Cho [31] using the following equation:

$$\rho_{nf} = \phi\rho_P + (1-\phi)\rho_w \quad (7)$$

where ρ_{nf} is the density of the nanofluids, ρ_p is the density of the nanoparticles, ρ_w is the density of the base fluid and ϕ is the volume fraction of the nanoparticles.

While the specific heat is calculated from Xuan and Roetzel [32] as follows:

$$\left(\rho C_p\right)_{nf} = \phi\left(\rho C_p\right)_p + (1-\phi)\left(\rho C_p\right)_w \quad (8)$$

where $\left(\rho C_p\right)_{nf}$ is the heat capacity of the nanofluids, $\left(\rho C_p\right)_w$ is the heat capacity of the base fluid and $\left(\rho C_p\right)_p$ is the heat capacity of the nanoparticles.

Analysis of the thermal resistance of the convective heat transfer of the nanofluids can be defined as

$$R_{th} = \frac{T_b - T_{nf,ave}}{Q_{nf}} \quad (9)$$

The uncertainties of measurements data and the relevant parameters obtained from the data reduction process are calculated. The maximum uncertainties of the relevant parameters in the data calculation are based on Coleman and Steel method [33]. The maximum uncertainties of relevant parameters are ±10% for heat transfer coefficient, ±10% for Nusselt number and ±5% for thermal resistance.

4. Results and Discussion

The supplied load into the CPU was adjusted by setting the operating condition of PC: full load and no load conditions. The relevant parameters are measured in the period time of 200 minutes. **Figure 3** shows effect of coolant flow rate on the variation of CPU temperature for the jet nanofluids impingement cooling systems. The full load operating condition generates the heat higher than the no load operating condition. Therefore, the CPU temperatures from the full load condition are higher than those from the no load condition for the whole range of the period time. For the four different coolant flow rates, a larger CPU temperature drop is found for a larger coolant flow rate. The reason for this is because a larger coolant flow rate results in higher heat transfer rate and consequently lower CPU temperature.

Figure 4 shows the comparison between the CPU temperatures obtained from the jet nanofluids impingement technique, the jet liquid impingement and the conventional liquid cooling techniques. The thermal conductivity of nanofluids depends on the sizes and species of the nanoparticles, the concentration of nanoparticles in the base fluid and the combination of the nanoparticles and the base fluid properties. However, there are various correlations are proposed to predict the thermal conductivity and

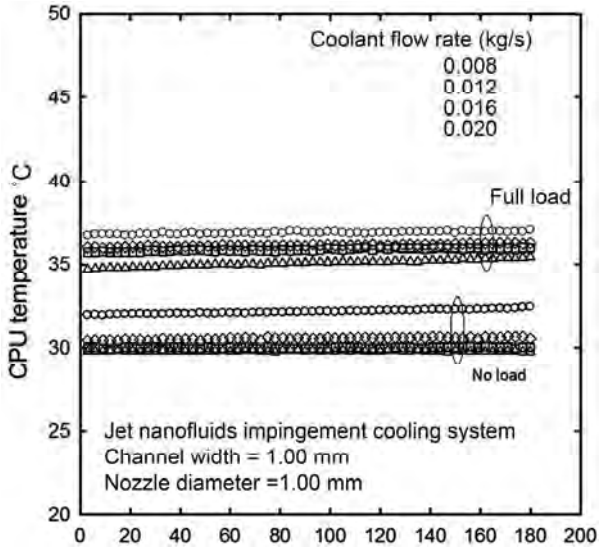

Figure 3. Effect of coolant flow rate on the CPU temperature for jet nanofluids impingement cooling system.

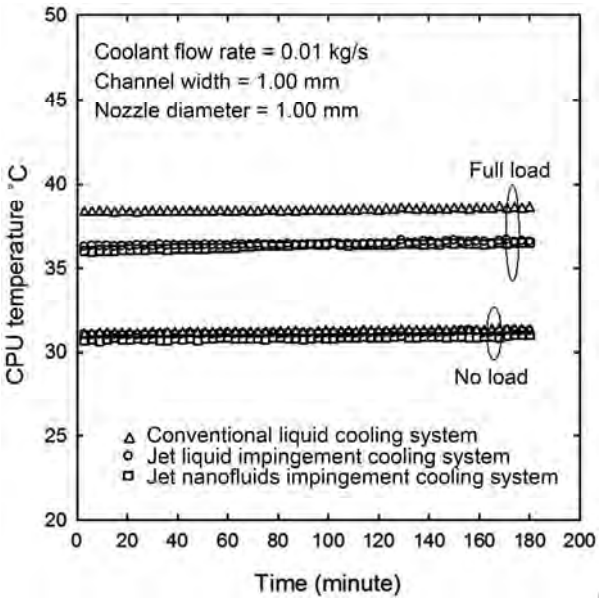

Figure 4. Comparison of CPU temperatures for different cooling techniques.

others properties of the nanofluids. Due to particle migration inside the heat sink, non-uniformity of the nanoparticles concentration has significant effect on the thermal conductivity and viscosity of the fluid. Therefore, in the present study, an average heat transfer characteristics are presented. At the same operating condition of CP, the CPU temperatures obtained from the jet nanofluids impingement cooling system are lower than those from the jet liquid impingement and from the conventional cooling systems, respectively. This is because the thermal conductivity of the nanofluids is higher than that of the base fluids therefore great potential for the enhancement of heat transfer.

Figure 5 shows the variation of the Nusselt number with nanofluids mass flow rate. As expected, the heat transfer rate is directly proportional to the nanofluids mass flow rate. In addition, **Figure 5** also shows the comparison of the average Nusselt number obtained from the jet nanofluids impingement cooling technique, jet liquid impingement cooling technique, and conventional liquid cooling technique. It can be seen that the jet nanofluids impingement technique gives the Nusselt number higher than two other cooling techniques. The application of the nanofluids to the working fluid has significantly changed the fluid transport properties and flow characteristics. Therefore, the Nusselt number obtained from the jet nanofluids impingement are higher than those obtained from two other cooling techniques.

In this study, the overall heat sink performance can be shown in the thermal resistance form. The heat sink thermal resistance is defined as shown in Equation (9). Using this definition, thermal resistance of heat sink is a function of heat transfer coefficient. Due to higher heat transfer rate, the heat sink thermal resistance decreases with increasing flow rate. Based on results shown in **Figure 6**, it is seen that the thermal resistance obtained from the jet nanofluids impingement cooling technique are lower than those from the jet liquid impingement and from the conventional cooling techniques. This result can be realized from Equation (9) and nanofluids transport properties. Due to the increase in thermal conductivity, the contribution to the thermal resistance is mainly improved. In addition, the reduction of the thermal resistance is clearly due to the thermal dispersion.

5. Conclusions

Due to high level of heat generation, space limitation for set up the cooling system, and air cooling limitation, the jet nanofluids impingement cooling in the mini-rectangular fin channel heat sink for CPU of PC has been investigated. The jet nanofluids impingement cooling with mini-rectangular fin heat sink system is introduced as the

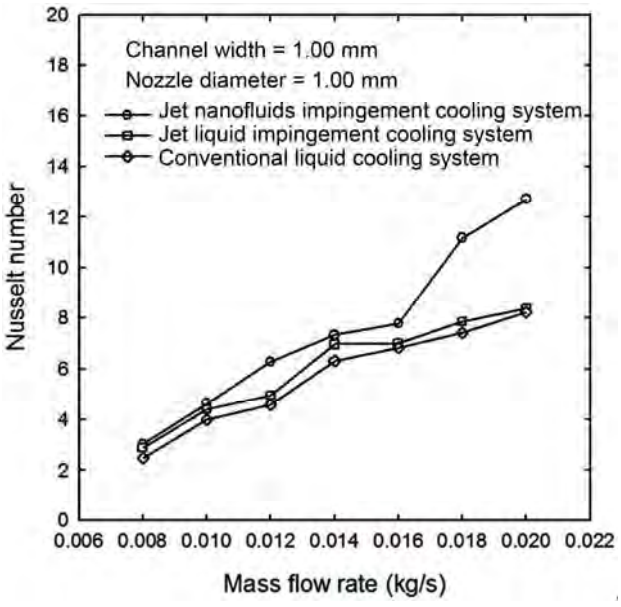

Figure 5. Variation of the Nusselt number versus mass flow rate for different cooling techniques.

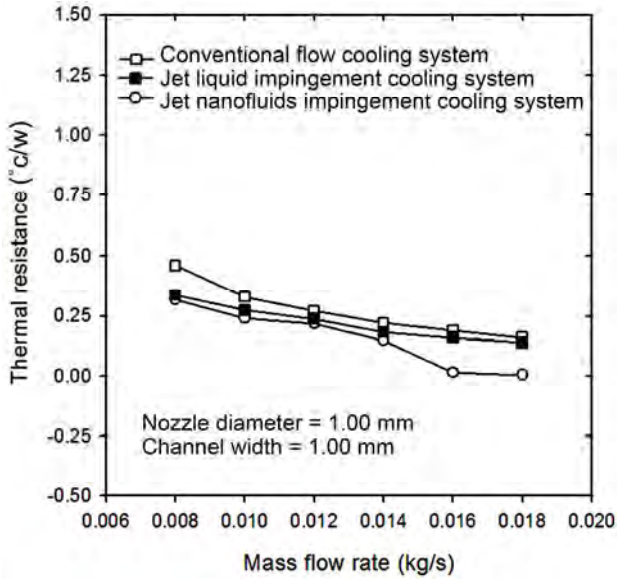

Figure 6. Comparison of thermal resistance versus mass flow rate for different cooling techniques.

couple active and passive heat transfer enhancement techniques. It is found that the CPU temperatures obtained from the jet nanofluids impingement cooling system are lower than those from the jet liquid impingement cooling system and the conventional liquid cooling system. However, this technique requires higher energy consumption. The results of this study are expected to lead to guidelines that will allow the design of the cooling system with improved thermal cooling performance for obtaining these devices in the specific temperature ranges.

6. Acknowledgements

The authors would like to express their appreciation to the Thailand Research Fund (TRF), the Srinakharinwirot University (SWU), and the King Mongkut's University of Technology Thonburi (KMUTT) for providing financial support for this study.

7. References

[1] H. Y. Zhang, D. Pingala, T. N. Wong, K. C. Toh and Y. K. Joshi, "Single-Phase Liquid Cooled Micro Channel Heat Sink for Electronic Packages," *Applied Thermal Engineering*, Vol. 25, No. 2, 2005, pp. 1472-1487. doi:10.1016/j.applthermaleng.2004.09.014

[2] X. Yu, "Development of a Plate-Pin Fin Heat Sink and Its Performance Comparisons with a Plate Fin Heat Sink," *Applied Thermal Engineering*, Vol. 25, No.1, 2005, pp. 173-182. doi:10.1016/j.applthermaleng.2004.06.016

[3] Y. Peles, A. Kosor, C. Mishra, C. J. Kuo and B. Schneider, "Forced Convective Heat Transfer across a Pin Fin Micro Heat Sink," *International Journal of Heat and Mass Transfer*, Vol. 48, No. 2, 2005, pp. 3615-3627. doi:10.1016/j.ijheatmasstransfer.2005.03.017

[4] A. Kosar and Y. Peles, "Convective Flow of Refrigerant (R123) across a Bank of Micro Pin," *International Journal of Heat and Mass Transfer*, Vol. 50, No. 1, 2007, pp. 1018-1034.

[5] K. Yukut, "Experimental Investigation of Thermal Resistance of a Heat Sink with Hexagonal Fins," *Applied Thermal Engineering*, Vol. 26, No. 2, 2006, pp. 2262-2271. doi:10.1016/j.applthermaleng.2006.03.008

[6] M. M. Mohamed, "Air Cooling Characteristics of a Uniform Square Modules Array for Electronic Device Heat Sink," *Applied Thermal Engineering*, Vol. 26, No. 2, 2006, pp. 486-493. doi:10.1016/j.applthermaleng.2005.07.013

[7] I. M. Didarul, "Study on Heat Transfer and Fluid Flow Characteristics with Short Rectangular Plate Fin of Different Pattern," *Experimental Thermal and Fluid Science*, Vol. 31, No. 1, 2007, pp. 367-379. doi:10.1016/j.expthermflusci.2006.05.009

[8] R. Chein and J. Chuang, "Experimental Microchannel Heat Sink Performance Studies Using Nanofluids," *International Journal of Thermal Sciences*, Vol. 46, No. 1, 2007, pp. 57-66. doi:10.1016/j.ijthermalsci.2006.03.009

[9] T. M. Jeng and S. C. Tzeng, "Pressure Drop and Heat Transfer of Square Pin-Fin Arrays in In-Line and Staggered Arrangements," *International Journal of Heat and Mass Transfer*, Vol. 50, No. 1, 2007, pp. 2364-2375. doi:10.1016/j.ijheatmasstransfer.2006.10.028

[10] W. Duangtongsuk and S. Wongwises, "A Critical Review of Convective Heat Transfer of Nanofluids," *Renewable and Sustainable Energy Review*, Vol. 11, No. 1, 2007, pp. 797-817. doi:10.1016/j.rser.2005.06.005

[11] V. Trisaksri and S, Wonwises, "Critical Review of Heat Transfer Characteristics of Nanofluids Review," *Renewable and Sustainable Energy Reviews*, Vol. 11, No. 2, 2007, pp. 512-523. doi:10.1016/j.rser.2005.01.010

[12] L. Godson, B. Raja, D. M. Lal and S. Wongwises, "Enhancement of Heat Transfer Using Nanofluids—An Overview," *Renewable and Sustainable Energy Reviews*, Vol. 14, No. 1, 2010, pp. 629-641. doi:10.1016/j.rser.2009.10.004

[13] C. J. Kobus and T. Oshio, "Development of a Theoretical Model for Predicting the Thermal Performance Characteristics of a Vertical Pin-Fin Array Heat Sink under Combined Forced and Natural Convection with Impinging Flow," *International Journal of Heat and Mass Transfer*, Vol. 48, No. 3, 2005, pp. 1053-1063. doi:10.1016/j.ijheatmasstransfer.2004.09.042

[14] H. Y. Li, S. M. Chao and G. L. Tsai, "Thermal Performance Measurement of Heat Sinks with Confined Impinging Jet by Infrared Thermography," *International Journal of Heat and Mass Transfer*, Vol. 48, Vol. 1, 2005, pp. 5386-5394.

[15] S. Geedipalli, A. K. Datta and V. Rakesh, "Heat Transfer in a Combination Microwave-Jet Impingement Oven," *Food and Bioproducts Processing*, Vol. 86, No. 1, 2008, pp. 53-63. doi:10.1016/j.fbp.2007.10.016

[16] M. K. Sung and I. Mudawar, "Single-Phase and Two-Phase Heat Transfer Characteristics of Low Temperature Hybrid Micro-Channel/Micro-Jet Impingement Cooling Module," *International Journal of Heat and Mass Transfer*, Vol. 51, No. 2, 2008, pp. 3882-3895. doi:10.1016/j.ijheatmasstransfer.2007.12.016

[17] M. K. Sung and I. Mudawar, "Single-Phase Hybrid Micro-Channel/Micro-Jet Impingement Cooling," *International Journal of Heat and Mass Transfer*, Vol. 51, No. 1, 2008, pp. 4342-4352. doi:10.1016/j.ijheatmasstransfer.2008.02.023

[18] M. F. Koseoglu and S. Baskaya, "The Effect of Flow Field and Turbulence on Heat Transfer Characteristics of Confined Circular and Elliptic Impinging Jets," *International Journal of Thermal Sciences*, Vol. 47, No. 2, 2008, pp. 1332-1346. doi:10.1016/j.ijthermalsci.2007.10.015

[19] V. Katti and S. V. Prabhu, "Heat Transfer Enhancement on a Flat Surface with Axisymmetric Detached Ribs by Normal Impingement of Circular Air Jet," *International Journal of Heat and Fluid Flow*, Vol. 29, No. 1, 2008, pp. 1279-1294. doi:10.1016/j.ijheatfluidflow.2008.05.003

[20] P. R. Kanna and M. K. Das, "Heat Transfer Study of Two-Dimensional Laminar Incompressible Offset Jet Flows," *International Journal of Thermal Sciences*, Vol. 47, No. 1, 2008, pp. 1620-1629. doi:10.1016/j.ijthermalsci.2008.01.003

[21] F. Cirillo and G. M. Isopi, "Glass Tempering Heat Transfer Coefficient Evaluation and Air Jets Parameter Optimization," *Applied Thermal Engineering*, Vol. 29, No. 2, 2009, pp. 1173-1179. doi:10.1016/j.applthermaleng.2008.06.005

[22] M. Goodro, J. Park, P. Ligrani, M. Fox and H. K. Moon, "Effects of Hole Spacing on Spatially-Resolved Jet Array

Impingement Heat Transfer," *International Journal of Heat and Mass Transfer*, Vol. 51, No. 1, 2008, pp. 6243-6253. doi:10.1016/j.ijheatmasstransfer.2008.05.004

[23] T. M. Jeng, S. C. Tzeng and H. R. Liao, "Flow Visualizations and Heat Transfer Measurements for a Rotating Pin-Fin Heat Sink with a Circular Impinging Jet," *International Journal of Heat and Mass Transfer*, Vol. 52, No. 2, 2009, pp. 2119-2131. doi:10.1016/j.ijheatmasstransfer.2008.10.028

[24] B. N. Hewakandamby, "A Numerical Study of Heat Transfer Performance of Oscillatory Impinging Jets," *International Journal of Heat and Mass Transfer*, Vol. 52, No. 2, 2009, pp. 396-406.

[25] C. T. Nguyen, N. Galanis, G. Polidori, S. Fohanno, C. V. Popa and A. L. Bechec, "An Experimental Study of a Confined and Submerged Impinging Jet Heat Transfer Using Al_2O_3-Water Nanofluids," *International Journal of Thermal Sciences*, Vol. 48, No. 3, 2009, pp. 401-411. doi:10.1016/j.ijthermalsci.2008.10.007

[26] M. F. Koseoglu and S. Baskaya, "Experimental and Numerical Investigation of Natural Convection Effects on Confined Impinging Jet Heat Transfer," *International Journal of Heat and Mass Transfer*, Vol. 52, No. 1, 2009, pp. 1326-1336. doi:10.1016/j.ijheatmasstransfer.2008.07.051

[27] S. W. Chang, T. L. Yang and D. W. Shih, "Jet-Array Impingement Heat Transfer in a Concentric Annular Channel with Rotating Inner Cylinder," *International Journal of Heat and Mass Transfer*, Vol. 52, No. 1, 2009, pp. 1254-1267. doi:10.1016/j.ijheatmasstransfer.2008.08.023

[28] M. A. R. Sharif and A. Banerjee, "Numerical Analysis of Heat Transfer Due to Confined Slot-Jet Impingement on a Moving Plate," *Applied Thermal Engineering*, Vol. 29, No. 1, 2009, pp. 532-540. doi:10.1016/j.applthermaleng.2008.03.011

[29] B. P. Whelan and A. J. Robinson, "Nozzle Geometry Effects in Liquid Jet Array Impingement," *Applied Thermal Engineering*, Vol. 29, No. 1, 2009, pp. 2211-2221. doi:10.1016/j.applthermaleng.2008.11.003

[30] W. Yu and S. U. S. Choi, "The Role of Interfacial Layers in the Enhanced Thermal Conductivity of Nanofluids: A Renovated Maxvell Model," *Journal of Nanoparticle Research*, Vol. 5, No. 1, 2003, pp. 167-171. doi:10.1023/A:1024438603801

[31] B. C. Pak and Y. I. Cho, "Hydrodynamic and Heat Transfer Study of Dispersed Fluids with Submicron Metallic Oxide Particles," *Experimental Heat Transfer*, Vol. 11, No. 2, 1998, pp. 151-170. doi:10.1080/08916159808946559

[32] Y. Xuan and W. Roetzel, "Conceptions of Heat Transfer Correlation of Nanofluids," *International Journal of Heat and Mass Transfer*, Vol. 43, No. 19, 2000, pp. 3701-3707. doi:10.1016/S0017-9310(99)00369-5

[33] H. W. Coleman and W. G. Steele, "Experimental and Uncertainty Analysis for Engineers," John Wiley & Sons, New York, 1989.

Nomenclatures

A_s : total heat transfer surface area of the heat sink, m^2.
D_{nozzle} : nozzle diameter, m.
$\bar{h}$: average heat transfer coefficient, $W/(m^2 K)$.
k_{nf} : thermal conductivity of the nanofluids, W/(m K).
$\bar{Nu}$: Nusselt number.
q_{nf} : heat flux, W/m^2.
R_{th} : thermal resistance, K/W.
T_b : the base temperature of the heat sink, ˚C.
T_{CPU} : CPU temperature, ˚C.
ΔT_{LMTD} : logarithm mean temperature difference, ˚C.

Greek Symbols

ρ_{nf} : density of the nanofluids.
$(\rho c_p)_{nf}$: heat capacity of the nanofluids.
$(\rho c_p)_p$: heat capacity of the nanoparticles.
μ_{nf} : viscosity of the nanofluids.

International Communications in Heat and Mass Transfer 38 (2011) 218–228

Contents lists available at ScienceDirect

International Communications in Heat and Mass Transfer

journal homepage: www.elsevier.com/locate/ichmt

Numerical investigation on the single phase forced convection heat transfer characteristics of TiO_2 nanofluids in a double-tube counter flow heat exchanger ☆

H. Demir [a,*], A.S. Dalkilic [a], N.A. Kürekci [a], W. Duangthongsuk [b], S. Wongwises [b,*]

[a] Heat and Thermodynamics Division, Department of Mechanical Engineering, Yildiz Technical University (YTU), Yildiz, Besiktas, Istanbul 34349, Turkey
[b] Fluid Mechanics, Thermal Engineering and Multiphase Flow Research Lab. (FUTURE), Department of Mechanical Engineering, King Mongkut's University of Technology Thonburi (KMUTT), Bangmod, Bangkok 10140, Thailand

ARTICLE INFO

Available online 21 December 2010

Keywords:
Heat transfer coefficient
Pressure drop
Wall shear stress
Nanofluid
Heat exchanger

ABSTRACT

In this study, forced convection flows of nanofluids consisting of water with TiO_2 and Al_2O_3 nanoparticles in a horizontal tube with constant wall temperature are investigated numerically. The horizontal test section is modeled and solved using a CFD program. Palm et al.'s correlations are used to determine the nanofluid properties. A single-phase model having two-dimensional equations is employed with either constant or temperature dependent properties to study the hydrodynamics and thermal behaviors of the nanofluid flow. The numerical investigation is performed for a constant particle size of Al_2O_3 as a case study after the validation of its model by means of the experimental data of Duangthongsuk and Wongwises with TiO_2 nanoparticles. The velocity and temperature vectors are presented in the entrance and fully developed region. The variations of the fluid temperature, local heat transfer coefficient and pressure drop along tube length are shown in the paper. Effects of nanoparticles concentration and Reynolds number on the wall shear stress, Nusselt number, heat transfer coefficient and pressure drop are presented. Numerical results show the heat transfer enhancement due to presence of the nanoparticles in the fluid in accordance with the results of the experimental study used for the validation process of the numerical model.

1. Introduction

Water, oil, and ethylene glycol mixture is one of the low thermal conductivity of widely used conventional heat transfer fluids that limits the enhancement of the performance and compactness of these devices belong to the electronic, automotive and aerospace industries. Improvements on the thermal conductivity by suspending small solid particles in the fluid are one of the solutions to prevent this disadvantage. Thermal conductivity is an important parameter in enhancing the heat transfer performance of a heat transfer fluid. Since the thermal conductivity of solid metals is higher than that of fluids, the suspended particles are expected to be able to increase the thermal conductivity and heat transfer performance. Many researchers have reported experimental studies on the thermal conductivity of nanofluids. Metallic, non-metallic and polymeric particles are used to form slurries by adding into fluids. Some of problems such as abrasion and clogging can be seen due to the suspended particles' sizes that are of millimeter dimensions. For that reason, these kinds of large particles are not suitable for heat transfer enhancement. Recently, advances in manufacturing technologies have made the production of particles in the nanometer scale possible (i.e., 10 nm<particle diameter<100 nm). The uniform and stable suspensions are obtained by means of these smaller sized particles. Thus, the nanofluids provide higher heat transfer enhancement than existing techniques. The use of particles of nanometer dimension was first continuously studied by a research group at the Argonne National Laboratory around a decade ago. Choi [1] was probably the first one who called the fluids with particles of nanometer dimensions 'nano-fluids'. The term 'nanofluid' refers to a two-phase mixture usually composed of a continuous liquid phase and dispersed nanoparticles in suspension.

In spite of the two phase mixture specialty of nanofluids, they are easily fluidized and can be nearly considered to behave as a fluid [2] due to the tiny size of solid particles. For that reason, it is possible for nanofluids to be treated as single phase flow. It is assumed that the fluid phase and particles are in thermal equilibrium and moving with the same velocity in certain conditions [3] considering the ultrafine and low volume fraction of the solid particles. The advantage of single phase flow is about its simplicity and required less computational time. It should be noted that experimental, numerical and theoretical solutions are strongly affected by physical properties of nanofluids. In addition, there is some inconsistency on this subject in the literature.

The most well-known nanoparticles are Al_2O_3, CuO, TiO_2 and they are used by many researchers in their experimental works together with the base fluids of water and ethylene glycol. In spite of the different size of the particles and type of base fluids, the enhancement

☆ Communicated by W.J. Minkowycz.

* Corresponding authors.
E-mail addresses: hdemir@yildiz.edu.tr (H. Demir), somchai.won@kmutt.ac.th (S. Wongwises).

0735-1933/$ – see front matter © 2010 Elsevier Ltd. All rights reserved.
doi:10.1016/j.icheatmasstransfer.2010.12.009

Nomenclature

Cp	specific heat, J kg^{-1} K^{-1}
CFD	Computational Fluid Dynamics
d	internal tube diameter, m
h	heat transfer coefficient, W m^{-2} K^{-1}
k	thermal conductivity, W m^{-1} K^{-1}
L	length of test tube, m
m	mass flow rate, kg s^{-1}
Nu	Nusselt number
ΔP	pressure drop, Pa
Pr	Prandtl number
Re	Reynolds number
Q	heat transfer rate, W
q''	heat flux, W m^{-2}
T	temperature, °C
μ	dynamic viscosity, Pa s
ρ	density, kg m^{-3}
τ	shear stress, N m^{-2}
φ	volume fraction, %
ν	kinematic viscosity, m^2 s^{-1}

Subscripts

avg	average
bf	base fluid
exp	experimental
ext	external
f	fluid
h	hot
i	inlet
m	mean
nf	nanofluid
num	numerical
p	particle
s	surface
o	outlet
w	water

of the thermal conductivity was seen during all the experimental conditions. Firstly, Maxwell [3,4] mentioned the enhancement on the thermal conductivity of a mixture by increasing volume fraction of solid particles. Besides this, the first empirical correlations for the determination of Nusselt number for laminar and turbulent flow of a nanofluid inside a tube were developed by Pak and Cho [5] and Xuan and Li [2,6] using the mixture of water and Cu, TiO_2 and Al_2O_3 nanoparticles. A significant increase in heat transfer performance was obtained in comparison to the water for the same Reynolds number. Liu et al. [7] conducted experiments on an industrial application and studied the effects of flow rates on the slurry pressure drop and heat transfer behavior. Choi [8] investigated augmentation of heat transfer that occurred by means of nanofluids considering little or no penalty in the pressure drop. Lee et al. [9] reported increase in thermal conductivity of the nanofluid approximately 20% at the volume concentration of 4% using oxide ceramic nanofluids consisting of CuO nanoparticles having a mean diameter of 35 nm in ethylene glycol, whereas an increase up to 10% was observed using larger particles with an average diameter of 40 nm. Masuda et al. [10] reported thermal conductivity enhancement by 30% using water–Al_2O_3 nanofluid having 13 nm mean diameter particles at 4.3% volume fraction. Rea et al. [11] investigated laminar convective heat transfer and viscous pressure loss for alumina–water and zirconia–water nanofluids in a flow loop with a vertical heated tube. The heat transfer

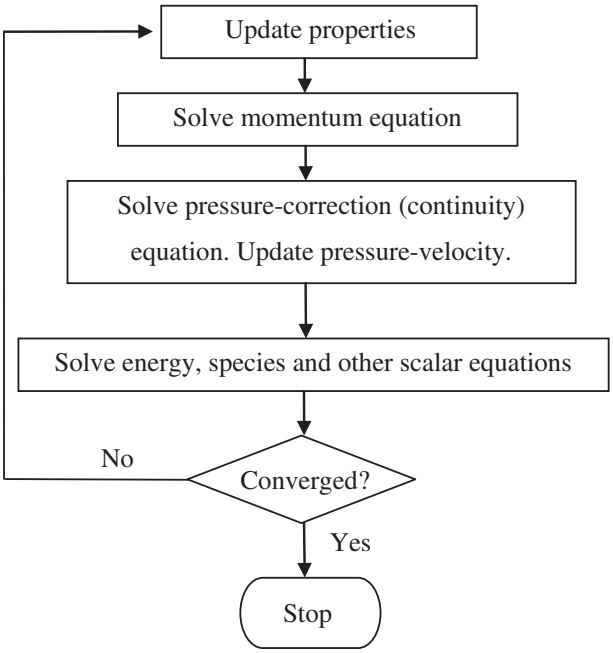

Fig. 1. Overview of the segregated method.

coefficients in the entrance region and in the fully developed region are found to be increased in 17% and 27%, respectively, for alumina–water nanofluid at 6 vol.% with respect to pure water. Bianco et al. [12] obtained heat transfer coefficient for the developing laminar forced convection flow of a water–Al_2O_3 nanofluid in a circular tube using single and two-phase models which have the maximum difference between them is about 11%. They also stated that convective heat transfer coefficient for nanofluids is greater than that of the base liquid. Heat transfer enhancement increases with the particle volume concentration, but it is accompanied by increasing wall shear stress values. Fard et al. [13] used CFD approach regarding single-phase and two-phase models to predict temperature, flow field, and calculation of heat transfer coefficient for the laminar convective heat transfer of nanofluids in a circular tube under constant wall temperature condition. Comparisons among two-phase model, single-phase model, theoretical models and experimental data were done and

Table 1
Operating conditions of the study.

Experimental study for the validation of numerical model	
Nanoparticle type, d_p	TiO_2, 21 nm
Test tube material, d, L	Copper, φ8.13 mm, 1500 mm
φ (wt.%)	0, 0.2, 0.6, 1
$T_{avg,f}$ (°C)	25–29–26.94
$T_{avg,s}$ (°C)	26.75–29.39
$T_{avg,h,w}$ (°C)	26.75–29.39
Re	4516.13–15,681.36
q'' (W m^{-2})	7233.13–13,340.99
Numerical study for the simulation of the case study	
Nanoparticle type, d_p	Al_2O_3, TiO_2, 21 nm
Test tube material, d, L	Copper, φ8 mm, 1000 m
φ (wt.%)	0, 1, 4
$T_{avg,f}$ (°C)	25.78, 28.34
$T_{avg,s}$ (°C)	26.19, 28.79
$T_{avg,h,w}$ (°C)	34.64, 36,64
Re	1000, 5000, 15,000, 25,000, 50,000, 75,000
q'' (W m^{-2})	1000, 5000, 10,000, 50,000

they reported that heat transfer coefficient clearly increases with an increase in particle concentration and two-phase model shows better agreement with experimental measurements.

Recently, Daungthongsuk and Wongwises [14] summarized the published subjects with respect to the forced convective heat transfer of the nanofluids both of experimental and numerical investigation in their review paper. Daungthongsuk and Wongwises [15] reported that thermal conductivity of nanofluids increased with increasing nanofluid temperatures and, conversely, the viscosity of nanofluids decreased with increasing temperature of nanofluids. Daungthongsuk and Wongwises [16] investigated the differences between using measured and computed thermophysical properties to describe the heat transfer performance of TiO_2–water nanofluids. Their results show that use of the models of thermo physical properties for calculating the Nusselt number of nanofluids gave similar results to use of the measured data. Daungthongsuk and Wongwises [17] presented the heat transfer coefficient and friction factor of the TiO_2–water nanofluids flowing in a horizontal double tube counter-flow

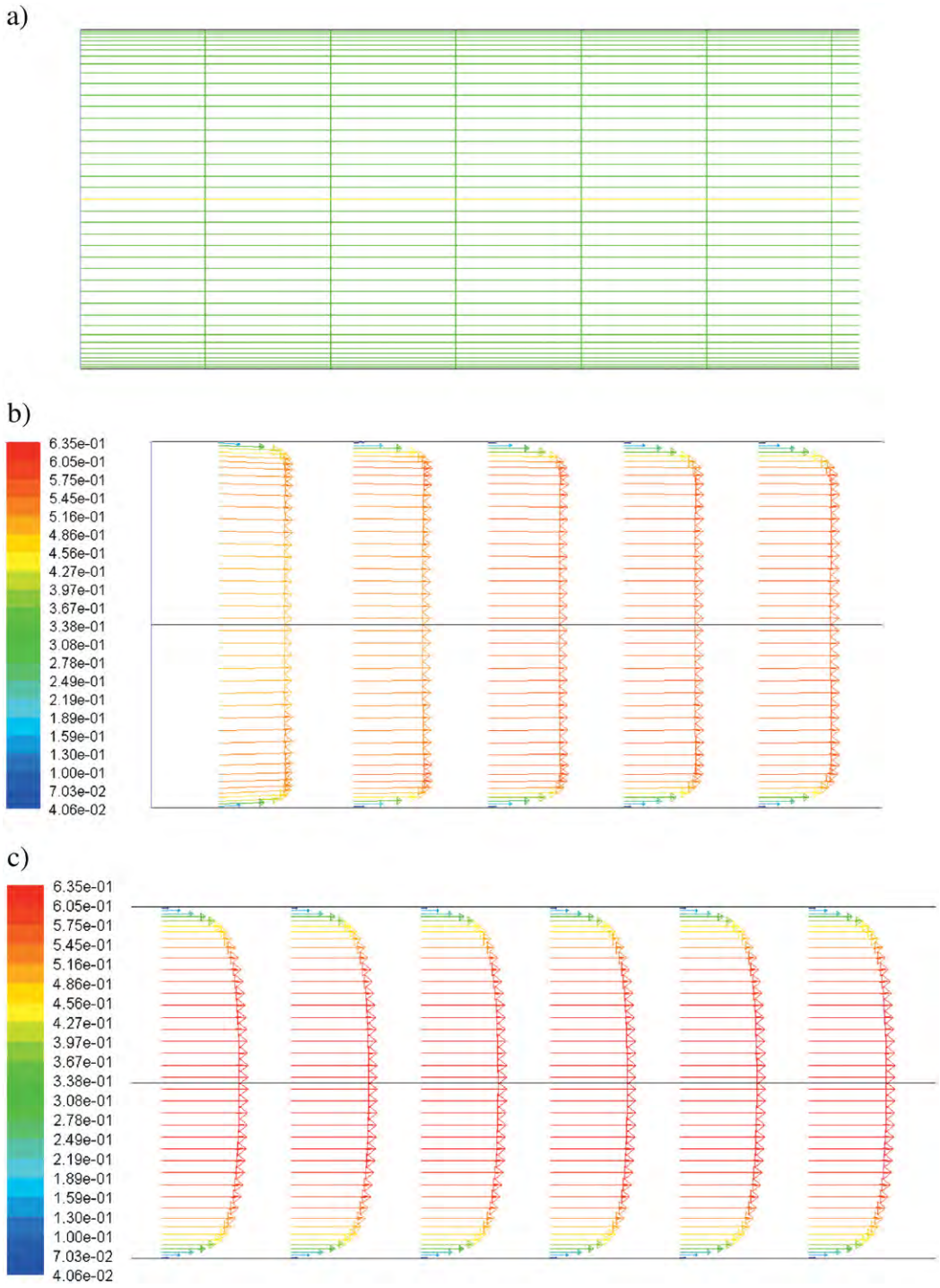

Fig. 2. Grid and velocity vectors for pure water ($Re = 4731$, $Q = 7233$ W). a) Solution grid generated in GAMBIT and used in the present analysis, axis-symmetric about *x*-axis. b) Velocity vectors at the inlet section of the test tube (m/s). c) Velocity vectors at the middle section of the test tube (m/s).

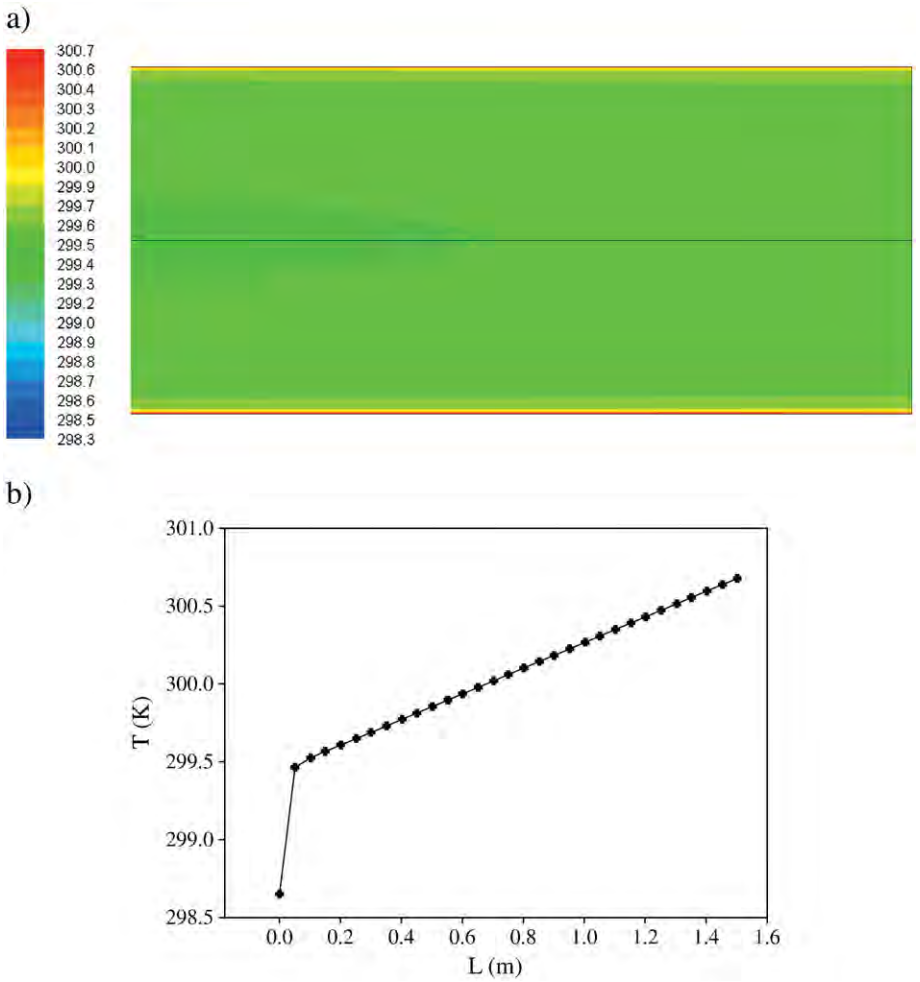

Fig. 3. Temperature distributions of outlet section and pipe surface for water and 0.6% TiO_2 nanoparticles ($Re = 14{,}880$, $Q = 11{,}862$ W). a) Temperature distribution at the outlet section of the tube. b) Surface temperature distribution along pipe.

heat exchanger under turbulent flow conditions, experimentally. Their results show that the heat transfer coefficient of nanofluid is higher than that of the base liquid and increased with increasing the Reynolds number and particle concentrations. Daungthongsuk and Wongwises [18] reported an experimental study on the forced convective heat transfer and flow characteristics of a nanofluid consisting of water and 0.2 vol.% TiO_2 nanoparticles. According to their experimental results, the heat transfer coefficient of the nanofluid increases with an increase in the mass flow rate of the hot water and nanofluid, and increases with a decrease in the nanofluid temperature, and the temperature of the heating fluid has no significant effect on the heat transfer coefficient of the nanofluid. Daungthongsuk and Wongwises [19] aimed in their paper to summarize the various models for predicting the thermophysical properties of nanofluids which have been commonly cited by a number of researchers and use them to calculate the experimental convective heat transfer coefficient of the nanofluid flowing in a double-tube counter flow heat exchanger. Daungthongsuk and Wongwises [20] summarized the published subjects with respect to the forced convective heat transfer of the nanofluids both of experimental and numerical investigation. Demir et al. [21] investigated laminar and turbulent forced convection flows of a nanofluid consisting of water and Al_2O_3 in a horizontal smooth tube with constant wall temperature numerically. Their numerical results show the heat transfer enhancement due to presence of the nanoparticles in the fluid.

Over the years, many studies have focused on the development of a model to predict the heat transfer enhancement of nanofluids. In the present work, the heat transfer behavior of a circular pipe flow has been modeled numerically in comparison to the distilled water as the base fluid with the nanofluid that is composed of distilled water and Al_2O_3 nanoparticles for a constant particle diameter and fluid temperature and various volume concentrations. Besides this, some significant experimental results reported in the study of Palm et al. [22] are used in the numerical solution. Before the modeling process in Fluent CFD program [23], validation of the model is performed using the experimental data belonging to the forced convection of nanofluids consisting of TiO_2 particles [16] regarding the comparison of calculated and measured Nusselt numbers, heat transfer coefficients and pressure drops. In addition to this, temperature distributions of inner surface and the fluids at the inlet and outlet sections of the tube, alteration of wall shear stress, Nusselt numbers, heat transfer coefficients and pressure drops with Reynolds numbers and particle concentrations, local heat transfer coefficients and pressure drops are also obtained from the numerical study and presented in the paper.

2. Sample preparation

In the present study, nanofluids provided by a commercial source (DEGUSSA, VP Disp. W740x) are used as working fluid. The detailed image of dispersed TiO_2 nanoparticles in water, taken by TEM, and

details of preparation of nanofluids can be seen from Duangthongsuk and Wongwises [16].

3. Experimental apparatus

Detailed descriptions of the experimental apparatus for studying single phase heat transfer performance of nanofluids inside a horizontal tube can be found in Duangthongsuk and Wongwises [16].

4. Data reduction

4.1. Thermal and physical properties of nanofluids

It is known that the determination of the nanofluid properties is problematic in the literature. There are also some correlations developed for this aim by Williams et al. [24]. Measurement of physical properties is performed by several researchers in the literature such as Rea et al. [11] and Duangthongsuk and Wongwises [15]. Calculation of the thermal and physical properties of the nanofluids can be done as follows:

Constant-value temperature independent densities based on nanoparticle volume fraction can be seen as follows:

$$\rho_{nf} = (1-\varphi)\rho_{bf} + \varphi\rho_p \quad (1)$$

The effective specific heat can be calculated as follows:

$$Cp_{nf} = (1-\varphi)Cp_{bf} + \varphi Cp_p \quad (2)$$

There is an alternate approach based on heat capacity concept to determine specific heat of nanofluids as follows:

$$(\rho Cp_{nf}) = (1-\varphi)(\rho Cp_{bf}) + \varphi\left(\rho Cp_p\right) \quad (3)$$

It should be noted that it is possible to have different results from Eqs. (2) and (3). Palm et al. [22] preferred to use Eq. (2) to calculate specific heat of nanofluids due to lack of experimental data on this subject.

Putra et al.'s [25] experimental data gives following equations, obtained by Palm et al.'s [22] analysis, to compute the nanofluid effective viscosity as a function of the local temperature for H_2O–Al_2O_3 nanofluid with 1% and H_2O–Al_2O_3 nanofluid with 4% respectively as follows:

$$\mu_{nf} = 2.910^{-7}T^2 - 2.10^{-4}T + 3.4.10^{-2} \quad (4)$$

$$\mu_{nf} = 3.410^{-7}T^2 - 2.310^{-4}T + 3.910^{-2} \quad (5)$$

According to the results of Palm et al.'s [22] study based on Putra et al.'s [25] experimental data, the effective thermal conductivity is determined for H_2O–Al_2O_3 nanofluid with 1% and H_2O–Al_2O_3 nanofluid with 4% respectively as follows:

$$k_{nf} = 0.003352T - 0.3708 \quad (6)$$

$$k_{nf} = 0.004961T - 0.8078 \quad (7)$$

4.2. Governing dimensionless numbers, heat flux, heat transfer coefficient and Nusselt number

In flow through ducts, the heat transfer surface surrounds and guides the stream, and the convection process is said to be internal. The velocity distribution in a duct has two distinct regions in laminar flow: first, the entrance region, where the walls are lined up by growing boundary layers, and, farther downstream, the fully developed region, where the longitudinal velocity is independent of the position along the duct. It is assumed that the duct geometry does not change with the longitudinal position. The flow through a straight duct ceases to be laminar when *Re* number exceeds approximately 2300. It is also observed that the turbulent flow becomes fully developed hydro dynamically and thermally after a relatively short entrance distance [26].

Reynolds number, Prandtl number are used in the theoretical analysis [22], the particle volume fraction (φ) and the ratios k_p/k_{bf} and

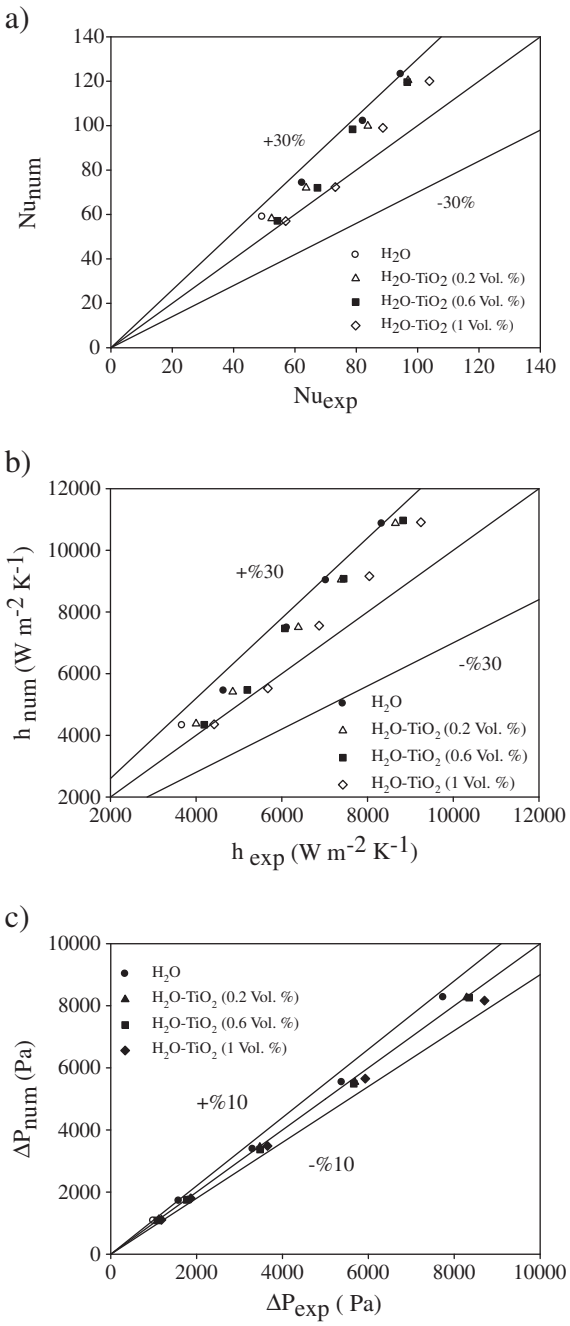

Fig. 4. Comparison of experimental and numerical Nusselt numbers, heat transfer coefficients and pressure drops using pure water with 0.2%, 0.6% and 1% TiO_2 particles data [21]. a) Experimental Nusselt numbers vs. numerical Nusselt numbers. b) Experimental heat transfer coefficient vs. numerical heat transfer coefficient. c) Experimental pressure drop vs. numerical pressure drop.

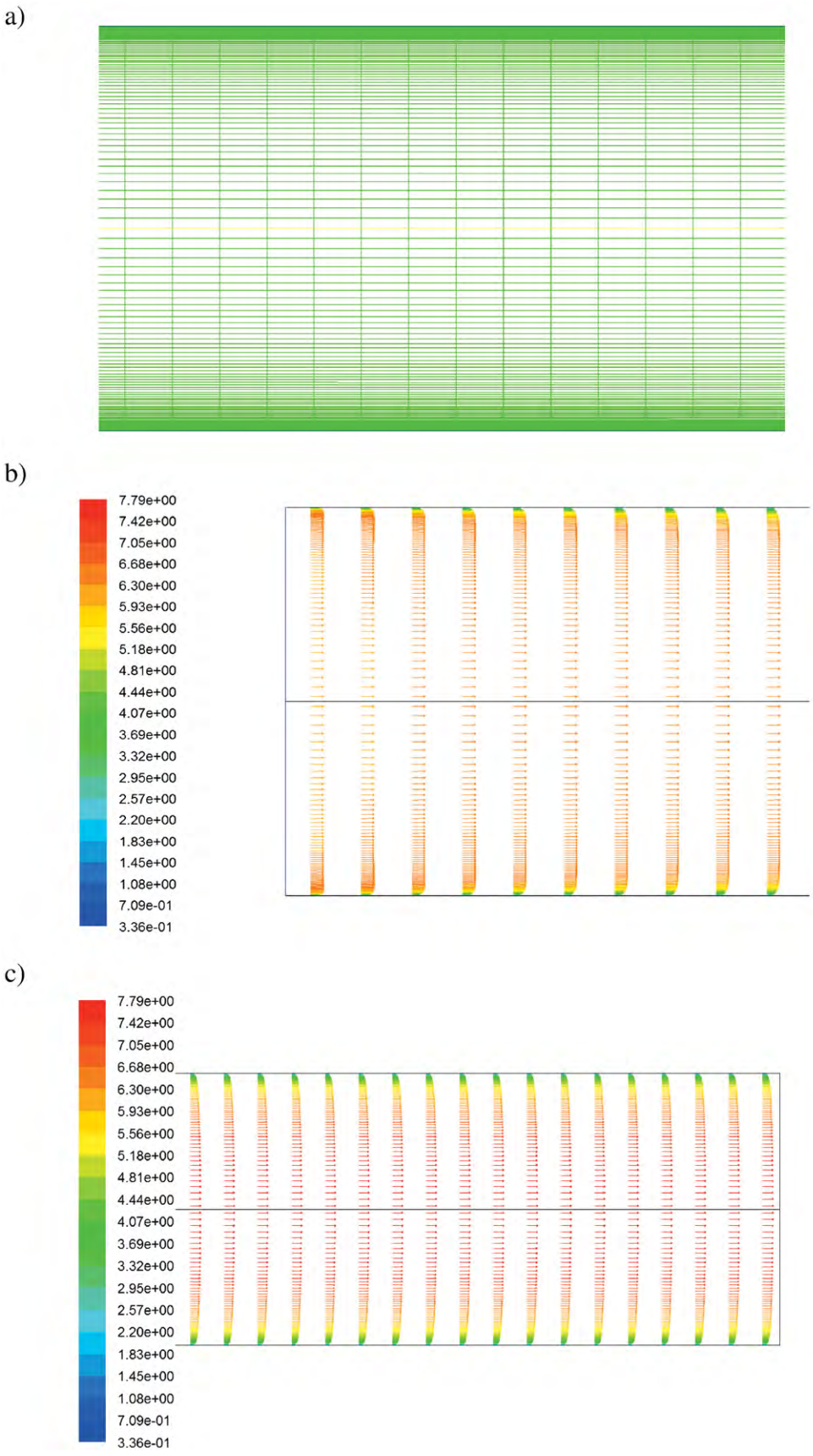

Fig. 5. Grid and velocity vectors layout obtained in the present analysis ($Re = 50{,}000$, $q'' = 10{,}000$ W m^{-2}, $T = 20$ °C). a) Solution grid generated in GAMBIT and used in the present analysis, axis-symmetric about x-axis. b) Velocity vectors at the inlet section of the test tube (m s^{-1}). c) Velocity vectors at the middle section of the test tube (m s^{-1}).

Cp_p/Cp_{bf} are used to characterize the problem and can be calculated as follows:

$$Re = \frac{2Q}{\pi d v} \tag{8}$$

$$Pr = \frac{Cp\mu}{k} \tag{9}$$

Heat flux in the test section is determined as follows:

$$q'' = \frac{m_w Cp_w (T_i - T_o)}{\pi d L} \tag{10}$$

Heat transfer coefficient of the base fluid and nanofluid can be calculated as follows:

$$h = \frac{q''}{\left(T_w - T_{f,m}\right)} \tag{11}$$

Nusselt number belongs to the base fluid and nanofluid can be calculated as follows:

$$Nu = \frac{hd}{k} \tag{12}$$

4.3. Numerical method

This problem was solved by means of the processes in Fluent CFD program [23]. FLUENT is commonly used software in CFD analysis in the literature and a detailed description of the mathematical model can be found in the Fluent User's Guide. This program uses a technique based on control volume theory to convert the governing equations to algebraic equations so they can be solved numerically. The control volume technique works by performing the integration of the governing equations about each control volume, and then generates discrimination of the equations which conserve each quantity based on control volume. The results are obtained thanks to the segregated solver algorithm shown in Fig. 1 in order to

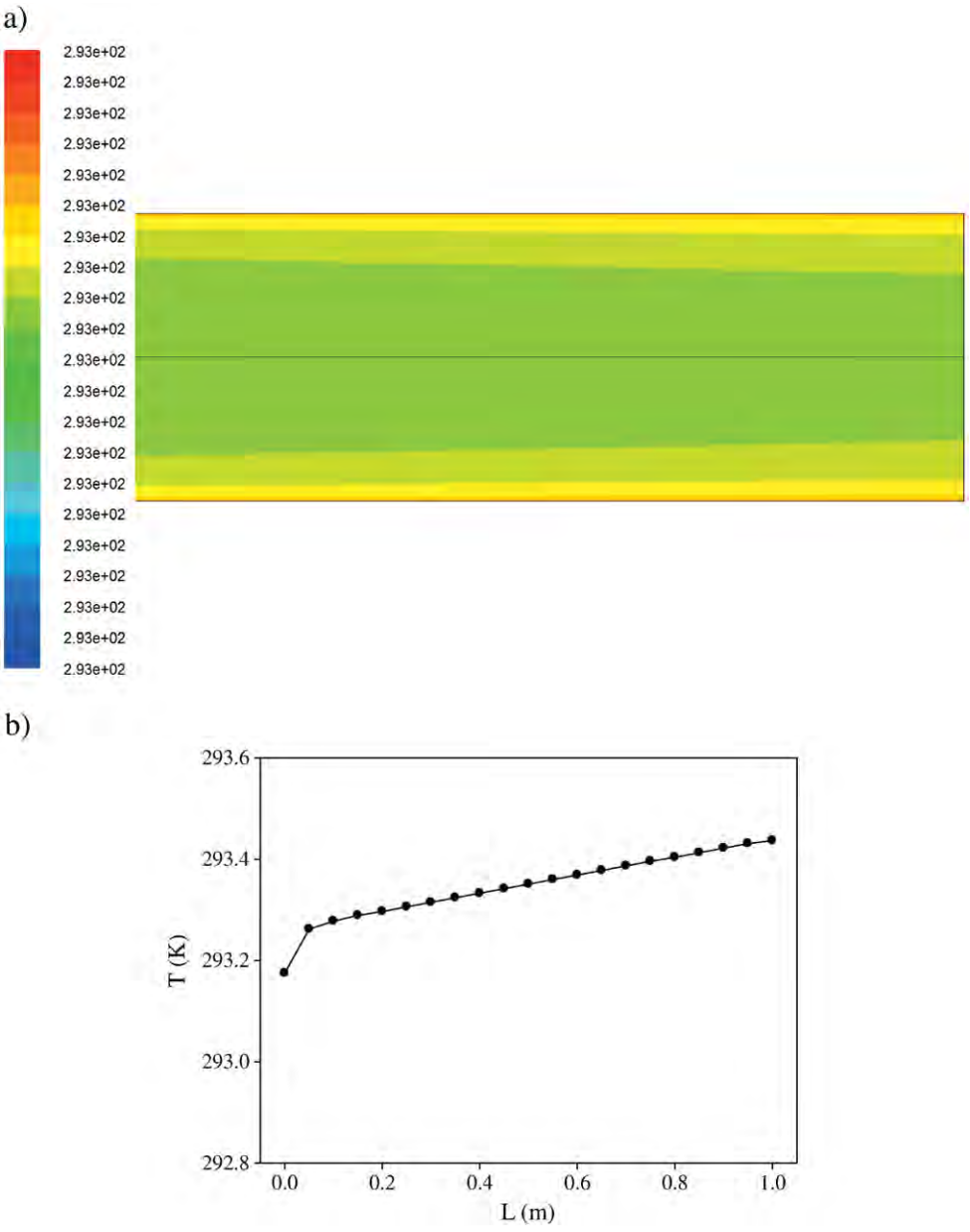

Fig. 6. Temperature distributions of inner surface and fluid in the tube ($Re = 50{,}000$, $q'' = 10{,}000\ W\ m^{-2}$, $T = 20\ °C$). a) Temperature distribution at the outlet section of the tube. b) Inner surface temperature distribution of the tube.

benefit from the experimental data reported in Palm et al.'s [22] study. According to this method the governing equations are solved sequentially, segregated one another. By means of this technique, each discrete equation is linearized implicitly respecting the equations dependent. Gambit program is used to form the model which is used for analyzing problems.

Classic single phase conservation equations were solved by control volume approach which makes possible numerical solution of governing equations by converting them to a set of algebraic equations. Governing equations have some results regarding convection terms, diffusion terms and other quantities which were discredited by second order upwind scheme. All scalar values and velocity components of the problem are calculated at the center of control volume interfaces where the grid schemes are used intensively. Semi Implicit Method for Pressure Linked Equations (SIMPLE) was used to pair the pressure and velocity. A point implicit (Gauss–Seidel) linear equation solver in conjunction with an algebraic multigrid method was used by Fluent CFD program [23] to solve the linear systems resulting from discretization schemes. Boundary conditions defined as velocity inlet at the pipe inlet and pressure outlet for the pipe exit. Turbulence intensity and hydraulic diameter defined for turbulence parameters. Constant heat flux applied to the pipe surface.

Monitor of the residuals was done during the iterative process thoroughly. All solutions were assumed to be converged when the residuals for all governing equations were lower than 10^{-6}. Optimal sizes of grid numbers were selected as 1000 (axial)×80 (radial) considering computation times and low variation with mesh size in temperature and pressure values for all conditions studied in this paper and they are placed highly near the radial flow channel entrance, as well as on all walls. Thus, it is provided that the solution became independent from the mesh size. This grid size was validated by our CFD results in all figures in the paper.

The equation for conservation of mass, or continuity equation, can be expressed as follows [23]:

$$\frac{\partial \rho}{\partial T} + \nabla\left(\rho \vec{v}\right) = S_m \tag{13}$$

Eq. (13) is the general form of the mass conservation equation and is valid for incompressible as well as compressible flows. The source S_m is the mass added to the continuous phase from the dispersed second phase and any user-defined sources.

For 2D axisymmetric geometries, the continuity equation is given by [23]

$$\frac{\partial \rho}{\partial T} + \frac{\partial}{\partial x}(\rho v_x) + \frac{\partial}{\partial r}(\rho v_r) + \frac{\rho v_r}{r}(\rho v_r) = S_m \tag{14}$$

where x is the axial coordinate, r is the radial coordinate, v_r is the radial velocity.

5. Results and discussion

A commercial software package FLUENT [23] is employed in the numerical study. It uses control volume technique to convert the governing equations to algebraic equations so they can be solved numerically. The control volume technique works by performing the integration of the governing equations about each control volume, and then generates discretization of the equations which conserve each quantity based on control volume [23]. GAMBIT was used to plot and mesh the model of the test tube. The problem under investigation is a two-dimensional (axisymmetric) steady, forced turbulent convection flow of nanofluid flowing inside a straight circular tube having diameter of 0.00813 m and a length of 1.5 m for TiO_2 and 0.008 m and 1 m for Al_2O_3. The operating conditions of the study can be seen from Table 1. The fluid enters the circular tube with uniform axial velocity and temperature. The flow and thermal fields are assumed to be axisymmetric with respect to the horizontal plane parallel to x-axis as shown in Fig. 2 for the validation study of the numerical model and Fig. 5 for the simulation study. The main frame of the grid is preferred to be intense near by the tube wall in order to investigate the alteration of boundary layer as shown in Figs. 2a and 5a.

Velocity vectors of the problems for the validation study using experimental data [16] and the simulation study using correlations of physical properties proposed by Palm et al. [22] based on the experimental data of Putra et al. [25] can be seen from Figs. 2a–b and 5a–b respectively. It should be noted that the uniformity of the flow at the inlet section of the tube and fully developed flow at the middle section of the tube can be seen from these figures respectively.

Fig. 3a for the validation study and Fig. 6a for the simulation study illustrate the temperature distribution of the flow in the outlet section of test tube. Due to the given heat flux applied to the surface of the tube, temperature values increased from center of the tube to the surface of the tube and this situation is shown in Figs. 3a and 6a. In accordance with these figures, inner surface temperature distributions of the tube can be seen from Figs. 3b and 6b for the single phase flow of the nanofluids consisting of TiO_2 particles and Al_2O_3 particles respectively.

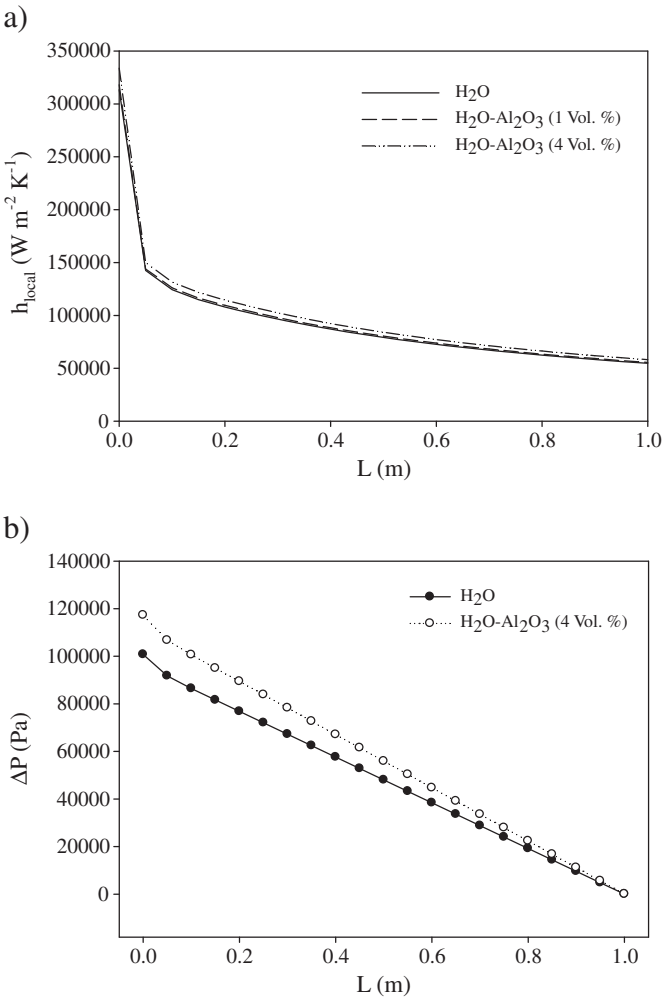

Fig. 7. Variation of local heat transfer coefficient and Pressure drop of water and nanofluid (Re = 50,000, q'' = 10,000 W, T = 20 °C, 4% concentration). a) Heat transfer coefficient—L. b) Pressure drop—L.

Validation process of numerical model is performed by means of the experimental data [16] as shown in Fig. 4 for some heat transfer characteristics of the problem. According to Fig 4, it can be clearly seen that the numerical model of Fluent [23] is in good agreement with the experimental values [16] in terms of the calculation of average Nusselt number within the range of ±30%, heat transfer coefficient within the range of ±30%, and pressure drop within the range of ±10% for the in-tube single phase flow of pure water and nanofluids with TiO_2 volume concentrations of 0.2%, 0.6% and 1%. Experimental and numerical studies are conducted for *Re* numbers between 4516 and 15681 and surface heat fluxes between 7233 and 13340 W m^{-2} (Figs. 2 and 3).

Fig. 7 shows the variation in local heat transfer coefficient and pressure drop along the length of the tube. The characteristics of the trend lines are found to be compatible with others in the literature. In addition to this, heat transfer enhancement due to nanoparticles can be seen from this figure. It is also noticed that a higher slope of relative local heat transfer coefficient can be seen at the entrance region of the tube in Fig. 7a. Fig. 7b shows the pressure drop distribution in the test tube including pure water and nanofluid with 4% Al_2O_3 concentration respectively. It can be seen from Fig. 7b that the volume concentration difference in small Reynolds numbers does not cause a significant effect, on the contrary, pressure drop increases with increasing Al_2O_3 concentration and Reynolds number in Fig. 7b.

From Fig. 8a, it is observed that wall shear stress increases with the increasing Reynolds number of the flow and also volume concentration of the nanoparticles in the tube as the mixture viscosity is increased strongly due to inclusion of nanoparticles. Fig. 8b and c displays the increase in Nusselt number, the heat transfer coefficient respectively by the various nanofluid volume concentrations over the base fluid of pure water for a fixed heat flux of 10,000 W m^{-2}. The increase in heat transfer coefficient is high for Al_2O_3, this is due to the higher Prandtl number and thermal conductivity of nanoparticles than the base fluid and also a large energy exchange process resulting from the chaotic movement of nanoparticles [27]. It should be noted that Nusselt number and heat transfer coefficient increase with increasing Reynolds number in these figures. The results complied with those obtained from Pak and Cho [5], Xuan and Li [28] and He et al. [29]. It can be seen from Fig. 8d that pressure drop increases with increasing the particle loading parameter and Reynolds number because of increasing velocity and viscosity of nanofluid.

From Fig. 9a, it is observed that wall shear stress increases with the increasing volume concentration of the nanofluid and Reynolds numbers. The shear stress has a significant increase at high Reynolds numbers. The effect of the particle concentration on the average Nusselt number and heat transfer coefficient can be clearly seen from Fig. 9b and c respectively. Nusselt number and heat transfer coefficient increase with increasing nanoparticle concentration and also Reynolds number in these figures. This shows the effect of particle concentration. It is evident that nanofluids give higher heat transfer coefficients compared to the base fluid. It can be clearly seen from Fig. 9d that there is a significant increase in pressure drop values especially at high Reynolds numbers and volume concentrations. From Fig. 9d, pressure drop increases with increasing Reynolds number and the particle loading parameter.

A large number of graphics could be generated from the output of the calculations; however, due to space limitations, only typical results are shown for limited data. It should also be noted that detailed

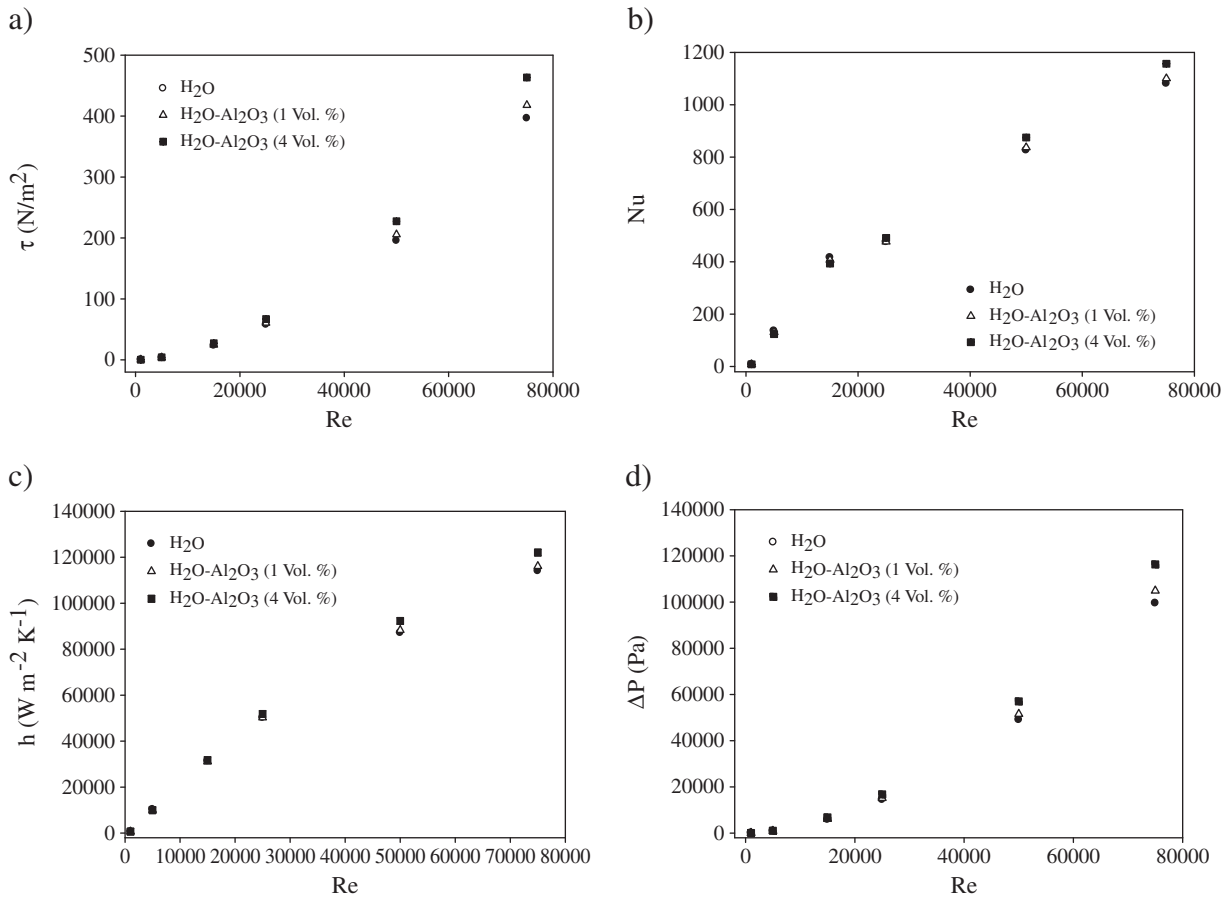

Fig. 8. Comparison of some heat transfer characteristics of different nanofluid concentrations over the base fluid of water ($q'' = 10{,}000$ W m^{-2}, $T = 20$ °C). a) Numerical wall shear stress vs. Re numbers. b) Numerical Nusselt numbers vs. Re numbers. c) Numerical heat transfer coefficient vs. Reynolds numbers. d) Numerical pressure drops vs. Reynolds numbers.

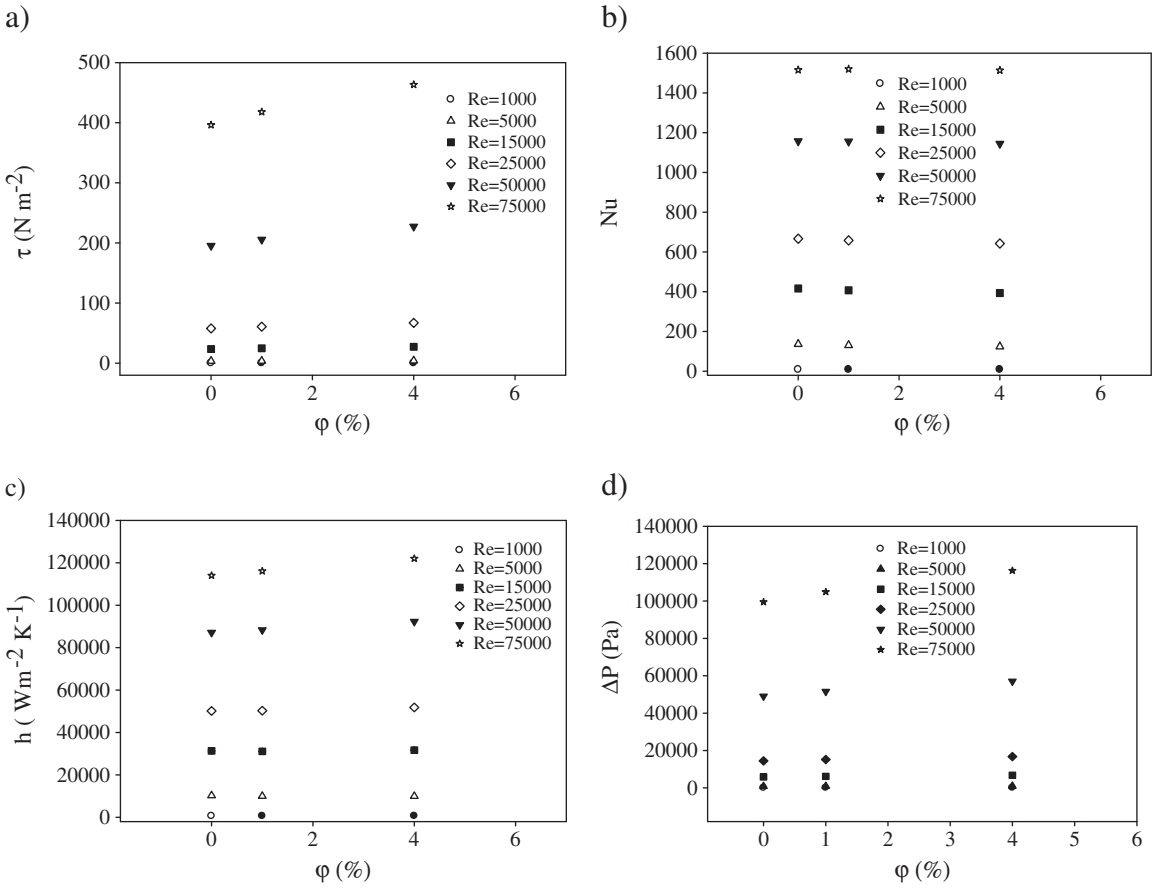

Fig. 9. Effect of particle loading φ on the some in laminar and turbulent flow ($q'' = 10{,}000\ \mathrm{W\,m^{-2}}$, $T = 20\ ^{\circ}\mathrm{C}$). a) Numerical wall shear stress vs. particle loading. b) Numerical Nusselt numbers vs. particle loading. c) Numerical heat transfer coefficient vs. particle loading. d) Numerical pressure drop vs. particle loading.

information on the explanations above and some additional figures with different experimental parameters related to this study can be seen in the authors' previous publications [14–21].

6. Conclusion

The heat transfer enhancement capabilities of nanofluids consisting of water–TiO_2 for a validation study and water–Al_2O_3 for a simulation study with various volume concentrations in a horizontal smooth tube have been investigated for forced flow conditions numerically using two dimensional governing equations.

Numerical results have clearly shown that the use of nanofluids can significantly increase heat transfer capabilities of nanofluids even for relatively small particle volume fractions.

Nanofluids with higher volume concentration have higher heat transfer enhancement and also have higher pressure drop. Therefore, judicious decision should be taken when selecting a nanofluid that will balance the heat transfer enhancement and the pressure drop penalty.

Although the nanofluid is actually a two-phase fluid in nature, the results show that the nanofluid behaves more like a pure fluid than a liquid–solid mixture.

Acknowledgments

The authors wish to thank DEGUSSA AG, Germany for the valuable donation of the nanoparticles used in the present study. The second author wishes to thank KMUTT for providing him with a Post-doctoral fellowship. The fifth author would like to thank the Thailand Research Fund, the Commission of Higher Education and the National Research University Project for providing financial support.

References

[1] U.S. Choi, Enhancing thermal conductivity of fluids with nanoparticles, ASME FED 231 (1995) 99–103.
[2] Y. Xuan, Q. Li, Heat transfer enhancement of nanofluids, Internatnal Journal of Heat Fluid Flow 21 (2000) 58–64.
[3] J.C. Maxwell, Electricity and Magnetism, Clarendon Press, Oxford, UK, 1873.
[4] J.C. Maxwell, A Treatise on Electricity and Magnetism, second ed., Oxford University Press, Cambridge, 1904, pp. 435–441.
[5] B.C. Pak, Y.I. Cho, Hydrodynamic and heat transfer study of dispersed fluids with submicron metallic oxide particles, Experimental Heat Transfer 11 (1998) 151–170.
[6] Y.M. Xuan, Q. Li, Investigation on convective heat transfer and flow features of nanofluids, Journal of Heat Transfer 125 (2003) 151–155.
[7] K.V. Liu, S.U.S. Choi, K.E. Kasza, Measurement of pressure drop and heat transfer in turbulent pipe flows of particulate slurries, Argonne National Laboratory Report, ANL-88-15, 1988.
[8] U.S. Choi, Enhancing thermal conductivity of fluid with nanoparticles, in: D.A. Singiner, H.P. Wang (Eds.), Development and Application of Non-Newtonian Flows, ASME, 231, 1995, pp. 99–105.
[9] S. Lee, S.U.S. Choi, S. Li, J.A. Eastman, Measuring thermal conductivity of fluids containing oxide nanoparticles, ASME Journal Heat Transfer 121 (1999) 280–288.
[10] H. Masuda, A. Ebata, K. Teramae, N. Hishinuma, Alteration of thermal conductivity and viscosity of liquid by dispersing ultra-fine particles (dispersions of c-Al_2O_3, SiO_2, and TiO_2 ultra-fine particles), Netsu Bussei (Japan) 4 (1993) 227–233.
[11] U. Rea, T. McKrell, L. Hu, J. Buongiorno, Laminar convective heat transfer and viscous pressure loss of alumina–water and zirconia–water nanofluids, International Journal of Heat and Mass Transfer 52 (2009) 2042–2048.
[12] V. Bianco, F. Chiacchio, O. Manca, S. Nardini, Numerical investigation of nanofluids forced convection in circular tubes, Applied Thermal Engineering 29 (2009) 3632–3642.
[13] M. H. Fard, M. N. Esfahany, M.R. Talaie, Numerical study of convective heat transfer of nanofluids in a circular tube two-phase model versus single-phase model, International Communications in Heat and Mass Transfer 37 (2010) 91–97.
[14] W. Daungthongsuk, S. Wongwises, A critical review of convective heat transfer of nanofluids, Renewable & Sustainable Energy Reviews 11 (2007) 797–817.
[15] W. Duangthongsuk, S. Wongwises, Measurement of temperature-dependent thermal conductivity and viscosity of TiO_2–water nanofluids, Experimental Thermal and Fluid Science 32 (2009) 706–714.

[16] W. Duangthongsuk, S. Wongwises, Comparison of the effects of measured and computed thermophysical properties of nanofluids on heat transfer performance, Experimental Thermal and Fluid Science 34 (2010) 616–624.
[17] W. Duangthongsuk, S. Wongwises, An experimental study on the heat transfer performance and pressure drop of TiO_2–water nanofluids flowing under a turbulent flow regime, International Journal of Heat and Mass Transfer 53 (2010) 334–344.
[18] W. Duangthongsuk, S. Wongwises, Heat transfer enhancement and pressure drop characteristics of TiO_2–water nanofluid in a double-tube counter flow heat exchanger, International Journal of Heat and Mass Transfer 52 (2009) 2059–2067.
[19] W. Duangthongsuk, S. Wongwises, Effect of thermophysical properties models on the predicting of the convective heat transfer coefficient for low concentration nanofluid, International Communications in Heat and Mass Transfer 35 (2008) 1320–1326.
[20] W. Duangthongsuk, S. Wongwises, A critical review of convective heat transfer of nanofluids, Renewable & Sustainable Energy Reviews 11 (2007) 797–817.
[21] H. Demir, A.S. Dalkilic, N.A. Kurekci, B. Kelesoglu, S. Wongwises, A numerical investigation of nanofluids forced convection flow in a horizontal smooth tube, International Heat Transfer Conference, ASME, 2010, August 8–13, USA.
[22] S.J. Palm, G. Roy, C.T. Nguyen, Heat transfer enhancement with the use of nanofluids in radial flow cooling systems considering temperature-dependent properties, Applied Thermal Engineering 26 (2006) 2209–2218.
[23] Fluent release 6.2.16, Fluent Incorporated, 2005.
[24] W.C. Williams, J. Buongiorno, L.W. Hu, Experimental investigation of turbulent convective heat transfer and pressure loss of alumina/water and zirconia/water nanoparticle colloids (nanofluids) in horizontal tubes, Journal of Heat Transfer 130 (2008) 042412.
[25] N. Putra, W. Roetzel, S.K. Das, Natural convection of nanofluids, Heat and Mass Transfer 39 (2003) 775–784.
[26] A. Bejan, G. Tsatsaronics, M. Moran, Thermal Design and Optimization, Wiley-Interscience Publication, 1996.
[27] Y. Xuan, W. Roetzel, Conceptions for heat transfer correlation of nanofluids, International Journal of Heat and Mass Transfer 43 (2000) 3701–3707.
[28] Y. Xuan, Q. Li, Investigation on convective heat transfer and flow features of nanofluids, ASME Journal of Heat Transfer 125 (2003) 151–155.
[29] Y. He, Y. Jin, H. Chen, Y. Ding, D. Cang, H. Lu, Heat transfer and flow behavior of aqueous suspensions of TiO_2 nanoparticles (nanofluids) flowing upward through a vertical pipe, International Journal of Heat and Mass Transfer 50 (2007) 2272–2281.

International Communications in Heat and Mass Transfer 38 (2011) 212–217

Contents lists available at ScienceDirect

International Communications in Heat and Mass Transfer

journal homepage: www.elsevier.com/locate/ichmt

Two-phase air–water flow in micro-channels: An investigation of the viscosity models for pressure drop prediction ☆

Sira Saisorn [a,b], Somchai Wongwises [b,*]

[a] Department of Engineering, King Mongkut's Institute of Technology Ladkrabang Chumphon Campus, Chumphon 86160, Thailand
[b] Fluid Mechanics, Thermal Engineering and Multiphase Flow Research Lab. (FUTURE), Department of Mechanical Engineering, King Mongkut's University of Technology Thonburi, Bangmod, Bangkok 10140, Thailand

ARTICLE INFO

Available online 16 December 2010

Keywords:
Two-phase flow
Micro-channel
Void fraction
Pressure drop

ABSTRACT

Adiabatic two-phase air–water flow is experimentally studied in this work. Two channels, made of fused silica, with different diameters of 0.53 and 0.15 mm are used as test sections. The void fraction data for both tubes are obtained by image analysis. For the larger channel, the void fraction is found to be a linear relationship with the volumetric quality. In the case of the smaller one, however, the non-linear void fraction is obtained. The measured frictional pressure drop data are compared with the predictions regarding the homogeneous flow assumption. Several well-known two-phase viscosity models are subsequently evaluated for applicability to micro-channels.

1. Introduction

Two-phase flow in micro-channel flow passages has been studied over the years. Clarification of micro-scale effects on two-phase flow and heat transfer characteristics has become more necessary due to the rapid development of microstructure devices used for several engineering applications including medical devices, high heat-flux compact heat exchangers, and cooling systems of various types of equipment such as high performance micro-electronics, supercomputers, and high-powered lasers.

Several investigators have proposed criteria to address the definition of a micro-channel. The proposed channel classifications are often based on different dimensionless parameters. For instance, arbitrary channel classifications based on the hydraulic diameter D_h have been proposed. Mehendale et al. [1] employed the hydraulic diameter as an important parameter for defining heat exchangers and Kandlikar [2] proposed criteria for small flow channels used in engineering applications.

Two-phase flow and heat transfer characteristics in small channels such as micro-channels and mini-channels are likely to be strongly dependent on surface tension effects in addition to viscosity and inertia forces, resulting in significant differences in two-phase flow phenomena between ordinarily sized channels and small channels.

In the past decade, a relatively small amount of publications have been available for both mini-channels and micro-channels compared to those for ordinarily sized channels.

Triplett et al. [3,4] studied adiabatic two-phase air-deionized water (DI water) flow characteristics in micro-channels with hydraulic diameters ranging from 1.1 to 1.5 mm. The flow patterns observed were bubbly, slug, churn, slug-annular, and annular. The measured void fraction and two-phase pressure drop in the relevant flow regimes were also investigated. The void fraction data were obtained based on image analysis.

Serizawa et al. [5] investigated the visualization of the two-phase flow pattern in circular micro-channels. The flowing mixture of air and water in channels 20, 25, and 100 μm in diameter and that of steam and water in a channel of 50 μm in diameter were studied experimentally. Two-phase flow patterns obtained from both air–water and steam–water flows were quite similar and their detailed structures were described. The study confirmed that the surface wettability had a significant effect on the two-phase flow patterns in very small channels.

Chung and Kawaji [6] performed an experiment to distinguish the two-phase flow characteristics in micro-channels from those in mini-channels. Four different circular diameters ranging from 50 to 526 μm were employed to examine a scaling effect on nitrogen-DI water two-phase flow. The results including the flow patterns, void fraction, and two-phase pressure drop were analysed.

A flow visualization study to clarify the flow patterns of a vertical upward gas–liquid two-phase flow in rectangular mini-channels with hydraulic diameters ranging from 1.95 to 5.58 mm was carried out by Satitchaicharoen and Wongwises [7]. Air–water, air — 20 wt.% glycerol solution, and air — 40 wt.% glycerol solution were used as working fluids. In the experiments, they employed various rectangular test sections: 20 mm × 2 mm, 40 mm × 1 mm, 40 mm × 2 mm, 40 mm × 3 mm, and 60 mm × 2 mm with an equal length of 1 m. The flow phenomena, which were classified as bubbly flow, cap-bubbly

☆ Communicated by W.J. Minkowycz.

* Corresponding author.
E-mail address: somchai.won@kmutt.ac.th (S. Wongwises).

0735-1933/$ – see front matter © 2010 Elsevier Ltd. All rights reserved.
doi:10.1016/j.icheatmasstransfer.2010.12.008

Nomenclature

C_o	confinement number
D	channel diameter (m)
D_b	capillary length (m)
D_h	hydraulic diameter (m)
f	friction factor
G	mass flux (kg/m^{2}s)
g	gravitational acceleration (m/s^2)
MAE	mean absolute error
$-dP_f/dz$	frictional pressure gradient (Pa/m)
Re	Reynolds number
x	mass quality

Greek symbols

α	void fraction
β	volumetric quality
μ	dynamic viscosity (Ns/m^2)
ρ	density (kg/m^3)
σ	surface tension (N/m)

Subscripts

G	gas phase
H	homogeneous
L	liquid phase
TP	two-phase

flow, slug flow, churn flow, and annular flow, were observed and recorded by a high-speed camera. The effects of gap size, channel width, and liquid viscosity on the flow pattern transitions were also discussed.

Saisorn and Wongwises [8] reported the influence of the working fluid on flow characteristics in a 0.53 mm diameter channel. Air, nitrogen gas, water and deionized water were used as working fluids. The results of the two-phase air–water system were found to agree with those of working fluids other than air–water mixture. A new correlation was also developed based on their experimental data.

From the previously mentioned review of the literature, it is noted that two-phase flow phenomena in micro-channels are not entirely consistent with those in ordinarily sized channels. However, some experimental data for micro-channels showed fair agreement with predictions developed based on ordinarily sized channels. In general, the prediction methods derived from the separated flow assumption were considered to be comparable with the data whereas the homogeneous flow assumption seemed to be unattractive to previous researchers. This is possibly due to the fact that the observed flow patterns are much less homogeneous under different conditions. Interestingly, it should be noted from Chung and Kawaji [6] and Saisorn and Wongwises [8] that although their observed flow patterns in micro-channels were not perfectly homogeneous, the linear void fraction is found to take place at a certain size of the channel. Such a linear relationship between the void fraction and volumetric quality indicates the homogeneous flow assumption, which may possibly be able to predict the two-phase flow behaviour in micro-channels. This work is, therefore, aimed at examining the applicability of several widely used viscosity models to the pressure drop prediction of air–water flow through different circular micro-channels.

2. Experimental apparatus and procedure

The experiments dealing with pressure drop measurements are carried out using the apparatus along with the instruments as shown in Fig. 1. Air and water are used as working fluids in the system. Instead of a conventional pump, which may contribute to pulsation and fluid contamination, air and the liquid-filled tank are combined and operated as a pneumatic pump to supply a constant flow rate of liquid through the test section. The mixing chamber is designed to introduce the air–water mixture smoothly along the channel. The mixture flows freely from the channel outlet where atmospheric pressure is realized. The gas flow rates can be measured by four sets of rotameters within the ranges of 5–50 sccm, 0.05–0.5, 0.2–2.0, and 1–10 SCFH, respectively. For liquid flow rate measurements, an electronic balance (320 ± 0.001 g) is used to measure the weight of the liquid flowing freely from the outlet over a time period. Test sections made of fused silica with two different inner diameters of 0.53 and 0.15 mm with corresponding lengths of 320 and 104 mm, respectively, are used in this work. The single-phase and two-phase pressure drops across the test section are determined by two pressure transducers installed at the channel inlet. The low range pressure transducer is calibrated from 0 to 250 kPa with a ± 0.5 kPa accuracy and the high range one is calibrated from 0 to 1000 kPa with a ± 2 kPa accuracy. Type T thermocouples are used to measure fluid temperatures. The degree of uncertainty of the temperature measurements is ± 0.1 °C.

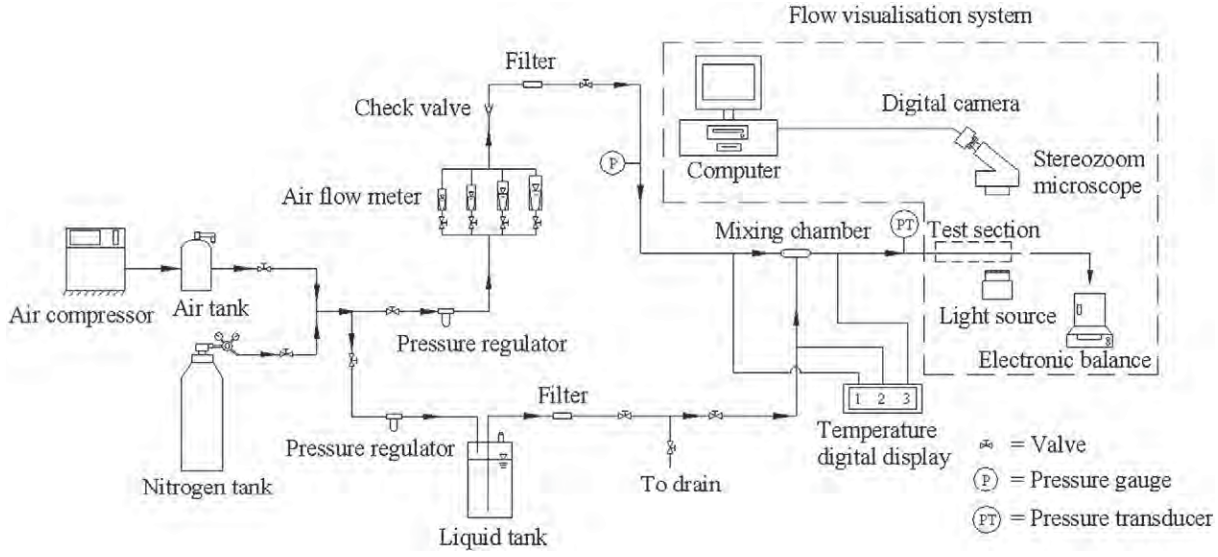

Fig. 1. Experimental apparatus.

Single-phase flow experiments with different fluids were the first to be performed. Following this, two-phase flow experiments were conducted at various gas and liquid flow rates. In this work, the gas flow rate was increased by small increments, while the liquid flow rate was kept constant at a pre-selected value. The system was allowed to approach steady conditions before the fluid flow rates, flow patterns, and pressure drops were recorded.

3. Results and discussion

3.1. Void fraction

Void fraction, the fraction of the channel cross-sectional volume that is occupied by the gas phase, is one of the most important parameters used to evaluate the pressure drop components existing in two-phase flows in various channels. In the case of a horizontal channel, for instance, the void fraction is required before the accelerational pressure drop can be calculated.

Different methods available for void fraction estimation have been used by previous researchers.

Conventional methods such as a constant electric current method generally used to measure void fraction in ordinarily sized channels were carried out by Kariyasaki et al. [9] to obtain void fractions in channels with three different diameters of 1, 2.4, and 4.9 mm. In a method based on quick-closing valves, Wongwises and Pipathattakul [10] measured the void fraction in an inclined narrow annular channel with a hydraulic diameter of 4.5 mm.

For channels with hydraulic diameters of less than 1 mm, it may be convenient to estimate volumetric void fraction by image analysis.

Prior to obtaining the present void fraction data based on image analysis, the detailed formation of each flow pattern has to be registered by a precise stereozoom microscope (Nikon SMZ-1) mounted together with a camera system having shutter speeds of 1/15 to 1/10,000 s. This flow visualization system provides continuous zoom so that the appropriate view field (L/D = 10) is obtained for channels with diameters of 0.53 and 0.15 mm. The region near the channel outlet is always selected as the viewing window.

In this work, the void fraction is the average value estimated from around 50–70 photographed images of flow pattern at a given flow condition. Slug flow, throat-annular flow, annular-rivulet flow, annular flow, liquid-alone flow, and serpentine-like gas core flow are taken into account in the estimation. However, the void fraction regarding churn flow is not measured due to the highly disruptive characteristics. The image analysis is considered by assuming symmetrical volumes, covering spherical and ellipsoidal segments as well as cylinders, formed by the gas–liquid interface. The volumetric void fraction is determined based on a micrometer scale with an accuracy of ±0.05 mm, and the effect of the curvature radius of the tube, which was first introduced by Kawahara et al. [11], is carefully considered in the analysis.

The void fraction data for the channel having a diameter of 0.53 mm are well compatible with the homogeneous flow model ($\alpha = \beta$), while a 0.15 mm diameter channel, in contrast, provides the non-linear void fraction as shown in Eq. (1).

$$\alpha = \frac{0.036\beta^{0.5}}{1-0.945\beta^{0.5}} \tag{1}$$

The non-linear relationship between the void fraction (α) and volumetric quality (β) was also reported by Kawahara et al. [11] and Kwak et al. [12]. Such non-linear characteristics may be contributed by the highly frequent appearance of the gas core flow patterns which have inherent flow with large slip ratios. Due to such different behaviours between the two channel sizes, the confinement number recommended by Kew and Cornwell [13] is used for checking whether the micro-scale effects are still important. The confinement number is defined as

$$C_o = \frac{D_b}{D_h}, \tag{2}$$

where D_b stands for capillary length, which is determined by

$$D_b = \sqrt{\frac{\sigma}{g(\rho_L - \rho_G)}}, \tag{3}$$

where σ is surface tension, g represents gravitational acceleration, and ρ_L and ρ_G are liquid and gas densities, respectively.

A confinement number below 0.5 refers to ordinarily sized channels. For all the present experimental conditions, channels with diameters of 0.53 and 0.15 mm correspond respectively to confinement numbers of around 5.07 and 17.98. These values of the confinement number indicate that surface tension plays a dominant role in the flow mechanisms, which implies the micro-scale point of view.

3.2. Frictional pressure drop

Prior to obtaining data for the two-phase frictional pressure drop, measurements of the total pressure drop are taken under various different conditions. In this work, the total pressure drop of two-phase flow in a horizontal channel is composed of three terms: frictional

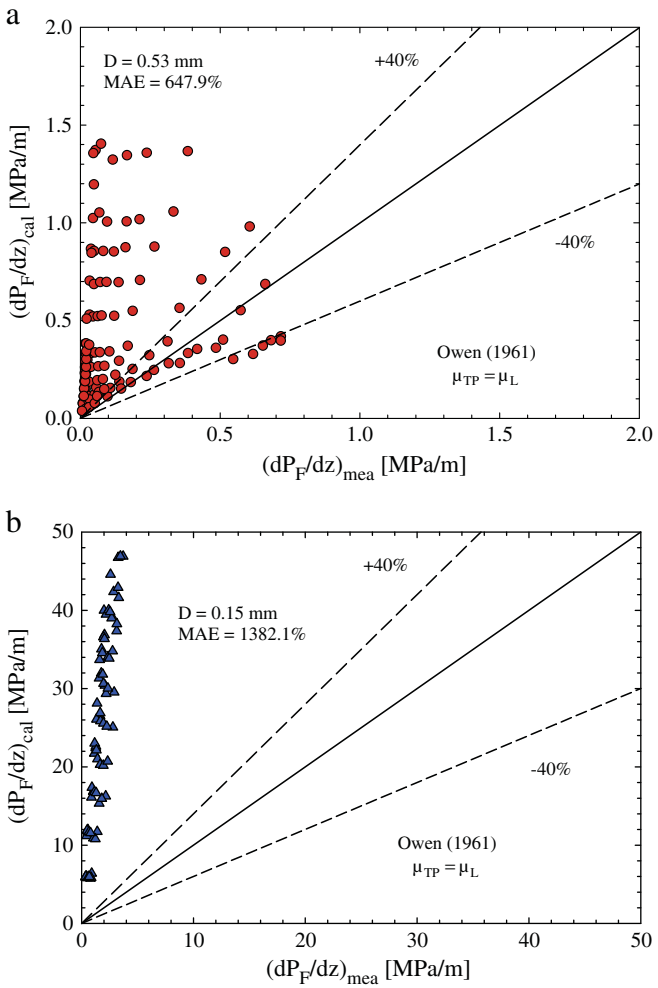

Fig. 2. Experimental data plotted against the predictions by Owen [16].

pressure drop, accelerational pressure drop, and pressure drop caused by an abrupt flow area. The latter component can be evaluated from an empirical correlation proposed by Abdelall et al. [14]. By subtracting the accelerational term and sudden contraction component from the total pressure drop, the frictional pressure drop data are obtained. Further details regarding the calculation method are available in Saisorn and Wongwises [15]. The obtained frictional pressure drop data are subsequently compared with the homogeneous flow predictions, taking into account several existing viscosity models.

The homogeneous flow model assumes that gas and liquid phases flow with equal velocity. The gas–liquid mixture is considered as a single-phase flow with average fluid properties.

For pressure drop calculations based on the homogeneous flow, it follows that

$$-\frac{dP_f}{dz} = \frac{f_{TP}G^2}{2D\rho_H} \tag{4}$$

$$\rho_H = \left[\frac{x}{\rho_G} + \frac{(1-x)}{\rho_L}\right]^{-1}. \tag{5}$$

In Eqs. (4) and (5), $(-dP_f/dz)$ is the two-phase frictional pressure gradient, G is the mass flux, D is the channel diameter, x is the mass quality, ρ_H is the average density of the homogeneous fluid, and ρ_L and ρ_G are liquid and gas densities, respectively. f_{TP} shown in Eq. (4) represents the two-phase Darcy friction factor, which is a function of the two-phase Reynolds number:

$$Re_{TP} = \frac{GD}{\mu_{TP}}. \tag{6}$$

For laminar flow ($Re_{TP} \leq 2100$),

$$f_{TP} = \frac{64}{Re_{TP}}. \tag{7}$$

For turbulent flow ($Re_{TP} < 100{,}000$) in a smooth channel,

$$f_{TP} = \frac{0.3164}{Re_{TP}^{0.25}}, \tag{8}$$

where μ_{TP} presented in Eq. (6) is the two-phase viscosity, for which various forms were proposed by different researchers as follows.

The two-phase viscosity was assumed by Owen [16] to be equal to the liquid viscosity as shown in Eq. (9).

$$\mu_{TP} = \mu_L \tag{9}$$

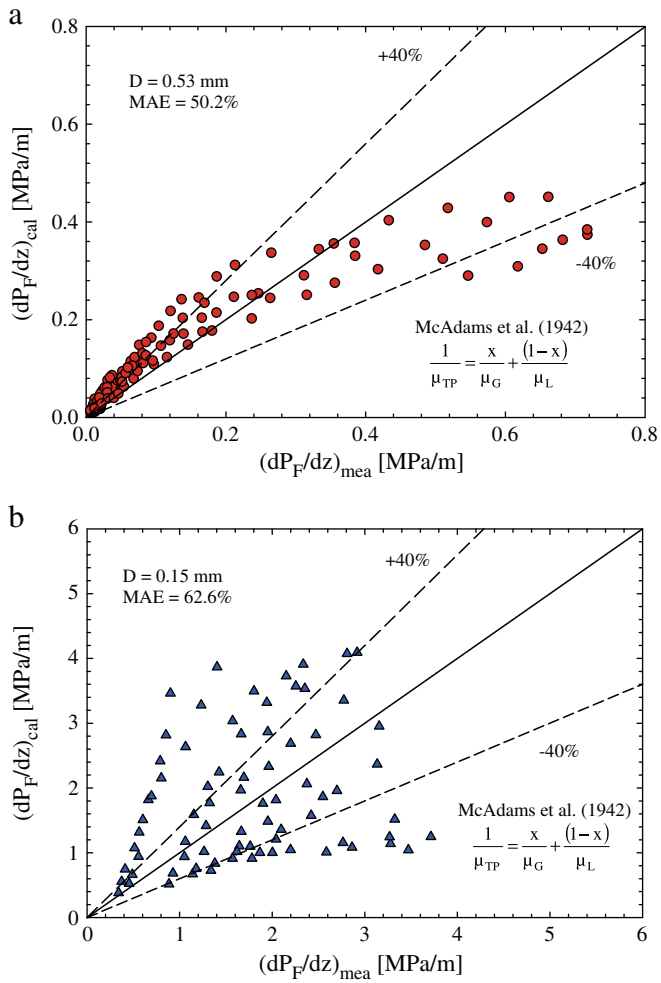

Fig. 3. Experimental data plotted against the predictions by McAdams et al. [17].

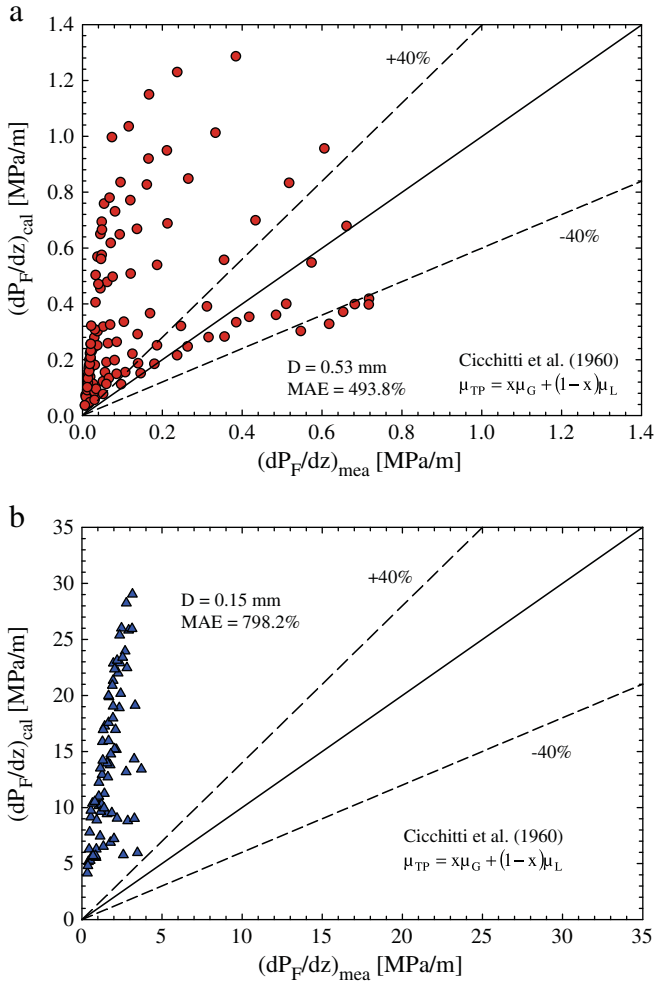

Fig. 4. Experimental data plotted against the predictions by Cicchitti et al. [18].

McAdams et al. [17] proposed the two-phase viscosity presented in Eq. (10), in which the viscosities of each phase are weighted by their corresponding mass quality.

$$\frac{1}{\mu_{TP}} = \frac{x}{\mu_G} + \frac{(1-x)}{\mu_L} \tag{10}$$

The two-phase viscosity of Eq. (11) was proposed by Cicchitti et al. [18] and the mass quality is an important parameter for the calculation.

$$\mu_{TP} = x\mu_G + (1-x)\mu_L \tag{11}$$

With the experimental data obtained from R-12 during vaporization in a capillary tube, Lin et al. [19] proposed the two-phase viscosity as follows.

$$\mu_{TP} = \frac{\mu_L \mu_G}{\mu_G + x^{1.4}(\mu_L - \mu_G)} \tag{12}$$

Dukler et al. [20] and Beattie and Whalley [21] developed two-phase viscosity models based on volumetric quality (β) as expressed respectively in Eqs. (13) and (14).

Dukler et al. [20]:

$$\mu_{TP} = \beta\mu_G + (1-\beta)\mu_L. \tag{13}$$

Beattie and Whalley [21]:

$$\mu_{TP} = \beta\mu_G + (1-\beta)(1 + 2.5\beta)\mu_L \tag{14}$$

In order to examine the applicability of the two-phase viscosity predictions for both tubes, the experimental pressure drop data are plotted against the values predicted by the corresponding models as presented in Figs. 2–7. The mean absolute error (MAE) indicated on these figures refers to the predictive accuracy of a given model. In general, the agreement between the experimental data and the predicted pressure drops is not good for a 0.15 mm diameter channel in which a non-linear void fraction is obtained. Nevertheless, better predictions are observed when a tube with a diameter of 0.53 mm, associated with the linear void fraction, is used. According to the previous discussion, different void fraction characteristics for the two channel sizes may result in the discrepancy in predictions. The comparisons shown in Figs. 2–7 also indicate that only the methods proposed by Beattie and Whalley [21] and by McAdams et al. [17] are roughly predictable. The prediction by Beattie and Whalley [21] is shown to be the best. The MAE values of 37.3% and 38.3% as well as 57.7% and 48.1% of the predicted data falling within a ±40% error band are obtained respectively for a 0.53 mm diameter channel and a 0.15 mm diameter channel. For the second best prediction, which is obtained by the method developed by McAdams et al. [17], the channels with diameters of 0.53 and 0.15 mm correspond respectively to the MAE values of 50.2% and 62.6%. Accordingly, 50.4% and 44.2% of the predicted values fall in the range of a ±40% error band.

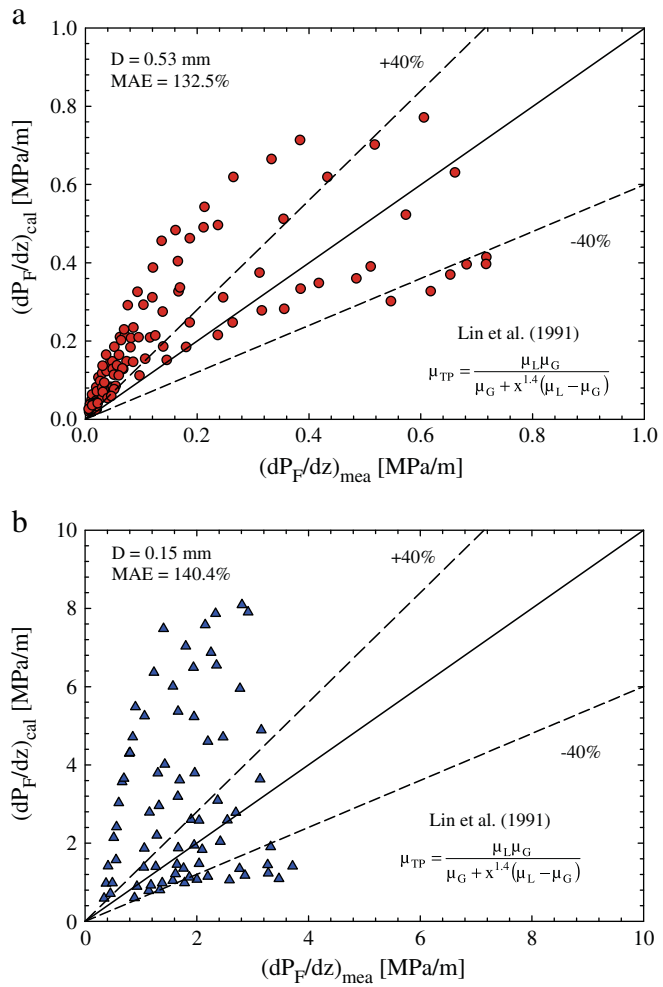

Fig. 5. Experimental data plotted against the predictions by Lin et al. [19].

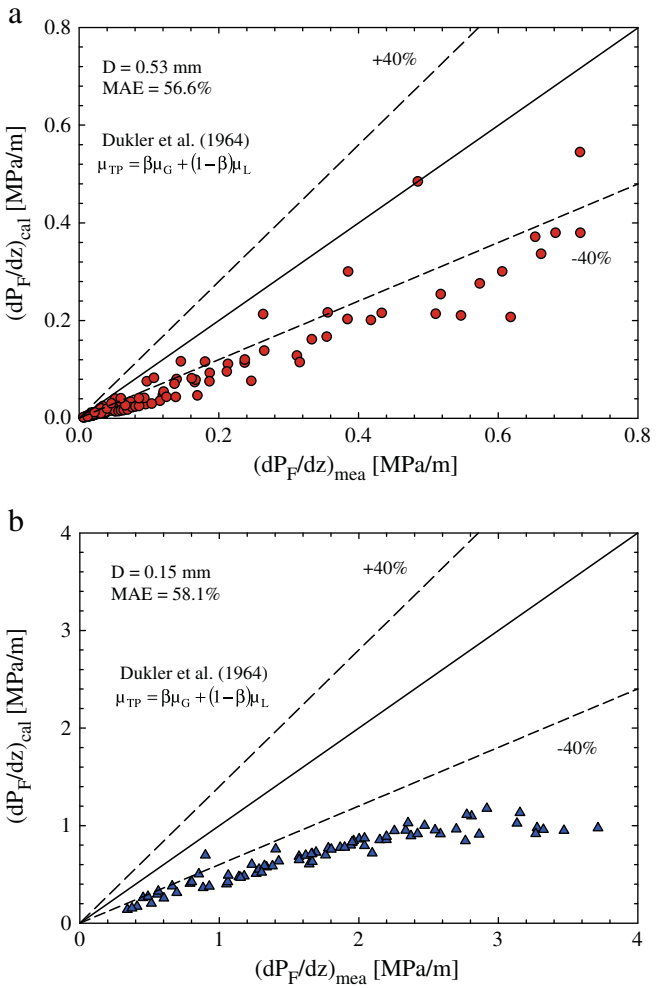

Fig. 6. Experimental data plotted against the predictions by Dukler et al. [20].

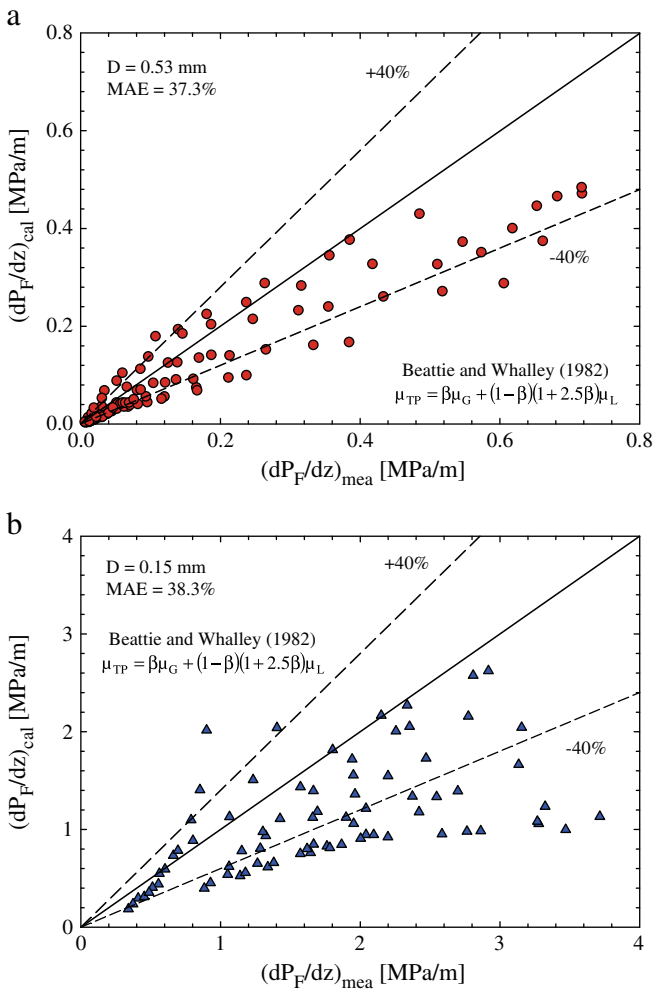

Fig. 7. Experimental data plotted against the predictions by Beattie and Whalley [21].

4. Conclusion

Two-phase pressure drop of air–water flow through circular channels having different diameters of 0.53 and 0.15 mm is experimentally investigated in this study. The test sections are made of fused silica. Void fraction data for both tubes are obtained by using a method based on image analysis. The linear void fraction is observed for the channel with a diameter of 0.53 mm whereas the non-linear void fraction is identified in the smaller channel. The frictional pressure drop data, determined by subtracting the accelerational component and the sudden contraction term from the total pressure drop, are compared with the predictions of several well-known two-phase viscosity models. The homogeneous flow assumption seems to unsatisfactorily predict the data corresponding to the channel with a diameter of 0.15 mm. However, better predictions are obtained for a 0.53 mm diameter channel in which the linear void fraction characteristics occur.

Acknowledgements

The authors would like to express their appreciation to the Thailand Research Fund, the Commission of Higher Education and the National Research University Project for providing financial support for this study.

References

[1] S.S. Mehendale, A.M. Jacobi, R.K. Ahah, Fluid flow and heat transfer at micro- and meso-scales with application to heat exchanger design, Appl. Mech. Rev. 53 (2000) 175–193.
[2] S.G. Kandlikar, Fundamental issues related to flow boiling in mini-channels and micro-channels, Exp. Therm. Fluid Sci. 26 (2002) 389–407.
[3] K.A. Triplett, S.M. Ghiaasiaan, S.I. Abdel-Khalik, D.L. Sadowski, Gas–liquid two-phase flow in microchannels Part I: two-phase flow patterns, Int. J. Multiphase Flow 25 (1999) 377–394.
[4] K.A. Triplett, S.M. Ghiaasiaan, S.I. Abdel-Khalik, A. LeMouel, B.N. McCord, Gas–liquid two-phase flow in microchannels Part II: void fraction and pressure drop, Int. J. Multiphase Flow 25 (1999) 395–410.
[5] A. Serizawa, Z. Feng, Z. Kawara, Two-phase flow in micro-channels, Exp. Therm. Fluid Sci. 26 (2002) 703–714.
[6] P.M.-Y. Chung, M. Kawaji, The effect of channel diameter on adiabatic two-phase flow characteristics in microchannels, Int. J. Multiphase Flow 30 (2004) 735–761.
[7] P. Satitchaicharoen, S. Wongwises, Two-phase flow pattern maps for vertical upward gas–liquid flow in mini-gap channels, Int. J. Multiphase Flow 30 (2004) 225–236.
[8] S. Saisorn, S. Wongwises, Flow pattern, void fraction and pressure drop of two-phase air–water flow in a horizontal circular micro-channel, Exp. Therm. Fluid Sci. 32 (2008) 748–760.
[9] A. Kariyasaki, T. Fukano, A. Ousaka, M. Kagawa, Characteristics of time-varying void fraction in isothermal air–water co-current flow in horizontal capillary tube, Trans. JSME 57 (1991) 4036–4043.
[10] S. Wongwises, M. Pipathattakul, Flow pattern, pressure drop and void fraction of two-phase gas–liquid flow in an inclined narrow annular channel, Exp. Therm. Fluid Sci. 30 (2006) 345–354.
[11] A. Kawahara, P.M.-Y. Chung, M. Kawaji, Investigation of two-phase flow pattern, void fraction and pressure drop in a microchannel, Int. J. Multiphase Flow 28 (2002) 1411–1435.
[12] Y. Kwak, D. Pence, J. Liburdy, V. Narayanan, Gas–liquid flows in a fractal-like branching flow network, Engineering Conference International Heat Transfer and Fluid Flow in Microscale III, Whistler, BC, Canada, 2008,, September 21–26.
[13] P.A. Kew, K. Cornwell, Correlations for the prediction of boiling heat transfer in small-diameter channels, Appl. Therm. Eng. 17 (8–10) (1997) 705–715.
[14] F.F. Abdelall, G. Hahn, S.M. Ghiaasiaan, S.I. Abdel-Khalik, S.S. Jeter, M. Yoda, D.L. Sadowski, Pressure drop caused by abrupt flow area changes in small channels, Exp. Therm. Fluid Sci. 29 (2005) 425–434.
[15] S. Saisorn, S. Wongwises, An experimental investigation of two-phase air–water flow through a horizontal circular micro-channel, Exp. Therm. Fluid Sci. 33 (2009) 306–315.
[16] W.L. Owen, Two-phase pressure gradient, Int. Dev. Heat Transfer, Pt II, ASME, New York, 1961.
[17] W.H. McAdams, W.K. Woods, L.C. Heroman, Vaporization inside horizontal tubes-III, Benzene-Oil Mixtures. Trans. ASME. 64 (1942) 193.
[18] A. Cicchitti, C. Lombardi, M. Silvestri, G. Solddaini, R. Zavalluilli, Two-phase cooling experiments — pressure drop, heat transfer and burnout measurement, Energy Nucl. 7 (1990) 407–425.
[19] S. Lin, C.C.K. Kwok, R.Y. Li, Z.H. Chen, Z.Y. Chen, Local frictional pressure drop during vaporization for R-22 through capillary tubes, Int. J. Multiphase Flow 17 (1991) 95–102.
[20] A.E. Dukler, M. Wicks III, R.G. Cleveland, Pressure drop and hold-up in two-phase flow, AIChE J. 10 (1964) 38–51.
[21] D.R.H. Beattie, P.B. Whalley, A simple two-phase flow frictional pressure drop calculation method, Int. J. Multiphase Flow 8 (1982) 83–87.

Heat Mass Transfer (2011) 47:629–640
DOI 10.1007/s00231-010-0748-6

ORIGINAL

Evaporation heat transfer and flow characteristics of R-134a flowing through internally grooved tubes

Somchai Wongwises · Suriyan Laohalertdecha · Jatuporn Kaew-on · Weerapun Duangthongsuk · Kanit Aroonrat · Kittipong Sakamatapan

Received: 8 November 2009 / Accepted: 29 November 2010 / Published online: 4 January 2011

Abstract This article describes experimental investigations of the heat transfer coefficient and pressure drop of R-134a flowing inside internally grooved tubes. The test tubes are one smooth tube and four grooved tubes. All test tubes are made from type 304 stainless steel, have an inner diameter of 7.1 mm, are 2,000 mm long and are installed horizontally. The test section is uniformly heated by a DC power supply to create evaporation conditions. The groove depth of all grooved tubes is fixed at 0.2 mm. The experimental conditions are conducted at saturation temperatures of 20, 25 and 30°C, heat fluxes of 5, 10 and 15 kW/m^2, and mass fluxes of 300, 500 and 700 kg/m^2 s. The effects of groove pitch, mass flux, heat flux, and saturation temperature on heat transfer coefficient and frictional pressure drop are discussed. The results illustrate that the grooved tubes have a significant effect on the heat transfer coefficient and frictional pressure drop augmentations.

S. Wongwises (✉) · S. Laohalertdecha · J. Kaew-on · W. Duangthongsuk · K. Aroonrat · K. Sakamatapan
Fluid Mechanics, Thermal Engineering and Multiphase Flow Research Lab. (FUTURE), Department of Mechanical Engineering, King Mongkut's University of Technology Thonburi, Bangmod, Bangkok 10140, Thailand
e-mail: somchai.won@kmutt.ac.th

S. Laohalertdecha
The Joint Graduate School of Energy and Environment (JGSEE), King Mongkut's University of Technology Thonburi, Bangmod, Bangkok 10140, Thailand

J. Kaew-on
Department of Physics, Faculty of Science, Thaksin University, Papayom, Phattalung 93110, Thailand

W. Duangthongsuk
Department of Mechanical Engineering, South-East Asia University, Bangkok 10160, Thailand

List of symbols

A	surface area of the test section (m^2)
c_p	specific heat at constant pressure (J/kg K)
G	mass flux (kg/m^2 s)
h	heat transfer coefficient (W/m^2 K)
I	current (A)
i	enthalpy (J/kg)
k	thermal conductivity (W/m K)
L	length of the test tube (m)
$\dot{m}$	mass flow rate (kg/s)
N	number of the thermocouples on the inner wall surface
ΔP	pressure drop (Pa)
$\dot{Q}$	heat transfer rate (W)
q''	heat flux (W/m^2)
r	radius (m)
T	temperature (^{o}C)
V	voltage (V)
x	average vapour quality
X	position of the test section (m)

Greek symbols

ρ	density (kg/m^3)
α	void fraction

Subscripts

a	acceleration
avg	average
f	friction
g	gravity
in	inlet
i	inside
l	liquid
out	outlet
o	outside

ph	pre-heater
ref	refrigerant
sat	saturation
TS	test section
v	vapor
w	water
wall	wall surface

1 Introduction

Nowadays, global warming and energy saving are major issues which many countries are addressing. All fluorocarbons, for example CFCs, HCFCs, HFCs are major sources of the global warming problem. Normally, Fluorocarbons are divided into two categories. The first group is the chemical substance containing chlorine or bromine, for example CFCs (R-11, R-12, R-502, etc.) and HCFCs (R-22, etc.), which are regulated by the Montreal Protocol. The production of CFCs and HCFCs have been or will be prohibited in developed countries from 1995 to 2030, respectively. The second group does not contain chlorine or bromine, for example HFCs (R-134a, R-404A, R-407C, etc.). The index for indicating the global warming problem is called "Global Warming Potential (GWP)". GWP is a measure of how much a given mass of greenhouse gas contributes to global warming. The details of GWPs for CFCs, HCFCs and HFCs are provided by IRR [1] as shown in Table 1. It is evident that R-134a shows the minimum value of GWP.

In order to reduce energy consumption, the thermal performance of heat transfer equipment should be improved. The rough surface technique is a heat transfer enhancement technique, which generally involves surface modification to promote turbulence in the flow field and increases the heat transfer surface area. In general, internally grooved tubes are used instead of smooth tubes in many heat exchangers to increase heat transfer performance by mixing and also limiting the fluid boundary layers close to the heat transfer surfaces. Moreover, they can promote two-phase heat transfer enhancement.

Table 1 GWPs of CFCs, HCFCs and HFCs [1]

CFCs		HCFCs		HFCs	
Refrigerant	GWP	Refrigerant	GWP	Refrigerant	GWP
R-11	3,800	R-22	1,500	R-134a	1,300
R-12	8,100			R-404A	3,260
R-502	5,500			R-407C	1,520
				R-410A	1,725
				R-507	3,300

Publications on the heat transfer and flow characteristics of single-phase flow in internally grooved tubes are summarized as follows:

Herman and Kang [2] investigated the heat transfer enhancement in a grooved channel with curved vanes. The unsteady temperature fields in the grooved channel with curved vanes were visualized by holographic interferometry. Air was used as the working fluid. The results demonstrated that heat transfer and pressure drop were enhanced by up to 1.5–3.5 and 3–5 times, respectively, compared to the basic grooved channel.

Bilen et al. [3] investigated the effect of groove shapes on heat transfer and friction characteristics in the turbulent flow regime. The experimental conditions corresponded to Reynolds numbers of 10,000–38,000. Circular, trapezoidal and rectangular grooved tubes with a ratio of tube length-to-diameter fixed at 33 were used in this study. Under given conditions, the experimental results showed that the maximum heat transfer coefficients were obtained from the circular groove, trapezoidal groove and rectangular groove, with enhancements of up to 63, 58 and 47%, respectively, in comparison with the smooth tube.

Bharadwaj et al. [4] studied experimentally the heat transfer and flow characteristics of water flowing in 75-start spirally grooved tube with a twisted tape insert. The test sections were internally grooved copper tubes, 1,040 mm long with 15.875 mm OD, inserted with clockwise and anticlockwise twist tape. The results illustrated that the maximum heat transfer enhancement obtained from the laminar range without and with twisted tape were 400 and 600%, respectively. In the turbulent range, the experimental results also showed that both maximum heat transfer enhancement without and with twisted tape is 140%.

Besides these, there are some publications concerned with the heat transfer and pressure drop characteristics of two-phase flow inside grooved tubes such as Graham et al. [5], Goto et al. [6] and Zhang et al. [7]. In 1999, Graham et al. [5] investigated the heat transfer and pressure drop characteristics of R-134a during condensation in an axially grooved tube. The experiment was performed at mass fluxes ranging between 75 and 450 kg/m^{2}s. Grooved tubes with 0 and 18^o helix angle were used as the inner tube. The results showed that the heat transfer coefficient and pressure drop obtained from grooved tubes were higher than from smooth tubes by factors of about 3 and 2, respectively.

Goto et al. [6] studied experimentally the condensation heat transfer of R-410A and R-22 fluids inside internally grooved horizontal tubes with an O.D. of 8.0 mm. The length of the test section was 1.0 m. The test conditions were run as follows: mass flux of 130–400 kg/m^{2}s, vapour pressure of 2.41 MPa for R-410A and 1.53 MPa for R-22. The new empirical correlation was proposed. The results

found that the majority of the data fall within ±20% of the proposed correlations.

The heat transfer coefficient of R-417A (R-125/R-134a/R-600) during evaporation flowing inside horizontal smooth and internally grooved tubes was investigated by Zhang et al. [7]. The test conditions were conducted with mass fluxes of 176–344 kg/m^{2}s, heat fluxes of 11–32 kW/m^2, saturation temperature of 0–5.5°C and vapour quality of 0.2–1. The test section was the three double tube type of heat exchangers. The results showed that the heat transfer coefficient of the grooved tube was much higher than the smooth tube. Moreover, R-22 was characterised by a higher heat transfer coefficient than R-417A, especially for the grooved tube.

Despite the heat transfer enhancement potential of grooved tube, as shown above, there are only few studies dealing with the heat transfer and pressure drop of flow of refrigerant changing the phase in grooved tubes. In the present study, the main concern is to experimentally study heat transfer enhancement and two-phase flow characteristics during evaporation of R134a in internally grooved tubes. Experimental data that have never been seen before on local heat transfer coefficient, average heat transfer coefficient and pressure drop under constant heat flux are presented.

2 Experimental apparatus and method

The experimental system consists mainly of a test section, refrigerant circulating loop, sub-cooling loop, a DC power supply and a data acquisition system as shown in Fig. 1.

For the refrigerant circulating loop, liquid refrigerant is forced by a gear pump which can be adjusted to the flow rate using an inverter. The refrigerant then passes in series through a filter/dryer, a refrigerant flow meter, pre-heater, a sight glass, and enters the test section. The inlet quality before entering the test section is controlled by the pre-heater. The heating water is used to apply the heat flux to the pre-heater, which can be controlled by adjusting the flow rate or the temperature of the hot water. Leaving the test section, the refrigerant vapour then condenses inside a sub-cooler and is collected in a receiver, returning to the refrigerant pump to complete the cycle. Instrumentation is installed at various positions, as shown in Fig. 1, to monitor the state of the refrigerant. All signals from the thermocouples and differential pressure transducer are recorded by a data acquisition system.

Details of the test section are shown schematically in Fig. 2. The dimensions of the test section are listed in Table 2. The test sections are a smooth tube (SMT), a straight grooved tube (SGT), a grooved tube with 8″ pitch (GT8), a grooved tube with 10″ pitch (GT10) and a grooved tube with 12″ pitch (GT12), which are made from type 304 stainless steel type. The cross section of grooved tube is shown in Fig. 3. The regulated DC power supply is used to provide the voltage for the test section. The voltage and electrical current values are measured by a multi-meter (Fluke 336 meter) which has an uncertainty of ±2% for voltage and ±1% for current. T-type thermocouples are installed at the inlet and outlet of the test section to measure the saturation temperature of the refrigerant. Similarly, the differential pressure transducer is installed in order to measure the pressure drop across the test section. The length between pressure taps is 2,000 mm. The twelve thermocouples are installed at the top, bottom, and side at four points along the test section to measure the wall temperatures. All of the thermocouples are fixed at the outer surface of the test section by the special glue (OMEGABOND 101) having a thermal conductivity of 1 W/mK. The test section is insulated with rubber foam with a thermal conductivity of 0.04 W/mK. All of the thermocouples are well calibrated with standard thermometers with a precision of 0.05°C. The refrigerant flow meter is a variable area type and is specially calibrated in the range of 0.2–1.8 LPM for R-134a by the manufacturer as was the differential pressure transducer.

In the experiments, the inlet quality of the test section is varied by small increments. The imposed heat flux, mass flux, and saturation temperature are kept constant at the desired values. The system is allowed to approach a steady state before any data are recorded. During experiments, the temperature and pressure are continuously recorded along the test section by the data acquisition system. The temperature profiles help us to know the limit of useful data because a large increase in wall temperature and outlet saturation temperature is noticed when dry-out takes place. The range of experimental conditions tested in this study is listed in Table 3. The uncertainties of measured quantities and calculated parameters are shown in Table 4.

3 Data reduction

In order to calculate the heat transfer performance of R-134a under evaporation conditions, the conversion of measured data into meaningful quantities is defined in the following equations.

The inlet vapour quality of the test section ($x_{\mathrm{TS,in}}$) can be calculated as follows:

$$x_{\mathrm{TS,in}} = \frac{i_{\mathrm{TS,in}} - i_{f@T_{\mathrm{TS,in}}}}{i_{\mathrm{fg}@T_{\mathrm{TS,in}}}} \quad (1)$$

where $i_{f@T_{\mathrm{TS,in}}}$ and $i_{fg@T_{\mathrm{TS,in}}}$ are the enthalpy of the saturated liquid and the enthalpy of vaporization, respectively, based

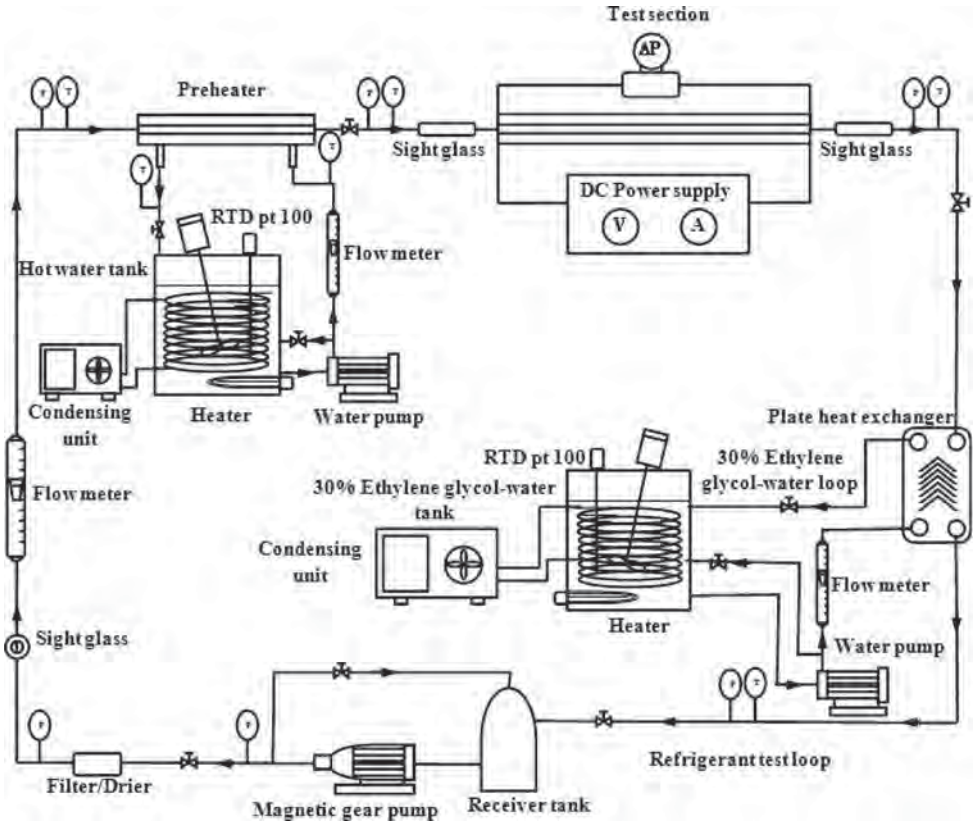

Fig. 1 Schematic diagram of the experimental apparatus

on the temperature at the test section inlet, and $i_{TS,in}$ is the enthalpy of refrigerant at the test section inlet which is calculated by the following equation:

$$i_{TS,in} = i_{ph,in} + \frac{\dot{Q}_{ph}}{\dot{m}_{ref}} \tag{2}$$

where $i_{ph,in}$ is the inlet enthalpy of the liquid refrigerant before entering the pre-heater, $\dot{m}_{ref}$ is the mass flow rate of the refrigerant and $\dot{Q}_{ph}$ is the heat transfer rate in the pre-heater:

$$\dot{Q}_{ph} = \dot{m}_{w,ph} c_{p,w} (T_{w,in} - T_{w,out})_{ph} \tag{3}$$

with $\dot{m}_{w,ph}$ the mass flow rate of water entering the pre-heater.

The outlet vapour quality of the test section ($x_{TS,out}$) can be calculated as follows:

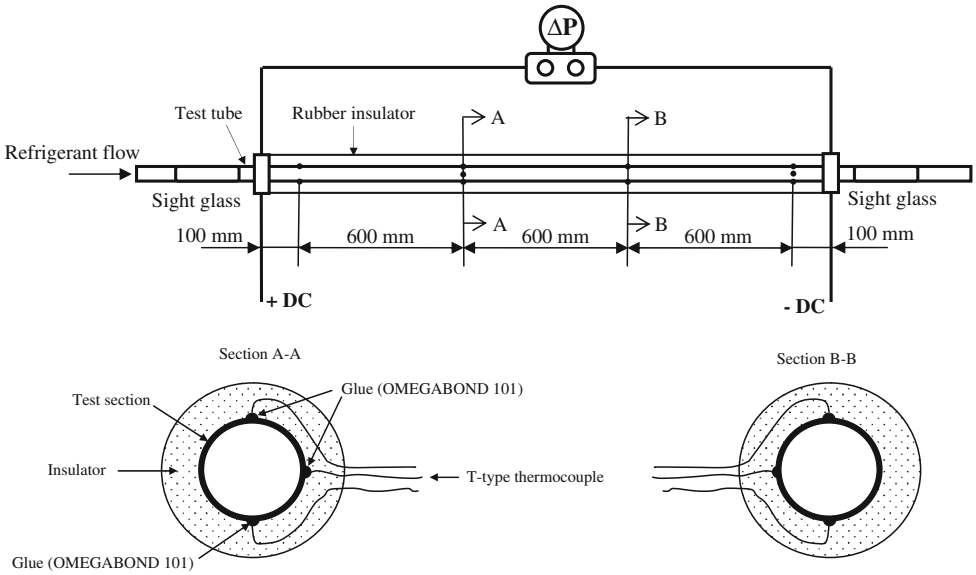

Fig. 2 Schematic diagram of the test section

Table 2 The details of the test sections

Parameter	Smooth tube (SMT)	Straight grooved tube (SGT)	Grooved tube with 8″ pitch (GT8)	Grooved tube with 10″ pitch (GT10)	Grooved tube with 12″ pitch (GT12)
Depth, e (mm)	–	0.2	0.2	0.2	0.2
Pitch, p (mm)	–	–	203	254	305
Outside diameter, D_o (mm)	9.5	9.5	9.5	9.5	9.5
Inside diameter, D_i (mm)	7.1	7.1	7.1	7.1	7.1
Actual inside cross section area (mm^2)	396	420	416	416	416
Actual inside tube area, A (mm^2)	44,611	54,210	52,658	52,641	52,632
Length of the test tube, L (mm)	2,000	2,000	2,000	2,000	2,000

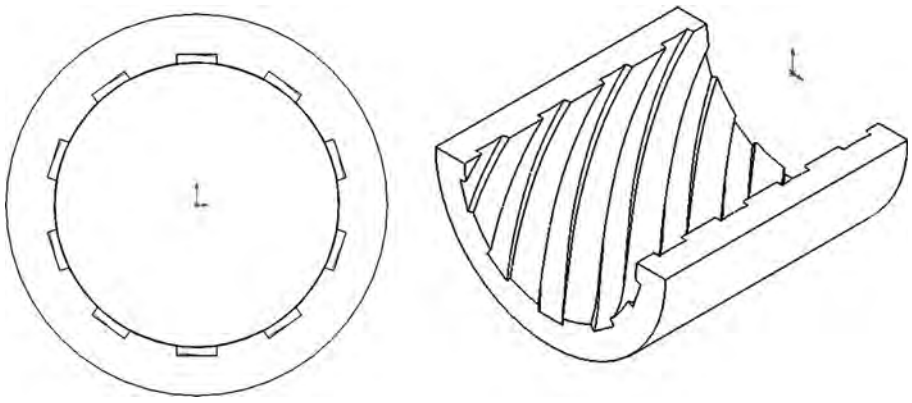

Fig. 3 The cross section of grooved tube

Table 3 Experimental conditions

Controlled variable	Range
Mass flux (kg/m^2s)	300, 500, 700
Heat flux (kW/m^2)	5, 10, 15
Saturation temperature (°C)	20, 25, 30
Tested tube material	Stainless steel type 304
Refrigerant	R-134a

Table 4 Uncertainties of measured quantities and calculated parameters

Parameter	Uncertainty
Temperature (°C)	±0.1
Pressure drop (Pa)	±370
Mass flow rate of refrigerant	±2% Full scale
Heat transfer rate of test section	±2.24%
Heat transfer rate of pre-heater	±2.24%
Heat transfer coefficient	±10%

$$x_{TS,out} = \frac{i_{TS,out} - i_{f@T_{TS,out}}}{i_{fg@T_{TS,out}}} \tag{4}$$

where $i_{\mathrm{TS,out}}$ is the refrigerant enthalpy at the test section outlet, $i_{f@T_{\mathrm{TS,out}}}$ is the enthalpy of the saturated liquid based on the temperature at the test section outlet, and $i_{fg@T_{\mathrm{TS,out}}}$ is the enthalpy of vaporization based on the temperature at the test section outlet. As a consequence, the outlet enthalpy of the refrigerant flow is calculated as:

$$i_{\mathrm{TS,out}} = i_{\mathrm{TS,in}} + \frac{\dot{Q}_{\mathrm{TS}}}{\dot{m}_{\mathrm{ref}}} \tag{5}$$

where the heat transfer rate in the test section is obtained from

$$\dot{Q}_{\mathrm{TS}} = IV \tag{6}$$

with I and V the current and voltage of the electric heater, respectively.

The average heat transfer coefficient can be calculated using the following equation:

$$h_{\mathrm{avg}} = \frac{\dot{Q}_{\mathrm{TS}}}{A_{\mathrm{i}}(T_{\mathrm{i,avg,wall}} - T_{\mathrm{avg,sat}})} \tag{7}$$

where $\dot{Q}_{\mathrm{TS}}$ is the heat transfer rate at the test section, $T_{\mathrm{avg,sat}}$ is the average temperature of the refrigerant at the test section inlet and outlet and A_i is the actual inside surface area of the test section. h_{avg} is the heat transfer coefficient averaged over the entire 2 m long tube. A total of 12 thermocouples are soldered to the outer wall of the tube at the top, bottom, and side (as shown in Fig. 2) at four

positions along the test section to measure the outer wall temperature ($T_{wall,o}$). These outer wall temperatures will be used to determine the inner wall temperatures. At each section, the temperatures at the inside wall of the tube ($T_{wall,i}$) at each position (top, bottom, and side of the tube) are determined based on heat conduction through the wall as follows:

$$T_{i,wall} = T_{o,wall} - \frac{q''_{TS} r_i \ln\left(\frac{r_o}{r_i}\right)}{k} \quad (8)$$

The circumferentially averaged values of the inner wall surface temperatures ($T_{i,avg,wall}$) of the test section are taken as the arithmetical mean of the 12 measurement points as follows:

$$T_{i,avg,wall} = \frac{\sum_{j=1}^{N} T_{i,wall}}{N} \quad (9)$$

The total pressure drop (ΔP_{total}) is measured by a pressure transducer installed between the inlet and outlet of the test section. The total pressure drop is expressed as the sum of the three different components, as follows:

$$\Delta P_{total} = \Delta P_f + \Delta P_a + \Delta P_g \quad (10)$$

The three terms on the right-hand side represent the frictional pressure drop (ΔP_f), acceleration pressure drop (ΔP_a) and gravitational pressure drop (ΔP_g), respectively. The gravitational pressure drop (ΔP_g) is zero in a horizontal tube. The acceleration pressure drop, ΔP_a, is proposed by Tran [8]:

$$\Delta P_a = G^2 \left(\left(\frac{x_{out}^2}{\rho_v \alpha_{out}} + \frac{(1-x_{out})^2}{\rho_l (1-\alpha_{out})} \right) - \left(\frac{x_{in}^2}{\rho_v \alpha_{in}} + \frac{(1-x_{in})^2}{\rho_l (1-\alpha_{in})} \right) \right) \quad (11)$$

where α is the void fraction and presented by Zivi's correlation [9] as follows:

$$\alpha = \left(1 + \frac{(1-x)}{x} \left(\frac{\rho_v}{\rho_l} \right)^{\frac{2}{3}} \right)^{-1} \quad (12)$$

The frictional pressure drop, ΔP_f, can be obtained by subtracting the acceleration pressure drop from the total measured pressure drop.

4 Results and discussion

4.1 Heat transfer coefficient

The comparison of the experimental data with published correlations proposed by Chaddock and Noerager [10], Choi et al. [11] and Wongsa-ngam et al. [12] for smooth tubes is shown in Fig. 4. Most of the correlations are in agreement with the present data to within 20%. How the heat transfer coefficient depends on flow regime, must first be observed. The flow pattern can be seen via sight glasses which are placed on the inlet and outlet of the test section. This observation found that the stratified flow pattern occurred at an average quality lower than 0.3 and the annular flow pattern occurred at an average quality higher than 0.3.

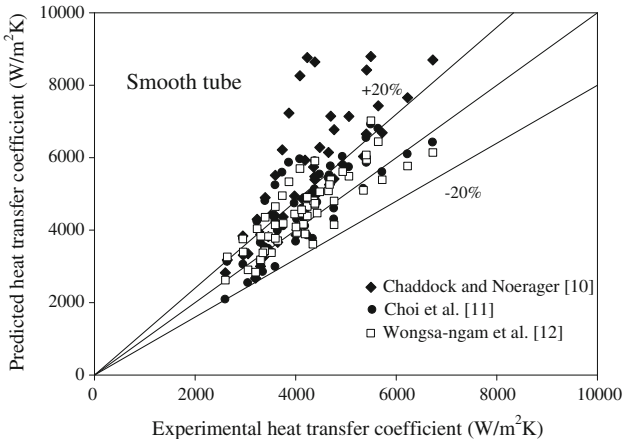

Fig. 4 Comparison of the heat transfer coefficient with existing correlations for the smooth tube

4.1.1 *Local heat transfer coefficient*

The variation of the measured inside wall temperature and refrigerant temperature along the test section (X/L) during evaporation of R-134a in internally grooved tubes at saturation temperatures between 30–32°C, mass flux of 500 kg/m^{2}s, and for different heat fluxes of 5 kW/m^2 (Fig. 5a) and 10 kW/m^2 (Fig. 5b) is shown in Fig. 5. Almost all the inside wall temperatures measured on the grooved tube are higher than those measured on a smooth tube. The results can be described in terms of the liquid film thickness decreasing as thermal resistance decreases. This is due to the fact that a grooved tube strongly increases the swirl flow. Moreover, the refrigerant temperature decreases with increasing (X/L) due to the effect of pressure drop.

Figure 6 illustrates the local heat transfer coefficient along the test section of R-134a during evaporation based on the inside wall temperature and refrigerant temperature obtained from Fig. 5. The result demonstrates that the local heat transfer coefficient gradually decreases with increasing (X/L) due to the effect of the entrance region. In the case of a grooved tube, the local heat transfer coefficient is higher than that obtained from a smooth tube. This is caused by the grooved tube promoting turbulence of the refrigerant flow.

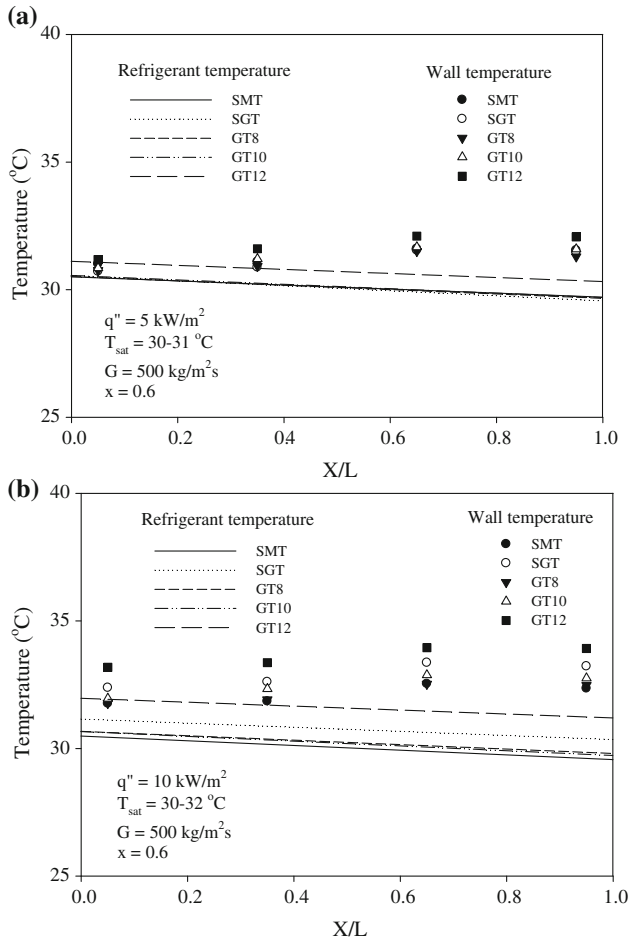

Fig. 5 The variation of the measured inside wall and refrigerant temperature along the test section

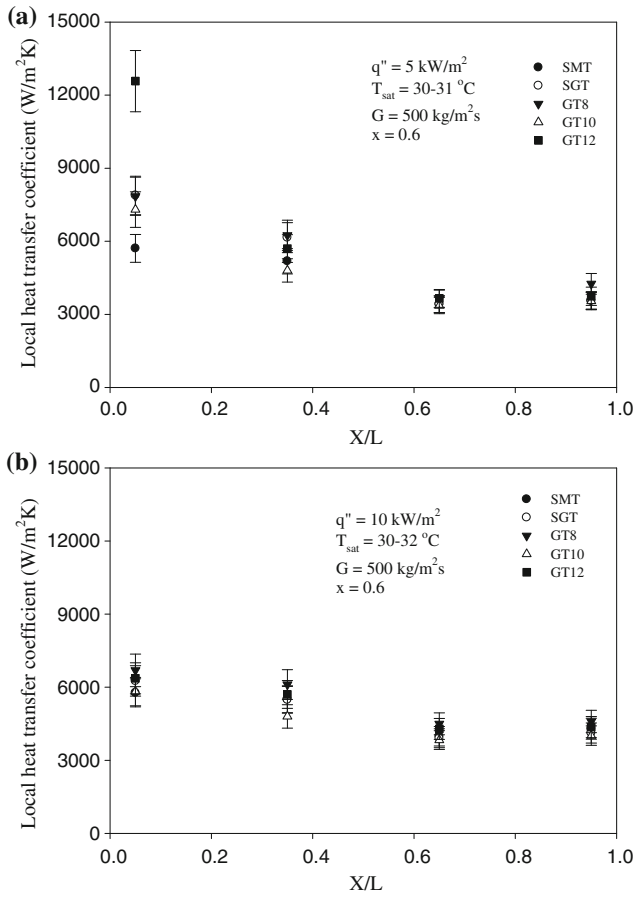

Fig. 6 The local heat transfer coefficient versus the position of the test section

4.1.2 *Effect of groove pitch on average heat transfer coefficient*

Figure 7 shows the variation of average evaporation heat transfer coefficient with average vapour quality of R134a at a saturation temperature of 30°C, mass flux of 500 kg/m^{2}s, and heat fluxes of 5 kW/m^2 (Fig. 7a) and 10 kW/m^2 (Fig. 7b). As shown in the figures, the heat transfer coefficient increase with an increase of average quality. However, at the same average quality, the groove pitch has only a small effect on the heat transfer coefficient. This may be caused by the spiral angles and small groove depth being too small. Similar trends of heat transfer coefficient are obtained under other test conditions.

4.1.3 *Effect of mass flux on average heat transfer coefficient*

Figure 8 shows the heat transfer coefficient as a function of average vapour quality of R-134 at constant saturation temperature and heat flux, for different mass fluxes of 300, 500, and 700 kg/m^{2}s. The results show that the heat transfer coefficient tends to increase with increasing average quality and mass flux. Moreover, the increase of the heat transfer coefficient becomes relatively smaller as the mass flux decreases.

The heat transfer coefficient increases significantly with increasing average vapour quality until the maximum heat transfer coefficient is reached ($x \approx 0.8$), and then decreases with increasing average vapour quality. This is due to dry-out taking place, so the wall temperature becomes higher and the heat transfer coefficient is reduced.

4.1.4 *Effect of heat flux on average heat transfer coefficient*

Figure 9 shows the experimental heat transfer coefficients plotted against average vapour quality at constant mass flux and saturation temperature for the different heat fluxes of 5, 10, 15 kW/m^2. As expected, an increase of heat flux results in an increase of the heat transfer

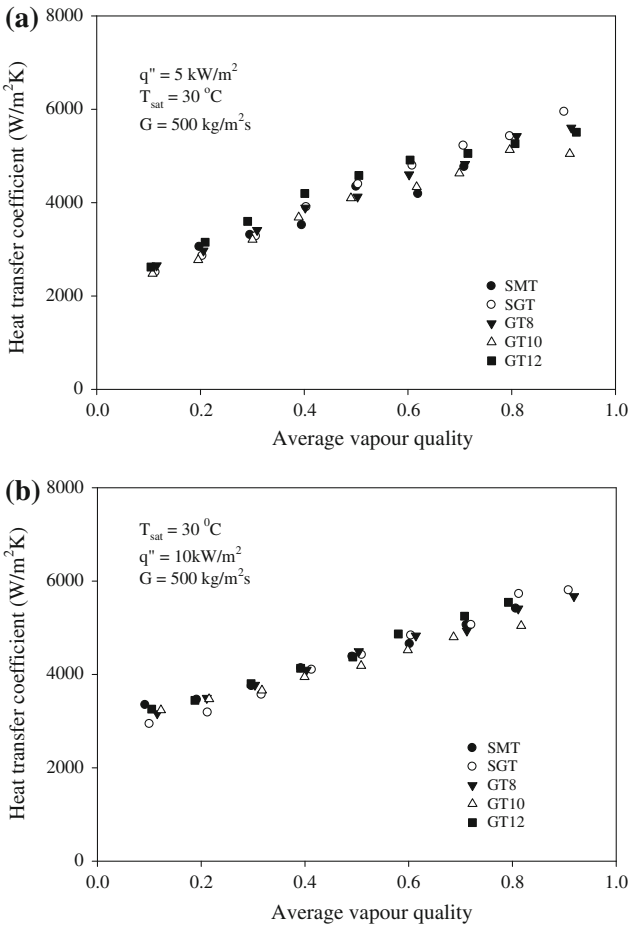

Fig. 7 Effect of groove pitch on average heat transfer coefficient

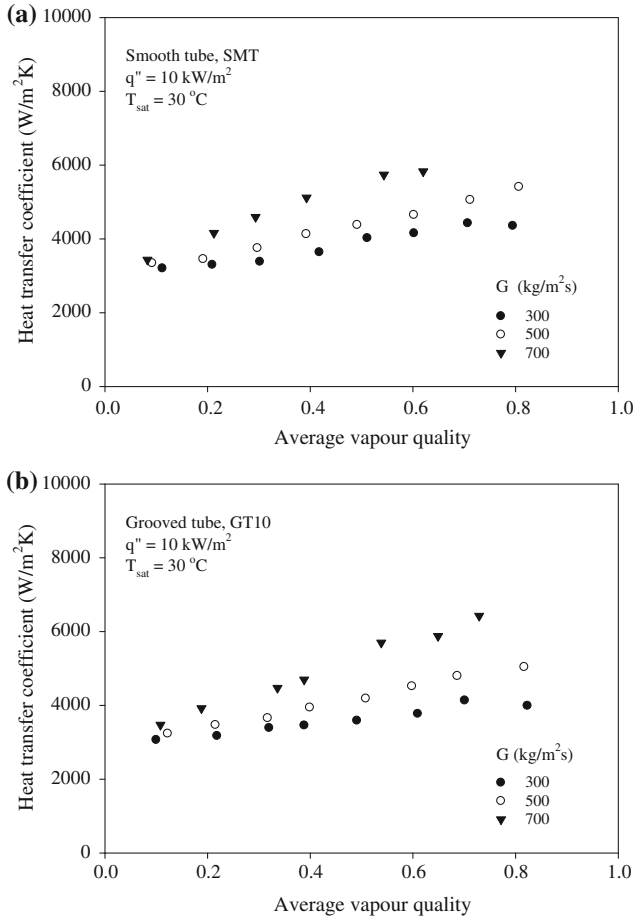

Fig. 8 Effect of mass flux on heat transfer coefficient

coefficients, before dry-out occurs. This can be explained by the increase in heat flux increasing the number of bubbles. These bubbles can induce turbulent flow in the liquid film, which accelerates the two-phase velocity and promotes the entrainment of droplet. On the other hand, the increase in the number of bubbles results in an increased entrainment of droplets and greater turbulence, resulting in a higher heat transfer coefficient.

4.1.5 Effect of saturation temperature on average heat transfer coefficient

Figure 10 presents the variation of heat transfer coefficient versus average vapour quality at constant mass flux and heat flux, for different saturation temperatures of 20, 25, and 30°C, respectively. The heat transfer coefficient increases with increasing saturation temperature across the range of quality. This is due to the evaporating temperature increasing and the two-phase viscosity decreasing. This results in increase of velocity and heat transfer coefficient.

4.2 Frictional pressure drop

The pressure drop is directly measured by the differential pressure transducer installed between the inlet and outlet of the test section. The comparison of the experimental data with well-known correlations proposed by Lockhart-Martinelli [13], Soliman and Azer [14], Friedel [15] and Wongsa-ngam et al. [12], for smooth tubes, is shown in Fig. 11. Most of the correlations are in agreement with the present data to within 30%.

4.2.1 Effect of grooved pitch on frictional pressure drop

Figure 12 shows the variation of the frictional pressure drop with average vapour quality during evaporation of R134a at a saturation temperature of 30°C, mass flux of 500 kg/m^{2}s, and heat fluxes of 5 kW/m^2 (Fig. 12a) and 10 kW/m^2 (Fig. 12b). Similar to the heat transfer coefficient, the frictional pressure drop increases with increasing average quality. At a given average quality, most of the frictional pressure drop in the grooved tube are slightly

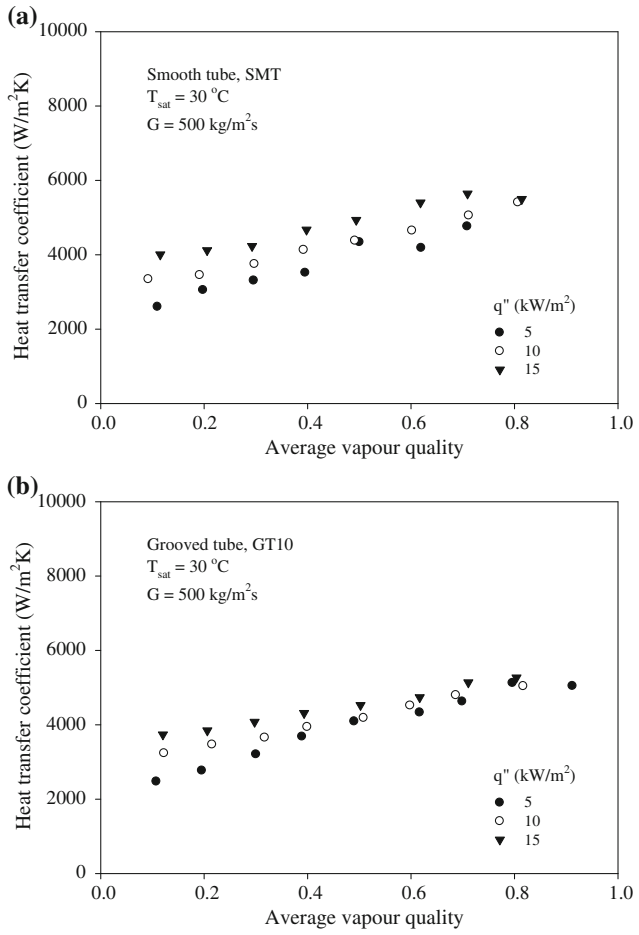

Fig. 9 Effect of heat flux on heat transfer coefficient

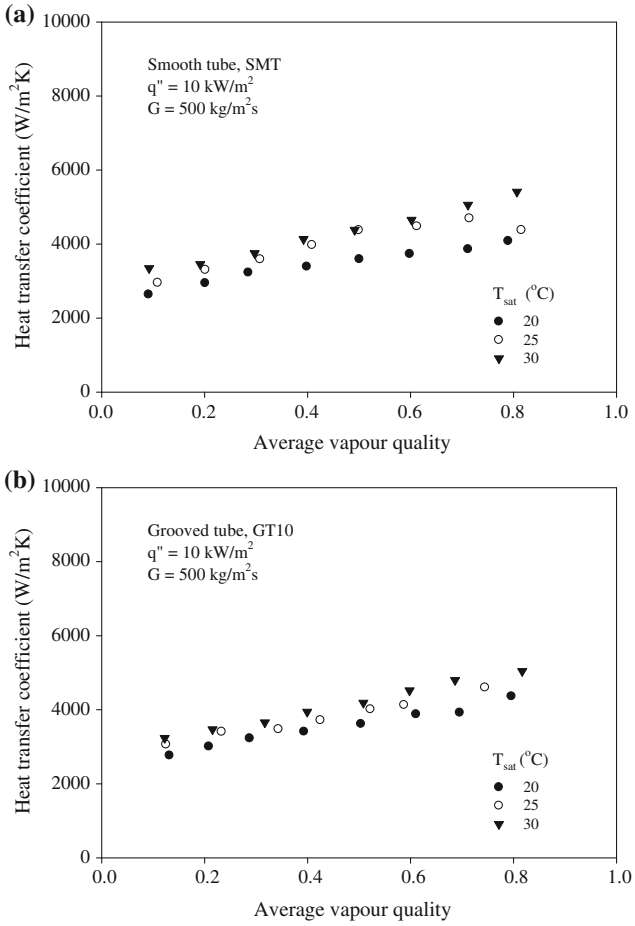

Fig. 10 Effect of saturation temperature on heat transfer coefficient

higher than those measured on the smooth tube. This may result from small differences in spiral angle or small groove depth. Similar trends of frictional pressure drop were found under the other test conditions.

4.2.2 *Effect of mass flux on frictional pressure drop*

Figure 13 shows the frictional pressure drop plotted against average vapour quality at constant saturation temperature and heat flux for mass fluxes of 300, 500, and 700 kg/m^{2}s. As shown, the frictional pressure drop increases with increasing average quality.

4.2.3 *Effect of heat flux on frictional pressure drop*

Figure 14 presents the variation of the measured frictional pressure drop with average vapour quality at mass flux of 500 kg/m^{2}s and saturation temperature of 30°C for heat fluxes of 5, 10 and 15 kW/m^2. These figures show that the frictional pressure drop increases significantly with increasing quality until the maximum frictional pressure drop is reached, and then reduces. Furthermore, it is also found that the heat flux has no significant effect on frictional pressure drop. This is because the increase in total rate of liquid film vaporization close to the wall surface is very small compared with the vapour flow rate at the inlet.

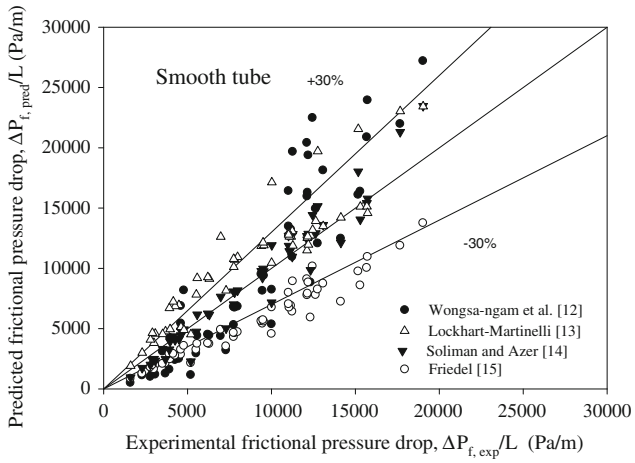

Fig. 11 Comparison of the experimental frictional pressure drop with existing correlations for the smooth tube

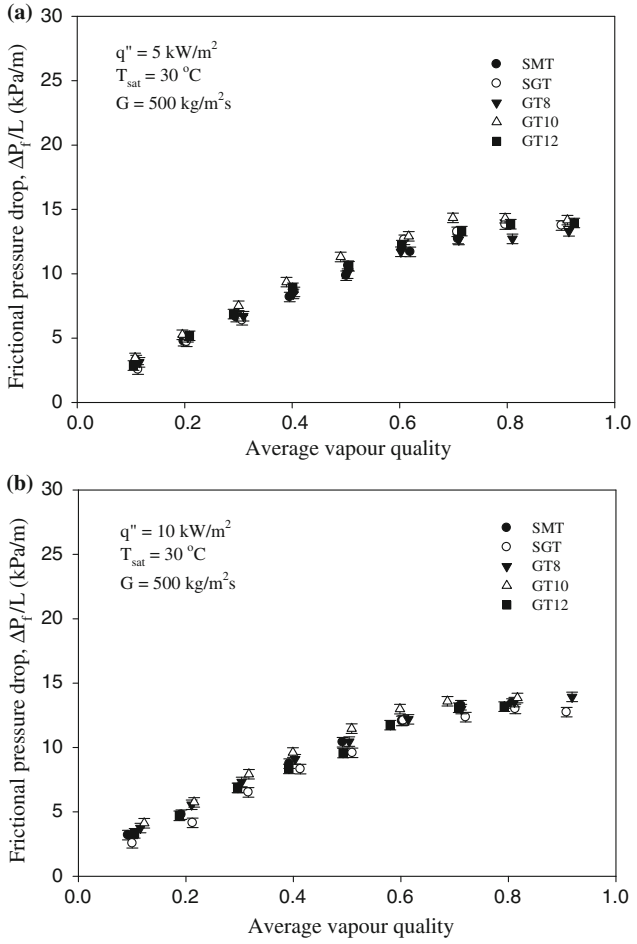

Fig. 12 Effect of grooved pitch on frictional pressure drop

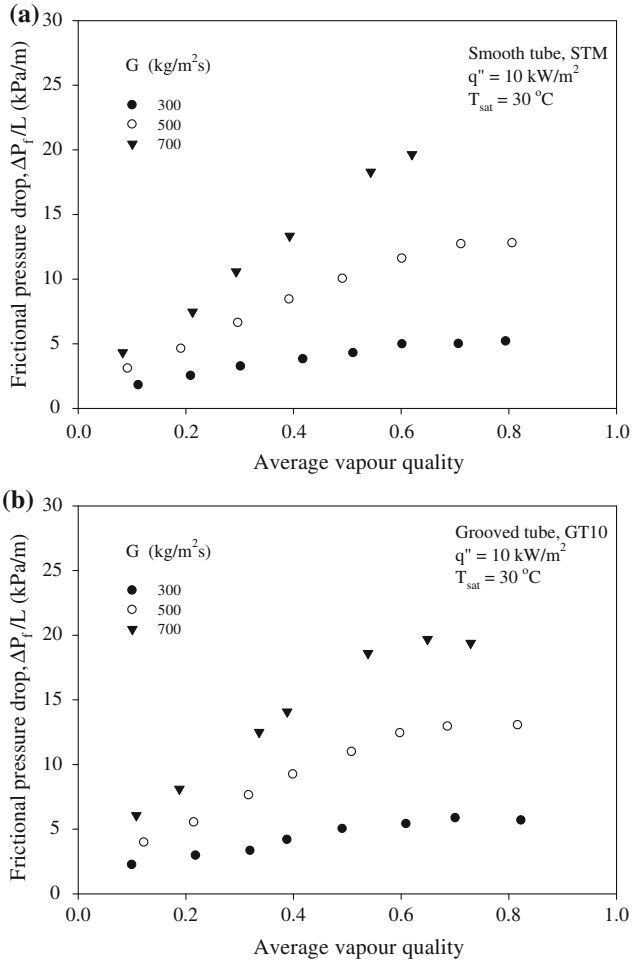

Fig. 13 Effect of mass flux on frictional pressure drop

4.2.4 Effect of saturation temperature on frictional pressure drop

Figure 15 shows the variation of frictional pressure drop versus average vapour quality at constant heat flux and mass flux for different saturation temperatures of 20, 25 and 30°C. It is found that the frictional pressure drop increases with a decrease in evaporation temperature. This is mainly due to a decrease in two-phase specific volume which results in a decrease in the velocity of the refrigerant.

5 Conclusions

In this work, the heat transfer coefficient and frictional pressure drop in grooved tubes during evaporation of R-134a were investigated experimentally. The tested tube configurations are as follows: smooth tube (SMT); straight grooved tube (SGT); grooved tube with 8″ pitch (GT8); grooved tube with 10″ pitch (GT10); and grooved tube with 12″ pitch (GT12). The tested tubes are made from type 304 stainless steel. The local heat transfer coefficient along the test section with (X/L) is presented. Moreover, the effects of groove pitch, mass flux, heat flux, and saturation temperature on the heat transfer coefficient and pressure drop are discussed. The ranges of mass flux, saturation temperature and heat flux studies were 300–700 kg/m^{2}s, 20–30°C and 5–15 kW/m^2, respectively. The important experimental results are concluded as follows:

1. The local heat transfer coefficient of R134a fluid during evaporation decreases with increasing (X/L), and is affected significantly by groove pitch.
2. The average heat transfer coefficient increases with increasing average quality, mass flux, and heat flux, but is little affected by groove pitch.
3. The frictional pressure drop increases with increasing average quality and mass flux, but decreases with increasing saturation temperature. Also, the heat flux has no significant effect on frictional pressure drop.

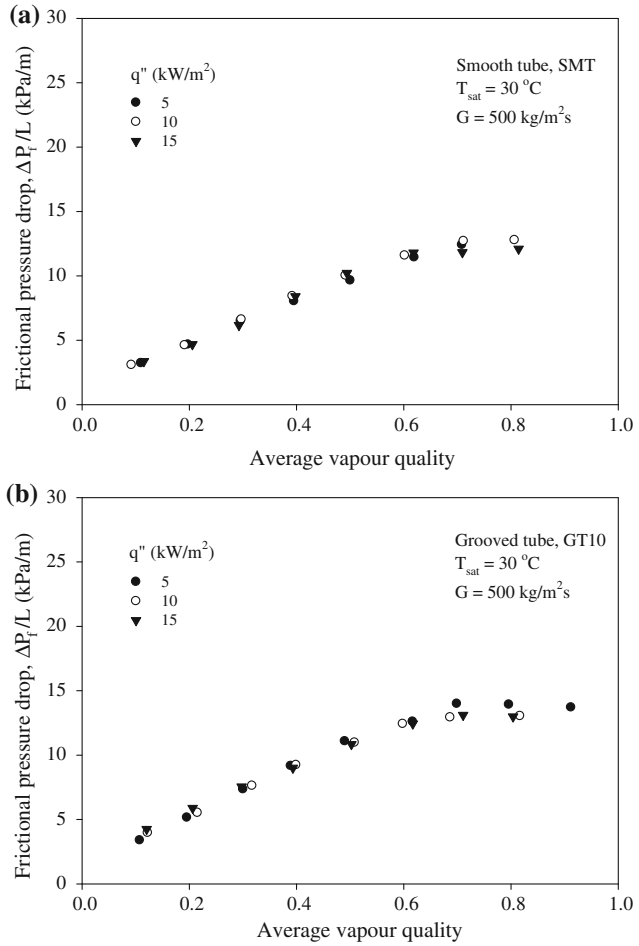

Fig. 14 Effect of heat flux on frictional pressure drop

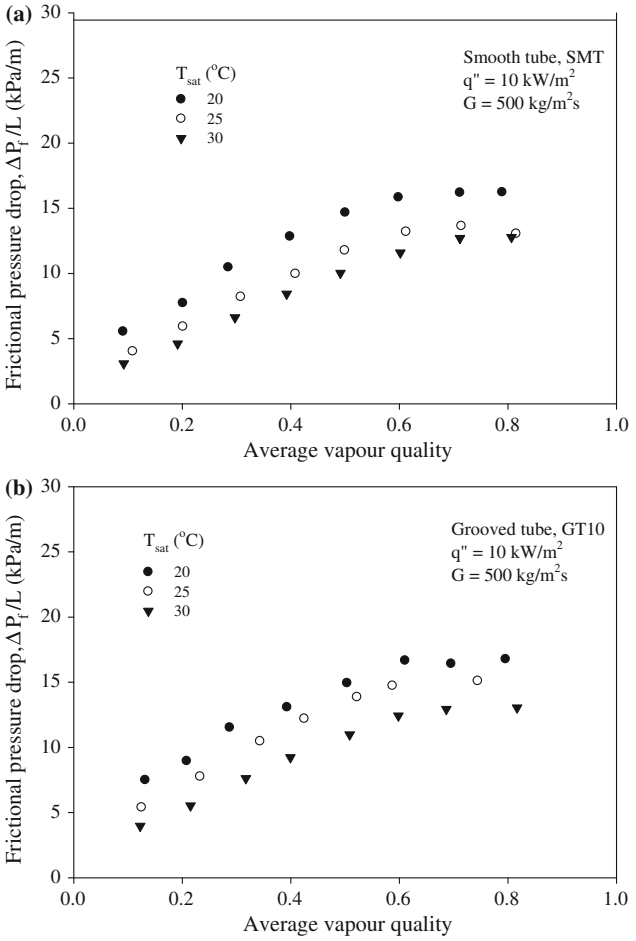

Fig. 15 Effect of saturation temperature on the frictional pressure drop

Finally, the frictional pressure drop increases slightly with increasing groove pitch.

Acknowledgments The present study was supported financially by the Thailand Research Fund (TRF), the Office of the Higher Education Commission and the National Research University Project, whose guidance and assistance are gratefully acknowledged. The authors also wish to acknowledge Thai-German Products Public Company Limited for providing the test tubes.

References

1. International Institute of Refrigerant (1997) 12th Informatory Note on Fluorocabons and Refrigeration
2. Herman C, Kang E (2002) Heat transfer enhancement in a grooved channel with curved vanes. Int J Heat Mass Transfer 45:3741–3757
3. Bilen K, Cetin M, Gul H, Balta T (2009) The investigation of groove geometry effect on heat transfer for internally grooved tubes. Appl Thermal Eng 29:753–761
4. Bharadwaj P, Khondge AD, Date AW (2009) Heat transfer and pressure drop in a spirally grooved tube with twisted tape insert. Int J Heat Mass Transfer 52:1938–1944
5. Graham D, Chato JC, Newell T (1999) Heat transfer and pressure drop during condensation of refrigerant 134a in an axially grooved tube. Int J Heat Mass Transfer 42:1935–1944
6. Goto M, Inoue N, Yonemoto R (2003) Condensation heat transfer of R410A inside internally grooved horizontal tubes. Int J Refrig 26:410–416
7. Zhang X, Zhang X, Chen Y, Yuan X (2008) Heat transfer characteristics for evaporation of R417A flowing inside horizontal smooth and internally grooved tubes. Energy Convers Managet 49:1731–1739
8. Tran TN (1998) Pressure drop and heat transfer study of two-phase flow in small channels. Ph.D. Dissertation, Texas Tech University, Lubbock
9. Zivi SM (1964) Estimation of steady-state steam void-fraction by mean of the principle of minimum entropy production. Trans ASME J Heat Transfer 86:247–252
10. Chaddock JB, Noerager JA (1966) Evaporation of refrigerant 12 in a horizontal tube with constant wall heat flux. ASHRAE Trans 72:90–101
11. Choi TY, Kim YJ, Kim MS, Ro ST (2000) Evaporation heat transfer of R-32, R-134a, R-32/134a, and R-32/125/134a inside a horizontal smooth tube. Int J Heat Mass Transfer 43:3651–3660
12. Wongsa-ngam J, Nualboonrueng T, Wongwises S (2004) Performance of smooth and micro-fin tubes in high mass flux region of R-134a during evaporation. Heat Mass Transfer 10:425–435

13. Lockhart RW, Martinelli RC (1949) Proposed correlation of data for isothermal two-phase, two-component flow in pipes. Chem Eng Prog 45:39–48
14. Soliman HM, Azer NZ (1971) Flow patterns during condensation inside a horizontal tube. ASHRAE Trans 77:210–224
15. Friedel L (1979) Improved friction pressure drop correlations for horizontal and vertical two-phase pipe flow. The European Two-Phase Flow Group Meeting, Paper E2. Ispra, Italy

Applied Mathematics and Computation 217 (2011) 8640–8654

Contents lists available at ScienceDirect

Applied Mathematics and Computation

journal homepage: www.elsevier.com/locate/amc

Study of storm surge due to Typhoon Linda (1997) in the Gulf of Thailand using a three dimensional ocean model

N. Aschariyaphotha [a,b], P. Wongwises [a], U.W. Humphries [b], S. Wongwises [c,*]

[a] The Joint Graduate School of Energy and Environment, King Mongkut's University of Technology Thonburi, Bangkok 10140, Thailand
[b] Department of Mathematics, King Mongkut's University of Technology Thonburi, Bangkok 10140, Thailand
[c] Department of Mechanical Engineering, King Mongkut's University of Technology Thonburi, Bangkok 10140, Thailand

ARTICLE INFO

Keywords:
Gulf of Thailand
Three dimensional ocean model
Storm surge
Typhoon Linda

ABSTRACT

Numerical integrations using the three dimensional ocean model based on the princeton ocean model (POM) were applied for the study of both sea level elevation and ocean circulation patterns forced by the wind fields during typhoons that moved over the Gulf of Thailand (GoT). The simulation concerned a case of Typhoon Linda which occurred during November 1–4, 1997. Typhoon Linda was one of the worst storms that passed the Gulf of Thailand and hit the southern coastal provinces of Thailand on November 3, 1997. It caused flooding and a strong wind covering large areas of agriculture and fisheries, which destroyed households, utilities and even human lives. The model is the time-dependent, primitive equation, Cartesian coordinates in a horizontal and sigma coordinate in the vertical. The model grid has 37×97 orthogonal curvilinear grid points in the horizontal, with variable spacing from 2 km near the head of the GoT to 55 km at the eastern boundary, with 10 sigma levels in the vertical conforming to a realistic bottom topography. Open boundary conditions are determined by using radiation conditions, and the sea surface elevation is prescribed from the archiving, validation and interpretation of satellite oceanographic data (AVISO). The initial condition is determined from the spin up phase of the first model run, which was executed by using wind stress calculated from climatological monthly mean wind, restoring-type surface heat and salt and climatological monthly mean freshwater flux. The model was run in spin up phase until an ocean model reached an equilibrium state under the applied force. A spatially variable wind field taken from the European Centre for Medium-Range Weather Forecasts (ECMWF) is used to compute the wind stress directly from the velocity fluctuations. Comparison of tendency between the sea surface elevations from model and the observed significant wave heights of moored buoys in the Gulf of Thailand under Seawatch project is investigated. The model predicts the sea level elevation up to 68.5 cm at the Cha-Am area located in the north of where the typhoon strands to the shore. Results of sea level elevation show that there is an area of peak set-up in the upper gulf, particularly in the western coast, and the effects of the storm surge are small at the lower gulf. During the entire period of this study, the surge in the gulf was induced by the northeasterly wind blowing over it.

1. Introduction

The Gulf of Thailand is located in Southeast Asia immediately to the west of the South China Sea (SCS). The gulf is a semi-enclosed sea that measures approximately 400- km by 800- km, covering an area of about 320,000 square km. Its location in

* Corresponding author.
E-mail address: somchai.won@kmutt.ac.th (S. Wongwises).

0096-3003/$ - see front matter © 2011 Elsevier Inc. All rights reserved.
doi:10.1016/j.amc.2011.03.105

the global map is between 6°N to 14°N latitudes and 99°E to 105°E longitudes surrounded by the kingdom of Cambodia, Malaysia, the kingdom of Thailand and the socialist republic of Vietnam (Fig. 1). It is a part of the sunda shelf which is a submerged connection between Southeast Asia, Malaysia, Sumatra, Java and Borneo, and is relatively shallow. The mean and maximum depths in the central part in the GoT are about 45 m and 80 m respectively. The living and non-living resources of the gulf are of great value to the people of four littoral countries.

The Gulf of Thailand is subjected to the monsoon system of the Western North Pacific Ocean or the South China Sea. Monsoons influence the surface currents, being clockwise during the southwest monsoon and counterclockwise during the northeast monsoon. There are several POM-based studied in the SCS connected to the GoT e.g. Yang et al. [5] used the POM to study the seasonal mean SCS circulation and its formation mechanisms. It reproduced well the observed sea surface height (SSH) annual cycle, and the sensitivity experiments show that the wind forcing dominates the seasonal variability of the SCS SSH, while the buoyancy forcing is of minor importance. The model also indicated that the Kuroshio current affects the SCS circulation by creating a loop current that exists throughout the year. Gan et al. [6] had studied the circulation and its seasonal variation in the SCS in response to the forcing of the Asian monsoon and the Kuroshio intrusion by using a three-dimensional ocean model. They found that the seasonal circulation in the SCS is mainly driven by the monsoonal wind stress and greatly influenced by the inflow from the Kuroshio intrusion.

Chu et al. [10] used POM to simulate the circulation and thermohaline variability for the SCS covering the GoT. They verified that the wind effect is the key factor for the generation of the SCS deep basin warm/cool eddy and that the lateral boundary forcing is the major factor for the formation of the strong western boundary currents. Afterwards, Chu et al. [11] simulated the SCS thermohaline structure, as well as the circulation, and investigated physical processes causing seasonal variability by using POM. They revealed that the POM model has the capability for simulating seasonal variations of the SCS circulation and thermohaline structure. The simulated SCS surface circulation is generally clockwise during the summer, and counterclockwise during the winter monsoon period with the strong western boundary currents.

In the early 1960's, a Typhoon name was not recorded for one that hit the Laem Talumpuk area located in Nakhon Si Thammarat province. This event was not announced in advance, hence it devastated human life and utilities. In 1989, Typhoon Gay originated in the southern part of GoT as a depression and then strengthened quickly to become a tropical storm. Typhoon Gay caused storm surge and enormous damage on the coast of Chumphon province and neighboring areas. Typhoon Linda in 1997 also caused a storm surge. Typhoon Linda, which formed in a westward pattern in the SCS, was one of the worst storms to hit Vietnam. Southern Vietnam was devastated by Typhoon Linda during the first two days of November 1997. The rapid development of the storm in the East Sea not far from the Vietnamese coast

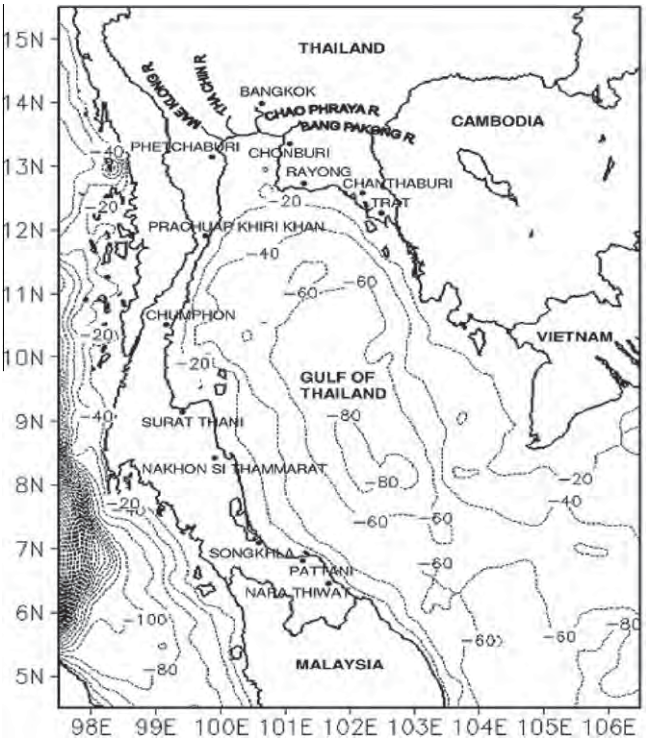

Fig. 1. Bathymetry (m) of the Gulf of Thailand.

meant that there was little time for warnings to be issued and acted upon. Over 600 people are known to have died in the storm's passing. Typhoon Linda, shown in Fig. 2, moved across the southern tip of Vietnam and was expected to hit Thailand's southern coastal provinces on November 3, 1997. When the storm passed over the southernmost coast of Vietnam it was estimated that the winds were reaching 28 ms^{-1} through the Gulf of Thailand, winds at its center were still over 25 ms^{-1}. As the storm tracked west through the Gulf of Thailand into the Bay of Bengal, it continued to wreak destruction, killing over 30 people in Cambodia and Thailand with around 200 fishermen reported missing. At least 330 people were killed in Vietnam and Thailand with approximately 2,250 people still missing. Regardless of its causes, Typhoon Linda demonstrated that even with a highly developed civil protection system, many thousands of individuals remain at risk when the warning time is limited by rapid storm development. Improved monitoring and prediction of storms such as Typhoon Linda must be a high priority.

Very few researches have been made about Typhoon Linda and its storm surge in the GoT. Schjølberg [12] used the Seawatch 3D model which is the three dimension model in vertical sigma coordinate developed in cooperation with Putch Company for studying the Typhoon Linda case. The research was run by two simulations, one with only the wind field forcing and another one with both wind and tide. The open boundary was applied by tidal forcing and used about 3 days of simulation before the typhoon actually entered the GoT in the sense of to spin up circulation. The model using the atmospheric forcing predicted the increase in sea level less than using the tidal forcing, and the result of the current speed compared with the buoy observation. Schjølberg concluded that the event quite well described when the Typhoon passed, although the maximum speed is underestimated by the model. In 2001, Kanbua et al.[20] used the wave analysis model (WAM), a third generation wave model, to forecast the significant wave height during the attack of Typhoon Linda in 1997 in the GoT. The WAM model is one of the best-tested wave models. Their results were also compared with the buoy observation in the Gulf of Thailand and Andaman Sea under the Seawatch project. The results indicated that the model fairly reproduces the observed characteristics of waves. Kanbua et al. [21] studied an investigation of wave field during Typhoon Linda in the GoT by two modeling approaches which were the WAM cycle 4.0 and the general regression neural network (GRNN) model. The results showed that the WAM model underestimates the wave height as much as 20%, while The GRNN gave the better forecasting results than the WAM model. They concluded that for short-term prediction within 24 h, the data-driven model, such as the GRNN, should be viewed as a strong alternative in operational forecasting.

The objective of this paper is to simulate the sea level and the ocean circulation patterns during the attack of Typhoon Linda for the GoT by using the POM model. In this paper, the focus is on how much of the surge generated due to meteorological forcing (wind forcing fields) and where the wind forcing fields affect the sea water elevation. During the entire period of this research, the northeasterly wind field was continuous and significant for determination of the sea level and ocean circulation patterns. The effects of atmospheric pressure differences are negligible. Consequences of difference parameter are presented along with the results of simulations illustrated in terms of sea surface elevations and sea surface anomalies. In this research, there are no observations of the sea surface height of the GoT to compare with the model results. The contents study only the effects of the Typhoon passing and illustrated the application of the three dimensional oceanic model. Comparison of tendency between the sea surface elevations from the model and the observed significant wave heights of moored buoys in the GoT under Seawatch project is investigated.

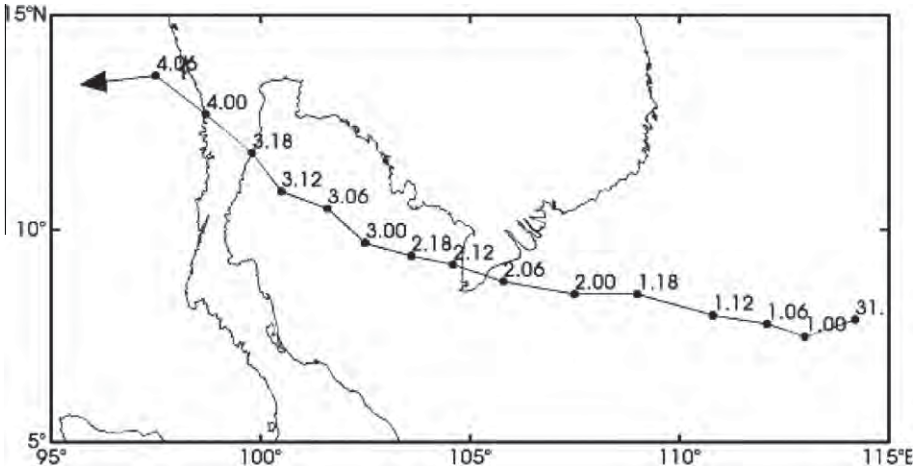

Fig. 2. The track of Typhoon Linda [18].

2. Model description

POM model is the time-dependent, primitive equation model formulated in Cartesian coordinates and vertical sigma coordinates. The model has been applied to simulate the storm surge and current patterns in the GoT. The model includes hydrostatic and Boussinesq approximations, realistic topography, a second-order turbulence closure model [4], horizontal diffusivity coefficients calculated by the Smagorinsky parameterization [7] and splitting modes, but the model does not include tidal forcing and river outflow. The Smagorinsky form of the horizontal viscosity is used to obtain a significantly smoother flow field which could be resolved on a model grid.

2.1. Three dimensional ocean model

Two approximations are used; first is the hydrostatic assumption, and second is the Boussinesq approximation [8]. The basic equations consist of the continuity, momentum, hydrostatic, temperature, salinity, density and by assuming that the ocean is incompressible.

In order to save computational time, the equations can be solved by the mode splitting method [13,17]. This method involves separating out the external (vertically averaged) and the internal (three dimension) modes and solving each of them separately at appropriate time steps. The vertical averaged currents (barotropic) are defined by:

$$\bar{u} = \int_{-1}^{0} u d\sigma \quad \text{and} \quad \bar{v} = \int_{-1}^{0} v d\sigma, \tag{2.1}$$

where u and v are the corresponding current components in the eastward and northward respectively. The value of σ ranges from $\sigma = 0$ at $z = \eta$ to $\sigma = -1$ at $z = -H(x,y)$, where $H(x,y)$ is the bottom topography, and η is the sea surface elevation. The barotropic equations are:

$$\frac{\partial \bar{u}D}{\partial x} + \frac{\partial \bar{v}D}{\partial y} + \frac{\partial \eta}{\partial t} = 0, \tag{2.2}$$

$$\frac{\partial \bar{u}D}{\partial t} + \frac{\partial \bar{u}^2 D}{\partial x} + \frac{\partial \bar{u}\bar{v}D}{\partial y} - \widetilde{F}^x - f\bar{v}D + gD\frac{\partial \eta}{\partial x} = - < wu(0) > + < wu(-1) > + G_x - \frac{gD}{\rho_0}\int_{-1}^{0}\int_{\sigma}^{0}\left(D\frac{\partial \rho'}{\partial x} - \sigma'\frac{\partial \rho'}{\partial \sigma'}\frac{\partial D}{\partial x}\right)d\sigma' d\sigma, \tag{2.3}$$

$$\frac{\partial \bar{v}D}{\partial t} + \frac{\partial \bar{u}\bar{v}D}{\partial x} + \frac{\partial \bar{v}^2 D}{\partial y} - \widetilde{F}^y + f\bar{u}D + gD\frac{\partial \eta}{\partial y} = - < wv(0) > + < wv(-1) > + G_y - \frac{gD}{\rho_0}\int_{-1}^{0}\int_{\sigma}^{0}\left(D\frac{\partial \rho'}{\partial y} - \sigma'\frac{\partial \rho'}{\partial \sigma'}\frac{\partial D}{\partial y}\right)d\sigma' d\sigma, \tag{2.4}$$

where $D = H + \eta$; t is time; ρ_0 is a reference density of the ocean; ρ is the density of sea water given by UNESCO [19]; $f = 2\Omega\sin\theta$ is the Coriolis parameter; Ω is the angular speed of the earth's rotation (7.2921×10^{-5} rad s^{-1}); g is magnitude of gravitational acceleration; the terms ($<wu(0)>$, $<wv(0)>$) and ($<wu(-1)>$, $<wv(-1)>$) are the transformed surface and bottom stresses (the stress components are opposite in sign) respectively. The terms $G_x, G_y, \widetilde{F}^x$ and $\widetilde{F}^y$ represent the horizontal viscosity and diffusion terms.

For the model grid, the rectangular horizontal grid was replaced by an orthogonal curvilinear grid to improve coastline representations with 37×97 horizontal grid points, as shown in Fig. 3. The horizontal grid spacing has ranged from 2 to 55 km. The vertical sigma coordinate has 10 levels. Aschariyaphotha et al. [9] has described the techniques that generate the model grid and interpolated the initial data by using cubic spline and bilinear interpolations.

2.2. Initialization

The bathymetry for the model was derived from the digital bathymetric data base 5- min (DBDB5) binary data file developed by the Naval Oceanographic Office (NAVOCEANO) with 1/12 degree longitude-latitude grided resolution. The numerical model integration was divided into spin up and simulation phases. In the spin up phase of the model run, the model was integrated with all three components of velocity initially set to zero, while the temperature and salinity were indicated by interpolating climatological monthly mean fields from Levitus94 [14,15] to the model grid. The spin up phase of the first model run was executed using wind stress calculated from climatological monthly mean wind, restoring-type surface temperature and salinity and climatological monthly mean freshwater flux taken from the European Centre for Medium-Range Weather Forecasts (ECMWF). The drag coefficient for wind stress (C_D) suggested by Matthias and Godfrey [16] is used in this paper. The C_D is calculated by

$$C_D = Min\{0.001 + 0.00007|\vec{V}_a|, 0.0025\}. \tag{2.5}$$

For spin up phase of the first model run, the wind velocities, $\vec{V}_a$, were taken from ECMWF climatological monthly mean wind velocity measured from 10 m above the sea surface.

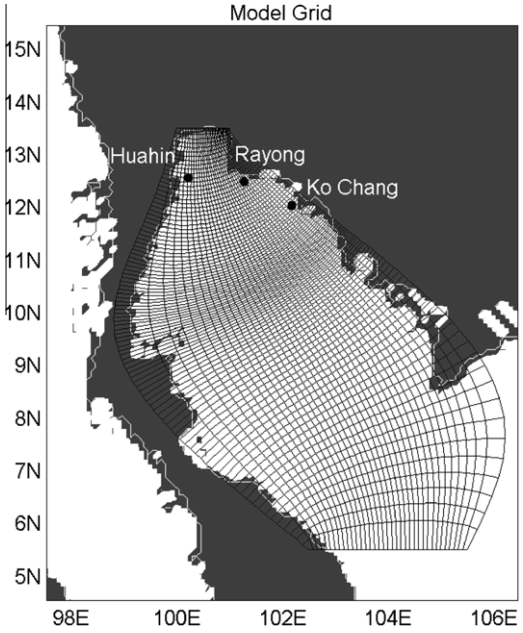

Fig. 3. The curvilinear model grid and three buoy locations in the Gulf of Thailand.

On the bottom of the gulf, the normal gradients of T and S are zero. Nevertheless there is an additional bottom friction force depending on the velocity adjacent to the boundary. A coefficient of bottom friction, C_z, will increase in value when wave effects are presented. This value taken from Blumberg and Mellor [1] can be obtained from the following expression:

$$C_z = Max\left\{\frac{\kappa^2}{\left[\ln\left\{\frac{(1+\sigma_{kb-1})H}{z_0}\right\}\right]^2}, 0.0025\right\}, \tag{2.6}$$

where κ is the Von Kraman constant; H is the bottom topography; kb is the total number of sigma vertical level, and z_0 is the bottom roughness parameter. In this paper, κ is taken to be 0.4, while $z_0 = 0.01$ m is used from Weatherly and Martin [2].

A radiation type of condition prescribes the normal currents across the open sea boundaries. As usual it is assumed that the motion in the sea is generated from an initial state of rest. Along the open boundaries the radiation conditions were applied

$$\frac{\partial}{\partial t}(T,S) + U_n\frac{\partial}{\partial n}(T,S) = 0, \tag{2.7}$$

where the subscript n is the direction normal to the boundary. The velocities and elevations at the open lateral boundary may be taken from observations if observed current and elevation data are available. In this paper, the boundary conditions of sea surface elevation are prescribed from You's model results [22]. The velocities at the open lateral boundary when inflow occur are calculated from the radiation condition for the $u-$ component and $v-$ component [3] as follows:

$$\frac{\partial u}{\partial t} \pm c_i\frac{\partial u}{\partial x} = 0, \tag{2.8}$$

$$\frac{\partial v}{\partial t} \pm c_i\frac{\partial v}{\partial y} = 0, \tag{2.9}$$

where c_i is the baroclinic phase speed.

In this paper, You's model outputs [22] are used as the value at the open boundary for the velocity. His model was run for simulating the circulation in the SCS covering the GoT with model resolution $1.125^\circ \times 1.125^\circ$ and $z-$ coordinate in the vertical. These data have been interpolated to the model grid. The model domain has two open boundaries, i.e. eastern boundary and southern boundary. At the eastern boundary the $u-$ component of the velocities was calculated from the radiation condition, and the $v-$ component was prescribed from You's results, while at the southern boundary the $u-$ component of the velocities was prescribed from You's results, and the $v-$ component was calculated from the radiation condition. The lateral boundary values of velocity and elevation taken from You's results are gradually increased from zero to the full values over the first 1/3 of a total runtime. The model was run with internal time step 900 s and 30 s for external time step until all variables were stable under the applied force. The results from this run were used as the initial data for simulation of storm surge, and the sea surface elevations and currents assumed to be the climatological value.

After spin up phase, the initial data for typhoon Linda simulation was wind field measured from 10 m above sea surface provided by ECMWF. The 6- h wind fields were taken from the period 00UTC on October 31 to 18UTC on November 7, 1997 with 1.125×1.1213 degree longitude-latitude grid resolution, and were interpolated by using cubic spline and bilinear interpolations to specify wind components at the model grid point. The sea surface elevation is prescribed from the AVISO sea surface height data.

2.3. Integration

The computation starts at 00UTC on October 31 and ends at 23UTC on November 7, 1997. The wind forcing field was added every 6 h, and the results were saved every one hour. Time steps used in this phase for the Typhoon Linda event were the internal time step 300 s and 10 s for the external time step.

3. Wind of Typhoon Linda

Fig. 4 shows the time series of the observed atmospheric pressure taken from ECMWF at the central part of the GoT (102.5°E, 10°N) and the typhoon's core passing. For Typhoon Linda, the atmospheric pressure in the center of the typhoon was only of the order of 10 hPa which is less than from the surroundings, consequently the effect from the pressure was very small. In addition, the GoT is shallow; the main effect is due to the strong wind stress. The effects of atmospheric pressure differences are negligible in this paper. The intense winds cause the sea water to pile up on the coast, leading to sudden inundation and flooding of coastal regions.

The availability of a wind field allows us to access how much and where the wind affects the sea levels in the gulf. The 6- h atmospheric wind fields during the Typhoon Linda period of from 00UTC on October 31 to 18UTC on November 7, 1997 shown in Fig. 5 were used to investigate the generated storm surge. These wind fields were obtained from ECMWF with 1.125×1.1213 degree longitude-latitude grid resolution. The wind in this event was a northeasterly wind. Typhoon Linda moved passing the southern tip of Vietnam on November 2. There is a strong counterclockwise wind circulation influenced by the northeasterly monsoon. The Typhoon moved into the GoT on the next day with the wind speed approximately 11.8 ms^{-1}, and then moved passing the center of the gulf with a speed of 12.7 ms^{-1}. At 18UTC on November 3, it was moving to the west and was approaching toward Huahin area with a maximum wind speed of 15.5 ms^{-1}. It was very close to Huahin 6 h later with the wind speed increasing up to 16.3 ms^{-1}, and then it moved passing further to the Bay of Bangal. The wind speed reduced after the Typhoon passed across the gulf.

4. Results

Although a three dimensional model is necessary to examine wind induced currents in the majority of storm surge calculations, the main emphasis is on changes in sea surface elevations and two dimensional models are used by Eqs. (2.2)–(2.4). For the results from the model run we will examine the time series of currents and sea surface elevations at only a limited number of locations, and consider for the whole GoT at the time during when the surge occurred. Three buoys, i.e. Huahin, Rayong and Ko Chang, located at the upper part of the gulf, as shown in Fig. 3, collected the significant wave height, so the simulated results at these three locations are examined. The positions of Huahin, Rayong and Ko Chang buoys are (100.17°E, 12.52°N), (101.23°E, 12.51°N) and (102.21°E, 12°N) respectively.

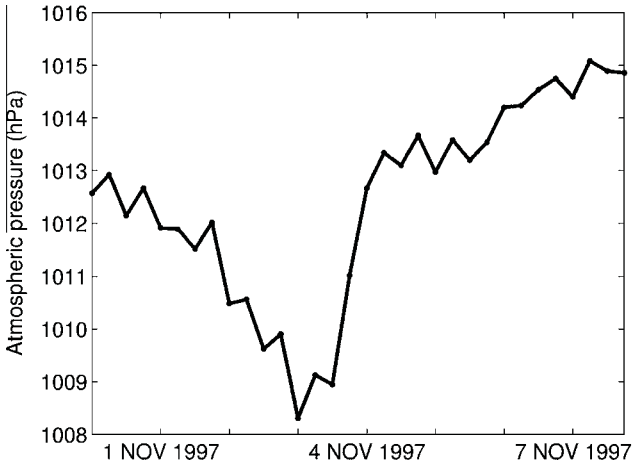

Fig. 4. The time series of the observed atmospheric pressure at point (102.5°E, 10°N).

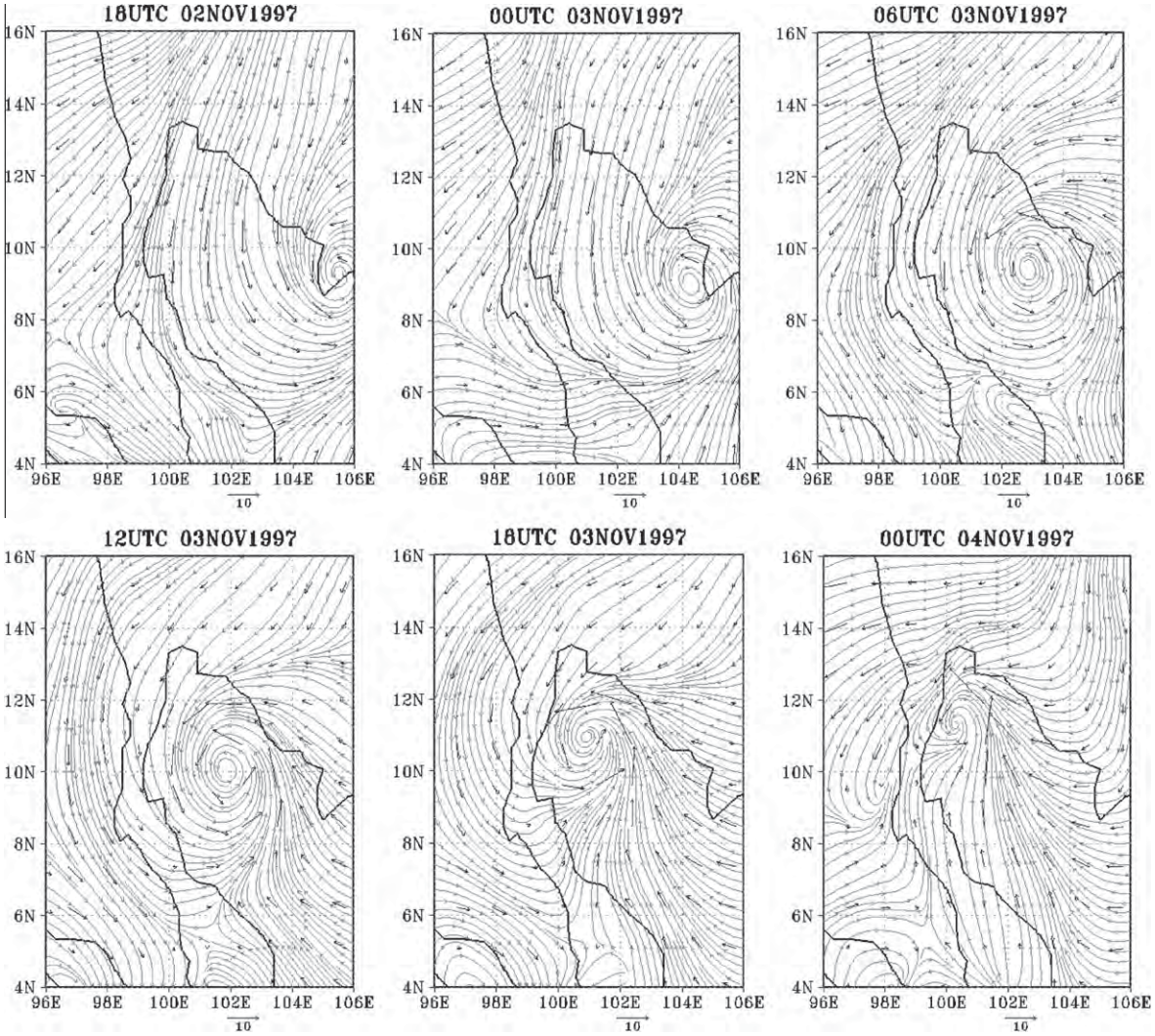

Fig. 5. The observed 6- h wind fields (ms^{-1}) of 18UTC on November 2 to 00UTC on November 4, 1997.

4.1. Determinations of drag coefficient

The formula of drag coefficient due to Matthias and Godfrey [16], which emphasize the dependency on wind speed, has been often used in oceanic models. On the other hand, the models with a constant drag coefficient have been mostly used for determination of the design heights of the sea level. For determining C_D, it may be appropriate to calculate wind stress and to produce sea surface elevation. In this paper, the observed sea surface anomaly on November 5, 1997 was used to determine the appropriate value of the drag coefficient. Fig. 6 shows the observed sea surface anomaly on November 5, 1997 taken from AVISO. The simulated sea surface anomalies on November 5 calculated using the drag coefficient as 1.3×10^{-3}, depending on the wind speed and 2.5×10^{-3} are shown in Fig. 7. The sea surface anomaly from the cases carried out using a constant drag coefficient, 1.3×10^{-3} and 2.5×10^{-3}, are compared with those using the drag coefficient depending on the wind speed. Using 1.3×10^{-3} for C_D gives a tendency to underestimate the sea surface anomaly, while using 2.5×10^{-3} was overestimated. It can be seen that the values from using C_D depending on the wind speed close to the observation. From the results, it may be concluded that the drag coefficient is reasonably taken for the calculation of storm surges in this research as C_D depending on the wind speed due to Mathias and Godfrey [16], and the sea surface elevation is substantially affected by the change of the drag coefficient. The value of drag coefficient can enhance or reduce the magnitude of the storm surge elevation.

In Fig. 8, the time series of sea surface elevations are shown for Huahin, Rayong and Ko Chang calculated in three cases; case 1 is calculated using bottom roughness parameter (z_0) as 0.01 m and bottom coefficient (C_z) calculated from the formula suggested by Mellor [3], case 2 estimated using $z_0 =$ 0.1 m and C_z also calculated from the same formula, and case 3

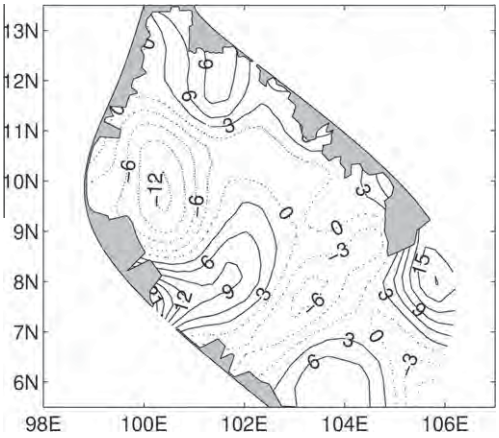

Fig. 6. The contours of observed sea surface anomaly (cm) taken from the AVISO near real-time sea surface anomaly data on November 5, 1997.

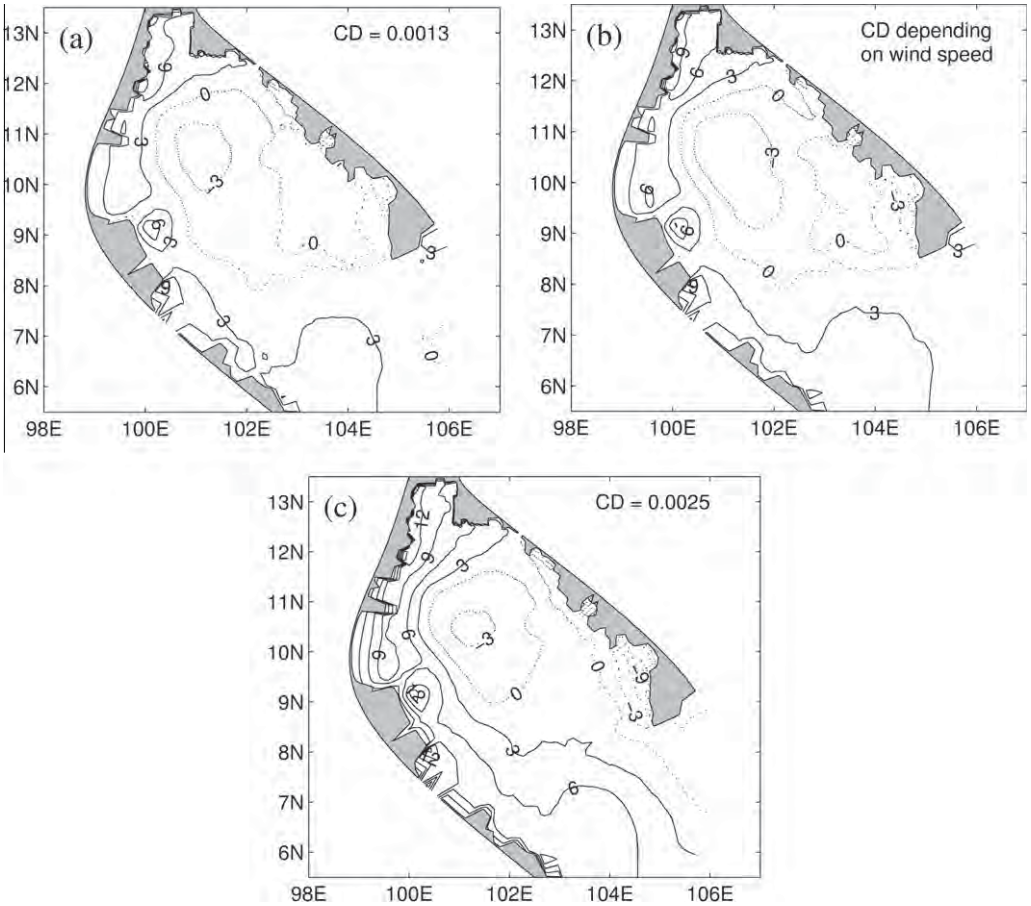

Fig. 7. The contours of simulated sea surface anomaly (cm) calculated using (a) $C_D = 1.3 \times 10^{-3}$, (b) C_D depending on the wind speed and (c) $C_D = 2.5 \times 10^{-3}$ on November 5, 1997.

estimated using $z_0 = 0.01$ m and constant $C_z = 3.3 \times 10^{-3}$. All three cases use the drag coefficient depending on the wind speed. The sea surface elevations of all three cases are the same. So that the changes of the bottom roughness parameter and bottom coefficient are insignificant to influence the calculation of sea surface elevation in the present study.

The results shown in the following were calculated using the drag coefficient due to the formula of Matthias and Godfrey [16], bottom roughness parameter as 0.01 m suggested by Weatherly and Martin [2] and bottom coefficient from calculation based on the logarithm law of the wall suggested by Mellor [3].

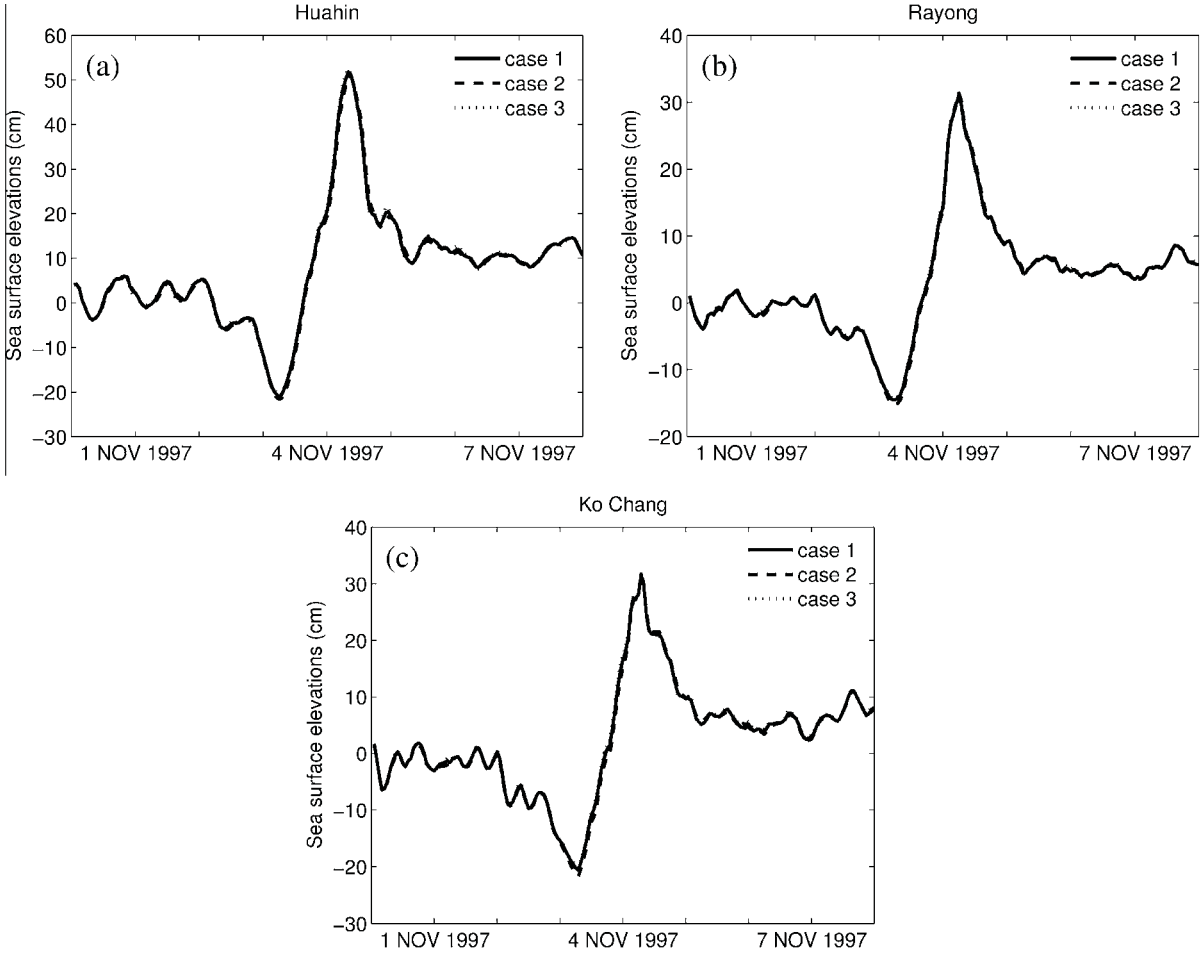

Fig. 8. The time series of sea surface elevations (cm) where case 1 estimated using $z_0 = 0.01$ m and C_z calculated from the formula suggested by Mellor [3], case 2 estimated using $z_0 = 0.1$ m and C_z also from calculation, and case 3 estimated using $z_0 = 0.01$ m and constant $C_z = 3.3 \times 10^{-3}$ at (a) Huahin (b) Rayong and (c) Ko Chang positions.

4.2. Simulated results of the current circulations

The simulated currents at the surface level induced by wind from observations are shown in Fig. 9. The actual storm surge is produced directly by the wind force. The wind induced circulation inside the gulf is characterized by the migration of water from the southeast to the north of the gulf as an effect of the wind force. It can be seen that the current circulation is counterclockwise during the typhoon passing. The positions of the center of the current circulation at the surface level correspond to the center of the typhoon at various times. When the typhoon moves northwestward from the SCS through the northern GoT, the current circulation also moves northwestward. A wind from the northeast drives a surface flow towards the land. The currents at the surface level, nearest surface, in offshore regions show a counterclockwise flow to the western coast with currents in some areas exceeding 0.8 ms^{-1} on November 4. A peak of the currents appeared to be associated with variations in wind stress. The currents in the area near the center of circulation are very low speeds which correspond to the existence of the area at the center of the typhoon where there is no relevant wind induced surge level.

Fig. 10 shows vectors of simulated currents at the surface level computed at 08UTC on November 4, 1997, around 8 h after the typhoon landfalls. The sea surface elevation rose to the maximum height at this time. The center of the counterclockwise circulation is quite a long way away from the shore, about 100 km south of Huahin. During this time, the counterclockwise circulation flow splits into two branches, one branch that flows directly toward the northeastern coast of the GoT, and another branch that flows directly to the north of Huahin with a speed of 0.8 ms^{-1}. A near-coast easterly flow is apparent along the northwestern coast of the GoT.

4.3. Simulated results of the sea surface elevations

The simulated sea surface elevations are shown in Fig. 11. As the wind blows, the water is pushed from the southwest to the north of the gulf. The area of set-up is permanently established in the northern part of the gulf. Following the spatial

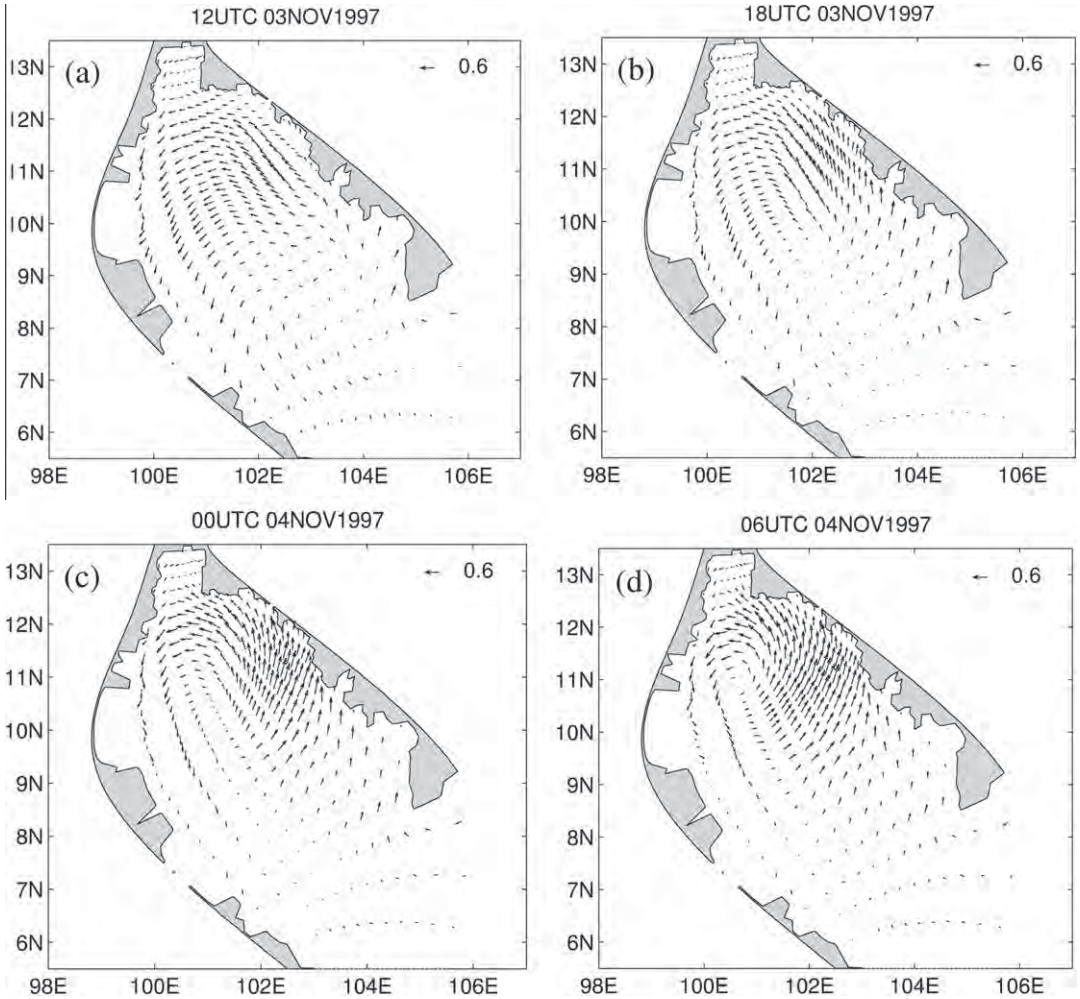

Fig. 9. The simulated the surface level current vectors (ms^{-1}) of 12UTC on November 3 to 06UTC on November 4, 1997.

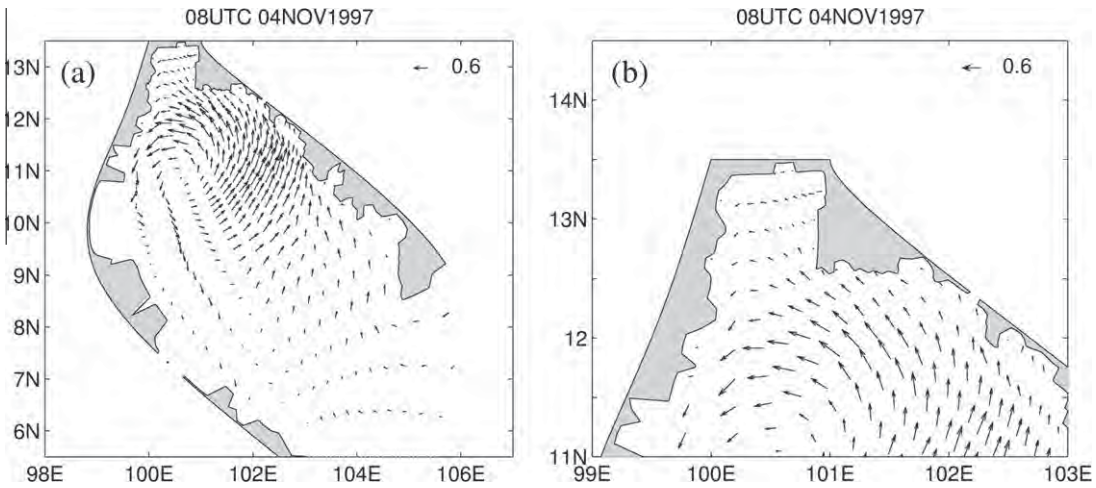

Fig. 10. The simulated (a) the surface level current vectors (ms^{-1}) and (b) the current vectors (ms^{-1}) in the upper of the GoT at 08UTC on November 4, 1997.

pattern of wind stress related to wind field, the gradient of sea levels is almost southwest-north. While the wind stress over the GoT increased, the sea level rose with very rapid increasing in the near-shore regions such as Cha-Am and Huahin.

Comparisons of the observed significant wave height provided by a network of moored data buoys called Seawatch buoys with the simulated sea surface height for three buoys, including the buoy at Huahin, Rayong and Ko Chang, are shown in Fig. 12. A peak has occurred in this observed wave height. At Huahin the peak of wave height, which appears to be 406.2 cm, appropriate to time of the peak of simulated sea surface elevation, which is 50.1 cm. At Rayong the peak of wave height, which is 296.9 cm, occurs at the same time as the peak of simulated sea surface elevation, which is 30.4 cm. At Ko Chang the peak of simulated sea surface elevation occurs after the peak of wave height by around 6 h. The 6- h delay may be caused by the errors in observation of initial wind. The peaks of wave height and simulated sea surface elevation at Ko Chang are 234.4 cm and 34.9 cm respectively. The Seawatch project, which was run by Schjølberg [12] using only the wind field, predicted an increase in sea level at 06UTC on November 4, 1997 to be 61 cm, calculated somewhere north of Cha-Am in the upper part of the gulf. In the model results, the highest sea surface elevation at this time was 61.4 cm. It agrees well with the Seawatch project. But the observation could not trace it. It is justified that the sea level does not elevate dramatically until the storm approaches the coast.

Fig. 13 shows the simulated sea surface heights in the upper part of the gulf at 08UTC on November 4, 1997. The time of peak surge agrees well with the time of peak wave height. The sea level raised to a maximum at this time at about 70 cm in the Cha-Am area, around latitude 12.8°N in the western coast of the upper GoT, very close to north of Huahin. For the Huahin position the maximum sea level was more than 51 cm. For the Rayong and Ko Chang positions located on the eastern coast of the upper GoT, the sea level calculated diminished down to 25 and 22 cm at this time, which is the time after the peak surge of these two locations occurring. It can be seen that the storm surge attains maximum values at the coastal region in the immediate vicinity of a storm's center slightly after storm passage. The climatological sea surface elevation taken from

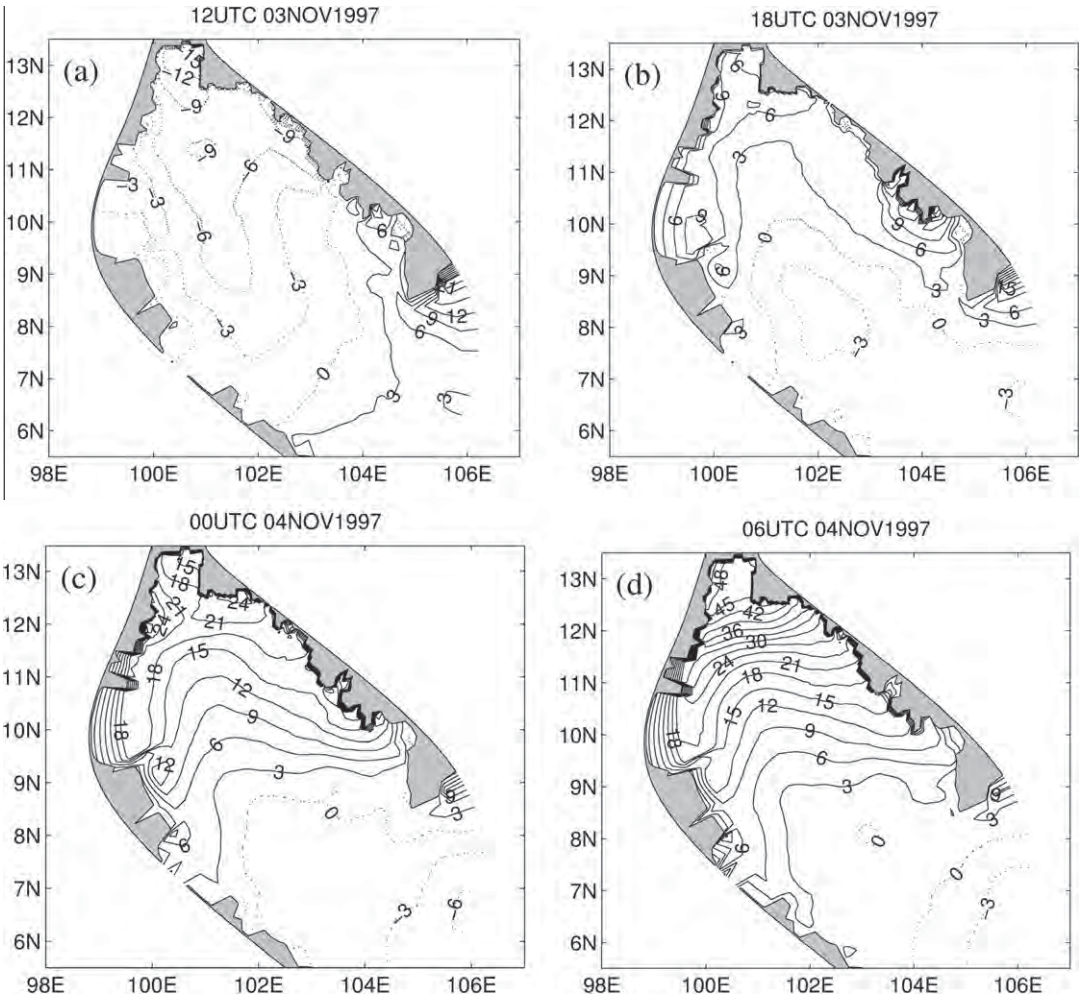

Fig. 11. The contours of simulated sea surface elevation (cm) of 12UTC on November 3 to 06UTC on November 4, 1997.

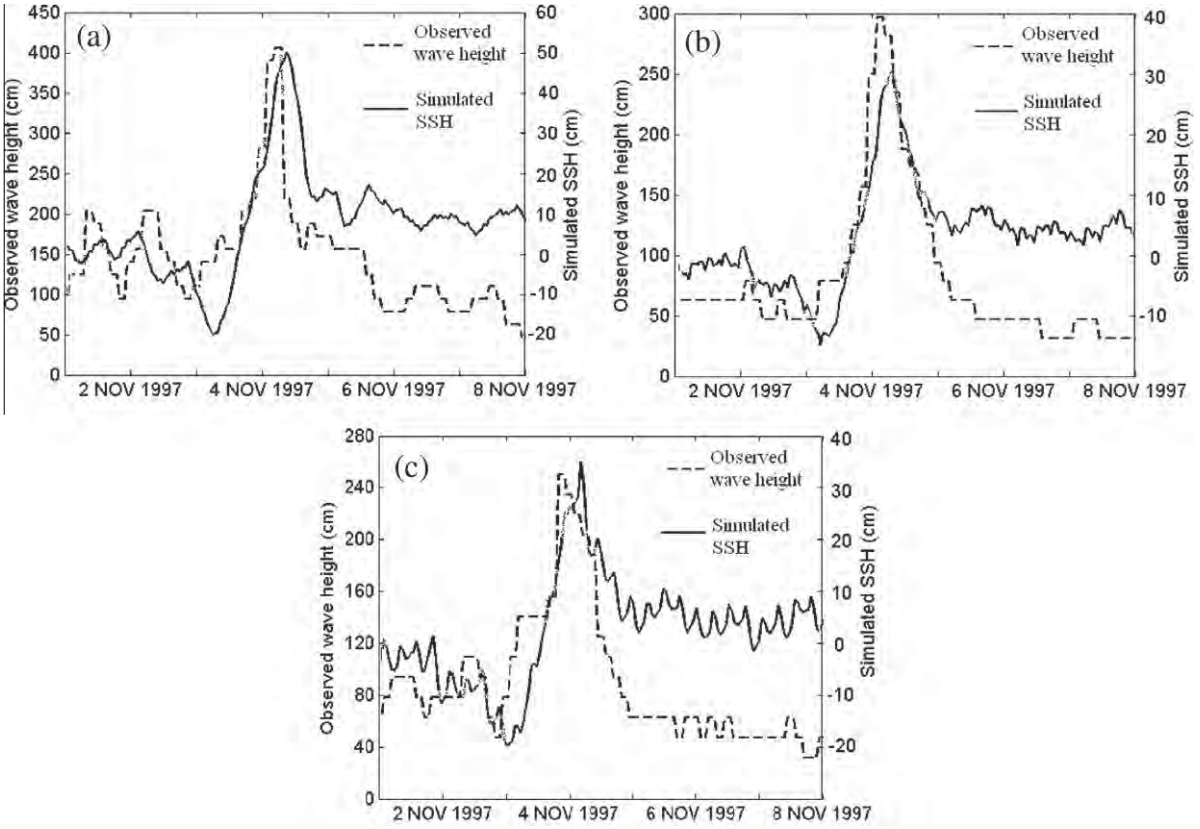

Fig. 12. The time series of the significant wave height (cm) from observation and the simulated sea surface elevation (cm) at (a) Huahin, (b) Rayong and (c) Ko Chang.

the spin up run on November and the simulated sea surface anomaly at 08UTC on November 4, 1997 are shown in Fig. 14. The big anomaly occurred in the upper part of the GoT in which the typhoon was passing toward the coast. The highest value of sea surface anomaly is about 60 cm in the Cha-Am area. At Huahin, Rayong and Ko Chang the sea surface anomalies are 46, 33 and 25 cm respectively. The averaged sea surface anomaly in the lower GoT is 5 cm, and in the upper GoT is 23 cm. It can be clearly concluded that the effects of the storm surge are a serious concern at the upper gulf when the typhoon moves northwestward through the northern GoT.

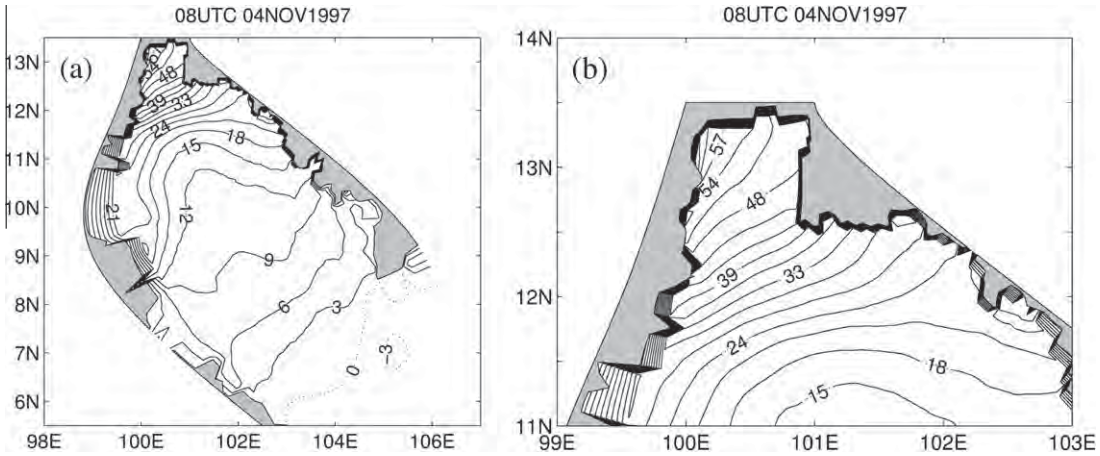

Fig. 13. The simulated (a) the contours of sea surface elevation (cm) and (b) the sea surface elevation (cm) in the upper of the GoT at 08UTC on November 4, 1997.

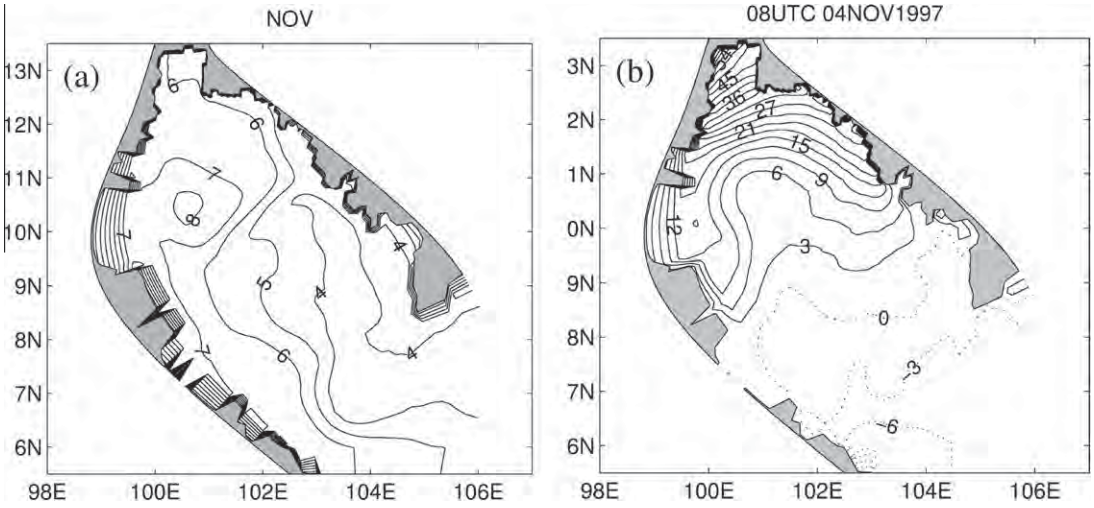

Fig. 14. The contours of (a) climatological sea surface elevation (cm) from spin up run for November and (b) simulated sea surface anomaly (cm) at 08UTC on November 4, 1997.

As we mentioned on the Cha-Am area, shown in Fig. 15, at a point near the shore the sea level elevations exceeded 70 cm. The maximum water set-up occurs at 08UTC on November 4, the maximum set-down at 08UTC on November 3. Thus around 24 h of time lag between the two maximum set-up and set-down with twenty-four hours of time lag correspond to the time between the high wave peak and the minimum taken from observation. The surges at the western coast region such as Hua-hin and Cha-Am rise higher than the eastern coast. The current speeds at this area are quite weak, the maximum current speed is 0.28 ms^{-1} occurring at 19UTC on November 3 which is the time before the typhoon landfalls. At the time of peak elevation, 08UTC on November 4, the current speed at Cha-Am is only 0.21 ms^{-1}, but the strong speed occur at the area around Cha-Am. That means the peak surge is not generated by the speed at that point, but it influenced by the strong speed around the peak area.

The variations of sea surface height can be divided into 3 stages that is the stage before storm surge occurred, the stage when storm surge existed, and the stage after the storm had passed. On November 3–4, a predominantly northeasterly wind was blowing over the GoT producing the surface elevation gradients, in which the surface elevation increases in the near coastal region.

The model contains the non-linear terms, and these terms are particularly important in shallow water, so we should be considering the energy for this study. Fig. 16 illustrates the kinetic energy and potential energy in units of Nm at various times in the GoT. Notice that potential energy is small compared to kinetic energy until the storm's center invades the gulf. Not that until the storm passes the coast does potential surpass kinetic energy. This suggests that the core of the storm when distant from the coast exclusively elevates the surface hydrostatically.

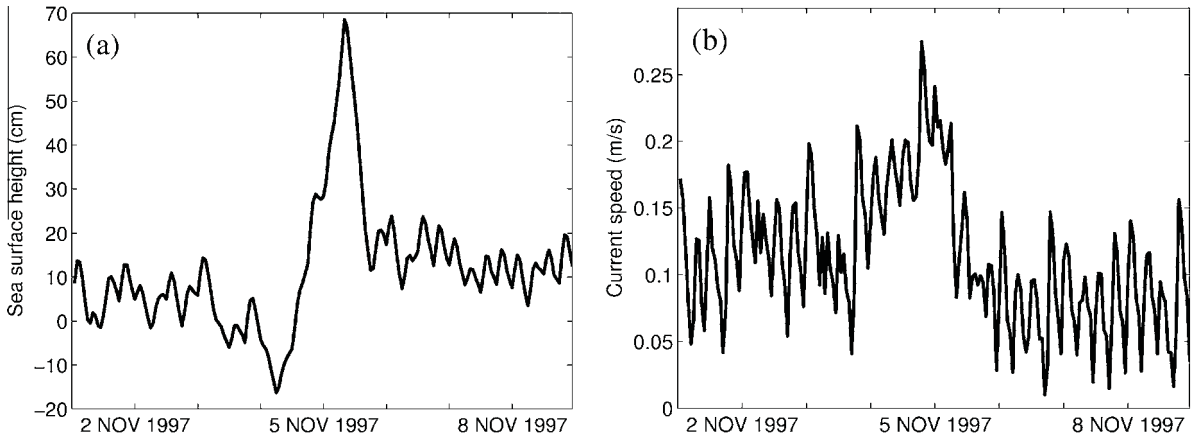

Fig. 15. The time series of (a) the simulated sea surface height (cm) and (b) the simulated first level current speed (ms^{-1}) at Cha-Am.

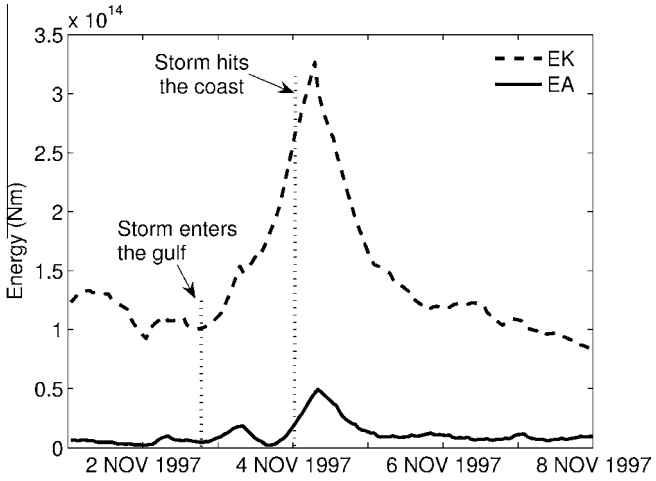

Fig. 16. The time series of kinetic energy (EK) and potential energy (EA) in units of Nm.

5. Conclusion

Numerical hindcast of storm surge caused by the Typhoon Linda in the Gulf of Thailand is conducted by using the three-dimensional ocean model (POM). In this case, the appropriate magnitude of drag coefficient depending on the wind speed is taken from the formula due to Matthias and Godfrey [16] which has been often used in storm surge models. It should be also noted that changes of bottom roughness parameter and bottom coefficient are checked not to influence the calculation of storm surge in this study. During the storm event, a northeasterly wind blew strongly over the southeastern coast of Thailand, which caused sea level elevation to rise in the northwestern part of GoT reaching a maximum value of 70 cm. Under the northeasterly wind, there is a contribution of sea water from the SCS into the GoT. A simulation has clearly revealed that the maximum sea elevation at the coast occurs not at the time of storm passage, but slightly after the storm strikes the coast. The wind forcing of a storm surge is the influential in controlling storm surges at a coastal region, whereas the initial value taken from the spin up phase is of minor importance. It is suitable to describe the storm from considerations presumed to hold at and near its center where the wind has the greatest effects.

The study of coastal storm surges for difference storm should be considered in the future. The results would be of immediate qualitative value to the typhoon warning service, and would provide insight on the relative importance of various mechanisms involved in storm surge generation.

Acknowledgements

This research was supported by the Thailand Research Fund (TRF), the Joint Graduate School of Energy and Environment (JGSEE) and the National Research University Project. The authors are greatly indebted to Prof. Dr. Jiang Zhu and Prof. Dr. Suphat Vongvisessomjai for valuable comments. We express our sincere thanks to the Institute of Atmospheric Physics (IAP), Chinese Academy of Sciences (CAS) and Department of Mathematics, King Mongkut's University of Technology Thonburi (KMUTT) for the facilities during this research and geo-informatics and space technology development agency (GISTDA) for the buoy data.

References

[1] A.F. Blumberg, G.L. Mellor, A description of a three-dimensional coastal ocean circulation model, in: N.S. Heaps (Ed.), Three Dimensional Coastal Ocean Models, American Geophysical Union, 1987, pp. 1–16.
[2] G. Weatherly, P.J. Martin, On the structure and dynamics of the ocean bottom boundary layer, Journal of Physical Oceanography 8 (1978) 557–570.
[3] G.L. Mellor, User's Guide for a Three-Dimensional, Primitive Equation, Numerical Ocean Model, Princeton University, New Jersey, 2004.
[4] G.L. Mellor, T. Yamada, Develop of a turbulence closure model for geophysical fluid problems, Reviews of Geophysics and Space Physics 20 (1982) 851–875.
[5] H.J. Yang, Q. Liu, Z. Liu, D. Wang, X. Liu, A general circulation model study of the upper ocean circulation of the South China Sea, Journal of Geophysical Research 107 (2002) C7.
[6] J. Gan, H. Li, E.N. Curchitser, D.B. Haidvogel, modeling South China Sea circulation: response to seasonal forcing regimes, Journal of Geophysical Research 111 (2006).
[7] J. Smagorinsky, General circulation experiments with the primitive equations, Monthly Weather Review 91 (1963) 99–164.
[8] K. Bryan, A numerical method for the study of circulation of the world ocean, Journal of Computing Physics 4 (1969) 357–376.
[9] N. Aschariyaphotha, P. Wongwises, U.W. Humphries, Interpolation of climatological data to numerical ocean modeling for the Gulf of Thailand, in: Proceedings of the Joint International Conference on Sustainable Energy and Environment, Huahin, Thailand, 2004, pp.784–789.
[10] P.C. Chu, Y. Chen, S. Lu, Wind-driven South China Sea deep basin warm-core/cool-core eddies, Journal of Oceanography 54 (1998) 347–360.
[11] P.C. Chu, N.L. Edmons, C.W. Fan, Dynamics mechanisms for the South China Sea seasonal circulation and thermohaline variabilities, Journal of Physical Oceanography 29 (1999) 2971–2989.

[12] P. Schjølberg, An operational ocean circulation model in the Gulf of Thailand: the Typhoon Linda case, in: Proceedings of the Seminar on The Seawatch Programmes in Asian Countries, Bangkok, Thailand, 2002, pp. 98–121.
[13] R.V. Madala, S.A. Piacsek, A semi-implicit numerical model for Baroclinic oceans, Journal of Computing Physics 23 (1977) 167–178.
[14] S. Levitus, T. Boyer, World ocean atlas, temperature, NOAA Atlas NESDIS, vol.4, U.S. Government Printing Office, Wasington, D.C., 1994.
[15] S. Levitus, R. Burgett, T. Boyer, World Ocean Atlas, Salinity, NOAA Atlas NESDIS, vol. 3, U.S. Government Printing Office, Wasington, D.C., 1994.
[16] T. Matthias, J.S. Godfrey, Regional Oceanography: An Introduction, Pergamon, Australia, 1994.
[17] T.J. Simons, Verification of numerical models of lake Ontario, Part I: circulation in spring and early summer, Journal of Physical Oceanography 4 (1974) 507–523.
[18] Tiempo Climate Cyberlibrary, Typhoon Linda hits Vietnam. Available from: <http://www.cru.uea.ac.uk/tiempo/floor0/recent/issue26/t26art5.htm>, 1997.
[19] UNESCO, Tenth Report of the Joint Panel on Oceanographic Tables and Standards, UNESCO Technical Pap. in Marine Science, UNESCO, Paris, 1981.
[20] W. Kanbua, I.W. Tang, B. Wiwatanapataphee, A study on ocean wave forecasting from Typhoon Linda by using the WAM model, in: Proceedings of ANSCES 2001, Bangkok, Thailand, 2001, pp. 22–28.
[21] W. Kanbua, S. Supharatid, I.W. Tang, Ocean wave forecasting in the Gulf of Thailand during Typhoon Linda 1997: WAM and neural network approaches, Science Asia 31 (2005) 243–250.
[22] X.B. You, R.F. Li, Q.C. Zeng, Numerical simulation of the current system in the China Sea by using a nested mesh model, Proceedings of the Nineth Asian Congress of Fluid Mechanics, Isfahan, Iran, 2002.

Experimental Thermal and Fluid Science 35 (2011) 887–895

Contents lists available at ScienceDirect

Experimental Thermal and Fluid Science

journal homepage: www.elsevier.com/locate/etfs

Two-phase flow of R-134a refrigerant during flow boiling through a horizontal circular mini-channel

Sira Saisorn [a,c], Jatuporn Kaew-On [b,c], Somchai Wongwises [c,*]

[a] King Mongkut's Institute of Technology Ladkrabang Chumphon Campus Chumphon 86160, Thailand
[b] Department of Physics, Faculty of Science, Thaksin University, Phattalung 93110, Thailand
[c] Fluid Mechanics, Thermal Engineering and Multiphase Flow Research Lab. (FUTURE), Department of Mechanical Engineering, King Mongkut's University of Technology Thonburi, Bangmod, Bangkok 10140, Thailand

ARTICLE INFO

Article history:
Received 18 December 2009
Received in revised form 24 October 2010
Accepted 21 January 2011
Available online 31 January 2011

Keywords:
Flow boiling
Mini-channel
Flow pattern
Heat transfer

ABSTRACT

This research focuses on heat transfer to R-134a during flow boiling in a 1.75 mm internal diameter tube. Flow visualisation and heat transfer experiments are conducted to obtain heat transfer coefficients for different flow patterns. The measured data in each flow regime are compared with predictions from a three-zone flow boiling model. The calculations are in fair agreement with the experimental results which correspond in particular to slug flow, throat-annular flow and churn flow regimes under conditions of low heat flux.

1. Introduction

In recent years, intense research effort has been devoted to the flow boiling heat transfer characteristics of small flow passages such as mini- and micro-channels owing to the rapid development of micro-scale devices used for several engineering applications including medical devices, high heat-flux compact heat exchangers, and cooling systems for various types of equipment.

Several advantages can be obtained when small channels are selected for applications. In compact heat exchanger implementations, for instance, small channels can provide a larger contact area with the fluid per unit volume and support high pressure operating conditions. Capillary force or surface tension is likely to play an important role in two-phase flow and heat transfer characteristics, resulting in significant differences in the flow phenomena between ordinarily sized channels and small channels.

The criteria for the classification of small channels have been given by different investigators as reported in Saisorn and Wongwises [1]. For instance, arbitrary channel classifications associated with the hydraulic diameter, D_h have been proposed. Mehendale et al. [2] employed the hydraulic diameter as an important parameter for defining the heat exchangers as follows:

- Micro-heat exchanger: 1 μm $\leqslant D_h \leqslant$ 100 μm
- Meso-heat exchanger: 100 μm $\leqslant D_h \leqslant$ 1 mm
- Compact heat exchanger: 1 mm $\leqslant D_h \leqslant$ 6 mm
- Conventional heat exchanger: $D_h >$ 6 mm

Kandlikar [3] proposed criteria for different-sized channels used in engineering applications:

- Micro-channels: 10 μm $\leqslant D_h \leqslant$ 200 μm
- Mini-channels: 200 μm $\leqslant D_h \leqslant$ 3 mm
- Conventional channels: $D_h >$ 3 mm

With regard to two-phase flow research, there have been a relatively small number of publications in the area of small channels compared with those done for ordinarily sized channels. Hydrodynamic and transport phenomena in small channels, which have limited and confined space, are less well understood compared to those in larger channels. Recent works concerned with two-phase heat transfer characteristics in mini- and micro-channels are outlined in the following paragraphs.

Huo et al. [4] studied experimentally boiling heat transfer of R-134a fluid flowing in small vertical tubes of 2.01 and 4.26 mm internal diameter. In the range of low vapour quality, the heat transfer coefficient in both tubes increased with increasing heat flux and saturated pressure but was independent of vapour quality. These results were attributed to nucleate boiling being the dominant heat transfer mode. Over other ranges of vapour quality, however, the dominant heat transfer mode was not addressed as a

* Corresponding author. Tel.: +66 2 470 9115; fax: +66 2 470 9111.
E-mail address: somchai.won@kmutt.ac.th (S. Wongwises).

0894-1777/$ - see front matter © 2011 Elsevier Inc. All rights reserved.
doi:10.1016/j.expthermflusci.2011.01.008

Nomenclature

Bo	boiling number
D	channel diameter (m)
G	mass flux (kg/m^{2}s)
h	heat transfer coefficient (W/m^2 K)
i	specific enthalpy (J/kg)
i_{LG}	latent heat of vapourization (J/kg)
MAE	mean absolute error
q	heat flux (W/m^2)
Re	Reynolds number
T	temperature (°C)
t	time (s)
We	Weber number
x	vapour quality
z	axial distance (m)

Greek symbols

τ	pair period (s)

Subscripts

A	annular flow
CB	coalescing bubble flow
dry	dry-out zone
film	liquid film between bubble and wall
G	vapour phase
GO	all-vapour
IB	isolated bubble flow
L	liquid phase
LO	all-liquid
sat	saturation
wall,in	inner wall

result of inconsistency in the experimental data. Under the same controlled conditions, they found that the nucleate boiling heat transfer coefficient was higher for the 2.01 mm tube than for the 4.26 mm tube.

Flow boiling heat transfer characteristics in micro-channels of 540 mm length with 25 circular flow channels of 0.81 mm diameter were investigated by Pettersen [5]. They reported that the increase in heat flux resulted in a higher heat transfer coefficient, which can be explained according to the dominant role of nucleate boiling over the low/moderate vapour quality region. Another point observed was that the dry-out effects were more noticeable at higher mass flux and temperature, resulting in a substantially reduced heat transfer coefficient at high vapour qualities. Besides, the pressure drop increased with mass flow and vapour quality but decreased as temperature increased. The measured heat transfer coefficient data corresponding to low vapour quality region were compared with various heat transfer correlations based on nucleate boiling mechanism. The frictional pressure drop data were also compared with the existing correlations.

Yun et al. [6] were concerned with flow boiling heat transfer characteristics in rectangular multi-channels with hydraulic diameters ranging from 1.08 to 1.54 mm. Working fluids tested were CO_2 and R-134a. Generally, the average heat transfer coefficient of CO_2 increased by around 53% as compared with that of R-134a. The effect of heat flux on heat transfer coefficient was much more obvious for CO_2 than for R-134a. The dry-out phenomenon was promoted by an increase in mass flux and it was also noted that the effect of mass flux on heat transfer coefficient was less sig-

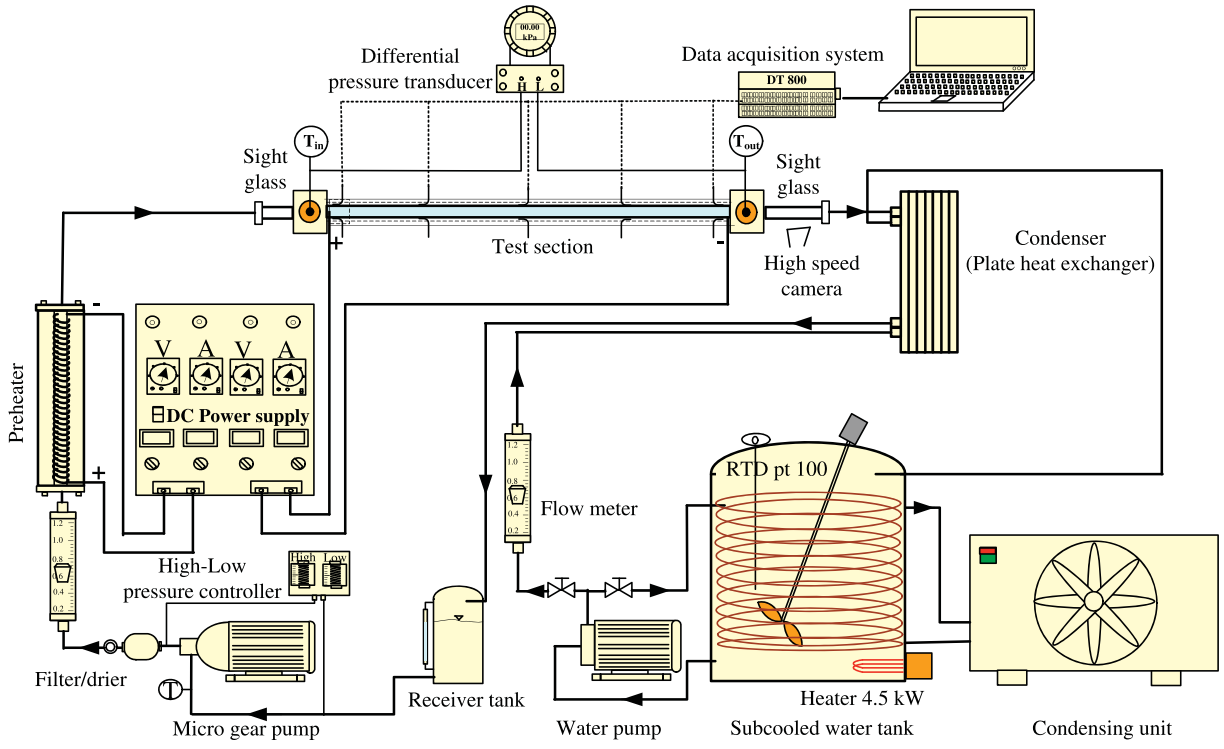

Fig. 1. Schematic diagram of experimental apparatus.

nificant than that of heat flux. As expected, the heat transfer coefficient increased with a decrease in hydraulic diameter.

Heat transfer of R-134a refrigerant during flow boiling in horizontal tubes with different diameters including 0.51, 1.12 and 3.1 mm was studied experimentally by Saitoh et al. [7]. Nucleate boiling was reported in the low vapour quality region whereas convective evaporation was dominant in the high vapour quality region. The latter mechanism was found to be less dominant as the tube diameter decreased. The smaller the tube diameter, the higher is the effect of saturation temperature on heat transfer coefficient. Flow instability was also discussed in this work.

Choi et al. [8] reported the heat transfer characteristics of CO_2 through horizontal mini-channels having diameters of 1.5 and 3 mm. They indicated that nucleate boiling was predominant in the low vapour quality region and a convective boiling heat transfer contribution appeared in moderate and high vapour quality regions. The variation of local heat transfer coefficient with heat flux, mass flux, vapour quality and saturation temperature was discussed. More vigorous nucleate boiling was observed and studied when the smaller diameter tube was used. Flow boiling heat transfer experiments with different refrigerants were continually carried out by Choi et al. [9]. They indicated that the use of CO_2 caused the heat transfer coefficient to be higher than with R-134a and R-22 fluids.

Shiferaw et al. [10] compared their flow boiling data with existing correlations. The data points were obtained from experiments with R-134a fluid flowing through small tubes with diameters of 4.26 and 2.01 mm. The comparison revealed that existing correlations do not predict their data very well. Comments and suggestions were provided by the authors for further development of the prediction. Similar experiments were conducted by Shiferaw et al. [11] to obtain data from a 1.1 mm diameter tube. Generally, the heat transfer characteristics showed that the heat transfer coefficient was not affected by mass flux or vapour quality, but increased with increasing heat flux and saturation pressure.

Three different refrigerants, R-134a, R-236fa and R-245fa, were tested for flow boiling in a 1.03 mm diameter tube by Ong and Thome [12]. Trends apparent in the data were investigated, showing that the heat transfer coefficient depended on heat flux at low vapour quality and on mass flux at high vapour quality. In terms of the refrigerants tested at low vapour quality, R-134a exhibited the highest heat transfer coefficient followed by R-236fa and R-245fa, respectively.

Interestingly, a number of researchers such as Lee and Lee [13], Sumith et al. [14] and Qu and Mudawar [15] have reported that flow boiling heat transfer is substantially controlled by convective boiling.

In addition to the mechanisms corresponding to nucleate boiling and convective boiling contributions, recently, a three-zone flow boiling model based on the elongated bubble flow regime, was developed by Thome et al. [16] and Dupont et al. [17] to predict heat transfer characteristics in micro-channels. The point they make is that heat transfer is controlled primarily by conduction through the evaporation film trapped between the elongated bubble and the tube wall.

From the above review of the literature, the characteristics of flow boiling heat transfer in small channels are not entirely consistent with those in ordinarily sized channel. Moreover, there is inconsistency in the micro-scale heat transfer results obtained from different researchers and, as a result, the major heat transfer mechanisms behind the phase-change phenomena are still unclear for small flow passages. Flow patterns have been expected to affect the heat transfer phenomena. Different flow patterns may give differences in flow boiling mechanisms. The current work is, therefore, aimed at examining the three-zone flow boiling model for various flow patterns observed in R-134a refrigerant flow boiling through a 1.75 mm tube.

2. Experimental apparatus and procedure

The present experimental apparatus, which is modified from that developed by Kaew-On and Wongwises [18] and is shown schematically in Fig. 1, is designed to investigate flow boiling of R-134a in a circular mini-channel placed horizontally. The main

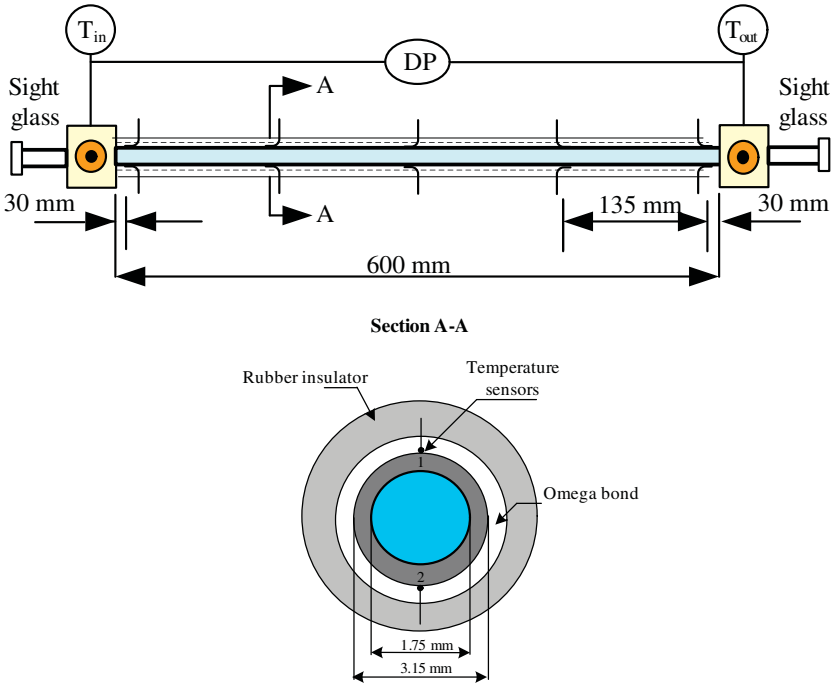

Fig. 2. Schematic diagram of the test section.

Table 1
Experimental conditions.

Refrigerant	R-134a
Diameter (mm)	1.75
Length (mm)	600
Mass flux (kg/m^2 s)	200–1000
Heat flux (kW/m^2)	1–83
Saturation pressure (bar)	8–13
Test section material	Stainless steel

Table 2
Uncertainties of measured quantities and calculated parameters.

Parameter	Uncertainty
Temperature	±0.1 (°C)
Mass flow rate of refrigerant	±0.1 (%) Full scale
Heat transfer rate of test section	±2.25%
Heat transfer rate of pre-heater	±2.25%
Heat transfer coefficient	±8.12%

components of the system include a test section, refrigerant loop, sub-cooling loop, and a data acquisition system.

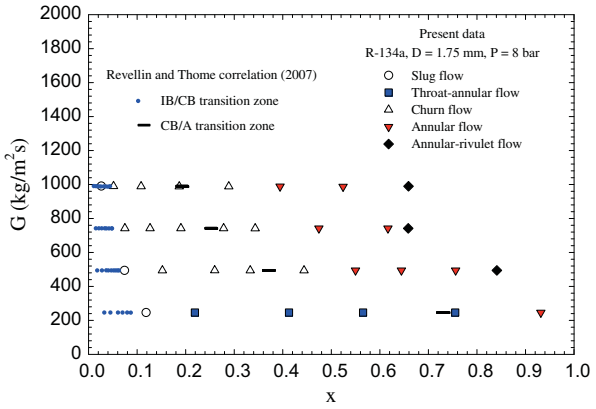

Fig. 4. The present flow regime map compared with the transition zones by Revellin and Thome [20].

For the refrigerant circulating loop, as seen in Fig. 1, liquid refrigerant is pumped by a gear pump which can be regulated by means of an inverter. The refrigerant then passes in series through a filter/dryer, a refrigerant flow metre, pre-heater, sight glass tube, and enters the test section. The inlet quality before entering the test section is controlled by the pre-heater with a DC power supply used to apply heat. Leaving the test section, the refrigerant vapour

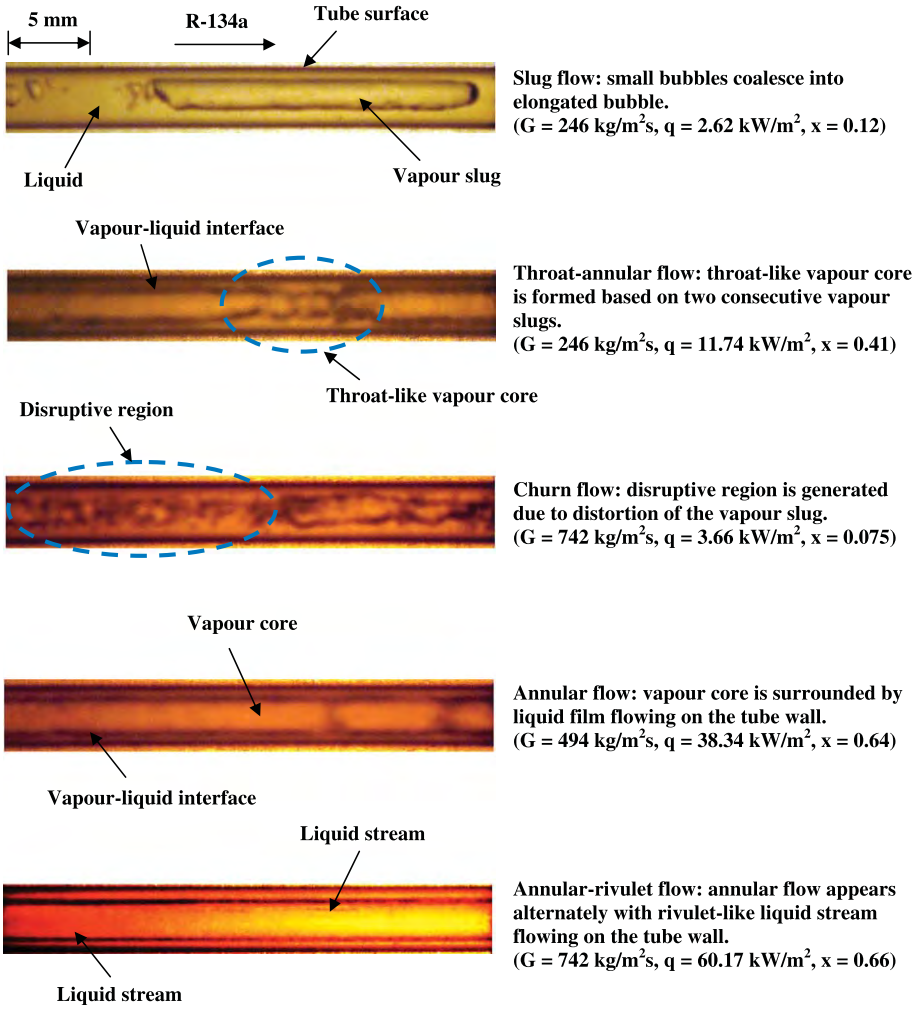

Fig. 3. Flow patterns for R-134a during flow boiling in a mini-channel with diameter of 1.75 mm (saturation pressure = 8 bar).

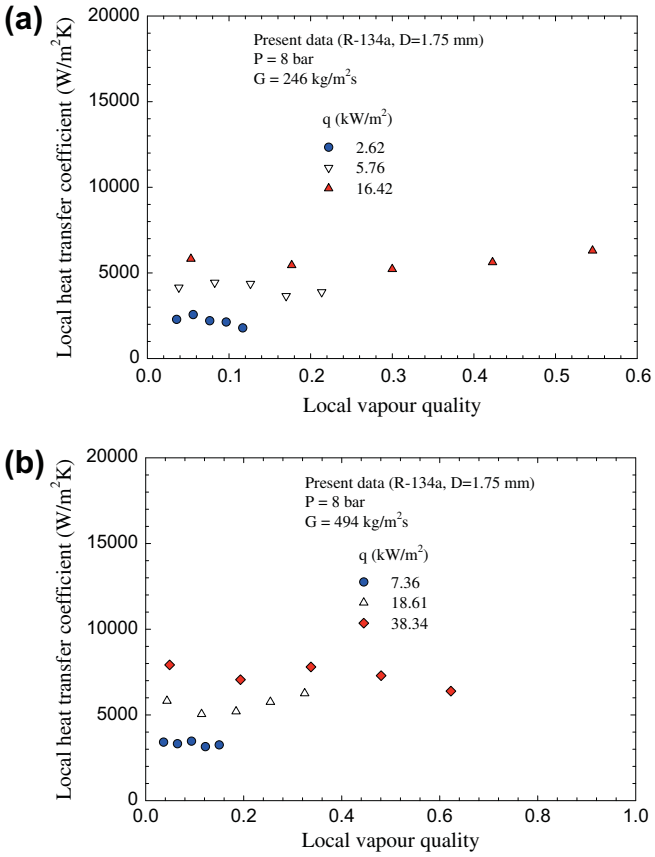

Fig. 5. Local vapour quality versus local heat transfer coefficient for various heat flux values.

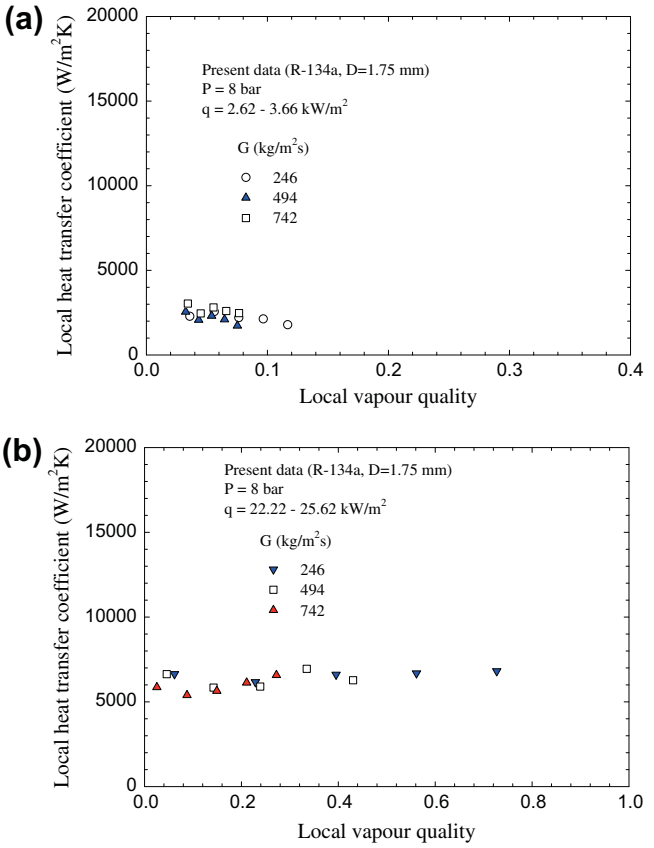

Fig. 6. Local vapour quality versus local heat transfer coefficient for various mass flux values.

subsequently condenses in a condenser which is a plate heat exchanger and then is collected in a receiver and returns to the refrigerant pump to complete the cycle. Instrumentation is installed at various positions, as shown in Fig. 1, to monitor the state of the refrigerant. All the signals from the thermocouples and pressure transducer are recorded by the data acquisition system.

Fig. 2 shows a schematic diagram of the test section, a stainless steel tube which is 600 mm long and 1.75 mm in diameter. A regulated DC power supply generating 80 A at 12 V is used to apply heat to the test section. The voltage and electric current values are measured by a multi-metre (Fluke 336 model) which has an uncertainty of ±2% for voltage and ±1% for current. T-type thermocouples are installed at the inlet and outlet of the test section to measure the system temperature. The 10 thermocouples are installed on the top and bottom sides at equal distances along the tube to measure the wall temperature. All thermocouples on the tube surface are fixed with special glue. The test section is well insulated by means of rubber foam with a thermal conductivity of 0.04 W/mK. A variable area type flow metre is specially calibrated in the range 0.02–0.2 LPM for R-134a by the manufacturer. All relevant instruments installed in the experimental apparatus, including the thermocouples and pressure transducer are well calibrated.

A 1.75 mm diameter transparent tube is installed to match up with the test section outlet and to serve as a viewing window for flow visualisation. The detailed formation of each flow pattern is registered by a high quality camera (Fujifilm FinePix S7000) having shutter speeds of 1/15–1/10,000 s. The camera, together with an adjustable light source consisting of 150 W halogen lamp and dimmer, are placed horizontally and normal to the viewing section.

In this work, the experiments were conducted in such a way that the heat applied to the test section is varied in small increments, while the refrigerant flow rate, saturation pressure, and inlet vapour quality in the test section are kept constant at the desired value. The system is allowed to approach a steady state before the flow pattern and relevant data are recorded. The steady state condition is verified by plotting a number of temperatures measured by the T-type thermocouples installed at pre-heater and test section, against time. Their variations are within the error range for a time of at least 120 s. During the experiment, the temperature and pressure are continuously recorded along the test section on the data acquisition system. The temperature profiles help us to know the limits of useful data because a large increase in wall temperature and outlet saturation temperature is observed when dry-out occurs. The range of experimental conditions is presented in Table 1. The uncertainties in the measured quantities and calculated parameters are shown in Table 2.

3. Results and discussion

Flow boiling of R-134a fluid in a horizontal tube of 1.75 mm inner diameter is carried out to obtain flow pattern and heat transfer coefficient data.

Photographs of the flow pattern are obtained through the viewing window located downstream of the test section. Fig. 3 illustrates the observed flow patterns which can be summarised as follows.

Slug flow: elongated bubbles which are larger in length than the channel diameter are developed from small bubbles.

Throat-annular flow: the two consecutive elongated bubbles coalesce into a throat like gas core.

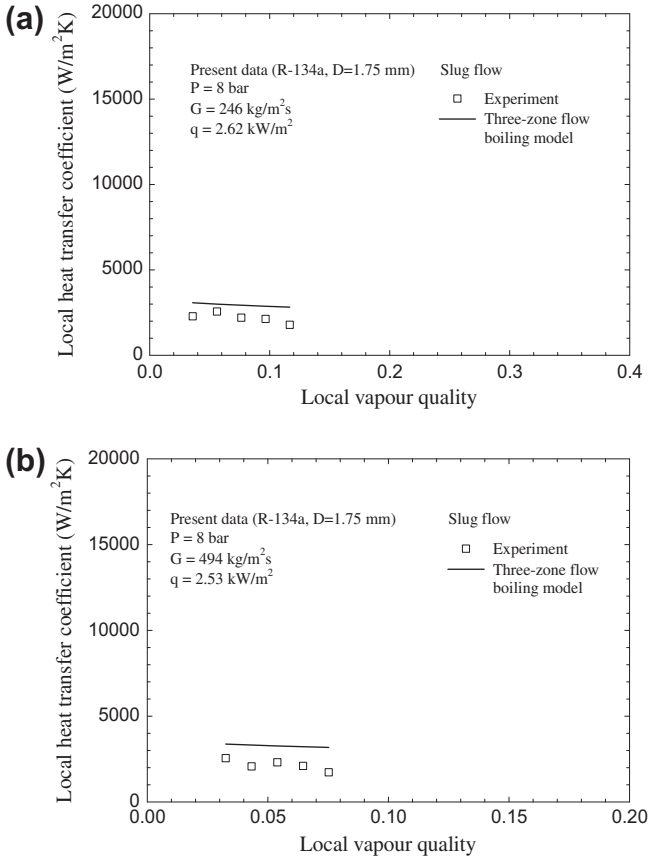

Fig. 7. Comparison of the local heat transfer coefficient data for slug flow regime with the three-zone flow boiling model.

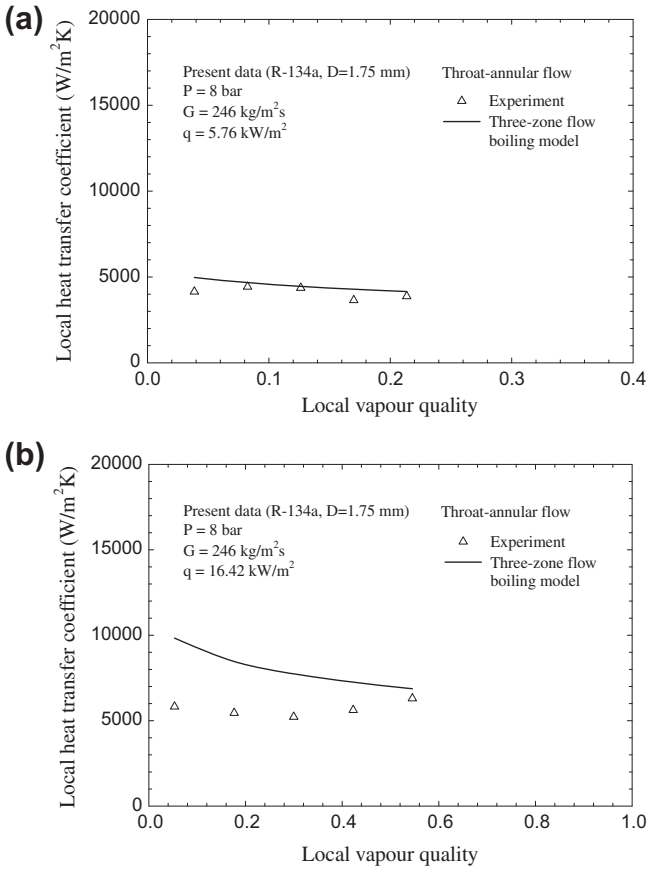

Fig. 8. Comparison of the local heat transfer coefficient data for throat-annular flow regime with the three-zone flow boiling model.

Churn flow: a disruptive region develops due to the distortion of the elongated bubbles.

Annular flow: liquid film flows on the tube wall and the tube core is occupied by continuous vapour flow.

Annular-rivulet flow: annular flow is observed alternately with flowing of a rivulet-like liquid stream on the tube surface.

It is remarkable to note from the figure that peculiar flow patterns, throat-annular flow and annular-rivulet flow, are also observed in the two-phase gas–liquid system for small channels as reported by Saisorn and Wongwises [19]. Such flow patterns have never been observed in ordinarily sized channels.

The usual method in the presentation of flow pattern data is to classify the flow pattern by visual observation and plot the data as a flow pattern map in terms of system parameters. The flow pattern map in terms of mass flux and vapour quality is presented in Fig. 4. The present data are also compared with the flow pattern map developed by Revellin and Thome [20] for flow boiling in micro-channels. Their flow regime map comprises different zones according to the bubble coalescence phenomena. The followings are a brief description of each zone located in the flow pattern map.

The isolated bubble (IB) regime corresponds to a relatively high bubble generation rate when compared with the bubble coalescence rate. Either or both of bubbly flow and slug flow are included in this regime. The coalescing bubble (CB) regime is defined when the bubble generation rate is smaller than the bubble coalescence rate.

The isolated bubble (IB) flow to coalescing bubble (CB) flow transition is given by

$$x_{IB/CB} = 0.763\left(\frac{Re_{LO}Bo}{We_{GO}}\right)^{0.41} \quad (1)$$

where Bo stands for Boiling number, Re_{LO} represents all-liquid Reynolds number and We_{GO} is all-vapour Weber number.

The transition from coalescing bubble flow to annular flow is determined by

$$x_{CB/A} = 0.00014Re_{LO}^{1.47}We_{LO}^{-1.23} \quad (2)$$

where We_{LO} is all-liquid Weber number.

These correlations take into account different effects including heat flux, viscosity and surface tension which are represented, respectively, by Boiling number, Reynolds number and Weber number. Their correlations were remarkably developed to generate a number of points representing the zone or vicinity of the transitions between flow regimes.

The comparison as indicated in Fig. 4 reveals that, in general, the present data correspond well with the transition zones proposed by Revellin and Thome [20]. The regions of churn flow and throat-annular flow obtained from the present study agree fairly well with their coalescing bubble regime whereas our annular flow and annular-rivulet flow are located in their annular region. The present slug flow data are found near the transition zone between their isolated bubble and coalescing bubble regions.

Heat flux, q, transferred to the test section is provided by the regulated DC power supply generating 80 A at 12 V. T-type thermocouples are installed at the inlet and outlet of the test section to measure the refrigerant temperatures. The two-phase conditions for flow boiling are provided at the test section inlet by using pre-heater as shown in Fig. 1. The saturation pressures at the test section inlet and outlet are obtained based on the corresponding saturation temperatures. Regarding the assumption of a linear

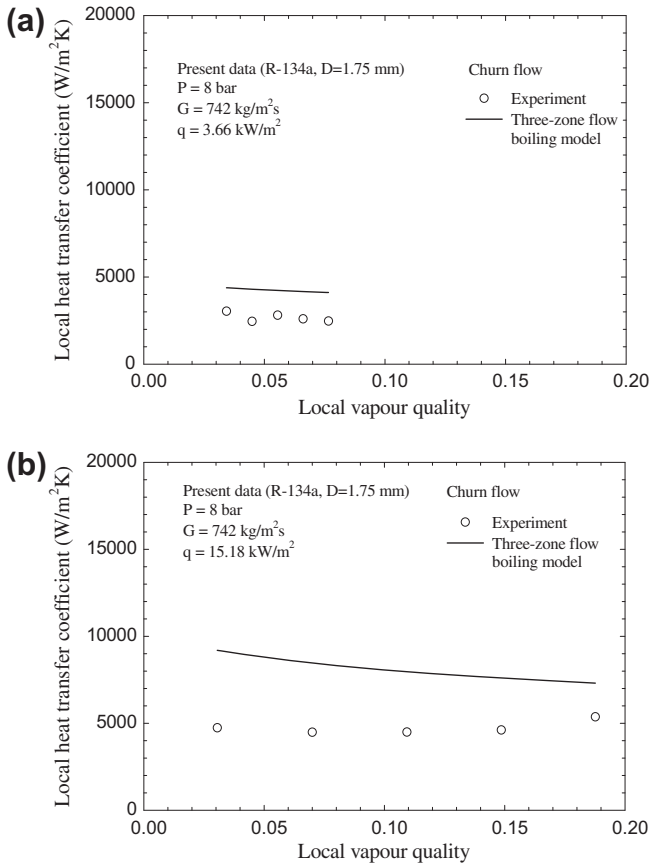

Fig. 9. Comparison of the local heat transfer coefficient data for churn flow regime with the three-zone flow boiling model.

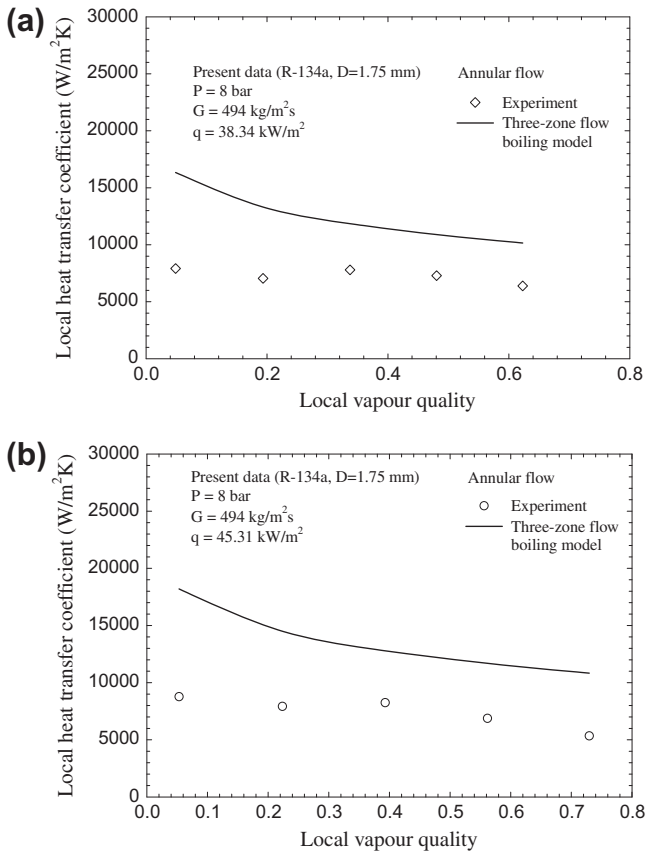

Fig. 10. Comparison of the local heat transfer coefficient data for annular flow regime with the three-zone flow boiling model.

variation of the saturation pressure along the tube, the local saturation temperatures, $T_{sat,loc}$, can subsequently be obtained.

As shown in Fig. 2, the 10 T-type thermocouples are installed on the top and bottom sides at equal distances along the tube to measure the tube surface temperature. For each position where the thermocouple is installed on the tube surface, the inner wall temperature at a given position is determined using the equations for steady state one-dimensional heat conduction through the tube wall with internal heat generation. At a given distance, hence, the average temperature of the inner wall at the top and bottom sides stands for the local temperature on the inner wall, $T_{wall,in,loc}$. Finally, the local heat transfer coefficient, h_{loc}, for flow boiling of R-134a along the test section is determined using the following equation.

$$h_{loc} = \frac{q}{(T_{wall,in,loc} - T_{sat,loc})} \tag{3}$$

The local vapour quality is determined based on thermodynamic properties, i.e.

$$x = \frac{(i - i_L)}{i_{LG}} \tag{4}$$

where i_L is the specific enthalpy of the saturated liquid, i_{LG} represents the latent heat of vaporisation and the local fluid enthalpy, i, is determined from an energy balance.

Figs. 5 and 6 show the variation of the heat transfer coefficient with vapour quality for different heat flux and mass flux values. Based on the experimental range, Fig. 5 shows the dependence of heat transfer coefficients on heat flux. The measured results increase with increasing heat flux and are less affected by vapour quality. Fig. 6 depicts the variation of the heat transfer coefficient with different values of mass flux. The results indicate that the measured heat transfer coefficients are mostly less dependent on mass flux. The similar behaviours as presented in Figs. 5 and 6 were also reported by different researchers such as Saitoh et al. [7] and Shiferaw et al. [11].

The experimental heat transfer coefficients for different flow patterns will be subsequently compared with predictions made with the three-zone flow boiling model which is discussed briefly next.

The modelling approach based on the elongated bubble flow regime, also known as the three-zone flow boiling model, was recently proposed by Thome et al. [16] and Dupont et al. [17]. It is a mechanistic flow boiling heat transfer model comprising heat transfer zones including a pair of liquid slug and elongated bubble zones, followed by vapour slug if dry-out occurs. Each zone is modelled as passing at a fixed location sequentially and cyclically. Rather than nucleate boiling, the heat transfer was proposed to be dominated by conduction through the thin liquid film trapped between the elongated bubble and the tube wall.

To describe the cyclic passage through each zone, a time-averaged local heat transfer coefficient is obtained as follows:

$$h(z) = \frac{t_L}{\tau} h_L(z) + \frac{t_{film}}{\tau} h_{film}(z) + \frac{t_{dry}}{\tau} h_G(z) \tag{5}$$

where the period of bubble generation, τ, which is the reciprocal of the frequency was determined empirically by Dupont et al. [17]. t_L represents the time needed for the liquid slug to pass by a fixed location z along the tube. t_{film} and t_{dry} are the times needed, respectively, for film formation and local wall dry-out. h_{film} stands for the heat transfer coefficient in the film, which is assumed to be

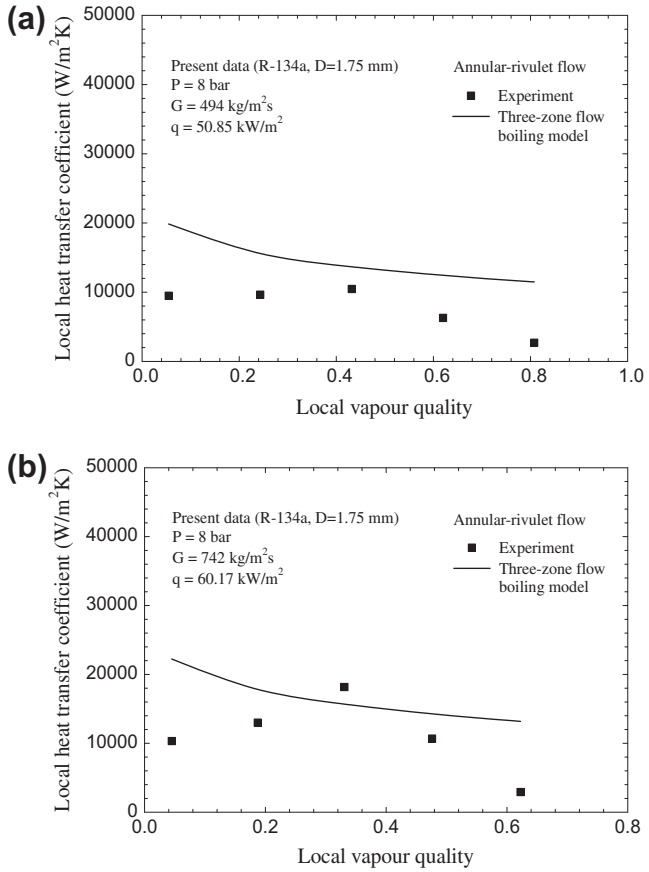

Fig. 11. Comparison of the local heat transfer coefficient data for annular-rivulet flow regime with the three-zone flow boiling model.

stagnant, across which one-dimensional conduction takes place. h_L and h_G are heat transfer coefficients in the liquid and vapour slugs, respectively, and are determined from their local Nusselt numbers.

Based on the general values for relevant parameters presented by Thome et al. [16] and Dupont et al. [17], our calculation is performed in order to examine the applicability of such a heat transfer model, whose dominant mechanism is transient conduction through the thin liquid film surrounding the confined and elongated bubble, to flow boiling heat transfer in different flow regimes.

Figs. 7–11 show a comparison of the present heat transfer coefficients for different flow regimes with predictions made with the three-zone flow boiling model.

Regarding the present flow pattern map shown in Fig. 4, the slug flow regime can be observed only in low vapour quality region. It is noted that the measured heat transfer coefficient for slug flow pattern tends to be not dependent with vapour quality. This corresponds well with the trends predicted by the model, excluding a contribution from nucleate boiling, as seen in Fig. 7.

In the throat-annular flow regime, which is developed from two consecutive vapour slugs (or elongated bubbles) coalescing into a throat-like vapour core, the measured heat transfer coefficient is not dependent on vapour quality but found to increase with heat flux as illustrated in Fig. 8. The observed characteristics, presented in Figs. 7 and 8, appear likely to agree with macro-scale ideas which suggest that nucleate boiling plays an important role in flow boiling heat transfer when the heat transfer coefficient is found to be strongly dependent on heat flux.

With regard to the predicted behaviour at increased heat flux, a relatively large enhancement of the predicted heat transfer coefficient is obtained when compared with the measured value, as indicated in Fig. 8. Based on transient conduction across the thin film being the dominant heat transfer mechanism, the heat transfer enhancement is due to the frequency of bubble generation which is strongly dependent on heat flux [17]. The model assumption seems to be compatible with the present results under low heat flux condition as seen in Fig. 8a.

The throat-annular flow is developed from the two consecutive elongated bubbles (vapour slugs) which coalesce to form the ripple, leading to a throat-like vapour core. As heat flux increases, however, the ripple appearing at the throat-like vapour core becomes thinner, and the annular flow is eventually established as illustrated by the flow regime map shown in Fig. 4. For throat-annular flow regime under a heat flux of 16.42 kW/m^2, the relevant position on the flow regime map is located near the transition from coalescing bubble flow to annular flow (CB/A transition zone). Such location is far from slug flow pattern from which the model was developed. As a consequence, the significant deviations of model predictions from the experimental results are observed in Fig. 8b.

Churn flow is characterised by a disruptive region caused by distortion of the vapour slug. This unstable condition, not included in the model which assumes a stagnant thin liquid film where one-dimensional conduction plays an important role in determining the local heat transfer coefficient, may explain why the prediction does not represent satisfactorily the experimental data as presented in Fig. 9. The deviation between measured and predicted values seems to get smaller as the heat flux decreases.

Up to this point, it is likely that the three-zone flow boiling model could also be roughly applicable to the throat-annular flow and churn flow regimes, in addition to the slug flow pattern from which the model was developed. It should be noted however, that the prediction is fairly reasonable under low heat flux conditions.

Figs. 10 and 11 show, respectively, the predictions compared with measured heat transfer coefficients for annular flow and annular-rivulet flow. In contrast to the results mentioned previously, the applicability of the model cannot extend to both annular and annular-rivulet flow regimes appearing under the present experimental range. In Fig. 11, a significant drop in the measured heat transfer coefficient near the test section outlet may be mainly attributed to partial dry-out intermittently appearing in annular-rivulet flow.

For the saturation pressure higher than 8 bar, the three-zone flow boiling model failed to predict the experimental data. Mean absolute error (MAE) of above 150% was obtained for all conditions as well as all flow patterns. As discussed in Saisorn et al. [21] and Choi et al. [9], the liquid film under high saturation pressure tends to break up easily, leading to the unstable condition near the tube wall. Such condition, which is not taken into account in the model assumption, results in the disagreement of the data with the model prediction.

4. Conclusion

Boiling of R-134a flowing through a mini-channel with diameter of 1.75 mm is studied. Five different flow patterns, including slug flow, throat-annular flow, churn flow, annular flow and annular-rivulet flow, are identified. The heat transfer coefficient increases with increasing heat flux but is mostly independent of mass flux and vapour quality. The heat transfer coefficients for each flow pattern are also compared with the predictions based on the three-zone flow boiling model. Although the model was developed to describe the slug flow regime, the comparison illustrates that the model tends to become roughly applicable for throat-annular flow and churn flow patterns, especially at low heat flux conditions.

Acknowledgements

The authors would like to express their appreciation to King Mongkut's University of Technology Thonburi, the Thailand Research Fund, the Office of the Higher Education Commission and the National Research University Project for providing financial support for this study.

References

[1] S. Saisorn, S. Wongwises, A review of two-phase gas–liquid adiabatic flow characteristics in micro-channels, Renew. Sust. Energy Rev. 12 (2008) 824–838.
[2] S.S. Mehendale, A.M. Jacobi, R.K. Ahah, Fluid flow and heat transfer at micro- and meso-scales with application to heat exchanger design, Appl. Mech. Rev. 53 (2000) 175–193.
[3] S.G. Kandlikar, Fundamental issues related to flow boiling in mini-channels and micro-channels, Exp. Therm. Fluid Sci. 26 (2002) 389–407.
[4] X. Huo, L. Chen, Y.S. Tian, T.G. Karayiannis, Flow boiling and flow regimes in small diameter tubes, Appl. Therm. Eng. 24 (2004) 1225–1239.
[5] J. Pettersen, Flow vaporization of CO_2 in microchannel tubes, Exp. Therm. Fluid Sci. 28 (2004) 111–121.
[6] R. Yun, Y. Kim, M.S. Kim, Convective boiling heat transfer characteristics of CO_2 in microchannels, Int. J. Heat Mass Transfer 48 (2005) 235–242.
[7] S. Saitoh, H. Daiguji, E. Hihara, Effect of tube diameter on boiling heat transfer of R-134a in horizontal small-diameter tubes, Int. J. Heat Mass Transfer 48 (2005) 4973–4984.
[8] K.I. Choi, A.S. Pamitran, J.T. Oh, Two-phase flow heat transfer of CO_2 vaporization in smooth horizontal minichannels, Int. J. Refrig. 30 (2007) 767–777.
[9] K.I. Choi, A.S. Pamitran, C.Y. Oh, J.T. Oh, Boiling heat transfer of R-22, R-134a, and CO_2 in horizontal smooth minichannels, Int. J. Refrig. 30 (2007) 1336–1346.
[10] D. Shiferaw, X. Huo, T.G. Karayiannis, D.B.R. Kenning, Examination of heat transfer correlations and a model for flow boiling of R134a in small diameter tubes, Int. J. Heat Mass Transfer 50 (2007) 5177–5193.
[11] D. Shiferaw, T.G. Karayiannis, D.B.R. Kenning, Flow boiling in a 1.1 mm tube with R134a: experimental results and comparison with model, Int. J. Therm. Sci. 48 (2009) 331–341.
[12] C.L. Ong, J.R. Thome, Flow boiling heat transfer of R134a, R236fa and R245fa in a horizontal 1.030 mm circular channel, Exp. Therm. Fluid Sci. 33 (2009) 651–663.
[13] H.J. Lee, S.Y. Lee, Heat transfer correlation for boiling flows in small rectangular horizontal channels with low aspect ratios, Int. J. Multiphase Flow 27 (2001) 2043–2062.
[14] B. Sumith, F. Kaminaga, K. Matsumura, Saturated flow boiling of water in a vertical small tube, Exp. Therm. Fluid Sci. 27 (2003) 789–801.
[15] W. Qu, I. Mudawar, Flow boiling heat transfer in two-phase microchannel heat sinks; experimental investigation and assessment of correlation methods, Int. J. Heat Mass Transfer 46 (2003) 2755–2771.
[16] J.R. Thome, V. Dupont, A.M. Jacobi, Heat transfer model for evaporation in microchannels. Part I: presentation of the model, Int. J. Heat Mass Transfer 47 (2004) 3375–3385.
[17] V. Dupont, J.R. Thome, A.M. Jacobi, Heat transfer model for evaporation in microchannels. Part II: comparison with the database, Int. J. Heat Mass Transfer 47 (2004) 3387–3401.
[18] J. Kaew-On, S. Wongwises, Experimental investigation of evaporation heat transfer coefficient and pressure drop of R-410A in a multiport mini-channel, Int. J. Refrig. 32 (2009) 124–137.
[19] S. Saisorn, S. Wongwises, Flow pattern, void fraction and pressure drop of two-phase air-water flow in a horizontal circular micro-channel, Exp. Therm. Fluid Sci. 32 (2008) 748–760.
[20] R. Revellin, J.R. Thome, A new type of diabetic flow pattern map for boiling heat transfer in microchannels, J. Micromech. Microeng. 17 (2007) 788–796.
[21] S. Saisorn, J. Kaew-On, S. Wongwises, Flow pattern and heat transfer characteristics of R-134a refrigerant during flow boiling in a horizontal circular mini-channel, Int. J. Heat Mass Transfer 53 (2010) 4023–4038.

International Journal of Heat and Mass Transfer 54 (2011) 4376–4388

Contents lists available at ScienceDirect

International Journal of Heat and Mass Transfer

journal homepage: www.elsevier.com/locate/ijhmt

Numerical investigation of effective parameters in convective heat transfer of nanofluids flowing under a laminar flow regime

Ehsan Ebrahimnia-Bajestan [a,*], Hamid Niazmand [a], Weerapun Duangthongsuk [b], Somchai Wongwises [c,d]

[a] Department of Mechanical Engineering, Ferdowsi University of Mashhad, Mashhad, Iran
[b] Department of Mechanical Engineering, South-East Asia University, Bangkok, Thailand
[c] Fluid Mechanics, Thermal Engineering and Multiphase Flow Research Laboratory (FUTURE), Department of Mechanical Engineering, King Mongkut's University of Technology Thonburi, Bangmod, Bangkok 10140, Thailand
[d] The Royal Institute of Thailand, Academy of Science, Sanam Sueapa, Dusit, Bangkok 10300, Thailand.

ARTICLE INFO

Article history:
Received 3 December 2010
Received in revised form 29 April 2011
Accepted 29 April 2011
Available online 27 May 2011

Keywords:
Nanofluids
Heat transfer performance
Pressure drop
Numerical study
Thermal conductivity

ABSTRACT

This article presents a numerical investigation on heat transfer performance and pressure drop of nanofluids flows through a straight circular pipe in a laminar flow regime and constant heat flux boundary condition. Al_2O_3, CuO, carbon nanotube (CNT) and titanate nanotube (TNT) nanoparticles dispersed in water and ethylene glycol/water with particle concentrations ranging between 0 and 6 vol.% were used as working fluids for simulating the heat transfer and flow behaviours of nanofluids. The proposed model has been validated with the available experimental data and correlations. The effects of particle concentrations, particle diameter, particles Brownian motions, Reynolds number, type of the nanoparticles and base fluid on the heat transfer coefficient and pressure drop of nanofluids were determined and discussed in details. The results indicated that the particle volume concentration, Brownian motion and aspect ratio of nanoparticles similar to flow Reynolds number increase the heat transfer coefficient, while the nanoparticle diameter has an opposite effect on the heat transfer coefficient. Finally, the present study provides some considerations for the appropriate choice of the nanofluids for practical applications.

1. Introduction

Common heat transfer fluids such as oil, water and ethylene glycol have inherently poor thermal conductivity compared to most solids. This problem is the primary obstacle to the high compactness, light in weight and effectiveness of heat exchangers. In order to enhance the thermal conductivity of conventional heat transfer fluids, it has been tried to develop a new type of modern heat transfer fluid by suspending ultrafine solid particles in base fluids. In 1993, Masuda et al. [1] studied the heat transfer performance of liquids with solid nanoparticles suspension. However, the term of "nanofluid" was first named by Choi [2] in 1995, and successively gained popularity. Because of the extensively greater thermal conductivity and heat transfer performance of the nanofluids as compared to the base fluids, they are expected to be ideally suited for practical applications.

Since a decade ago, research publications related to the use of nanofluids as working fluids have been reported both numerically and experimentally. There are also some review papers that elaborate on the current stage in the thermal behaviours, thermophysical properties and flow characteristics of nanofluids [3–6]. However, this article is aimed at reviewing only the novel literature considering convective heat transfer of nanofluids with a numerical approach. These studies are briefly described as follows.

Mirmasoumi and Behzadmehr [7] reported the effect of nanoparticle diameter on convective heat transfer performance of Al_2O_3/water nanofluid flowing under a fully developed laminar flow regime numerically. In their study, a two-phase mixture model was used. The results demonstrated that the heat transfer coefficient of the nanofluid dramatically increases with decreasing the diameter of nanoparticle. Moreover, the results also indicated that nanoparticle diameter has no significant effect on the skin friction coefficient.

Kalteh et al. [8] numerically studied forced convective heat transfer of Cu/water nanofluid inside an isothermally heated microchannel under a laminar flow regime. An Eulerian two-fluid model was used to simulate the heat transfer characteristic of the nanofluid. The results indicated that the heat transfer performance increases with increasing Reynolds number as well as particle volume fraction. On the contrary, heat transfer enhancement increases with decreasing nanoparticle diameter. Finally, the results also showed that the pressure drop of nanofluids is slightly higher than that of base fluids.

* Corresponding author. Tel.: +98 915 300 6795; fax: +98 511 876 3304.
E-mail address: ehsan.ebrahimnia@gmail.com (E. Ebrahimnia-Bajestan).

0017-9310/$ - see front matter © 2011 Elsevier Ltd. All rights reserved.
doi:10.1016/j.ijheatmasstransfer.2011.05.006

Mirmasoumi and Behzadmehr [9] investigated the laminar mixed convection heat transfer of Al_2O_3/water nanofluid flowing through a horizontal tube numerically. A two-phase mixture model was used to describe the hydrodynamic and thermal behaviour of the nanofluid. The numerical results indicated that in the fully developed region the particle concentration has insignificant effects on the hydrodynamic parameters, while it has important effects on the thermal parameters. Moreover, the results showed that nanoparticle concentration is higher at the bottom of the test tube and at the near wall region.

Akbarinia [10] and Akbarinia and Behzadmehr [11] numerically investigated the fully developed laminar mixed convection of Al_2O_3/water nanofluid flowing through a horizontal curved tube. In their studies, three-dimensional elliptic governing equations were used. The effects of the buoyancy force, centrifugal force and particle concentration on the heat transfer performance were presented. The results showed that the particle concentration has no direct effect on the secondary flow, axial velocity and skin friction coefficient. However, when the buoyancy force is more important than the centrifugal force, the effect of particle concentration on the entire fluid temperature can affect the hydrodynamic parameters. Moreover, the results also indicated that the buoyancy force decreases the Nusselt number whereas the particle concentration has a positive effect on the heat transfer enhancement and on the skin friction reduction.

Izadi et al. [12] studied the hydrodynamic and thermal behaviours of an Al_2O_3/water nanofluid flowing through an annulus under a laminar flow regime. In their study, a single-phase model was used for nanofluid simulation. The results indicated that the particle volume concentration has no significant effect on the dimensionless axial velocity, but affects the temperature field and increases the heat transfer coefficient.

He et al. [13] numerically studied the convective heat transfer of a nanofluid with TiO_2 nanoparticles dispersed in water under laminar flow conditions. A single-phase model and combined Euler and Lagrange methods were used to investigate the effects of volume concentration, Reynolds number and aggregate size on the convective heat transfer and flow behaviour of the nanofluid. Their results indicated that the nanofluid significantly enhances the Nusselt number, especially in the entrance region. Moreover, the numerical results were consistent with experimental data.

Bianco et al. [14] investigated the heat transfer performance of an Al_2O_3/water nanofluid flowing through a circular tube under a laminar flow regime numerically. A single-phase model and two-phase model were used to determine the heat transfer coefficient of the nanofluid. The results demonstrated that the heat transfer performance increases with increasing Reynolds number as well as particle volume concentration. Moreover, differences in the average heat transfer coefficient between the single-phase and two-phase models were observed as approximately 11%.

Kumar et al. [15] used a single-phase thermal dispersion model to numerically investigate the thermal properties and flow field of a Cu/water nanofluid in a thermally driven cavity. The results indicated that the Grashof number, particle volume fraction and particle shape factor augment the average Nusselt number of nanofluids.

Talebi et al. [16] presented the numerical formulation to evaluate the laminar mixed convection heat transfer of Cu/water nanofluid flowing through a square lid-driven cavity. They found that, at a given Reynolds number, the particle concentration affects the thermal behaviour and flow characteristic at larger Rayleigh numbers. Moreover, the effect of particle concentration decreased with increasing Reynolds number.

Shahi et al. [17] reported a numerical investigation to simulate the heat transfer performance of Cu/water nanofluid flowing through a square cavity under a laminar flow regime. Their results indicated that the average Nusselt number of the nanofluid increases with increasing particle concentration. In contrast, the results also showed that the bulk temperature of the nanofluid decreases with increasing particle concentration.

Akbarinia and Laur [18] presented the laminar mixed convection heat transfer of Al_2O_3/water nanofluid flows in a circular curved tube numerically. A two-phase mixture model and the control-volume technique were used to investigate the effect of particle diameter on the hydrodynamic and thermal parameters. Their results indicated that the Nusselt number and secondary flow decrease with increasing the particle diameter and uniform distribution of nanoparticles is observed.

Zeinali Heris et al. [19] numerically investigated the convective heat transfer of nanofluid in a circular tube with constant wall temperature, employing a dispersion model. Their results showed that decreasing nanoparticle size and increasing nanoparticle concentration augment the heat transfer coefficient.

Raisi et al. [20] carried out a numerical study on laminar convective heat transfer of Cu/water nanofluid inside a microchannel with slip and no slip boundary conditions. They investigated the effect of different parameters such as Reynolds number, particle concentration, and slip velocity coefficient on the nanofluid heat transfer characteristics. The results indicated that the particle concentration and slip velocity coefficient have significant effects on the heat transfer rate at high Reynolds numbers.

Ghasemi and Aminossadati [21] investigated the natural convective heat transfer of CuO/water nanofluid inside an inclined enclosure with top and bottom wall at different temperatures. The effects of Rayleigh number, inclination angle, and particle concentration on heat transfer performance were studied. The results showed that the flow pattern, temperature field and heat transfer rate are affected by inclination angle at high Rayleigh numbers. Furthermore, it was found that the heat transfer rate is maximised at specific particle concentration and inclination angle.

Zhou et al. [22] presented the lattice Boltzman method (LB method) to study the microscale characteristics of the multicomponent flow of nanofluids. In this method, the computation domain was separated into fine mesh and coarse mesh regions, respectively. The multicomponent LB method was used in the fine mesh region and the single-component LB method was applied in the coarse mesh region. The results indicated that the present model can be used to predict the microscopic characteristics of the nanofluid and the computational efficiency can be significantly improved.

Although numerous papers are currently available on the numerical study of laminar convective heat transfer of nanofluids, there is no comprehensive study on different effective parameters in this field. The effect of several parameters such as nanoparticle shape, based fluid type and nanoparticle material are not considered in literature. On the other hand, naturally the increase in heat transfer performance due to the nanofluids is accompanied by several undesirable effects such as an increase in pressure drop. Therefore, it needs to find the suitable nanofluid for optimum operation. No significant attention is paid to find some criteria for the choice of appropriate nanofluids in different heat transfer applications. In the present study a modified single-phase model for predicting the heat transfer performance of nanofluids is proposed and a home-made FORTRAN computer program is developed. The model has been validated against the measured data of Kim et al. [23] and the predicted values from Shah and London [24] for the base fluid. The effects of particle concentration, mean particle diameter, Reynolds number, Brownian motion, nanoparticle material and shape, and type of base fluid on the heat transfer performance of nanofluids are then investigated in detail. Finally, some guidelines related to choice of the appropriate nanofluid for particular applications are provided.

2. Mathematical modelling

Normally, two different approaches can be used in predicting the heat transfer performance of nanofluids. One is the two-phase model, where solid particles are treated as a solid phase in the base fluid, and the other is the single-phase model, where the presence of the nanoparticles is accounted for by introducing the effective thermophysical properties for the nanofluid. A single-phase model is simpler to implement and requires less computational time, and therefore, adopted here to describe the heat transfer characteristics of nanofluids flowing through a straight circular tube under constant wall heat flux and laminar flow regime, as shown in Fig. 1. On the basis of this model, the governing equations are as follows.

For continuity equation:

$$\iint \rho_e \vec{V} \cdot d\vec{A} = 0. \tag{1}$$

For momentum equation:

$$\int_{\forall} \rho_e \frac{\partial \vec{V}}{\partial t} d\forall + \iint \vec{V} \rho_e \vec{V} \cdot d\vec{A} = -\iint p\vec{n} \cdot d\vec{A} + \iint \mu_e \vec{\nabla} \vec{V} \cdot d\vec{A} \tag{2}$$

For energy equation:

$$\int_{\forall} (\rho C_p)_e \frac{\partial T}{\partial t} d\forall + \iint (\rho C_p)_e T\vec{V} \cdot d\vec{A} = \iint k_e \vec{\nabla} T \cdot d\vec{A} \tag{3}$$

where $\vec{V}$, p, T, t, $\forall$, $\vec{A}$ and $\vec{n}$ are the velocity vector, pressure, temperature, time, volume, cross-sectional area vector and normal unit vector, respectively. The effective thermophysical properties of the nanofluid indicated by the subscript e are density (ρ), thermal conductivity (k), dynamic viscosity (μ), and heat capacity (C_p). These effective properties are modelled as temperature dependent variables using available correlations and experimental data as follows.

Density:

$$\rho_e(\phi, T) = (1-\phi)\rho_f(T) + \phi\rho_p \tag{4}$$

Heat capacity:

$$C_{p,e}(\phi, T) = \frac{(1-\phi)(\rho(T)C_p(T))_f + \phi(\rho_p C_p)_p}{(1-\phi)\rho_f(T) + \phi\rho_p} \tag{5}$$

where ϕ is the volume fraction of the nanoparticles, and the subscripts p and f indicate the nanoparticle and base fluid, respectively.

Regarding the dynamic viscosity and thermal conductivity of nanofluids two different methods have been considered. In the first method, available measured data of these properties in static condition are used. However, in the second method, available models for dynamic viscosity and thermal conductivity of nanofluids, where different effects such as base fluid type, Brownian motions, volume concentration, and nanoparticle diameters are also included are employed. Clearly, these models are designed to accurately predict the heat transfer coefficient.

In the present study, the measured data of Kim et al. [23] is used to develop the following correlations for predicting the effective thermal conductivity and viscosity of the nanofluids according to the first method.

$$\mu_e = -0.0001953 + \frac{0.0475745}{T} - \frac{0.42561}{T^2} \quad \text{for } 20\,^\circ\text{C} \leqslant T \leqslant 80\,^\circ\text{C} \tag{6}$$

$$k_e = 0.65 + 4.864 \times 10^{-7} T^3 \quad \text{for } 22\,^\circ\text{C} \leqslant T \leqslant 52\,^\circ\text{C} \tag{7}$$

where T is the temperature in Celsius. However, it should be mentioned that above correlations are valid only for Al_2O_3/water nanofluid containing 3 vol.% of suspended particles.

As for the second method, the Vajjha et al.'s [25] model is taken for viscosity with two parameters A and B, which are determined according to the experimental data of Kim et al. [23].

$$\mu_e = \mu_f(T) A \exp(B\phi) \tag{8}$$

This correlation applies for $20\,^\circ\text{C} \leqslant T \leqslant 90\,^\circ\text{C}$ and $1\% \leqslant \phi \leqslant 10\%$, with $A = 0.9$ and $B = 10.0359$.

For thermal conductivity, the model presented by Koo and Kleinstreuer [26] and modified by Vajjha and Das [27] is employed. The model consists of static thermal conductivity based on the Maxwell's theory and dynamic thermal conductivity to include Brownian motion of nanoparticles. This model is expressed as follows:

$$k_e = \left[\frac{k_p + 2k_f - 2(k_f - k_p)\phi}{k_p + 2k_f + (k_f - k_p)\phi}\right] k_f + (5 \times 10^4 \beta\phi\rho_f C_{p,f}) \times \sqrt{\frac{\kappa(T + 273.15)}{\rho_p d_p}} f(T, \phi) \tag{9}$$

$$f(T, \phi) = (2.8217 \times 10^{-2}\phi + 3.917 \times 10^{-3}) \frac{(T + 273.15)}{(T_0 + 273.15)} + (-3.0669 \times 10^{-2}\phi - 3.91123 \times 10^{-3}) \tag{10}$$

$$\beta = 8.4407(100\phi)^{-1.07304} \tag{11}$$

where κ is the Boltzmann constant (1.381×10^{-23} J/K), d_p is the nanoparticle diameter (m), and T is the temperature (°C). $T_0 = 0\,^\circ\text{C}$ is the reference temperature. The correlation is valid for $25\,^\circ\text{C} \leqslant T \leqslant 90\,^\circ\text{C}$ and the volume fractions between 1% and 10% for Al_2O_3 nanofluids [27]. It should be mentioned that all thermophysical properties of the base fluid (μ_f, k_f, $C_{p,f}$ and ρ_f) are considered as functions of temperature. For water as the base fluid, density, heat capacity and thermal conductivity are obtained from the curve-fits applied to available data [28], while for dynamic viscosity the following correlation is employed [29]:

$$\mu_{water} = 0.00002414 \times 10^{[247.8/(T+133)]} \tag{12}$$

The above methods for effective viscosity (Eqs. (6) and (8)) have been compared with measured data of Kim et al. [23] for 3.0 vol.% Al_2O_3/water nanofluids, where reasonable agreements are observed (Fig. 2). Similarly, the temperature variations of thermal

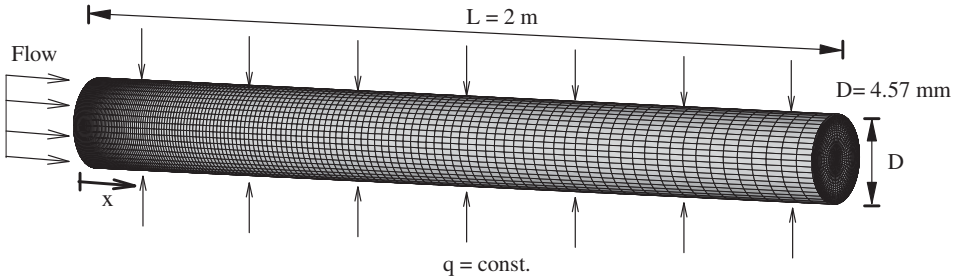

Fig. 1. Flow geometry and numerical grid distributions.

conductivity according to Eqs. (7) and (9) have been compared with the measured data of Kim et al. [23] as shown in Fig. 3. It can be seen that Eq. (9) over predicts the thermal conductivity as compared to the measured data, however it can predict the heat transfer coefficient more accurately as compared to Eq. (7) as will be discussed later.

3. Solution methodology

In order to evaluate the heat transfer coefficient of nanofluids numerically, the following assumptions are required.

As for boundary conditions for velocity filed, a uniform velocity profile is assumed at the inlet, while zero gradients are applied to all hydrodynamic variables at the outlet, with no-slip condition at walls. For the thermal field, constant heat flux of 60 W (2089.56 W/m^2) and the inlet temperature of 22 °C are employed corresponding to the data of Kim et al. [23], while constant temperature gradient is applied at the outlet.

In order to simulate the nanofluid flow, pipe geometry with 4.57 mm in diameter and 2 m long has been adopted according to the flow geometry in the experimental work of Kim et al. [23] as shown in Fig. 1. The problem under investigation is steady, however, in the numerical scheme the steady solution is obtained through sufficient integrations in time. The governing equations are solved numerically in a body-fitted coordinate system using a control-volume technique. The numerical solution is based on a projection-type method which solves the flow field in two steps. Firstly, an intermediate velocity field is obtained using the available pressure field. Secondly, velocity and pressure corrections

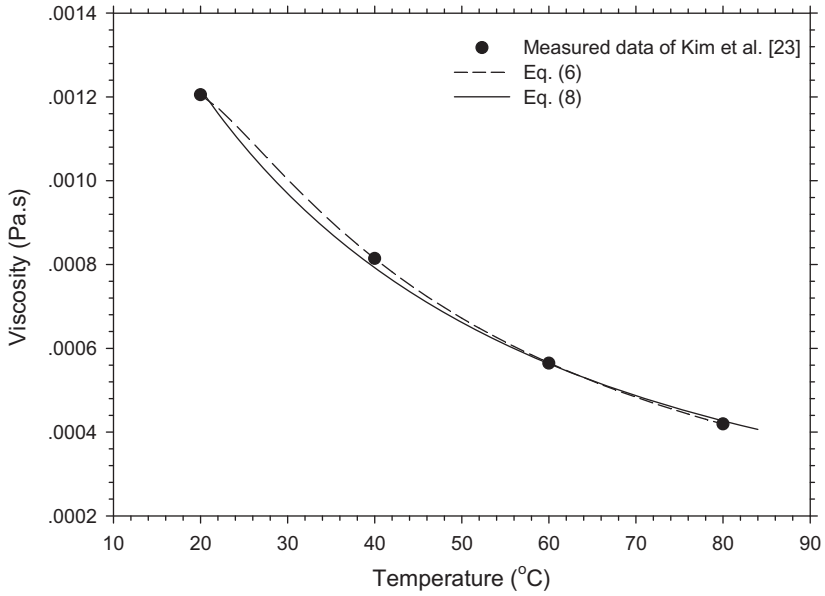

Fig. 2. Comparison of the predicted viscosity using Eqs. (6) and (8) with the measured data.

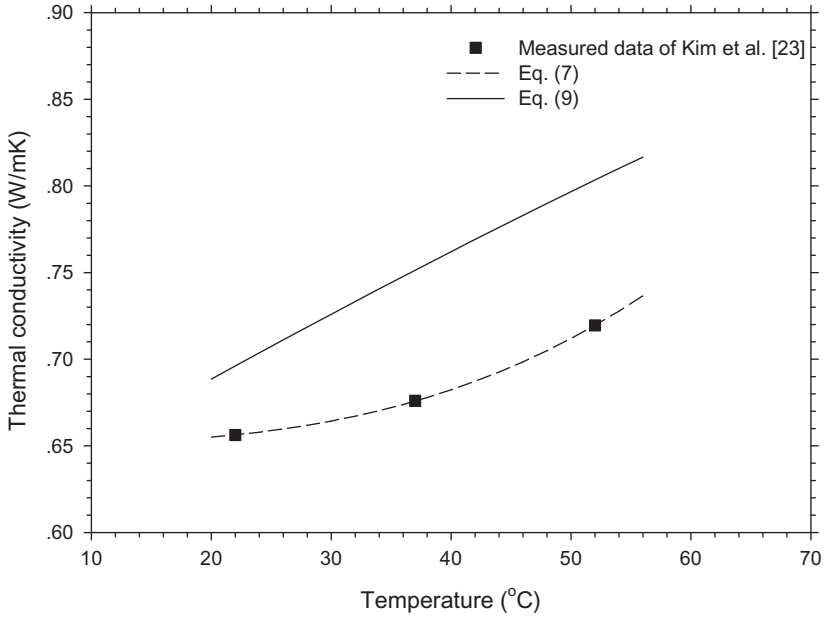

Fig. 3. Comparison of the predicted thermal conductivity using Eqs. (7) and (9) with the measured data.

are calculated from a Poisson equation designed to satisfy the continuity equation. The numerical scheme was originally developed by Chorin [30] and improved further by Dwyer [31] as well as Renksizbulut and Niazmand [32].

Moreover, extensive computations have been performed to identify the number of grid points that produce reasonably grid independent results. In Fig. 4 the grid resolution effects on the axial variations of the centreline velocity (nondimensionalized with the inlet velocity) and the heat transfer coefficient for just four different mesh distributions are presented. It is clear that the grid system of $41 \times 50 \times 150$ points in respective directions of radial, azimuthal, and axial adequately resolve the velocity and thermal fields with reasonable accuracy. Uniform grid spacing is used in the azimuthal direction, while the expansion ratios of 1.15 and 1.02 are employed in the radial and axial directions.

4. Model validation

For validating the present numerical scheme, the axial variations of the local Nusselt number have been compared with the experimental data of Kim et al. [23] and the results of Shah and London [24] as shown in Fig. 5. A laminar water flow in a straight circular pipe geometry, as mentioned above, has been considered under the constant heat flux condition of 60 W (2089.56 W/m^2) at Reynolds number of 1620. The Shah and London [24] equation for the axial variations of the local Nusselt number is expressed as:

$$Nu(x) = \begin{cases} 3.302x_*^{-1/3} - 1; & x_* \leqslant 0.00005 \\ 1.302x_*^{-1/3} - 0.5; & 0.00005 < x_* < 0.0015 \\ 4.264 + 8.68(10^3 x_*)^{-0.506}\exp(-41x_*); & x_* > 0.001 \end{cases} \quad (13)$$

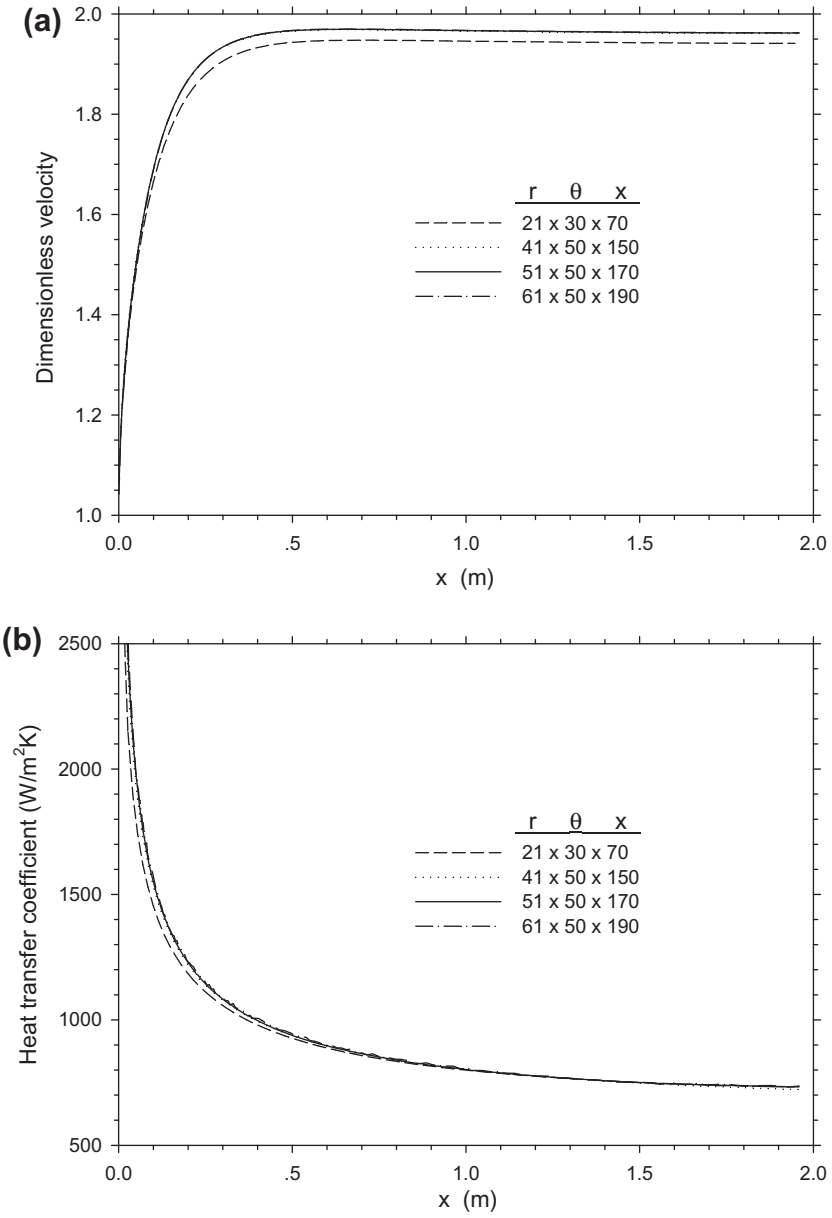

Fig. 4. Grid resolution effects on the axial variations of (a) dimensionless centreline velocity and (b) heat transfer coefficient for 6.0 vol.% Al_2O_3/water nanofluid at Reynolds number of 1460.

where $x_* = \frac{x/D}{\mathrm{Re}\,\mathrm{Pr}}$. Excellent agreements between the results can be observed in Fig. 5.

For the validation of the effective nanofluid properties models, the convective heat transfer of nanofluid in a straight pipe has been considered. Fig. 6 shows the axial variations of heat transfer coefficient of Al_2O_3/water nanofluid containing 3.0 vol.% of nanoparticles for Reynolds number of 1460. The results indicate that the second method (Eqs. (8) and (9)) agrees better with the measured data of Kim et al. [23] as compared to the first method (Eqs. (6) and (7)). This implies that the changes in thermal conductivity of nanofluids at static condition cannot justify the enhancement in heat transfer coefficient of nanofluids and a model, which adjusts the thermal conductivity to accurately estimate the heat transfer coefficient, is required.

Other numerical scheme validations for nanofluids can be found in Ebrahimnia-Bajestan et al. [33], which are not repeated here for conciseness.

5. Results and discussion

As shown in Fig. 6, the second method of nanofluid properties models predicts the heat transfer coefficient more accurately than the first method. In addition, the second method is more general than the first method, which is only valid for 3.0 vol.% Al_2O_3/water. Therefore, the second method has been employed for the evaluations of the effective thermal conductivity and viscosity in all numerical computations reported here. Moreover, the effects of

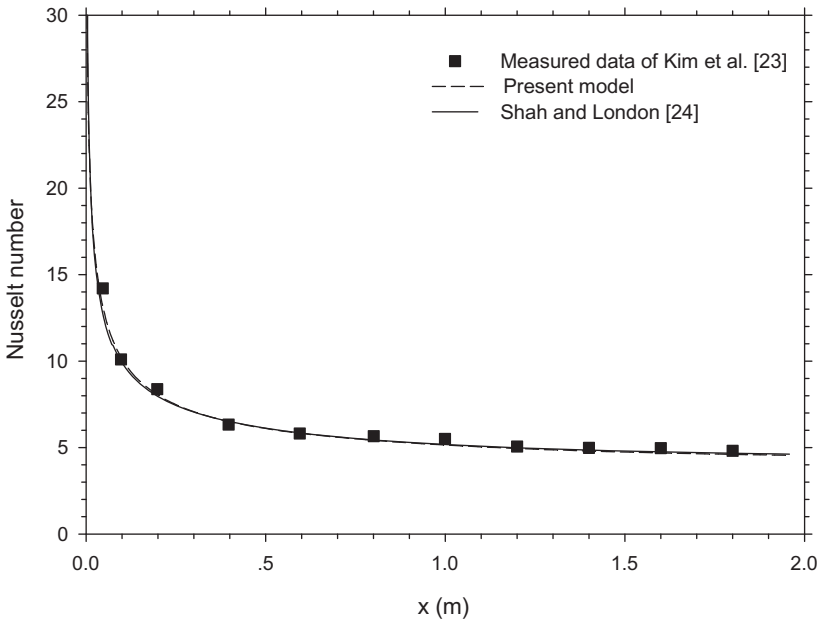

Fig. 5. Comparison of the axial variations of the Nusselt number with available data in literature at Reynolds number of 1620.

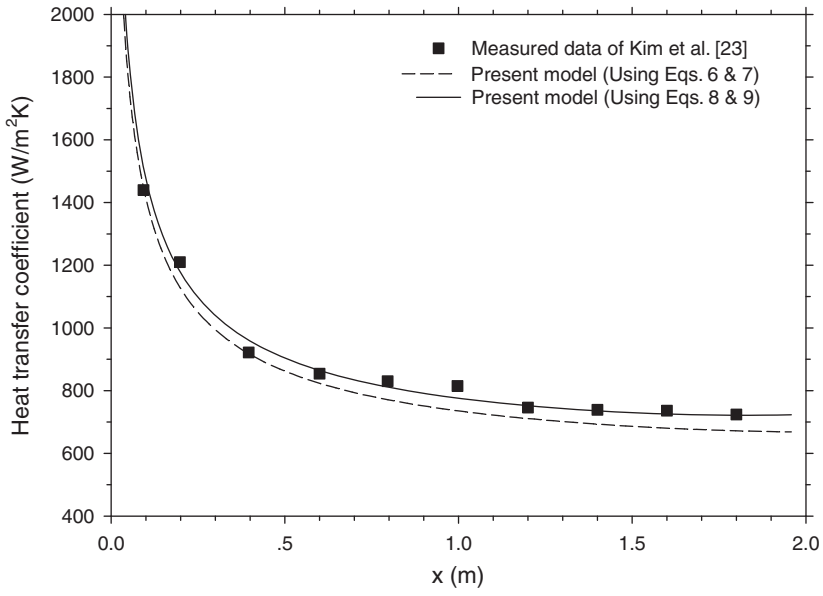

Fig. 6. Comparison of the local heat transfer coefficient with measured data of 3.0 vol.% Al_2O_3/water nanofluid at Reynolds number of 1460.

several parameters on the convective heat transfer characteristics of nanofluids will be examined in detail.

5.1. The effect of nanoparticle concentration

Fig. 7 shows the effect of particle volume concentration on the heat transfer coefficient along the pipe for Reynolds number of 1460 and heat flux of 2089.56 W/m^2. The results indicate that the heat transfer coefficient of nanofluid increases with increasing particle volume concentration. According to Eq. (9), nanofluids with higher particle concentrations have higher static and dynamic thermal conductivities, which in turn increase the heat transfer coefficient. For example, in the case of 6.0 vol.%, the local heat transfer coefficient is about 22% larger than pure water at the end of the pipe.

5.2. The effect of nanoparticle diameter

The effect of nanoparticle diameter on the heat transfer performance of nanofluid for Reynolds number of 1460 and heat flux of 2089.56 W/m^2 is shown in Fig. 8. The results show that the nanofluid with smaller nanoparticle diameter slightly increases the heat transfer coefficient as compared to the larger particle diameter, especially at lower volume concentrations. In general, according to Eq. (9) the nanoparticle diameter has a negative effect on the thermal conductivity and consequently on the heat transfer coefficient.

5.3. The effect of Reynolds number

Fig. 9 presents the effect of Reynolds number on the heat transfer coefficient along the pipe for Al_2O_3/water nanofluid with

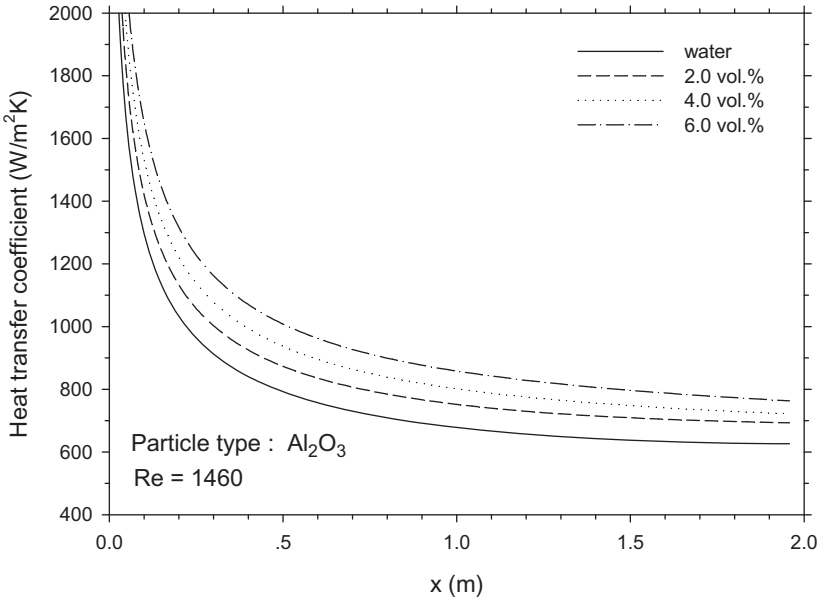

Fig. 7. Axial variations of heat transfer coefficient for different particle volume concentrations of Al_2O_3/water nanofluid at Reynolds number of 1460.

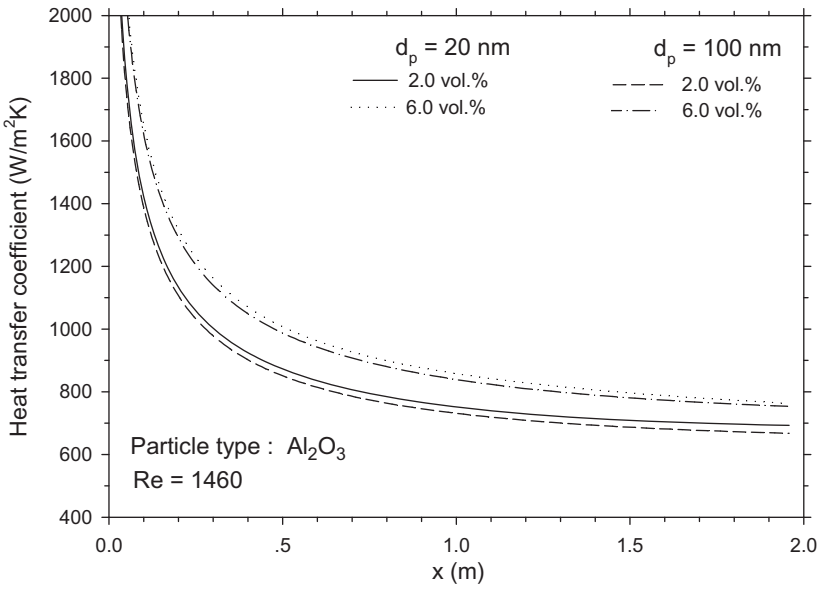

Fig. 8. Axial variations of heat transfer coefficient for different particle diameters and concentrations of Al_2O_3/water nanofluid at Reynolds number of 1460.

particle diameter of 20 nm. The results indicate that the heat transfer coefficient of nanofluid increases with increasing Reynolds number. This is due to the fact that higher Reynolds numbers lead to higher velocity and temperature gradients at the pipe wall.

5.4. The effect of Brownian motion of nanoparticles

According to Eq. (9), the second term is related to the dynamic thermal conductivity and reflects the Brownian motion effects on the thermal characteristics of nanofluids. In order to study the effects of Brownian motion on the heat transfer performance of nanofluids, Eq. (9) without the dynamic thermal conductivity term is used to simulate the convective heat transfer. It means that the classical two-phase model of Maxwell is employed and compared with the new nanofluid thermal conductivity model. Fig. 10 compares the axial variations of the heat transfer coefficient of Al_2O_3/water nanofluid with and without Brownian motion effects on thermal conductivity model for various particle concentrations at Reynolds number of 1460 and particle diameter of 20 nm. It is clearly seen that the Brownian motion has significant effects on the heat transfer coefficient of the nanofluids.

5.5. The effect of nanoparticle material

The nanoparticle material affects the nanofluid properties and consequently is an important factor in heat transfer performance. In order to study the effect of nanoparticle material, the CuO/water nanofluid is selected to compare with the results of the Al_2O_3/

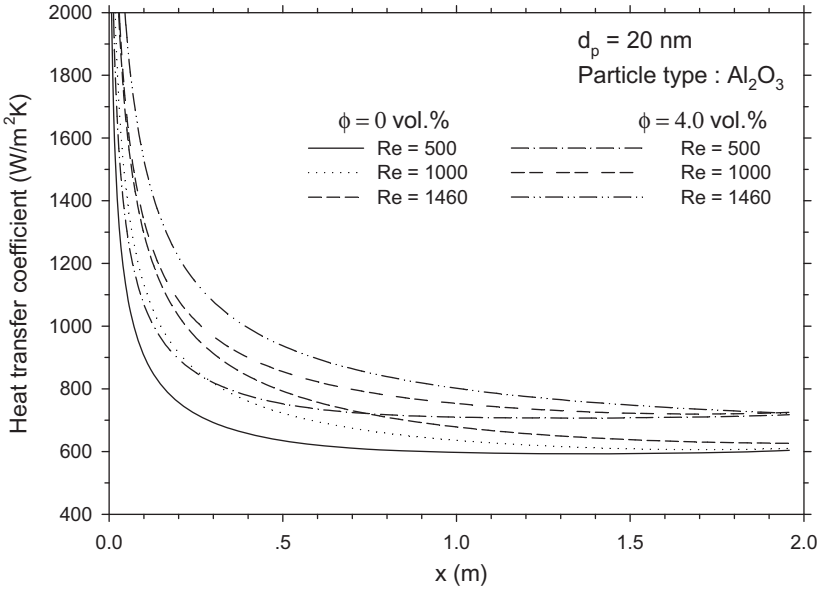

Fig. 9. Axial variations of heat transfer coefficient for different Reynolds numbers and particle concentrations of Al_2O_3/water nanofluid.

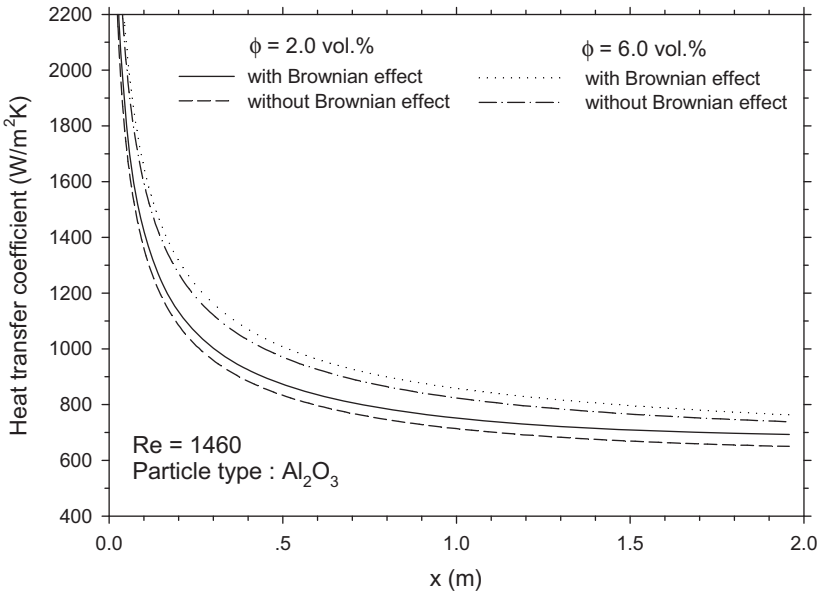

Fig. 10. Effects of Brownian motion on the local heat transfer coefficient as a function of particle concentration for Al_2O_3/water nanofluid at Reynolds number of 1460.

water nanofluid. For the viscosity of the CuO/water nanofluid, Eq. (8) is employed, where constants $A = 0.9197$ and $B = 22.8539$ are obtained following Vajjha et al. [25]. The thermal conductivity of CuO/water is evaluated based on Eqs. (9) and (10), however, the parameter β is determined from [27] as expressed below, which is valid for $25\ ^\circ C \leqslant T \leqslant 90\ ^\circ C$ and $1\% \leqslant \phi \leqslant 6\%$.

$$\beta = 9.881(100\phi)^{-0.9446} \tag{14}$$

As shown in Fig. 11, CuO/water nanofluids give higher convective heat transfer coefficients than the Al_2O_3/water nanofluids. For example, the heat transfer coefficient of 4.0 vol.% CuO/water nanofluids is greater than that of the 6.0 vol.% Al_2O_3/water nanofluids. This is because of the fact that the thermal conductivity of CuO nanoparticles is much larger than the thermal conductivity of Al_2O_3 nanoparticles.

5.6. The effect of base fluid properties

Another important factor in the heat transfer characteristics of nanofluids is the type of base fluid. In addition to water, a common base fluid consists of 60% ethylene glycol and 40% water (60% EG/water) by mass has also been considered. This kind of heat transfer fluid is common in cold regions of the world because of its low freezing point. The thermophysical properties of 60% EG/water as functions of temperature are obtained from [34] as follows:

$$\rho_{60\%EG/water} = -2.475 \times 10^{-3}T^2 - 0.35T + 1090.93 \tag{15}$$

$$C_{p,60\%EG/water} = 4.248T + 3042.74 \tag{16}$$

$$k_{60\%EG/water} = -3.196 \times 10^{-6}T^2 + 7.54 \times 10^{-4}T + 0.34 \tag{17}$$

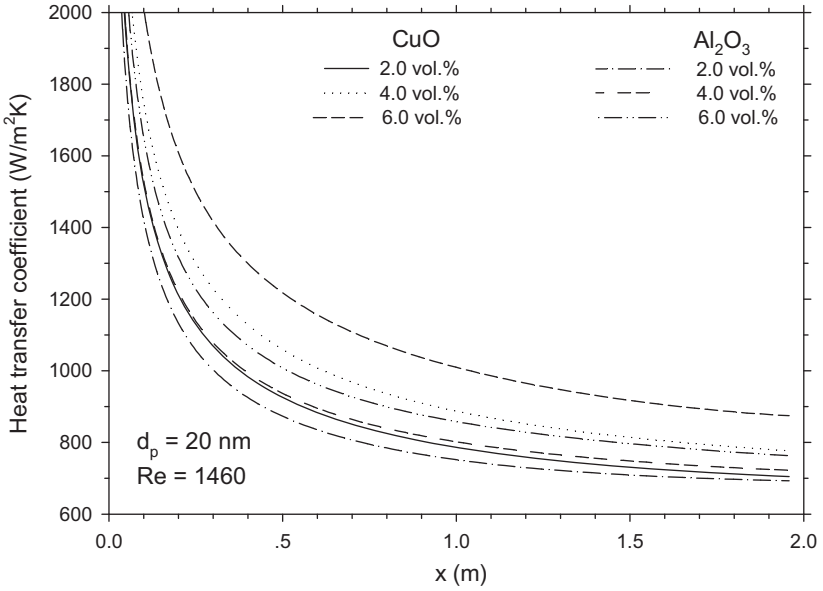

Fig. 11. Effects of particle type and particle concentration on the local heat transfer coefficient at Reynolds number of 1460 and particle diameter of 20 nm.

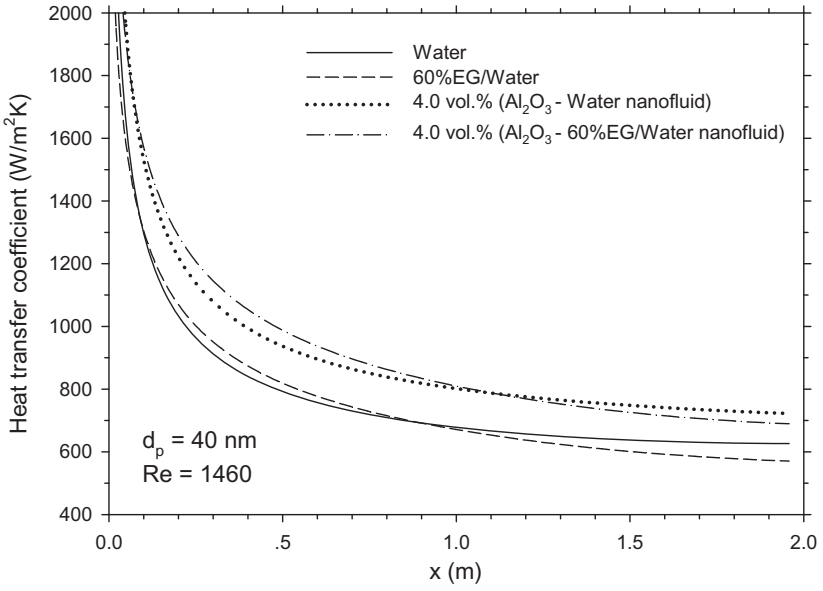

Fig. 12. Axial variations of heat transfer coefficient for different base fluids at Reynolds number of 1460 and particle diameter of 20 nm.

Table 1
Properties of CNT/water and TNT/water nanofluids.

Nanofluids	Nanoparticles aspect ratio	Nanoparticles concentration (vol.%)	Viscosity (Pa s)	Thermal conductivity (W/m K) $k = a + bT + cT^2$		
				a	b	c
CNT/water	>100	0.0384	0.00308	51.88156	−0.35487	6.14×10^{-4}
TNT/water	≈10	0.6	0.0015	0.42548	6.4×10^{-4}	0

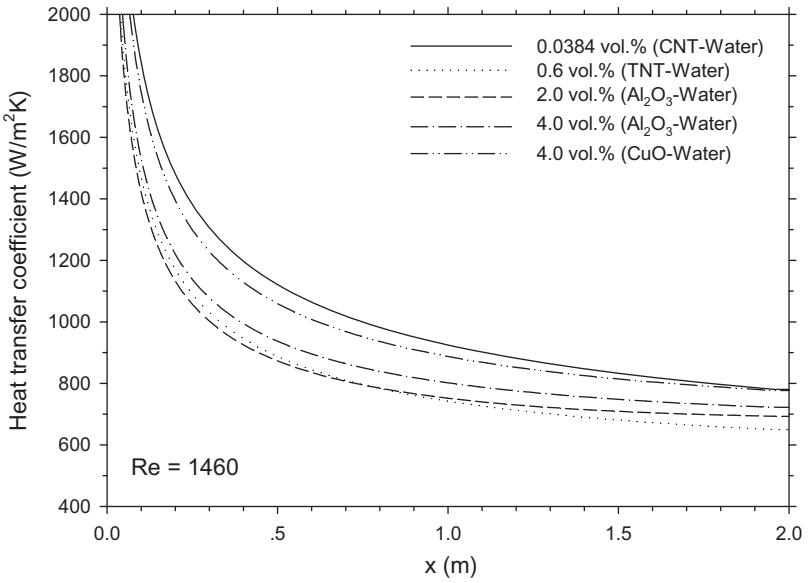

Fig. 13. Effects of particle shape on the local heat transfer coefficient at Reynolds number of 1460.

$$\mu_{60\%EG/water} = 0.001 \exp\left(\frac{3135.6}{T + 273.15} - 8.9367\right) \quad (18)$$

These correlations are valid for $0\ ^\circ C \leqslant T \leqslant 97\ ^\circ C$.

According to Vajjha and Das [27], Eqs. (8)–(11) are still applicable for the evaluation of viscosity and thermal conductivity of 60% EG/water base nanofluids.

In Fig. 12, the heat transfer coefficients of Al_2O_3 nanoparticles in both water and 60% EG/water base fluids are compared. The results indicate that the heat transfer characteristics of nanofluids are strongly influenced by the type of the base fluid.

5.7. The effect of nanoparticle shape

It has been shown that nanofluids containing nanoparticles with a higher aspect ratio have better thermal properties [35,36]. For example, the cylindrical nanoparticles give higher thermal conductivity and heat transfer coefficient than the spherical nanoparticles. To study the effect of nanoparticle shape, two kinds of cylindrical nanoparticles, which are CNT and TNT are used and then compared with the nanofluids with spherical nanoparticles. He et al. [35] studied the heat transfer performance of CNT/water nanofluid containing 0.1 wt.% (0.0384 vol.%) and TNT/water nanofluid containing 2.5 wt.% (0.6 vol.%) numerically and experimentally. They indicated that, at a given temperature, the shear viscosity of both nanofluids decreases with increasing shear rate, exhibiting a shear thinning behaviour. Moreover, the shear viscosity approaches a constant minimum value at higher shear rate. The measured viscosity did not show an important change versus share rate, more than the shear rates of 200 1/s and 500 1/s for the CNT/water and TNT/water nanofluids, respectively. They simulated the convective heat transfer of nanofluids as both Newtonian and non-Newtonian fluids. Their results showed that the heat transfer coefficients based on the non-Newtonian model agree well with the measured data. Furthermore, they indicated that, when the

Table 2
Different nanofluids flow conditions simulated in the present study and their corresponding temperature increase, pressure drop, and pumping power.

Type of working fluids	Re	d_p (nm)	ϕ (vol.%)	ΔT (°C)	ΔP (Pa)	Pump power (W)
Al_2O_3/60% EG/water	1460	20	4	0.56	43240	1.38
60% EG/water	1460	–	–	0.68	26240	0.69
CNT/water	1460	$L_p/d_p > 100$	0.038	0.9	9625	0.16
CuO/water	1460	20	6	1.05	8838	0.12
CuO/water	1460	20	4	1.52	3830	0.04
TNT/water	1460	$d_p = 10$, $L_p = 100$	0.6	1.8	2241	0.017
Al_2O_3/water	1460	100	6	2.05	2020	0.014
Al_2O_3/water	1460	40	6	2.06	2020	0.014
Al_2O_3/water	1460	20	6	2.08	2020	0.014
CuO/water	1460	20	2	2.18	1670	0.011
Al_2O_3/water	1460	40	4	2.39	1416	0.008
Al_2O_3/water	1460	20	4	2.39	1417	0.008
Al_2O_3/water	1460	20	3	2.52	1188	0.007
Water	1620	–	–	2.6	974	0.005
Al_2O_3/water	1460	20	2	2.72	996	0.005
Al_2O_3/water	1460	100	2	2.72	995	0.005
Al_2O_3/water	1460	40	2	2.73	995	0.005
Water	1460	–	–	2.78	869	0.004
Al_2O_3/water	1000	20	4	3.44	936	0.004
Water	1000	–	–	4.08	572	0.002
Al_2O_3/water	500	20	4	6.91	438	0.0009
Water	500	–	–	8.19	266	0.0004

nanofluid is considered as Newtonian with the constant minimum value of viscosity, the heat transfer coefficient has also reasonable agreement with the result of non-Newtonian model.

In the present work, the constant minimum value of viscosity presented by He et al. [35] was adopted as the effective viscosity. Similarly, the thermal conductivity of nanofluids as a function of temperature is taken from [35] as listed in Table 1.

Fig. 13 presents the comparison of axial heat transfer coefficients for nanoparticles with different aspect ratios at Reynolds number of 1460. The results show that the heat transfer coefficient of the CNT/water nanofluid is significantly greater than that of the other nanofluids, which can be attributed to its large aspect ratio (>100) as listed in Table 1. In addition to the nanoparticle shape, the higher thermal conductivity of CNTs compared with Al_2O_3 and CuO is the reason of substantial thermal characteristics enhancement of CNT/water nanofluids, even at low concentrations.

On the other hand, because of the low aspect ratio of TNT (≈10) and its lower thermal conductivity as compared with Al_2O_3, CuO and CNT, the heat transfer coefficient of TNT/water nanofluid is lower than those. Yet, it should be mentioned that the concentration of TNT is lower than Al_2O_3, CuO. The TNT/water nanofluid containing 0.6 vol.% nanoparticle shows approximately the same heat transfer coefficient as that of Al_2O_3/water nanofluid containing 2 vol.%, which also indicates the considerable effect of nanoparticle shape on the heat transfer characteristics of nanofluids.

Thus far, several influential parameters on the heat transfer of nanofluids are investigated; yet the important question is which nanofluid is more appropriate for a specific application. In this article, considering a constant wall heat flux condition, two important factors are considered as the criteria for the choice of proper nanofluids. These factors are pressure drop and temperature difference along the pipe. For a constant wall heat flux condition with a given

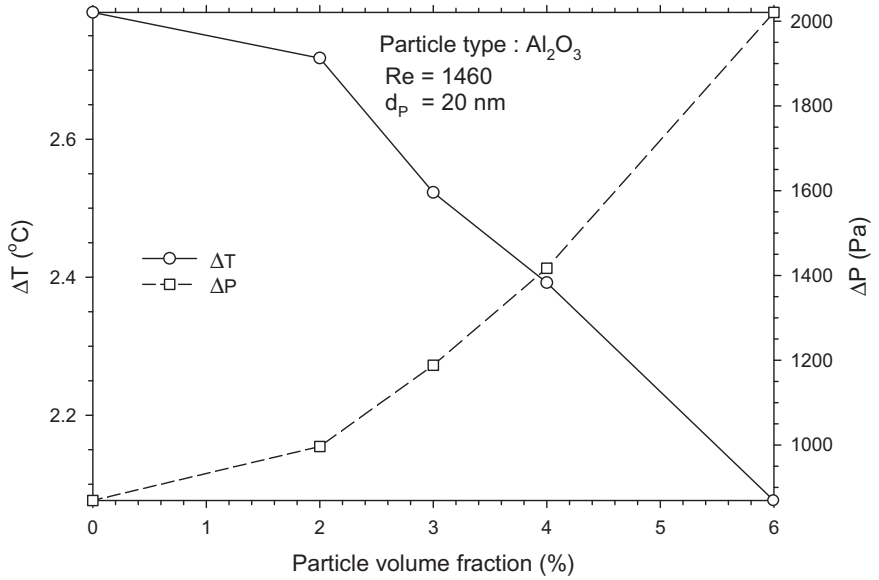

Fig. 14. Temperature differences and pressure drops for different particle volume concentrations of Al_2O_3/water nanofluid at Reynolds number of 1460 and particle diameter of 20 nm.

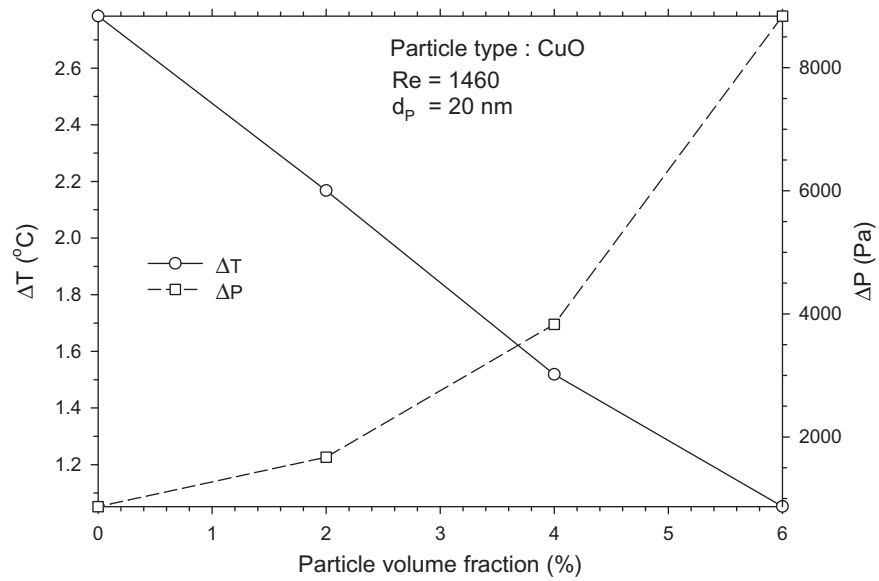

Fig. 15. Temperature differences and pressure drops for different particle volume concentrations of CuO/water nanofluid at Reynolds number of 1460 and particle diameter of 20 nm.

amount of heat transfer to the fluid, the lower temperature difference along the pipe can be considered as an advantage in some applications. On the other hand, lower pressure drop reduces the pumping cost.

In the view of these two criteria, all cases simulated in the present study are listed in Table 2, which have been sorted by pressure drop. It can be concluded from the table that almost all cases with lower pressure drops have higher temperature differences, which also implies that nanofluids should be selected according to the application requirements.

From Table 2 it is observed that considerable pressure drop are associated with high particle concentration of nanofluids, while much less pressure drop has been reported in numerical studies of [37,38] for similar flow conditions. It must be emphasised that the viscosity model, $\mu_e = \mu_f(1-\phi)^{-2.5}$, which has been used in these studies produces much lower values for viscosity as compared to the present experimental data [23] and consequently leads to relatively lower pressure drops. However, the applied viscosity model in the present study (Eq. (8)) represents the experimental data with reasonable accuracy and therefore, the resulting pressure drops are higher.

Another related issue to the pressure drop is the relative increase in viscosity with respect to thermal conductivity as the nanoparticle concentration increases. In general, the advantage of the nanofluids for the heat transfer applications is directly related to the amount of the thermal conductivity increase, leading to the heat transfer enhancement, to the amount of the viscosity increase associated with higher pressure drops. For the nanofluids used in the present study, the viscosity of the base fluid increases faster than its thermal conductivity as nanoparticle concentration increases, and therefore, the heat transfer enhancements come at the expense of relatively considerable pressure drop.

Considering Table 2, the temperature increase along the pipe and the pressure drop behave in an opposite manner. In Figs. 14 and 15 these parameters are plotted versus the particle volume fraction to see if an optimum nanoparticle concentration for a specific application can be identified. Fig. 14 shows the Al_2O_3 nanoparticles in water with particle diameter of 20 nm and Reynolds number of 1460. From this figure, the optimum choice for the Al_2O_3/water nanofluid is the volume fraction of about 4 vol.%, which has more reasonable temperature increase and pressure drop. Similarly, Fig. 15 indicates that for the case of the CuO/water nanofluid with particle diameter of 20 nm and Reynolds number of 1460, the proper choice is the volume fraction of about 3.7 vol.%.

Another limitation for nanofluids applications is the toxicity of nanoparticles. Clearly, the green nanofluids with no environmental, health and safety dangers are desirable. There are some studies on toxicity of nanoparticles considered in this article, Al_2O_3 [39], CuO [40], CNT [41,42] and TiO_2 [40]. Among them, the high toxicity of CuO nanoparticles has been reported [40]. Moreover, Bottini et al. [42] indicated that CNTs nanofluids can be very toxic at high particle concentrations.

In addition, the economical justification is one of the important considerations in nanofluid selection. In the present study, CNT/water nanofluid with a low concentration of 0.038 vol.% but high heat transfer coefficient seems to be a low cost nanofluid as compared with the others. Finally, the chemical reaction of nanofluids with the pipe wall is a consideration, especially in the case of surfactants, which may affect the nanofluids applications.

6. Conclusions

The laminar convective heat transfer performance and pressure drop of different nanofluids flowing in a straight circular pipe under a constant heat flux condition were numerically investigated. The effects of particle concentration, Reynolds number, Brownian motion, particle diameter, particle shape, particle material and type of base fluid on the heat transfer performance of nanofluids are examined in details. Major findings can be summarised as follows:

- The predicted heat transfer coefficients based on the thermophysical properties of nanofluids in a static condition are lower than the experimental data. This means that the static thermal conductivity increase is not the only reason of convective heat transfer enhancement of nanofluids.
- A thermal conductivity model which considers the effect of Brownian motion of nanoparticles predicts the heat transfer coefficient of nanofluids more accurately as compared to the models based on the pure static conditions of the nanofluids.
- The particle volume concentration, Brownian motion and aspect ratio of nanoparticles similar to the flow Reynolds number increase the heat transfer coefficient of nanofluids, while the particle diameter has an opposite effect. Moreover, the heat transfer characteristics of nanofluids are strongly influenced by the type of both base fluid and nanoparticle.
- There are several parameters to select the proper nanofluids for convective heat transfer of nanofluids in pipes. These parameters are the amount of heat transfer enhancement, pump power, stability, cost, toxicity and chemical corrosion of pipe wall. Also, there are some other restrictions in the special applications such as low freezing temperature nanofluids as the anti-refrigerant fluids in cold region.

Acknowledgements

The authors wish to thank Ferdowsi University of Mashhad (Iran), South-East Asia University (Thailand), King Mongkut's University of Technology Thonburi (Thailand) for the valuable support in the present study. The fourth author would like to acknowledge the Thailand Research Fund and the National Research University Project for financial supporting.

References

[1] H. Masuda, A. Ebata, K. Teramae, N. Hishinuma, Alteration of thermal conductivity and viscosity of liquid by dispersing ultra-fine particles (dispersion of Al_2O_3, SiO_2 and TiO_2 ultra-fine particles), Netsu Bussei (in Japanese) 7 (4) (1993) 227–233.
[2] S.U.S. Choi, Enhancing thermal conductivity of fluids with nanoparticles, in: Proceedings of the 1995 ASME International Mechanical Engineering Congress and Exposition, ASME, New York, 1995, pp. 99–105.
[3] W. Duangthongsuk, S. Wongwises, A critical review of convective heat transfer of nanofluids, Renew. Sustain. Energy Rev. 11 (2007) 797–817.
[4] V. Trisaksri, S. Wongwises, Critical review of heat transfer characteristics of the nanofluids, Renew. Sustain. Energy Rev. 11 (3) (2007) 512–523.
[5] X.Q. Wang, A.S. Mujumdar, Heat transfer characteristics of nanofluids: a review, Int. J. Therm. Sci. 46 (1) (2007) 1–19.
[6] L. Godson, B. Raja, D. Mohan Lal, S. Wongwises, Enhancement of heat transfer using nanofluids – an overview, Renew. Sustain. Energy Rev. 14 (2) (2010) 629–641.
[7] S. Mirmasoumi, A. Behzadmehr, Effect of nanoparticles mean diameter on mixed convection heat transfer of a nanofluid in a horizontal tube, Int. J. Heat Fluid Flow 29 (2) (2008) 557–566.
[8] M. Kalteh, A. Abbassi, M. Saffar-Avval, J. Harting, Eulerian–Eulerian two-phase numerical simulation of nanofluid laminar forced convection in a microchannel, Int. J. Heat Fluid Flow 32 (1) (2011) 107–116.
[9] S. Mirmasoumi, A. Behzadmehr, Numerical study of laminar mixed convection of a nanofluid in a horizontal tube using two-phase mixture model, Appl. Therm. Eng. 28 (7) (2008) 717–727.
[10] A. Akbarinia, Impacts of nanofluid flow on skin friction factor and Nusselt number in curved tubes with constant mass flow, Int. J. Heat Fluid Flow 29 (1) (2008) 229–241.
[11] A. Akbarinia, A. Behzadmehr, Numerical study of laminar mixed convection of a nanofluid in horizontal curved tubes, Appl. Therm. Eng. 27 (8–9) (2007) 1327–1337.
[12] M. Izadi, A. Behzadmehr, D. Jalali-Vahida, Numerical study of developing laminar forced convection of a nanofluid in an annulus, Int. J. Therm. Sci. 48 (11) (2009) 2119–2129.

[13] Y. He, Y. Men, Y. Zhao, H. Lu, Y. Ding, Numerical investigation into the convective heat transfer of TiO_2 nanofluids flowing through a straight tube under the laminar flow conditions, Appl. Therm. Eng. 29 (10) (2009) 1965–1972.
[14] V. Bianco, F. Chiacchio, O. Manca, S. Nardini, Numerical investigation of nanofluids forced convection in circular tubes, Appl. Therm. Eng. 29 (17) (2009) 3632–3642.
[15] S. Kumar, S.K. Prasad, J. Banerjee, Analysis of flow and thermal field in nanofluid using a single phase thermal dispersion model, Appl. Math. Model. 34 (3) (2010) 573–592.
[16] F. Talebi, A.H. Mahmoudi, M. Shahi, Numerical study of mixed convection flows in a square lid-driven cavity utilizing nanofluid, Int. Commun. Heat Mass Transfer 37 (1) (2010) 79–90.
[17] M. Shahi, A.H. Mahmoudi, F. Talebi, Numerical study of mixed convective cooling in a square cavity ventilated and partially heated from the below utilizing nanofluid, Int. Commun. Heat Mass Transfer 37 (2) (2010) 201–213.
[18] A. Akbarinia, R. Laur, Investigating the diameter of solid particles effects on a laminar nanofluid flow in a curved tube using a two phase approach, Int. J. Heat Fluid Flow 30 (4) (2009) 706–714.
[19] S. Zeinali Heris, M. Nasr Esfahany, G. Etemad, Numerical investigation of nanofluid laminar convective heat transfer through a circular tube, Numer. Heat Transfer, Part A: Appl. 52 (11) (2007) 1043–1058.
[20] A. Raisi, B. Ghasemi, S.M. Aminossadati, A numerical study on the forced convection of laminar nanofluid in a microchannel with both slip and no-slip conditions, Numer. Heat Transfer, Part A: Appl. 59 (2) (2011) 114–129.
[21] B. Ghasemi, S.M. Aminossadati, Natural convection heat transfer in an inclined enclosure filled with a water–CuO, Numer. Heat Transfer, Part A: Appl. 55 (8) (2009) 807–823.
[22] L. Zhou, Y. Xuan, Q. Li, Multiscale simulation of flow and heat transfer of nanofluid with lattice Boltzmann method, Int. J. Multiphase Flow 36 (5) (2010) 364–374.
[23] D. Kim, Y. Kwon, Y. Cho, C. Li, S. Cheong, Y. Hwang, J. Lee, D. Hong, S. Moon, Convective heat transfer characteristics of nanofluids under laminar and turbulent flow conditions, Curr. Appl Phys. 9 (2) (2009) e119–e123.
[24] R.K. Shah, A.L. London, Laminar Flow Forced Convection in Ducts, Academic Press, New York, 1978. p.128.
[25] R.S. Vajjha, D.K. Das, P.K. Namburu, Numerical study of fluid dynamic and heat transfer performance of Al_2 O_3 and CuO nanofluids in the flat tubes of a radiator, Int. J. Heat Fluid Flow 31 (4) (2010) 613–621.
[26] J. Koo, C. Kleinstreuer, A new thermal conductivity model for nanofluids, J. Nanopart. Res. 6 (6) (2004) 577–588.
[27] R.S. Vajjha, D.K. Das, Experimental determination of thermal conductivity of three nanofluids and development of new correlations, Int. J. Heat Mass Transfer 52 (21–22) (2009) 4675–4682.
[28] F.P. Incropera, D.P. DeWitt, T.L. Bergman, A.S. Lavine, Fundamentals of Heat and Mass Transfer, sixth ed., John Wiley & Sons, 2006. p. 949.
[29] R.W. Fox, A.T. McDonald, P.J. Pritchard, Introduction to Fluid Mechanics, sixth ed., John Wiley & Sons, Berlin, 2004. p. 724.
[30] A.J. Chorin, Numerical solution of the Navier–Stokes equations for an incompressible fluid, Math. Comput. 22 (104) (1968) 745–762.
[31] H.A. Dwyer, Calculations of droplet dynamics in high temperature environments, Prog. Energy Combust. Sci. 15 (2) (1989) 131–158.
[32] M. Renksizbulut, H. Niazmand, Laminar flow and heat transfer in the entrance region of trapezoidal channels with constant wall temperature, J. Heat Transfer 128 (1) (2006) 63–74.
[33] E. Ebrahimnia-Bajestan, H. Niazmand, M. Renksizbulut, Flow and heat transfer of nanofluids with temperature dependent properties, in: Proceedings of the ASME 2010 Third Joint US–European Fluids Engineering Summer Meeting and Eighth International Conference on Nanochannels, Microchannels, and Minichannels, Montreal, 2010.
[34] R. Strandberg, D.K. Das, Finned tube performance evaluation with nanofluids and conventional heat transfer fluids, Int. J. Therm. Sci. 49 (3) (2010) 580–588.
[35] Y. He, Y. Men, X. Liu, H. Lu, H. Chen, Y. Ding, Study on forced convective heat transfer of non-Newtonian nanofluids, J. Therm. Sci. 18 (1) (2009) 20–26.
[36] H. Chen, W. Yang, Y. He, Y. Ding, L. Zhang, C. Tan, A.A. Lapkin, D.V. Bavykin, Heat transfer and flow behaviour of aqueous suspensions of titanate nanotubes (nanofluids), Powder Technol. 183 (1) (2008) 63–72.
[37] J. Li, C. Kleinstreuer, Thermal performance of nanofluid flow in microchannels, Int. J. Heat Fluid Flow 29 (4) (2008) 1221–1232.
[38] R. Chein, G. Huang, Analysis of microchannel heat sink performance using nanofluids, Appl. Therm. Eng. 25 (17–18) (2005) 3104–3114.
[39] W. Lin, I. Stayton, Y. Huang, X.D. Zhou, Y. Ma, Cytotoxicity and cell membrane depolarization induced by aluminum oxide nanoparticles in human lung epithelial cells A549, Toxicol. Environ. Chem. 90 (5) (2008) 983–996.
[40] V. Aruoja, H.C. Dubourguiera, K. Kasemets, A. Kahru, Toxicity of nanoparticles of CuO, ZnO and TiO_2 to microalgae Pseudokirchneriella subcapitata, Sci. Total Environ. 407 (4) (2009) 1461–1468.
[41] J. Miyawaki, M. Yudasaka, T. Azami, Y. Kubo, S. Iijima, Toxicity of single-walled carbon nanohorns, ACS Nano 2 (2) (2008) 213–226.
[42] M. Bottini, S. Bruckner, K. Nika, N. Bottini, S. Bellucci, A. Magrini, A. Bergamaschi, T. Mustelin, Multi-walled carbon nanotubes induce T lymphocyte apoptosis, Toxicol. Lett. 160 (2) (2006) 121–126.

Heat Mass Transfer (2011) 47:1219–1227
DOI 10.1007/s00231-011-0783-y

ORIGINAL

Performance characteristics of HFC-134a and HFC-410A refrigeration system using a short-tube orifice as an expansion device

Kitti Nilpueng · Chietta Supavarasuwat · Somchai Wongwises

Received: 24 March 2010 / Accepted: 8 March 2011 / Published online: 27 March 2011

Abstract In the present article, the effect of heat source temperature, heat sink temperature, short-tube orifice diameter and short-tube orifice length on the performance characteristics of HFC-140A and HFC-134a refrigeration system using a short-tube orifice as expansion device, i.e., mass flow rate, cooling capacity, compressor pressure ratio, power consumption, and second law efficiency are experimentally studied. The short-tube orifices diameters ranging from 0.849 to 1.085 mm with length ranging from 10 to 20 mm are used in this examination. The test run are done at heat source temperature ranging between 16.5 and 18.5°C, and heat sink temperature ranging between 30 and 35°C. The results show that the tendency of second law efficiency is increased as the short-tube orifice diameter and heat source temperature are enhanced, but it is decreased by increasing the short-tube orifice length and heat sink temperature. Under the similar conditions, the mass flow rate, cooling capacity, and compressor power consumption obtained from HFC-410A are higher than those obtained from HFC-134a.

List of symbols

COP_{actual}	Actual coefficient of performance
COP_{carnot}	Carnot coefficient of performance
$c_{p,\ hw}$	Specific heat at constant pressure of the hot water, kJ/kg K
D	Short-tube orifice diameter, m
L	Short-tube orifice length, m
$\dot{m}_{hw}$	Mass flow rate of hot water, kg/s
$\dot{m}_{cw}$	Mass flow rate of cold water, kg/s
Q_{evap}	Heat transfer rate at evaporator, kW
T_{sink}	Heat sink temperature, °C
T_{source}	Heat source temperature, °C
$T_{hw,\ in}$	Hot water temperature at the inlet of the evaporator, °C
$T_{hw,\ out}$	Hot water temperature at the outlet of the evaporator, °C
ΔT_{sub}	Degree of subcooling, °C
ΔT_{sup}	Degree of superheat, °C
W_{comp}	Electrical power supplied to the compressor, kW

1 Introduction

Due to the destruction of the earth's ozone layer by chlorine molecules from chlorofluorocarbon (CFC), many companies have been developed the alternative refrigerants to replace CFC refrigerant and hydrochlorofluorocarbon (HCFC) refrigerant in the refrigeration and air-conditioning applications for example, HFC-417A, HFC-404A, HFC-407C, HFC-134a, and HFC-410A. However, since the properties of refrigerant are changed, it may cause the variation of system performance. Therefore, the inspection in the performance of refrigeration system with using the new hydrofluorocarbon (HFC) refrigerants is very important.

An expansion device is a necessary element in the refrigeration system which is utilized to reduce the pressure of the refrigerant from the condenser pressure to the evaporator pressure and to regulate the mass flow rate of refrigerant flowing from the condenser to the evaporator.

K. Nilpueng · S. Wongwises (✉)
Fluid Mechanics, Thermal Engineering and Multiphase Flow Research Lab (FUTURE), Department of Mechanical Engineering, King Mongkut's University of Technology Thonburi, Bangmod, Bangkok 10140, Thailand
e-mail: somchai.won@kmutt.ac.th

C. Supavarasuwat
C Aircon Tech Co., Ltd., Bangkae, Bangkok 10160, Thailand

Basically, it can be divided into two main categories: variable-restriction type and constant-restriction type. In the prior, the flow area can be adjusted by the control system for example the automatic expansion valve and thermostatic expansion valve. In the latter, the flow area of the expansion device is fixed. An instance of most popular device of this type is capillary tube, ejector and short-tube orifice. Recently, however, it is discovered that the short-tube orifice have been widely used as the expansion device in residential and automotive air-conditioning systems. This is because of its simplicity, low initial cost, high reliability and ease of maintenance. Accordingly, a clear understanding of performance characteristics of air-conditioning system using as expansion device is more important.

In the past decade, the experimental investigation about the performance of vapour compression refrigeration system working with new HFC refrigerants and the refrigerant flow behaviour inside short-tube orifices have been investigated by the a number of researchers which are described in the following paragraphs.

1.1 Performance of the vapour compression refrigeration system with new HFC refrigerants

The performance characteristic of water chiller and heat pump and cold storage were experimentally studied by Aprea et al. [2] and Aprea and Renno [1]. HCFC-22 and HFC-417A were used as working fluid. The effect of cold storage air temperature on the coefficient of performance, compression ratio, volumetric efficiency, discharge temperature, and exergy destroy were presented. The results showed that *COP* and exergetic efficiency obtained from HFCF-22 was higher than those obtained from HFC-417A. Navarro-Esbrı′ et al. [13] estimated the effect of internal heat exchanger on the energy efficiency of a vapour compression plant working with HCFC-22, HFC-134a, and HFC-407C. The comparison between the results obtained from an experimental compression vapour plant with and without the internal heat exchanger was reported. They stated that the internal heat exchanger can have positive or negative effects on the plant efficiency, depending on the working fluid and the operating conditions. Cabello et al. [3] developed the mathematical model for analyzing the effect of operating conditions on performance of a single-stage vapour compression plant, including mass flow rate, cooling capacity, compressor power consumption and coefficient of performance. The results indicated that evaporating or condensing conditions have no significant effect on the change of mass flow rate and other energetic parameter. Llopis et al. [12] evaluated the performance of HFC-404A and HFC-507A in a double-stage vapour compression plant. The experiment was performed at evaporating temperature range between −36 and −20°C for a constant condensing temperature of 40°C. They reported that the performance of the HFC-404A was higher than that gained from the HFC-507A when the plant was operated without inter- stage systems. The performance of refrigeration system using an ejector as expansion device was experimentally investigated by Disawas and Wongwises [6], Wongwises and Disawas [19], Chaiwongsa and Wongwises, [4], and Chaiwongsa and Wongwises [5]. The impact of the external parameters, i.e., heat sink and heat source temperature on primary mass flow rate of refrigerant, secondary mass flow rate of refrigerant, compressor ratio, discharge temperature, cooling capacity and coefficient of performance were reported. The results indicated that the use of two-phase ejector enabled the evaporator to be flooded by refrigerant. Thus, the heat transfer rate in the evaporator was increased comparing with the standard cycle. However, although the ejector cycle has higher performance over the standard cycle, some disadvantage such as high refrigerant charge, high refrigerant flow, piping insulation and installation cost should be considered.

1.2 Flow characteristics of refrigerant through the short-tube orifices

Kim [9] experimentally investigated the flow of two-phase and subcooled HFC-134a through short-tube orifices with length-to-diameter ratios ranging between 7 and 20. For two-phase flow entering the short tube, he noticed that the mass flow rate decreased with increases in the dryness fraction. The flow characteristics of HFC-407C through mini short-tube orifices with diameters of 1.09–1.94 mm were studied by Payne and O'Neal [16]. They found that the addition of oil into refrigerant increased the mass flow rate by more than 12% for a two-phase flow entering the short tube but had little effect on mass flow rate at a high degree of subcooling. Singh et al. [17] presented experimental data on refrigerant HFC-134a flow through short-tube orifices with and without inlet and outlet screens. The experimental results indicated that the inlet and outlet screens had an insignificant effect on the mass flow rate. Liu et al. [11] explored the characteristics of R744 flow through short-tube orifices. The experimental results showed that choked flow existed under a wide range of operating conditions. They reported that the inlet and outlet chamfer depths had no evident effects on the mass flow rate. Kim et al. [10] examined the mass flow rate of HFC-410A through short-tube orifices at upstream pressures approaching the critical point. They found that the decrease in mass flow rate with a reduction in subcooling became more significant when upstream pressure increased beyond 3,604 kPa, due to a greater density change. Tu et al. [18]

presented the experimental results of HFC-134a flowing through micro-orifices with diameters of 31.0 and 52.0 mm. The experimental results indicated that flow was not choked, even when the downstream pressure was reduced to more than 400 kPa below the saturation pressure for liquid-upstream/two-phase-downstream flow. Nilpueng and Wongwises [14] and Nilpueng et al. [15] experimentally investigated the two-phase flow characteristics of HFC-134a, including flow pattern, mass flow rate, pressure distribution, and temperature distribution through short-tube orifices. The results indicated that metastable flow exists inside short-tube orifices over the whole range of testing conditions. However, the choked flow phenomenon disappears inside the short-tube orifice when L/D is less than 2.91.

As mentioned above, the studies about the performance of vapour compression refrigeration system with HFC refrigerants which is used to replace the CFC and HCFC refrigerants is currently available. However, there are still limited on the inspection of the system performance by using the short-tube orifice as expansion device; especially, HFC-134a and HFC-410A which is popularly used in the residential and automobile air conditioner. Therefore, the knowledge about performance characteristics is important for designing the air-conditioning system. The main aim of this article is to explore the impacts of short-tube orifice diameter, short-tube orifice length, heat source temperature, and heat sink temperature on the performance characteristics of refrigeration system, i.e., mass flow rate, cooling capacity, compressor pressure ratio, compressor power consumption, and second law efficiency. The comparison of vapour compression refrigeration system performance obtained from HFC-134a to HFC-410A are also presented.

2 Experimental apparatus

The experimental apparatus used for testing the performance of refrigeration system is setup as shown in Fig. 1. It consists of the three main loops: the refrigerant loop, the hot water loop and the cold water loop. The refrigerant loop consists of the main refrigeration system components: compressor, condenser, short-tube orifice (expansion device), evaporator, and other accessory parts: oil separator, liquid receiver, filter/drier, sight glass, sub-cooler and accumulator. Refrigerant is circulated by a two-cylinder single stage reciprocating compressor along with an inverter. The compressor speed is maintained at 450 rpm by controlling the inverter frequency. A helical oil separator is used to minimize the effect of lubricating oil on refrigerant which is discharged from the compressor. Compact plate heat exchangers are used as condenser, evaporator and sub-cooler. A schematic diagram of the short-tube orifice which is used as an expansion device is illustrated in Fig. 2. As shown in this figure, in order to fix the brass short-tube orifice with the copper tube, it is pressed by pressing machine. The short-tube orifice diameter ranging between 0.849 and 1.085 mm with length ranging between 10 and 20 mm are used in this experiment. The hot water loop and cold water loop are used for transferring heat to evaporator and from condenser, respectively. The hot water is heated by electric heater inside an insulated tank and supplied through the evaporator by the circulating pump. The cold water is cooled by a separated refrigeration system.

Normally, the examination of the cycle performance can be made by two approaches. The first one is based on internal parameters i.e., evaporating and condensing temperatures. The second one is based on external parameters such as the inlet temperature and the flow rate of the heat transfer fluid [7, 8]. In this paper, the cycle performance is examined by using the second method because it is more likely in real life. Thus, hot water acts as a heat source of the evaporator and heat source temperature means temperature of hot water. While cold water acts as a heat sink of the condenser and heat sink temperature means temperature of cold water. The test runs are done at heat source temperatures ranging between 16.5 and 18.5°C and heat sink temperatures ranging between 30 and 35°C. The volume flow rate of hot water and cold water are kept constant at 8 LPM and 6 LPM, respectively.

A microscope (Olympus BX51) is used to measure the diameter of the short-tube orifice. The length of the short-tube orifice is measured with a digital calliper. The accuracies of diameter and length measurements are ±0.001 and ±0.01 mm, respectively. The flow of hot water and cold water are measured by the rotameters within the ranges 2–20 LPM. The accuracy of the water volumetric flow rates is ±2%. The pressure is detected by pressure transducers calibrated from 0 to 30 bar with ±20 mbar accuracy. *T*-type thermocouples are used to measure fluid temperature. The uncertainty of the temperature measurement is ±0.1°C. The differential transducer had an accuracy of ±0.1% of its calibrated span. The flow rate of refrigerant through the short-tube orifice is measured by a Coriolis mass flow meter (ABB FCM2000) with an accuracy of ±0.25%. The uncertainty of the calculation of cooling capacity is ±13.2%.

3 Results and discussion

In this section, the performance characteristics of refrigeration system using short-tube orifice as expansion device

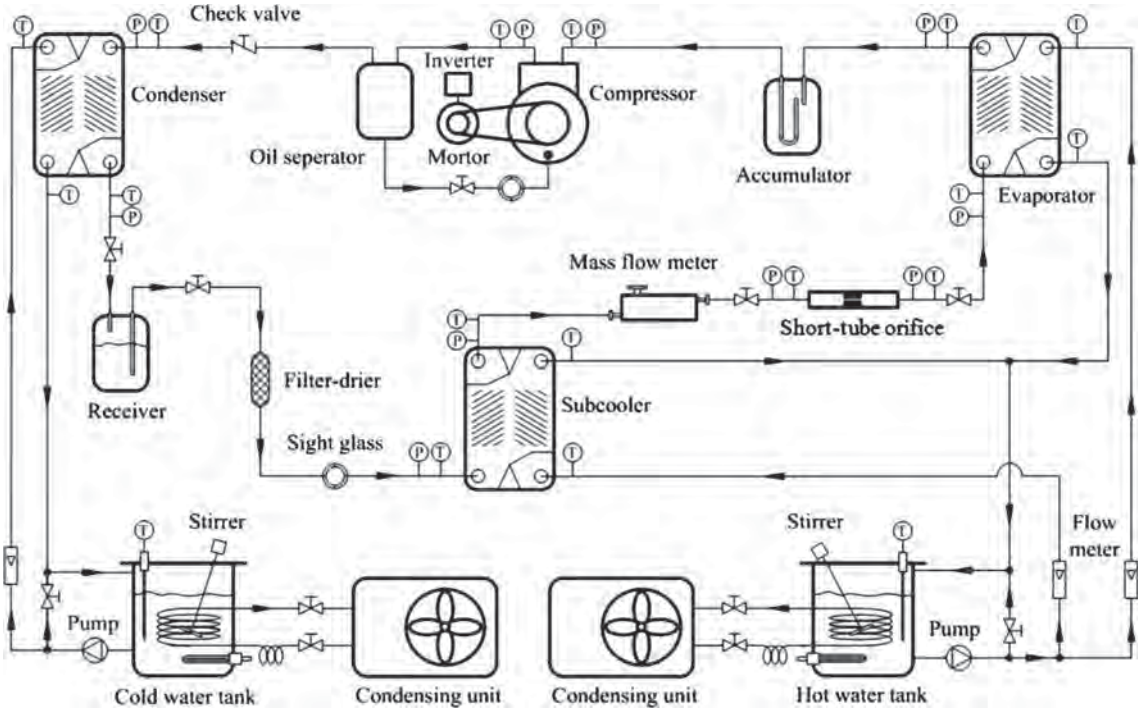

Fig. 1 Schematic diagram of experimental apparatus

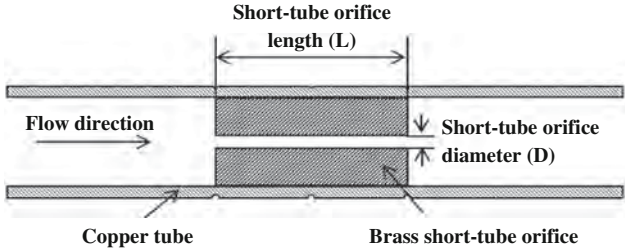

Fig. 2 Schematic diagram of the short-tube orifice

are described. The impacts of relevant parameters, i.e., heat source temperature, heat sink temperature, short-tube orifice diameter and short-tube orifice length on the mass flow rate, cooling capacity, compressor power consumption, and second law efficiency are explained.

3.1 Refrigerant mass flow rate

The variation of refrigerant mass flow rate with the heat source temperature is illustrated in Fig. 3. The results indicate that the mass flow rate is very little affected by the change of heat source temperature. However, it is found that the drop of heat source temperature causes the flow rate to increase by 1.03–1.60%. In this case, there are two explanations about the change of mass flow rate. The first one is related to the refrigerant density at the compressor inlet. When heat source temperature is reduced, the evaporation pressure is reduced whereas the degree of superheating is slightly increased. This leads to the decrease of refrigerant density which leads to a decrease of mass flow rate through compressor. The second reason is associated to the refrigerant velocity inside the short-tube orifice. The drop of heat source temperature causes the decrease of evaporation pressure which results in an increase of the pressure difference across the short-tube orifice. Therefore, refrigerant velocity and mass flow rate through short-tube orifice slightly increases. The reduction of mass flow rate inside compressor dominates the increase of mass flow rate inside the short tube orifice. As a result, the reduction of heat source temperature results in a very slight increase of mass flow rate in the refrigeration system. As shown in Fig. 3, it also can be seen that, when lifting the heat sink temperature, the mass flow rate is increased. The reason for this is similar to the one as mentioned above. That is, the increase of heat sink temperature leads to the rise of condensing pressure and pressure difference across the short-tube orifices, resulting in a higher refrigerant velocity and mass flow rate along the short-tube orifice. On the other hand, the increase of condensing pressure causes an increase of the compressor pressure ratio which results in the decrease of volumetric efficiency of compressor. As a result, the mass flow rate through the compressor is slightly reduced. Consequently, at the steady condition, the mass flow rate in the refrigeration system increases with increasing the heat sink temperature. In addition, at the same conditions, the mass flow rate of HFC-410A is higher than that of HFC-134a by about 85.3%.

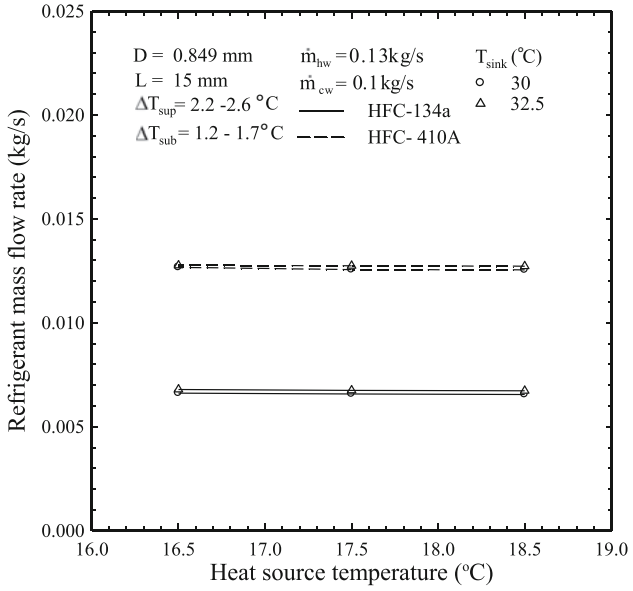

Fig. 3 Effect of heat source temperature on the refrigerant mass flow rate

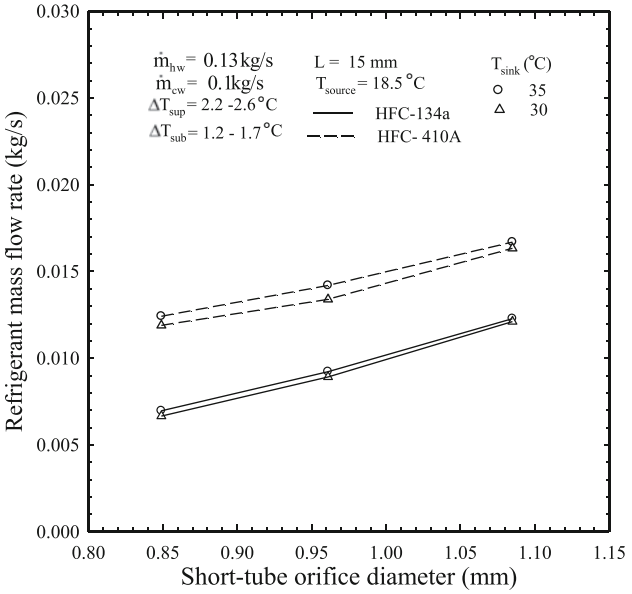

Fig. 4 Effect of short-tube orifice diameter on the refrigerant mass flow rate

The relationship between the refrigerant mass flow rate and short-tube orifice diameter is illustrated in Fig. 4. As expected, the refrigerant mass flow rate is greatly enhanced as the orifice diameter increases. This is because the enlargement of orifice diameter leads to an increase of mass flow rates of refrigerant flowing through short-tube orifice and evaporator. In addition to this, the density of suction vapour at the compressor inlet also increases due to a decrease of degree of superheating, resulting in a higher mass flow rate along the compressor. Consequently, the refrigerant flow rate in the air-conditioning system is increased.

As shown in Fig. 5, it is found that the decrease of refrigerant mass flow rate is the result of the enlargement of short-tube orifice length. The mass flow rate is found to decrease by about 0.31 and 0.38 kg/h/mm for HFC-134a and HFC-410A, respectively. This is due to the fact that the extension of length causes the increase of frictional pressure drop which lead to the drop of velocity and mass flow rate along the short-tube orifice. In addition, at this condition, the density of vapour at the evaporator outlet decreases because the evaporation pressure is reduced whereas the degree of superheating is slightly increased. The volumetric efficiency of compressor is also decreased as the pressure ratio enlarged. As a result, the mass flow rate of refrigerant flowing through compressor is also decreased. These two impacts cause the refrigerant flow rate to decrease.

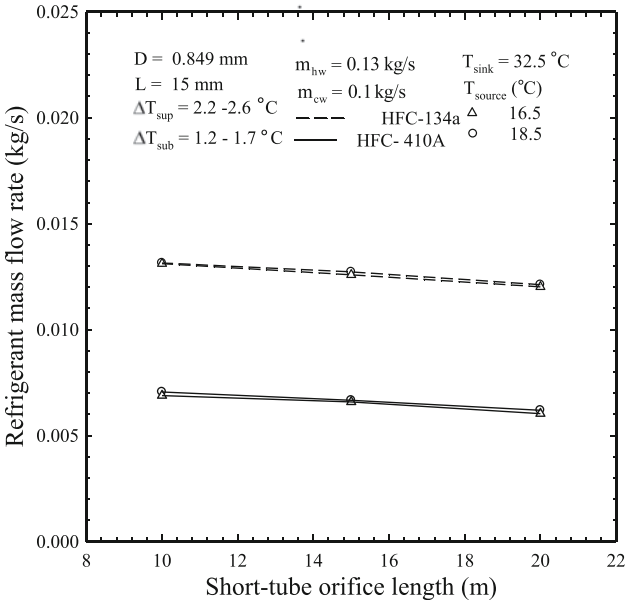

Fig. 5 Effect of short-tube orifice length on the refrigerant mass flow rate

3.2 Cooling capacity

In this experiment, the cooling capacity of the refrigeration system can be calculated from the following equation:

$$Q_{\text{evap}} = \dot{m}_{\text{hw}} c_{\text{p,hw}} (T_{\text{hw,in}} - T_{\text{hw,out}}) \quad (1)$$

where $\dot{m}_{\text{hw}}$ is mass flow rate of hot water (kg/s), $c_{\text{p,hw}}$ is specific heat at constant pressure of hot water (kJ/kg K), $T_{\text{hw,in}}$ is hot water temperature at the inlet of evaporator (°C), $T_{\text{hw,out}}$ is hot water temperature at the outlet of evaporator (°C).

As seen in Fig. 6, the cooling capacity is reduced by increasing the heat sink temperature. This is because, the

increase in heat sink temperature leads to a decrease of temperature difference between refrigerant inside the condenser and cold water, resulting in a decrease of the heat rejection from condenser. Therefore, based on the energy conservation, the cooling capacity is also decreased. This figure also shows that the rise of heat source temperature leads to an increase of cooling capacity. An increase of the heat source temperature leads to a slight increase of the evaporating pressure. As a result, the refrigerating effect and the density of the suction vapour at the compressor are increased. These effects lead to an increase of cooling capacity.

As seen in Fig. 7, it can be seen that the cooling capacity increases when the orifice diameter is enlarged. This is due to the fact that, at the similar operating conditions, the increase of short-tube orifice diameter results in an enhancement of refrigerant mass flow rate. Therefore, the heat absorption into the evaporator or cooling capacity is also increased.

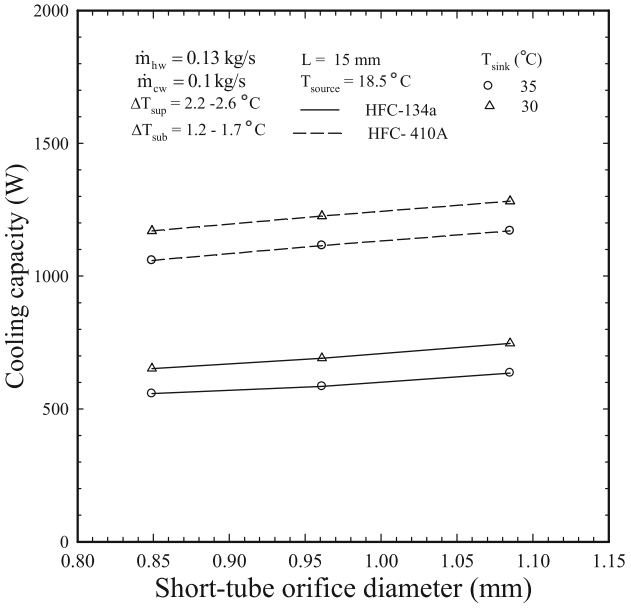

Fig. 7 Effect of short-tube orifice diameter on the cooling capacity

3.3 Compressor power consumption

The variation of compressor pressure ratio and electrical power consumption of compressor with the heat sink temperature is shown in Fig. 8. In this study, the electrical power consumption of compressor is directly measured by the built-in function of the inverter. The plots show that the electrical power consumption of compressor increases with increasing heat sink temperature, but it tends to decrease when the heat source temperature increases. This is because, as the heat sink temperature increases, the pressure ratio is increased. As we known, the volumetric efficiency of compressor is directly proportional with the pressure ratio. Conversely, it is found that the pressure ratio is decreased by increasing heat source temperature which results in an increase of volumetric efficiency of compressor. Therefore, the power consumption of compressor is reduced as the heat source temperature increases.

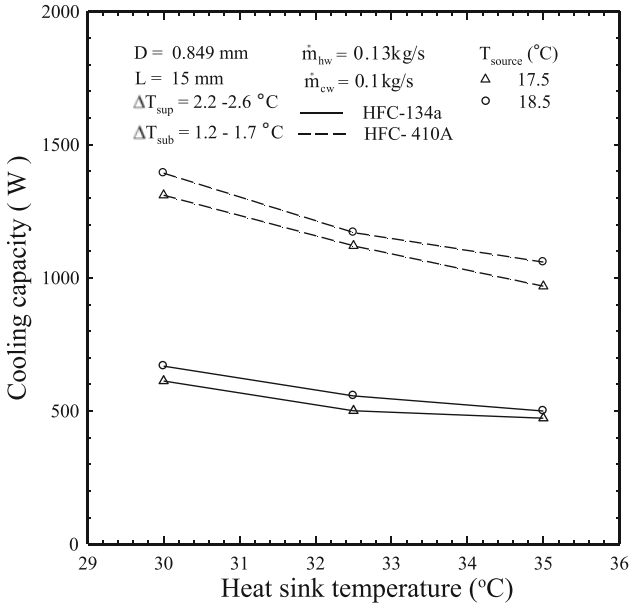

Fig. 6 Effect of heat sink temperature on the cooling capacity

As shown in Fig. 9, the power consumption of compressor slightly decreases with increasing the short-tube orifice diameter. This is because the expansion of diameter is the cause of the decrease of pressure drop due to sudden contraction which leads to the higher average evaporation pressure. This results in the decrease of compressor pressure ratio which leads to an increase of volumetric efficiency of compressor. Accordingly, the power consumption of compressor is lessened with enlarging the short-tube orifice diameter.

3.4 Second law efficiency

The identification of refrigeration system performance is presented by the second law efficiency (η_{II}) which is defined as the ratio of actual coefficient of performance (COP_{actual}) to the Carnot coefficient of performance (COP_{Carnot}) as shown by the following equation:

$$\eta_{II} = \frac{COP_{actual}}{COP_{Carnot}} \tag{2}$$

$$COP_{Carnot} = \frac{1}{\frac{T_H}{T_L} - 1} \tag{3}$$

where T_H is temperature of refrigerant inside the condenser (K) and T_L is temperature refrigerant inside the evaporator

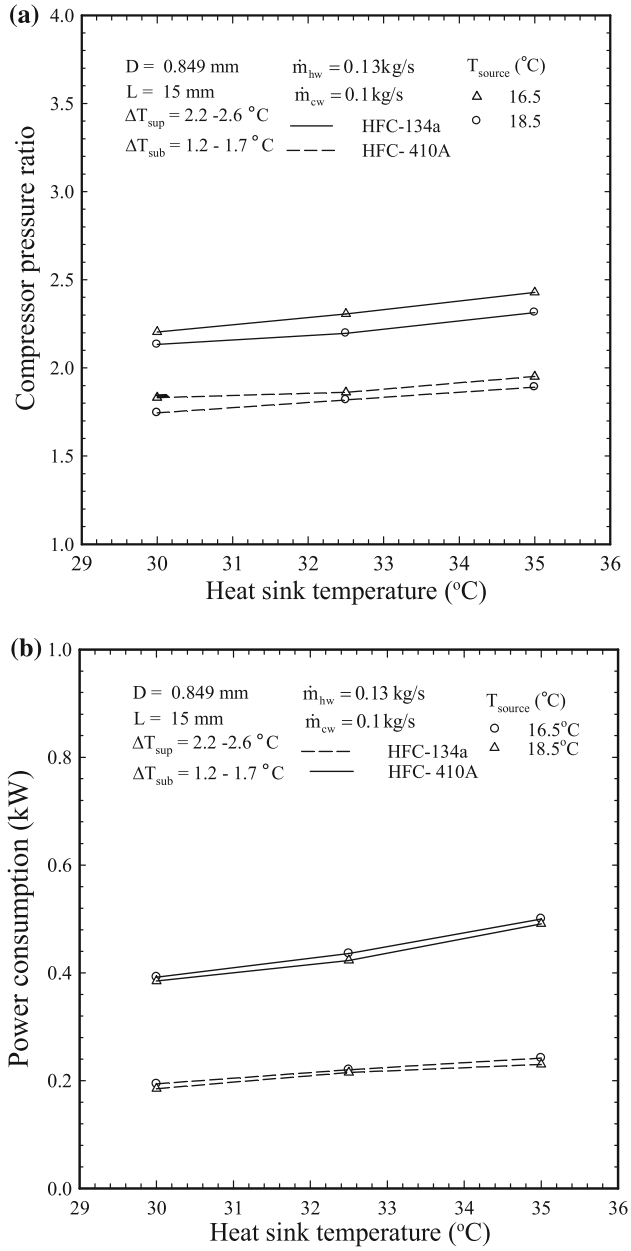

Fig. 8 Effect of heat sink temperature on the compressor pressure ratio and power consumption

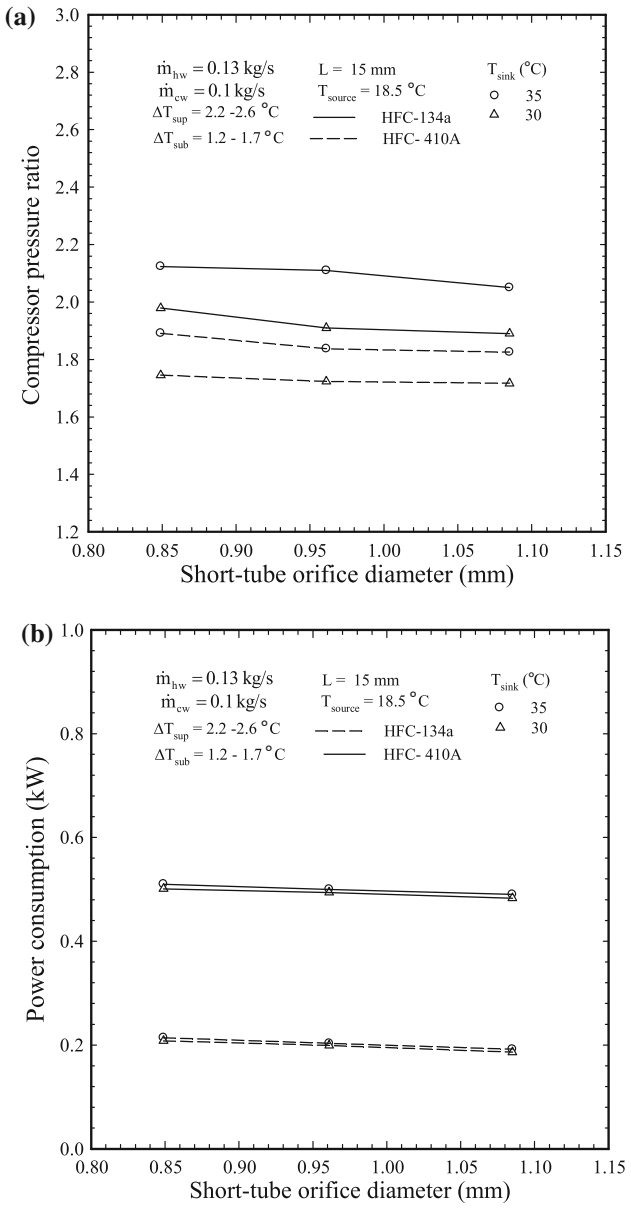

Fig. 9 Effect of short-tube orifice diameter on the compressor pressure ratio and power consumption

(*K*). The actual coefficient of performance is the ratio between the cooling capacity (Q_{evap}) and the electrical power supplied to the compressor (W_{comp}) as follows:

$$COP_{\text{actual}} = \frac{Q_{\text{evap}}}{W_{\text{comp}}} \tag{4}$$

The effect of heat source temperature on the second law efficiency is shown in Fig. 10. The results show that the second law efficiency is augmented when the heat source temperature increases. The average second law efficiency is 24.21 and 27.39% for HFC-410A and HFC-134a, respectively. This is because the refrigerant temperature inside evaporator slightly increases with increasing heat source temperature which produces an increase of Carnot *COP*. The increase of heat source temperature causes the actual *COP* of HFC-134a and HFC-410A to increase. The reason for this is that, when the heat source temperature increases, the cooling capacity also increases due to an increase of refrigerating effect. Conversely, the power consumption of compressor is reduced because the pressure ratio decreased. These influences lead to an increase of actual *COP*. However, the increment of actual *COP* is

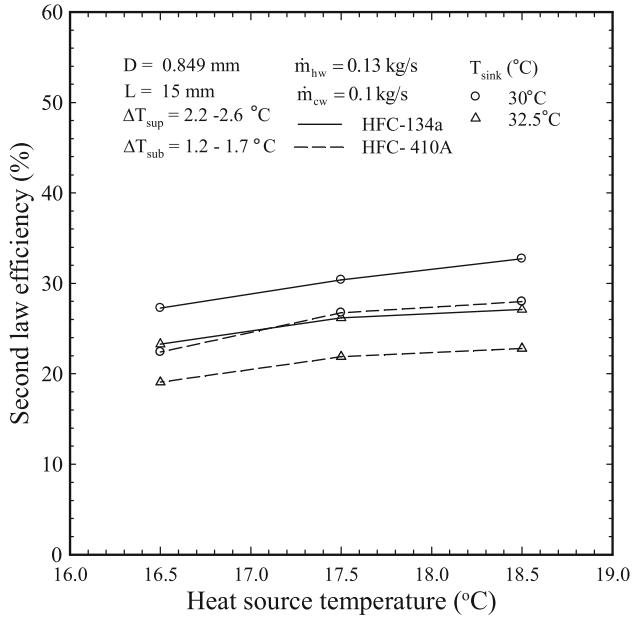

Fig. 10 Effect of heat source temperature on the second law efficiency

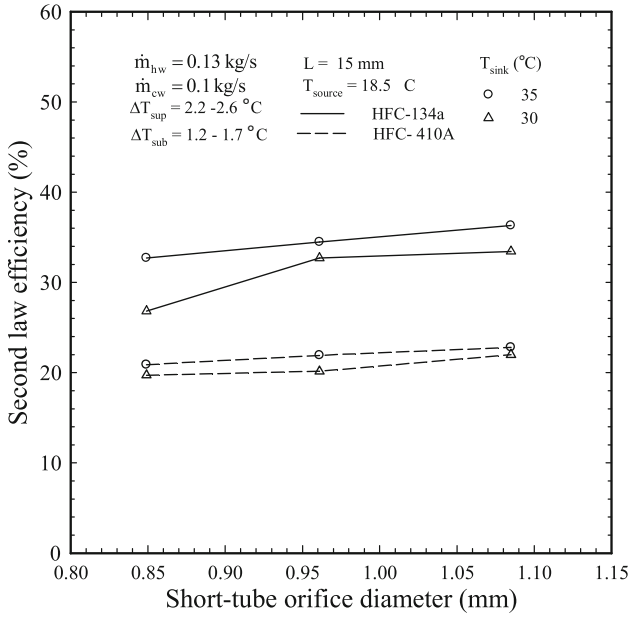

Fig. 11 Effect of short-tube orifice diameter on the second law efficiency

higher than the increment Carnot *COP* which causes the increase of second law efficiency.

Considering the second law efficiency of the short-tube orifice diameters ranging between 0.849 and 1.085 mm (Fig. 11), it is found that the average second law efficiency is 21.25 and 32.75% for HFC-410A and HFC-134a, respectively. As aforementioned from Figs. 4, 7 and 9, it is found that the enlargement of orifice diameter leads to an increase of refrigerant mass flow rate and cooling capacity. Conversely, the power consumption is slightly reduced as the orifice diameter is expanded due to the decrease of pressure ratio. This leads to the increase of actual *COP*. As a result, second law efficiency slightly increases with increasing short-tube orifice diameters.

As shown in Fig. 12, the second law efficiency tends to decrease as the short-tube orifice length increases. As described earlier, it is indicated that the wall friction increases when short-tube orifice length increases which leads to a decrease of the mass flow rate and cooling capacity. In addition, it is also found that electrical power consumption becomes higher when pressure ratio is higher due to the extension of short-tube orifice length. Similarly, the increase of short-tube orifice length results in the slight reduction of refrigerant temperature inside evaporator, resulting in a slight decrease of Carnot *COP*. Therefore, both actual *COP* and Carnot *COP* tend to decrease as the short-tube orifice length increases. Finally, the second law efficiency tends to decrease with increasing short-tube orifice length.

4 Conclusion

New experimental data of the performance characteristics of refrigeration system using a short-tube orifice as expansion device is presented. The impacts of working conditions and short-tube orifice dimension on mass flow rate, cooling capacity, compressor pressure ratio, compressor power consumption, and second law efficiency are

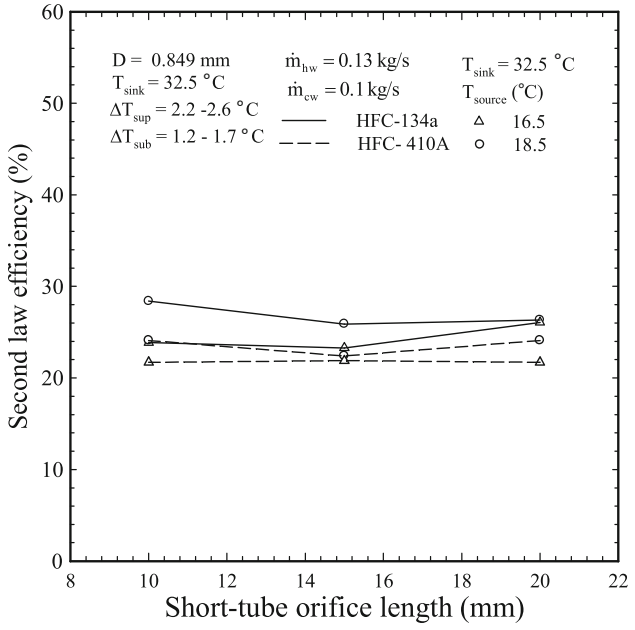

Fig. 12 Effect of short-tube orifice length on the second law efficiency

described. The performance characteristics of refrigeration system obtained from HFC-410A and HFC-134a are also compared. The short-tube orifice having diameter of 0.849, 0.961 and 1.085 mm with the length of 10, 15, and 20 mm are used in this experiment. Based on the foregoing discussions, the following summaries can be given:

1. The increases of short-tube orifice diameter and heat source temperature result in an increase of cooling capacity, but the increases of heat sink temperature lead to a reduction of cooling capacity.
2. The compressor power consumption is increased by increasing the heat sink temperature, but it is decreased with increasing the short-tube orifice diameter and heat source temperature.
3. Under the similar conditions, the mass flow rate, cooling capacity, and power consumption of compressor obtained from HFC-410A are higher than those obtained from HFC-134a.
4. Based on the testing conditions, the tendency of second law efficiency is increased when increasing short-tube orifice diameter and heat source temperature. On the other hand, it is decreased by increasing short-tube orifice length and heat sink temperature.

Acknowledgments The authors would like to express their appreciation to the Thailand Research Fund (TRF), the Office of the Higher Education Commission and the National Research University Project for providing financial support for this study.

References

1. Aprea C, Renno C (2004) Experimental comparison of R22 with R417A performance in a vapour compression refrigeration plant subjected to a cold store. Energy Convers Manag 45:1807–1819
2. Aprea C, Mastrullo R, Renno C (2004) An analysis of the performances of a vapour compression plant working both as a water chiller and a heat pump using R22 and R417A. Appl Therm Eng 24:487–499
3. Cabello R, Navarro-Esbrı′ J, Llopis R, Torrella E (2007) Analysis of the variation mechanism in the main energetic parameters in a single-stage vapour compression plant. Appl Therm Eng 27:167–176
4. Chaiwongsa P, Wongwises S (2007) Effect of throat diameters of the ejector on the performance of the refrigeration cycle using a two-phase ejector as an expansion device. Int J Refrig 30:601–608
5. Chaiwongsa P, Wongwises S (2008) Experimental study on R-134a refrigeration system using a two-phase ejector as an expansion device. Appl Therm Eng 28:467–477
6. Disawas S, Wongwises S (2004) Experimental investigation on the performance of the refrigeration cycle using a two-phase ejector as an expansion device. Int J Refrig 27(6):587–594
7. Giuliani G, Hewitt NJ, Marchesi Donati F, Polonara F (1999) Composition shift in liquid-recirculation refrigeration systems: an experimental investigation for the pure fluid R134a and the mixture R32/134a. Int J Refrig 22(6):486–498
8. Hoegberg M, Vamling L, Berntsson T (1993) Calculation methods for comparing the performance of pure and mixed working fluids in heat pump applications. Int J Refrig 16(6):403–413
9. Kim Y (1993) Two-phase flow of HFC134a and HCFC22 through short tube orifices PhD thesis. Texas A&M University, USA
10. Kim Y, Payne V, Choi J, Domanski P (2005) Mass flow of R410A through short tube working near the critical point. Int J Refrig 28:547–553
11. Liu JP, Niu YM, Chen JP, Chen ZJ, Feng X (2004) Experimental and correlation of R744 two-phase flow through short tubes. Exp Therm Fluid Sci 28:565–573
12. Llopis R, Torrella E, Cabello R, S′anchez D (2009) Performance evaluation of R404A and R507A refrigerant mixtures in an experimental double-stage vapour compression plant. Appl Energy, (in press)
13. Navarro-Esbrı′ J, Cabello R, Torrella E (2005) Experimental evaluation of the internal heat exchanger influence on a vapour compression plant energy efficiency working with R22, R134a and R407C. Energy 30:621–636
14. Nilpueng K, Wongwises S (2009) Experimental investigation of two-phase flow characteristics of HFC-134a through short-tube orifices. Int J Refrig 32:854–864
15. Nilpueng K, Supavarasuwat C, Wongwises S (2009) Flow pattern, mass flow rate, pressure distribution, and temperature distribution of two-phase flow of HFC-134a inside short-tube orifices. Int J Refrig 32:1864–1875
16. Payne WV, O'Neal DL (1998) Mass flow characteristics of R407C through short-tube orifices. ASHRAE Trans 104(3):197–209
17. Singh GM, Hrnjak PS, Bullard CW (2001) Flow of refrigerant R134a through orifice tubes. Int J HVAC&R Res 7:245–262
18. Tu X, Hrnjak PS, Bullard CW (2006) Refrigerant 134a liquid flow through micro-scale short tube orifices with/without phase change. Exp. Therm. Fluid Sci 30(3):253–262
19. Wongwises S, Disawas S (2005) Performance of the two-phase ejector expansion refrigeration cycle. Int J Heat Mass Trans 48:4282–4286

Springer

KSME

Journal of Mechanical Science and Technology 25 (10) (2011) 2683~2701
www.springerlink.com/content/1738-494x
DOI 10.1007/s12206-011-0618-2

Investigation of empirical correlations on the determination of condensation heat transfer characteristics during downward annular flow of R134a inside a vertical smooth tube using artificial intelligence algorithms †

Muhammet Balcılar[1], Ahmet Selim Dalkılıç[2,*], Berna Bolat[3] and Somchai Wongwises[4,5,**]

[1]*Computer Engineering Department, Yildiz Technical University, Yildiz, Besiktas, Istanbul 34349, Turkey*
[2]*Heat and Thermodynamics Division, Department of Mechanical Engineering, Yildiz Technical University, Yildiz, Besiktas, Istanbul 34349, Turkey*
[3]*Design Division, Department of Mechanical Engineering, Yildiz Technical University,Yildiz, Besiktas, Istanbul 34349, Turkey*
[4]*Fluid Mechanics, Thermal Engineering and Multiphase Flow Research Lab. (FUTURE), Department of Mechanical Engineering, King Mongkut's University of Technology Thonburi, Bangmod, Bangkok 10140, Thailand*
[5]*Academy of Science, The Royal Institute of Thailand, Sanam Suea Pa, Dusit, Bangkok 10300, Thailand*

(Manuscript Received November 3, 2010; Revised June 7, 2011; Accepted June 15, 2011)

Abstract

The heat transfer characteristics of R134a during downward condensation are investigated experimentally and numerically. While the convective heat transfer coefficient, two-phase multiplier and frictional pressure drop are considered to be the significant variables as output for the analysis, inputs of the computational numerical techniques include the important two-phase flow parameters such as equivalent Reynolds number, Prandtl number, Bond number, Froude number, Lockhart and Martinelli number. Genetic algorithm technique (GA), unconstrained nonlinear minimization algorithm-Nelder-Mead method (NM) and non-linear least squares error method (NLS) are applied for the optimization of these significant variables in this study. Regression analysis gave convincing correlations on the prediction of condensation heat transfer characteristics using ±30% deviation band for practical applications. The most suitable coefficients of the proposed correlations are depicted to be compatible with the large number of experimental data by means of the computational numerical methods. Validation process of the proposed correlations is accomplished by means of the comparison between the various correlations reported in the literature.

Keywords: Condensation; Heat transfer coefficient; Pressure drop; Genetic algorithm; Unconstrained nonlinear minimization algorithm; Nelder-mead method; Non-linear least squares

1. Introduction

Artificial intelligence methods such as genetic algorithm (GA) and artificial neural network (ANN) modeling validated by the experimental works have been gaining increased popularity in correlating two-phase flows in tubes. However, there still are not enough investigations on the prediction of in-tube condensation's characteristics by means of artificial intelligence techniques in the literature. Existing numerical studies in this subject regarding the two-phase flows in the literature are summarized in the following paragraphs.

Jenkins [1] mentioned the definition of the GA as "survival of the fittest" and ANN as "human brain activity" in his study. The principal subject of his paper is on application of the GA to find the optimum combination of design variables of a space condensation heuristic.

Akin and Demiral [2] defined the primary flow parameters required to model multiphase flow in porous media as relative permeability and capillary pressure and showed that the performance of the algorithm depends on the probabilities of crossover and mutation, and the proper usage of the fitness function of genetic algorithm.

Alizadehdakhel et al. [3] studied the two-phase flow regimes and pressure drops in a 2 cm diameter and 6 m length tube, and the flow in the test tube is modeled using a computational fluid dynamics (CFD) program and also ANN analysis. As a result of their analysis, the CFD results are more accurate than the ANN evaluations compared to their experimental results.

Magee and Boyle [4] presented a system, based on re-sampling condensation proposed by Isard and Blakes [5], for the tracking and classification of livestock movements. They reported that re-sampling condensation relies on the variation within the shape model being separated into pseudo-

† This paper was recommended for publication in revised form by Associate Editor Jae Dong Chung

* Corresponding author. Tel.: +902123832819, Fax.: +902122616659
** Co-corresponding author. Tel.: +6624709115, Fax.: +6624709111
E-mail address: dalkilic@yildiz.edu.tr, somchai.won@kmutt.ac.th

independent components regarding analogous to genes.

Nasseh et al. [6] focused on the two-phase pressure drop, which is the most important factor affecting the dust collection efficiency in venturi scrubbers in their paper. As a conclusion of their study, their neural network model is optimized by genetic algorithm, and it was selected as the best model due to its compatibility with experimental data and easier usage than the mathematical models.

Salgado et al. [7] presented a new approach, based on gamma-ray pulse height distributions pattern recognition by means of ANNs, for the identification of flow regimes and prediction of volume fraction in water-gas-oil multiphase systems. Their ideal and static theoretical models are developed for annular, stratified and homogeneous regimes using MCNP-X mathematical code. The training, test and validation data for the ANNs was performed using their mathematical code. Finally, their proposed ANNs were in good agreement related with the identification of all three different regimes and prediction of the volume fraction in water-gas-oil multiphase system.

Shang [8] developed a new numerical calculation method, a novel algorithm for CFD using the concept of artificial intelligence, based on the nonlinear analysis characteristics of ANN. Finally, they applied the model to the determination of the vapor-water two-phase flows in a tube with uniform and no uniform heating successfully.

Sunde et al. [9] investigated a non-intrusive method of two-phase flow identification for the bubbly and slug flow regimes in their measurements. Consequently, they classified the flow regime types by an ANN algorithm in agreement with their experimental work.

Tambouratzis and Pazsit [10] proposed a general regression ANN for the identification of the two-phase flow in the coolant channels of boiling water reactors. In conclusion, their cross validation tests validated accurate on-line flow regime identification.

Tarca et al. [11] used ANN validated with experimental data successfully for the modeling of multiphase reactors. They correlated the two-phase pressure drop in randomly packed beds with countercurrent flow by means of the new approach illustrated in their paper as a case study.

Vins and Vacek [12] presented some experimental results of fluorinate refrigerant R218, used in some special vapor cooling circuits, e.g., in various particle detectors, two-phase flow through a capillary tube. They compared two approaches such as the conventional power law function with the correlation determined with the use of an ANN in their paper.

Zhang et al. [13] investigated the alternative correlations of two-phase friction pressure drop and void fraction for mini-channels based on the separated flow model and drift-flux model by applying the artificial neural network on the dominant parameters to correlate the two-phase friction multiplier and void fraction.

Allen et al. [14] presented a procedure for the design of the components of a heat exchanger network including condensers using a GA in order to minimize its total annual cost. Eleven design variables related to the exchanger geometry are considered in their study. In consequence of their study, the optimal solution is determined for the minimum temperature difference providing the more economical heat exchanger network.

Wang et al. [15] developed an ANN correlation for boiling heat transfer coefficient of R22 and its alternative refrigerants R134a, R407C and R410A inside horizontal smooth tubes in their paper. They compared the trained ANN with the experimental data in terms of the average, mean and root-mean-square deviations successfully.

Demir et al. [16] presented an ANN correlation for the experimental data belonging to the condensation heat transfer coefficient of alternative refrigerant R600a inside horizontal tube in their paper. Eventually, the results from the trained network showed good agreement with the experimental data and better results than the some well-known correlations in the literature.

In this study, the main idea is to determine the proper coefficients of correlations, related with heat transfer coefficient and frictional pressure drop, characterizing the two-phase annular downward condensation flow in a vertical tube by means of computational numerical methods such as genetic algorithm (GA), unconstrained nonlinear minimization algorithm- Nelder-Mead method (NM) and non-linear least squares error method (NLS). However, there is no work regarding the numerical solution using GA, NM and NLS for the condensation heat transfer coefficient and frictional pressure drop of HFC-134a either in a horizontal or vertical tube apart from the ANN work just for the condensation of R600a in a horizontal tube, recently carried out by Demir et al. [16]. For these reasons, there remains room for further research. Especially, it can be also noted that all of the numerical and experimental investigations on in-tube condensation do not have any, considering contents and operating parameters, which are concerned with the authors' previous studies [17-29]. Finally, in the present study, the main concern is to fill the gap in the literature. The results for the solution of computational numerical methods on the two-phase heat transfer coefficient, frictional pressure drop, two-phase friction factor which have never before appeared in open literature are presented and compared with the results from the in-tube condensation database of KMUTT whose accuracy was proven in many papers in the literature. The results are evaluated with a genetic algorithm (GA), unconstrained nonlinear minimization algorithm-Nelder-Mead method (NM) and a non-linear least squares (NLS) method, and a least squares error method (LS), respectively.

2. Experimental apparatus and method

A schematic diagram of the test apparatus is shown in Fig. 1. The refrigerant loop consists of a pre-heating loop, test section, cooling loop and chilling loop. The refrigerant is circulated by

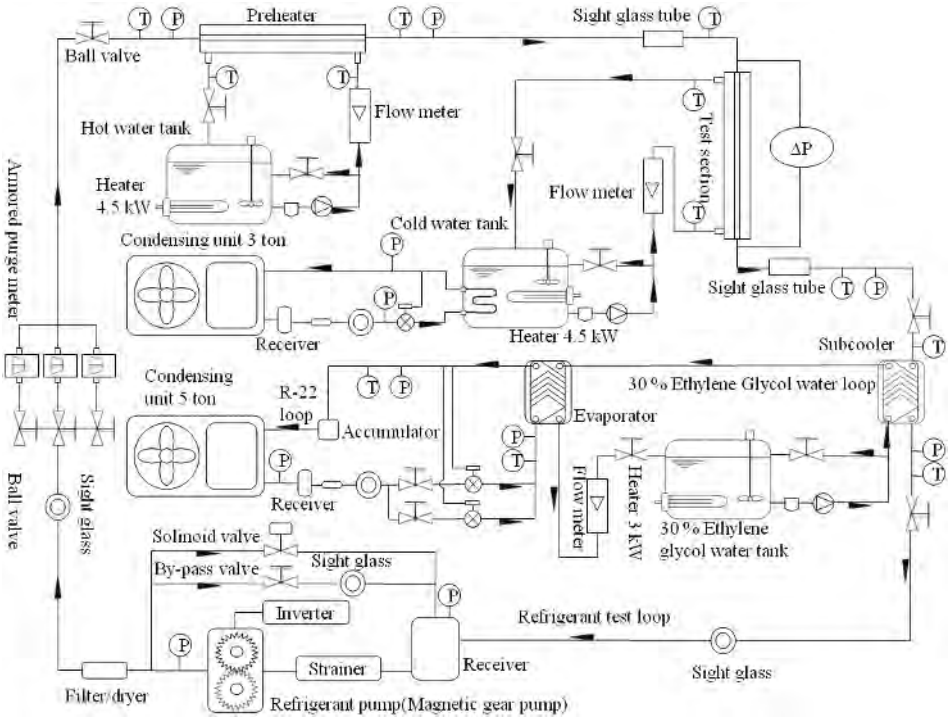

Fig. 1. Schematic diagram of experimental apparatus.

a gear pump controlled by an inverter. The refrigerant flows in series through a filter/dryer, a sight glass tube, a refrigerant flow meter and a preheater and enters the test section. A spiral counter-flow double tube heat exchanger is designed to supply heat to control the inlet quality of the refrigerant before entering the test section. After exiting the test section, the chilling loop condenses and sub-cools the refrigerant and removes the heat input from the pre-heater and test section, and ejects it into the surroundings. After leaving the chilling loop, the refrigerant changes from the two-phase refrigerant to a subcooled state. Eventually, the refrigerant returns to the refrigerant pump to complete the cycle.

The test section, well insulated with a proper material to minimize the heat loss, is a vertical counter-flow tube-in-tube heat exchanger with refrigerant flowing downward (co-current liquid and vapor of R134a's down flow) in the inner tube and cooling water flowing upward in the annulus. The inner and outer tubes are made from smooth vertical copper having inner diameters of 8.1 and 26 mm, respectively. The length of the heat exchanger is 0.5 m. Fig. 2 shows the detailed dimensions of the heat exchanger and the location of the thermocouples.

T-type thermocouples are used to measure refrigerant temperature and the tube wall temperatures in the test section. A total of ten thermocouples are located on the sidewall at five points along the test tube. A thermostat is used to control the inlet temperature of the water. All the temperature-measuring devices are calibrated in a controlled temperature bath using standard precision mercury glass thermometers. The uncertainty of the temperature measurements is ±0.1 °C. All static pressure taps are mounted on the tube wall. The refrigerant flow meter is a variable area type. The flow meter was calibrated in the range of 0-2.2 gal min^{-1} for HFC-134a by the manufacturer. Pressure drop is measured by a differential pressure transducer installed between the inlet and outlet of the test section. The length between pressure taps is 0.7 m. A low temperature thermostat is used to control the system pressure of the refrigerant flow. The differential pressure transducer and pressure gauges are calibrated against a primary standard, the dead weight tester. All signals from thermocouples and pressure transducers are recorded by a data logger. Tests are performed in the steady state.

The test runs were performed at average condensing temperatures of 40°C and 50°C in a copper smooth tube having an inner diameter of 8.1 mm and length of 0.5 m. The mass fluxes were varied from 260 to 515 kg $m^{-2}s^{-1}$ and the heat fluxes were between 10.16 and 66.61 kW m^{-2}. Accuracy of the dataset was proven in many papers in the literature.

3. Data reduction and experimental uncertainty

The data reductions of the measured results such as inlet and outlet vapor quality of the test section are presented in detail in the authors' previous publications in the literature.

3.1 The average heat transfer coefficient

$$h_{exp} = \frac{Q_{TS}}{A_i(T_{ref,sat} - T_{wi})} \quad (1)$$

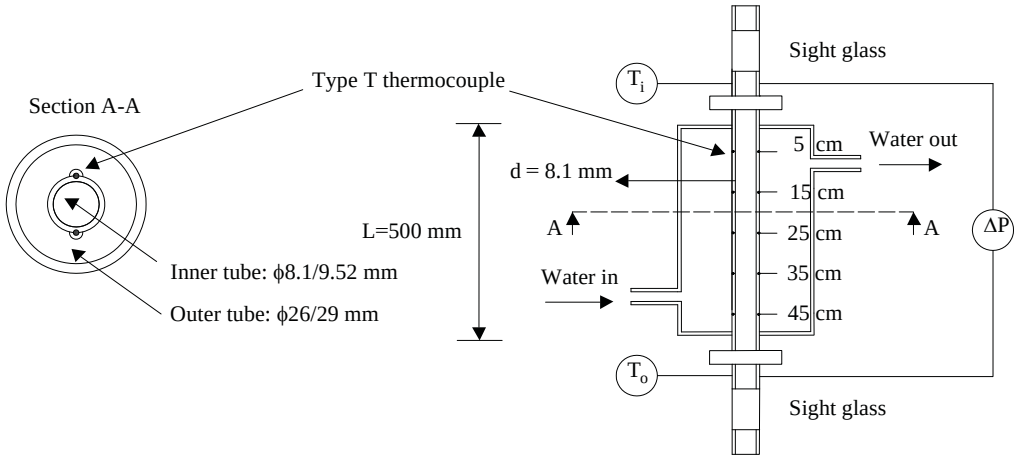

Fig. 2. Schematic diagram of test section.

where h_{exp} is the experimental average heat transfer coefficient, Q_{TS} is the heat transfer rate in the test section, T_{wi} is the average temperature of the inner wall, $T_{ref,sat}$ is the average temperature of the refrigerant at the test section inlet and outlet, and Ai is the inside surface area of the test section:

$$A_i = \pi dL \tag{2}$$

where d is the inside diameter of the test tube. L is the length of the test tube.

3.2 Error analysis

Error analysis of the study is performed by means of Eqs. (3), (4) and (5). In these equations, N is the element number of test group, h^i_{exp} and h^i_{calc} are the experimental and calculated results of heat transfer coefficient obtained from "i" number of test data, respectively, and $\overline{h_{exp}}$ and $\overline{h_{calc}}$ are the average values of experimental and calculated results of heat transfer coefficient obtained from the numerical analysis. It should be noted that error analysis of frictional pressure drop and two-phase multiplier was done similarly.

R square error is determined as follows:

$$E_{Rsquare} = \frac{\left(\sum_{i=1}^{N}(h^i_{exp} - \overline{h_{exp}})(h^i_{calc} - \overline{h_{calc}})\right)^2}{\left(\sum_{i=1}^{N}(h^i_{exp} - \overline{h_{exp}})^2\right)\left(\sum_{i=1}^{N}((h^i_{calc} - \overline{h_{calc}})^2\right)} \tag{3}$$

$$E_{ratio} = \frac{100}{N}\sum_{i=1}^{N}\frac{\left|h^i_{exp} - h^i_{calc}\right|}{h^i_{exp}} \tag{4}$$

$$E_{square} = \sqrt{\frac{1}{N}.\sum_{i=1}^{N}(h^i_{exp} - h^i_{calc})^2}. \tag{5}$$

3.3 Calculation procedure for the genetic algorithm (GA)

GA is a search technique used in computing to find good solutions for optimization and search problems. GA uses the techniques inspired by Darwin's evolution theory and it is a particular class of evolutionary algorithms that solves hard problems quickly, reliably and accurately [30-32]. GA is applied to find a good solution that meets the system requirements. GA strongly differs in conception from other stochastic search methods and traditional optimization methods. While other methods always process single points in the search space, the GA maintains a population of potential solutions [33] as a basic difference. The GA starts with a large number of randomly generated chromosomes which are necessary for the problem, and each chromosome represents different solutions of the problem. Chromosomes are created to encode the potential solutions as a mathematical representation for solutions according to the type of problem. Each solution in the population is evaluated from the fitness function which is always dependent to the problem. The chromosomes are selected from best to worst by means of an objective function. In every generation, the genetic operators are applied to create a new population. GA uses the operators of reproduction, crossover and mutation. Reproduction selects and recombines the individuals from the population and produces offspring for the next generation. There are several techniques for the usage of reproduction operators. The most frequently used reproduction methods are roulette wheel and linear selection methods. Crossover is used to change the information between randomly selected two parents without losing any important information. There are also many crossover techniques which are one-point, two-point, multiple point, shuffle-exchange and uniform. One of the operators of GA is the mutation which is applied to chromosomes by changing the gene values. The basic steps of genetic algorithm are as follows:

(1) The initial population type and number is determined.
(2) Initial population is generated.
(3) Each individual's fitness function value of the population is calculated.
(4) The fitness is determined according to the scale method.
(5) All individuals of the population are binary matched ac-

cording to the selection method.
(6) New individuals are created among the individuals who are binary matched, by the crossing over operators.
(7) A mutation is applied to the newly formed individual.
(8) Fitness value of the mutated individual is calculated and added to population.
(9) The most well-defined number of individuals (elitism) are stored for the next generation.
(10) To fix the increased number of population to the initially defined number, individuals with high fitness values (poor individuals) are removed from the population randomly.
(11) And the individual with the lowest fitness value (best individual) is assigned as the global best.
(12) If the stop condition is not fulfilled then step 4 is followed again.

Genetic algorithms are search and optimization methods, working in a similar way as the evolutionary process observed in nature. They look for the best global solution, according to the principle of survival of the good, in a complex multi-dimensional search space. Basic principles of genetic algorithms have been first proposed by John Holland at the University of Michigan. First, Holland used the laws of evolution in genetic algorithms for optimization problems [34].

Genetic algorithms produce a set of solutions to problems, rather than a single solution. Thus, many points are evaluated in the search space at the same time while the possibility of reaching ultimately global solution increases. The solutions in the solution set are completely independent of each other. Each one is a vector of multi-dimensional space.

In practice, a bit-based population was used, consisting of 200 individuals. Each coefficient candidate has been expressed by 20 bits. Each parameter was searched between -5 to +5. If all of the bits, corresponding to any parameter, are 1, it means that this parameter is at 5, and if all of the bits are 0, then this means that it's at -5. Since, 2^{20} -1 different states can be expressed by 20 bits, the sensitivity for each parameter becomes (5- (-5)) / (2^{20} -1). The used population is simulated in Table 1.

Bit sequence of the individuals in initial population was determined in a uniform random manner. And the fitness function is square error (MSE) between the calculated value and the actual value. Therefore, the genetic algorithm searches the formula coefficients, which give the smallest MSE, between experimentally obtained values and the output of the heuristic formula.

The rank scale method, which is used as the scale method, is based on calculation of the fitness in accordance with the individual's rank number, after sorting each individual by their fitness. The roulette selection method is used as the selection method. According to this method, individuals are selected by a lottery with the odds being maximum for the best individual and the odds being minimum for the worst individual. In this way, even the worst individuals have the possibility to produce new individuals and to remain in the next generation.

A crossing-over process is performed among selected pairs

Table 1. The simulated population for GA analysis.

	20 bits															
	1.coefficient				2.coefficient				3.coefficient				4.coefficient			
1. individual	0	1	....	0	1	1	....	1	0	1	....	0	0	1	....	1
2. individual	0	0	....	1	1	1	....	0	0	1	....	1	0	0	....	1
3. individual	1	1	....	0	0	1	....	1	0	0	....	0	1	1	....	0
	⋮	⋮	⋮	⋮	⋮	⋮	⋮	⋮	⋮	⋮	⋮	⋮	⋮	⋮	⋮	⋮
200 individual	1	1	....	0	1	0	....	1	0	1	....	0	0	1	....	1

to maintain diversity. This process is the process of creating a new individual, with a mixture of the two selected individual's bit sequences. In practice, scatter crossing-over is used. This process is to rearrange every bit of the new individual by 50% probability from the first individual and by 50% probability from the second individual.

Mutation is a procedure that increases the diversity in new individuals. In this step, any randomly selected bit of randomly selected 10% of individuals is changed from 0 to 1 or 1 to 0.

The elitism number is taken as 2 in the algorithm. Thus, the best two individuals in each generation are always guaranteed to remain in the next generation. The individuals which are not going to be in the next generation are again selected according to the selection method, by determining their fitness. Thus, 1 generation is completed.

In practice, the determined stopping condition should be 1000 generations, or the best value should never be changed for consecutive 200 generations. This algorithm stops when one of these two stop conditions is fulfilled, and the globally best known individual so far is presented as the solution.

3.4 Unconstrained nonlinear minimization algorithm Nelder-Mead method (NM)

Nelder and Mead developed a simplex method to determine a local minimum of a function of several variables. It is a good alternative method when the differential of the fitness function is complex either analytically or numerically. A simplex forms triangle for two variables and function values at the three vertices of this triangle are compared by means of the pattern search method. The new vertex is found by replacing with the rejected worst vertex where f (x, y) is largest. Then, the search is continued when the new vertex is formed. A sequence of triangles, which might have different shapes, is generated by each iteration when values at the vertices get smaller and smaller. Reduction of the size of the triangles is performed and the coordinates of the minimum point are found. Generally, this effective method begins to the simplex having “n+1” vertex for the minimization of the fitness function having “n” variables.

The Nelder-Mead algorithm is a local optimization method which attempts to find better points by removing the worst of m+1 points at each step of its iterative methods, that starts

with m+1 initial guesses in an m dimension space, without using a derivative information. The Nelder-Mead technique is a technique for minimizing a fitness function in a many-dimensional space.

It is used to find the optimal value of the predetermined function parameters, which expresses the experimental data collected from the environment, in this study. For this, an error function was coded, and minimization of this error function with desired parameters is provided by the above mentioned method.

Assume we have n data points with 3 inputs and 1 output. Where, input parameters are denoted by x, y, z and the output parameter is denoted by f. In this case, our data points can be expressed as follows:

$$(x_1,y_1,z_1,f_1),(x_2,y_2,z_2,f_2),(x_3,y_3,z_3,f_3)\ldots(x_n,y_n,z_n,f_n). \quad (6)$$

The non-linear function to be fitted to these points is denoted by g, and if the m coefficients to be found are β_1, β_2, $\beta_3\ldots\beta_m$ then it can be expressed as $f_i = g(x_i,y_i,z_i,\beta)$. Here, f_i is the real value and $g(x_i,y_i,z_i,\beta)$ are the calculated values. If we call total squared error as E, between these two values, equivalent of E becomes as follows:

$$E(\beta) = \sum_{i=1}^{n} (f_i - g(x_i,y_i,z_i,\beta))^2 . \quad (7)$$

The goal of the method is to find the β value which makes the E(β) function minimum.

There are five operators in the Nelder-Mead algorithm used for this purpose as shown in Fig. 3. These operators are briefly described as follows:

Reflection: Its operation, where the worst candidate among m+1 guesses is moved to a symmetrical point according to the center of gravity of other remaining m candidates.

Expansion: The worst candidate point is to be moved beyond its point of reflection. The distance of expansion point to the reflection point equals the distance of the worst candidate to the center of gravity of the remaining points.

Inside contraction: The worst candidate point is to be moved to the exact center, where it is the center of gravity of other points together with itself.

Outside contraction: The worst candidate point is to be moved to the exact center, where it is the center of gravity of other points together with the reflection point.

Shrink: Except the best point, is to be moved to the exact center of all points and itself.

The steps of the algorithm are as follows [36]:

(1) Determine m+1 starting point for m parameter guess.

$x_1 = [\beta_1^1, \beta_2^1, \ldots \beta_m^1]$, $x_2 = [\beta_1^2, \beta_2^2, \ldots \beta_m^2]$, $x_{m+1} = [\beta_1^{m+1}, \beta_2^{m+1}, \ldots \beta_m^{m+1}]$

(2) Sort by fitness function $E(x_1)<E(x_2)<E(x_3)\ldots<E(x_{m+1})$.

(3) Calculate the reflection point x_r of the point x_{m+1}.

(4) If $E(x_1) \le E(x_r) < E(x_m)$ then $x_{m+1}=x_r$.

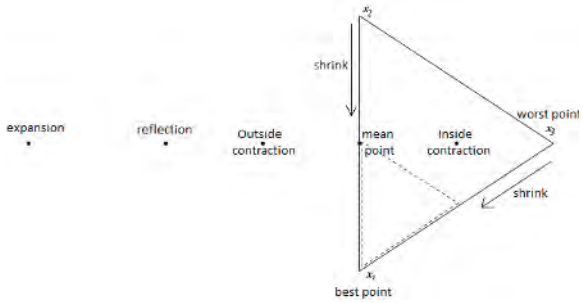

Fig. 3. Operators in Nelder-Mead algorithm.

(5) Else if $E(x_r) < E(x_1)$ then calculate the expansion point x_θ.

If $E(x_\theta) < E(x_r)$ then $x_{m+1} = x_\theta$ else $x_{m+1}=x_r$.

(6) Else if $E(x_r) \ge E(x_m)$ then

a. If $E(x_m) \le E(x_r) < E(x_{m+1})$ then

i. Calculate inside contraction x_{ic} and outside contraction x_{oc}.

ii. If $E(x_{oc}) < E(x_r)$ then $x_{m+1}=x_{oc}$.

iii. Else if $E(x_{ic}) < E(x_{m+1})$ then $x_{m+1}=x_{ic}$.

iv. Else shrink.

b. Else shrink.

(7) If var $(x_1,x_2,x_3\ldots x_{m+1}) > \varepsilon$ go to step 2.

(8) Take the x_1 as candidate solution.

The stop condition in this algorithm is that the variance of m+1 candidate solution points is smaller than a certain epsilon. As the algorithm progresses, each m+1 candidate solution points will approach mutually. When the loop ends, the best of the m+1 candidate is determined as the result.

3.5 Calculation procedure for the non-linear least squares algorithm (NLS)

Gauss [37] described the LS method, which is one of the standard approaches to the approximate solution of over determined systems or inexactly specified systems of equations in an approximate sense. It can be used when the sets of equations in which there are fewer unknowns than equations. LS means that the overall solution minimizes the sum of the squares of the errors made in solving every single equation instead of solving the equations exactly.

The data fitting is the most important application of LS. The minimization of the sum of squared residuals is sensed by the best fit in the LS and a residual causes the difference between an observed value and the value provided by a model. LS matches with the maximum probability criterion if there is a normal distribution of the experimental errors.

LS problems consist of linear least squares and non-linear least squares (NLS) depending on whether or not the residuals are linear in all unknowns. Most statistical regression analysis has linear LS problems; it has a closed form solution. The non-linear problem, usually solved by iterative refinement, has no closed solution. The system is approximated by a linear one at each iteration in order to have similar results for the

core calculation in both cases.

The non-linear least square (NLS) method allows determination of the most optimal non-linear function coefficients, in order to fit data collected from an experimental environment to a non-linear function (non-linear curve fitting). This method tries to minimize the mean square error, beginning from the first estimated values determined by the user [38]. Since it advances step by step by optimizing this point, starting from this initial point, it finds the local minimum and not the global minimum. The method is tested by starting from different initial points, and the point which finds global minimum is tried to be predicted.

Mathematical basis of the method is as follows:

Assume we have n data points with 3 inputs and 1 output, where input parameters are denoted by x, y, z and the output parameter is denoted by f. In this case, our data points can be expressed as in Eq. (6).

The non-linear function to be fitted to these points is denoted by g, and if the m coefficients to be found are $\beta_1,\beta_2,\beta_3 \ldots \beta_m$ then it can be expressed as $f_i=g(x_i, y_i, z_i, \beta)$. Here, f_i is the real value and $g(x_i, y_i, z_i, \beta)$ are the calculated values. If we say that the total squared error between these two values is S, then equivalent of S is as follows:

$$S=\sum_{i=1}^{n}(f_i-g(x_i,y_i,z_i,\beta))^2 \ . \quad (8)$$

The β values, which make the S value minimum, are the coefficient vectors to be found. The point where S is minimum is the point where the partial derivatives of S are equal to zero. Therefore the following equation is written, where j=1...m

$$\frac{\partial S}{\partial \beta_j}=2.\sum_{j=1}^{n}(f_i-g(x_i,y_i,z_i,\beta)).\frac{(f_i-g(x_i,y_i,z_i,\beta))}{\partial \beta_j}=0. \quad (9)$$

The iterative steps to be applied in order to find the β values, which equate the above equation to zero, are as follows:

(1) k is determined as the iteration counter and k=0 value is assigned.
(2) The β^k initial values are determined randomly.
(3) The vector with n elements $\Delta f_i = f_i - g(x_i, y_i, z_i, \beta^k)$ is calculated (i=1..n).
(4) If the $J_{i,j}$ expression is stated in terms of a partial derivative of the error function according to β_j, with the values at i^{th} data point, then that J matrix becomes the Jacobian matrix (i=1..n, j=1..m).
(5) $\beta^{k+1} = \beta^k + (J^T J)^{-1} J^T \Delta f$ is updated.
(6) If $\left|\beta^{k+1} - \beta^k\right| > \varepsilon$ then k is increased by one, and continued from the 3rd step.
(7) The searched coefficients are found as β^{k+1}.

In the study, coefficients are searched by starting the above algorithm for each problem at 100 different initial points. The results of these 100 experiments, which give the best curve fits, are presented as the output.

3.6 Correlation development

Determination of heat transfer characteristics of compact systems such as heat transfer coefficient, frictional pressure drop, flow type between the fluids, heat transfer surface area in heat exchangers should be known accurately for the optimum design. The two-phase heat transfer systems have higher thermal heat transfer performance than single-phase heat transfer systems in limited apparatus volumes. Advantage of high thermal performance in comparison to the single-phase applications includes smaller, more compact systems regarding tube length, tube diameter, and internal tube geometry shape in a wide variety of applications, e.g., refrigeration and air conditioning systems, power engineering and other thermal processing plants. Before doing any numerical work on this subject, validation process of the experimental setup and data is a very significant for reliability of the study. The correctness of experimental data should be evaluated by either graphics regarding the characteristics of trend lines [17-29] such as alteration of heat transfer coefficient vs. quality, heat flux vs. temperature difference between the vapor and inlet wall temperature, pressure drop vs. vapor quality etc., or widely accepted correlations in the literature and desired working conditions should be agreeable with the heat balance correlations and flow type observations by means of sight glasses at the different points of experimental apparatus.

There have been a number of studies on the in-tube condensation heat transfer coefficient and pressure drop. The frictional, acceleration, and gravitational components determine the two-phase total pressure drop in tubes. Determination of the void fraction is required to compute the acceleration and gravitational components, and in a similar way, determination of either the two-phase friction factor or the two-phase frictional multiplier is required to compute the frictional component of pressure drop. Generally, empirical methods have been used to compute the condensation heat transfer coefficients and pressure drops in tubes. Most of these proposed models are modifications of the Dittus-Boelter single-phase forced convection correlation [39], as in Akers et al. [40], Cavallini and Zecchin [41], and Shah [42].

3.6.1 Correlation proposal for the convective condensation heat transfer coefficient

The correlation for the laminar and turbulent flow inside the test tube was developed as a form of Dittus and Boelter's [39] correlation in Eq. (10) by means of several dimensionless numbers which were defined and used by Akers et al. [40] for Reynolds equivalent number in Eq. (11), by Koyama et al. [43] for the ratio of density to dynamic viscosity in Eq. (12), by Lockhart and Martinelli [44] for their parameter in Eq. (14), by Dobson and Chato [41] for the form of Lockhart and Martinelli's [44] parameter with specific constant numbers in Eq. (10) and by Cavallini et al. [46, 47] for the usage of Bond and Froude numbers together in Eqs. (15)-(16). As a result, Eq. (10) is formed to predict the convective condensation heat

transfer coefficient in terms of the above explanations as follows:

$$h = A\left(\frac{k_l}{d}\right)Re_{eq}{}^{B}(PrR)^{C}\left[\frac{D}{X^{E}}+F\right](BoFr)^{G} \tag{10}$$

where the all liquid equivalent Re number is determined from:

$$Re_{eq}=\frac{G_{eq}d}{\mu_l} \tag{11}$$

and equivalent liquid mass flux is defined as:

$$G_{eq}=G\left((1-x)+x(\frac{\rho_l}{\rho_g})^{0,5}\right) \tag{12}$$

and the ratio of density to dynamic viscosity is defined as:

$$R=\frac{\rho_l\mu_l}{\rho_g\mu_g} \tag{13}$$

and Bond number is defined as:

$$Bo = g(\rho_l - \rho_g)\left(\frac{(d/2)^2}{\sigma}\right) \tag{14}$$

and Froude number is defined as:

$$Fr = \frac{G^2}{gd\rho_{TP}{}^2} \tag{15}$$

where the two-phase density is determined from:

$$\rho_{TP} = \left(\frac{x}{\rho_g}+\frac{1-x}{\rho_l}\right)^{-1} \tag{16}$$

and Lockhart and Martinelli [44] parameter is expressed as:

$$X=\sqrt{\frac{\left(\frac{dp}{dz}\right)_l}{\left(\frac{dp}{dz}\right)_g}} \tag{17}$$

where the two-phase frictional pressure gradient can be related to the Fanning friction factor [48] in terms of mass flux and mass quality for liquid flowing alone as follows:

$$\left(\frac{dp}{dz}\right)_l=\frac{f_l G^2(1-x)^2}{2d\rho_l} \tag{18}$$

and liquid phase's friction factors are determined for laminar flow by Darcy and Weisbach [49, 50] in Eq. (19) and turbulent flow by Blasius [51] in Eq. (20) as follows:

$$f_l=\frac{64}{Re_l}, \tag{19}$$

$$f_l=\frac{0.316}{Re_l^{0.25}} \tag{20}$$

where the Reynolds number equation can be expressed in terms of mass flux and mass quality for liquid flowing alone as:

$$Re_l=\frac{Gd(1-x)}{\mu_l} \tag{21}$$

and the gas phase's pressure drop in Eq. (17) is calculated in a similar way with Eq. (14) as:

$$\left(\frac{dp}{dz}\right)_g=\frac{f_g G^2x^2}{2d\rho_g} \tag{22}$$

where all of the gas phase's friction factors, valid for Re_g>20000, are determined by Blasius [51] for turbulent flow in this study as:

$$f_g=\frac{0.184}{Re_g^{0.2}} \tag{23}$$

and the two-phase gas Reynolds number is defined as:

$$Re_g=\frac{Gdx}{\mu_g}. \tag{24}$$

It should be noted that Lockhart and Martinelli [44] parameter in Eq. (17) is calculated by means of the equations from 17 to 24 according to the situation for the laminar or turbulent flows of liquid and gas phases of R134a in the test tube. The detailed information on the basis of Lockhart and Martinelli's development [44] can be obtained from Chisholm [52]'s investigation.

3.6.2 Correlation proposal for the two phase multiplier

The separated flow model is the most used method to calculate heat transfer characteristics. Lockhart and Martinelli's [44] method is one of the most well-known for the determination of two-phase frictional pressure drop. It is a combination of the inertial and viscous forces of both phases. Chisholm and Laird's [53] two-phase frictional multiplier is commonly used in the literature as follows:

$$\phi_l^2=\frac{\left(\frac{dp}{dz}\right)_F}{\left(\frac{dp}{dz}\right)_l}=1+\frac{C}{X}+\frac{1}{X^2} \tag{25}$$

where Chisholm parameter C varies from 5 to 20 depending on whether the phases of liquid and gas are laminar or turbulent for conventional channels. As a result, Eq. (25) is modified to predict the frictional pressure drop regarding with the explanations above as follows:

$$\phi_l^2 = A + \frac{B}{X^C} + \frac{D}{X^E}. \quad (26)$$

The two-phase frictional pressure drop can be obtained by subtracting the gravitational and momentum terms from the total measured pressure drop as follows:

$$\left(\frac{dP}{dz}\right)_F = \left(\frac{dP}{dz}\right)_{exp} - \left(\frac{dP}{dz}\right)_G - \left(\frac{dP}{dz}\right)_M. \quad (27)$$

Pressure drop due to gravity can be determined from:

$$(\Delta P)_G = g(\alpha\rho_g + (1-\alpha)\rho_l)L \quad (28)$$

where the void fraction, α, can be determined from Chisholm [54] correlation below:

$$\alpha = \frac{1}{1 + \left(\frac{1-x}{x}\right)\left(\frac{\rho_g}{\rho_l}\right)S}, \quad (29)$$

$$S = \left(1 - x + x\frac{\rho_l}{\rho_g}\right)^{1/2}. \quad (30)$$

The momentum transfer term contributes to the overall pressure drop during condensation due to the mass transfer that occurs at the phase's interface. The momentum pressure gradient can be written according to the results of the one-dimensional two-phase separated-flow analysis which can be defined as follows:

$$\left(\frac{dP}{dz}\right)_M = -G^2 \frac{d}{dz}\left[\frac{x^2}{\rho_g\alpha} + \frac{(1-x)^2}{\rho_l(1-\alpha)}\right]. \quad (31)$$

Eq. (31) can be rearranged as follows:

$$\Delta P_M = G^2\left[\left\{\frac{(1-x)^2}{\rho_l(1-\alpha)} + \frac{x^2}{\rho_g\alpha}\right\}_o - \left\{\frac{(1-x)^2}{\rho_l(1-\alpha)} + \frac{x^2}{\rho_g\alpha}\right\}_i\right]. \quad (32)$$

3.6.3 Validation of the proposed correlations by means of heat transfer correlations

The Shah correlation [55] has been investigated by researchers commonly for turbulent condensation conditions especially in vertical tubes [56] and is considered to be the most comparative condensation model for annular flow regime in a tube [57]. The Shah correlation is based on the liquid heat transfer coefficient, which is valid for $Re_l \geq 350$. It has a two-phase multiplier for annular flow regime of high pressure steam and refrigerants [56, 57]. Dobson and Chato [58] developed a correlation using a two-phase multiplier for an annular flow regime. They also provided a correlation for a wavy flow regime. Their correlations are commonly used in the literature for zeotropic refrigerants. Chato [59] developed Dittus and Boelter's correlation [39] using a two-phase multiplier for an annular flow regime. Sweeney [60] provided a modification of the Dobson and Chato model [58]. He studied zeotropic mixtures for annular flow. He also offered a correlation for wavy flow. Cavallini et al. [61] developed a semi empirical correlation for the condensation of various organic refrigerants in both vertical and horizontal orientations. Fujii [62] developed the following correlation for smooth tubes. He also offered a correlation for gravity controlled regimes. His equation was used for shear-controlled regimes in Table 5. Tang et al. [63] modified the Shah [55] equation for annular flow condensation of R410A, R134a and R22 in i.d. 8.81 mm tube with Frso > 7. Bivens and Yokozeki [64] modified Shah correlation [3] for various flow patterns of R22, R502, R32/R134a, R32/R125/R134a. Tandon et al. [65] modified the Akers and Rosson [66] correlation for shear controlled annular and semi-annular flows with $Re_g > 30000$. It should be noted that there is another correlation for gravity-controlled wavy flows with $Re_g < 30000$ which belongs to Tandon et al. [65]. Traviss et al. [66] investigated flow regime maps for condensation inside tubes. Their correlation was suggested for the condensation of R134a inside tubes specifically. Variation in the quality of the refrigerant was considered using Lockhart-Martinelli parameter [44]. Akers and Rosson [67] modified the Dittus and Boelter [39] single-phase forced convection correlation. Their correlation was recommended for turbulent annular flow in small diameter circular tubes and rectangular channels. Table 2 shows the correlations mentioned above.

3.7 Uncertainties

The uncertainties of the Nusselt number and condensation heat transfer coefficient in the test tube varied from ±7.64% to ±10.71%. It should be noted that similar ranges of uncertainty with minimum and maximum values exist in the literature. The procedures of Kline and McClintock [68] were used for the calculation of all uncertainties. Various uncertainty values of the study can be seen from authors' previous works and the details are given in Table 3.

4. Results and discussion

The present study was done at the Fluid Mechanics, Thermal Engineering and Multiphase Flow Research Lab. (FUTURE) in KMUTT for the correlation development belong to the convective heat transfer coefficient and two-phase multiplier during the downward two-phase flow of pure R134a in a vertical round tube with inner diameter of 8.1 mm.

Table 2. The existing heat transfer coefficient correlations from literature for the comparison.

Researcher	Correlation
Shah [55]	$h_{shah} = h_{sf}\left(\frac{1.8}{Co^{0.8}}\right)$ $Co = \left(\frac{1}{x}-1\right)^{0.8}\left(\frac{\rho_g}{\rho_l}\right)^{0.5}$ $h_{sf} = h_l(1-x)^{0.8}$ $h_l = \frac{k_l}{d}\left(0.023\left(\frac{Re_l}{1-x}\right)^{0.8} Pr_l^{0.4}\right)$ $P_{red} = P_{sat}/P_{critic}$ $Re_l = \frac{Gd(1-x)}{\mu_l}$
Dobson and Chato [58]	for $G > 500$ kg m^{-2} s^{-1} $Nu = 0.023Re_l^{0.8}Pr_l^{0.4}\left[1+\frac{2.22}{X^{0.89}}\right]$ for $Re_l > 1250$ and $Fr_{so}>18$ $Nu = 0.023Re_l^{0.8}Pr_l^{0.3}\frac{2.61}{X^{0.805}}$ $X = \left(\frac{1-x}{x}\right)^{0.9}\left(\frac{\rho_g}{\rho_l}\right)^{0.5}\left(\frac{\mu_l}{\mu_g}\right)^{0.1}$
Chato [59]	$Nu = 0.023Re_l^{0.8}Pr_l^{0.4}\left[\frac{2.47}{X^{1.96}}\right]$
Sweeney [60]	$Nu = 0.7\left(\frac{G}{300}\right)^{0.3} Nu_{Dobson,Chato}$
Cavallini et al. [61]	$Nu_l = 0.05Re_{eq}^{0.8}Pr^{0.33}$ $Re_{eq} = Re_g\left(\mu_g/\mu_l\right)\left(\rho_l/\rho_g\right)^{0.5} Re_l$
Fujii [62]	$Nu_l = 0.0125\left(Re_l\sqrt{\rho_l/\rho_g}\right)^{0.9}\left(\frac{x}{1-x}\right)^{0.1x+0.8} Pr_l^{0.63}$
Tang et al. [63]	$Nu = 0.023Re_l^{0.8}Pr_l^{0.4}\left[1+4.863\left(\left(-\ln(P_{red})\frac{x}{1-x}\right)^{0.836}\right]\right.$ $Fr_{so} = c_3Re_l^{c_4}\left(\frac{1+1.09X^{0.039}}{X}\right)^{1.5}\frac{1}{Ga^{0.5}}$ $Ga = \frac{\rho_l(\rho_l-\rho_g)gd^3}{\mu_l^2}$ $R_{el} \leq 1250$ $c_3 = 0.025c_4 = 1.59$ $R_{el}>1250$ $c_3 = 1.26$ $c_4 = 1.04$
Bivens and Yokozeki [64]	$Nu = Nu_{Shah}\left(0.78738+\frac{6187.89}{G^2}\right)$ $Nu_{Shah} = 0.023Re_l^{0.8}Pr_l^{0.4}\left[1+\frac{3.8}{P_{red}^{0.38}}\left(\frac{x}{1-x}\right)^{0.76}\right]$
Tandon et al [65]	$Nu = 0.084Re_g^{0.67}Pr_l^{1/3}\left[\frac{1}{Ja_l}\right]^{1/6}$
Travis et al. [66]	$Nu = Re_l^{0.9}Pr_l\frac{F_1(X)}{F_2(Re_l,Pr_l)}$ $F_1(X) = 0.15\left[\frac{1}{X}+\frac{2.83}{X^{0.476}}\right]$ $F_2 = 5Pr_l+5\ln(1+5Pr_l)+2.5\ln(0.00313Re_l^{0.812})$ for $Re_l>1125$
Akers and Rosson [67]	$Nu = 0.0265Re_{eq}^{0.8}Pr_l^{1/3}$ $Re_{eq} = \frac{G_{eq}d}{\mu_l}$ $G_{eq} = G\left[(1-x)+x\left(\rho_l/\rho_g\right)^{0.5}\right]$

The results will be discussed in turn as follows.

The determination of convective heat transfer coefficient and frictional pressure drop by means of computational numerical techniques is presented in the following paragraphs using relevant measured data such as 178 numbers of 40°C data and 191 numbers of 50°C data during the downward laminar and turbulent condensation of R134a at a high mass flux in a vertical smooth tube over a wide range of experimental conditions. 89 of 178 at 40°C data and 95 of 191 at 50°C data were separated from others to form the test group. The rest of them were used to form the training group.

The thermal resistance is increased due to the increase in film thickness during condensation, hence, the heat transfer rate decreases. The heat transfer coefficient is larger when the inlet quality is higher. This is due to the result of smaller liquid film thickness together with higher vapor velocity at the

Table 3. Uncertainty of experimental parameters.

Parameters	Uncertainty
$T_{ref,sat}$ (°C)	0.19
x_i	±6.96-8.24%
ΔT (K)	±0.191
$(T_{w,o}-T_{w,i})_{TS}$ (K)	±0.045
$(T_{w,i}-T_{w,o})_{ph}$ (K)	±0.13
m_{ref} (g s^{-1})	±0.023
$m_{w,TS}$ (g s^{-1})	±0.35
$m_{w,ph}$ (g s^{-1})	±0.38
q_{TS} (kW m^{-2})	±6.55-8.93%
q_{ph} (kW m^{-2})	±12-14.81%
h_{ref} (W m^{-2}K^{-1})	±7.64-10.71%.
ΔP (kPa)	±0.15

vapor-liquid interface in comparison to the lower inlet quality with larger film thickness. Finally, the average heat transfer coefficient increases with increasing inlet quality. The heat transfer coefficient decreases with decreasing mass flux. This is due to the increase of vapor velocity of R134a. On the contrary, it decreases with increasing saturation temperature due to alteration of the physical properties of refrigerant by condensation temperature or pressure. Therefore, film thickness at high saturation temperature is thicker than that of low saturation temperature. The increase in condensation temperature difference between saturation and inner wall temperature, condensation rate and heat flux increases the film thickness due to the constant latent heat of condensation for a specific saturation temperature of condensation. Therefore, the average convective condensation heat transfer coefficient decreases with increasing condensation temperature difference regarding Eq. (1). It is also known that the increase in condensation rate causes an increase in mass flux and heat flux. Besides this, vapor quality decreases with decreasing void fraction. The increase in mass flux increases the total pressure drop at the same condensing temperature due to the increase of shear stress at the interface of phases. It is also known that the pressure drop decreases with increasing with system pressure or condensing at the same mass flux. In the same way, frictional pressure drop increases with increasing mass flux as well. Thus, the specific volume of R-134a vapor and the viscosity of R134a are decreased by the increase of saturation temperature. For that reason, the flow resistance is also decreased. All of these factors lower the pressure drop due to the increase in condensing pressure. Also, the pressure drop decreases with decreasing vapor quality generally. The decrease in vapor quality can occur by the increase in heat flux, which increases with increasing condensation rate. Also, total pressure drop increases with increasing mass flux at the same condensing temperature difference. The increase in the vapor velocity and the flow turbulence can occur by the increase of mass flux at a specific vapor quality. As a result of the increase in the shear stress at the interface of the vapor and liquid film, there is an increase in pressure drop. It can be noted that two-phase friction factor increases with decreasing equivalent Reynolds numbers. The results of correlation development study in this paper are found to be in good agreement with this fundamental knowledge of in-tube condensation as expected.

Table 4 shows the detailed results of the study. First, the convective heat transfer coefficient was obtained by means of the computational numerical methods such as genetic algorithm (GA), unconstrained nonlinear minimization algorithm- Nelder-Mead method (NM) and non-linear least squares method (NLS), and their correlations can be seen from the table separately. All the results of the computational numerical methods seem to have low proportional error rate values calculated from Eqs. (3) to (5). The unconstrained nonlinear minimization algorithm-Nelder-Mead method (NM) has the lowest proportional error rates as a result of the analysis. For that reason, dependency analysis was only done for this method. Second, the term (k_l/d), obtained by the division of the liquid thermal conductivity (k_l) to inner tube diameter (d), was a constant parameter in Eq. (10) due to its unit of "W $m^{-2}K^{-1}$". Other parameters such as equivalent Reynolds number, Prandtl number, Lockhart and Martinelli number, Bond number and Froude number are changed in Table 4 to show the dependency of convective heat transfer coefficient to them. It can be seen clearly from Table 4 that the convective heat transfer coefficient has the highest dependency to equivalent Reynolds number among others together with the ratio of liquid thermal conductivity to inner tube diameter; in other words, equivalent Reynolds number is found to be the dominant parameter for the determination of convective heat transfer coefficient by means of Eq. (10).

Figs. 4 to 6 show the comparison of convective condensation heat transfer coefficients obtained by the computational numerical methods of GA, NM, NLS and experiment (Eq. (1)) for all mean mass fluxes from 260 to 515 kg m^{-2} s^{-1} at the saturation temperatures of 40-50°C separately. These figures clearly show that the distribution of the data between the errors bands of ±30% seems quite balanced as expected from the results shown in Table 4. In addition, it is also shown that convective heat transfer coefficients increase with increasing mass flux of R134a as explained above. This result also shows that results of the numerical analysis are reasonable and compatible with the fundamental issues of condensation heat transfer.

Table 5 demonstrates the proposed equations for the two-phase multipliers and their error rates obtained from Eqs. (3) to (5). Lockhart and Martinelli parameter was the single parameter regarding with the form of Chisholm and Laird [53]'s two-phase frictional multiplier in Eq. (26). All proposed correlations' results using computational numerical methods are found to be successful according to their error rates in Table 5. NM method seems the most predictive one among others as a result of the analysis. For that reason, the last two equations' development is performed using NM in a different form from Chisholm and Laird's [53] two-phase frictional multiplier. It can be clearly seen from Table 5 that the last correlation in this table has the lowest proportional error rate.

Figs. 7 to 9 illustrate the comparison of the two-phase multipliers calculated from the computational numerical methods of GA, NM, NLS and experiment (Eq. (21)) for all mean mass fluxes from 260 to 515 kg m^{-2} s^{-1} at the saturation temperatures of 40-50°C separately. The 98.36% of the data for GA and NM, and 96.73% of the data for LS falls within the ±30% deviation line in these figures. The results also show the success due to the usage of Lockhart and Martinelli parameter in Eq. (25).

Figs. 10 to 12 show the comparison of frictional pressure drops between the computational numerical methods and the experiment (Eq. (23)) for condensation of R134a inside the vertical tube at the mean mass fluxes from 260 to 515 kg m^{-2} s^{-1} at the saturation temperatures of 40-50°C. The 89.66% of the data falls within the ±30% deviation line in these figures for all investigated computational numerical methods. It can be clearly seen from figures that the distribution of the data between the error bands of ±30% seems quite balanced apart

Table 4. The most predictive combinations of input parameters for Eq. (10) and proposed correlations for the condensation heat transfer coefficient.

Inputs for Eq. (10)					Input number	Error analysis			Proposed equations	Method		
k_l/d ($W m^{-2}K^{-1}$)	Re_{eq}	PrR	X	BoFr		R^2	Prop. (%)	Square law	h ($W m^{-2}K^{-1}$)	GA	NM	NLS
1	1	0	0	0	2	0.683	12.154	923.252	$h = 0.0436\left(\frac{k_l}{d}\right)Re_{eq}^{0.85}$	0	1	0
1	0	1	0	0	2	0.623	23.158	1622.576	$h = 404.86\left(\frac{k_l}{d}\right)(PrR)^{0.08}$	0	1	0
1	0	0	1	0	2	0.685	22.428	1569.877	$h = 12.64\left(\frac{k_l}{d}\right)\left[\frac{0.000172}{X^{2.914}} + 52.886\right]$	0	1	0
1	0	0	0	1	2	0.619	12.712	1012.119	$h = 21.479\left(\frac{k_l}{d}\right)(BoFr)^{0.368}$	0	1	0
1	1	1	1	1	4	0.675	12.389	934.468	$h = 0.332\left(\frac{k_l}{d}\right)Re_{eq}^{0.619}(PrR)^{0.032}\left[\frac{0.648}{X^{-0.00152}} + 0.127\right](BoFr)^{0.0713}$	1	0	0
1	1	1	1	1	4	0.688	11.969	916.376	$h = 0.0536\left(\frac{k_l}{d}\right)Re_{eq}^{0.999}(PrR)^{-0.06}\left[\frac{-0.739}{X^{-0.0239}} + 1.248\right](BoFr)^{-0.0875}$	0	1	0
1	1	1	1	1	4	0.647	12.388	974.128	$h = 0.591\left(\frac{k_l}{d}\right)Re_{eq}^{0.327}(PrR)^{0.297}\left[\frac{0.222}{X^{-0.0815}} + 0.0782\right](BoFr)^{0.281}$	0	0	1

Table 5. The most predictive coefficients of the proposed correlations for two-phase multiplier by means of the computational numerical methods.

Inputs for Eq. (25)	Input number	Error analysis			Proposed equations	Method		
X		R^2	Prop. (%)	Square law	φ_l^2	GA	NM	NLS
1	1	0.965	18.624	269.826	$\varphi_l^2 = -2.272 + \frac{2.188}{X^{1.987}} + \frac{0.337}{X^{1.553}}$	1	0	0
1	1	0.965	18.43	270.42	$\varphi_l^2 = -0.0283 + \frac{2.253}{X^{1.988}} - \frac{0.351}{X^{0.247}}$	0	1	0
1	1	0.965	18.604	270.215	$\varphi_l^2 = -29.483 + \frac{28.283}{X^{0.0166}} + \frac{2.314}{X^{1.98}}$	0	0	1
1	1	0.966	16.114	267.695	$\varphi_l^2 = 46462.2e^{-125.788X} + 2746.01e^{-24.944X}$	0	1	0
1	1	0.966	13.608	267.122	$\varphi_l^2 = 6019149e^{(-((X+0.1034)/0.0456)^2)} + 2045.276e^{(-((24.944X+0.0377)/0.09)^2)}$	0	1	0

from the data belonging to the mass flux of 260 kg $m^{-2}s^{-1}$ at 50°C. As explained above, the frictional pressure drop increases with increasing mass flux in these figures, and this situation shows the compatibility of the computational numerical models with the condensation heat transfer fundamental issues. As a result of the analysis of the authors' previous publications on the prediction of the proper void faction models and correlations, the reported agreeable void fraction correlations give quite similar frictional pressure drops. For that reason, the Chisholm correlation [54] is used as a constant void faction correlation in this numerical study.

The fitness function is defined to perform the optimization process considering its maximization in the GA analysis. The performances of the method of GA, NM and NLS with suitable architecture were found to be in good agreement predicting the experimental condensation heat transfer coefficient, two-phase friction multiplier and frictional pressure drop for all tested conditions. In addition, their prediction success can be realized and comparable with the results published in the authors' previous publications, especially for the condensation heat transfer coefficient [22] and pressure drop [23].

Table 6 shows the deviations of investigated heat transfer coefficient correlations shown in Table 2. The first proposed heat transfer coefficient correlation shown in Table 4, which depends only on k_l/d and Re_{eq}, and obtained from NM analysis, is also selected for the comparison. A large number of data points are used to show the success of the proposed correlation. The deviations of the different condensing temperatures are found to be similar with each other. For that reason, Table 6 also shows the accuracy of the experiments according to different condensing temperatures of 40 and 50°C in terms of the consistency of the deviations. Considering all data points, the proposed correlation has the best predictability among the reported correlations with the deviation of 2.52%. Akers and Rosson's [67] correlation has the largest one with the deviation of 50.39%. As explained above, artificial intelligence techniques have a learning process including test and training processes using a limited number of experimental data. As shown in Table 4, the proposed correlation in Table 6 has the $E_{Rsquare}$ (R^2) value of 0.683. In spite of its low R^2 value obtained from the testing process, it has lower deviations in comparison to the most of the correlations in Table 6. The

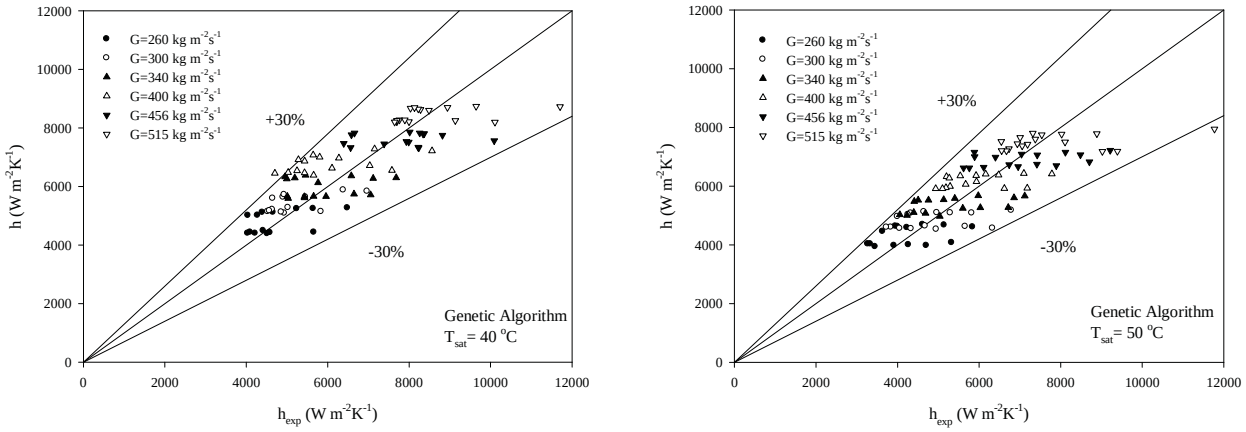

Fig. 4. Comparisons of experimental convective heat transfer coefficients with the method of genetic algorithm for the mass fluxes of 260, 340, 456 kg $m^{-2}s^{-1}$ and (a) T_{sat}=40°C and (b) 50°C.

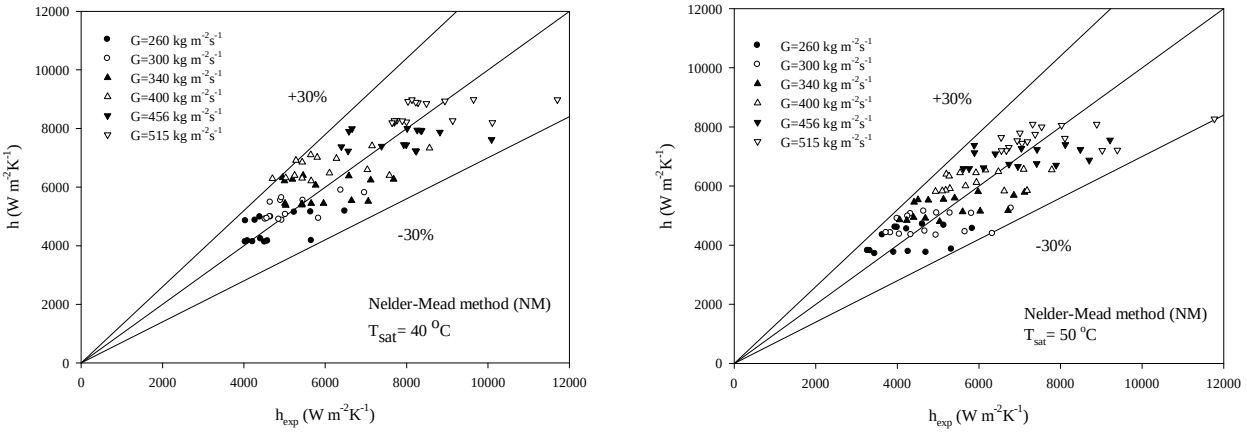

Fig. 5. Comparisons of experimental convective heat transfer coefficients with the method of non-linear least squares for the mass fluxes of 260, 340, 456 kg $m^{-2}s^{-1}$ and (a) T_{sat}=40°C and (b) 50°C.

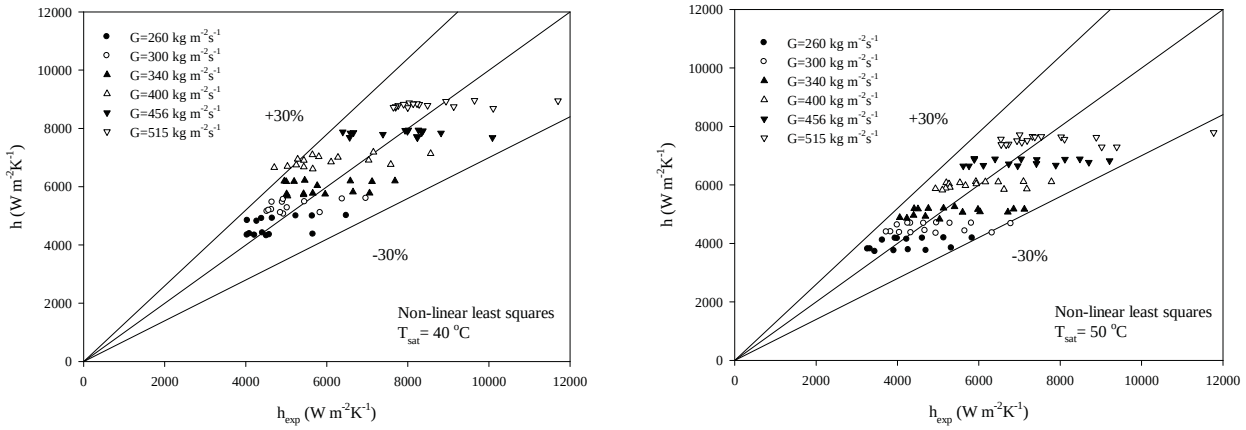

Fig. 6. Comparisons of experimental convective heat transfer coefficients with the method of least squares for the mass fluxes of 260, 340, 456 kg $m^{-2}s^{-1}$ and (a) T_{sat}=40°C and (b) 50°C.

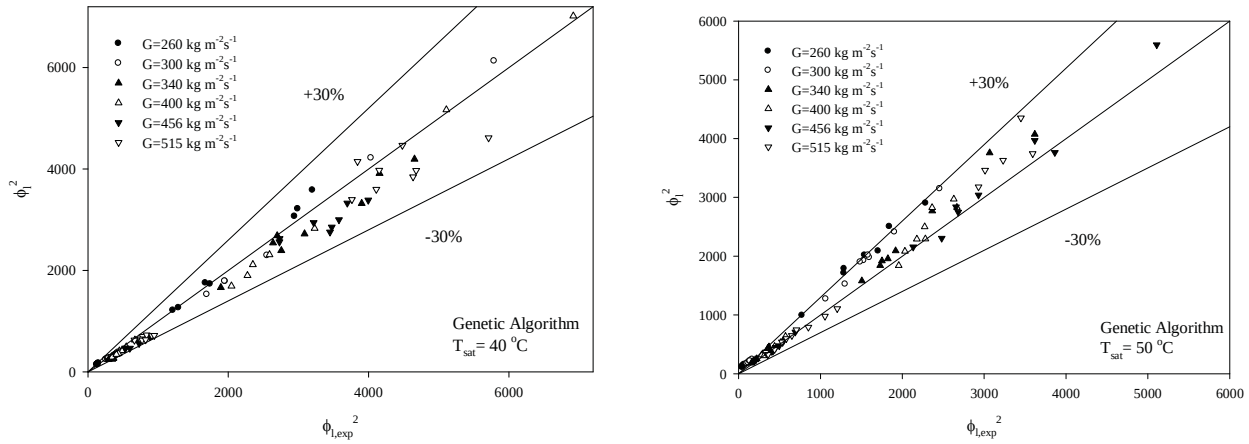

Fig. 7. Comparisons of experimental two-phase multiplier with the method of genetic algorithm for the mass fluxes of 260, 340, 456 kg $m^{-2}s^{-1}$ and (a) T_{sat}=40°C and (b) 50°C.

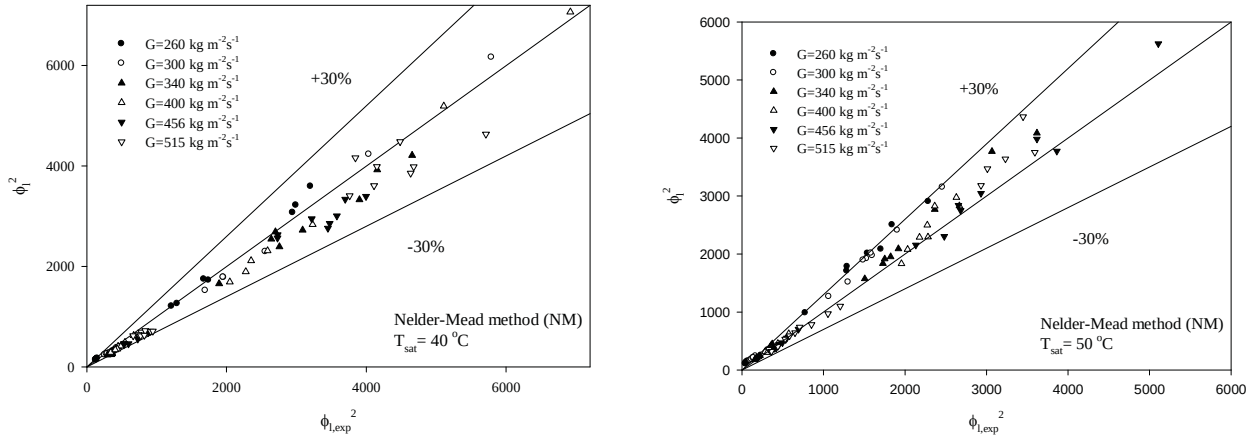

Fig. 8. Comparisons of experimental two-phase multiplier with the method of non-linear least squares for the mass fluxes of 260, 340, 456 kg $m^{-2}s^{-1}$ and (a) T_{sat}=40°C and (b) 50°C.

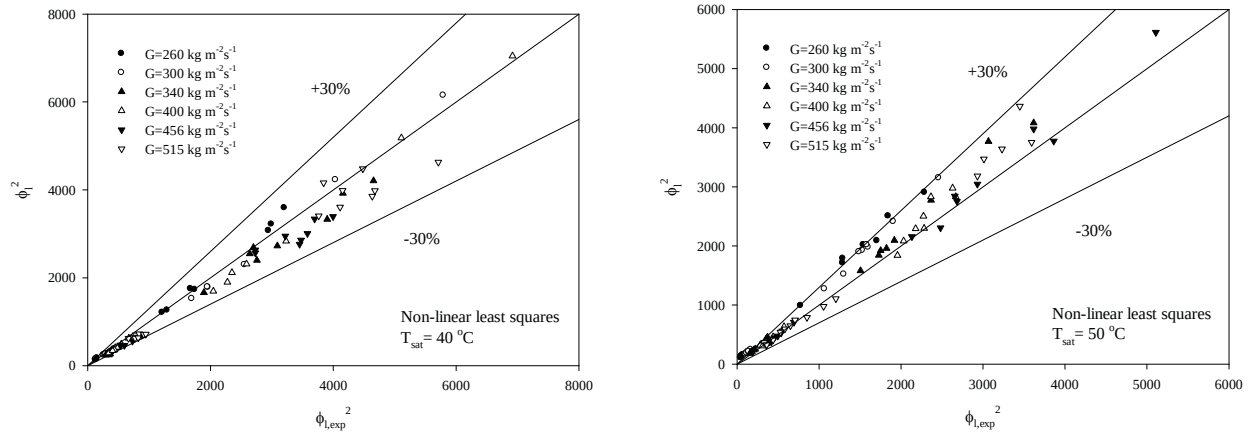

Fig. 9. Comparisons of experimental two-phase multiplier with the method of least squares for the mass fluxes of 260, 340, 456 kg $m^{-2}s^{-1}$ and (a) T_{sat}=40°C and (b) 50°C.

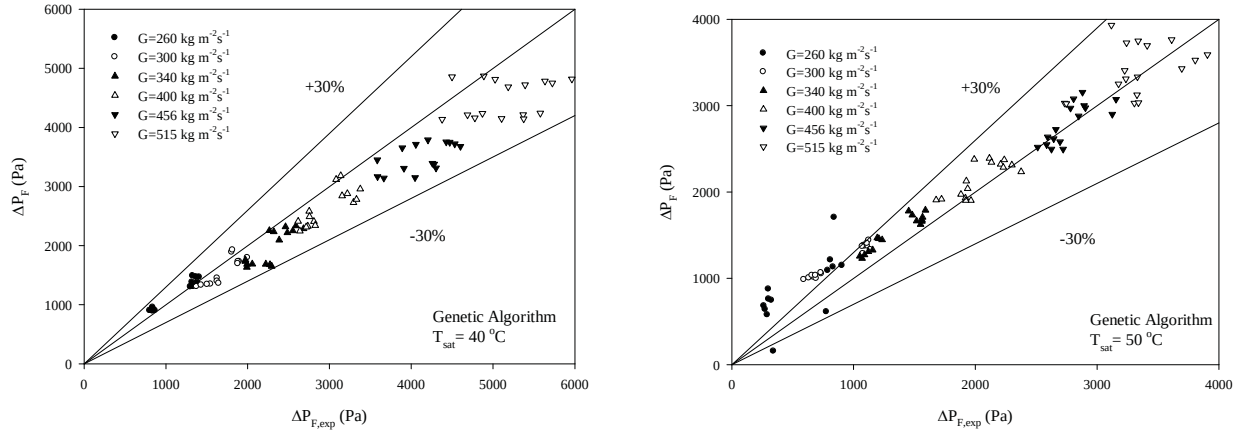

Fig. 10. Comparisons of experimental frictional pressure drop with the method of genetic algorithm for the mass fluxes of 260, 340, 456 kg $m^{-2}s^{-1}$ and (a) T_{sat}=40°C and (b) 50°C.

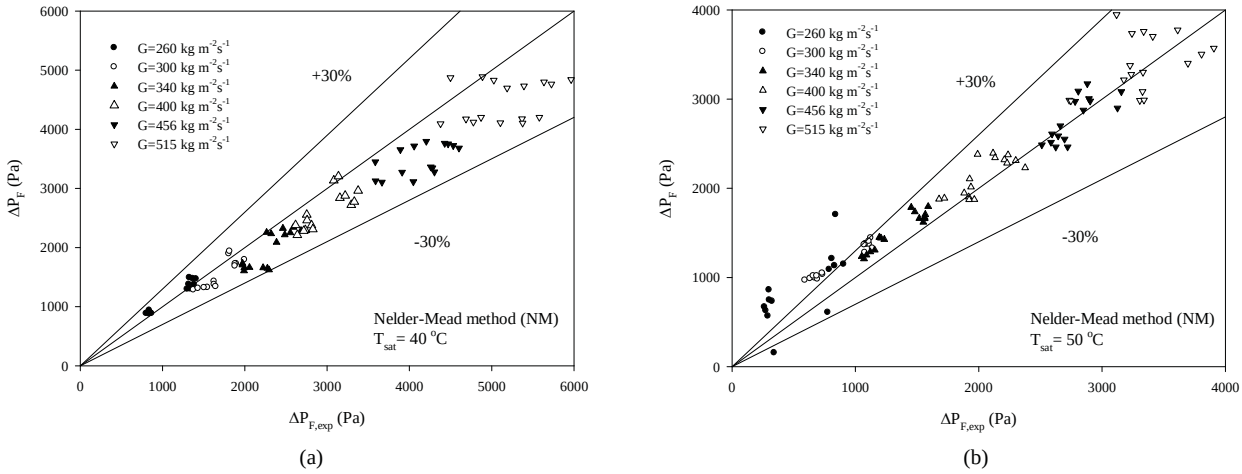

Fig. 11. Comparisons of experimental frictional pressure drop with the method of non-linear least squares for the mass fluxes of 260, 340, 456 kg $m^{-2}s^{-1}$ and (a) T_{sat}=40°C and (b) 50°C.

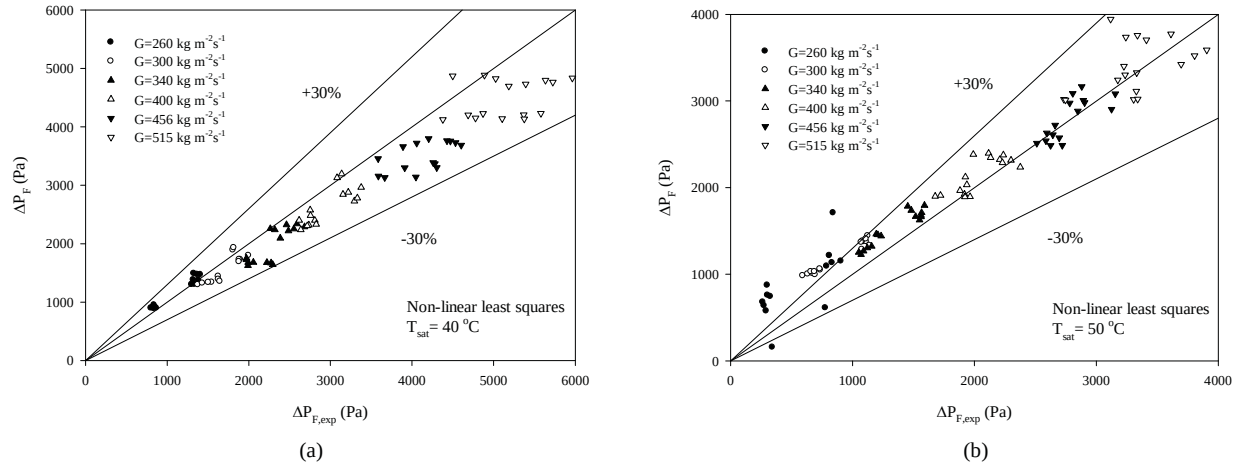

Fig. 12. Comparisons of experimental frictional pressure drop with the method of least squares for the mass fluxes of 260, 340, 456 kg $m^{-2}s^{-1}$ and (a) T_{sat}=40°C and (b) 50°C.

Table 6. The existing heat transfer coefficient correlations and one of the proposed correlations for the validation for the mass fluxes ranging between 260 and 515 kg $m^{-2}s^{-1}$.

Researcher	Data of 40 °C (178 data points) deviation (%)	Data of 50 °C (191 data points) deviation (%)	All data (369 data point) deviation (%)
Shah [55]	21.29	18.89	20.09
Dobson and Chato [58]	5.08	3.76	4.42
Dobson and Chato [58]	26.19	24.34	25.26
Chato [59]	27.22	26.2	26.71
Sweeney [60]	28.9	28.05	28.47
Cavallini et al. [61]	-4.34	-5.56	-4.95
Fujii [62]	3.08	3.25	3.16
Tang et al. [63]	8.88	12.07	10.48
Bivens and Yokozeki [64]	34.13	32.04	33.09
Tandon et al. [65]	40.43	40.91	40.67
Travis et al. [66]	17.29	15.07	16.18
Akers and Rosson [67]	50.73	50.04	50.39
Proposed correlation $h = 0.0436\left(\frac{k_l}{d}\right)Re_{eq}^{0.85}$	3.73	1.31	2.52

two-phase friction multipliers shown in Table 4 have the average deviation of 0.96%. It is obvious that they are supposed to predict the measured pressure drop values better than other correlations.

In addition, detailed explanations and some additional figures and tables with different experimental parameters related to the study on the void fraction models and correlations, film thickness models, friction factors and frictional pressure drop models, heat transfer and pressure drop characteristics can be seen from the series of the authors' previous publications [17-29]. A general application of computational numerical techniques to in-tube condensation on the correlation development is performed in this paper.

A large number of graphics could be generated from the output of the calculations; however, due to space limitation, only typical results are shown for limited data of the experimental database of the authors. It should be also noted that detailed information on the heat transfer characteristics of the study with some additional figures and different experimental parameters can be seen from the authors' previous publications.

5. Conclusion

Experiments have been conducted to determine the convective condensation heat transfer coefficient, two-phase friction factor and frictional pressure drop by means of computational numerical techniques. This paper reports that in spite of the numerous studies on the determination of convective condensation heat transfer coefficient in tubes, application of computational numerical techniques to the in-tube condensation for the aim of correlation development does not exist in the literature. For that reason, the content of this study is expected to fill this gap in the literature.

The calculated heat transfer coefficients, two-phase friction factors and frictional pressure drops by means of all computational numerical methods such as genetic algorithm (GA), unconstrained nonlinear minimization algorithm- Nelder-Mead method (NM) and non-linear squares error method (NLS) are found to be quite near to each other and also be in good agreement with the 369 numbers of laminar and turbulent flow experimental data.

It is shown clearly that the proposed correlations, obtained from artificial intelligence algorithms, have better predictability of heat transfer characteristics than the existing correlations in the literature.

Acknowledgments

The second author wishes to thank King Mongkut's University of Technology Thonburi for providing him with a Post-doctoral fellowship and Yıldız Technical University (Research Project No: 29-06-01-01). The fourth author would like to thank the Thailand Research Fund and the National Research University Project, for the financial support.

Nomenclature

A : Surface area, m^2
ANN : Artificial neural network
Bo : Bond number
CFD : Computational fluid dynamics
Co : Parameter in Shah correlation
D : Internal tube diameter, m
E : Error

f : Friction factor
Fr : Froude number
G : Mass flux, kg m^{-2} s^{-1}
GA : Genetic algorithm
Ga : Galileo number
h : Heat transfer coefficient, W $m^{-2}K^{-1}$
k : Thermal conductivity, W $m^{-1}K^{-1}$
L : Length of test tube, m
LS : Least square
N : Element number
NLS : Non-linear least squares
NM : Nelder-Mead method
Nu : Nusselt number
P : Pressure, N m^{-2}
ΔP : Pressure drop, N m^{-2}
Pr : Prandtl number
$Prop$: Proportional
R : ρ-μ ratio
Re : Reynolds number
S : Slip ratio
Q : Heat transfer rate, W
T : Temperature, °C
X : Lockhart and Martinelli parameter
x : Average vapor quality

Greek symbols

φ_l^2 : Two-phase multiplier
ρ : Density, kg m^{-3}
μ : Dynamic viscosity, kg m^{-1} s^{-1}
α : Void fraction
σ : Surface tension, N m^{-1}

Subscripts

$calc$: Calculated
$critic$: Critical
eq : Equivalent
exp : Experimental
F : Frictional term
G : Gravitational term
g : Gas/vapor
sf : Superficial
so : Soliman
i : Inlet
l : Liquid
M : Momentum term
ph : Preheater
o : Outlet
red : Reduced
ref : Refrigerant
sat : Saturation
TP : Two-phase
TS : Test section
wi : Inner wall

References

[1] W. M. Jenkins, On the application of natural algorithms to structural design optimization, *Eng. St.,* 19 (4) (1997) 302-308.

[2] S. Akin, B. Demiral, Genetic algorithm for estimating multi-phase flow functions from unsteady-state displacement experiments, *Comp. and Geosci.,* 24 (3) (1998) 251-258.

[3] A. Alizadehdakhel, M. Rahimi, J. Sanjari and A. A. Alsairafi, CFD and artificial neural network modeling of two-phase flow pressure drop, *Int. Comm. in Heat and Mass Tr.,* 36 (8) (2009) 850-856.

[4] D. R. Magee and R. D. Boyle, Detecting lameness using 'Re-sampling Condensation' and 'multi-stream cyclic hidden Markov models', *Im. and Vis. Comp.,* 20 (8) (2002) 581-594.

[5] M. Isard and A. Blake, Condensation-conditional density propagation for visual tracking, *Int. J. of Comp. Vis.,* 29 (1) (1998) 5-28.

[6] S. Nasseh, A. Mohebbi, A. Sarrafi and M. Taheri, Estimation of pressure drop in venturi scrubbers based on annular two-phase flow model, artificial neural networks and genetic algorithm, *Chem. Eng. J.,* 150 (1) (2009) 131-138.

[7] C. M. Salgado, C. M. N. A. Pereira, R. Schirru and L. E. B. Brandao, Flow regime identification and volume fraction prediction in multiphase flows by means of gamma-ray attenuation and artificial neural networks, *Prog. in Nuc. En.,* 52 (6) (2010) 555-562.

[8] Z. Shang, Application of artificial intelligence CFD based on neural network in vapor-water two-phase flow, *Eng.App. of Artificial Int.,* 18 (6) (2005) 663-671.

[9] C. Sunde, S. Avdic and I. Pazsit, Classification of two-phase flow regimes via image analysis and neuro-wavelet approach, *Prog. in Nuc. En.,* 46 (3-4) (2005) 348-358.

[10] T. Tambouratzis and I. Pazsit, A general regression artificial neural network for two-phase flow regime identification, *Ann. of Nuc. En.,* 37 (5) (2010) 672-680.

[11] L. A. Tarca, B. P. A. Grandjean and F. Larachi, Reinforcing the phenomenological consistency in artificial neural network modeling of multiphase reactors, *Chem. Eng. and Proc.,* 42 (8-9) (2003) 653-662.

[12] V. Vins and V. Vacek, Mass flow rate correlation for two-phase flow of R218 through a capillary tube, *Appl. Th. Eng.,* 29 (14-15) (2009) 2816-2823.

[13] W. Zhang, T. Hibiki and K. Mishima, Correlations of two-phase frictional pressure drop and void fraction in mini-channel, *Int. J. of Heat and Mass Tr.,* 53 (1-3) (2010) 453-465.

[14] B. Allen, M. Savard-Goguen and L. Gosselin, Optimizing heat exchanger networks with genetic algorithms for designing each heat exchanger including condensers, *Appl. Th. Eng.,* 29 (16) (2009) 3437-3444.

[15] W. Wang, L. X. Zhao and C. L. Zhang, Generalized neural network correlation for flow boiling heat transfer of R22 and its alternative refrigerants inside horizontal smooth tubes, *Int. J. of Heat and Mass Tr.,* 49 (15-16) (2006) 2458-2465.

[16] H. Demir, Ö. Agra and Ş. Ö. Atayılmaz, Generalized neural network model of alternative refrigerant (R600a) inside a

smooth tube, *Int. Comm. in Heat and Mass Tr.*, 36 (2) (2009) 744-749.

[17] A. S. Dalkilic, S. Laohalertdecha and S. Wongwises, Effect of void fraction models on the two-phase friction factor of R134a during condensation in vertical downward flow in a smooth tube, *Int. Comm. in Heat and Mass Tr.*, 35 (8) (2008) 921-927.

[18] A. S. Dalkilic, S. Yildiz and S. Wongwises, Experimental investigation of convective heat transfer coefficient during downward laminar flow condensation of R134a in a vertical smooth tube, *Int. J. of Heat and Mass Tr.*, 52 (1-2) (2009) 142-150.

[19] A. S. Dalkilic, S. Laohalertdecha and S. Wongwises, Two-phase friction factor in vertical downward flow in high mass flux region of refrigerant HFC-134a during condensation, *Int. Comm. in Heat and Mass Tr.*, 35 (9) (2008) 1147-1152.

[20] A. S. Dalkilic, S. Laohalertdecha and S. Wongwises, Effect of void fraction models on the film thickness of R134a during downward condensation in a vertical smooth tube, *Int. Comm. in Heat and Mass Tr.*, 36 (2) (2009) 172-179.

[21] A. S. Dalkilic and S. Wongwises, Intensive literature review of condensation inside smooth and enhanced tubes, *Int. J. of Heat and Mass Tr.*, 52 (15-16) (2009) 3409-3426.

[22] A. S. Dalkilic, S. Laohalertdecha and S. Wongwises, Experimental investigation on heat transfer coefficient of R134a during condensation in vertical downward flow at high mass flux in a smooth tube, *Int. Comm. in Heat and Mass Tr.*, 36 (10) (2009) 1036-1043.

[23] A. S. Dalkilic, O. Agra, I. Teke and S. Wongwises, Comparison of frictional pressure drop models during annular flow condensation of R600a in a horizontal tube at low mass flux and of R134a in a vertical tube at high mass flux, *Int. J. of Heat and Mass Tr.*, 53 (9-10) (2010) 2052-2064.

[24] A. S. Dalkilic and S. Wongwises, An investigation of a model of the flow pattern transition mechanism in relation to the identification of annular flow of R134a in a vertical tube using various void fraction models and flow regime maps, *Exp. Th. and Fl. Sci.*, 34 (6) (2010) 692-705.

[25] A. S. Dalkilic, S. Laohalertdecha and S. Wongwises, Validation of void fraction models and correlations using a flow pattern transition mechanism model in relation to the identification of annular vertical downflow in-tube condensation of R134a, *Int. Comm. in Heat and Mass Tr.*, 37 (7) (2010) 827-834.

[26] A. S. Dalkilic, S. Laohalertdecha and S. Wongwises, New experimental approach on the determination of condensation heat transfer coefficient using frictional pressure drop and void fraction models in a vertical tube, *En. Conv. and Man.*, 51 (12)(2010) 2535-2547.

[27] A. S. Dalkilic and S. Wongwises, A performance comparison of vapour compression refrigeration system using various alternative refrigerants, *Int. Comm. in Heat and Mass Tr.*, 37 (9) (2010) 1340-1349.

[28] A. S. Dalkilic, S. Laohalertdecha and S. Wongwises, Experimental study of the condensation heat transfer coefficients in high mass flux region in annular flow regime of HFC-134a inside the vertical smooth tube, *H. Tr. Eng.*, 32 (1) (2011) 1-12.

[29] A. S. Dalkilic, I. Teke and S. Wongwises, Experimental analysis for the determination of the convective heat transfer coefficient by measuring pressure drop directly during annular condensation flow of R134a in a vertical smooth tube, *Int. J. of Heat and Mass Tr.*, 54 (4) (2011) 1008-1014.

[30] J. H. Holland, *Adaptation in natural and artificial systems*, University of Michigan Press, Michigan, USA (1975).

[31] J. Koza, *Genetic programming: on the programming of computers by means of natural selection*, MIT Press/ Cambridge, Massachusetts, USA (1992).

[32] D. E., Goldberg, *Genetic algorithms in search optimization and machine learning*, Addison Wesley Longman Publishing Co., Boston (1989).

[33] G. Renner, A. Ekart, Genetic algorithms in computer aided design, *Comp.-Aided Des.*, 35 (2003) 709-726.

[34] J. H. Holland, *Adaptation in natural and artificial systems: an introductory analysis with applications to biology, Control and Artificial Intelligence*, MIT Press/Bradford Books Ed., USA (1992).

[35] J. A. Nelder and R. Mead, A simplex method for function minimization, *Comp. J.*, 7 (15) (1965) 308-313.

[36] J. Nocedal and S. J. Wright, *Numerical optimization*, Springer, New York, USA (2006).

[37] C. F. Gauss, Theory of the combination of observations least subject to errors: part one, part two, supplement (repost), translated by G.W. Stewart, *Soc. for Ind. Engi.*, 1987.

[38] M. J. Box, D. Davies and W. H. Swann, *Non-linear optimization techniques*, Oliver and Boyd, Edinburg, Scotland (1969).

[39] F. W. Dittus and L. M. E. Boelter, Heat transfer in automobile radiators of the tubular type, *Univ. of California* Pub. on Eng., 2 (1930) 443-461.

[40] W. W. Akers, H. A. Deans and O. K. Crosser, Condensation heat transfer within horizontal tubes, *Chemical Engineering Prog. Sym. Ser.*, 55 (1959) 171-176.

[41] A. Cavallini and R. Zecchin, A dimensionless correlation for heat transfer in forced convection condensation, *Proceedings of the Sixth Int. Heat Tr. Conf.*, 3 (1974) 309-313.

[42] M. M. Shah, A general correlation for heat transfer during film condensation inside pipes, *Int. J. of Heat and Mass Tr.*, 22 (1979) 547-556.

[43] S. Koyama, A. Miyara, H. Takamatsu and T. Fujii, Condensation heat transfer of binary refrigerant mixtures of R22 and R114 inside a horizontal tube with internal spiral grooves, *Int. J. of Ref.*, 13 (4) (1990) 256-263.

[44] R. W. Lockhart and R. C. Martinelli, Proposed correlation of data for isothermal two-phase, two-component flow in pipes, *Chem. Eng. Prog.*, 45 (1949) 39-48.

[45] M. K. Dobson and J. C. Chato, Condensation in smooth horizontal tubes, J. of Heat Tr., 120 (1998) 193-213.

[46] A. Cavallini, G. A. Longo and L. Rossetto, Condensation heat transfer and pressure drop of refrigerants in tubes of finned tube heat exchangers, *Rec. Dev. in Finned Tube Heat Exc., Theo. and Prac. Aspects*, Denmark (1993) 160-204.

[47] A. Cavallini, L. Doretti, N. Klammsteiner, G. A. Longo and L. Rossetto, Condensation of new refrigerants inside smooth and enhanced tubes, *Proceedings 19th Int. Cong. of Ref.*, Holland, 4 (1995) 105-114.
[48] J. T. Fanning, *A practical treatise on hydraulic and water supply engineering*, *Van Nostrand*, New York, USA (1877) Revised ed. 1886.
[49] H. Darcy, *Recherches experimentales relatives au mouvement de l'Eau dans les Tuyaux, Mallet-Bachelier*, Paris, France (1857).
[50] J. Weisbach, Lehrbuch der ingenieur und maschinen-mechanik, *Braunschwieg*, 1845.
[51] H. Blasius, Grenzschichten in Flüssigkeiten mit kleiner Reibung, *Z. Math. u. Phys*., 56 (1908) 1-37.
[52] D. Chisholm, A theoretical basis for the Lockhart-Martinelli correlation for two-phase flow, *Int. J. of Heat and Mass Tr.*, 10 (1967) 1767-1778.
[53] D. Chisholm and A. D. K. Laird, Two-phase flow in rough tubes, *Trans. of ASME*, 80 (2) (1958) 276-286.
[54] D. Chisholm, *Two phase flow in pipelines and heat exchangers*, George Godwin in association with The Institution of Chemical Engineers, *London*, UK (1983).
[55] M. M. Shah, A general correlation for heat transfer during film condensation inside pipes, *Int. J. of Heat and Mass Tr.*, 22 (4) (1979) 547-556.
[56] S. J. Kim and H. C. No, Turbulent film condensation of high pressure steam in a vertical tube, *Int. J. of Heat and Mass Tr.*, 43 (21) (2000) 4031-4042.
[57] L. Lienberg, J. P. Bukasa, M. F. K. Holm, J. P. Meyer and A. E. Bergles, Towards a unified approach for modelling of refrigerant condensation in smooth tubes, *Proc. of the Int. Sym. on Comp. Heat Exch.*, (2002) 457-462.
[58] M. K. Dobson and J. C. Chato, Condensation in smooth horizontal tubes, *J. of Heat Tr., Trans. of ASME*, 120 (2) (1998) 193-213.
[59] J. C. Chato, Laminar Condensation inside horizontal and inclined tubes, *ASHRAE J.*, 4 (2) (1962) 52-60.
[60] K. A. Sweeney, *The heat transfer and pressure drop behavior of a zeotropic refrigerant mixture in a micro-finned tube*, M.S. thesis, Dept. of Mech. and Ind. Eng., Univ. of Illinois at Urbana-Champaign, Illinois, USA (1996).
[61] A. Cavallini, J. R. Smith and R. Zecchin, A dimensionless correlation for heat transfer in forced convection condensation, *6th Int. Heat Tr. Conf.*, Tokyo, Japan (1974) 309-313.
[62] T. Fujii, Enhancement to condensing heat transfer-new developments, *J. of Enhanced Heat Tr.*, 2 (1-2) (1995) 127-137.
[63] L. Tang, M. M. Ohadi and A. T. Johnson, Flow condensation in smooth and microfin tubes with HCFC-22, HFC-134a, and HFC-410 refrigerants. part II: Design equations, *Journal of Enh. Heat Tr.*, 7 (5) (2000) 311-325.
[64] D. B. Bivens and A. Yokozeki, Heat transfer coefficient and transport properties for alternative refrigerants, *Proc. 1994 Int. Ref. Conf.* (1994) 299-304.
[65] T. N. Tandon, H. K. Varma and C. P. Gupta, Heat transfer during forced convection condensation inside horizontal tube, *Int. J. of* Ref., 18 (3) (1995) 210-214.
[66] D. P. Travis, W. M. Rohsenow and A. B. Baron, Forced convection inside tubes: a heat transfer equation for condenser design, *ASHRAE Trans.*, 79 (1) (1973) 157-165.
[67] W. W. Akers and H. F. Rosson, Condensation inside a horizontal tube, *Chem. Eng. Prog.* Symp. Series, 56 (30) (1960) 145-149.
[68] S. J. Kline and F. A. McClintock, Describing uncertainties in single sample experiments, *Mech. Eng.*, 75 (1) (1953) 3-8.

Muhammet Balcılar is currently a Research Assistant of Computer Engineering at Yildiz Technical University, İstanbul, Turkey. He is a Ph.D student in Computer Engineering from the same university. His research interest is on artificial intelligence, video editing, optimization and signal processing.

Ahmet Selim Dalkılıç is currently an Assistant Professor of Mechanical Engineering at Yildiz Technical University, İstanbul, Turkey. He received his Ph.D in Mechanical Engineering from the same university. His current research interest is in enhanced heat transfer, convection heat transfer, two-phase flow of new refrigerants and mixture refrigerants and applications in heat exchangers. Dr. Ahmet Selim Dalkılıç is the member of Innovation Explorer for Scientific Researchers Community sponsored by Elsevier and American Society of Mechanical Engineers.

Berna Bolat is currently an Assistant Professor of Mechanical Engineering at Yildiz Technical University, İstanbul, Turkey. She received her Ph.D in Mechanical Engineering from the same university. Her current research interest is in computer aided design, vertical transportation, elevator traffic modeling and simulation and genetic algorithms.

Somchai Wongwises is currently a Professor of Mechanical Engineering at King Mongkut's University of Technology Thonburi, Bangmod, Thailand. He received his Doktor-Ingenieur (Dr.-Ing.) in Mechanical Engineering from the University of Hannover, Germany, in 1994. His research interests include two-phase flow, heat transfer enhancement, and thermal system design. He is the head of the Fluid Mechanics, Thermal Engineering and Multiphase Flow Research Labarotory (FUTURE).

Particuology 9 (2011) 626–631

Contents lists available at SciVerse ScienceDirect

Particuology

journal homepage: www.elsevier.com/locate/partic

Convective heat transfer of nanofluids with correlations

Lazarus Godson Asirvatham[a,*], Balakrishnan Raja[b], Dhasan Mohan Lal[a], Somchai Wongwises[c,d]

[a] R&AC Division, Department of Mechanical Engineering, College of Engineering, Guindy, Anna University, Chennai 600 025, Tamil Nadu, India
[b] Indian Institute of Information Technology, Design and Manufacturing (IIITD&M)-Kancheepuram, Chennai 600 048, India
[c] Fluid Mechanics, Thermal Engineering and Multiphase Flow Research Lab (FUTURE), Department of Mechanical Engineering, King Mongkut's University of Technology Thonburi, 126 Bangmod, Tongkru, Bangkok 10140, Thailand
[d] The Academy of Science, The Royal Institute of Thailand, Sanam Suea Pa, Dusit, Bangkok 10300, Thailand

ARTICLE INFO

Article history:
Received 1 May 2010
Received in revised form 17 February 2011
Accepted 31 March 2011

Keywords:
Convective heat transfer
Silver
Nanofluid
Correlation
Laminar
Turbulent
Transition

ABSTRACT

To investigate the convective heat transfer of nanofluids, experiments were performed using silver–water nanofluids under laminar, transition and turbulent flow regimes in a horizontal 4.3 mm inner-diameter tube-in-tube counter-current heat transfer test section. The volume concentration of the nanoparticles varied from 0.3% to 0.9% in steps of 0.3%, and the effects of thermo-physical properties, inlet temperature, volume concentration, and mass flow rate on heat transfer coefficient were investigated. Experiments showed that the suspended nanoparticles remarkably increased the convective heat transfer coefficient, by as much as 28.7% and 69.3% for 0.3% and 0.9% of silver content, respectively. Based on the experimental results a correlation was developed to predict the Nusselt number of the silver–water nanofluid, with ±10% agreement between experiments and prediction.

1. Introduction

Energy costs have soared rapidly in the last decade and there is tremendous need for new kinds of heating/cooling fluids, to improve heating system performance and to reduce equipment size and energy consumption. Nanofluids are new-generation heat transfer fluids for various industrial and automotive applications because of their excellent thermal performance (Eastman, Phillpot, Choi, & Keblinski, 2004). Nanofluids consist of nanometer-sized particles (<100 nm) dispersed in a base fluid such as water, engine oil or ethylene glycol. Addition of high thermal-conductivity metallic nanoparticles (e.g., copper, aluminum, silicon and silver) increases the thermal conductivity of such mixtures, thus enhancing their overall energy transport capability (Xuan & Li, 2003).

Eastman, Choi, Li, Yu, and Thompson (2001) showed a 40% increase in thermal conductivity by adding 0.3 vol% copper nanoparticles to ethylene glycol. For convective heat transfer, Xuan and Li (2004) studied the single phase heat transfer of Cu–water nanofluid with volume fraction of Cu, $\varphi = 0.3$–2.0% in the turbulent flow regime (Reynolds number between 10,000 and 25,000), and proposed a heat transfer correlation. The convective heat transfer coefficient increased by more than 60% with increase in Cu volume–fraction and flow velocity, yet with negligible penalty in pumping power. Li, Xuan, Jiang, and Xu (2005) measured the convective heat transfer of the Cu–water nanofluid in a small-hydraulic-diameter flat tube under laminar flow and found that the Nusselt number of the nanofluid with $\varphi = 1.5\%$ increased by more than 39% as compared to pure water. Zhou (2004) investigated the enhancement of heat transfer of Cu–acetone nanofluids with average Cu particle sizes in the range of $\gamma = 80$–100 nm and concentrations up to 4.0 g/L, and found that the heat transfer coefficient was much higher when compared to that of the base fluid. Faulkner, Rector, Davison, and Shekarriz (2004) investigated the convective heat transfer of a carbon nanotube (CNT)–water nanofluid in a micro channel, with a hydraulic diameter of 355 μm, at a Reynolds number between 2 and 17 and $\varphi = 1.1\%$, 2.2% and 4.4%, showing enhanced heat transfer coefficient of CNT–water at the higher concentrations. Yang, Zhang, Grulke, Anderson, and Wu (2005) investigated the convective heat transfer of graphite nanoparticles dispersed in a liquid in laminar flow in a horizontal tubular heat exchanger, and reported that at 2.5 wt% the heat transfer coefficient of the nanofluids increased by 22%. Ding, Alias, Wen, and Williams (2006) tested nanofluids with multi-walled carbon nanotubes (MCNT with $\varphi = 0.1$–1.0% with 0.5 wt% in aqueous solution) in a horizontal tube, and obtained a maximum enhancement of heat transfer of 350% at a Reynolds number of 800.

* Corresponding author. Tel.: +91 42 22614430; fax: +91 42 2615615.
E-mail addresses: godasir@yahoo.co.in (L.G. Asirvatham), rajab@iiitdm.ac.in (B. Raja), mohanlal@annauniv.edu (D. Mohan Lal), somchai.won@kmutt.ac.th (S. Wongwises).

1674-2001/$ – see front matter © 2011 Chinese Society of Particuology and Institute of Process Engineering, Chinese Academy of Sciences. Published by Elsevier B.V. All rights reserved.
doi:10.1016/j.partic.2011.03.014

Nomenclature

A	cross sectional area, m^2
C_p	specific heat, J/(kg K)
D	tube diameter, m
h	heat transfer coefficient, W/(m^2 K)
k	thermal conductivity, W/(m K)
m	mass flow rate, kg/s
Nu	Nusselt number
Pr	Prandtl number
Re	Reynolds number
T	temperature, K

Greek symbols

φ	volume fraction
ρ	density, kg/m^3
μ	dynamic viscosity, kg/m s
γ	particle size (nm)

Subscript

bf	base fluid
i	inner wall
nf	nanofluid
o	outer wall
p	nanoparticle
x	axial distance
w	tube wall

In this study, the enhancement of convective heat transfer of a silver–water nanofluid flowing in a concentric-tube countercurrent flow heat exchanger in which the heated nanofluid flowed in the inner tube while chilled water flowed through the annulus was experimentally studied. The effect of inlet temperature, concentration of silver, friction factor and flow rate on convective heat transfer was investigated.

2. Experimental

2.1. Nanofluid preparation

The silver nanoparticles manufactured by Sigma Aldrich (product number-576832, 99.5% metal, particle size <100 nm) were mixed with deionized water without any additive or stabilizer for 12 h under ultrasonic vibration using a Roop-Telsonic TEC-40 Model mixer with power density of 750 W at frequency of 20 kHz, to ensure complete dispersion of the nanoparticles in water. The volume concentrations used in this study were 0.3%, 0.6%, and 0.9% with pH values of 7.4, 7.1 and 6.8, respectively. A scanning electron microscope (SEM) was used to monitor the dispersion and size of the silver nanoparticles, as shown in Fig. 1. The figure shows that the nanoparticles were nearly spherical in shape, with a size of about 80 nm and the distribution in the base fluid was essentially uniform, though not without some agglomeration of the particles.

2.2. Measurement of thermal conductivity and viscosity

In this study, the transient-hot-wire method, which involves measuring the slope of the rise in the wire's temperature against the logarithmic time interval, was used to measure the effective thermal conductivity of the nanofluids. And the Cannon-Fenske Opaque reverse-flow viscometer was used to measure the viscosity of the Ag–water nanofluid. The uncertainty of the thermal conductivity and viscosity measurements was around 1.5% and 2%, respectively, while the uncertainties of temperature and volume fraction measurements were estimated to be ±0.15 °C and $\pm 10^{-5}$ g, respectively. Details on these measurements were given in a previous paper of the present authors (Godson, Raja, Mohan Lal, & Wongwises, 2010).

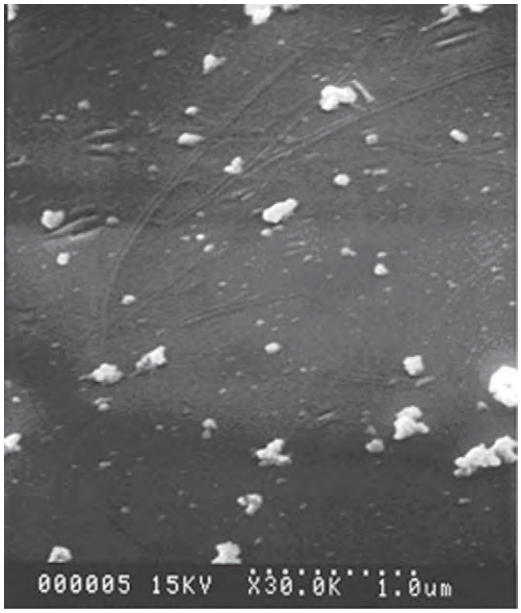

Fig. 1. SEM image of 0.6 vol% dispersed silver nanoparticles in water.

2.3. Convective heat transfer coefficient

Fig. 2 shows the schematic layout of the test facility to measure convective heat transfer coefficient, which comprises two flow circuits, chilled water and nanofluid. Each circuit consists of a constant temperature bath, of chilled water and of nanofluid bath respectively, with its own temperature controller, pump and flow meter. The test section is a 2.94 m long counter flow horizontal concentric-tube heat exchanger with nanofluid flowing inside the inner tube and chilled water inside the annular space. The inner tube is 4.3 mm in inside diameter, while the outer tube, 10.5 mm in inside diameter. The test section is thermally insulated by ceramic wool to reduce heat loss. A differential pressure transducer with 0.075% accuracy and two RTDs are mounted at both ends of the test section to measure respectively the pressure drop between the inlet and outlet and the bulk temperatures of the nanofluid. Six RTDs (PT100 RTD sensors with ±0.15 °C accuracy) are mounted longitudinally on the surface of the outside wall to measure the temperature distributions along the length of the test section. The nanofluid is heated in an insulated cylindrical tank with a 0.5 kW electric heater coupled to a proportional-integral-derivative controller (PID-C). Heated nanofluid is tapped out from the bottom of the tank and pumped by a centrifugal pump through a mass flow meter into the test section, counter-current to the chilled water. The nanofluid flow rate is measured using a Coriolis type mass flow meter with ±0.1% accuracy. Similarly, the outflowing water is cooled in a chilling unit of 0.5 TR (refrigeration ton) capacity with a 1 kW heater coupled to a PID controller in order to keep the temperature of the chilled water constant. A stirrer operating at 1500 rpm is mounted inside the chilled water tank to ensure uniform temperature. All inter connecting tubes for the nanofluid and chilled water are insulated to avoid heat loss to the surroundings. Error analysis for the heat transfer coefficient of the nanofluid is carried out by applying the uncertainty analysis suggested by Moffat

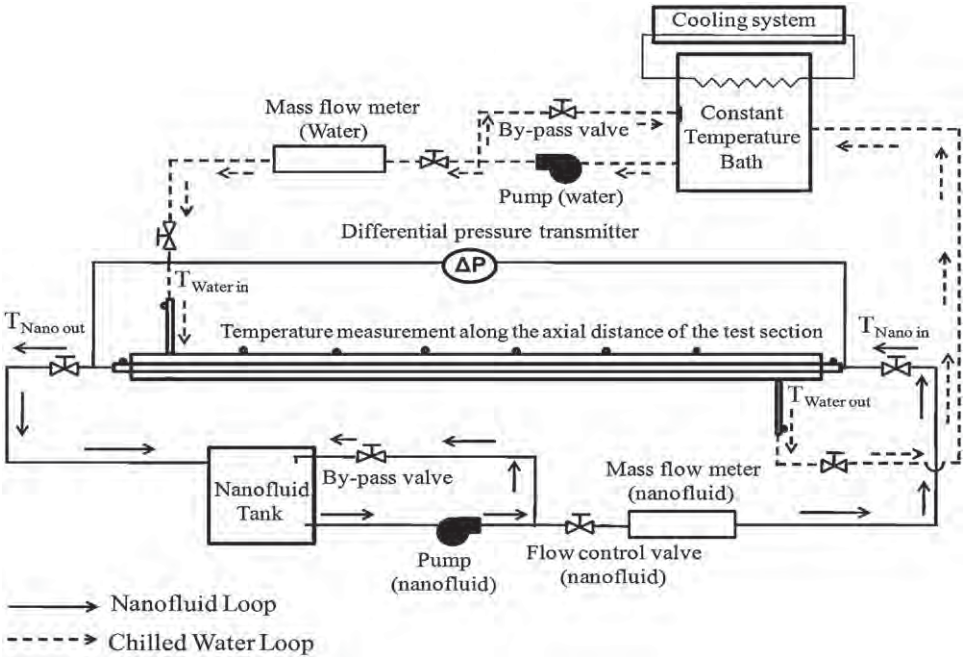

Fig. 2. Schematic diagram of the experimental apparatus.

Table 1
Experimental conditions.

D (mm)	Re	T_{nano} (°C)	T_{water} (°C)	m_{water} (kg/s)
4.3	900–12,000	48, 57, 65	26, 30, 35	0.016

(1988). The uncertainty of the heat transfer coefficient was found to be 4.44%. During a test run, the inlet and exit temperatures of the chilled water and nanofluids, and temperatures of the wall of the test tubes, mass flow rates of the chilled water and nanofluid, and the pressure difference in the nanofluid are measured. Table 1 lists the experimental conditions used in this study.

2.4. Data reduction

The heat transfer rate from the hot fluid is defined as:

$$Q_{h_{nf}} = m_{h_{nf}} C_{P_{h_{nf}}} (T_{in_{nf}} - T_{out_{nf}}), \tag{1}$$

$$\frac{1}{U_i A_i} = \frac{1}{h_i A_i} + \frac{\ln\,(d_o/d_i)}{2\pi k L} + \frac{1}{h_o A_o}, \tag{2}$$

$$Nu_{nf} = \frac{h_{nf} D}{k_{nf}}, \tag{3}$$

where $Q_{h_{nf}}$ is the heat transfer rate of the hot nanofluid, $m_{h_{nf}}$ is the mass flow rate of the hot nanofluid, $h_i = h_{nf}$ is the heat transfer coefficient of the nanofluid, h_o the heat transfer coefficient of chilled water in the annulus, k is the thermal conductivity of the copper tube, U_i is the overall heat transfer coefficient of the inner tube, Nu_{nf} is the Nusselt number of the nanofluid, D is the inner diameter of the test tube and k_{nf} is the thermal conductivity of the nanofluid.

The thermo-physical properties such as density, specific heat, thermal conductivity and viscosity of the nanofluid are calculated using the following published correlations.

Density is calculated from Pak and Cho (1998) using the following equation:

$$\rho_{nf} = \varphi\rho_p + (1-\varphi)\rho_w. \tag{4}$$

Specific heat is calculated from Xuan and Roetzel (2000) as follows:

$$(\rho C_p)_{nf} = \varphi(\rho C_p)_p + (1-\varphi)(\rho C_p)_w, \tag{5}$$

Where $(\rho C_p)_{nf}$ is the heat capacity of the nanofluid, $(\rho C_p)_p$ the heat capacity of the nanoparticles and $(\rho C_p)_w$ the heat capacity of the base fluid.

The thermal conductivity and viscosity of the nanofluid are calculated by correlations developed elsewhere by the present authors (Godson et al., 2010), both correlated as linear and quadratic functions of particle volume fraction. And the coefficients of silver–water nanofluid for the tested volume concentration and temperature are achieved using linear regression as shown below for water and nanofluid at their average bulk temperature:

$$\frac{k_{nf}}{k_w} = (0.9692\varphi + 0.9508), \tag{6}$$

$$\frac{\mu_{nf}}{\mu_w} = (1.005 + 0.497\varphi - 0.1149\varphi^2). \tag{7}$$

3. Correlation

The heat transfer coefficient, Nusselt number, of the nanofluid depends on various factors such as thermal conductivity, heat capacity of both the base fluid and the nanoparticles, viscosity of the nanofluid, volume fraction of the suspended particles, and dimension and shape of the particles, and can be expressed as follows:

$$Nu_{nf} = f\left(Re,\ Pr,\ \frac{k_{nf}}{k_w} \times \frac{(\rho C_p)_{nf}}{(\rho C_p)_w},\ \varphi,\ \text{dimension and shape of particles}\right).$$

In the present study, an additive method is used for developing a correlation to predict the Nusselt number with closest fit to

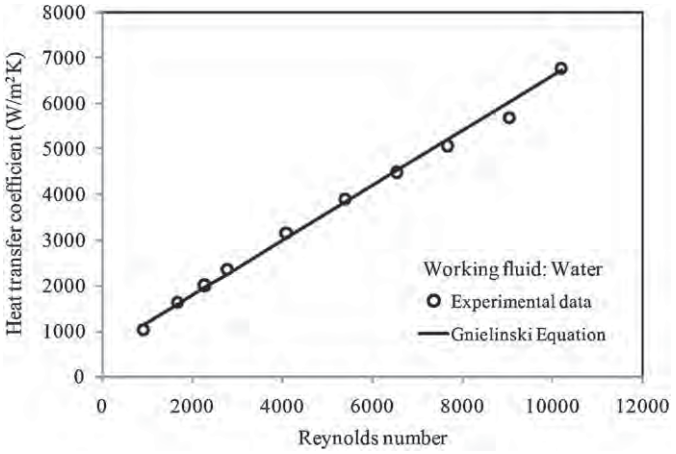

Fig. 3. Comparison between measured heat transfer coefficients and those calculated from Gnielinski (1976) equation.

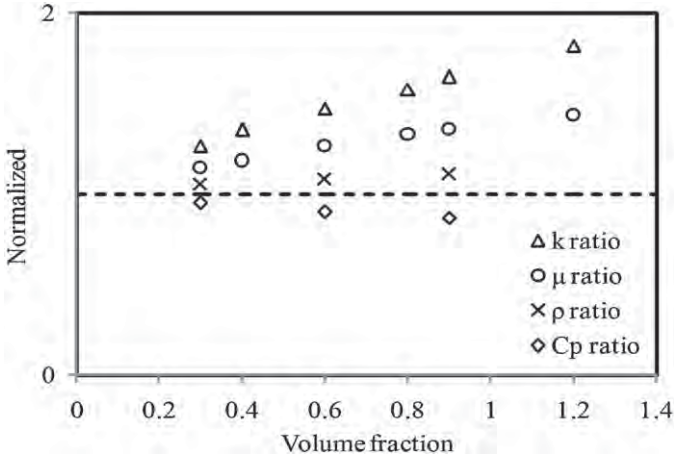

Fig. 4. Thermo-physical property ratios against silver nanoparticle volume fraction.

experimental data for silver–water nanofluid. The present correlation includes the effect of Reynolds number, Prandtl number, volume concentration and the temperature-dependent thermo-physical properties of silver–water nanofluid. The experimental data are correlated against Reynolds and Prandtl numbers ($Nu = C\ Re^a\ Pr^b$), in a manner resembling that of Pak and Cho (1998) and of Maiga et al. (2006). Such technique is used for the entire database for experimental values for Ag concentrations of 0.3%, 0.6% and 0.9%. The coefficient C and exponents a and b are calculated using multiple regression techniques. The difference between the nanofluid experimental Nusselt numbers and the single phase Nusselt number calculated using Dittus and Boelter (1930) correlation is then used to develop the new correlation. The current experiments showed that the Nusselt number of the nanofluid under test conditions is always higher than that for the single-phase base fluid. The difference in Nusselt numbers is thus once again correlated against Reynolds and Prandtl number ($Nu = C\ Re^a\ Pr^b$) and the coefficient C and exponents a and b are calculated using multiple regression. Hence, a generalized correlation is developed, where the constant and exponents of the correlation are functions of volume concentration in percentage. The coefficient of determination, R^2, is used in the context of correlation models with the main purpose of predicting Nusselt number on the basis of other related information. It is the proportion of variability in a data set that is accounted for by the statistical model, and provides a measure of how well outcomes are likely to be predicted by the model. The value of the coefficient of determination for all the correlations was above 0.98, thus testifying to the credibility of the correlation. The following is the correlation developed using the experimental data after careful removal of outliers from the database. Detailed comparisons of the predicted correlation with those from existing correlations and experimental results are discussed in the following sections. $Nu_{nf} = 0.023\,Re^{0.8}\ Pr^{0.3} + (0.617\ \varphi - 0.135)Re^{(0.445\varphi - 0.37)}Pr^{(1.081\varphi - 1.305)}$

4. Results and discussion

Experiments were carried out for the conditions given in Table 1. The effect of thermo-physical properties, mass flow rate, heat flux and concentration on the heat transfer coefficient to develop a new correlation are discussed in the following subsections. The experimental results for water are compared with those obtained from the Gnielinski (1976) equation as shown in Fig. 3, showing agreement within ±4.5%, thus validating the test facility for its repeatability and accuracy.

4.1. Dependence of thermo-physical properties on volume fraction of nanoparticles

Dependence of the thermo-physical property ratios on volume fraction of silver nanoparticles is shown in Fig. 4. All the observed values of the thermo-physical property data are normalized. It can be seen that the dependence of thermal conductivity k ratio on volume fraction of silver nanoparticles is significantly higher than the other thermo-physical properties such as ratios of density, viscosity and heat capacity. For 0.3% volume concentration, the thermal conductivity ratio is 1.27. Similarly for the same concentration the ratios for density, viscosity and heat capacity are 1.05, 1.14 and 0.95, respectively. Likewise, the thermal conductivity ratio enhancement increases to 1.64 for 0.9% volume concentration, whereas the ratio enhancement for density, viscosity and heat capacity are 1.1, 1.36 and 0.87, respectively, much lower than that for the thermal conductivity ratio. Evidently, the influence on thermal conductivity plays a major role in heat transfer enhancement. Both Brownian diffusion and thermophoresis are found to be the potential mechanisms for enhancement of thermal conductivity in the absence of turbulent eddies, that is, these mechanisms are responsible for an increase in temperature which leads to the enhancement in convective heat transfer coefficient at higher Reynolds number as well as with higher volume concentration of the nanoparticles (Xuan & Roetzel, 2000).

4.2. Effects of Reynolds number, Nusselt number and silver nanoparticle volume fraction on heat transfer coefficient

Fig. 5 shows increases of average heat transfer coefficients of nanofluids with Reynolds number and volume concentration, for example, as much as 28.3%, 47.6% and 69.3% for 0.3%, 0.6% and 0.9% volume concentration respectively at Reynolds number of 11,000. Similar enhancement has been observed by Xuan and Li (2004) who investigated convective heat transfer characteristics of copper–water nanofluid finding that the Nusselt number of the nanofluid with $\varphi = 1.5\%$ increased by 60% as compared to pure water. A possible reason for this enhancement is the enhancement of thermal conductivity by the chaotic movement of the nanoparticles, as reported by Xuan and Roetzel (2000). Fig. 6 shows the variation of the average Nusselt number with Reynolds number and volume concentration of nanoparticles, e.g., an increase by 47%

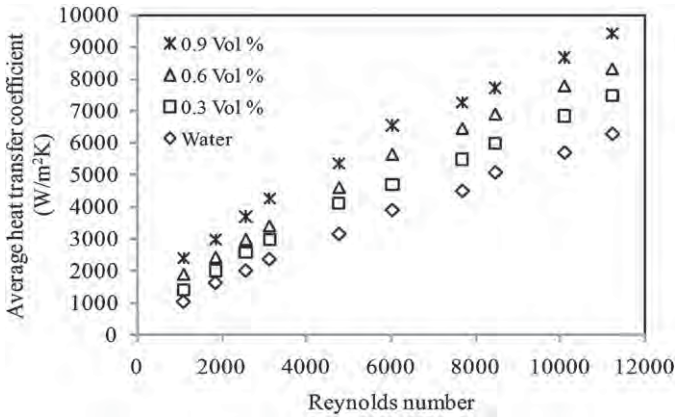

Fig. 5. Variation of the average heat transfer coefficient against Reynolds number.

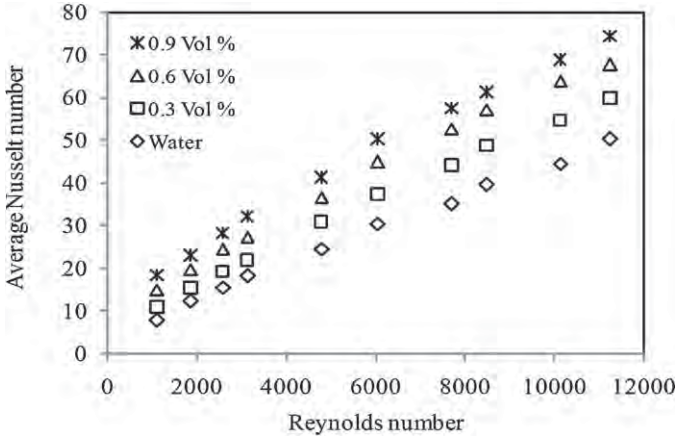

Fig. 6. Variation of the average Nusselt number against Reynolds number.

in the turbulent region, by 33% in the transition region and by 25% in the laminar region, even for the small volume concentration of 0.6% of silver nanoparticles.

Fig. 7 shows the significant variation of heat transfer coefficient with volume fraction for Reynolds numbers of 1800, 4600 and 9500, corresponding to a flow regime transition from laminar through transition to turbulent. Also, for a given Reynolds number, heat transfer coefficient clearly augments with increasing particle loading, e.g. for laminar flow condition with $Re = 1800$, the heat

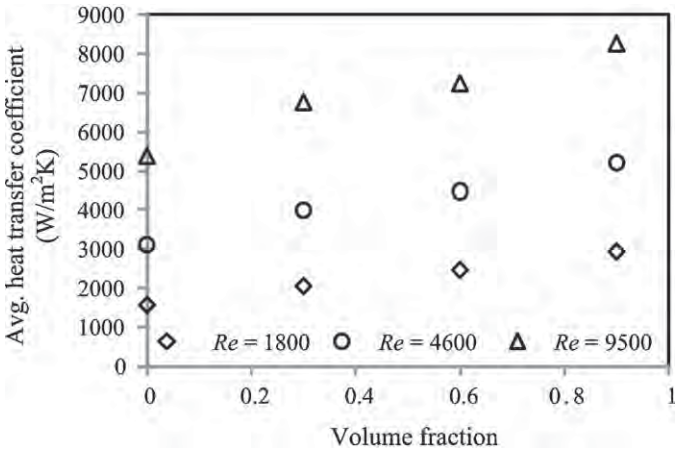

Fig. 7. Variation of heat transfer coefficient against volume fraction.

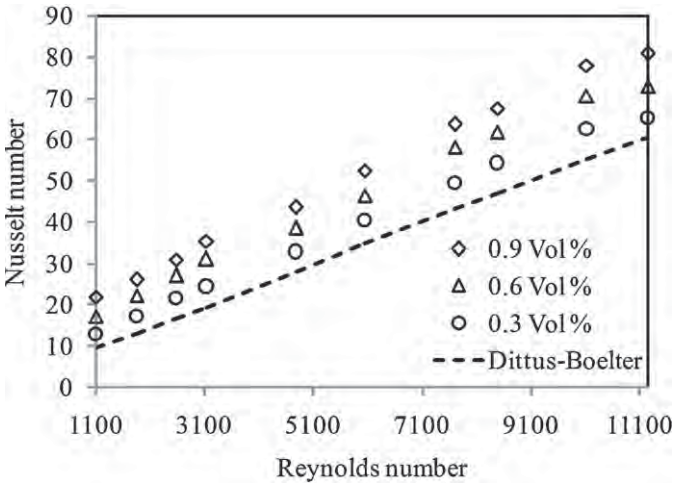

Fig. 8. Comparison between experimental Nusselt number and Dittus–Boelter correlation against Reynolds number.

transfer coefficient increases from 1560 W/(m^2 K) at 0% nanoparticles to 2930 W/(m^2 K) at 0.9%. Combination of particle loading and Reynolds number can produce rather high wall heat transfer rate, a conclusion very useful for advanced and special thermal applications.

4.3. Correlation results

Fig. 8 compares experimental Nusselt number for nanofluid with the Dittus and Boelter (1930) correlation for a single phase fluid (i.e. 0% volume concentration) against Reynolds number, showing how the Nusselt number increases with increasing nanoparticle concentration. For 0.9% volume concentration of nanoparticles, an average increase of 50.5% is observed for Nusselt number with respect to the pure fluid. The observed experimental results for Nusselt number are compared with those obtained by Dittus and Boelter (1930), Pak and Cho (1998), Gnielinski (1976), Xuan and Li (2003) as shown in Fig. 9.

A comparison of the experimental Nusselt number with that predicted from the familiar existing correlations for nanofluids such as Pak and Cho (1998) and Maiga et al. (2006), respectively, are shown in Fig. 10(a) and (b). It is clearly observed that the Pak and Cho (1998) correlation under predicts the experimental data

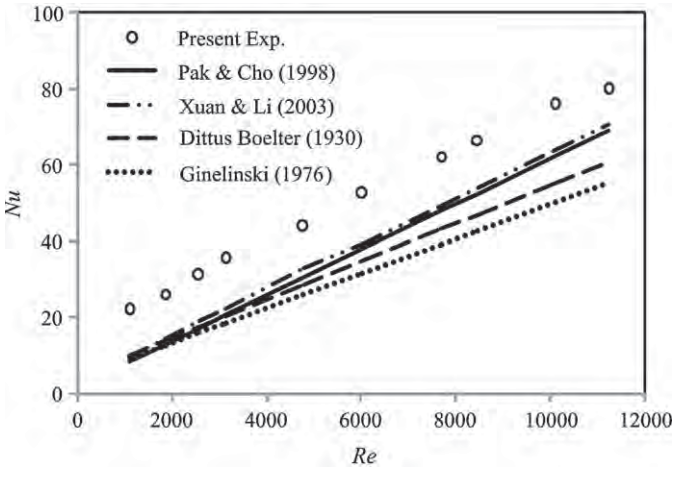

Fig. 9. Comparison of experimental and theoretical Nusselt number obtained from various correlations.

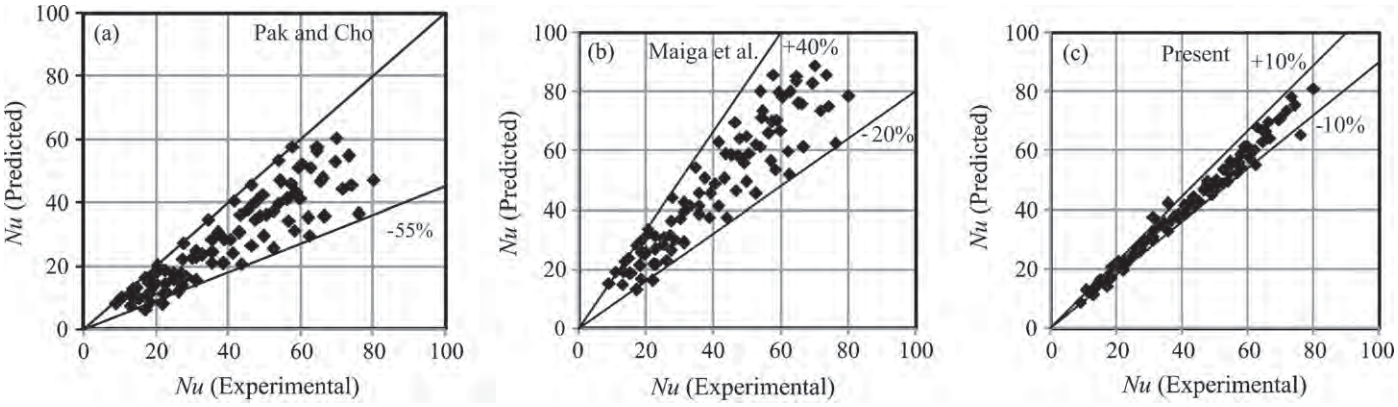

Fig. 10. Mean deviation between predicted Nusselt number (a) by Pak and Cho (1998) correlation, (b) by Maiga et al. (2006) correlation, and (c) by the proposed correlation, with experimental Nusselt number.

by 50%. Likewise, Maiga et al. (2006) correlation predicts fairly well with present experimental data of silver–water nanofluid, and the deviation of the predicted data and the experimental ones lies between +40% and −20%. In both case, the prediction accuracy of the correlation is poor as the volume concentration increases. However, the latter predicts better than the former. The distribution of the percentage deviation of the new correlation between the predicted and the experimental Nusselt number for the entire database is shown in Fig. 10(c). This new correlation is generalized for all the volume concentration. The date from the new correlation predicts the Nusselt number reasonably well within ±10% deviation. This correlation can be used for predicting the Nusselt number for the following ranges of the parameters: Reynolds number from 800 to 12,000; Prandtl number from 4 to 10 and volume concentration from 0 to 2%.

5. Conclusions

The convective heat transfer coefficient of silver–water nanofluids was investigated experimentally in a 4.3 mm inside diameter tube. Experimental results show that the suspended nanoparticles remarkably increase the heat transfer performance of the base fluid, water, under the same Reynolds number. The addition of 0.9 vol% silver particles in water enhances the heat transfer coefficients by 69.3%. Considering the factors affecting convective heat transfer characteristics of nanofluids, such as flow velocity, transport properties, volume fraction of nanoparticles, a new convective heat transfer correlation for nanofluids suspending metal nanoparticles has been developed. Comparison between experimental data and calculated results indicates that the correlation could take into account the main factors that affect heat transfer of the nanofluid and could be used to predict heat transfer coefficient of nanofluids with ±10% deviation.

Acknowledgements

The fourth author wishes to express his indebtedness to King Mongkut's University of Technology Thonburi, the Thailand Research Fund, the Office of the Higher Education Commission and the National Research University Project for supporting his study.

References

Ding, Y., Alias, G., Wen, D. & Williams, R. A. (2006). Heat transfer of aqueous suspensions of carbon nanotubes (CNT nanofluids). *International Journal of Heat and Mass Transfer*, *49*, 240–250.

Dittus, F. W. & Boelter, L. M. K. (1930). *Heat transfer in automobile radiators of the tubular type* Berkeley: University of California Publications in Engineering., pp. 443–461.

Eastman, J. A., Choi, S. U. S., Li, S., Yu, W. & Thompson, L. J. (2001). Anomalously increased effective thermal conductivities of ethylene glycol-based nanofluids containing copper nanoparticles. *Applied Physics Letters*, *78*, 718–720.

Eastman, J. A., Phillpot, S. R., Choi, S. U. S. & Keblinski, P. K. (2004). Thermal transport in nanofluids. *Annual Review of Materials Research*, *34*, 219–246.

Faulkner, D. J., Rector, D. R., Davison, J. J. & Shekarriz, R. (2004). Enhanced heat transfer through the use of nanofluids in forced convection. In *Proceedings of the ASME International Mechanical Engineering Congress and Exposition (IMECE '04)* Anaheim, USA, (pp. 219–224).

Gnielinski, V. (1976). New equations for heat and mass transfer in turbulent pipe and channel flow. *International Chemical Engineering*, *16*, 359–368.

Godson, L., Raja, B., Mohan Lal, D. & Wongwises, S. (2010). Experimental investigation on the thermal conductivity and viscosity of silver-deionized water nanofluid. *Experimental Heat Transfer*, *23*(4), 317–332.

Li, Q., Xuan, Y., Jiang, J. & Xu, J. W. (2005). Experimental investigation on flow and convective heat transfer feature of a nanofluid for aerospace thermal management. *Journal of Astronautics*, *26*, 391–394 (in Chinese).

Maiga, S. B., Nguyen, C. T., Galanis, N., Roy, G., Mare, T. & Coqueux, M. (2006). Heat transfer enhancement in turbulent tube flow using Al_2O_3 nanoparticle suspension. *International Journal of Numerical Methods for Heat and Fluid Flow*, *16*, 275–292.

Moffat, R. J. (1988). Describing the uncertainties in experimental results. *Experimental Thermal and Fluid Science*, *1*, 3–17.

Pak, B. C. & Cho, Y. I. (1998). Hydrodynamic and heat transfer study of dispersed fluids with sub-micron metallic oxide particles. *Experimental Heat Transfer*, *11*, 151–170.

Xuan, Y. & Li, Q. (2003). Investigation on convective heat transfer and flow features of nanofluids. *ASME Journal of Heat Transfer*, *125*, 151–155.

Xuan, Y. & Li, Q. (2004). Flow and heat transfer performances of nanofluids inside small hydraulic diameter flat tube. *Journal of Engineering Thermophysics*, *25*, 305–307.

Xuan, Y. & Roetzel, W. (2000). Conceptions for heat transfer correlation of nanofluids. *International Journal of Heat and Mass Transfer*, *43*, 3701–3707.

Yang, Y., Zhang, Z. G., Grulke, E. A., Anderson, W. B. & Wu, G. (2005). Heat transfer properties of nanoparticle-in-fluid dispersions (nanofluids) in laminar flow. *International Journal of Heat and Mass Transfer*, *48*, 1107–1116.

Zhou, D. W. (2004). Heat transfer enhancement of copper nanofluid with acoustic cavitation. *International Journal of Heat and Mass Transfer*, *47*, 3109–3117.

International Communications in Heat and Mass Transfer 38 (2011) 1406–1413

Contents lists available at SciVerse ScienceDirect

International Communications in Heat and Mass Transfer

journal homepage: www.elsevier.com/locate/ichmt

Correlations for evaporation heat transfer coefficient and two-phase friction factor for R-134a flowing through horizontal corrugated tubes ☆

Suriyan Laohalertdecha [a,b], Ahmet Selim Dalkilic [c], Somchai Wongwises [b,d,*]

[a] The Joint Graduate School of Energy and Environment (JGSEE), King Mongkut's University of Technology Thonburi, Bangmod, Bangkok 10140, Thailand
[b] Fluid Mechanics, Thermal Engineering and Multiphase Flow Research Lab. (FUTURE), Department of Mechanical Engineering, King Mongkut's University of Technology Thonburi, Bangmod, Bangkok 10140, Thailand
[c] Heat and Thermodynamics Division, Department of Mechanical Engineering, Yildiz Technical University (YTU), Yildiz, Besiktas, Istanbul 34349, Turkey
[d] The Academy of Science, The Royal Institute of Thailand, Sanam Suea Pa, Dusit, Bangkok 10300, Thailand

ARTICLE INFO

Available online 27 August 2011

Keywords:
Two-phase friction factor
Heat transfer
Temperature
R-134a
Corrugated tube

ABSTRACT

Correlations for the evaporation heat transfer coefficient and two-phase friction factor of R-134a flowing through horizontal corrugated tubes are proposed. In the present study, the test section is a horizontal counter-flow concentric tube-in-tube heat exchanger with R-134a flowing in the inner tube and hot water flowing in the annulus. Smooth tube and corrugated tubes with inner diameters of 8.7 mm and lengths of 2000 mm are used as the inner tube. The corrugation pitches are 5.08, 6.35, and 8.46 mm and the corrugation depths are 1, 1.25, and 1.5 mm, respectively. The outer tube is made from smooth copper tube with an inner diameter of 21.2 mm. The correlations presented are formed by using approximately 200 data points for five different corrugated tube geometries and are then proposed in terms of Nusselt number, equivalent Reynolds number, Prandtl number, corrugation pitch and depth, and inside diameter.

1. Introduction

Heat transfer enhancement techniques can produce superior heat exchanger performance. One such technique is the use of corrugated tube instead of smooth tube. Corrugated tubes can enhance the heat transfer coefficient on both the outer and inner heat transfer surface area without a significant increase in pressure drop. Typically, corrugated tubes can improve the heat transfer performance of the heat exchanger by increasing fluid mixing, unsteadiness, turbulence flow or by limiting the growth of fluid boundary layers close to the heat transfer surface. Corrugated tubes are sometimes chosen for the design of industrial shell-and-tube heat exchangers in order to reduce the size of the heat exchangers. However, use of corrugated tubes to replace conventional smooth tubes has only been reported over the past two decades. It is still a new method for improving the heat transfer performance of heat transfer equipment. So far, the heat transfer and flow characteristics of corrugated tube have been reviewed as described in the following subsections and in Table 1.

Nozu et al. [1,2] investigated local heat transfer and pressure gradients of pure R-114, R-113 and a zeotropic refrigerant mixture during condensation in the annulus of a double-tube coil consisting of three U-bends and four straight lengths. A corrugated copper tube with an ID of 17.2 mm was used as the test section. Mass fluxes were tested in the range of 80 to 240 kg/sm^2. The results showed that the local heat transfer coefficient decreased along the tube length and that the U-bends showed higher heat transfer coefficients than straight lengths.

Dong et al. [3] experimentally determined the turbulent friction and heat transfer characteristics for four spirally corrugated tubes with various geometrical parameters. Water and oil were used as the working fluid. The experimental conditions were tested at Reynolds numbers ranging between 6000 and 93,000 for water, and from 3200 to 19,000 for oil. Compared with a smooth tube, their results showed that the heat transfer coefficient enhancement varied from 30% to 120%, while the friction factor increased from 60% to 160%.

Barba et al. [4] experimentally studied single-phase heat transfer and flow behaviour of corrugated tube used in the chemical and food industry. The tested conditions were done at moderate Reynolds numbers ranging from 100 to 800. In this study, ethylene glycol was used as the working fluid. The results offered a heat transfer enhancement ranging from 4.27 to 16.79, while the friction factor increased by up to 1.83–2.45 times compared to the smooth tube. Based on the experimental data, Nusselt number and friction factor correlations were proposed.

Rainieri and Pagliarini [5] experimentally investigated the thermal performance of corrugated tubes. Helical and transverse corrugated tubes with different pitches were used as the test section. Ethylene glycol was employed as the working fluid. The experimental conditions were conducted at Reynolds numbers ranging from 90 to 800.

☆ Communicated by W.J. Minkowycz.

* Corresponding author at: Fluid Mechanics, Thermal Engineering and Multiphase Flow Research Lab. (FUTURE), Department of Mechanical Engineering, King Mongkut's University of Technology Thonburi, Bangmod, Bangkok 10140, Thailand. Tel.: +66 2 470 9115; fax: +66 2 470 9111.
E-mail address: somchai.won@kmutt.ac.th (S. Wongwises).

0735-1933/$ – see front matter © 2011 Elsevier Ltd. All rights reserved.
doi:10.1016/j.icheatmasstransfer.2011.08.014

Nomenclature

A	surface area of the test section (m^2)
c_p	specific heat at constant pressure (J/kg K)
d	inner diameter (m)
D	outer diameter (m)
e	corrugation depth (mm)
f	friction factor
G	mass flux (kg/m^2 s)
h	heat transfer coefficient (W/m^2 K)
i	enthalpy (J/kg)
i_f	enthalpy of the saturated liquid (J/kg)
i_{fg}	enthalpy of the vaporisation (J/kg)
k	thermal conductivity (W/m K)
L	length of test section (m)
$LMTD$	logarithmic mean temperature difference
m	mass flow rate (kg/s)
Nu	Nusselt number
p	corrugation pitch (mm)
Pr	Prandtl number
ΔP	pressure drop (Pa/m)
Q	heat transfer rate (W)
Re	Reynolds number
q''	heat flux (W/m^2)
T	temperature (°C)
U	overall heat transfer coefficient (W/m^2 K)
w	corrugation wide (mm)
x	average vapour quality

Greek letters

α	void fraction
β	helix angle (degree)
ρ	density (kg/m^3)
u	dynamic viscosity (Pa.s)

Subscripts

a	acceleration
avg	average
c	corrugated tube
eq	equivalent
f	friction
g	gravitation
in	inlet
i	inside
l	liquid
out	outlet
o	outside
ph	pre-heater
ref	refrigerant
s	smooth tube
sat	saturation
tp	two-phase
TS	test section
v	vapour
w	water

As a comparison of helical corrugated tubes, transverse corrugated tubes and a smooth tube, the results demonstrated that the transverse corrugated tubes showed greater heat transfer enhancement than the helical corrugated and smooth tubes.

Among all of these previous studies, the most productive studies have been performed by Zimparov [6]. The heat transfer enhancement of a combination of three-start spirally corrugated tubes with a twisted tape was investigated. Two three-start spirally corrugated tubes combined with five twisted tape inserts with different relative pitches were employed as the test section. The experimental conditions were conducted at Reynolds number ranging from 3000 to 60,000. The height to diameter ratio (e/d_i) and relative pitch (p/d_i) parameters were 0.0407, 0.0569 and 15.3, 12.2, 7.7, 5.8, 4.7, respectively.

Zimparov [7] presented the heat transfer enhancement using a combination of single-start spirally corrugated tubes with a twisted tape. The friction factors and heat transfer coefficients obtained from these tubes were higher than those of the smooth tube under the same conditions. In addition, Zimparov [8,9] applied a simple mathematical model to predict the friction factor and heat transfer coefficient for a spirally corrugated configuration combined with twisted tape inserts flowing in a turbulent flow regime. The friction factors and heat transfer coefficients calculated were compared with the experimental data. The results showed good agreement between the predicted and experimental data.

Vicente et al. [10,11] presented measurements of mixed convection heat transfer and isothermal pressure drop in corrugated tubes for laminar, transition and turbulent flow regions. Water and ethylene glycol were used as the working fluids. Their results indicated that the corrugated tubes gave a higher pressure drop and heat transfer coefficient than the smooth tube under given conditions. Moreover, the pressure drop obtained from laminar flow to transition flow and from transition flow to turbulent flow increased by up to 25% and 300%, respectively. Similarly, the Nusselt number obtained from laminar flow to transition flow and transition flow to turbulent flow increased by up to 30% and 250%, respectively.

Targanski and Cieslinski [12] experimentally studied the heat transfer coefficient and pressure drop of pure R-407C and R-407C/oil mixtures during evaporation inside a smooth stainless steel tube, smooth copper tubes and two enhanced tubes. The inlet and exit vapour quality were controlled at 0 and 0.7, respectively, the mass flow varied from 250 to 500 kg/m^2.s, and the average saturation temperature was controlled at 0 °C. It was found that the heat transfer coefficient and pressure drop for the enhanced tubes were distinctly higher than those of the smooth tube. The maximum enhancement factor and penalty factor for corrugated tube were 1.25 and 1.8, respectively.

Laohalertdecha and Wongwises [13,14] experimentally investigated the effect of pitch on the heat transfer coefficient and pressure drop of R-134a flowing in corrugated tubes during condensation and evaporation conditions. The results demonstrated that the heat transfer coefficient and pressure drop obtained from corrugated tube are higher than those of the smooth tube for all experimental conditions. Moreover, the results also showed that the corrugation surface significantly promotes turbulent flow. However, the effect of pitch on the heat transfer coefficient absolutely has significance at high average quality. On the other hand, the effect of pitch on the pressure drop was insignificant.

In 2011, Laohalertdecha and Wongwises [15] continuously studied the condensation heat transfer and flow characteristics of R-134a flowing through corrugated tubes. The test section was a horizontal counter-flow concentric tube-in-tube heat exchanger, 2000 mm in length. A smooth copper tube and corrugated copper tubes with inner diameters of 8.7 mm were used as the inner tube. The outer tube was made from smooth copper tube with an inner diameter of 21.2 mm. The corrugation pitches used in this study were 5.08, 6.35, and 8.46 mm. Similarly, the corrugation depths were 1, 1.25, and 1.5 mm, respectively. The results found that the Nusselt number and two-phase friction factor obtained from the corrugated tubes were significantly higher than those obtained from the smooth tube. Moreover, new correlations were proposed for predicting the Nusselt number and two-phase friction factor of the corrugated tubes.

Table 1
Experimental investigations on the corrugated tube.

Sources	d_i (mm)	e/d_i	p/d_i	β (deg)	Phase
Nozu et al. [1,2]	17.2	0.0174	0.407	–	Two-phase (Condensation)
Dong et al. [3]	16.04–22.82	0.0243–0.0398	0.438–0.623	78.8–82.1	Single phase
Barba et al. [4]	14.5	0.103	0.793	45	Single phase
Rainieri and Pagliarini [5]	14	0.107	1.143–4.571	–	Single phase
Zimparov [6]	13.68–13.73	0.0407–0.0569	4.7–15.3	67.4–68	Single phase
Zimparov [7]	13.39–13.65	0.0371–0.0441	2.4–7.7	79.3–82.2	Single phase
Zimparov [8,9]	12.44–13.90	0.0224–0.0569	7.45–21.17	67.4–90	Single phase
Vicente et al. [10,11]	18	0.0239–0.0572	0.608–1.229	68–80	Single phase
Targanski and Cieslinski [12]	8.8	0.0511	0.681	77.75	Two phase (Evaporation)
Laohalertdecha and Wongwises [13]	8.7	0.1724	0.584–0.9724	74.2–79.47	Two phase (Condensation)
Laohalertdecha and Wongwises [14]	8.7	0.1724	0.584–0.9724	74.2–79.47	Two phase (Evaporation)
Laohalertdecha and Wongwises [15]	8.7	0.115–0.1724	0.584–0.9724	74.2–79.47	Two phase (Condensation)

As described above, most of the papers to date examine single-phase heat transfer in corrugated tube. There are very few studies, however, dealing with heat transfer enhancement using a corrugated tube in two-phase flow. However, although some information is currently available on two-phase heat transfer enhancement by using corrugated tube, there are no suitable correlations including important relevant parameters yet available for heat transfer and pressure drop characteristics. In the present study, correlations for predicting the heat transfer coefficient and two-phase friction factor for R-134a flowing in horizontal corrugated tubes during the evaporation process, are presented. These correlations, which have never before appeared in open literature, include several important relevant parameters such as corrugation depth and corrugation pitch.

2. Experimental apparatus

A schematic diagram of the test apparatus is shown in Fig. 1. The experimental apparatus was designed to determine the heat transfer coefficient and pressure drop of pure R-134a over the length of the test tube. The test loop consists of a test section, refrigeration loop, cooling water flow loops, sub-cooling loop and relevant instrumentation. The objective of the water loop before the test section is to provide a controlled inlet vapour quality. The second water loop located in the test section provides a controlled heat output from the test section. The sub-cooling loop is used to prevent any two-phase flow condition of the refrigerant occurring before it enters the refrigerant pump.

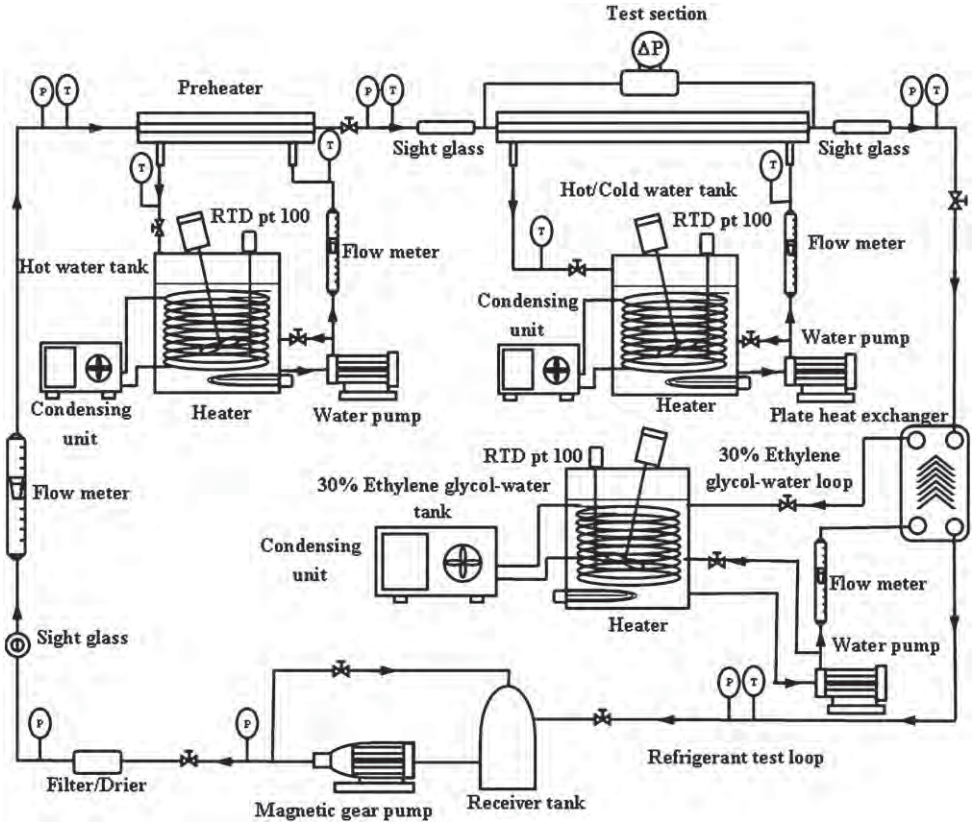

Fig. 1. Schematic diagram of the experimental apparatus.

For the refrigeration circulating loop, liquid refrigerant is discharged by a gear pump regulated by an inverter. The refrigerant passes in series through a filter/dryer, a sight glass tube, flow metre, pre-heater and enters the test section. The inlet vapour quality before entering the test section is controlled by the pre-heater. The pre-heater is a spiral counter flow heat exchanger that supplies energy to provide a controlled inlet vapour quality for vaporisation of the refrigerant. On leaving the test section, the refrigerant is then condensed and sub-cooled by a chilling loop that removes the heat input from the pre-heater and test section and then it returns from the two-phase refrigerant to a sub-cooled state, which later collects in a receiver and eventually returns to the refrigerant pump to complete the cycle.

The test section is a horizontal counter-flow double tube heat exchanger. The length of the heat exchanger is 2000 mm. The detailed dimensions of the heat exchanger and the location of the thermocouples are shown in Fig. 2. A photograph of a corrugated tube and nomenclature to describe the geometry is shown in Fig. 3. The dimensions of the test section are shown in Table 2.

The inlet temperature of the water is controlled by a thermostat. A differential pressure transducer and thermocouples are installed in the test section to measure the pressure drop and temperature across the test section. The length between pressure taps is 2500 mm. In the present study, the pressure of the refrigerant is mainly controlled by a high-pressure limit switch. High-pressure limit switches (Danfoss Type KP 5) are devices for regulating the pressure of a system so that the pressure is maintained near a desired set point pressure in order to prevent the damage to the apparatus.

The refrigerant temperature and tube wall temperature in the test section are measured by Type T thermocouples. A total of 15 thermocouples are soldered to the top, bottom and at five points along side of the tube as shown in Fig. 2. All the temperature measuring devices are well calibrated in a controlled temperature bath using standard precision mercury glass thermometers. The uncertainty of the temperature measurements as recorded by the data acquisition system is ±0.1 °C. All static pressure taps are mounted on the tube wall. The refrigerant flow metre is a variable area type and specially calibrated in the range 0.2–3.4 LPM for R-134a by the manufacturer. Also, the differential pressure transducer is calibrated by the manufacturer.

Experiments were conducted with various flow rates of refrigerant, vapour qualities of refrigerant entering the test section, heat flows and temperatures of refrigerant condensing in the test section. In the experiments, the refrigerant flow rate in the test section was controlled by adjusting the speed of the magnetic gear pump. To vary the vapour quality at the inlet of the test section, the heating water flow and the cooling water flow rates were varied by small increments while the refrigerant flow rate was kept constant. The hot water in the test section was re-circulated by a centrifugal pump to supply heat from the water to the refrigerant. During each experiment, the heat transferred from the test section was kept at a desired value. This might be obtained by simultaneously adjusting and controlling the temperature and flow rate of the hot water entering the test section. The system was allowed to approach a steady state before any data was recorded. After stabilisation, the temperature on the tube wall, the temperature of the refrigerant at the locations mentioned above, the inlet and outlet temperatures of the heating water and flow rates of heating water and refrigerant were all recorded. The pressure drop was measured by a differential pressure transducer installed between the inlet and outlet of the test section. The experiments could be carried out by increasing the refrigerant flow rate while the saturation temperature in the test section was kept constant. The accuracy of the direct measurements and the uncertainties in the derived experimental values are shown in Table 3.

3. Data reduction

The data reduction for calculating the two-phase heat transfer coefficient and pressure drop of R-134a flowing in horizontal smooth and corrugated tubes under evaporation conditions can be summarised as follows.

3.1. The inlet vapour quality of the test section ($x_{TS,in}$)

The inlet vapour quality entering the test section can be calculated as follows:

$$x_{TS,in} = \frac{i_{TS,in} - i_{f,T_{TS,in}}}{i_{fg,T_{TS,in}}} \tag{1}$$

where i_f is the enthalpy of the saturated liquid based on the temperature of the test section inlet, i_{fg} is the enthalpy of vaporisation based on the temperature of the test section inlet, $i_{TS,in}$ is the refrigerant enthalpy at the test section inlet and is given by:

$$i_{TS,in} = i_{ph,in} + \frac{Q_{ph}}{m_{ref}} \tag{2}$$

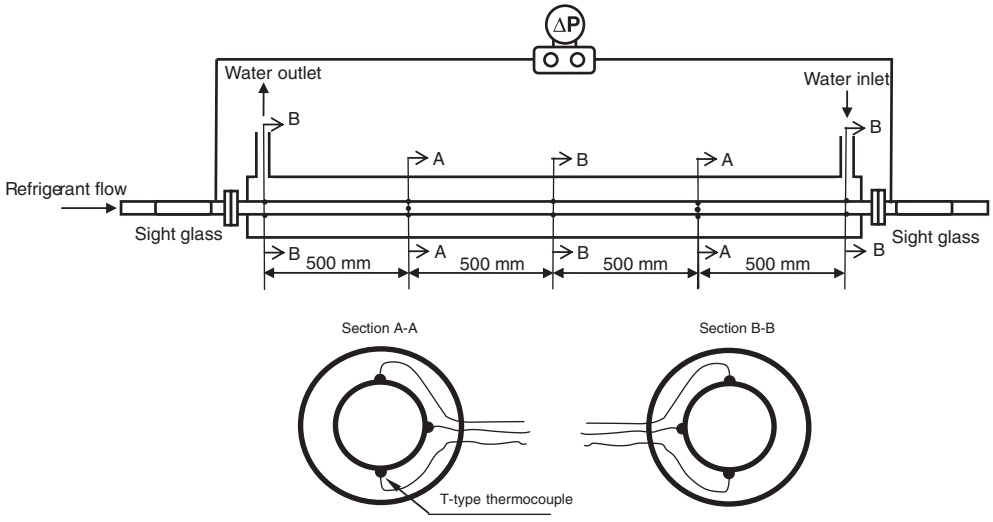

Fig. 2. Schematic diagram of the test section.

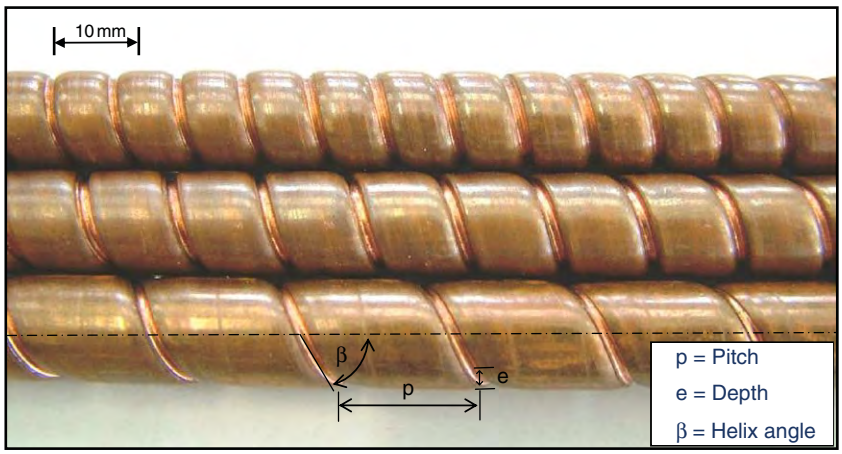

Fig. 3. Photograph of corrugated tubes.

where $i_{ph,in}$ is the inlet enthalpy of the liquid refrigerant before entering the pre-heater, m_{ref} is the mass flow rate of the refrigerant and Q_{ph} is the heat transfer rate in the pre-heater which is calculated by Eq. (3)

$$Q_{ph} = m_{w,ph} c_{p,w} \left(T_{w,in} - T_{w,out}\right)_{ph} \tag{3}$$

where $m_{w,ph}$ is the mass flow rate of water entering the pre-heater.

3.2. The outlet vapour quality of the test section ($x_{TS,out}$)

Similarly, Eq. (4) was used to calculate the exit vapour quality of the test section.

$$x_{TS,out} = \frac{i_{TS,out} - i_{f,T_{TS,out}}}{i_{fg,T_{TS,out}}} \tag{4}$$

where $i_{TS,out}$ is the refrigerant enthalpy at the test section outlet, i_f is the enthalpy of the saturated liquid based on the temperature of the test section outlet, and i_{fg} is the enthalpy of vaporisation. As a consequence, the outlet enthalpy of the refrigerant flow is calculated as:

$$i_{TS,out} = i_{TS,in} + \frac{Q_{TS}}{m_{ref}} \tag{5}$$

where the heat transfer rate in the test section is obtained from:

$$Q_{TS} = m_{w,TS} c_{p,w} \left(T_{w,in} - T_{w,out}\right)_{TS} \tag{6}$$

where $m_{w,\ TS}$ is the mass flow rate of the water entering the test section.

3.3. The inside heat transfer coefficient (h_i)

The inside heat transfer coefficient is calculated as follows:

$$h_i = \frac{1}{\left(\frac{1}{U_i}\right) - \left(\frac{1}{2k}\right) d_i \ln\left(\frac{d_o}{d_i}\right) - \left(\frac{d_i}{d_o}\right)\left(\frac{1}{h_o}\right)} \tag{7}$$

where U_i is the overall heat transfer coefficient based on inside surface area, k is the thermal conductivity of tube material and h_o is the outside heat transfer coefficient.

$$U_i = \frac{Q_{TS}}{A_i (LMTD)} \tag{8}$$

where A_i is the inside tube surface, $LMTD$ is the logarithmic mean temperature difference which is defined as follows:

$$LMTD = \frac{\Delta T_1 - \Delta T_2}{\ln\left(\frac{\Delta T_1}{\Delta T_2}\right)} \tag{9}$$

$$\Delta T_1 = T_{w,out} - T_{ref,in} \tag{10}$$

$$\Delta T_2 = T_{w,in} - T_{ref,out} \tag{11}$$

where $T_{w,in}$ and $T_{w,out}$ denote the inlet and outlet temperatures of the water on the annulus. $T_{ref,in}$ and $T_{ref,out}$ are the inlet and outlet refrigerant temperatures.

$$h_o A_o = \frac{Q_{TS}}{T_{w,avg} - T_{wall,avg}} \tag{12}$$

where Ao is the outside tube surface, $T_{wall,avg}$ is average wall temperature and $T_{w,avg}$ is average water temperature.

Table 2
The dimensions of the test section.

Number	p (mm)	e (mm)	w (mm)	β (degree)	d_i (mm)	L (mm)
1	5.08	1	1	79.47	8.7	2000
2	5.08	1.25	1	79.47	8.7	2000
3	5.08	1.5	1	79.47	8.7	2000
4	8.46	1.5	1	74.20	8.7	2000
5	6.35	1.5	1	76.56	8.7	2000
6	Smooth tube				8.7	2000

Table 3
Uncertainties of measured quantities and calculated parameters.

Parameter	Uncertainty
Temperature, T (°C)	±0.1
Pressure drop, ΔP (kPa)	±0.37
Mass flow rate of refrigerant, m_{ref}	±2%
Mass flow rate of water, m_w	±2%
Heat transfer rate at test section, Q_{TS}	±10%
Heat transfer rate at pre-heater, Q_{ph}	±5%
Evaporation heat transfer coefficient, h	±10%
Average vapour quality, x	±5%

The Nusselt number is determined as:

$$Nu = \frac{hd}{k_l} \tag{13}$$

where k_l is thermal conductivity of the liquid phase refrigerant.

3.4. The frictional pressure drop (ΔP_f)

The total pressure drop, ΔP_{total}, is expressed as the sum of the three different components, as follows:

$$\Delta P_{total} = \Delta P_f + \Delta P_a + \Delta P_g. \tag{14}$$

The three terms on the right-hand side represent the frictional pressure drop (ΔP_f), acceleration pressure drop (ΔP_a) and gravitational pressure drop (ΔP_g). The gravitational pressure drop (ΔP_g) is zero in a horizontal tube. The acceleration pressure drop, ΔP_a, is as proposed by Tran [16]:

$$\Delta P_a = G^2\left(\left(\frac{x^2{}_{out}}{\rho_v\alpha_{out}} + \frac{(1-x_{out})^2}{\rho_l(1-\alpha_{out})}\right) - \left(\frac{x^2{}_{in}}{\rho_v\alpha_{in}} + \frac{(1-x_{in})^2}{\rho_l(1-\alpha_{in})}\right)\right) \tag{15}$$

where α is the void fraction and presented by Zivi's correlation [17] as follows:

$$\alpha = \left(1 + \frac{(1-x)}{x}\left(\frac{\rho_v}{\rho_l}\right)^{\frac{2}{3}}\right)^{-1}. \tag{16}$$

The frictional pressure drop, ΔP_f, can be obtained by subtracting the acceleration pressure drop from the total measured pressure drop.

The two-phase friction factor is defined in terms of equivalent mass flux (G_{eq}) as proposed by Akers et al. [18] and shown in Eq. (17).

$$f_{tp} = \frac{d_i \Delta P_f \rho_l}{2G_{eq}^2} \tag{17}$$

$$G_{eq} = G\left[(1-x) + \left(\frac{\rho_l}{\rho_v}\right)^{0.5}\right] \tag{18}$$

3.5. Equivalent Reynolds number (Re_{eq})

The equivalent Reynolds number is defined as:

$$\mathrm{Re}_{eq} = \mathrm{Re}_l + \mathrm{Re}_v\left(\frac{\mu_v}{\mu_l}\right)\left(\frac{\rho_l}{\rho_v}\right)^{0.5} \tag{19}$$

where Re_l is the liquid Reynolds number defined as:

$$\mathrm{Re}_l = \frac{Gd_i(1-x)}{\mu_l} \tag{20}$$

where Re_v is the vapour Reynolds number defined as:

$$\mathrm{Re}_v = \frac{Gd_i x}{\mu_v} \tag{21}$$

4. Results and discussion

In this study, correlations for evaporation heat transfer coefficient and two-phase friction factor of R-134a flowing through horizontal corrugated tubes are proposed as a function of Nusselt number, equivalent Reynolds number, Prandtl number, corrugation pitch and depth, and inside diameter. The corrugation pitches used in this study are 5.08, 6.35, and 8.46 mm. Similarly, the corrugation depths are 1, 1.25, and 1.5 mm, respectively. The database of the present correlation includes about 200 data points for five different corrugation geometries. The physical properties of the refrigerants are obtained from REFPROP, Version 6.01 [19]. The important results are presented as follows.

4.1. Comparison of experimental heat transfer coefficient and frictional pressure drop for smooth tube with exiting data

Comparison between the experimental data and the data of heat transfer coefficient obtained from Wongsa-ngam et al. [20], Silva Lima et al. [21] and Rossi et al. [22] are shown in Fig. 4a. Almost all the existing data yield relatively good agreement with the experimental data, except Rossi's data which produces a relatively high difference in heat transfer coefficient compared to the experimental data, especially at higher average vapour quality. This may be due to differences in the saturation temperature. Similarly, the frictional pressure drop data are compared with existing data obtained from Filho et al. [23] and Wellsandt and Vamling [24] as shown in Fig. 4b. In this figure, the frictional pressure drops of experimental data give good agreement with existing data.

4.2. Comparison of experimental Nusselt number with the proposed correlations

Fig. 5 shows a comparison of the experimental Nusselt number for the smooth tube and corrugated tube with the proposed correlations.

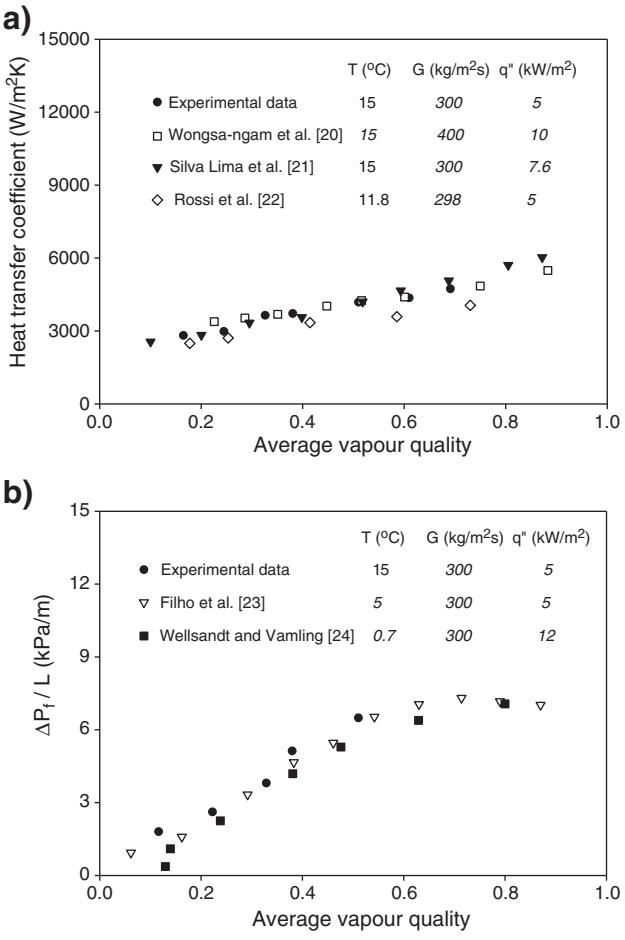

Fig. 4. Comparisons of experimental heat transfer coefficient and frictional pressure drop data for smooth tube with data obtained from literature.

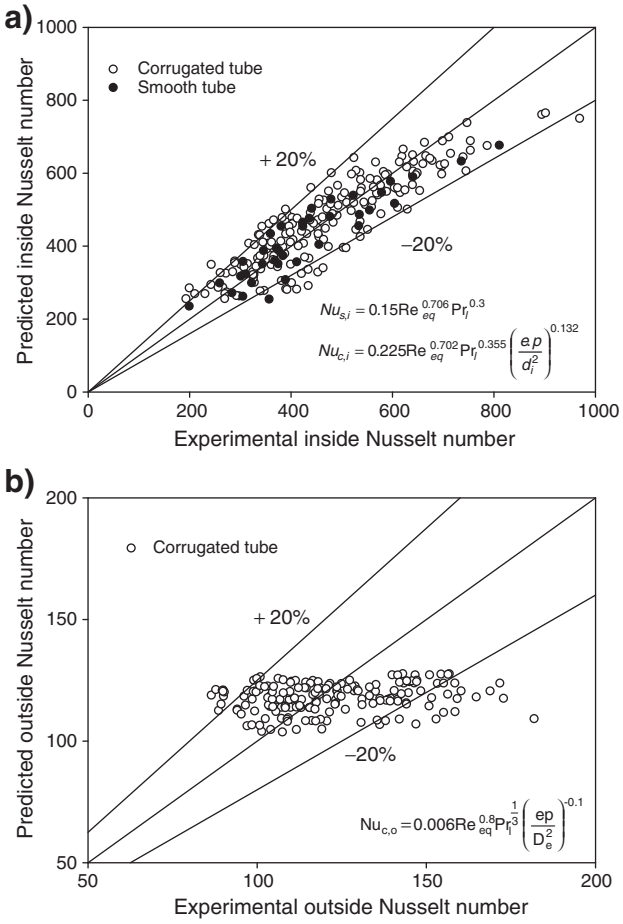

Fig. 5. Inside and outside Nusselt number obtained from the proposed correlations versus the experimental data.

The tests are performed at saturation temperatures of 10–20 °C, heat fluxes of 5–10 kW/m^2, mass fluxes of 300–500 kg/m^2.s, and equivalent Reynolds numbers of 20,000–90,000. The proposed correlations are established based on the Buckingham's Pi theorem and presented in terms of Nusselt number, equivalent Reynolds number, Prandtl number, corrugation pitch and depth, and inside diameter. The Nusselt number correlations for flow in smooth and corrugated tubes are expressed as follows:

- For smooth tube

$$Nu_{s,i} = 0.15\,\mathrm{Re}_{eq}^{0.706}\,\mathrm{Pr}_l^{0.3} \tag{22}$$

- For corrugated tube

$$Nu_{c,i} = 0.225\,\mathrm{Re}_{eq}^{0.702}\,\mathrm{Pr}_l^{0.355}\left(\frac{ep}{d_i^2}\right)^{0.132} \tag{23}$$

The inside Nusselt number is determined from

$$Nu_i = \frac{h_i d_i}{k_{l,ref}}. \tag{24}$$

Similarly, the Nusselt number correlation for flow outside the corrugated tubes is defined as follows:

$$Nu_{c,o} = 0.006\mathrm{Re}_{eq}^{0.8}\mathrm{Pr}_l^{\frac{1}{3}}\left(\frac{ep}{D_{eq}^2}\right)^{-0.1} \tag{25}$$

The outside Nusselt number is determined from

$$Nu_o = \frac{h_o D_{eq}}{k_w} \tag{26}$$

where D_{eq} is the equivalent diameter which is defined as follows:

$$D_{eq} = \frac{D_i^2 - d_o^2}{d_o}. \tag{27}$$

The inside Nusselt number correlations for smooth tube and corrugated tubes are displayed in Fig. 5a. The results show that approximately 90% of data fall within a deviation of ±20%. Equally, the outside Nusselt number correlation for corrugated tube is shown in Fig. 5b. The results show that approximately 85% of the data are correlated within a deviation of 20%.

4.3. Comparison of experimental frictional pressure drop with proposed correlations

The pressure drops are obtained by dividing the measured pressure drop by the length of the test section between pressure taps. In this study, the length between pressure taps is 2500 mm while the length of the heat exchanger is 2000 mm.

Fig. 6 shows the variation of the two-phase friction factor with equivalent Reynolds number for smooth tube and corrugated tubes. The result shows the two-phase friction factor obtained from corrugated tubes depends on the equivalent Reynolds number and tube geometry. Moreover, the result also shows that the two-phase friction factors obtained from smooth and corrugated tubes increase by decreasing the equivalent Reynolds number.

Similar to the Nusselt number, the proposed correlations are presented as function of equivalent Reynolds number, corrugation pitch and depth, and inside diameter. The proposed correlations are shown as follows:

- For smooth tube

$$f_{tp,s} = 13.64\mathrm{Re}_{eq}^{-0.625} \tag{28}$$

- For corrugated tube

$$f_{tp,c} = 33.368\mathrm{Re}_{eq}^{-0.68}\left(\frac{ep}{d_i^2}\right)^{0.1}. \tag{29}$$

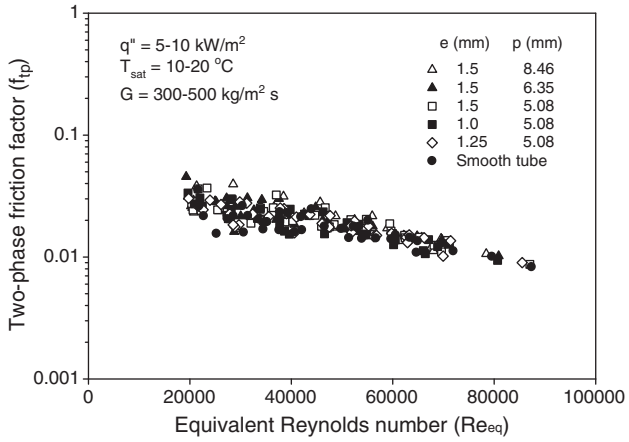

Fig. 6. Two-phase flow friction factor versus equivalent Reynolds number for smooth and corrugated tubes.

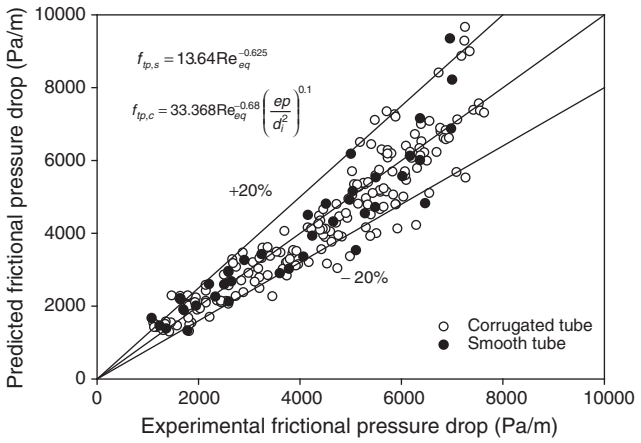

Fig. 7. Frictional pressure drop obtained from the proposed two-phase friction factor correlations versus the experimental data.

Fig. 7 illustrates a comparison of the experimental frictional pressure drop for the smooth tube and corrugated tubes with the proposed correlations. As illustrated in Fig. 7, the results show that approximately 95% of data fall within a deviation of ±20%.

5. Conclusion

Correlations for evaporation heat transfer coefficient and two-phase friction factor of R-134a flowing through horizontal corrugated tubes have been proposed. The test section is a horizontal counter-flow concentric tube-in-tube heat exchanger with R-134a flowing in the inner tube and hot water flowing in the annulus. The Buckingham's *Pi* theorem was used to analyse and form the correlations, and were then presented in terms of Nusselt number as a function of equivalent Reynolds number, Prandtl number, corrugation pitch and depth, and inside diameter. The results show that approximately 85–90% of Nusselt number data fall within a deviation of ±20%. Similarly, the two-phase friction factor results show that approximately 95% of data fall within a deviation of ±20%.

Acknowledgements

The present study was supported financially by the Thailand Research Fund, the Office of the Higher Education Commission and the National Research University Project, whose guidance and assistance are gratefully acknowledged.

References

[1] S. Nozu, H. Honda, H. Nakata, Condensation of refrigerants CFC11 and CFC113 in the annulus of a double-tube coil with an enhanced inner tube, Exp. Therm. Fluid Sci. 11 (1995) 40–51.
[2] S. Nozu, H. Honda, S. Nishida, Condensation of a zeotropic CFC 114–CFC 113 refrigerant mixture in the annulus of a double-tube coil with an enhanced inner tube, Exp. Therm. Fluid Sci. 11 (1995) 364–371.
[3] Y. Dong, L. Huixiong, C. Tingkuan, Pressure drop, heat transfer and performance of single-phase turbulent flow in spirally corrugated tubes, Exp. Therm. Fluid Sci. 24 (2001) 131–138.
[4] A. Barba, S. Rainieri, M. Spiga, Heat transfer enhancement in a corrugated tube, Int. Commun. Heat Mass Transfer 29 (2002) 313–322.
[5] S. Rainieri, G. Pagliarini, Convective heat transfer to temperature dependent property fluids in the entry region of corrugated tubes, Int. J. Heat Mass Transfer 45 (2002) 4525–4536.
[6] V. Zimparov, Enhancement of heat transfer by a combination of three-start spirally corrugated tubes with a twisted tape, Int. J. Heat Mass Transfer 44 (2001) 551–574.
[7] V. Zimparov, Enhancement of heat transfer by a combination of a single-start spirally corrugated tubes with a twisted tape, Exp. Therm. Fluid Sci. 25 (2002) 535–546.
[8] V. Zimparov, Prediction of friction factors and heat transfer coefficients for turbulent flow in corrugated tubes combined with twisted tape inserts. Part 1: friction factors, Int. J. Heat Mass Transfer 47 (2004) 589–599.
[9] V. Zimparov, Prediction of friction factors and heat transfer coefficients for turbulent flow in corrugated tubes combined with twisted tape inserts. Part 2: heat transfer coefficients, Int. J. Heat Mass Transfer 47 (2004) 385–393.
[10] P.G. Vicente, A. Garcia, A. Viedma, Experimental investigation on heat transfer and friction factor characteristics of spirally corrugated tubes in turbulent flow at different Prandtl number, Int. J. Heat Mass Transfer 47 (2004) 671–681.
[11] P.G. Vicente, A. Garcia, A. Viedma, Mixed convection heat transfer and isothermal pressure drop in corrugated tubes for laminar and transition flow, Int. Commun. Heat Mass Transfer 31 (2004) 651–662.
[12] T. Targanski, J.T. Cieslinski, Evaporation of R407C/oil mixtures inside corrugated and micro-fin tubes, Appl. Therm. Eng. 27 (2007) 2226–2232.
[13] S. Laohalertdecha, S. Wongwises, The effects of corrugation pitch on the condensation heat transfer coefficient and pressure drop of R-134a inside horizontal corrugated tube, Int. J. Heat Mass Transfer 53 (2010) 2924–2931.
[14] S. Laohalertdecha, S. Wongwises, An experimental study into the evaporation heat transfer and flow characteristics of R-134a refrigerant flowing through corrugated tubes, Int. J. Refrig. 34 (2011) 280–291.
[15] S. Laohalertdecha, S. Wongwises, Condensation heat transfer and flow characteristics of R-134a flowing through corrugated tubes, Int. J. Heat Mass Transfer 54 (2011) 2673–2682.
[16] T.N. Tran, Pressure drop and heat transfer study of two-phase flow in small channels. Ph.D. Dissertation, Texas Tech University, Lubbock, Texas, 1998
[17] S.M. Zivi, Estimation of steady-state steam void-fraction by mean of the principle of minimum entropy production, Trans. ASME, J. Heat Transfer 86 (1964) 247–252.
[18] W.W. Akers, H.A. Deans, O.K. Crasser, Condensing heat transfer within horizontal tubes, Chem. Eng. Prog. Symp. 55 (1959) 171–176.
[19] REFPROP, Refrigerant Properties Database Version 6.01, NIST, Gaithersburg, MD, 1998.
[20] J. Wongsa-ngam, T. Nualboonrueng, S. Wongwises, Performance of smooth and micro-fin tubes in high mass flux region of R-134a during evaporation, Heat Mass Transfer 10 (2002) 425–435.
[21] R.J. Silva Lima, J.M.Q. Quibén, J.R. Thome, Flow boiling in horizontal smooth tubes: New heat transfer results for R-134a at three saturation temperatures, Appl. Therm. Eng. 29 (2009) 1289–1298.
[22] F. Rossi, A.W. Mauro, A. Rosato, Local heat transfer coefficients and pressure gradients for R-134a during flow boiling at temperatures between −9 °C and +20 °C, Energy Convers. Manage. 50 (2009) 1714–1721.
[23] E.P.B. Filho, J.M.S. Jabardo, P.E.L. Barbieri, Convective boiling pressure drop of refrigerant R-134a in horizontal smooth and micro-fin tubes, Int. J. Refrig. 27 (2004) 895–903.
[24] S. Wellsandt, L. Vamling, Evaporation of R134a in a horizontal herringbone micro-fin tube heat transfer and pressure drop, Int. J. Refrig. 28 (2005) 889–900.

American J. of Engineering and Applied Sciences 4 (4): 540-547, 2011
ISSN 1941-7020

Improvement of the Runner Design of Francis Turbine using Computational Fluid Dynamics

[1]Suthep Kaewnai and [1,2]Somchai Wongwises
[1]Department of Mechanical Engineering,
Thermal Engineering and Multiphase Flow Research Lab (FUTURE),
Faculty of Engineering, King Mongkut's University of Technology Thonburi,
Bangkok 10140, Thailand
[2]The Academy of Science, the Royal Institute of Thailand,
Sanam Suea Pa, Dusit, Bangkok 10300, Thailand

Abstract: Problem statement: The objective of this study is to improve runner design of the Francis turbine and analyze its performance with the Computational Fluid Dynamics (CFD) technique. **Approach:** A runner design process uses a direct method with the following design conditions: flow rate of 3.12m^3/sec head of 46.4 m and speed of 750 rpm or dimensionless specific speed of 0.472. **Results:** The first stage involves the calculation of various dimensions such as the blade inlet and exit angle at hub and the mean and shroud positions to depict the meridional plane. The second stage deals with the CFD simulation. Various results were calculated and analyzed for factors affecting runner's performance. Results indicated that the head rise of the runner at the design point was approximately 39 m, which is lower than the specified head. Based on past experiences, the meridional plane was modified and blade inlet and lean angles were corrected. The process of meridional plane modification was repeated until the head rise was nearly equal to the specified head. Velocity vector and streamline should be a uniform stream. **Conclusion/Recommendations:** Results from calculating runner's performance were approximately 90% at design point. Existing absolute velocity component from CFD simulation pointed out that swirling flow occurred at the exit of runner. Based on the comparison of runner's performance between simulation results and experimental data from previous work reported in the literature, it is possible to use this method to simulate runner's performance of the Francis turbine.

Key words: Meridional plane, Francis turbine, runner, theoretical calculation, Best Efficiency Point (BEP), streamline

INTRODUCTION

Difficulty in construction of large dams to produce electricity leads to the study of the small turbine. Owing to the progress of the numerical method and computer capacity, a runner design of the Francis turbine can be analyzed by computer programs such as 3D-Navier-Stokes or CFD code to predict its performance before real production. Nevertheless, both the prediction and the design cannot be done easily without an existing database and past experiences. If results from the CFD predictions differ from the design, the turbine should be redesigned before real production. During the past decades, the Francis turbine was studied by many researchers.

Sebestyen and Keck studied flow in the Francis turbine at low head for EGLISU electrical plant (Sebestyen and Keck, 1995). The runner design was improved to fit with existing casing and draft tube by analyzing with CFD technique. The efficiency was improved by 7% and its real efficiency was measured by 5% at design point.

Milos and Barglazan explained that the hydraulic runner design process for Francis turbine usually took a long duration, even for experienced designers (Milos and Barglazan, 2004). They proposed a streamline function of the flow through the runner to enable a quicker design process (Keck *et al*., 1996; 1997; Krishna, 1997; Vu and Shy, 1994; Wu *et al*., 2007).

MATERIALS AND METHODS

There are explanations for runner design processes and CFD prediction techniques, there is no available

Corresponding Author: Suthep Kaewnai, Department of Mechanical Engineering, Thermal Engineering and Multiphase Flow Research Lab (FUTURE), Faculty of Engineering, King Mongkut's University of Technology Thonburi, Bangmod, Bangkok 10140, Thailand

data for one-dimensional hydraulic runner design, which is a starting point of the design process. Even though there is much research on the Francis turbine, there is still a large gap for further study. Therefore, this study focuses on the following main issues:

- Data for improvement of runner design
- Prediction of total head rise at various flow rates
- Checking of speed and streamline through the runner
- Checking of speed distribution along meridian plane at the runner inlet and outlet
- Checking of circumferential component at the absolute velocity to determine swirling flow at the runner outlet

Runner design process: In general, there are two approaches to runner design: the direct method and the inverse method. This study uses a direct method. Figure 1 show the runner design process that begins with the setting of Q (volume flow rate), H (head) and n (speed).

Basic equation in runner design: Basic theory in runner design assumes that flow occurs in one dimension. A momentum equation is applied to determine the runner's head Euler Eq. 1:

$$H = \frac{U_1 C_{u1}}{g} \quad (1)$$

The Free vortex used in the design assumes that head is static with no swirl at the runner blade outlet.

Dimensionless specific speed Eq. 2:

$$\nu = \frac{\omega\sqrt{(Q/\pi)}}{(2gH)^{0.75}} \quad (2)$$

Meridional component of absolute velocity Eq. 3:

$$C_m = \frac{Q}{A_v} \quad (3)$$

Inlet or outlet area with blockage Eq. 4:

$$A_v = \pi Db - ZS_u b \quad (4)$$

Blade blockage Eq. 5:

$$S_u = \frac{S}{\sin(\beta)} \quad (5)$$

Average diameter Eq. 6:

$$D_{ave} = \frac{D_{hub} + D_{shroud}}{2} \quad (6)$$

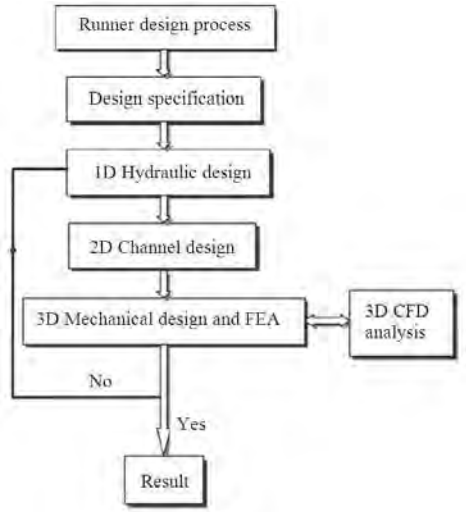

Fig. 1: Design process of runner

Circumferential speed Eq. 7:

$$U = \frac{\pi Dn}{60} \quad (7)$$

Basic mathematical equation of the model: This study uses CFX 5.5 software for three-dimensional flow. The fluid is incompressible and unsteady. The mass conservation and momentum equations for coordinate rotation system can be described as follows:

Mass conservation Eq. 8:

$$\frac{\partial \rho}{\partial t} + \vec{\nabla} \cdot \rho \vec{V} = 0 \quad (8)$$

Momentum Eq. 9:

$$\rho \frac{d\vec{V}}{dt} + \vec{\nabla} P = \rho \vec{g} + \mu\left(\nabla^2 \cdot \vec{V}\right) - 2\rho\vec{\Omega} \times \vec{V} - \rho\vec{\Omega} \times \left(\vec{\Omega} \times \vec{r}\right) \quad (9)$$

Parameters for efficiency calculation: In CFD-code analysis, speed and pressure on the controlled surface at the runner's upstream and downstream could be determined by Eq. 10.

Total head rise:

$$H_{total} = \left(\frac{\overline{P_{1total}} - \overline{P_{2total}}}{\rho g}\right) \quad (10)$$

Table 1: Details at runner inlet

Position	Hub	Mean	Shroud
Circumferential speed (m/sec)	23.562	26.196	28.588
Circumferential component of the absolute velocity (m/sec)	19.277	17.339	15.888
Blade angle (Degree)	61.112	41.245	31.446

Table 2: Details at runner outlet without preswirl

Position	Hub	Mean	Shroud
Circumferential speed (m/sec)	12.802	22.408	28.431
Blade angle (Degree)	30.22	18.109	14.697

Table 3: Conditions used for the simulation

Parameters	CFD Code, CFX 5.5
Flow simulation domain	Single runner flow channel
Mesh	Structured
Fluid	Water at 25°C
Inlet	Total pressure
Outlet	Mass flow rate, Variable (kg/sec)
Wall	No slip
Turbulence model	k,ε
Maximum residual convergence	10^{-4} (RMS)

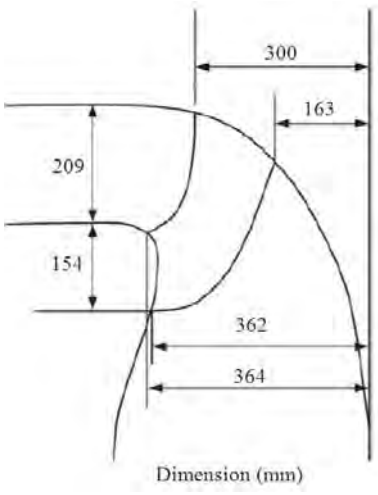

Fig. 2: Dimension of Francis turbine runner in meridional plane (Dimension: mm)

Theoretical head Eq. 11:

$$H_{th} = \frac{\overline{U_1C_{u1}} - \overline{U_2C_{u2}}}{g} \quad (11)$$

Runner efficiency Eq. 12:

$$\eta_{runner} = \frac{\text{Total head rise}}{\text{Theoretical head}} \quad (12)$$

Analysis of runner's flow: Analysis of the Francis turbine runner was done on the given design quantities: volume flow rate of 3.12 m^3/sec, head of 46.4 m, circumferential speed of 750 rpm or dimensionless specific speed of 0.472 and 11 blades of runner. The calculation shows that the Meridional component of the absolute velocity at the runner inlet, C_{m1} is 7.766 m/sec and Meridional component of the absolute velocity at the runner outlet, C_{m2} is 7.457 m/sec. Various dimensions of the runner are shown in Fig. 2. Blade angle, circumferential speed and the circumferential component of the absolute velocity at the runner inlet and outlet could be summarized in Table 1 and 2.

Dimension of runner in meridional plane is shown in Fig. 2. The analysis began with mesh generation and mesh refinement on runner domain. (The domain is the runner channel through which the fluid flows). Secondly, initial conditions and boundary conditions were specified for the mesh-refined domain. Finally, several calculations were made and displayed to determine factors affecting runner's performance. Results from CFD code included pressure; speed on x, y and z axes and specific data that could be further analyzed. If the CFD code prediction gives incorrect results, the runner design can be corrected. Regarding the simulation using CFD code, the conditions used are shown in Table 3.

RESULTS AND DISCUSSION

Drafting domain of runner channel by 3D-CAD programs began as shown in Fig. 4. Then, the domain was entered into CFD code analysis to generate mesh, as shown in Fig. 5.

Analysis of simulation results: In this study, only the inlet and outlet of the fluid were considered to determine the effect on domain. To get better results, a finer mesh should be generated. Figure 6 shows the streamline distribution of the fluid and Fig. 7 shows the velocity distribution on the domain. Notably, the distributions are non-uniform. The results from simulation using CFD Code before improving the runner of Francis turbine are concluded in Table 4 and 5.

Runner design process: At the specified flow rate, results from simulation showed that the head rise was lower than specified head in the design:

- The design improvement process began by reshaping the meridian plane. The shape of the meridian plane is the first priority in designing fluid machinery that requires much experience. In Fig. 8, the shorter length of the meridian plane, compared to Fig. 3, does not signify the shorter length of the runner blade. The length of the runner blade depends on wrap angle (λ), which is normally between 20-80 degrees.

Table 4: Results from the simulation before runner improvement

Mass flow rate	3120	kg /sec
Volume flow rate	3.12	m^3/sec
Head rise	39.00	m

Table 5: Results from simulation after runner improvement at design point

Mass flow rate	3120	kg /sec
Volume flow rate	3.12	m^3/sec
Head rise	46.3	m

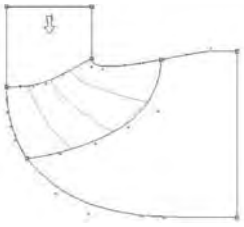

Fig. 3: Meridional plane of Fig. 2 corresponding to CFD Code

Fig. 4: Domain of runner channel

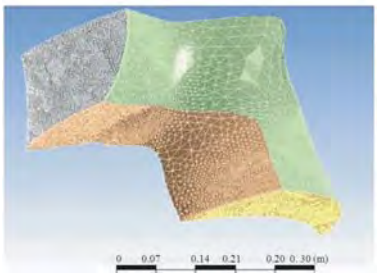

Fig. 5: Mesh on domain for numerical calculation

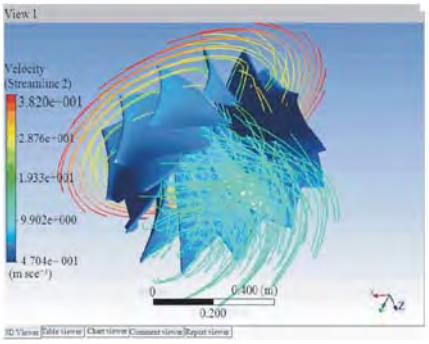

Fig. 6: Streamline distribution on runner

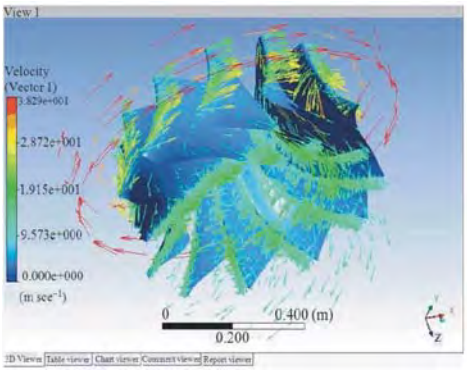

Fig. 7: Velocity distribution on runner

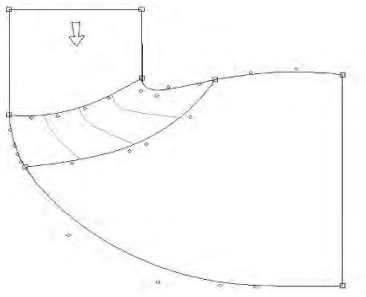

Fig. 8: Meridional plane after improvement

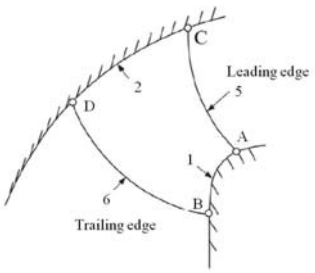

Fig. 9: Location of Meridional plane for Fig. 10

- Lean angle (β) at runner blade inlet was adjusted to 10-30 degrees. Characteristic of lean angle is shown in Fig. 9-10
- Plan view of runner blade was adjusted as shown in Fig. 10
- Inlet angle of runner blade was adjusted to the value shown in Fig. 11. At the dimensionless specific speed 0.472, the angles at the Hub and Shroud were changed to 64 and 73 Degrees, respectively. It is noticeable that the shroud angle is larger than the hub angle, which is contrary to the results from the theoretical calculation given in Table 1

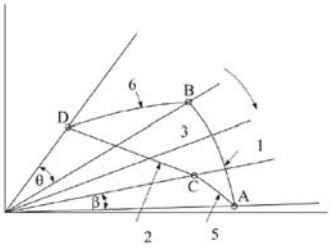

Fig. 10: Plan view of a runner blade

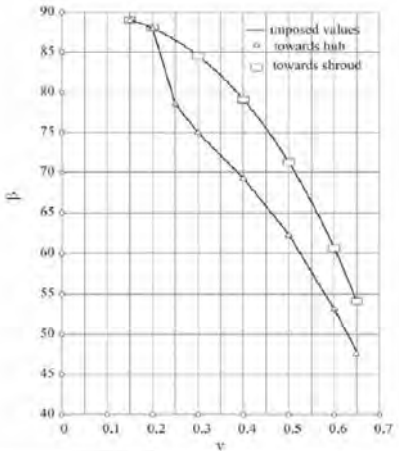

Fig. 11: Inlet and outlet angle of runner blade

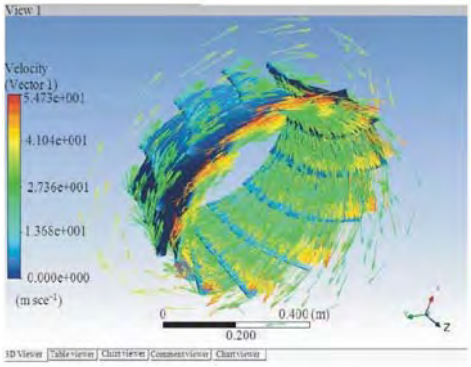

Fig. 12: Velocity distribution on runner after improvement

Results from runner design process: Figure 12 and 13 show that the velocity and streamline distributions on domain are uniform.

Runner performance: Runner performance from this study is shown in Fig. 14-17. Head rise at the specified design point is 46.4 m. From Fig. 14, the head rise is 46.3 m at the same flow rate.

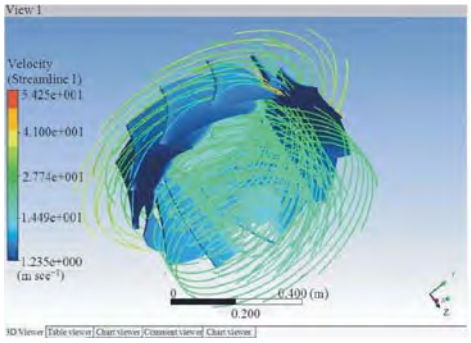

Fig. 13: Streamline distribution on runner after improvement

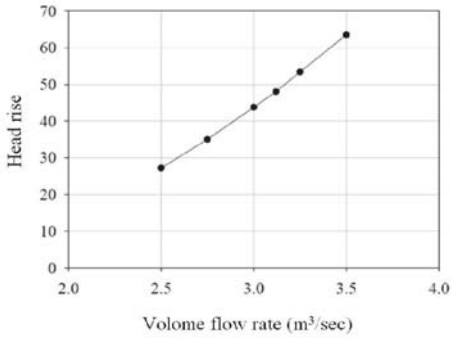

Fig. 14: Head rise Vs volume flow rate

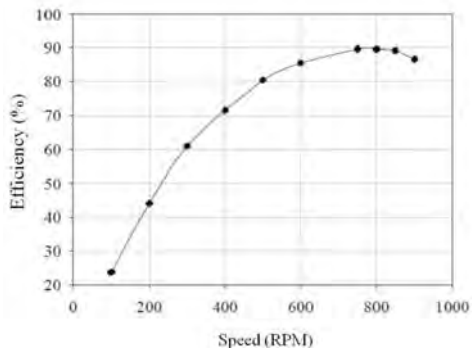

Fig. 15: Runner efficiency Vs speed

It could be seen that improvement of runner design leads to better head rise and head obtained from the simulation is close to the specified design point.

Figure 15 shows that, at the speed of 750 rpm, the runner's efficiency is 90%. In real use, the runner is assembled with casing, draft tube and bearing; thus, the turbine's overall efficiency might be reduced because of friction. Figure 16 shows a relationship between head rise and speed.

It is found that at the designed speed, the head rise that has occurred is not the maximum head, which should be rotated at 400 rpm.

Figure 17 shows the speed of the meridian plane from CFD code from hub to shroud. One notices that the speed of meridian plane is maximum at the hub and minimum at the shroud, with an average of 6.931 m/sec. This differs slightly from the value gained from theoretical calculation.

Figure 18 shows that the circumferential component of the absolute velocity, at the runner inlet decreases from hub to shroud. Figure 19 shows that the speed of the meridian plane at the runner outlet is nearly stable.

Figure 20-21 show that the circumferential component of the absolute velocity at the runner outlet and distance from Hub is not equal to zero.

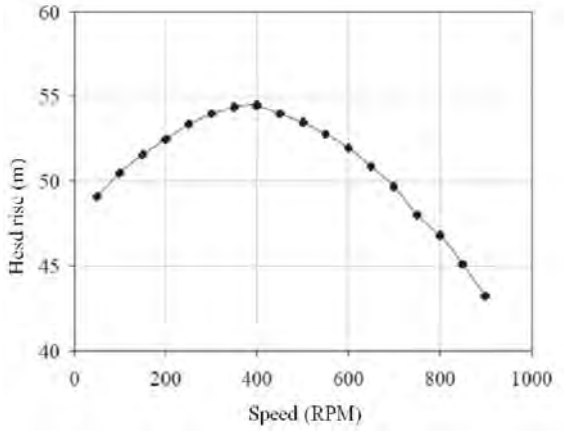

Fig. 16: Head rise Vs speed

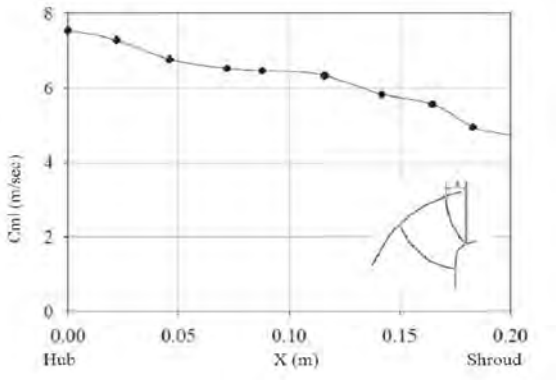

Fig. 17: Variation of meridional component of the absolute velocity at runner inlet with distance from hub

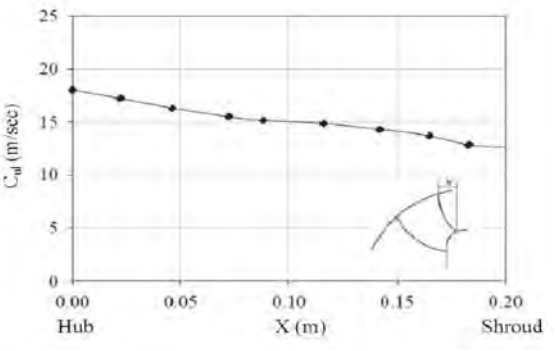

Fig. 18: Variation of circumferential component of the absolute velocity at runner inlet with distance from hub

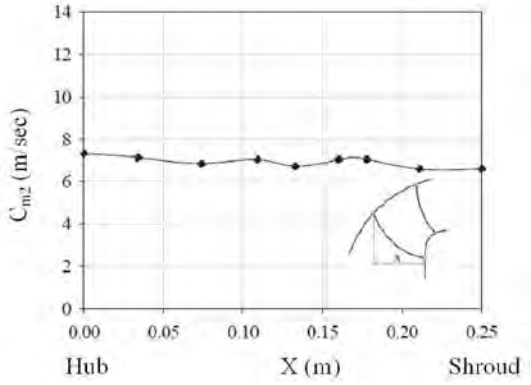

Fig. 19: Variation of meridional component of the absolute velocity at runner outlet with distance from hub

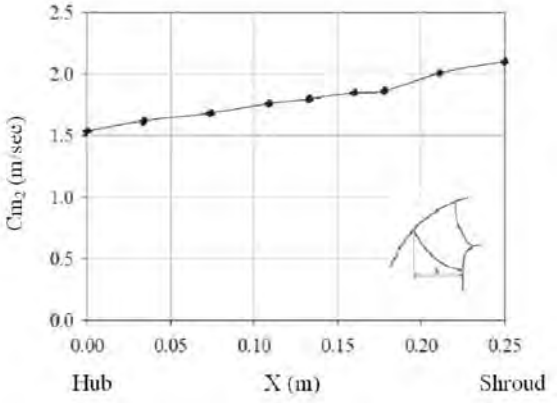

Fig. 20: Variation of circumferential component of the absolute velocity at runner outlet with distance from hub

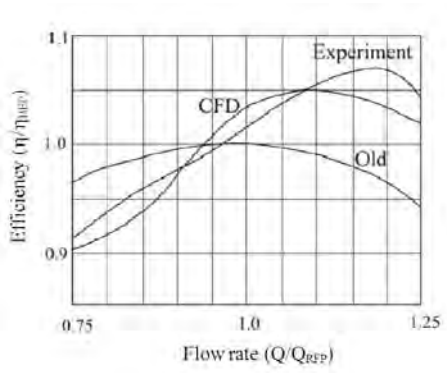

Fig. 21: Comparison between calculation and measurement; efficiency and volume flow rate referred to best efficiency point

This means that there is a pre-swirl at the runner outlet. Hence, the design that sets to zero is not correct.

Confirmation from CFD: This study did not conduct any experiment because of the high cost. However, the study by Sebestyen and Keck shows corresponding results between analysis and test (Sebestyen and Keck, 1995). The runner is redesigned for EGLISU electrical plant. CFD analysis indicated higher efficiency by 7%. Then, the new runner was installed into the old casing and tested. It was found that the efficiency of the new runner-not including friction in casing, draft tube and bearing-was better by 5%, close to results from CFD analysis. The highest point of efficiency was at.

CONCLUSION

The improvement of runner design of the Francis turbine to get the desired head rise and high efficiency relied on experienced correction of meridional plane and angle of runner blade inlet as shown in Fig. 11. It took a long time to complete this step. CFD analysis indicated that the runner efficiency at the design point was 90%. At the flow rate close to the Best Efficiency Point (BEP), the runner's efficiency was quite high and became lower when the flow rate was far from the BEP. Checking the speed from CFD code revealed that the circumferential component of the absolute velocity at runner outlet was not equal to zero. Thus, the flow at the runner outlet caused swirl. However, the analysis only gave very small value. On the other hand, the meridional component of the absolute velocity at the runner outlet was nearly stable.

ACKNOWLEDGMENT

The researchers would like to express their appreciation to the Thailand Research Fund (TRF), the Office of Higher Education Commission and the National Research University Project for providing financial support for this study.

List of symbols:

A_v	Inlet or outlet area (m^2)
b	Width of channel in the meridional section (m)
C_{m1}	Meridional component of the absolute velocity at runner inlet (m/sec)
C_{m2}	Meridional component of the absolute velocity at runner outlet (m/sec)
C_{u1}	Circumferential component of the absolute velocity at runner inlet (m/sec)
C_{u2}	Circumferential component of the absolute velocity at runner outlet (m/sec)
CFD	Computational Fluid Dynamics
D	Diameter (m)
FEA	Finite element analysis
G	Gravitational acceleration (m/sec^2)
H	Design head of runner (m)
H_{total}	Total head rise
H_{th}	Theoretical head
K	Turbulence kinetic energy
n	Speed (rpm)
P	Pressure (N/m^2)
p_w	Power (Watt)
P_{1total}	Total pressure at runner inlet (N/m^2)
p_{2total}	Total pressure at runner outlet ($N\ m^2$)
Q	Volume flow rate (m^3/sec)
R	Radius from the reference point (m)
S	Blade thickness (m)
S_u	Blade thickness with blockage (m)
U_1	Circumferential speed at runner inlet (m/sec)
U_2	Circumferential speed at runner outlet (m/sec)
$\vec{V}$	Velocity vector (m)
Z	Number of blade
β	Blade angle
η	Efficiency
ν	Dimensionless specific speed
ε	Turbulence eddy dissipation
ρ	Density of water (kg/m^3)
$\vec{\Omega}$	Angular velocity (rad/sec)
$\vec{\nabla}$	Operator

REFERENCES

Keck, H., P. Drtina and M. Sick, 1996. Numerical hill chart prediction by mean of CFD stage simulation for a complete Francis turbine. Porceedings of the IAHR Symposium Hydraulic Machinery and Cavitation, (HMC' 96), Valencia.

Keck, H., P. Drtina and M. Sick, 1997. A breakthrough–CFD flow simulation for a complete turbine. Sulzer Hydro Ltd., Switzerland.

Krishna, H.C.R., 1997. Hydraulic Design of Hydraulic Machinery. 1st Edn., Avebury, Aldershot, ISBN: 0291398510, pp: 570.

Milos, T. and M. Barglazan, 2004. CAD technique used to optimize the francis runner design. Proceedings of the 6th International Conference on Hydraulic Machinery and Hydrodynamics Timisoara, Oct. 21-22, Politehnica University, Romania, pp: 125-130.

Sebestyen, A. and H. Keck, 1995. Uprating of ultra-low francis units based on numerical flow analysis. Sulzer Hydro Ltd., Switzerland.

Vu, T.C. and W. Shy, 1994. Performance prediction by viscous flow analysis for francis turbine runner. J. Fluid Eng., 116: 116-120.

Wu, J., K. Shimmei, K. Tani, K. Niikura and J. Sato, 2007. CFD-based design optimization for hydro turbines. J. Fluid Eng. ASME, 129: 159-168.

Experimental Thermal and Fluid Science 36 (2012) 107–117

Contents lists available at SciVerse ScienceDirect

Experimental Thermal and Fluid Science

journal homepage: www.elsevier.com/locate/etfs

Flow boiling pressure drop of R134a in the counter flow multiport minichannel heat exchangers

Jatuporn Kaew-On [a,b], Kittipong Sakamatapan [b], Somchai Wongwises [b,c,*]

[a] The Joint Graduate School of Energy and Environment (JGSEE), King Mongkut's University of Technology Thonburi, Bangmod, Bangkok 10140, Thailand
[b] Fluid Mechanics, Thermal Engineering and Multiphase Flow Research Lab. (FUTURE), Department of Mechanical Engineering, King Mongkut's University of Technology Thonburi, Bangmod, Bangkok 10140, Thailand
[c] The Academy of Science, The Royal Institute of Thailand, Sanam Suea Pa, Dusit, Bangkok 10300, Thailand

ARTICLE INFO

Article history:
Received 8 April 2011
Received in revised form 29 July 2011
Accepted 4 September 2011
Available online 22 September 2011

Keywords:
Flow boiling pressure drop
Multiport minichannels
Tube-in-tube heat exchanger
R134a

ABSTRACT

In the present study, the pressure drop characteristics during the boiling of R134a as it flows through the multiport minichannel heat exchangers are presented. The heat exchangers are counter flow tube-in-tubes. The refrigerant flow runs through the inner tube, while the hot water flows through the 25.4 mm round tube at outer edge of the heat exchanger. Two inner test sections are made from aluminium tubing with hydraulic diameters of 1.1 mm for 14 channels and 1.2 mm for eight channels. The experiments were carried out at mass fluxes ranging from 350 to 980 kg/(m^2 s), heat fluxes ranging from 18 to 80 kW/m^2, and saturation pressures of 4, 5 and 6 bar, at constant inlet quality of 0.05. The effect of relevant parameters on the frictional pressure drop, such as the saturation pressure, mass flux, heat flux, and aspect ratio, are examined and discussed in detail. Finally, the nine existing correlations that are based on both conventional tubes and small tubes are selected for comparison with the experimental results.

1. Introduction

Multiport minichannels have been considered to be of great interest in the compact evaporator applications of both automotive air-conditioning and heat pump systems. The greatest advantages of the minichannels are their high heat transfer coefficient, high compactness, and lower required fluid mass. The greater heat transfer in minichannels is obtained by a higher surface area. The decreasing size also allows heat exchangers to achieve a significant weight reduction, a lower fluid inventory, a low capital and installation cost, and enhanced energy savings. Despite such advantages, the pressure drop in the minichannels is still higher than that which occurs with a conventional tube due to the increased wall friction. Thus, the designs of multiport minichannels that are used as evaporators for air conditioning or heat pumps are needed in order to overcome the practical obstructions that relate to flow boiling. In the last decade, the pressure drop characteristics of refrigerant in small channels have been studied by a number of researchers. However, most of them were studied with a singleport minichannel. Thus, the pressure drop and flow characteristics of refrigerant in multiport minichannels have received little attention in existing literature. So far, some examples of the most productive studies that address both single port and multiport minichannels are summarized as follows:

Zhang and Webb [1] measured the single phase and adiabatic two-phase flow pressure drop of R134a, R22, and R404A flowing in a multiport extruded aluminium minichannel with a hydraulic diameter of 2.13 mm. They concluded that the Blasius friction correlation gave supported the experimental data for a single-phase flow. In contrast, Friedel's [2] correlation showed over-predicted values for two-phase data. They also proposed the two-phase multiplier based on their experimental results as a function of the refrigerant quality and reduced pressure.

In 2002, Ould Didi et al. [3] presented experimental data for evaporation in two horizontal test sections of 10.92 and 12.00 mm diameter for five refrigerants (i.e., R134a, R123, R402A, R404A and R502) over mass fluxes from 100 to 500 kg/(m^2 s). They showed the comparisons between the experimental results and the seven two-phase frictional pressure drop predictions method. From the comparisons, they concluded that the method of Müller-Steinhagen and Heck [4] and the method of Gronnerud [5] consistently gave the best predictions, while the Friedel [2] method was the third best in comparisons of seven leading predictive methods.

In 2005, Cavallini et al. [6] investigated the pressure drop characteristics in multiport minichannels during the adiabatic

* Corresponding author at: Fluid Mechanics, Thermal Engineering and Multiphase Flow Research Lab. (FUTURE), Department of Mechanical Engineering, King Mongkut's University of Technology Thonburi, Bangmod, Bangkok 10140, Thailand. Tel.: +662 470 9115; fax: +662 470 9111.
E-mail address: somchai.won@kmutt.ac.th (S. Wongwises).

0894-1777/$ - see front matter © 2011 Elsevier Inc. All rights reserved.
doi:10.1016/j.expthermflusci.2011.09.002

Nomenclature

Bo	boiling number, $Bo = \frac{q''}{Gi_{lv}}$
C_c	coefficient of sudden contraction (−)
d_h	hydraulic diameter (m)
f	fanning friction factor (−)
G	mass flux (kg/(m^2 s))
i	enthalpy (kJ/kg)
k	thermal conductivity (W/(m K))
N	number of channel
P	pressure (kPa)
q''	heat flux (kW/m^2)
Re	Reynolds number, $Re = \frac{Gd}{\mu}$
v	specific volume (m^3/kg)
We	Weber number, $We = \frac{G^2 d}{\rho\sigma}$
X	Lockhart–Martinelli parameter (−)
x	vapor quality

Greek letters

α	void fraction
β	aspect ratio
$\frac{\Delta P}{\Delta z}$	pressure gradient (kPa/m)
μ	dynamic viscosity (Pa s)
ρ	density (kg/m^3)
σ	surface tension (N/m)
σ_c	the ratio of A_1/A_2 in sudden contraction equation (−)
σ_e	the ratio of A_1/A_2 in sudden expansion equation (−)
ϕ^2	two-phase frictional multiplier (−)

Subscripts

A	annular
a	acceleration
CB	coalescing bubble
$cont$	contraction
cr	critical
exp	expansion
f	friction
l	liquid
lo	all liquid
lv	liquid–vapor
v	vapor
vo	all vapor
IB	isolated bubble
in	inlet
out	outlet
tot	total
tp	two-phase

two-phase flow of R236ea, R134a, and R410A. They performed the wide range of the reduced pressure (varying from 0.1 up to 0.5). Their results showed that the frictional pressure drop of R410A gave the lowest values when comparison with those of R134a and R234ea at the same conditions. Moreover, the experimental results were used to compare with the existing correlations. The results showed that the frictional pressure drop of R134a supported the available correlations.

Nino et al. [7] proposed correlations based on a flow-regime for predicting the frictional pressure drop in the intermittent and annular flow regime. For the intermittent flow regime, the average kinetic energy of the mixture was used to develop the correlation based on the homogenous flow model. They found that the relation between the two-phase pressure drop and the average kinetic energy of the mixture is linear. For the annular flow regime, they developed the new separated flow model by using the correlation of Lockhart and Martinelli [8].

Mauro et al. [9] compared their experimental pressure drop data for different refrigerants (R22, R134a, R404A, R407C, R417A, and R507A) and different experimental conditions to the prediction method by using a general model. They found that the method by Quiben and Thome [10] was able to yield reliable predictions in the annular, intermittent, and dry-out flow regime, while the Gronnerud [5] method worked well up to the annular flow regime.

In 2008, Pamitran et al. [11] studied the two-phase pressure drop of CO_2 during vaporization in horizontal smooth minichannels. The test section was made of stainless steel tubes with inner diameters of 1.5 mm and 3.0 mm and lengths of 2000 and 3000 mm. The electric current was supplied to the test section directly in order to meet the uniform wall heat flux. They concluded that the pressure drop is higher for a smaller inner tube diameter, lower saturation temperature, and for higher mass flux and heat flux. They also showed that the two-phase pressure drop is a function of mass flux, inner diameter, surface tension, density and viscosity. Finally, the new correlation based on the Lockhart–Martinelli [8] method was presented.

Revellin and Haberschill [12] compared the experimental frictional pressure drop database for smooth tubes to four well-known correlations (Gronnerud [5], Friedel [2], Müller-Steinhagen and Heck [4], and Jung and Radermacher [13]) and the model proposed by Quibem and Thome [10]. They found that the Gronnerud [5] correlation and the model of Quiben and Thome [10] displayed the best prediction.

Kaew-On and Wongwises [14] experimentally studied the evaporation of 410A in three ports minichannels with a 3.48 mm hydraulic diameter. The experimental results indicated that the average heat transfer coefficient tended to increase with increasing average quality, mass flux, and heat flux. On the contrary, the heat transfer coefficient tended to decrease with increasing saturation temperature. Moreover, the pressure drop increased with increasing mass flux and decreased with an increased saturation temperature. The results also showed that the heat flux has no significant effect on the pressure drop. Finally, the correlations for predicting the heat transfer coefficient and frictional pressure drop were also proposed. The comparison of the frictional pressure drop of R134a and 410A in multiport are reported by the studied of Kaew-On and Wongwises [15]. They found that the frictional pressure drops of R410A were lower than those of R134a by approximately 30–50%.

In recently, Zhang et al. [16] proposed the new method to correlate the two-phase friction multiplier by applying the artificial neural network. They found that the newly developed correlations are extensively evaluated with a variety of data sets collected from the literature.

1.1. The existing correlations for predicting frictional pressure drop

The overview of two-phase frictional pressure drop correlations for both conventional channels and small channels are presented as follows:

1.2. Conventional channel correlations

The existing correlations for conventional channel are frequently seen in the open literature are follows:

1.2.1. Lockhart and Martinelli correlation [8]

For calculating the frictional pressure drop of two-phase flow, Martinelli and Nelson [17] and Lockhart and Martinelli [8] defined

key multipliers which are ratios of a two-phase to single-phase pressure drop. These two-phase multipliers, ϕ_l^2, ϕ_v^2, ϕ_{lo}^2 and ϕ_{vo}^2 are defined as follows:

$$\phi_l^2 = \frac{(dp_f/dz)_{tp}}{(dp_f/dz)_l}, \quad \phi_v^2 = \frac{(dp_f/dz)_{tp}}{(dp_f/dz)_v}, \\ \phi_{lo}^2 = \frac{(dp_f/dz)_{tp}}{(dp_f/dz)_{lo}}, \quad \phi_{vo}^2 = \frac{(dp_f/dz)_{tp}}{(dp_f/dz)_{vo}}. \tag{1}$$

The single-phase frictional pressure gradient, $(dp_f/dz)_l$, $(dp_f/dz)_v$, $(dp_f/dz)_{lo}$ and $(dp_f/dz)_{vo}$ are defined as:

$$(dp_f/dz)_l = \frac{2f_l(1-x)^2G^2}{d\rho_l}, \quad (dp_f/dz)_v = \frac{2f_v x^2 G^2}{d\rho_v}, \\ (dp_f/dz)_{lo} = \frac{2f_{lo}G^2}{d\rho_l}, \quad (dp_f/dz)_{lo} = \frac{2f_{lo}G^2}{d\rho_l}. \tag{2}$$

Factors f_{lo} and f_{vo} are the fanning friction factors which assume that only liquid or only vapor is flowing alone at the same mass flux of the two-phase flow. Further, f_l and f_v are Fanning friction factors which assume that only liquid or only vapor is flowing alone at the same superficial velocity of the phase. Moreover, Lockhart and Martinelli [8] proposed the parameter to correlate their experimental results, well known as the Lockhart–Martinelli parameter.

$$X = \left(\frac{1-x}{x}\right)^{0.875}\left(\frac{\rho_v}{\rho_l}\right)^{0.5}\left(\frac{\mu_l}{\mu_v}\right)^{0.125}. \tag{3}$$

1.2.2. Chisholm correlation [18]

The two-phase multiplier is related to the Lockhart–Martinelli parameter through the Chisholm correlation [18], which is defined as:

$$\phi_l^2 = 1 + \frac{C}{X} + \frac{1}{X^2}, \tag{4}$$

where the value C depends on the flow regime of the liquid and vapor.

1.2.3. Friedel correlation [2]

One of the most widely used correlations for predicting the two-phase frictional pressure drop was suggested by Friedel [2]. He proposed correlation based on 25,000 data points. He correlated his experimental data with ϕ_{lo}^2 as a function of the Lockhart–Martinelli parameter, Froude number, Weber number, quality, friction factor, and physical properties.

$$\phi_{lo}^2 = E + \frac{3.24FX}{F_r^{0.045}We_l^{0.035}}, \tag{5}$$

where

$$F_r = \frac{G^2}{gd\rho_{tp}}, \quad F = x^{0.78}(1-x)^{0.224}, \quad We_l = \frac{G^2 d}{\sigma\rho_l}, \tag{6}$$

$$E = (1-x)^2 + x^2\frac{\rho_l f_{vo}}{\rho_v f_{lo}}. \tag{7}$$

1.2.4. Müller-Steinhagen and Heck correlation [4]

$$(dP_f/dz)_{tp} = F(1-x)^{1/3} + (dP_f/dz)_{lo}x^3, \tag{8}$$

where

$$F = (dP_f/dz)_{lo} + [(dP_f/dz)_{vo} - (dP_f/dz)_{lo}]. \tag{9}$$

1.3. Small channel correlations

There are many correlations for predicting the frictional pressure drop in a small channel. The following correlations for small channels were presented in extant literatures.

1.3.1. Mishima and Hibiki correlation [19]

Mishima and Hibiki [19] proposed the correlation based on the Lockhart–Martinelli correlation [8]. They modified the constant C as a function of hydraulic diameter, which is presented as follows:

$$C = 21(1 - e^{-319d_h}); \quad (d_h \text{ in mm}). \tag{10}$$

The constant C proposed by Mishima and Hibiki [19] was developed using the available air–water two-phase data, which was obtained in circular and rectangular channels with a hydraulic diameter of 1–4 mm.

1.3.2. Zhang and Webb correlation [1]

In 2000, Zhang and Webb [1] proposed the two-phase multiplier based only on liquid flow as a function of the refrigerant quality and reduced pressure.

$$\phi_{lo}^2 = (1-x)^2 + 2.87x^2\left(\frac{P}{P_{cr}}\right)^{-1} + 1.68x^{0.25}(1-x)^2\left(\frac{P}{P_{cr}}\right)^{-1.64}. \tag{11}$$

1.3.3. Lee and Mudawar correlation [20]

Lee and Mudawar [20] proposed two correlations for calculating the constant C values which depend on the flow regimes of liquid and vapor.

For laminar liquid and laminar vapor flows

$$C = 2.16Re_{lo}^{0.047}We_{lo}^{0.23}. \tag{12}$$

For laminar liquid and turbulent vapor flows

$$C = 1.45Re_{lo}^{0.25}We_{lo}^{0.23}. \tag{13}$$

1.3.4. Saisorn and Wongwises correlation [21]

Saisorn and Wongwises [21] developed the correlation for predicting the two-phase frictional multiplier according to their experimental data of adiabatic two-phase air–water flowing through 0.53 mm inner diameter. The correlation they presented is as follow:

$$\phi_l^2 = 1 + \frac{6.627}{X^{0.761}}. \tag{14}$$

1.3.5. Kaew-On and Wongwises correlation [14]

Recently, Kaew-On and Wongwises [14] proposed the correlation for predicting the frictional pressure drop as a function of constant C, which was defined as follows:

$$C = -3.356 + 41.863e^A + B, \tag{15}$$

where A and B were defined as

$$A = -69.475\beta f_l d_h, \tag{16}$$

$$B = 498\beta f_l d_h. \tag{17}$$

1.3.6. Zhang et al. correlation [16]

Zhang et al. [16] developed the correlations for predicting the pressure drop in minichannels and microchannels.

For an adiabatic liquid–vapor two-phase flow:

$$C = 21[1 - e^{(-0.674/Lo^*)}]. \tag{18}$$

For a diabatic liquid–gas two-phase flow:

$$C = 21[1 - e^{(-0.142/Lo^*)}], \tag{19}$$

where Lo^* is the non-dimensional Laplace constant, which is defined as

$$Lo^* = \left[\frac{\sigma}{g(\rho_l - \rho_v)}\right]^{0.5} / d_h. \tag{20}$$

They recommended that the application ranges of their correlation are as follows:

$0.014 \leqslant d_h \leqslant 6.25$ mm, $Re_l \leqslant 2000$ and $Re_g \leqslant 2000$.

As previously mentioned, it is clearly evident that some information is available on the boiling flow characteristics in minichannels and microchannels, especially which pertains to the single port channel. However, despite worthwhile applications in industrials, relatively little information is currently available on flow boiling characteristics in a multiport minichannel. As a consequence, this article, which is a continuation of our previous paper (Kaew-On et al. [22]), is aimed at determining the frictional pressure drop of refrigerant R134a during a flow boiling condition. The effects of the mass flux, heat flux, and saturation pressure on the frictional pressure drop are presented. Moreover, the comparisons of a frictional pressure drop at a different aspect ratio of the channel are also presented. In addition, the nine existing correlations for predicting frictional pressure drop are compared with the present data.

2. Experimental apparatus and method

The experimental apparatus is schematically presented in Fig. 1. The main components of the system are the test section, refrigerant flow loop, hot water flow loop, subcooling loop, and a data acquisition system.

As indicated by Fig. 1, which portrays the refrigerant circulating loop, liquid refrigerant is pumped by a gear pump with a regulated flow rate by means of an inverter. The refrigerant then passes in a series through a filter/dryer, refrigerant flow meter, pre-heater, and sight glass tube and enters the test section. The inlet quality before entering the test section is controlled by the pre-heater. The DC power supply is used to supply the imposed heat flux to the pre-heater, which can be controlled by adjusting the supply voltage and current. Leaving the test section, the refrigerant vapor then condenses in a subcooler and is later collected in a receiver; it eventually returns to the refrigerant pump to complete the cycle. Instrumentation is installed at various positions, as is also clearly shown in Fig. 1, to monitor the refrigerant state. All of the signals from the thermocouples and pressure transducer are recorded by a data logger.

The complete schematic diagram and the drawing of the test section are shown in Figs. 2 and 3, respectively. The heat exchanger was designed as the counter flow tube-in-tube heat exchanger with refrigerant flowing in the inner tube and heating water in the gap between the outer and inner tubes. Therefore, the supply heat fluxes from the heating water to the refrigerant are based on the outer surface area of the multiport minichannel test section. Two inner tubes were made from extruded multiport aluminium with the internal hydraulic diameter of 1.1 mm for 14 numbers of channels (tube No. 1) and 1.2 mm for eight numbers of channels (tube No. 2). The outer surface areas of two inner test sections are 5979 mm^2 and 6171 mm^2, while the inner surface areas are 13,545 mm^2 and 8856 mm^2 for tube No. 1 and tube No. 2, respectively. Additional details about the test sections are presented in Table 1. The outer tube of the heat exchanger was made from a circular acrylic tube with an internal hydraulic diameter of 25.4 mm. The test section is connected with a header at the inlet and outlet. T-type thermocouples are installed at the inlet and outlet on the side of header to measure the saturation temperature of the refrigerant. At the other side of the header, the differential pressure transducer is installed in order to measure the pressure drop across the test section. The accuracy of the differential pressure transducer is ±0.25% of the full scale or ±0.125 kPa. The water outside of the test section is insulated through the use of rubber foam with a thermal conductivity of 0.04 W/(mK). The refrigerant flow meter is a variable area type. The flow meter is specially calibrated in the range of 0.2–1.8 LPM for R134a by the manufacturer. The details of the test conditions and the uncertainties of measured quantities and calculated parameters are presented in Tables 2 and 3, respectively.

3. Data reduction

For all calculations, the thermophysical properties of the refrigerant are evaluated by using the REFPROP, Version 6.01 [23]. The

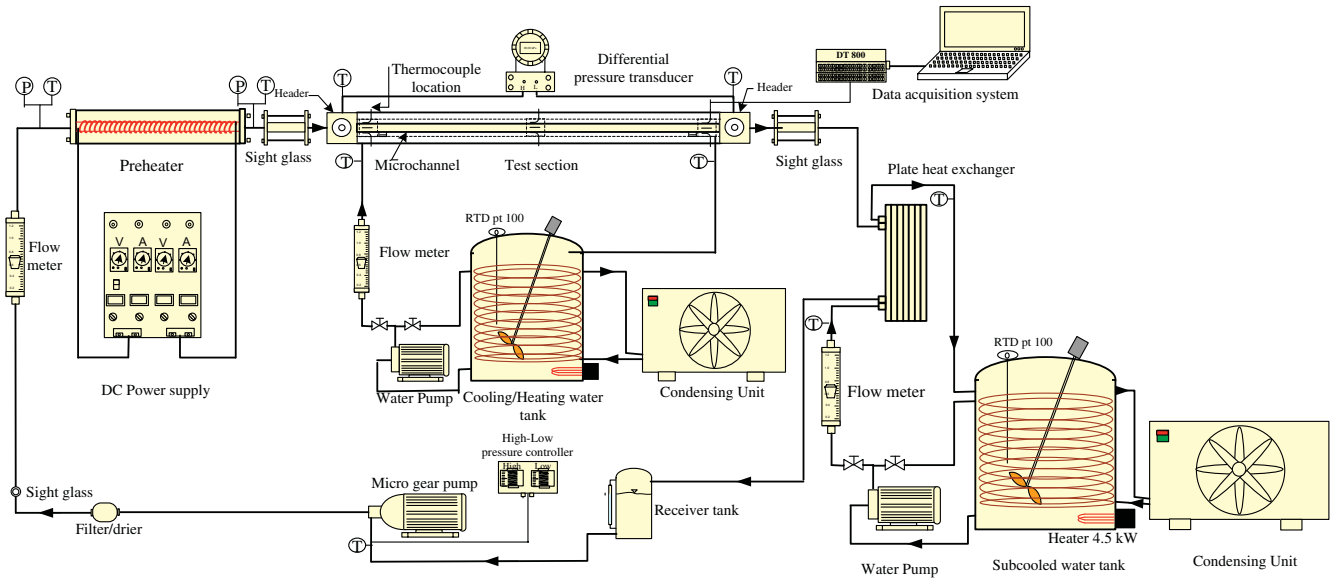

Fig. 1. Schematic diagrams of the experimental apparatus.

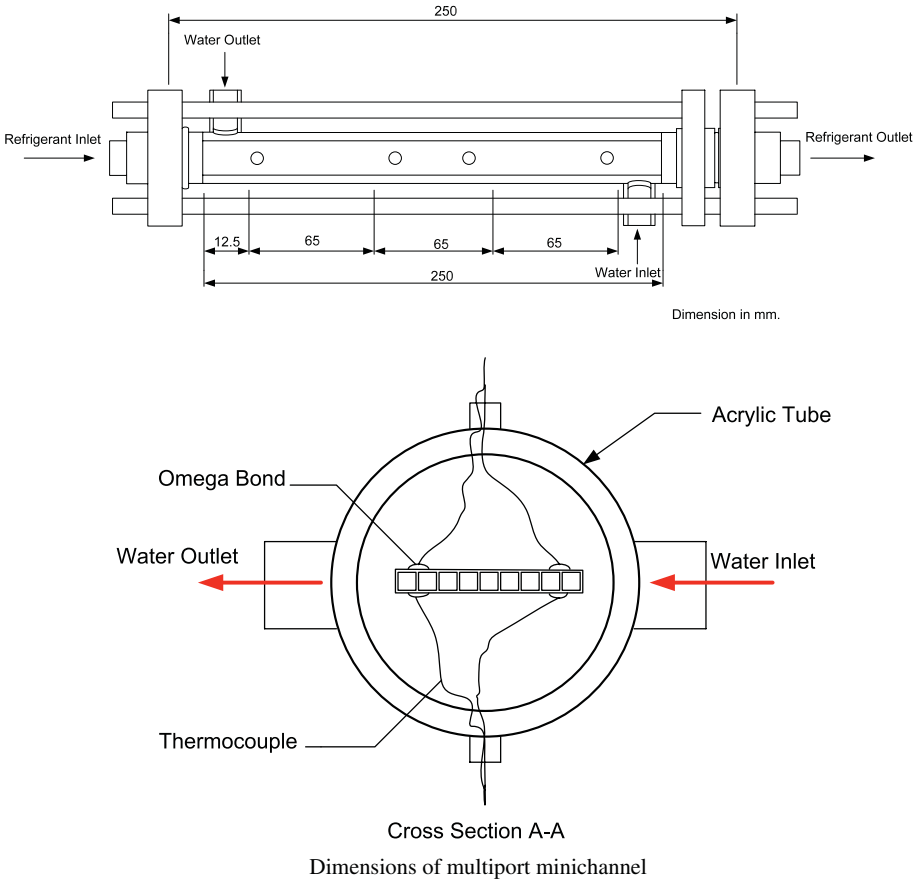

Fig. 2. Schematic diagram of the test section.

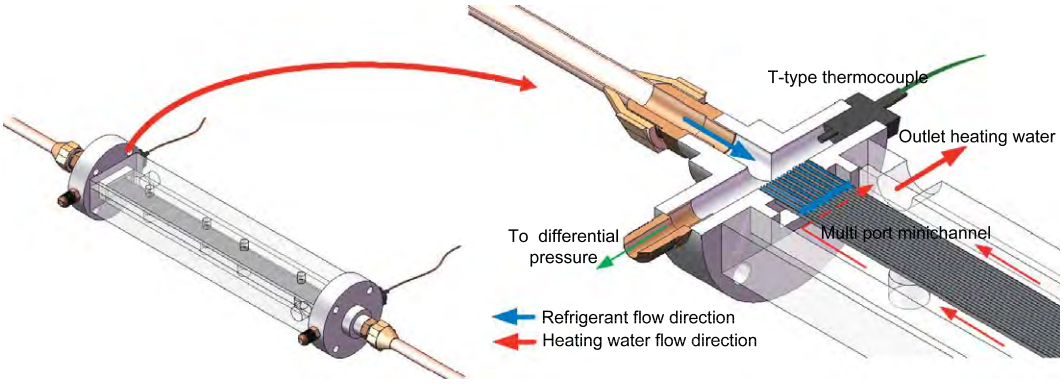

(a) Overall test section (b) Inlet manifold

Fig. 3. Illustration of the test section, (a) overall test section, and (b) inlet manifold.

Table 1
The details of test sections.

Test no.	Hydraulic diameter (mm)	Number of channel	Channel width (mm)	Channel height (mm)	Aspect ratio	Inner surface (mm^2)	Outer surface (mm^2)
1	1.1	14	1	1.25	1.25	13,545	5979
2	1.2	8	1.8	0.9	0.5	8856	6171

data reduction of the measured results is summarized in the following procedures.

The total boiling pressure drop was measured by the differential pressure transducer which was installed between the inlet and exit of the test section. The main components of the total pressure gradient are the frictional pressure gradient, the sudden contraction pressure gradient or the loss at the minichannels inlet, the sudden expansion pressure gradient and the acceleration or momentum

Table 2
Experimental conditions.

Refrigerant	R134a
Mass flux (kg/m^2 s)	350–980
Heat flux (kW/m^2)	18–80
Saturation pressure (bars)	4, 5, 6

Table 3
Uncertainties of measured quantities and calculated parameters.

Parameter	Uncertainty
Temperature	±0.1 °C
Differential pressure transducer	±0.25% of full scale
Mass flow rate of refrigerant	±0.1% of full scale
Heat transfer rate of pre-heater	±2.25%
Heat transfer rate of the test section	±8.5%
Vapor quality inlet	±3.25%
Vapor quality outlet	±9.00%

pressure gradient. Therefore, the total pressure gradient between the upstream and downstream portion of the test section can be expressed as follows:

$$(\Delta p/\Delta z)_{tot} = (\Delta p_f/\Delta z) + (\Delta p_{cont}/\Delta z) + (\Delta p_{\exp}/\Delta z) + (\Delta p_a/\Delta z). \tag{21}$$

The sudden contraction pressure gradient is calculated from the following correlation that Collier and Thome proposed [24].

$$(\Delta p_{cont}/\Delta z) = \frac{G^2 v_l}{2}\left[\left(\frac{1}{C_c}-1\right)^2 + \left(1-\frac{1}{\sigma_c^2}\right)^2\right]\left[1+\frac{v_{lv}x_{in}}{v_l}\right]. \tag{22}$$

Similarly, the sudden expansion pressure gradient is also determined from Collier and Thome [24], which is expressed as follows:

$$(\Delta P_{exp}/\Delta z) = G^2\sigma_e(1-\sigma_e)v_l\left[1+\frac{v_{lv}x_{out}}{v_l}\right]. \tag{23}$$

The acceleration or momentum pressure gradient is the loss due to the phase change which can be determined from following equation.

$$(\Delta p_a/\Delta z) = G^2\left\{\left[\frac{(1-x)^2}{\rho_l(1-\alpha)}+\frac{x^2}{\rho_v\alpha}\right]_{out} - \left[\frac{(1-x)^2}{\rho_l(1-\alpha)}+\frac{x^2}{\rho_v\alpha}\right]_{in}\right\}, \tag{24}$$

where the void fraction, α, can be calculated by the correlation of Zivi [25] as follows:

$$\alpha = \left[1+\frac{(1-x)}{x}\left(\frac{\rho_v}{\rho_l}\right)\right]^{-1}. \tag{25}$$

The frictional pressure gradient can be obtained through the Eqs. (22)–(26). The experimental frictional pressure gradient results are then compared with values predicted by the existing correlation for both the conventional channel correlations and small channel correlations.

4. Results and discussion

4.1. Flow patterns

The patterns of the refrigerant as it flows through the multiport minichannel are a very important parameter which influences the changing pressure drop. Therefore, an investigation into the flow patterns is necessary. Due to the visualized investigation of the flow patterns, additional instruments are needed and the material of the test section must be transparent. Therefore, this study cannot be performed through the observation of the flow pattern. However, the available existing flow regimes map the correlation in previous studies and can be used to estimate the flow patterns. In 2007, the two-phase flow pattern map for flow boiling in a micro-channel was developed by Revellin and Thome [26]. They proposed a flow regime map comprised of different zones according to the bubble coalescence phenomena. The following is a brief description of each zone located in the flow map.

The isolated bubble (IB) regime corresponds to a relatively high bubble generation rate in comparison to the bubble coalescence rate. Either or both of the bubbly flow and the slug flow are included in this regime. The coalescing bubble (CB) regime is defined when the bubble generation rate is smaller than the bubble coalescence rate.

The isolated bubble (IB) flow to coalescing bubble (CB) flow transition is given by

$$x_{IB/CB} = 0.763\left(\frac{Re_{lo}Bo}{We_{vo}}\right)^{0.41}, \tag{26}$$

where Bo stands for the boiling number, Re_{lo} represents the all-liquid Reynolds number, and We_{vo} is the all-vapor Weber number.

The transition from the coalescing bubble flow to the annular flow is determined by

$$x_{CB/A} = 0.00014Re_{lo}^{1.47}We_{lo}^{-1.23}. \tag{27}$$

where We_{vo} is the all-liquid Weber number.

Fig. 4 presents flow pattern maps in terms of mass flux and vapor quality which are compared with Revellin and Thome [26] transition zones. It was found that all of the present experimental data is located in the coalescence bubble (CB) or semi-annular zone.

Recently, a new update macro-to-micro scale flow pattern map was proposed by Ong and Thome [27]. They proposed new flow pattern transition lines as follows:

1. Isolated bubble/coalescing bubble (IB/CB)

$$x_{IB/CB} = 0.36Co^{0.20}\left(\frac{\mu_v}{\mu_l}\right)^{0.65}\left(\frac{\rho_v}{\rho_l}\right)^{0.9}Re_v^{0.75}Bo^{0.25}We_l^{-0.91}. \tag{28}$$

2. Coalescing bubble/annular (CB/A)

$$x_{CB/A} = 0.047Co^{0.05}\left(\frac{\mu_v}{\mu_l}\right)^{0.7}\left(\frac{\rho_v}{\rho_l}\right)^{0.6}Re_v^{0.8}We_l^{-0.91}. \tag{29}$$

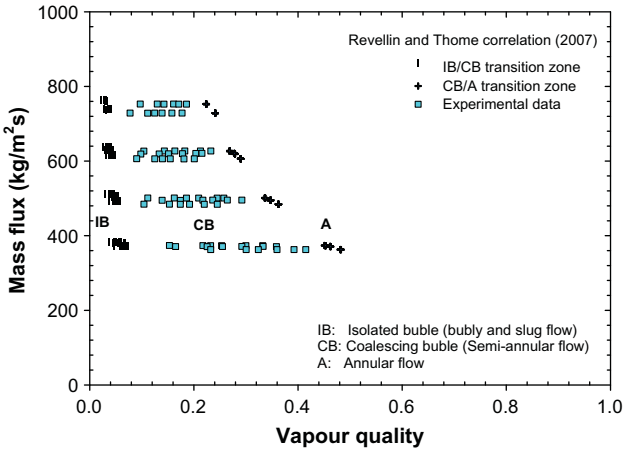

Fig. 4. The comparison of the experimental flow patterns with the transition lines by Revellin and Thome correlation [26].

3. Plug–slug/coalescing bubble (S–P/CB) if ($x_{S-P/CB} < x_{CB/A}$)

$$x_{S-P/CB} = 9(Co^{0.20})\left(\frac{\rho_v}{\rho_l}\right)^{0.9} Fr_l^{-1.2} Re_l^{0.1}. \quad (30)$$

4. Plug–slug/annular (S–P/A) if ($x_{S-P/CB} > x_{CB/A}$)

$$x_{S-P/A} = x_{CB/A}, \quad (31)$$

where Re_v, Re_l, Bo, We_l and Fr_l are respectively defined as:

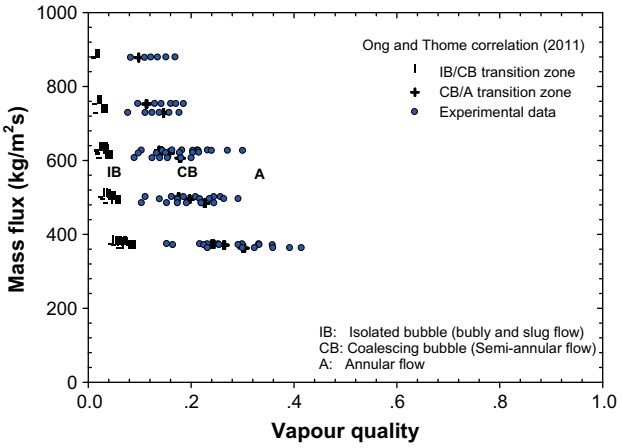

Fig. 5. The comparison of the experimental flow patterns with the transition lines by Ong and Thome correlation [27].

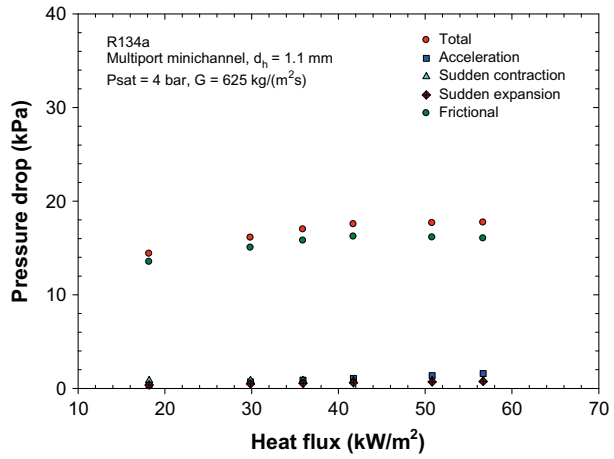

Fig. 6. The pressure drop components as a function of heat flux.

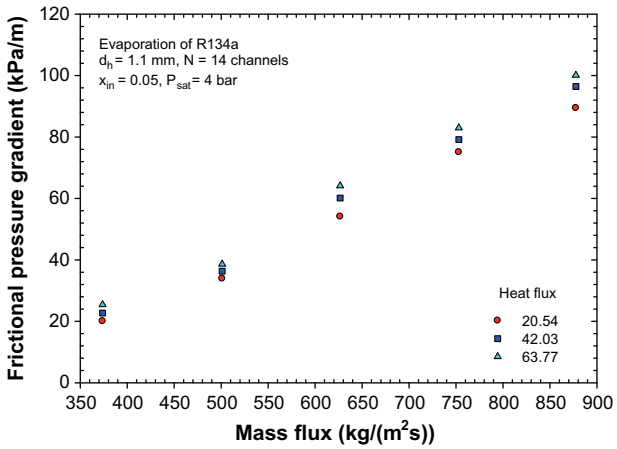

Fig. 7. The frictional pressure gradient as a function of mass flux for different levels of heat flux.

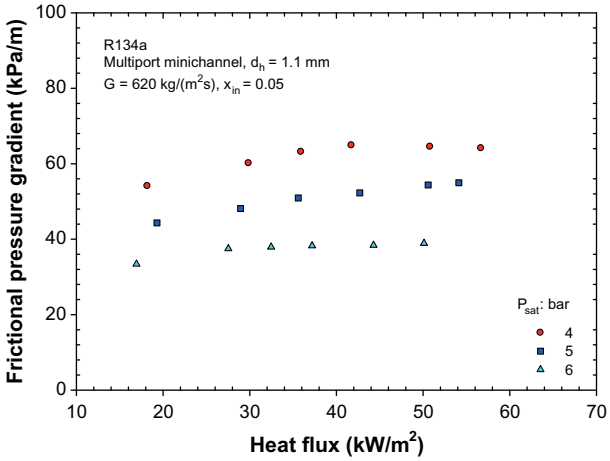

Fig. 8. The frictional pressure gradient as a function of heat flux for different levels of saturation pressure.

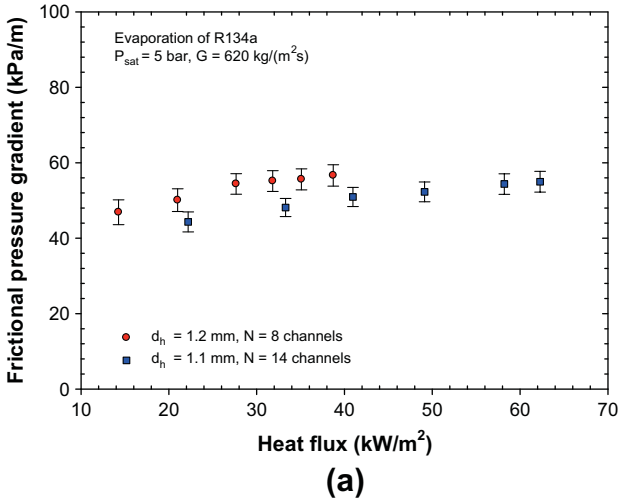

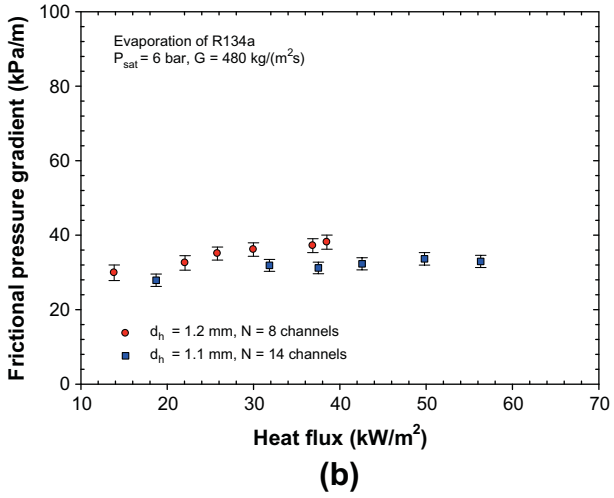

Fig. 9. Comparison the frictional pressure gradient as a function of heat flux for different numbers of channels.

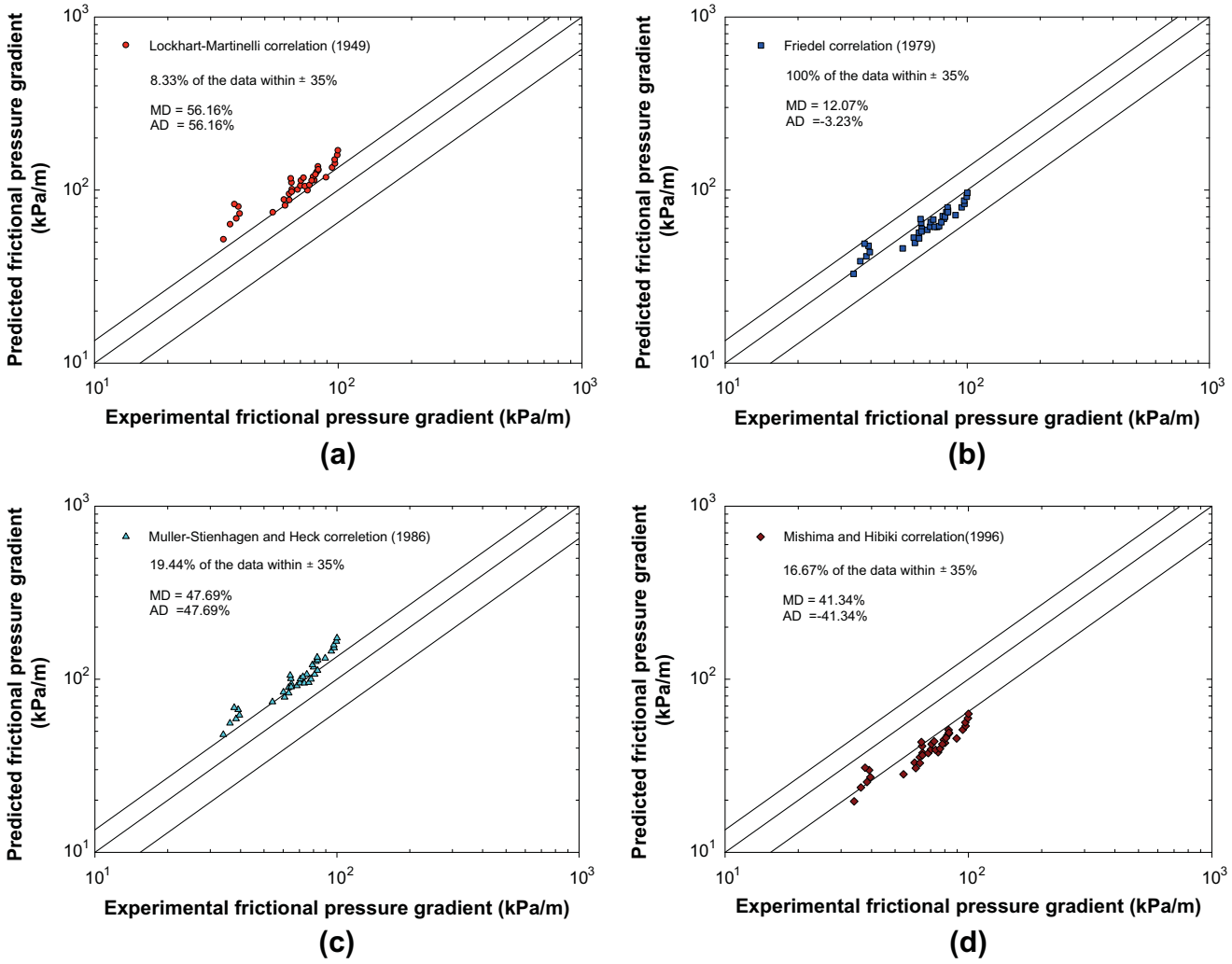

Fig. 10. Comparison of experimental pressure gradient with existing correlations proposed by (a) Lockhart–Martinelli [8], (b) Friedel [2] (c) Müller-Steinhagen and Heck [4], (d) Mishima and Hibiki [19], (e) Zhang and Webb [1], (f) Lee and Mudawar [20], (g) Saisorn and Wongwises [21], (h) Kaew-On and Wongwises [14] and (i) Zhang et al. [16].

$$Re_v = \frac{Gd_h}{\mu_v},\ Re_l = \frac{Gd_h}{\mu_l},\ Bo = \frac{q''}{Gh_{lv}},\ We_l = \frac{G^2 d_h}{\sigma\rho_l},\ Fr_l = \frac{G^2}{\rho_l^2 g d_h}.$$

From the comparison with the flow patterns map of Ong and Thome [27], as presented in Fig. 5, it is found that all experimental data are in all three transition zones (i.e., the isolated bubble zone, coalescing bubble zone, and annular flow zone). From the comparisons of the two flow pattern models, therefore, it can be concluded that the most experimental data in this study are semi-annular and annular flow patterns.

4.2. The pressure drop components

The total pressure drops are composed of the frictional pressure drop, the momentum pressure drop, the sudden contraction pressure drop, and the sudden expansion pressure drop. The components of the pressure drop with the variation of heat fluxes are presented in Fig. 6. The results were obtained at a mass flux of 625 kg/(m^2 s) and the saturation pressure was kept constant at 4 bar. The results show that the frictional pressure drop dominates all other pressure drop components which possess values ranging between 90% and 95% of the total pressure drop. The acceleration pressure drop that is attributed to the change of momentum is about 4–5% of the total pressure drop. In addition, the sudden contraction pressure drop and sudden expansion pressure drop are between 3–5% and 2–4% of the total pressure drop, respectively. This figure also shows that the frictional pressure drop slightly increases with an increase in the supposed heat flux. This is due to the increase of the heat fluxes, which causes the vapor-phase fraction and mean quality to increase. Therefore, the frictional pressure drop increases with an increasing heat flux.

4.3. Frictional pressure gradient

The variations of the frictional pressure gradient with mass flux are presented in Fig. 7. The experiment carried out by varying mass flux from 370 to 980 kg/(m^2 s) for various heat fluxes of 20.54, 42.03, and 63.77 kW/m^2 at a constant saturation pressure of 4 bar and inlet quality of 0.05. The results indicate that the frictional pressure gradient increase when the mass flux increases. This is due to higher shear stress at the tube wall and interfacial shear at the liquid–vapor interface. Moreover, this figure also illustrates that the pressure gradient slightly increases with an increasing heat flux. The increasing heat flux results in a higher vaporization and then leads to an increase in the average fluid vapor quality and flow velocity.

Fig. 8 presents the influence of saturation pressure on the frictional pressure gradient. At constant mass flux and heat flux, the

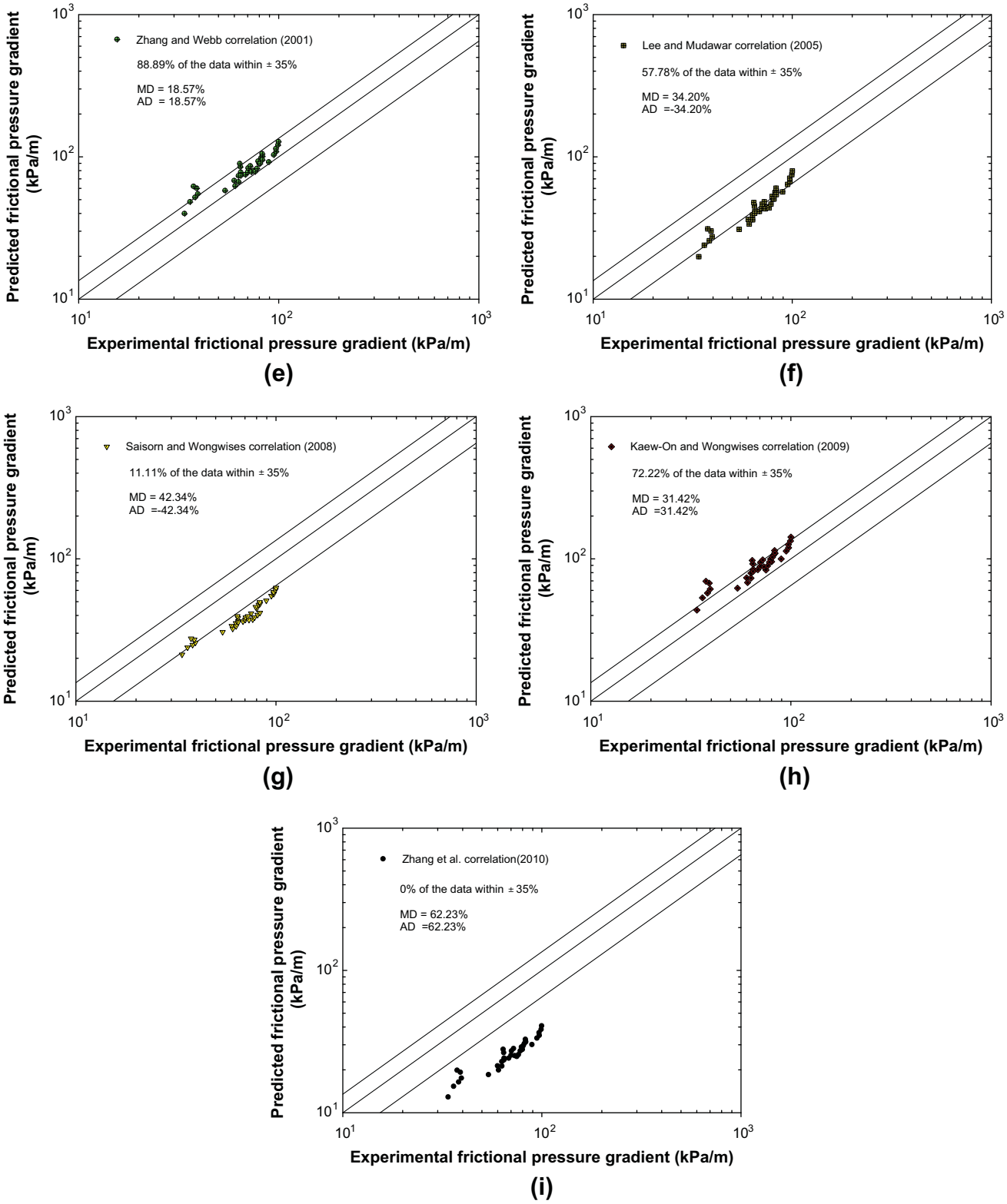

Fig. 10 (*continued*)

results indicate that the frictional pressure gradient increases with decreasing saturation pressure. This can be explained by the difference in the properties of the liquid and vapor phases. Considering that the saturation pressure decreased from 6 to 4 bar, it found that the viscosity ratio, μ_l/μ_v, increased from 17.73 to 21.81 (22.99%), similarity, the density ratio, ρ_l/ρ_{lv}, increase from 41.85 to 64.77 (54.76%). The increasing liquid density and liquid viscosity resulted in a lower liquid velocity, whereas the decreasing vapor density and vapor viscosity result in higher vapor velocity. Moreover, surface tension forces are more dominant at lower pressures, thus the interface between liquid and vapor is less wavy. At lower pressures, the pressure drop increases because of higher liquid

viscosity and an increase relative phase densities. The result is a higher interfacial shear. Therefore, the frictional pressure gradients increase when saturation pressure decreases.

4.4. Comparison results at two different inner tubes

Fig. 7 presents the comparison results that were obtained from the two heat exchangers that contain different inner tube geometries. Two inner tubes were made from extruded multiport aluminium with internal hydraulic diameters of 1.1 mm for 14 numbers of channels (tube No.1) and 1.2 mm for eight numbers of channels (tube No.2). Additional details about the test section are presented in Table. 1. As shown in Fig. 9, the results show that the frictional pressure drop of tube No. 1 is lower than that of tube No. 2 (i.e., approximately 15–20% for Fig. 9a and 10–15% for Fig. 9b). This finding can be explained by the different of geometries of the tubes that were tested. According to the details of the test section as shown in Table 1, although the two test sections are of a similar hydraulic diameter, but there are so different of the aspect ratio, 1.25 for tube No. 1 and 0.5 for tube No. 2. In their investigation, Akbari et al. [28] defined the term of the Poiseuille number, *fRe*, for the microchannel rectangular cross section as follows:

$$fRe = \frac{4\pi^2(1+\beta^2)}{3\sqrt{\beta}(1+\beta)}. \tag{32}$$

As the same mass flux condition, it can be seen from their correlation that the friction factor is only a function of the aspect ratio, β; that is, in support of the present experimental data, the friction factor increased when the aspect ratio decreased. The experimental result in Fig. 9a also reveals similar trends that emerged in Fig. 9b.

4.5. Comparison of experimental data with existing correlations

In this section, the frictional pressure drop obtained from the presented study is compared with the values predicted by both conventional and minichannel tubes. The nine well-known correlations, proposed by Lockhart–Martinelli [8], Friedel [2], Müller-Steinhagen and Heck[4], Mishima and Hibiki [19], Zhang and Webb [1], Lee and Mudawar [20], Saisorn and Wongwises [21], Kaew-On and Wongwises [14], and Zhang et al. [16] are compared to this author's experimental results. The results of the comparisons between the predicted and experimental frictional pressure gradient are presented in Fig. 10. The error band of ±35% is also presented by the solid lines in these figures. The mean and average deviations of the comparisons between the experimental data and predicted values are summarized in Table 4. For all of the comparisons, the Friedel correlation [2] predicted the current experimental data better than the other correlations (i.e., mean and average deviations of 12.07% and −3.23%, respectively). The correlations of Zhang and Webb [1] and Kaew-On and Wongwises [14] reasonably correlated to the current experimental data (i.e., 88.89% and 72.22% fell within ±35% of the error band, respectively). The correlations of Mishima and Hibiki [19], Lee and Mudawar [20], Saisorn and Wongwises [21], and Zhang et al. [16] are under-predicted, while the correlation of Lockhart–Martinelli [8] and Müller-Steinhagen and Heck [4] are over-predicted.

Table 4
Deviation of the frictional pressure gradient comparison between the present data and the existing correlations.

Correlation	Mean deviation %	Average deviation %
Lockhart–Martinelli [8]	56.16	56.16
Friedel [2]	12.07	−3.23
Muller-Stienhagen and Heck [4]	47.69	47.69
Mishima and Hibiki [19]	41.34	−41.34
Zhang and Webb [1]	18.57	18.57
Lee and Mudawar [20]	34.20	−34.20
Saisorn and Wongwises [21]	42.34	−42.34
Kaew-On and Wongwises [14]	31.42	31.42
Zhang et al. [16]	62.23	−62.23

5. Conclusions

This study presents the experimental investigations of the pressure drop of R134a flowing through the two multiport heat exchangers. The heat exchangers include the counter flow tube-in-tube heat exchangers. The experimental process has been applied for a wide range of experimental conditions: Mass fluxes from 350 to 980 kg/(m^2 s), heat fluxes from 18 to 80 kW/m^2, and saturation pressures from 4 to 6 bar. The major finding of this study are summarized as follows:

1. The results of Revelin and Thome [26] and Ong and Thome [27] are applied to determine the flow patterns of the present data. It was determined that most of the experimental data are located within semi-annular and annular flow patterns.
2. According to the total pressure drop components, the frictional pressure drop, acceleration pressure drop, sudden contraction pressure drop, and sudden expansion pressure drop are 90–95%, 4–10%, 3–5%, and 2–4% of the total pressure drop, respectively.
3. According to the effects of the relevant parameters on the frictional pressure drop, the mass flux has a more significant influence on the frictional pressure drop over the others, whereas the frictional pressure drop slightly increases with increasing heat flux. In addition, the frictional pressure drop decreases as the saturation pressure increase.
4. From the comparisons of the frictional pressure drop of two types of heat exchange inner tubes, it was found that the frictional pressure drops of tube No. 1 are lower than those of tube No. 2 (i.e., approximately 10–20%).
5. The Friedel correlation [2] provided the best predictions with the mean deviation of 12.07% and the average deviation of −3.23%, while the Zhang and Webb correlation [1] and Kaew-On and Wongwises correlation [14] satisfactorily predicted all of the data.

Acknowledgements

The present study was supported financially by the Thailand Research Fund, the Office of Higher Education Commission and the National Research University Project, whose guidance and assistance are gratefully acknowledged.

References

[1] M. Zhang, R.L. Webb, Correlation of two-phase friction for refrigerants in small-diameter tubes, Exp. Thermal Fluid Sci. 25 (2001) 131–139.
[2] L. Friedel, Improved frictional pressure drop correlation for horizontal and vertical two-phase flow, European two-phase flow group meeting, 1979.
[3] M.B. Ould Didi, N. Kattan, J.R. Thome, Prediction of two-phase pressure gradients of refrigerants in horizontal tubes, Int. J. Refrig. 25 (2002) 935–947.
[4] H. Müller-Steinhagen, K. Heck, A simple friction pressure drop correlation for two-phase flow in pipes, Chem. Eng. Process 20 (1986) 297–300.
[5] R. Gronnerud, Investigation of liquid hold-up, flow resistance and heat transfer in circulation type evaporators, part iv: two-phase flow resistance in boiling refrigerants, Bull de 1'Inst. Du Froid, 1979 (Annexe, 1972-1).
[6] A. Cavallini, D. Del Col, L. Doretti, M. Matkovic, L. Rossetto, C. Zilio, Two-phase frictional pressure gradient of R236ea, R134a and R410A, Exp. Thermal Fluid Sci. 29 (2005) 861–870.

[7] V.G. Nino, E.W. Jassim, P.S. Hrnjak, T.A. Newell, Flow-regime-based model for pressure drop predictions in microchannels, HVAC&R Research 12 (2005) 17–34.
[8] R.W. Lockhart, R.C. Martinelli, Proposed correlation of data for isothermal two-phase, Two-component flow in pipes, Chemical Engineering Progress 45 (1949) 39–48.
[9] A.W. Mauro, J.M. Quiben, J.R. Thome, Comparison of experimental pressure drop data for two phase flows to prediction methods using a general model, Int. J. Refrig. 30 (2007) 1358–1367.
[10] J.M. Quiben, J.R. Thome, Flow pattern based two-phase frictional pressure drop model for horizontal tubes, part II: new phenomenological model, Int. J. Heat fluid flow 28 (2007) 1060–1072.
[11] A.S. Pamitran, K.-I. Choi, J.-T. Oh, H.-K. Oh, Two-phase pressure drop during CO_2 vaporization in horizontal smooth minichannels, Int. J. Refrig. 31 (2008) 1375–1383.
[12] R. Revellin, P. Haberschill, Prediction of frictional pressure drop during flow boiling of refrigerants in horizontal tubes: Comparison to an experimental database, Int. J. Refrig. 32 (2009) 487–497.
[13] D.S. Jung, R. Radermacher, Prediction of pressure drop during horizontal annular flow boiling of pure and mixed refrigerants, Int. J. Heat Mass Transfer 32 (1989) 2435–2446.
[14] J. Kaew-On, S. Wongwises, Experimental investigation of evaporation heat transfer coefficient and pressure of R410A in multiport minichannel, Int. J. Refrig. 32 (2009) 124–137.
[15] J. Kaew-On, S. Wongwises, Experimental study of evaporation heat transfer characteristics and pressure drops of R410A and R134a in a multiport mini-channel, Proceedings of the 7th International Conference on Nanochannels, Microchannels and Minichannels 2009, ICNMM2009 (PART A), 581–588.
[16] M. Zhang, T. Hibiki, K. Mishima, Correlation of two-phase frictional pressure drop and void fraction in min-channel, Int. Heat and Mass Transfer 53 (2010) 453–465.
[17] R.C. Martinelli, D.B. Nelson, Prediction of pressure drop during forced circulation boiling of water, Trans. ASME 70 (1948) 695–702.
[18] D. Chisholm, Pressure gradients due to friction during the flow of evaporating two-phase mixtures in smooth tubes and channels, Int. Heat and Mass Transfer 16 (1973) 347–358.
[19] K. Mishima, T. Hibiki, Some characteristics of air-water two-phase flow in small diameter tube, J. Multiphase Flow 22 (1996) 703–712.
[20] J. Lee, I. Mudawar, Two-phase flow in high-heat-flux micro-channel heat sink for refrigeration cooling applications: Part I—pressure drop characteristics, Int. J. Heat Mass Transfer 48 (2005) 928–940.
[21] S. Saisorn, S. Wongwises, Flow pattern, void fraction and pressure drop of two-phase air–water flow in a horizontal circular micro-channel, Exp. Thermal Fluid Sci. 32 (2008) 748–760.
[22] J. Kaew-On, K. Sakamatapan, S. Wongwises, Flow Boiling Heat Transfer of R134a in the Multiport Minichannel Heat Exchangers, Exp. Thermal Fluid Sci. 35 (2011) 364–374.
[23] REFPROP, NIST, Refrigerant Properties Database 23, Gaithersburg, MD, 1998, Version 6.01.
[24] J.G. Collier, J.R. Thome, Convective boiling and condensation, 3rd ed., Oxford University Press, Oxford, U.K., 1994.
[25] S.M. Zivi, Estimation of steady-state steam void–fraction by mean of the principle of minimum entropy production, Trans. ASME, J. Heat Transfer 86 (1964) 247–252.
[26] R. Revellin, J.R. Thome, A new type of diabatic flow pattern map for boiling heat transfer in microchannels, J. Micromech. Microeng 17 (2007) 788–796.
[27] C.L. Ong, J. Thome, Macro-to-microchannel transition in two-phase flow: part 1 – two-phase flow patterns and film thickness measurements, Exp. Thermal Fluid Sci. 35 (2011) 37–47.
[28] M. Akbari, D. Sinton, M. Bahrami, Pressure drop in rectangular microchannels as compared with theory based on arbitrary cross section, J. Fluid Eng. 131 (2009) 1–8.

Heat Transfer Engineering
Publication details, including instructions for authors and subscription information:
http://www.tandfonline.com/loi/uhte20

Selected Papers on Advances in Heat Transfer

Sujoy K. Saha [a] , Gian P. Celata [b] & Somchai Wongwises [c]

[a] Mechanical Engineering Department, Bengal Engineering and Science University, West Bengal, India

[b] ENEA, Energy Department, Institute of Thermal Fluid Dynamics, Rome, Italy

[c] Department of Mechanical Engineering, King Mongkut's University of Technology Thonburi, Bangmod, Bangkok, Thailand

Available online: 18 Nov 2011

To cite this article: Sujoy K. Saha, Gian P. Celata & Somchai Wongwises (2012): Selected Papers on Advances in Heat Transfer, Heat Transfer Engineering, 33:4-5, 281-283

To link to this article: http://dx.doi.org/10.1080/01457632.2012.614157

Heat Transfer Engineering, 33(4–5):281–283, 2012

ISSN: 0145-7632 print / 1521-0537 online
DOI: 10.1080/01457632.2012.614157

editorial

Selected Papers on Advances in Heat Transfer

SUJOY K. SAHA,[1] GIAN P. CELATA,[2] and SOMCHAI WONGWISES[3]

[1]Mechanical Engineering Department, Bengal Engineering and Science University, West Bengal, India
[2]ENEA, Energy Department, Institute of Thermal Fluid Dynamics, Rome, Italy
[3]Department of Mechanical Engineering, King Mongkut's University of Technology Thonburi, Bangmod, Bangkok, Thailand

Advancement of technology in virtually all fields, in one way or another, has been due to simultaneous advances in thermal engineering. Design objectives of space stations, hazardous-waste destruction, high-speed transport, electronics, materials processing and manufacturing, etc. are fulfilled by proper energy management, heat-flow control, and temperature control.

The scale of thermal engineering ranges from the very large to the near-molecular level and from very high temperatures of thousands of degrees to very low ones approaching absolute zero. Thermal energy transport occurs in every walk of human existence.

In the recent past and of course with the passage of time, tremendous progress has been made in the field of thermal science and engineering. It is a continuous process and the quest of knowledge is truly unending.

In this special issue of the journal, an attempt has been made to collate some scattered knowledge in the advances in heat transfer. Leading international heat transfer experts from the diverse fields of heat transfer have contributed in this special issue. It should be useful to the readers of the journal. This special issue is a compendium of the following 10 papers.

- The first paper is "Thermal Design of Multistream Plate Fin Heat Exchangers—A State-of-the-Art Review" by Prasanta Kumar Das and Indranil Ghosh:

Address correspondence to Professor Sujoy K. Saha, Mechanical Engineering Department, Bengal Engineering and Science University, Shibpur, Howrah 711 103, West Bengal, India. E-mail: sujoy_k_saha@hotmail.com

Multistream plate fin heat exchangers are useful and important innovations in the design of heat exchangers. These heat exchangers encounter direct/indirect crossover in temperatures due to several thermal communications among the fluid streams, and their thermal performance depends on "stacking pattern." Extension of the commonly used design/simulation techniques like ε-NTU or the LMTD method, applicable for two-stream heat exchangers, fails miserably in case of multistream units. Though several techniques have been suggested over the years, the "thermal design" method of multistream plate fin heat exchangers is far from being perfect even today.

A state-of-the-art review of the thermal design of multistream plate fin heat exchangers is presented by the authors. Different methods of analysis including "area splitting" and "successive partitioning" along with their merits and demerits are discussed. Basic thermal design methodology and its optimization, the techniques adopted for accounting variable fluid properties, axial heat conduction in the solid matrix, and thermal communication with the environment are discussed. Need for further research is emphasized.

- The second paper is "Dropwise Condensation Studies on Multiple Scales" by Basant Singh Sikarwar, Sameer Khandekar, Smita Agarwal, Sumeet Kumar, and K. Murlidhar:

New surfaces are being engineered by nanotechnology, chemical texturing technologies, thin film coatings, and physical texturing using advanced manufacturing techniques. Dropwise condensation rather than film condensation occurs on those special surfaces. Superior experimental techniques are now available to study the thermo-fluid dynamics of dropwise condensation. Phenomena at different hierarchical length

scales, e.g., surface modification at the microscale, nuclei formation, formation of clusters, macroscopic droplet ensemble, and drop coalescence, are involved. Atomistic modeling of initial nucleation, droplet–substrate interaction, surface preparation, preliminary results on simulation of fluid motion inside sliding drops, experimental determination of the local and average heat transfer coefficient, and a macroscopic model of the complete dropwise condensation process underneath horizontal and inclined surfaces are discussed.

- The third paper is "Modified Wilson Plots for Enhanced Heat Transfer Experiments: Current Status and Future Perspectives" by E. van Rooyen, M. Christians, and J. R. Thome:

Performance of enhanced heat transfer tubes is evaluated indirectly using the "Wilson plot" method to first characterize the thermal performance of one side (heating or cooling supply) and then obtaining the heat transfer data for the enhanced side based on the Wilson plot results. Wilson plot evolution and alternative methods to the Wilson plot including the advantages and disadvantages are discussed. The existing method has been modified so that the experimental errors can be propagated through the method and the error in the generated correlations may be estimated. A new method based on unconstrained minimization is proposed as an alternative to the least-squares regression.

- The fourth paper is "A State-of-the-Art Review of Compact Vapor Compression Refrigeration Systems and Their Applications" by Jader R. Barbosa, Jr., Guilherme B. Ribeiro, and Pablo A. de Oliveira:

Literature on the fundamentals, design, and application aspects of compact and miniature mechanical vapor compression refrigeration systems has been critically reviewed. Vapor compression enables the attainment of low evaporating temperatures while maintaining a large cooling capacity per unit power input to the system. Miniaturization of system components, particularly the compressor, has been the significant development. When compared with competing cooling technologies, such as flow boiling in microchannels, jet impingement and spray cooling refrigeration is the only one capable of lowering the junction temperature to values below the ambient temperature. The simultaneous use of vapor compression refrigeration with the aforementioned technologies is also possible, necessary, and beneficial, since it increases greatly the potential for reducing the system size. The paper sheds some light on the thermodynamic and thermal aspects of the cooling cycle and on the recent developments regarding its components (compressor, heat exchangers and expansion device). Issues and challenges associated with the different cycle designs have been addressed. An overview of the ongoing efforts in competing technologies is also presented.

- The fifth paper is "Modeling of Evaporation and Combustion of Droplets in a Spray Using the Unit Cell Approach: A Review" by Achintya Mukhopadhyay and Dipankar Sanyal:

Modeling of evaporation and combustion of liquid fuel droplets using "unit cell" approach has been reviewed extensively. Different regimes of droplet combustion and other techniques used for evaluating mutual interaction of droplets are discussed first, followed by the detailed presentation of the cell model. Gas-phase convection, high pressure, and multicomponent composition of fuels are reviewed for both dense and dilute sprays.

- The sixth paper is "Loop Heat Pipes: A Review of Fundamentals, Operation, and Design" by Amrit Ambirajan, Abhijit A. Adoni, Jasvanth S. Vaidya, Anand A. Rajendran, Dinesh Kumar, and Pradip Dutta:

The loop heat pipe (LHP) is a passive two-phase heat transport device. LHPs are used in spacecraft thermal control system and in avionics cooling and submarines. A major advantage of a loop heat pipe is that that the porous wick structure is confined to the evaporator section, and connection between the evaporator and condenser sections is by smooth tubes, thus minimizing pressure drop. Basic fundamentals, construction details, operating principles, typical operating characteristics, and current developments in modeling of thermohydraulics and design methodologies of LHPs are discussed.

- The seventh paper is "Augmentation of Heat Transfer by Creation of Streamwise Longitudinal Vortices Using Vortex Generators" by Gautam Biswas, Himadri Chattopadhyay, and Anupam Sinha:

A state-of-the-art review of improving heat exchanger surfaces using streamwise longitudinal vortices is presented. Fin-tube cross-flow heat exchangers and the plate-fin heat exchangers are focused on. Protrusions in certain forms such as delta wing or winglet pairs and rectangular winglet pairs act as vortex generators, creating longitudinal vortices, disrupting growth of the thermal boundary layer, and promoting mixing between fluid layers, resulting in enhanced heat transfer from the flat or louvered surfaces. The flow fields are dominated by a swirling motion associated with a modest pressure penalty. Both computational and experimental investigations on flow and heat transfer in the heat exchanger passages with built-in vortex generators are reviewed.

- The eighth paper is "Frictional and Heat Transfer Characteristics of Single-Phase Microchannel Liquid Flows" by Ranabir Dey, Tamal Das, and Suman Chakraborty:

The literature on friction and heat transfer characteristics of single-phase liquid flows through microchannels has been reviewed. The disagreement of experimental results with theoretical predictions has been brought to the fore. Theoretical models and empirical correlations are highlighted. Aspects of microscale liquid flow and heat transfer requiring further scrutiny are identified and possible future research directions are prescribed.

- The ninth paper is "Recent Trends in Computation of Turbulent Jet Impingement Heat Transfer" by Anupam Dewan, Rabijit Dutta, and Balaji Srinivasan:

> A review of the current status of computation of turbulent impinging jet heat transfer has been made. Flow and heat transfer characteristics of single jet impingement on a flat surface are considered. The effect of different sub-grid scale models, boundary conditions, numerical schemes, grid distribution, and size of the computational domain adopted in various large eddy simulations of this flow configuration is dealt with in detail. Direct numerical simulation and Reynolds-averaged Navier–Stokes modeling of the same geometry are discussed. Other complex impinging flows are also presented. A listing of some important findings and future directions in the computation of impinging flows is presented.

- The tenth paper is "Two-Phase Natural Circulation Loops: A Review of the Recent Advances" by Souvik Bhattacharyya, Dipankar N. Basu, and Prasanta K. Das:

> Experimental and theoretical studies of two-phase natural circulation loops abound in the literature. A comprehensive review has been made by the authors. Different forms of thermal-hydraulic instabilities and coupled nuclear instabilities are discussed. Further research direction is delineated.

We thank the authors for their contributions, and the reviewers, who have played a great role in improving the quality of the papers. We also thank the editor-in-chief of *Heat Transfer Engineering*, Professor Afshin Ghajar, for his willingness to publish this special issue highlighting the current research going on worldwide.

Sujoy K. Saha is a professor of mechanical engineering at Bengal Engineering and Science University Shibpur, India. He specializes in heat transfer enhancement, heat transfer in microchannels, biomimetics, and circulating fluidized bed. Prof. Saha is an associate editor of *ASME Journal of Heat Transfer*, editor of *Experimental Thermal and Fluid Science*, associate editor of *Heat Transfer Engineering*, regional editor of the *Journal of Enhanced Heat Transfer,* and guest editor of *Frontiers of Heat and Mass Transfer*. Prof. Saha has published about 60 articles in international and national peer-reviewed journals and conferences.

Gian P. Celata is director of the Division of Advanced Technologies for Energy and Industry of ENEA, Italy. He is a member of the European Academy of Sciences, of several scientific boards in Italy (UIT, past-President, ANIMP, AIDIC), and also of international scientific boards (EUROTHERM, past president, AIHTC, AWC, vice-president, ICHMT, Executive Committee). Dr. Celata is also the editor-in-chief of the *Journal of Experimental Thermal and Fluid Science* and associate editor of the *International Journal of Thermal Sciences*. He is also the editor of *Thermopedia and Heat Exchangers Design Handbook*. His areas of expertise are heat transfer and two-phase flow, CHEx, microscale heat transfer, bubbly flow, two-phase critical flow, and CHF. He has about 200 articles in international journals and international conferences, and one patent, and is the editor of many scientific books.

Somchai Wongwises is a professor of mechanical engineering at King Mongkut's University of Technology Thonburi, Bangmod, Thailand. He received his Dr.-Ing. (Doktor Ingenieur) in mechanical engineering from the University of Hannover, Germany, in 1994. His research interests include two-phase flow, heat transfer enhancement, and thermal system design. Professor Wongwises is the head of the Fluid Mechanics, Thermal Engineering and Multiphase Flow Research Laboratory (FUTURE).

INTERNATIONAL JOURNAL OF REFRIGERATION 35 (2012) 27–35

Available online at www.sciencedirect.com

SciVerse ScienceDirect

journal homepage: www.elsevier.com/locate/ijrefrig

Review

Review on the experimental studies of refrigerant flow mechanisms inside short-tube orifices

Kitti Nilpueng [a], Somchai Wongwises [a,b,*]

[a] Fluid Mechanics, Thermal Engineering and Multiphase Flow Research Lab (FUTURE), Department of Mechanical Engineering, King Mongkut's University of Technology Thonburi, Bangmod, Bangkok 10140, Thailand

[b] The Academy of Science, The Royal Institute of Thailand, Sanam Suea Pa, Dusit, Bangkok 10300, Thailand

ARTICLE INFO

Article history:
Received 24 May 2011
Received in revised form
7 September 2011
Accepted 24 September 2011
Available online 2 October 2011

Keywords:
Expansion valve
Flow rate
Critical pressure
Temperature variation

ABSTRACT

A short-tube orifice is a kind of an expansion device. The advantages of a short-tube orifice are simplicity, low cost, and low starting torque of the compressor as the pressures across the short-tube orifice equalise during the off-cycle. The two-phase flow mechanisms of refrigerant inside the short-tube orifice are very complicated although its physical configurations are simple. During the past decade, investigations of the mass flow rate of various refrigerants inside short-tube orifices, which is useful for selecting the proper size in practical applications, have been reported by many researchers. However, few researchers focused on the flow pattern, choked flow, and metastable flow phenomena inside short-tube orifices, which are necessary for a clear understanding of the flow behaviour and developing suitable calculation techniques. The aim of this paper is to summarise the evolution of the experimental research on refrigerant flow characteristics inside short-tube orifices to provide guidelines for future research.

Passage en revue des études expérimentales sur les mécanismes du débit du frigorigène dans les orifices de tubes courts

Mots clés : détendeur ; débit ; pression critique ; variation de température

1. Introduction

An expansion device is one of the four important components of the vapour compression refrigeration system. The main purposes of the expansion device are to reduce the pressure of the refrigerant from the condenser pressure to the evaporator pressure and to regulate the mass flow rate of refrigerant flowing from the condenser to the evaporator at a rate equal to

* *Corresponding author*. Fluid Mechanics, Thermal Engineering and Multiphase Flow Research Lab (FUTURE), Department of Mechanical Engineering, King Mongkut's University of Technology Thonburi, Bangmod, Bangkok 10140, Thailand. Tel.: +662 470 9115; fax: +662 470 9111.
E-mail address: somchai.won@kmutt.ac.th (S. Wongwises).

0140-7007/$ – see front matter © 2011 Elsevier Ltd and IIR. All rights reserved.
doi:10.1016/j.ijrefrig.2011.09.011

Nomenclature

D	diameter, m
f	fanning friction factor
G	mass flux, kg m^{-2} s^{-1}
P_v	actual vapourisation pressure, Pa
P_{inlet}	inlet pressure, Pa
P_c	critical pressure, Pa
z_m	length of short-tube orifice in metastable region, mm

Greek symbols

ρ	density, kg m^{-3}
v	specific volume, m^3 kg^{-1}
μ	viscosity, kg m^{-1} s^{-1}

Subscripts

c	critical
f	liquid-phase
g	gas-phase

the evaporation rate in the evaporator. During the flow of liquid refrigerant through the expansion device, the pressure decreases rapidly below the saturation pressure and the refrigerant is changed from a subcooled liquid or saturated liquid to a liquid–vapour mixture. This behaviour is defined as a flashing process.

Basically, there are two types of expansion devices: the variable-restriction type and the constant-restriction type. In the former, the flow area can be varied depending on the control system, such as automatic expansion valve or thermostatic expansion valve. In the latter, the flow area of the expansion device, for example, a capillary tube, ejector, or short-tube orifice, is fixed.

In recent years, the short-tube orifice has been popularly used as an expansion device in residential and automotive air conditioners. The short-tube orifices used in small residential air conditioners are made from extremely small bore hollow brass ingots with lengths of 10–13 mm and L/D = 3–20, while the diameter and L/D of short-tube orifices for automotive applications are 1–2 mm and 21–35, respectively (Fang, 2001). The advantages of the short-tube orifice over the thermostatic expansion valve are simplicity, low initial cost, and low starting torque of the compressor, as the pressures across the short-tube orifice equalise during the off-cycle.

Although the short-tube orifice's physical configuration is very simple, the two-phase flow behaviours inside the tube are complicated. Experimental results from previous studies (Aaron and Domanski, 1990; Kim, 1993; Liu et al., 2004; Nilpueng and Wongwises, 2009a) indicated that the choked flow and metastable flow phenomena existed inside a short-tube orifice under the normal operating conditions of an air conditioner and heat pump. As a result, the refrigerant flow characteristics inside a short-tube orifice not only depended on the working conditions, but were also significantly affected by these flow phenomena.

The aim of this paper is to review the literature on the refrigerant flow characteristics including flow pattern, pressure and temperature distribution, metastable flow, choked flow, and mass flow rate inside short-tube orifices and to suggest guidelines for future research work.

2. Flow pattern

During the flashing process, the flow of liquid refrigerant changes from a subcooled liquid or saturated liquid to a liquid–vapour two-phase flow. It is not possible to understand the refrigerant flow mechanism without a clear understanding of the flow patterns encountered, as it is expected that the flow patterns will influence the two-phase pressure drop, holdup, system stability, exchange rates of momentum, and heat and mass transfer during the phase change. Therefore, investigation of the flow pattern inside the channel is very useful.

Pasqua (1953) studied the flow behaviour of subcooled and saturated liquid CFC-12 through glass short tubes with length to diameter ratios ranging between 4 and 24. He found four distinct flow patterns when the pressure differential between upstream and downstream was increased as shown in Fig. 1. At a very low pressure differential (Regime AB), the flow of refrigerant remained in the liquid state at the entrance and exit of the short-tube orifice. It was also observed that the vena contracta appeared inside the short-tube orifice. When the pressure differential was increased (Regime BC), the liquid refrigerant started to evaporate between the vena contracta and the solid wall because the refrigerant pressure reached the saturation pressure. The flow pattern was in the form of a liquid jet encircled by a ring of two-phase mixture as the pressure differential was higher (Regime CD). He noted that the refrigerant at the central core of the tube was in a metastable state. At a high pressure differential (Regime DE), it was seen that the liquid refrigerant at the vena contracta changed into the mist jet of a two-phase mixture. He stated that the liquid refrigerant began to flash inside the short-tube orifice when the downstream pressure was approximately at or below the saturation pressure. In addition, he concluded that the metastable liquid diameter decreased as the fluids proceeded to the exit. According to Pasqua's results, it may be concluded that the flow pattern in regimes CD and DE appeared in the short-tube orifice when the downstream pressure used in the common air conditioner was lower than the saturation pressure.

The flow pattern of saturated and nearly saturated water flowing through a short-tube orifice with a ratio of length to diameter less than 6 was also observed by Zaloudek (1963). He reported that the results were similar to the photograph obtained by Pasqua (1953).

Fauske (1965) and Henry (1970) investigated the flow pattern of subcooled and saturated liquid inside sharp-edged short-tube orifices with different length to diameter ratios. They found that three flow patterns appeared inside the short-tube orifice when the length to diameter ratio was varied (Fig. 2). For L/D < 3, a superheated liquid commonly flowed at the central core of the tube in the form of a free streamline jet and was surrounded by a vapour annulus. For the short-tube orifice with 3 < L/D < 12, the liquid jet at the

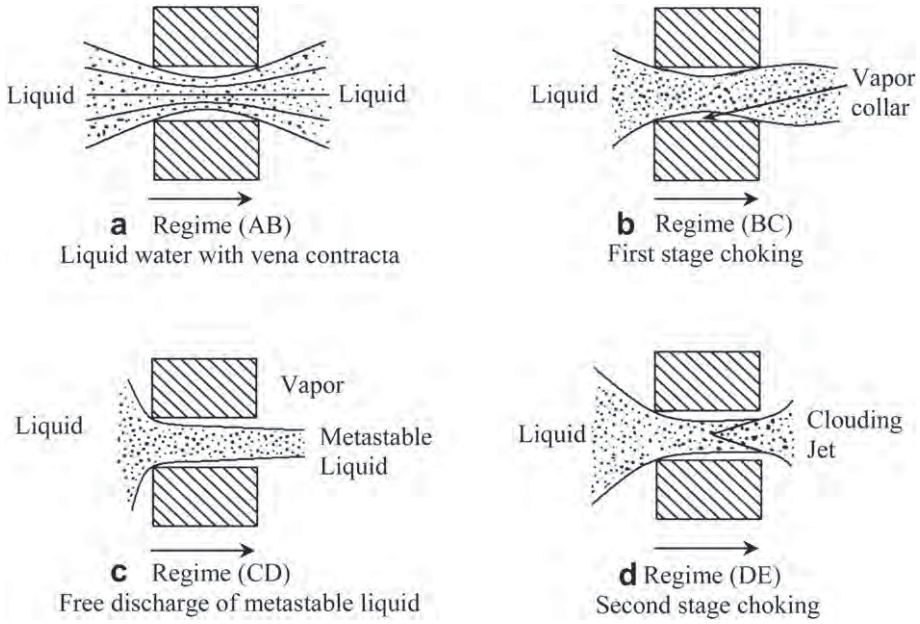

Fig. 1 – Flow patterns inside the short-tube orifice (Pasqua, 1953).

exit region of the tube was broken and changed into bubbles at the surface of the jet. When the length to diameter ratio was higher than 12,it was found that the flow pattern was divided into two regions: a superheated liquid jet flow region and a dispersed two-phase flow region. In the superheated liquid jet flow region, a liquid jet flowed at the central core of the tube and was surrounded by a vapour annulus. In the dispersed two-phase flow region, the mixture of the two-phase flow covered the entire cross-sectional flow area.

Aaron and Domanski (1990) observed the flow pattern of subcooled liquid HCFC-22 at the inlet and outlet of short-tube orifices with $5 < L/D < 20$. In order to fix a brass short-tube orifice with a glass short-tube and prevent refrigerant leakage, the perimeter of the brass short-tube orifice was tightened by a rubber o-ring. The results indicated that the refrigerant existed in the liquid state at the inlet and outlet of short-tube orifices even though the downstream pressure reached saturation pressure. They explained that under this condition, the two-phase mixture recondensed into liquid refrigerant inside the tube. However, under the normal downstream pressure of an air conditioner, the microscopic bubbles suspended in the liquid covered the short-tube orifice outlet in a homogeneous form over several inches.

The flow behaviours of HCFC-22 and HFC-134a along the short-tube orifice were visually investigated by Kim (1993). In order to observe the refrigerant flow at the entrance region, exit region, and inside the short-tube orifice, a glass short-tube orifice was connected with two glass tubes using frame solder. The glass short-tube orifice was attached to a copper tube using a Swagelok connector and Teflon ferrule to prevent leakage of the refrigerant. The results obtained from HFC-134a showed that the metastable liquid core which was enclosed by the two-phase mixture appeared inside the short-tube orifice when subcooled liquid entered the short-tube orifice. It was also found that the flashing point of refrigerant moved to the inlet section as the degree of subcooling decreased. In the case of a two-phase flow entering the short-tube orifice, bubbly flow and stratified wavy flow occurred at low inlet quality ($x < 4\%$) and high inlet quality ($x > 4\%$), respectively. Considering the effect of oil concentration on the flow pattern at a high degree of subcooling ($\Delta T_{sub} > 8.3\ ^{\circ}C$), the flashing point of refrigerant moved slightly to the exit region as the oil concentration increased. They stated that the variations in flow pattern of HCFC-22 and HFC-134a inside the short-tube orifice were similar.

Nilpueng and Wongwises (2009a) and Nilpueng and Wongwises (2009b) investigated the flow pattern of HFC-134a inside short-tube orifices under general operating conditions. Glass tubes without flame solder were specially designed to ensure that the entrance and exit of the short-tube orifice were sharp-edged. In order to prevent leakage of the refrigerant, the glass short-tube orifice and the glass tube were fitted into an acrylic tube and rubber o-rings were inserted between the glass tubes. The flow pattern of refrigerant inside the short-tube orifice was registered by a digital camera with a shutter speed of 1/2000 s mounted together with a 20X magnification lens. The flow pattern of refrigerant inside the short-tube orifice was divided into two regions: the metastable liquid flow region and the two-phase flow region (Fig. 3). From the images in this study, the light (white) area represented the liquid refrigerant flow while the dark (black) area represented the two-phase refrigerant flow of liquid and vapour. In the metastable liquid flow region, the liquid refrigerant, which had the appearance of a cone shape, flowed in the central core of the tube while the two-phase flow, which had many tiny bubbles mixed in the liquid refrigerant, covered the liquid refrigerant. In the two-phase flow region, there were many tiny bubbles mixed with the liquid refrigerant so that it looked misty. They reported that the length of metastable liquid flow increased when the upstream pressure

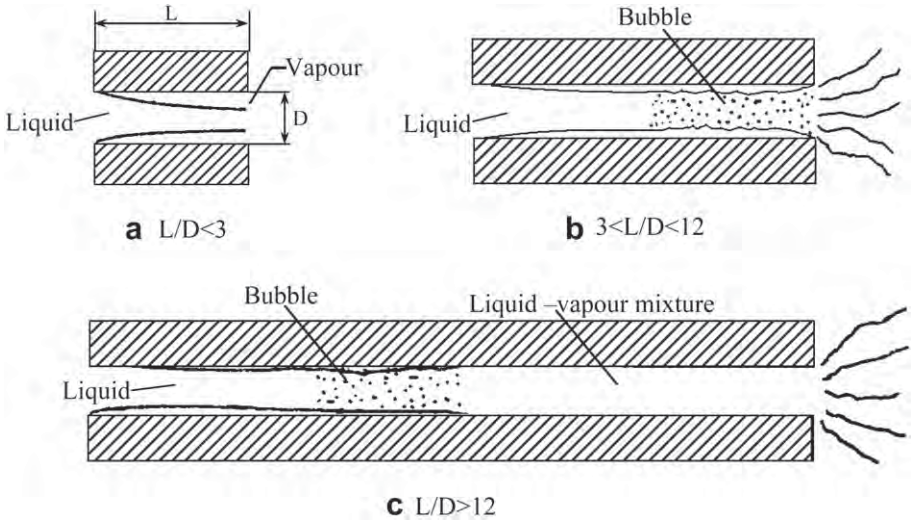

Fig. 2 – Flow patterns of saturated or subcooled liquid through sharp-edge orifices at different ratio of length to diameter (Fauske, 1965; Henry, 1970).

and degree of subcooling were increased. In addition, it was also found from Fig. 4 that at length-to-diameter ratios ranging between 1.87 and 33 the metastable liquid flow inside the short-tube orifice was divided into three different forms: metastable liquid core flow ($L/D < 2.91$), conical metastable liquid core flow ($2.91 \leq L/D < 24.9$), and full metastable liquid flow ($L/D \geq 24.9$).

3. Pressure and temperature distribution

One of the purposes of a refrigerant expansion device is to reduce the refrigerant pressure from the condenser pressure to the evaporator pressure, which also results in a temperature drop. Over the years, pressure and temperature distributions inside short-tube orifices have been studied and published by some researchers (Aaron and Domanski, 1990; Kim, 1993; Liu et al., 2004; Nilpueng and Wongwises, 2009a,b; Chen et al., 2004).

The pressure distribution of HCFC-22 through a short-tube orifice with $L = 12.7$ mm and $D = 1.35$ mm was presented by Aaron and Domanski (1990). Six pressure taps having diameters of 0.08 mm were drilled along the tube length. Pressure transducers with an accuracy of ±0.15% were used to measure the pressure distribution.

Kim (1993) investigated the pressure distribution inside three short-tube orifices: (1) $L = 12.83$ mm and $D = 1.33$ mm, (2) $L = 25.35$ mm and $D = 1.34$ mm, and (3) $L = 12.69$ mm and $D = 1.63$ mm. HCFC-22 and HFC-134a were used as working fluids. Five or six pressure taps with diameter of 0.2 mm were drilled along the length of the short-tube.

The pressure and temperature distributions of carbon dioxide in a short-tube orifice with $D = 1.35$ mm and $L = 12.92$ mm were studied by Liu et al. (2004) and Chen et al. (2004). In order to decrease the effect of taps on the measurement of refrigerant flow rate, low pressure and low temperature taps ($D = 0.1$ mm) were bored by laser equipment. The difference in mass flow rate in cases before and after perforation was measured. It was discovered that the deviation in measurement was ±1.5%.

Nilpueng and Wongwises (2009a) and Nilpueng and Wongwises (2009b) observed the pressure and temperature distribution of HFC-134a inside short-tube orifice. A short-tube orifice diameter of 0.961 mm and lengths of 10 mm, 15 mm, and 20 mm were used in the experiment. Along the short-tube length, six pressure and temperature taps were bored to 0.2 mm using a wire cutting machine. Based on the results obtained from the above researchers, it was found that the pressure distribution along the short-tube orifice could be divided into three regions: inlet section, constant cross-section, and

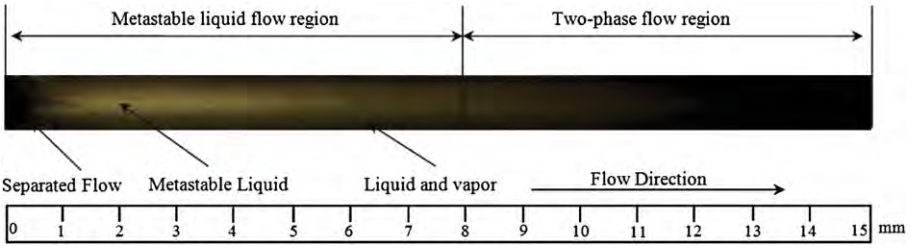

Fig. 3 – Flow pattern of HFC-134a inside a short-tube orifice (Nilpueng and Wongwises, 2009a).

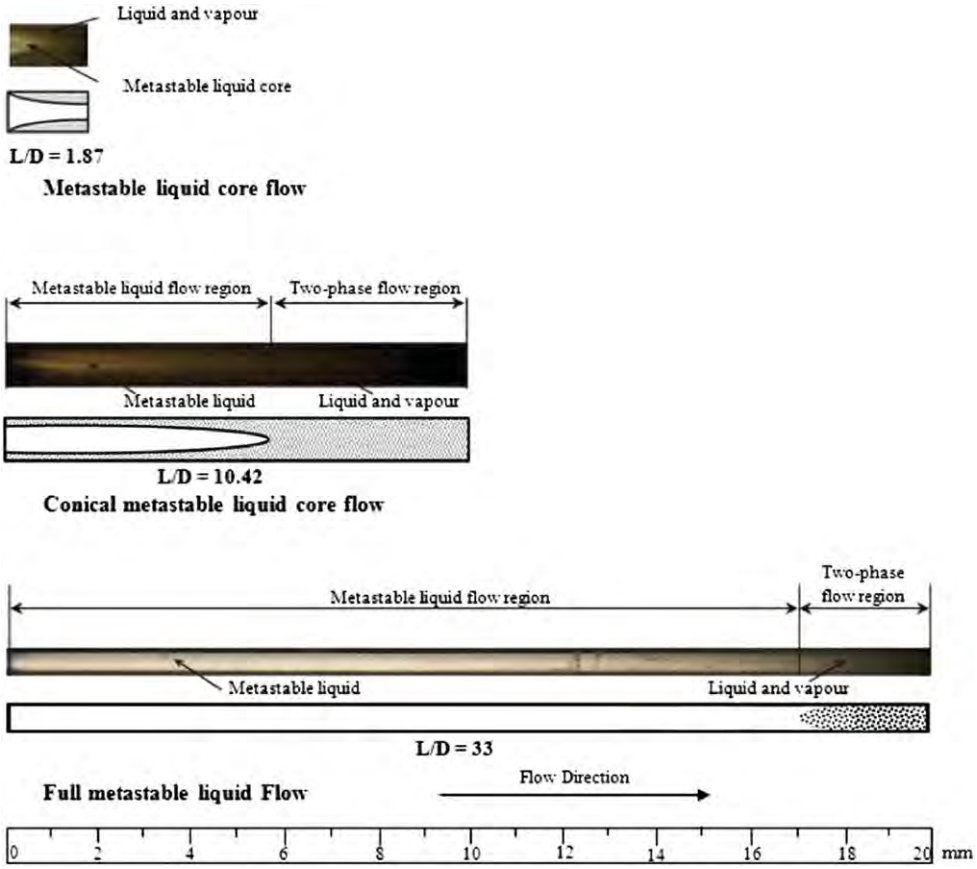

Fig. 4 – Effect of length-to-diameter ratio of short-tube orifice on flow pattern inside a short-tube orifice (Nilpueng and Wongwises, 2009b).

outlet section. The typical pressure and temperature distribution of HFC-134a along a short-tube orifice is illustrated in Fig. 5. It was clear that the pressure decreased rapidly at the inlet and outlet sections, while the pressure decreased slightly inside the constant cross-section under the normal working conditions of the air conditioner (P_{down} = 300–400 kPa). The reason for the enormous pressure drop at the inlet section was explained by the rapid change in acceleration and the loss of flow due to sudden contraction. That is, the upstream pressure was suddenly converted into kinetic energy and the pressure loss was produced due to an inertial effect and wall shear stress at the inlet section. With a constant cross-section, the pressure of HCFC-22 and HFC-134a increased slightly and then decreased steadily inside the constant cross-section. The reason for this was explained by the slight increase in the refrigerant flow area at the beginning of the constant cross-section and the shear stress between the refrigerant and tube wall along the constant cross-section, respectively. They also concluded that the vena contracta appeared at the beginning of the constant cross-section (Aaron and Domanski, 1990; Kim, 1993; Nilpueng and Wongwises, 2009a,b).

However, for carbon dioxide, the refrigerant pressure along the constant cross-section gradually decreased. That is, the increase in pressure at the beginning of the constant cross-section did not appear (Liu et al., 2004; Chen et al., 2004). When considering the pressure variation at the outlet section, it was found that the pressure decreased greatly. This implied that the flow behaviour of the refrigerant was not in agreement with the incompressible fluid flow theory but was similar to compressible flow through a converging nozzle when the velocity in the exit plane reached sonic speed. Under this condition, they stated that the pressure decreased discontinuously from the exit plane to the downstream pressure value. This behaviour was defined as the choked flow phenomenon. Conversely, the refrigerant flow behaviour agreed with incompressible flow when the downstream pressure was higher than the saturation pressure.

Considering the change in temperature inside the short-tube orifice, it was discovered that the temperature distribution was related to the pressure distribution. This means that the temperature decreased rapidly at the inlet and outlet sections, while it decreased slightly inside the constant cross-section. This was because the refrigerant pressure was lower than the saturation pressure corresponding to the upstream pressure when refrigerant passed the inlet plane. Therefore, refrigerant temperature varied directly with refrigerant pressure (Nilpueng and Wongwises, 2009a,b).

4. Metastable flow

During the refrigerant flow through the expansion device, the liquid refrigerant changes into a liquid–vapour mixture. Under thermodynamic equilibrium, the refrigerant inside the

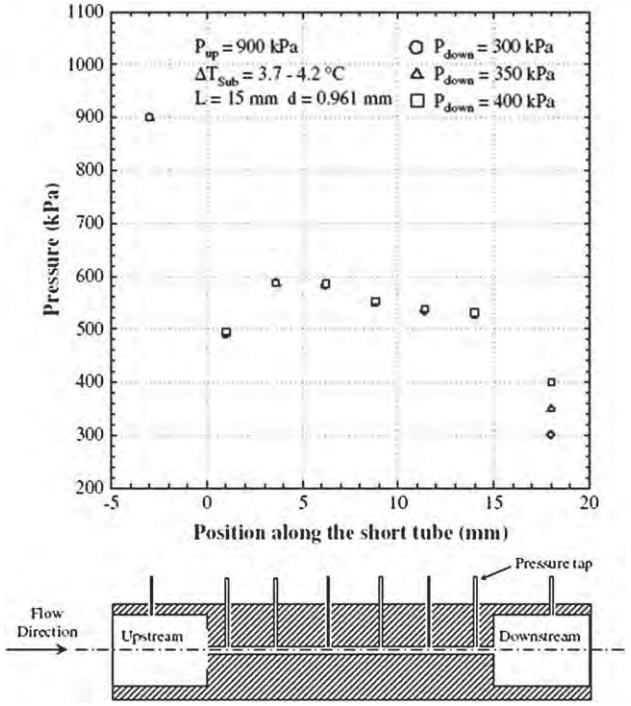

Fig. 5 – Pressure profile along short-tube orifice with L = 15 mm and D = 0.961 mm (Nilpueng and Wongwises, 2009a).

short-tube orifice was evaporated under the saturated condition. However, previous studies of metastable flow inside short-tube orifices have been discussed and reported by some publications.

Pasqua (1953) explored the appearance of metastable flow of CFC-12 inside a short-tube orifice. The photograph of the flow pattern showed that although the pressure was lower than the saturation pressure, the flow of liquid refrigerant was in the form of a liquid core along the tube length. His results implied that the metastable flow phenomenon existed inside the short-tube orifice. This phenomenon was consistent with the results of water flow through short-tube orifices observed by past researches (Fauske, 1965; Henry, 1970; Baily, 1951). He concluded that the flow rate increased in the metastable liquid core flow compared with the flashing flow of refrigerant inside the tube.

The existence of metastable flow of HCFC-22 inside a short-tube orifice was reported by Kim (1993) and Kim and O'Neal (1994). The relationship between the pressure distribution and visual studies along the short-tube orifice was used to identify the metastable flow. Their results showed that the refrigerant pressure was lower than the saturation pressure corresponding to the upstream temperature when it passed the inlet section. However, the visual studies indicated that the refrigerant remained in a liquid state. They noted that the flashing of refrigerant inside the short-tube orifice was delayed. In order to develop a mathematical model for calculating the mass flow rate inside the short-tube orifice, the location of inception of vapourisation was presented in terms of a single-phase frictional pressure drop as follows.

$$z_m = \frac{2D\rho_f(P_v - P_{inlet})}{fG^2} \quad (1)$$

where

$$\frac{P_v - P_{inlet}}{P_c} = 0.000693\left(\frac{GD}{\mu_f}\right)^{3.1146} - 0.3165\left(\frac{v_g}{v_g - v_f} - 1.0469\right) \quad (2)$$

$$f = 1.7649\left(\frac{GD}{\mu_f}\right)^{-0.1685} \quad (3)$$

Where z_m is the fraction of the short-tube length in the metastable region (mm), D is the short-tube orifice diameter (mm), P_v is actual vapourisation pressure (kPa), P_{inlet} is inlet pressure (kPa), P_c is critical pressure (kPa), f is the fanning friction factor, G is mass flux (kg m^{-2} s^{-1}), ρ_f is liquid density (kg m^{-3}), μ_f is liquid dynamic viscosity (kg m^{-1} s^{-1}), v_f is liquid specific volume (m^3 kg^{-1}), and v_g is vapour specific volume (m^3 kg^{-1}).

Nilpueng and Wongwises (2009a) and Nilpueng and Wongwises (2009b) observed the metastable flow of HFC-134a inside short-tube orifices. The existence of metastable flow inside the short-tube orifice was verified by considering the relation of flow pattern, pressure distribution, and temperature distribution. The results showed similar behaviour to that found by previous researchers. That is, the refrigerant remained in the liquid state although the pressure was lower than saturation pressure. The metastable liquid which flowed at the central core of the tube in a cone shape existed inside the short-tube orifice under the general operating conditions of the air conditioner. They stated that with the same short-tube orifice size, the mass flow rate increased as the metastable liquid flow region increased. Moreover, it was also reported that metastable two-phase flow occurred inside the short-tube orifice.

5. Choked flow

Choked flow is a limiting condition which occurs inside a short-tube orifice when the velocity of refrigerant is increased to sonic velocity. Under this condition, the flow of refrigerant through the short-tube orifice corresponds to the critical flow rate, which is the maximum flow rate that can be attained by reducing the downstream pressure under given upstream conditions.

In order to use a short-tube orifice as an expanding device in an air-conditioning system, it is found that the flow of refrigerant should be choked flow to achieve an appropriate distribution of refrigerant under working conditions. This is because under non-choked flow, the refrigerant mass flow rate which is discharged to the evaporator is reduced when the evaporator pressure or cooling load of the system increases, but is increased as the evaporator pressure or cooling load of the system decreases. This flow behaviour is inappropriate for air-conditioning systems. Therefore, to achieve proper performance and reliability, the short-tube orifice should be insensitive to the downstream pressure.

Over the years, the choked flow phenomenon inside short-tube orifices has been investigated and carried out by

a number of researchers. Baily (1951) investigated the occurrence of choked flow of saturated and nearly saturated water through a short tube with $5 < L/D < 20$. In the experiment, the upstream pressure was kept at atmospheric pressure, while the downstream pressure was varied by using a vacuum pump. The flow behaviour was divided into three regions as shown in Fig. 6.In regime AB, the flow rate increased approximately as a function of the square root of the pressure differential across the short-tube orifice. He reported that the instability of the flow appeared near point B before the curve AB moved to curve CD. However, the relationships between the mass flow rate and the pressure differential across the short-tube orifice of the two curves were similar. Beyond this point, the mass flow rate remained constant although the pressure differential was augmented. Therefore, he concluded that critical flow or choked flow occurred in the region DE.

The choked flow phenomenon of water through a short-tube orifice with $L/D < 6$ was studied by Zaloudek (1963). He stated that his results showed the same behaviour as those obtained by Baily (1951). However, the instability between curve AB and curve CD did not appear, but the mass flow rate in this region remained constant as shown by a dotted line. This flow phenomenon was named as the first-stage critical flow. It was also discovered that the same flow behaviour occurred in the region DE. He stated that this flow phenomenon was established at the end of the tube when the downstream pressure was below the saturation pressure, and termed it the second-stage critical flow.

Mei (1982) explored the choked flow phenomenon of HCFC-22 along a short-tube orifice with $7 < L/D < 12$. The results within the normal heat pump operating range indicated that first-stage choking appeared at a degree of subcooling ranging between 19.4 and 22.2 °C, but the second-stage choking disappeared inside the short-tube orifice. Therefore, under any operating condition, the refrigerant flow rate through the short-tube orifice was related to the square root of the pressure differential.

An investigation of the choked flow of HCFC-22 inside a short-tube orifice with $5 < L/D < 12$ was reported by Aaron and Domanski (1990). The experiment was run at upstream pressures ranging from 1448 to 2006 kPa, downstream pressures ranging from 345 to 827 kPa, and degrees of subcooling ranging from 5.6 to 13.9 °C, which were the normal working conditions of the heat pump. The results showed that the mass flow rate was insensitive to the downstream pressure

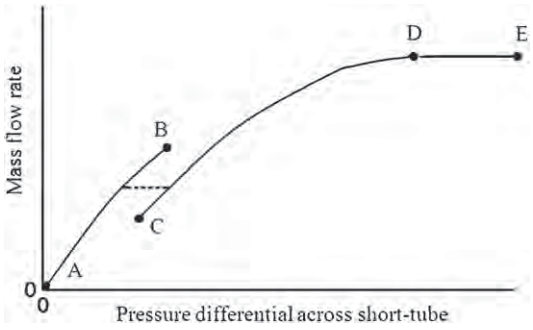

Fig. 6 – Relationship between mass flow rate and pressure differential across short-tube orifice (Baily, 1951).

when the downstream pressure was reduced below saturation pressure. They noted that the tendency of the mass flow rate was similar to curve CDE presented by Baily (1951). However, the flow rate was found to increase by about 3–8% with the downstream pressure. Therefore, the flow behaviour was defined as non-ideal choked flow. They concluded that non-ideal choked flow appeared inside the short-tube orifice used in the heat pump because the evaporator pressure under working conditions was lower than the saturation pressure. In addition, under these conditions, it was noted that the pressure drop in the exit region was large.

Kim (1993) and Kim and O'Neal (1994) observed the existence of choked flow of two-phase HCFC-22 flowing through short-tube orifices. The experiment was performed at upstream pressures ranging from 1448 to 2006 kPa, qualities ranging from 0 to 10%, and degrees of subcooling ranging from 0 to 13.9 °C. The effect of downstream pressure on the relevant parameter, including the flow rate change, pressure distribution change, and flow pattern change, was used to identify the choked flow phenomenon. The results indicated that the mass flow rate depended on the downstream pressure when the pressure was above the saturation pressure. Conversely, when the downstream pressure was below the saturation pressure, the mass flow rate changed slightly. It was also found that the pressure drop at the exit region decreased greatly when the downstream pressure was lower than the saturation pressure. Under this condition, they concluded that the refrigerant flow was choked.

The choked flow of HFC-134a inside short-tube orifices was studied by Kim (1993), Nilpueng and Wongwises (2009a,b). The change in mass flow rate, pressure distribution, and flow pattern with downstream pressure was used to confirm the appearance of choked flow. The results demonstrated that the mass flow rate, pressure distribution, and length of metastable liquid flow inside the short-tube orifice were affected very little by the change in downstream pressure. This flow behaviour agreed well with the theory of compressible flow through a converging nozzle. Therefore, they concluded that there was a choked flow phenomenon in HFC-134a flow through a short-tube orifice. However, Nilpueng and Wongwises (2009b) reported that choked flow appeared inside a short-tube orifice with $L/D > 2.91$ but disappeared with $L/D < 2.91$.

In addition, the existence of choked flow of other refrigerants such as HFC-407C, HFC-410A, and carbon dioxide was confirmed by Payne and O'Neal (1998), Payne and O'Neal (1999) and Kim et al. (2005). According to all the experimental results obtained from previous publications, it was indicated that the mass flow rate was very little affected by the change in downstream pressure. Therefore, they concluded that choked flow appeared inside short-tube orifices under the normal operating conditions of an air conditioner and heat pump. This was because the liquid refrigerant suddenly changed to a liquid and vapour mixture. As a result, the refrigerant velocity accelerated until it reached sonic velocity at the exit plane of the short-tube orifice. Moreover, it was obvious that the inception of choked flow occurred when the downstream pressure was nearly at saturation pressure. Nonetheless, the investigation of HFC-134a flowing through micro-orifices with diameters of 31.0 and 52.0 μm showed different flow

behaviours. That is, the flow was not choked even though the downstream pressure was reduced to more than 400 kPa below the saturation pressure. They recorded that the refrigerant cannot flash in a micro-tube when the downstream pressure is equal to saturation pressure. The reason for this was attributed to the strengthening of the metastable effect in a micro-tube (Tu et al., 2006).

6. Mass flow rate

As mentioned earlier, although the refrigerant mass flow rate is insensitive to downstream pressure under the choked flow condition, it depends on the relevant parameters, for example upstream pressure, degree of subcooling, upstream quality, short-tube orifice length, short-tube orifice diameter, and inlet and outlet chamfering. The data of mass flow rate obtained from the experiments are directly useful for selecting the proper short-tube orifice size in air conditioners. Therefore, the impacts of the operating conditions and short-tube orifice dimensions on the refrigerant mass flow rate are studied and presented in most published researches.

Early experimental investigations of refrigerant flow inside short-tube orifices focused exclusively on CFC-12 and HCFC-22. Kim et al. (1994) investigated the flow rate of CFC-12 through short-tube orifices with $5 < L/D < 20$. They reported that the mass flow rate was greatly affected by the upstream condition. The refrigerant mass flow rate was augmented when the degree of subcooling increased and reduced when the upstream quality increased. Also, changes in the short-tube orifice diameter resulted in large changes in mass flow rate. However, the effect of diameter on the flow rate was lower when the two-phase flow entered the short-tube orifice.

The influence of relevant parameters on the mass flow rate of HCFC-22 was explored by Mei (1982), Aaron and Domanski (1990), Kuehl and Goldschmidt (1992), Kim (1993), and Kim and O'Neal (1994). It was found that the mass flow rate was directly proportional to the cross-sectional area, upstream pressure, and degree of subcooling and was greatly affected by the inlet and outlet chamfering. Conversely, the mass flow rate was inversely proportional to the short-tube orifice length. For two-phase flow entering the short-tube orifice, it could be seen that increases in the upstream quality led to decreases in the mass flow rate.

Due to environmental concerns about depletion of the ozone layer and global warming, CFC and HCFC refrigerants have been replaced by alternative refrigerants. Therefore, several researchers have concentrated on HFC-134a, HFC-407C, R744, and HFC-410A.

The mass flow rate of HFC-134a inside short-tube orifices has been studied by Kim and O'Neal (1994), Singh et al. (2001), Nilpueng and Wongwises (2009a,b). The results indicated that the variation in mass flow rate with relevant parameters was similar to those obtained in previous works. That is, the mass flow rate strongly increased with the upstream pressure and degree of subcooling but decreased with increases in the short-tube orifice length. The flow rate increased approximately as a function of the square of the short-tube orifice diameter. In addition, a change in the orientation of the short-tube orifice and the installation of upstream and downstream screens had negligible effects on the mass flow rate.

Payne and O'Neal (1998) and Payne and O'Neal (1999) presented results for the mass flow rates of HFC-407C and HFC-410A through short-tube orifices. The effects of upstream subcooling, upstream pressure, downstream pressure, tube length, tube diameter, and lubricant concentration on the mass flow rate were tested. They reported that the variation in refrigerant mass flow rate with operating conditions and short-tube orifice sizes for the refrigerant mixtures followed the same trend as those achieved with HCFC-22 and HFC-134a. However, for two-phase flow entering the short-tube orifice, the flow rate was directly related to the short-tube orifice diameter. Moreover, they found that the addition of oil to the refrigerant led to an increase in the mass flow rate for two-phase flow entering the short-tube orifice but had little effect on the mass flow rate at a high degree of subcooling. The mass flow rate result of HFC-410A inside short-tube orifices at upstream pressures approaching the critical point was reported by Kim et al. (2005). Test runs were performed at upstream pressures ranging from 2619 to 4551 kPa, degrees of subcooling ranging from 2.8 to 11.1 °C, and downstream pressures ranging from 772 to 1274 kPa. They reported that the flow rate varied greatly with upstream pressure, degree of subcooling, and short-tube diameter. This was similar to the normal condition in general air-conditioning system. Nonetheless, they found that the decrease in the mass flow rate with a reduction in subcooling became more significant when the upstream pressure increased beyond 3604 kPa, due to a higher density change.

The flow of carbon dioxide through short-tube orifices was observed by Liu et al. (2004) and Chen et al. (2004). They stated that the flow characteristics of carbon dioxide through short-tube orifices differed from those obtained from conventional refrigerants such as HFC-134a when the trans-critical fluid was not directly changed into the two-phase region. The results showed that the mass flow rate decreased as the upstream temperature increased but was insignificantly affected by the inlet and outlet chamfer depths.

7. Conclusions

Recent developments in research work on refrigerant flow mechanisms inside short-tube orifices are presented in this paper. Based on a review of the open literature, the conclusions can be summarised as follows:

- Most of the research works have been focused on the mass flow rate inside short-tube orifices, but studies of flow pattern, pressure distribution, temperature distribution, and metastable flow have rarely been reported.
- The refrigerant pressure and temperature decreased suddenly at the inlet and outlet of the short-tube orifice, but gradually decreased along the constant cross-section.
- Only one correlation which is generated for predicting the HFC-134a metastable liquid length inside short-tube orifice has been reported in the literature.
- The experimental results indicated that choked flow and metastable flow phenomena exist inside short-tube orifices

under the normal operating conditions of an air conditioner and heat pump. Under the choked flow condition, the refrigerant flow rate through the short-tube orifice is increased with increases in the upstream pressure, degree of subcooling, short-tube orifice diameter, and chamfer depth.

At the present time, although short-tube orifices have been popularly used in residential and automobile air conditioners, a clear understanding of the refrigerant flow phenomena, especially, flow pattern, choked flow and metastable flow are still needed for developing suitable calculation techniques. Therefore, future research work on refrigerant flow mechanisms inside short-tube orifices remains important.

Acknowledgements

The authors would like to express their appreciation to the Thailand Research Fund (TRF), the Office of Higher Education Commission and the National Research University Project for providing financial support for this study.

REFERENCES

Aaron, A.A., Domanski, P.A., 1990. Experimentation, analysis, and correlation of refrigerant-22 flow through short tube restrictors. ASHRAE Trans. 96, 729–742.

Baily, J.F., 1951. Metastable flow of saturated water. Trans. ASME 73, 1109–1116.

Chen, J.P., Liu, J.P., Chen, Z.J., Niu, Y.M., 2004. Trans-critical R744 and two-phase flow through short tube orifices. Int. J. Thermal Sci. 43, 623–630.

Fang, X., 2001. Flow calculations for fixed- area expansion device. ASHRAE Trans. 107, 130–139.

Fauske, H.K., 1965. The discharge of saturated water through tube. Chem. Eng. Symp. 61, 210–216.

Henry, R.E., 1970. The two-phase critical discharge of initially saturated or subcooled liquid. Nucl. Sci. Eng. 41, 336–343.

Kim, Y., 1993. Two-phase flow of HFC134a and HCFC22 through short tube orifices. PhD thesis, Texas A&M University, USA.

Kim, Y., O'Neal, D.L., 1994. Two-phase flow of refrigerant-22 through short tube orifices. ASHRAE Trans. 100, 323–334.

Kim, Y., O'Neal, D.L., Yuan, X., 1994. Two-phase flow of HFC-134a and CFC-12 through short-tube orifices. ASHRAE Trans. 100, 582–591.

Kim, Y., Payne, V., Choi, J., Domanski, P., 2005. Mass flow of R410A through short tube working near the critical point. Int. J. Refrig. 28, 547–553.

Kuehl, S.J., Goldschmidt, V.W., 1992. Flow of R-22 through short-tube restrictors. ASHRAE Trans. 98, 59–64.

Liu, J.P., Niu, Y.M., Chen, J.P., Chen, Z.J., Feng, X., 2004. Experimental and correlation of R744 two-phase flow through short tubes. Exp. Therm. Fluid Sci. 28, 565–573.

Mei, V.C., 1982. Short tube refrigerant flow restrictors. ASHRAE Trans. 88, 157–169.

Nilpueng, K., Wongwises, S., 2009a. Experimental investigation of two-phase flow characteristics of HFC-134a through short-tube orifices. Int. J. Refrig. 32, 854–864.

Nilpueng, K., Wongwises, S., 2009b. Flow pattern, mass flow rate, pressure distribution, and temperature distribution of two-phase flow of HFC-134a inside short-tube orifices. Int. J. Refrig. 32, 1864–1875.

Pasqua, P.F., 1953. Metastable flow of Freon-12. Refrig. Eng. 61, 1084–1088.

Payne, W.V., O'Neal, D.L., 1998. Mass flow characteristics of R407C through short-tube orifices. ASHRAE Trans. 104, 197–209.

Payne, W.V., O'Neal, D.L., 1999. Multiphase flow of refrigerant 410A through short tube orifices. ASHRAE Trans. 105, 66–74.

Singh, G.M., Hrnjak, P.S., Bullard, C.W., 2001. Flow of refrigerant R134a through orifice tubes. HVAC&R Res. 7, 245–262.

Tu, X., Hrnjak, P.S., Bullard, C.W., 2006. Refrigerant 134a liquid flow through micro-scale short tube orifices with/without phase change. Exp. Therm. Fluid Sci. 30, 253–262.

Zaloudek, R.R., 1963. The Critical Flow of Hot Water through Short Tube. HW77594, Hanford Lab. Richland, Washington.

International Journal of Heat and Mass Transfer 55 (2012) 1403–1411

Contents lists available at SciVerse ScienceDirect

International Journal of Heat and Mass Transfer

journal homepage: www.elsevier.com/locate/ijhmt

Technical Note

Effect of number of tube rows on the air-side performance of crimped spiral fin-and-tube heat exchanger with a multipass parallel and counter cross-flow configuration

Parinya Pongsoi [a], Santi Pikulkajorn [b], Chi-Chuan Wang [c], Somchai Wongwises [a,d,*]

[a] Fluid Mechanics, Thermal Engineering and Multiphase Flow Research Lab. (FUTURE), Department of Mechanical Engineering, King Mongkut's University of Technology, Thonburi, Bangmod, Bangkok 10140, Thailand
[b] Somchai Industry Co., Ltd., Bangkok 10150, Thailand
[c] Department of Mechanical Engineering, National Chiao Tung University, Hsinchu 300, Taiwan
[d] The Royal Institute of Thailand, Academy of Science, Sanam Suea Pa, Dusit, Bangkok 10300, Thailand

ARTICLE INFO

Article history:
Received 11 March 2011
Received in revised form 23 June 2011
Accepted 23 June 2011
Available online 21 October 2011

Keywords:
Crimped fin
Heat transfer
Heat exchanger
Air–water
Extended surface

ABSTRACT

The air-side performance of crimped spiral fin and tube heat exchangers at high Reynolds number (3000–13,000) is investigated in this study. The test heat exchangers have a new type of multipass parallel and counter cross-flow water flow arrangement which is a combination of parallel cross-flow and counter cross-flow. The test samples are made from copper and aluminium with different number of tube rows (N_{row} = 2, 3, 4 and 5). The effects of number of tube rows and fin material on the heat transfer and friction characteristics are studied. The results show that no significant effect for either number of tube rows or fin materials on the heat transfer performance is found at high Reynolds number. In addition, the correlation of the air-side performances of this type of the heat exchangers at high Reynolds number is developed for industrial applications.

1. Introduction

The heat exchanger is a basic component that is used for thermal systems in many industrial processes involving heat transfer. The most favourable type of heat exchanger used in industrial applications is the fin-and-tube heat exchanger. It is very important to consider the heat transfer rate, which is normally limited by the thermal resistance on the air-side of the heat exchanger. One way to augment the heat transfer rate on the air-side of the heat exchanger is to improve the fin geometry. However, this method may lead to the need for increased fan power because of the penalty associated with the pressure drop. Many researchers had studied the effect of the plate fin geometry, such as plain fin, slit fin, wavy fin, louvered fin, compounded fin, etc., on the heat transfer performance and frictional characteristic. On the other hand, there are only few researches on the crimped spiral fin-and-tube heat exchanger as found in [1–4].

Nuntaphan et al. [1] studied the air-side of crimped spiral fin heat exchanger to analyse the effect of tube diameter, fin spacing, transfer tube pitch, and tube arrangement and proposed correlations between heat transfer and friction characteristics in the case of low Reynolds numbers. Moreover, heat exchangers using crimped spiral finned tubes were investigated by Srisawad and Wongwises [2] who focused on the air-side performance of helically coiled crimped spiral finned tube heat exchangers in dry-surface conditions. Pongsoi et al. [3] studied the effect of fin pitch on the air-side heat transfer characteristics of crimped spiral fin-tube heat exchangers having multipass parallel and counter cross-flow under sensible heating conditions and purpose the ε–*NTU* relation equation for this new water flow arrangement. Tang et al. [4] studied the air-side heat transfer and friction characteristics of five kinds of fin-and-tube heat exchangers i.e. crimped spiral fin, plain fin, slit fin, fin with delta-wing longitudinal vortex generators, and mixed fin. The number of tube rows (N_{row}) was 12. The diameter of tubes (d_o) was 18 mm. Reynolds number was varied from 4000 to 10,000. According to their results, although the crimped spiral fin gave high pressure drop, it provided higher air-side heat transfer performance than several types of heat exchangers.

According to these literatures, crimped spiral fin is proved to be quite reliable in industrial applications. The crimped spiral fin

* Corresponding author at: Fluid Mechanics, Thermal Engineering and Multiphase Flow Research Lab. (FUTURE), Department of Mechanical Engineering, King Mongkut's University of Technology, Thonburi, Bangmod, Bangkok 10140, Thailand. Tel.: +66 24709115.
E-mail address: Somchai.won@kmutt.ac.th (S. Wongwises).

0017-9310/$ - see front matter © 2011 Elsevier Ltd. All rights reserved.
doi:10.1016/j.ijheatmasstransfer.2011.09.064

Nomenclature

A_{min}	minimum free flow area, m^2
A_o	total surface area, m^2
A_p	cross-sectional or profile area of fin, m^2
Al	aluminium material
C^*	capacity rate ratio, dimensionless
Cu	copper material
f	Fanning friction factor, dimensionless
Gc	mass flux of the air based on minimum free flow area, kg/m^2 s
h	heat transfer coefficient, $W/(m^2 K)$
j	Colburn factor, dimensionless
NTU	number of transfer units, dimensionless
Nu	Nusselt number, dimensionless
Pr	Prandtl number, dimensionless
ΔP	pressure drop, Pa
Re_{do}	Reynolds number based on tube outside diameter (d_o)
U	overall heat transfer coefficient, $W/(m^2 K)$
V_{fr}	air frontal velocity, m/s
V_{max}	maximum velocity across heat exchanger, m/s
ε_c	heat exchanger effectiveness for multipass counter cross-flow
ε_p	heat exchanger effectiveness for multipass parallel cross-flow
ε_{pc}	heat exchanger effectiveness for multipass parallel and counter cross-flow
η_f	fin efficiency, dimensionless
ϕ	combination of terms, dimensionless

Table 1
Experimental conditions.

Inlet-air-dry bulb temperature, °C	31.5 ± 0.5
Inlet-air frontal velocity, m/s	2–6 or Re_{do}(3000–13,000)
Inlet-water temperature, °C	55–70
Water flow rate, LPM	12–14

features a sine-shaped fin which gives rise to a higher heat transfer rate on the air-side through the increase in the contact surface between the fin base and tube. However, up to now, none of the experimental investigations found in the literature had reported the effect of the number of tube rows on the air-side performance of crimped spiral fin-and-tube heat exchangers. Upon the foregoing studies, Nuntaphan et al. [1] is the only experimental work that examined the effect of fin geometry and tube arrangement on the air-side performance of crimped spiral fin-and-tube heat

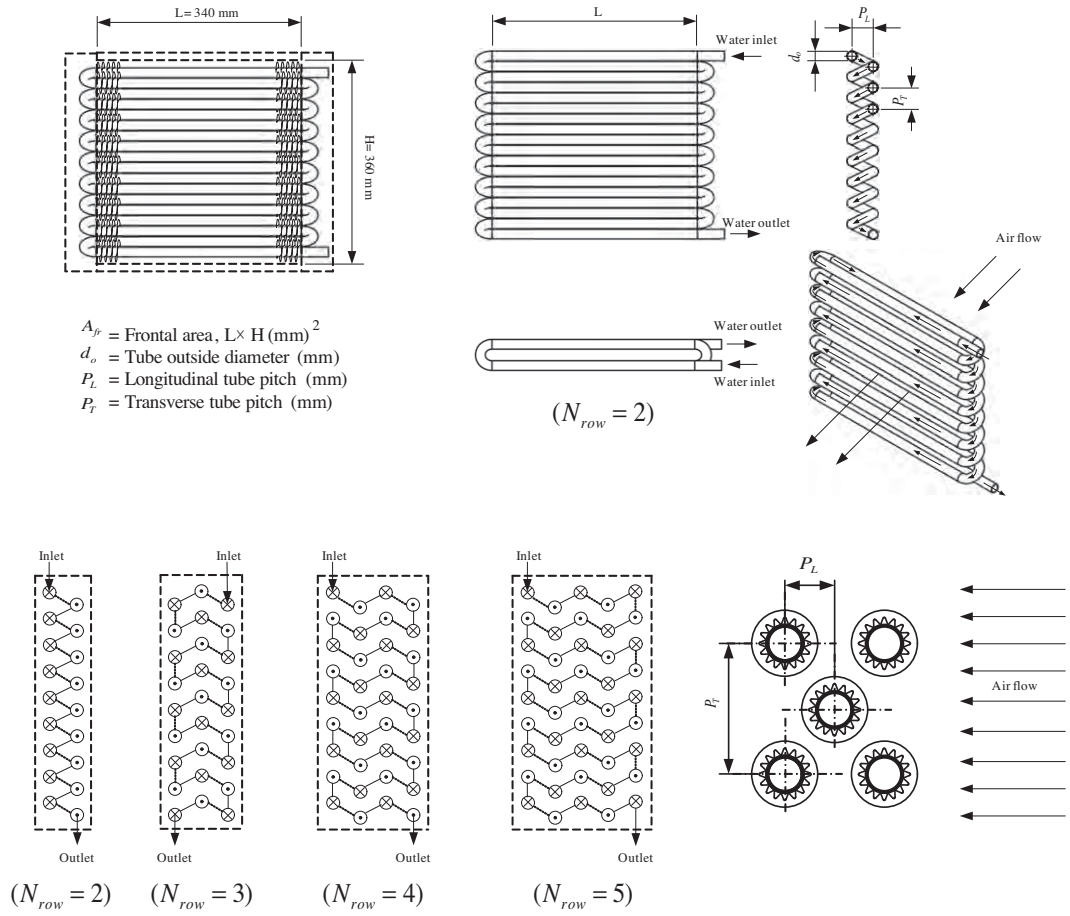

Fig. 1. Geometric details of multipass parallel-and-counter cross flow heat exchangers and water flow circuit inside the heat exchanger. N_{row} = 2, 3, 4 and 5 (× and • signs indicates that water flows into or out of the paper, respectively).

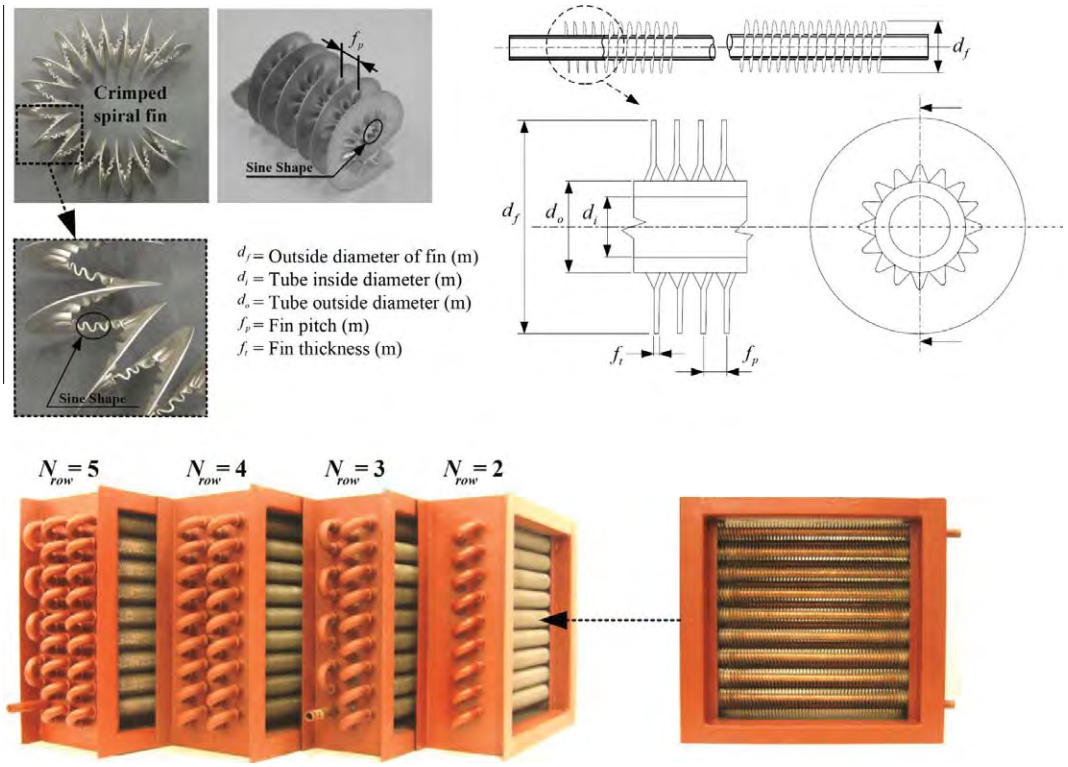

Fig. 2. The photos of the tested crimped spiral fin and tube heat exchangers and schematic diagram of crimped spiral fin.

exchangers. However, their tests were conducted at a very low air frontal velocity (0.5–1.5 m/s) which limited the applicability of the test results. In practice, especially in industrial service, the operation velocity is normally much higher as reported by Xie et al. [5]. Therefore, it is the main purpose of this study is to extend the applicable range (V_{fr} up to 6 m/s) of the crimped spiral fin-and-tube heat exchangers subject to the influence of the number of tube rows and fin materials. Moreover, the test samples are of this study is of large diameter tubes (about 16 mm) which are very popularly used in ventilator and fan-coil units [6,7].

2. Data reduction

This present work is conducted by using the experimental apparatus of Wongwises and Chokeman [8], including the test section, air supply, water loop, instrumentation, and data acquisition. Air and hot water are used as working fluids. Detailed descriptions of the relevant components can be seen from the previous study.

In the experiment, the inlet water temperature and the water flow rate are fixed while varying the air flow rate. Tests are then conducted at the steady state with tested conditions being tabulated in Table 1.

The tests heat exchangers are of fin-and-tube configurations with copper tube being finned with either copper or aluminium. The water-side circuitry arrangement and detailed dimensions of the tested fin-and-tube heat exchangers are shown in Fig. 1. Photos of the crimped spiral fin pattern are shown in Fig. 2. The geometric parameters of the heat exchangers are summarized in Table 2. Tests are performed under steady state condition, and the overall resistance can be obtained from the *UA* product of transfer units (ε–*NTU*), yet the total resistance is the sum of the individual resistances as follows:

$$\frac{1}{UA} = \frac{1}{h_i A_i} + \frac{\ln(d_o/d_i)}{2\pi k_t L} + \frac{1}{\eta_o h_o A_o} \tag{1}$$

The ε–*NTU* relationships with one fluid mixed and one fluid unmixed in cross-flow was employed to determine the overall heat transfer coefficient. From Fig. 1, the present mixed circuitry arrangement is a combination of parallel and counter cross-flow. Therefore, the ε–*NTU* relationships developed by Pongsoi et al. [3] is selected to calculate the heat exchanger effectiveness. This relation combines both effect of parallel and counter cross-flow configuration of water flow arrangement from [9–11], as shown in Eqs. (2)–(9):

For multipass parallel cross-flow with N_{row} = 2, 3, 4 and 5:

$$(N_{row} = 2), \quad \varepsilon_P \left(1 - \frac{K}{2}\right)\left(1 - e^{-2K/C_A^*}\right), \quad K = 1 - e^{-NTU_A(C_A^*/2)} \tag{2}$$

Table 2
Detailed geometric parameters of the test samples.

No.	Fin type	d_i (mm)	d_o (mm)	d_f (mm)	P_L (mm)	P_T (mm)	f_t (mm)	n_t	N_{row}	f_p (mm)	Fin material
1, 2	Crimped	13.5	16.35	35.0	35	40	0.5	9	3, 4	6.3	Cu
3–6	Crimped	13.5	16.35	35.0	35	40	0.5	9	2, 3, 4, 5	6.3	Al

d_f = outside diameter of fin; d_i = tube inside diameter; d_o = tube outside diameter; f_p = fin pitch; f_t = fin thickness; P_L = longitudinal tube pitch; P_T = transverse tube pitch; n_t = number of tubes in row; N_{row} = number of tube rows. Tube layouts of all heat exchangers are staggered layout (Al = aluminium, Cu = copper).

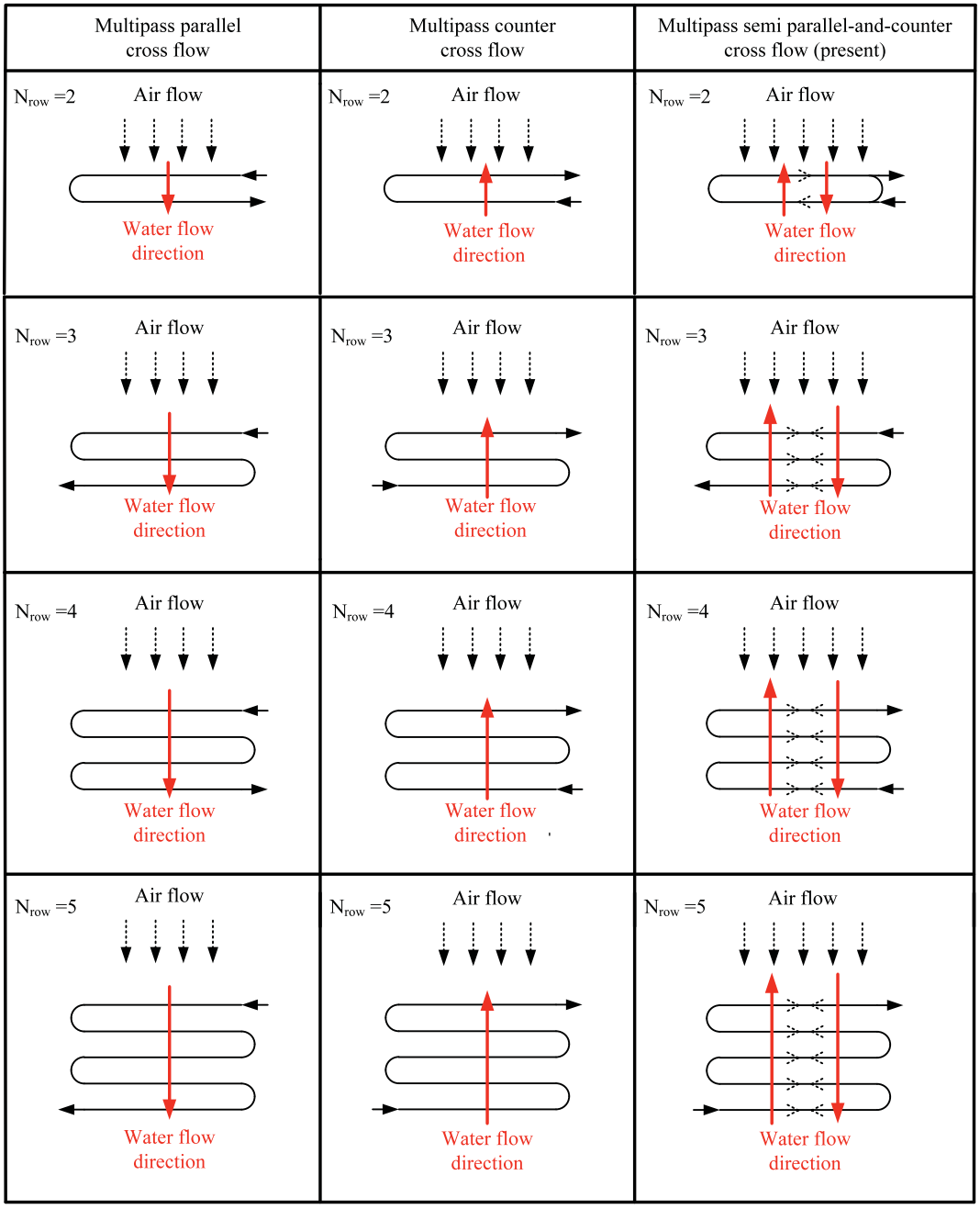

Fig. 3. Schematic diagram of the heat exchangers algorithm for multipass parallel cross flow, multipass counter cross flow and multipass parallel and counter cross-flow (N_{row} = 2, 3, 4 and 5).

$$(N_{row}=3),\quad \varepsilon_P = 1-\left(1-\frac{K}{2}\right)^2 e^{-3K/C_A^*} - K\left[1-\frac{K}{4}+\frac{K}{C_A^*}\left(1-\frac{K}{2}\right)\right]e^{-K/C_A^*},\quad K=1-e^{-NTU_A(C_A^*/3)} \tag{3}$$

$$(N_{row}=4),\quad \varepsilon_P = 1-\frac{K}{2}\left(1-\frac{K}{2}+\frac{K^2}{4}\right)-K\left(1-\frac{K}{2}\right)\left(1+2\frac{K}{C_A^*}\left[1-\frac{K}{2}\right]\right)e^{-2K/C_A^*}-\left(1-\frac{K}{2}\right)^3 e^{-4K/C_A^*},\quad K=1-e^{-NTU_A(C_A^*/4)} \tag{4}$$

$$(N_{row}=5 \text{ or } \infty),\quad \varepsilon_P = \frac{1-e^{-NTU_A(1+C_A^*)}}{1+C_A^*} \tag{5}$$

For multipass counter cross-flow with N_{row} = 2, 3, 4 and 5:

$$(N_{row}=2),\quad \varepsilon_c = 1-\left[\frac{K}{2}+\left(1-\frac{K}{2}\right)e^{2K/C_A^*}\right]^{-1},\quad K=1-e^{-NTU_A(C_A^*/2)} \tag{6}$$

$$(N_{row}=3),\quad \varepsilon_c = 1-\left\{\left(1-\frac{K}{2}\right)^2 e^{3K/C_A^*} + k\left[K\left(1-\frac{K}{4}\right)-\left(1-\frac{K}{2}\right)\frac{K^2}{C_A^*}\right]e^{K/C_A^*}\right\}^{-1},\quad K=1-e^{-NTU_A(C_A^*/3)} \tag{7}$$

$$(N_{row}=4),\quad \varepsilon_c = 1-\left\{\frac{K}{2}\left(1-\frac{K}{2}+\frac{K^2}{4}\right)+K\left(1-\frac{K}{2}\right)\times\left[1-2\frac{K}{C_A^*}\left(1-\frac{K}{2}\right)\right]e^{2K/C_A^*}+\left(1-\frac{K}{2}\right)^3 e^{4K/C_A^*}\right\}^{-1},\quad \times K=1-e^{-NTU_A(C_A^*/4)} \tag{8}$$

$$(N_{row} = 5 \text{ or } \infty), \quad \varepsilon_c = \frac{1 - e^{-NTU_A(1-C_A^*)}}{1 - C_A^* e^{-NTU_A(1-C_A^*)}} \tag{9}$$

where $C^* = C_{min}/C_{max}$ is equal to C_c/C_h or C_h/C_c depending on the value of hot and cold fluid heat capacity rates

$$\varepsilon_{pc} = \frac{\varepsilon_P + \varepsilon_C}{2} \quad \text{for } N_{row} = 2, 3, 4 \text{ and } 5 \tag{10}$$

The schematic diagram of circuitry arrangement for $N_{row} = 2$, 3, 4 and 5 are shown in Fig. 3.

The heat transfer performance is calculated by the method of Kays and London. Further details about the data reduction can be seen from Wongwises and Chokeman [8], The efficiency of a radial fin with rectangular profile is based on the derivation of Gardner [12], i.e.,

$$\eta_f = \frac{2\psi}{\phi(1+\psi)} \frac{I_1(\phi R_o)K_1(\phi R_i) - I_1(\phi R_i)K_1(\phi R_o)}{I_0(\phi R_i)K_1(\phi R_o) + I_1(\phi R_o)K_0(\phi R_i)} \tag{11}$$

where

$$\phi = (r_o - r_i)^{3/2} \left(\frac{2h_o}{k_f A_p}\right)^{1/2} \tag{12}$$

Accordingly, the air-side heat transfer coefficient (h_o) can be calculated from Eq. (1). The air-side heat transfer characteristics of the heat exchanger are often in terms of dimensionless Colburn j factor:

$$j = \frac{Nu}{Re_{do}\Pr^{1/3}} = \frac{h_o}{\rho_a V_{\max} c_P}(\Pr)^{2/3} \tag{13}$$

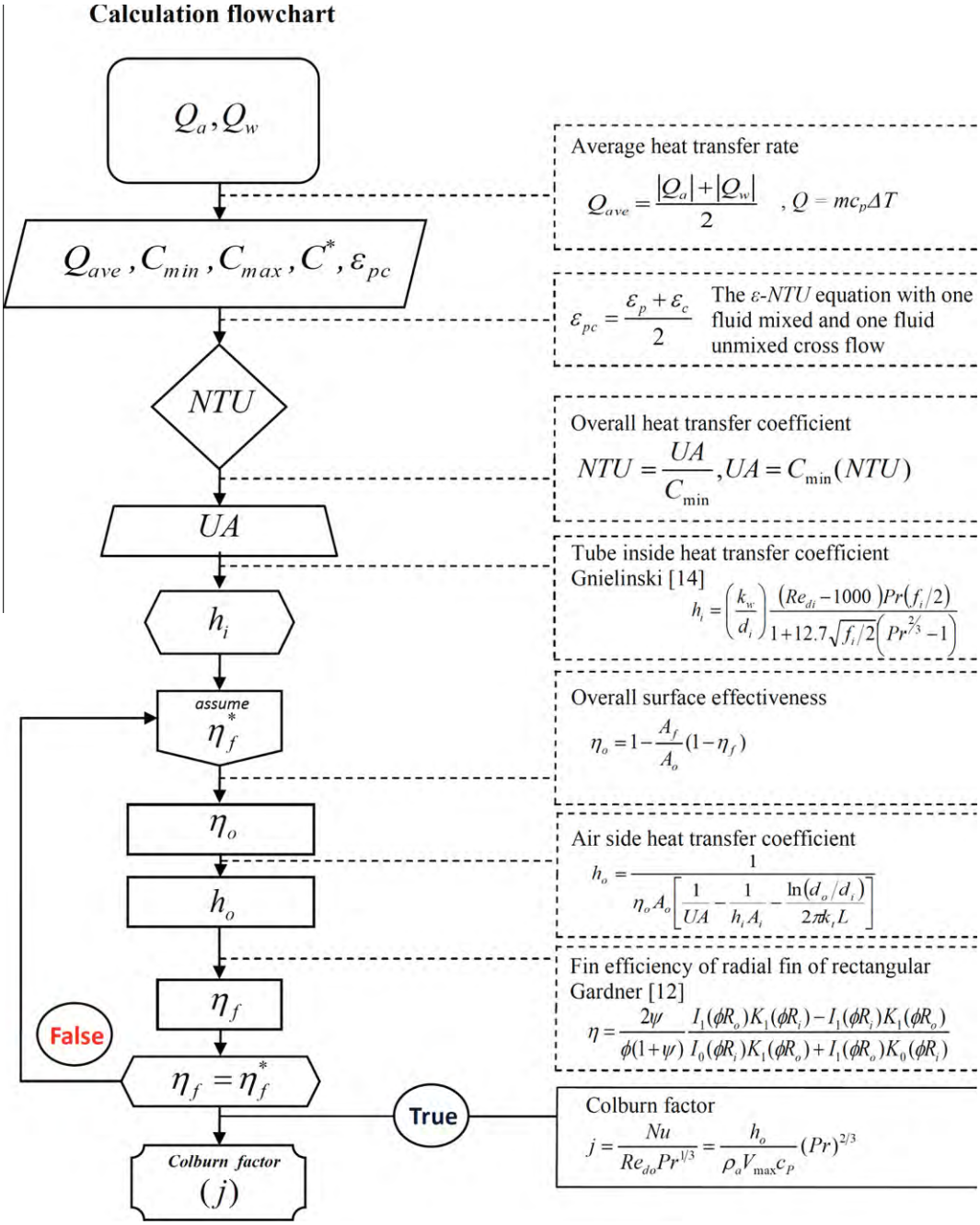

Fig. 4. Flowchart of the data reduction for air-side heat transfer performance (j-factor). (See above-mentioned reference for further information.)

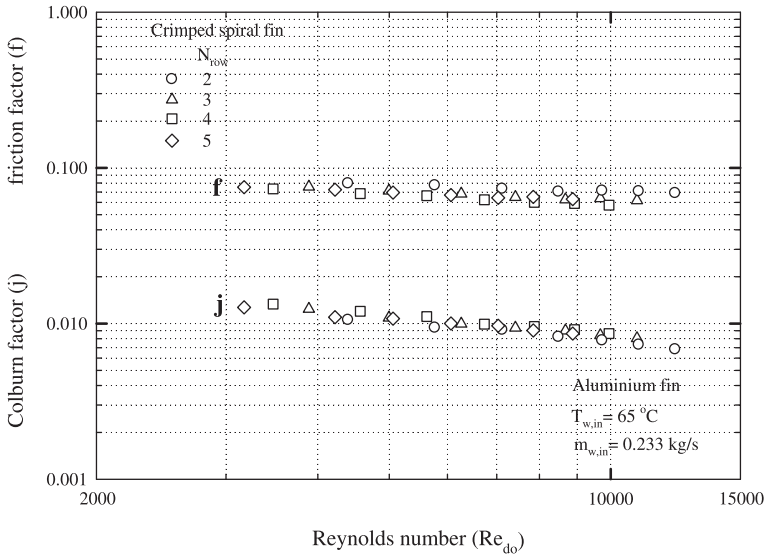

Fig. 5. Effect of number of tube rows on the Colburn factor and friction factor of crimped spiral fin and tube heat exchangers.

The frictional characteristics are termed with Fanning friction factor, as depicted by Kays and London [13]:

$$f = \left(\frac{A_{\min}}{A_o}\right)\left(\frac{\rho_m}{\rho_1}\right)\left[\frac{2\Delta P\rho_1}{G_c^2} - (1+\sigma^2)\left(\frac{\rho_1}{\rho_2} - 1\right)\right] \tag{14}$$

where G_c is the mass flux of the air based on minimum free flow area, A_o is the total heat transfer area, A_{min} is the minimum free flow area. The flow chart showing the reduction of the data is shown in Fig. 4.

The experiments are conducted following the ANSI/ASHRAE 33 Standards [15] in which the energy un-balance between air and water of the crimped spiral fin-and-tube heat exchangers, denoting $|Q_a - Q_w|/Q_{ave}$, is less than 0.05. The uncertainties are calculated from the root mean sum square method, the maximum uncertainties are 3.5% for the Re_{do}, 13.0% for the j-factor and 11.5% for f-factor. The uncertainties decreased as Reynolds number increased.

3. Results and discussion

In experiments, the analysis of air-side heat transfer and friction characteristics of all the heat exchangers examined are presented in terms of a dimensionless number including the Colburn factor (j) and friction factor (f) plotted against the Reynolds number (Re_{do}) and the Reynolds number based on the outside diameter of the tube. As expected, both the Colburn factor (j) and the friction factor (f) decrease an increasing Reynolds number.

Fig. 5 shows the effect of the number of tube rows on the heat transfer and friction characteristic. The number of tube row of the heat exchangers are from 2 to 5. As can be seen in Fig. 5, the number of tube rows casts no significant effect on the Colburn factor (j) at high Reynolds numbers (3000–13,000). This phenomenon is similar to the plain fin data as reported by Rich [16] and Wang et al. [17] in which the effect of the number of tube rows diminishes as the Reynolds number is increased over 2000. This is due to the downstream turbulence eddies shed from the tubes that

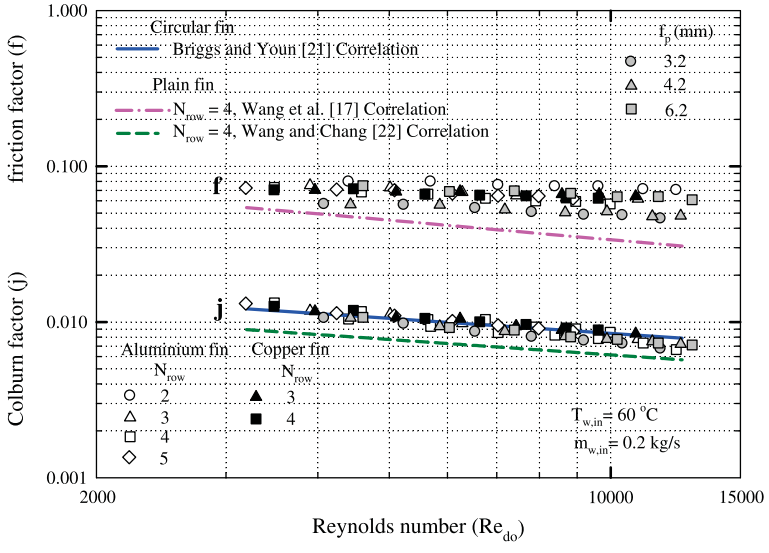

Fig. 6. The comparison of j and f factors between presented data with correlation of plain fin and circular fin.

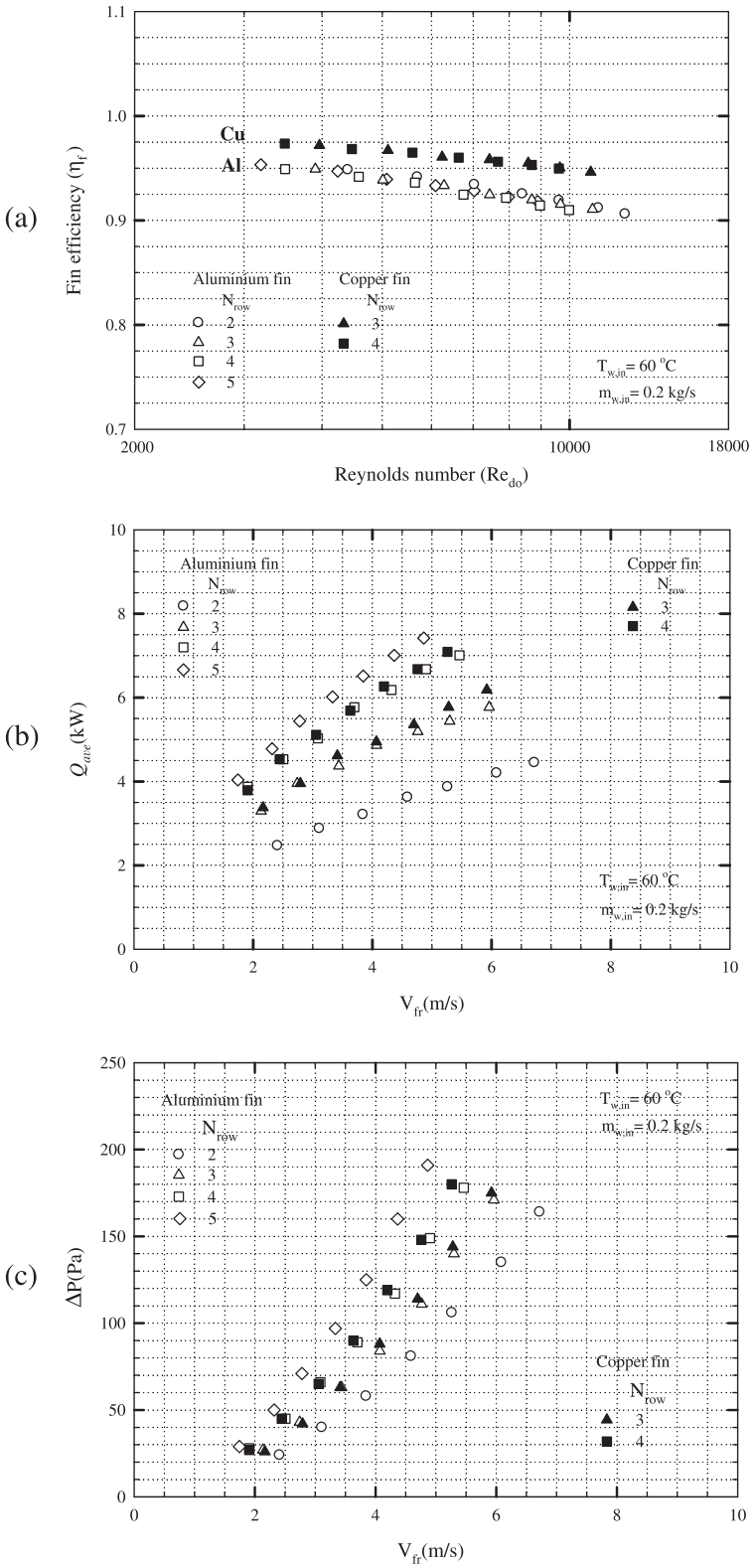

Fig. 7. Effect of number of tube rows on the fin efficiency (a), heat transfer rate (b) and pressure drop (c) of crimped spiral fin and tube heat exchangers (N_{row} = 2, 3, 4 and 5).

cause good mixing in the downstream fin region. Moreover, the fact that the effect of the number of tube rows on the heat transfer characteristics vanishes for Reynolds numbers over 2000 can also be found in the works of [18–20] with fin-and-tube heat exchangers having wavy, louver and slit geometry, respectively. The data point in Fig. 5 shows that the number of tube row (N_{row}) does not affect the friction factor (f) over the range of Reynolds numbers being examined.

For a comparison of the present test samples with previous studies, the Briggs and Young [21] correlation for circular fin-and-tube heat exchanger is chosen to compare with the present experimental results as illustrated in Fig. 6. Note that the configu-

ration of circular fin is very similar to that of the tested crimped spiral fin. Therefore, the calculated Colburn factor (j) of circular fins reveals a similar trend and magnitude as the present crimped spiral fins. Also, the Colburn factor (j) and friction factor (f) correlations of plain fin-and-tube heat exchangers, which is proposed by Wang and Chang [22] and Wang et al. [17], respectively, are selected to compare with the tested results. As shown in Fig. 6, it is found that crimped spiral fins have a similar trend with the plain fins as well. However, due to the corrugated folding at the base of the present fin configuration, it appears that crimped spiral fins give a higher friction factor (f) than that plain fins at the same Reynolds number. Moreover, as shown in Fig. 6, there is no significant effect of fin material on both the Colburn factor (j) and friction factor (f).

Fig. 7(a) illustrated the effect of the number of tube rows on the fin efficiency (η_f) of both fin material. It can be seen that no significant effect of number of tube rows is found under the same experimental conditions. The reason may be explained by Eqs. (11) and (12), which show that an increase in the number of tube rows has no significant differences in terms of ϕ and fin efficiency (η_f) at the same Reynolds number because the fin efficiency depends only on size, shape and material of fin. In the meantime, it can be clearly seen that the fin efficiency (η_f) of the copper fin is higher than that of aluminium fin due to a higher thermal conductivity of copper.

Moreover, the heat transfer rate for both fins is shown in Fig. 7(b). It seems that the heat transfer rate for copper fin only marginally higher than that of aluminium fin due to its very minor difference in fin efficiency. On the other hand, the number of tube rows had significant effect on average heat transfer rate at the same air frontal velocity.

A comparison of the results for the effect of the number of tube rows on the pressure drop of crimped spiral fin-and-tube heat exchangers is presented in Fig. 7(c). As seen, the pressure drop increases with the frontal air velocity while the friction factor decreases with increasing Reynolds number. It can be seen that the pressure drop for $N_{row} = 5$ is two times higher than those for $N_{row} = 2$. The reason for this result can be explained by the increase in the blocking flow area when N_{row} is increased.

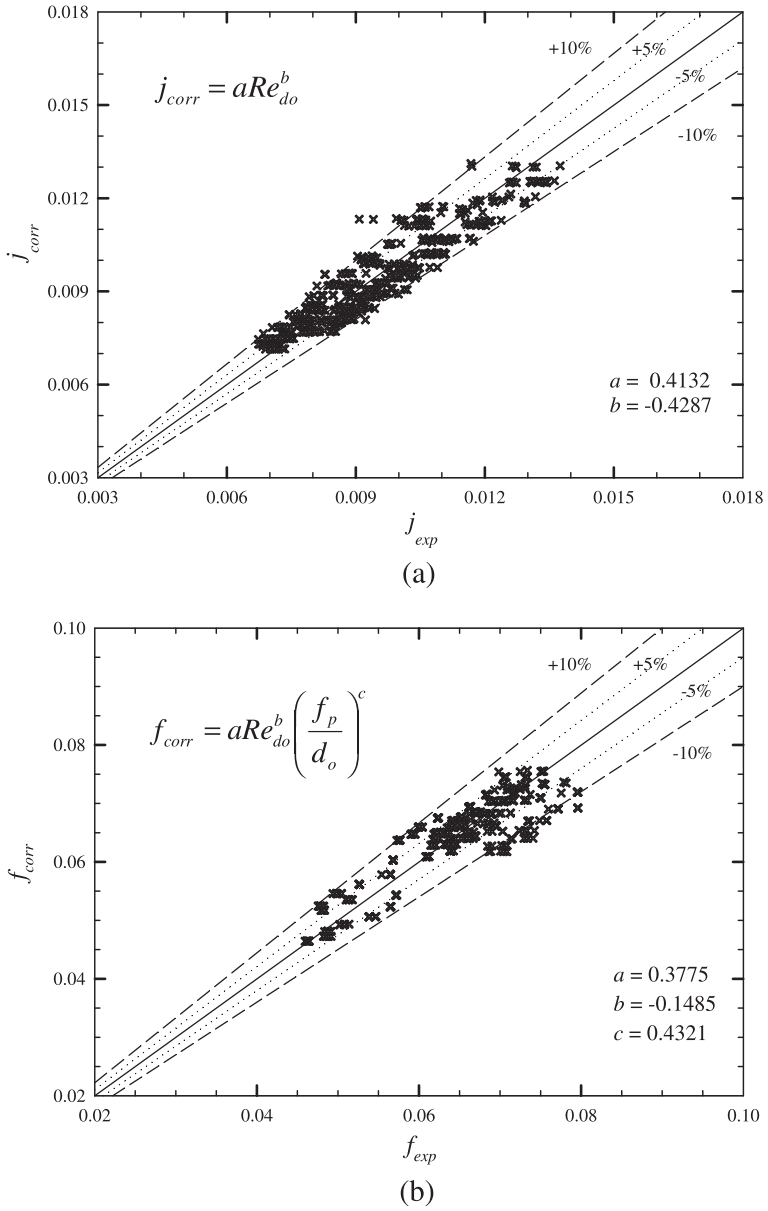

Fig. 8. Comparison of the proposed correlations with experimental data: (a) Colburn factor and (b) friction factor.

To determine the heat transfer coefficient of crimped spiral fin-and-tube heat exchangers, an empirical correlation between the Colburn factor (j) and the friction factor (f) is proposed in this work. The correlations may be valuable for industrial usage in order to design the heat exchangers operating at air flows of high Reynolds number.

An empirical correlation for j and f factors for crimped spiral fin-and-tube heat exchanger is developed in this work. The correlation also includes the experimental data used to study the effect of fin pitch as reported in Pongsoi et al. [3]. It must be noted that number of tube rows cast negligible influence on both j and f factors as foregoing discussions. As a result, the number of tube row is not included in the correlations. The test results are correlated as suggested by Wang et al. [23] in the form of $j = aRe_{do}^{b}$ and $f = aRe_{do}^{b}$ where a and b are the empirical constants obtained from least-square fitting of the experimental data. Furthermore, based on the data analysis, the f factor of crimped spiral fin-and-tube heat exchanger were also proportional to the fin pitch. Therefore, the present correlation for f factor is modified by including the dimensionless fin pitch (f_p) normalized by the tube outside diameter (d_o). The final correlation for the j and f factors takes the following form:

$$j_{corr} = 0.4132Re_{do}^{-0.4287} \tag{15}$$

$$f_{corr} = 0.3775Re_{do}^{-0.1485}\left(\frac{f_p}{d_o}\right)^{0.4321} \tag{16}$$

$$\text{Mean deviations} = \frac{1}{M}\left[\sum_{1}^{M}\frac{|\Phi_{corr} - \Phi_{exp}|}{\Phi_{exp}}\right] \times 100\% \tag{17}$$

As shown in Fig. 8, the proposed heat transfer and friction correlations Eqs. (15) and (16) can describe 95.04% and 91.07% of the j and f factors to be within ±10%, respectively. The mean deviations Eq. (17) of the proposed heat transfer and friction correlations are 5.09% and 4.53%, respectively. However, Eq. (15) and (16) can be used only (N_{row} = 2–5), (f_p = 3.2–6.3 mm) when staggered arrangement.

4. Conclusion

This study has investigated the effect of number of tube rows on the air-side performance of crimped spiral fin and tube heat exchangers having multipass parallel and counter cross-flow under sensible heating conditions at high Reynolds number (3000–13,000) based on the tube outside diameter. The following conclusions based on the tests are obtained:

- The number of tube rows cast a negligible influence on the air-side heat transfer performance at high Reynolds number (3000–13,000). Moreover, it could be clearly seen that the airside performance is independent of fin material.
- The average heat transfer rate and pressure drop increase with increasing the number of tube rows.
- The correlation of Colburn factor (j) and friction factor (f) of crimped spiral fin-and-tube heat exchangers at high Reynolds number are proposed in this paper. The mean deviations of the proposed heat transfer and friction correlations are 5.09% and 4.53%, respectively.

Acknowledgments

The authors are indebted to the Thailand Research Fund and the National Research University Project for supporting this study. The third author also expresses gratitude for support funding from the National Science Council of Taiwan (99-2218-E-009-012-MY2).

References

[1] A. Nuntaphan, T. Kiatsiriroat, C.C. Wang, Air side performance at low Reynolds number of cross-flow heat exchanger using crimped spiral fins, Int. Commun. Heat Mass Transfer 32 (1-2) (2005) 151–165.
[2] K. Srisawad, S. Wongwises, Heat transfer characteristics of a new helically coiled crimped spiral finned tube heat exchanger, Heat Mass Transfer 45 (4) (2009) 381–391.
[3] P. Pongsoi, S. Pikulkajorn, C.C. Wang, S. Wongwises, Effect of fin pitches on the air-side performance of crimped spiral fin-and-tube heat exchangers with a multipass parallel and counter cross-flow configuration, Int. J. Heat Mass Transfer 54 (9–10) (2011) 2234–2240.
[4] L.H. Tang, M. Zeng, Q.W. Wang, Experimental and numerical investigation on air-side performance of fin-and-tube heat exchangers with various fin patterns, Exp. Thermal Fluid Sci. 33 (2009) 818–827.
[5] G. Xie, Q. Wang, B. Sunden, Parametric study and multiple correlations on air-side heat transfer and friction characteristics of fin-and-tube heat exchangers with large number of large-diameter tube rows, Appl. Therm. Eng. 29 (1) (2009) 1–16.
[6] Y.C. Liu, S. Wongwises, W.J. Chang, C.C. Wang, Airside performance of fin-and-tube heat exchangers in dehumidifying conditions – data with larger diameter, Int. J. Heat Mass Transfer 53 (7-8) (2010) 1603–1608.
[7] C.C. Wang, J.S. Liaw, B.C. Yang, Airside performance of herringbone wavy fin-and-tube heat exchangers – data with larger diameter tube, Int. J. Heat Mass Transfer 54 (5–6) (2011) 1024–1029.
[8] S. Wongwises, Y. Chokeman, Effect of fin pitch and number of tube rows on the air side performance of herringbone wavy fin and tube heat exchangers, Energy Convers. Manage. 46 (13–14) (2005) 2216–2231.
[9] ESDU 86018, Effectiveness-NTU Relations for the Design and Performance Evaluation of two-stream heat exchangers, Engineering Science Data Unit 86018 with Amendment, London ESDU International plc, 1991, pp. 92–107.
[10] H.A. Navarro, L. Cabezas-Gomez, A new approach for thermal performance calculation of cross-flow heat exchanger, Int. J. Heat Mass Transfer 48 (18) (2005) 3880–3888.
[11] L. Cabezas-Gomez, H.A. Navarro, J.M. Saiz-Jabardo, Thermal performance of multipass parallel and counter-cross-flow heat exchangers, J. Heat Transfer 129 (3) (2007) 282–290.
[12] K.A. Gardner, Efficient of extended surface, ASME Trans. 67 (1945) 621.
[13] W.M. Kays, A. London, Compact Heat Exchangers, third ed., McGraw-Hill, New York, 1984.
[14] V. Gnielinski, New equation for heat and mass transfer in turbulent pipe and channel flow, Int. Chem. Eng. 16 (1976) 359–368.
[15] ANSI/ASHRAE Standard 33-2000, Method of Testing Forced Circulation Air Cooling and Air Heating Coils, 2000.
[16] D.G. Rich, The effect of the number of tube rows on heat transfer performance of smooth plate fin-and-tube heat, ASHRAE Trans. 81 (1) (1975) 307–317.
[17] C.C. Wang, Y.J. Chang, Y.C. Hsieh, Y.T. Lin, Sensible heat and friction characteristics of plate fin-and-tube heat exchangers having plane fins, Int. J. Refrig. 19 (4) (1996) 223–230.
[18] C.C. Wang, W.L. Fu, C.T. Chang, Heat transfer and friction characteristics of typical wavy fin-and-tube heat exchangers, Exp. Thermal Fluid Sci. 14 (2) (1997) 174–186.
[19] C.C. Wang, K.-Y. Chi, Y.-J. Chang, Y.-P. Chang, An experimental study of heat transfer and friction characteristics of typical louver fin-and-tube heat exchangers, Int. J. Heat Mass Transfer 41 (4-5) (1998) 817–822.
[20] Y.J. Du, C.C. Wang, An experimental study of the airside performance of the superslit fin-and-tube heat exchangers, Int. J. Heat Mass Transfer 43 (24) (2000) 4475–4482.
[21] D.E. Briggs, E.H. Young, Convective heat transfer and pressure drop of air flowing across triangular pitch banks of finned tubes, Chem. Eng. Prog. Symp. Ser. 59 (41) (1963) 1–10.
[22] C.C. Wang, C.T. Chang, Heat and mass transfer for plate fin-and-tube heat exchangers, with and without hydrophilic coating, Int. J. Heat Mass Transfer 41 (20) (1998) 3109–3120.
[23] C.C. Wang, K.Y. Chi, C.J. Chang, Heat transfer and friction characteristics of plain fin-and-tube heat exchangers: Part II. Correlation, Int. J. Heat Mass Transfer 43 (15) (2000) 2693–2700.

International Journal of Heat and Mass Transfer 55 (2012) 1475–1485

Contents lists available at SciVerse ScienceDirect

International Journal of Heat and Mass Transfer

journal homepage: www.elsevier.com/locate/ijhmt

Unconfined laminar nanofluid flow and heat transfer around a square cylinder

Vahid Etminan-Farooji [a], Ehsan Ebrahimnia-Bajestan [a,*], Hamid Niazmand [a], Somchai Wongwises [b,c]

[a] Department of Mechanical Engineering, Ferdowsi University of Mashhad, Mashhad, Iran
[b] Fluid Mechanics, Thermal Engineering and Multiphase Flow Research Lab. (FUTURE), Department of Mechanical Engineering, King Mongkut's University of Technology Thonburi, Bangmod, Bangkok, Thailand
[c] The Academy of Science, The Royal Institute of Thailand, SanamSueaPa, Dusit, Bangkok 10300, Thailand

ARTICLE INFO

Article history:
Received 13 April 2011
Received in revised form 10 October 2011
Accepted 10 October 2011
Available online 12 December 2011

Keywords:
Nanofluid
Square cylinder
Peclet number
Thermophysical properties
Unconfined flow
Heat transfer enhancement

ABSTRACT

The momentum and forced convection heat transfer for a laminar and steady free stream flow of nanofluids past an isolated square cylinder have been studied numerically. Different nanofluids consisting of Al_2O_3 and CuO with base fluids of water and a 60:40 (by mass) ethylene glycol and water mixture were selected to evaluate their superiority over conventional fluids. Recent correlations for the thermal conductivity and viscosity of nanofluids, which are functions of particle volumetric concentration as well as temperature, have been employed in this paper. The simulations have been conducted for $Pe = 25$, 50, 100 and 200, with nanoparticle diameters of 30 and 100 nm and particle volumetric concentrations ranging from 0% to 4%. The results of heat transfer characteristics of nanofluid flow over a square cylinder showed marked improvement comparing with the base fluids. This improvement is more evident in flows with higher Peclet numbers and higher particle volume concentration, while the particle diameter imposes an adverse effect on the heat transfer characteristics. In addition, it was shown that for any given particle diameter there is an optimum value of particle concentration that results in the highest heat transfer coefficient.

1. Introduction

Due to the immense theoretical and practical importance of cross flow past bluff bodies, this field of study has received substantial attention from researchers. Common examples of this kind of flow include flow in tubular and pin-type heat exchangers, the use of thin cylinders as measuring probes as well as sensors, and in the continuous thermal treatment of food particles (such as slices and chips of carrots and potatoes) in viscous fluids (high Prandtl number). Over the years, a considerable amount of information dealing with different aspects of the heat transfer and flow over bluff bodies has been added to the literature, a great majority of which relates to the flow over a circular cylinder [1–5]. In contrast to much theoretical, experimental and numerical data on the flow around circular cylinders over a wide range of Reynolds numbers, there are a limited number of similar studies and information available on flow around square bodies. However, in recent years there have been some efforts to expand the knowledge of flow over square cylinders in the literature. Turki et al. [6] presented a numerical study to analyse the unsteady flow field and heat transfer characteristics in a horizontal channel with a built-in heated square cylinder. The study was carried out for two channel blockage ratios ($B = 1/4$ and 1/8), and different Reynolds and Richardson numbers ranging from 62 to 200 and from 0 to 0.1 respectively at $Pr = 0.71$. They showed that the overall heat transfer of a square cylinder was slightly affected by the blockage ratio and presented correlations for $B = 1/4$ and $B = 1/8$.

Sharma and Eswaran [7] have carried out a detailed study on heat and fluid flow over square cylinders. In a study concerning the unconfined two dimensional laminar regime for Reynolds numbers between 1 and 160, they showed that the transition to unsteadiness occurs between $Re = 40$ and 50. The results indicated that the heat transfer characteristics in the steady flow regime ($Re \leqslant 40$) and unsteady periodic 2-D flow regime ($50 \leqslant Re \leqslant 160$) are markedly different. The time-averaged rear-surface Nusselt number is more strongly dependent on Reynolds numbers in the periodic flow regime, in contrast to the other faces of the cylinder. Finally, heat transfer correlations for both constant temperature and constant-heat-flux boundary conditions were proposed.

Dihman et al. [8] researched the flow and heat transfer characteristics of an isolated square cylinder in a crossflow placed symmetrically in a channel for the range of conditions of $1 \leqslant Re \leqslant 45$, $0.7 \leqslant Pr \leqslant 4000$, $Pe \leqslant 4000$ and $B = 1/8$, 1/6 and 1/4. It was shown

* Corresponding author. Tel.: +98 915 300 6795; fax: +98 511 876 3304.
E-mail address: ehsan.ebrahimnia@gmail.com (E. Ebrahimnia-Bajestan).

0017-9310/$ - see front matter © 2011 Elsevier Ltd. All rights reserved.
doi:10.1016/j.ijheatmasstransfer.2011.10.030

Nomenclature

B	blockage ratio, $B = L/H$
c_d	drag coefficient
c_p	specific heat, J/kg K
d	diameter, m
h	heat transfer coefficient, W/m^2 K
H	height of the computational domain, m
k	thermal conductivity, W/m K
L	side of the square cylinder, m
n	normal direction to the surface, m
Nu	Nusselt number, $Nu = hL/k$
P	pressure, Pa
Pe	Peclet number, $Pe = Re \times Pr$
Pr	Prandtl number, $Pr = \mu c_p/k$
Re	Reynolds number, $Re = \rho u_\infty L/\mu$
T	temperature, K
V	velocity, m/s
x	streamwise coordinate, $x = x'/L$
X_d	downstream face distance of the cylinder from the outlet, m
X_u	upstream face distance of the cylinder from the inlet, m
y	transverse coordinate, $y = y'/L$

Greek symbols

δ	size of the CV clustered around the cylinder, m
Δ	size of the CV far away from the cylinder, m
μ	dynamic viscosity, kg/m s
Φ	particle volumetric concentration, %
ρ	density, kg/m^3
κ	Boltzmann constant, 1.381×10^{-23} J/K

Subscripts

∞	inlet condition
bf	base fluid
nf	nanofluid
np	nanoparticle
w	wall

that under the same conditions of B, Re and Pr, the use of the constant heat flux boundary condition yields slightly higher values of the Nusselt number than constant temperature case. The results indicated that for a fixed block ratio, the increase in Prandtl and/or Reynolds number ends in the enhancement of the average Nusselt number. Finally, heat transfer correlations were obtained for the constant temperature and constant heat flux cases of the solid square cylinder in the previously mentioned range of physical parameters. In a recent study [9] on the effects of Reynolds and Prandtl numbers on the heat transfer from a square cylinder, a numerical study has been carried out in a 2D unsteady crossflow for the range of conditions $60 \leqslant Re \leqslant 160$ and $0.7 \leqslant Pr \leqslant 50$ (the maximum value of Peclet number being 4000). The results showed that the overall mean Nusselt number increases with the Reynolds and Prandtl numbers. It was also shown that the Nusselt number profiles for the two boundary conditions were qualitatively similar, though the constant heat flux case had a numerically higher mean Nu, for identical conditions. The front surface of the cylinder exhibited the highest value of the surface average Nusselt number; however the value for the rear face exceeded the values at the top or bottom surfaces at high Reynolds and Prandtl numbers.

One of the main difficulties with industrial fluids such as water, mineral oils and ethylene glycol is their poor heat transfer properties that impose a limitation in improving the heat transfer augmentation and compactness of the heat exchangers. There are several methods to improve the heat transfer characteristics, such as employing the flow inserts and nanofluids. Recently, much research [10,11] has been done on the suspension of nanoparticles in conventional heat transfer fluids named nanofluid, due to their anomalous thermal conductivity enhancement. Applying this new generation of heat transfer fluids eliminates the limitation of low thermal conductivity of conventional heat transfer fluids. Several effective parameters on the thermal conductivity of nanofluids have been presented, such as nanofluid temperature [12,13], nanoparticle size [12], concentration [12,13], shape [14] and materials [13]. Furthermore, some researchers believe that the Brownian motion of nanoparticles inside the fluid is a key mechanism of heat transfer in nanofluids [15]. A number of models are presented to consider these different effective parameters on the conductive heat transfer of nanofluids [13,15,16] and other thermophysical properties such as viscosity [17,18].

Ding et al. [19] conducted experiments on the laminar convective heat transfer of a Carbone nanotube-water mixture flowing through a horizontal tube. They reported a maximum enhancement of 3.5 times the heat transfer coefficient of the nanofluid relative to pure water. They showed that the effect of shape and concentration of nanoparticles is significant in determining the convective heat transfer coefficient. An experimental investigation on the convective heat transfer characteristics in the developing region of tube flow was carried out by using water/Al_2O_3 nanofluids by Anoop et al. [20]. Their results indicated that nanofluids with a smaller average particle size result in higher heat transfer coefficient.

The effect of types of nanoparticle on the laminar convective heat transfer of nanofluids was studied by Rea et al. [21]. They showed that water/Al_2O_3 nanofluid increases the heat transfer coefficient more than water/ZrO_2 nanofluid. Zeinali et al. [22] investigated the heat transfer performance of water/Al_2O_3 and water/CuO nanofluids flowing through a circular tube under a laminar flow regime. The results of their experiments indicated that the water/Al_2O_3 nanofluids cause a greater enhancement in heat transfer coefficient compared with CuO/water. They suggested that it may result from the large particle size of CuO nanoparticles compared with Al_2O_3. Ebrahimnia-Bajestan et al. [23] carried out a numerical study on the effects of different parameters on the convective heat transfer of nanofluids inside a straight circular pipe. Their results indicated that increasing particle concentration, aspect ratio of nanoparticles and flow Reynolds number enhance the heat transfer while increasing nanoparticle diameter reduces the heat transfer coefficient. Furthermore, the results demonstrated that the heat transfer characteristics of nanofluids are significantly affected by Brownian motion of particles as well as types of base fluid and nanoparticles.

Due to the outstanding potential of nanofluids in enhancing heat transfer many researchers have studied their effects and characteristics, but most of these studies are oriented toward simple geometries. To the best of the authors' knowledge, no research on nanofluids flow and heat transfer over bluff bodies has been documented in the literature. In this study, the unconfined flows of two conventional fluids as well as various types of nanofluids over a square cylinder are numerically simulated. The convective heat transfer coefficients of these flows are determined and the

effect of using nanofluids in enhancing the heat transfer from the cylinder to the flow is carefully studied. The conventional fluids (also base fluids) were chosen to be water and a 60% ethylene glycol and 40% water mixture by mass (EG:W) which are widely used as the heat transfer fluid in heat exchangers, building heating and automobile radiators. The material of the nanoparticles were selected as Al_2O_3 and CuO with two different diameters of d_{np} = 30 and 100 nm. The values of the nanoparticle volumetric concentration φ were also chosen to be 2% and 4%. All the simulations were conducted at four different Peclet numbers of 25, 50, 100 and 200.

2. Mathematical modelling

2.1. Geometrical configuration

The system of interest in this case is the unconfined flow around a two-dimensional square cylinder with side L, which is also the non-dimensionalising length scale. In this system, the square cylinder (block) is placed symmetrically between the upper and lower boundaries and is maintained at a constant temperature T_w. The block is exposed to a free stream with uniform velocity u_∞ and temperature T_∞ (Fig. 1). In addition, the free slip condition is used for artificial confining boundaries. Sohankar et al. [24] have shown that for avoiding the misleading effects of the presence of the upper and lower boundaries on the flow characteristics near the cylinder, the blockage ratio B which is defined as L/H should not be more than 5. Therefore, H/L = 20 has been used in the present work as the channel blockage ratio. Moreover, the non-dimensional upstream distance between the channel inlet and the front surface of the cylinder, X_u/L, is taken as 8 and the non-dimensional downstream distance between the rear surface of the cylinder and channel outlet, X_d/L, is taken as 15. More details on the procedure of choosing these values are presented in Section 2.4.

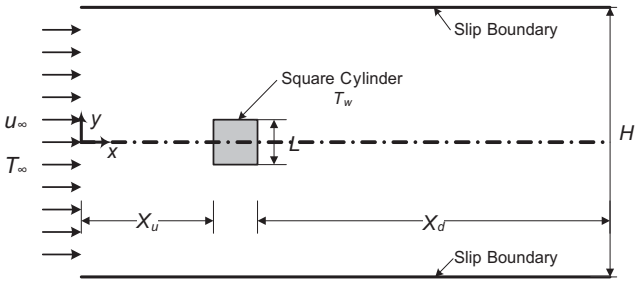

Fig. 1. Schematics of the flow and the computational domain.

2.2. Governing equations

The unconfined flow of water and the mixture of ethylene glycol and water (60:40 EG:W)can be considered to be incompressible. It is also reasonable to neglect viscous dissipation. Under these conditions, the following conservation equations were solved numerically in a two-dimensional flow field using the computational fluid dynamics software Fluent6.3 [25]:

– *Continuity*

$$(\nabla \cdot V) = 0, \tag{1}$$

– *Momentum*

$$\rho_{nf}(\nabla \cdot V)V = -\nabla P + \nabla.(\mu_{nf}\nabla V), \tag{2}$$

– *Energy*

$$\rho_{nf}c_{P,nf}(V \cdot \nabla)T = \nabla.(k_{nf}\nabla T). \tag{3}$$

2.3. Numerical method

The system of governing Eqs. (1)–(3) was solved by the control volume method using Fluent [25]. Discretization of convection terms, diffusion terms, and other quantities resulting from the governing equations was carried out using the first-order upwind scheme. The pressure–velocity coupling was modelled with the SIMPLE algorithm. Fluent uses a point implicit linear equation in conjunction with an algebraic multi-grid (AMG) method to solve the resultant block system of equations for all dependent variables in each cell. For all the simulations performed in this study, the solutions were only considered to be converged when the residuals were lower than 10^{-9}. The resulting data were then post-processed to obtain the streamlines, temperature field and convective heat transfer coefficients of the block walls.

2.4. Choice of numerical parameters

It has been shown that in numerical simulations of flow around bluff bodies, the numerical parameters such as blockage ratio B, upstream computational domain X_u, downstream computational domain X_d and grid size, $M \times N$, are of great importance and should be chosen carefully [24,26]. Since there is no available information on nanofluids flow around a square cylinder, the values of aforementioned parameters used when studying the air flow over bluff bodies were used as initial guesses. In order to study the confining upper and lower boundaries, three blockage ratios of 1/15, 1/20 and 1/25 were tested for nanofluid EG:W/Al_2O_3 4% (d_{np} = 30 nm) at the lowest Peclet number (Pe = 25). A monotonic behaviour was discovered in the variation of c_d and Nu with blockage ratio, and the changes in the values of c_d and Nu were 1.68% and 0.47%, respectively as the blockage ratio reduced from 1/20 to 1/25. Therefore, B = 1/20 was found to be adequate to simulate nanofluid unconfined flow.

In order to explore the influence of the upstream distance between the inlet and the front surface of the cylinder, four values of X_u/L = 5, 8, 10 and 15 were studied while keeping X_d/L constant at 40. Once again the nanofluid EG:W/Al_2O_3 4% (d_{np} = 30 nm) was simulated at Pe = 25 and results showed that relative percentage changes in the values of c_d and Nu were about 0.042% and 0.012% for X_u/L = 8 with respect to X_u/L = 15, respectively. Thus X_u/L = 8 was found to be an appropriate value, which is consistent with earlier research [7,8,27].

An extensive study on the influence of the downstream distance of the cylinder from the outlet X_d is carried out in [24] and also in a number of other studies including [8,28]. Based on the values used in these papers, four values of X_d/L = 10, 15, 20 and 30 were tested for water/CuO 4% (d_{np} = 100 nm) at the highest Peclet number (Pe = 200), while keeping X_u/L constant at 8. This experiment revealed that the resulting gain in the accuracy of c_d and Nu were as small as 0.019% and 0.01%, respectively, at the expense of a considerable increase in CPU time when increasing the X_d/L from 15 to 30. As a result, X_d/L = 15 is used for all the calculations in this study.

2.5. Grid structure

The grid structure approach adopted in [7,8] was found to be adequate for simulating the unconfined flow of interest. First, a uniform fine grid with constant cell size δ was distributed around the cylinder over a distance of 1.5 units to adequately capture wake-wall interactions. A much coarser mesh with constant cell size Δ was made outside the region around the cylinder that extended 4 units upstream, downstream, and to the sides. An

Table 1
Details of the grids used at $Pe = 200$ for grid independence study.

	δ	Δ	X_u	X_d	B	Size (M × N)
Grid 1	0.015	0.5	8	15	1/20	163 × 67
Grid 2	0.01	0.25	8	15	1/20	274 × 129
Grid 3	0.008	0.2	8	15	1/20	342 × 162
Grid 4	0.006	0.15	8	15	1/20	458 × 210

algebraic expression was used to generate the grid between these two regions.

2.6. Grid independence study

A grid independence study was carried out using the different non-uniform grids listed in Table 1. Four values of δ and Δ were tested to study the effects of near-region and far-field grid resolution for $Pe = 200$ and a blockage ratio of $B = 1/20$. The fluid was chosen to be water/CuO4% ($d_{np} = 100$ nm) and the upstream distance X_u/L and downstream distance X_d/L were kept constant at 8 and 15, respectively. The results of grids 1 and 2 demonstrate considerable differences while the relative changes in the value of c_d and Nu for grid 3 relative to grid 4 is only 0.31% and 0.74%, respectively. The excessive computation time taken to solve grid 4 justifies the small errors involved in using grid 3. Therefore, grid 3 is used in this study for unconfined ($B = 1/20$) flow. The grid structure was generated using Gambit [29] and is shown in Fig. 2. It shows the non-uniform grid for the whole computational domain (Fig. 2(a)) and a magnified view near the block (Fig. 2(b)).

2.7. Nanofluid modelling

The thermophysical properties of nanofluids such as density, specific heat, thermal conductivity and viscosity are calculated based on relationships presented in the literature. These formulas are listed below:

- *Density*
  The density of the nanofluids is calculated based on the equation proposed by Pak and Cho [30]:

$$\rho_{nf} = (1-\phi)\rho_{bf} + \phi\rho_{np}. \tag{4}$$

- *Specific heat*
  The specific heat of nanofluids is determined using the equation given by Xuan and Roetzel [31] that assumes thermal equilibrium between the base fluid and the nanoparticles:

$$C_{p,nf} = \frac{(1-\phi)(\rho c_p)_{bf} + \phi(\rho c_p)_{np}}{(1-\phi)\rho_{bf} + \phi\rho_{np}}. \tag{5}$$

- *Thermal conductivity*
  Koo and Kleinstreuer [15] presented their thermal conductivity model as a two-term function which takes into account the effect of particle size d_{np}, particle volumetric concentration ϕ, temperature T and the properties of the base fluid as well as the effect of the Brownian motion of nanoparticles. Later, Vajjha and Das [32] revised this relation using a broader set of data:

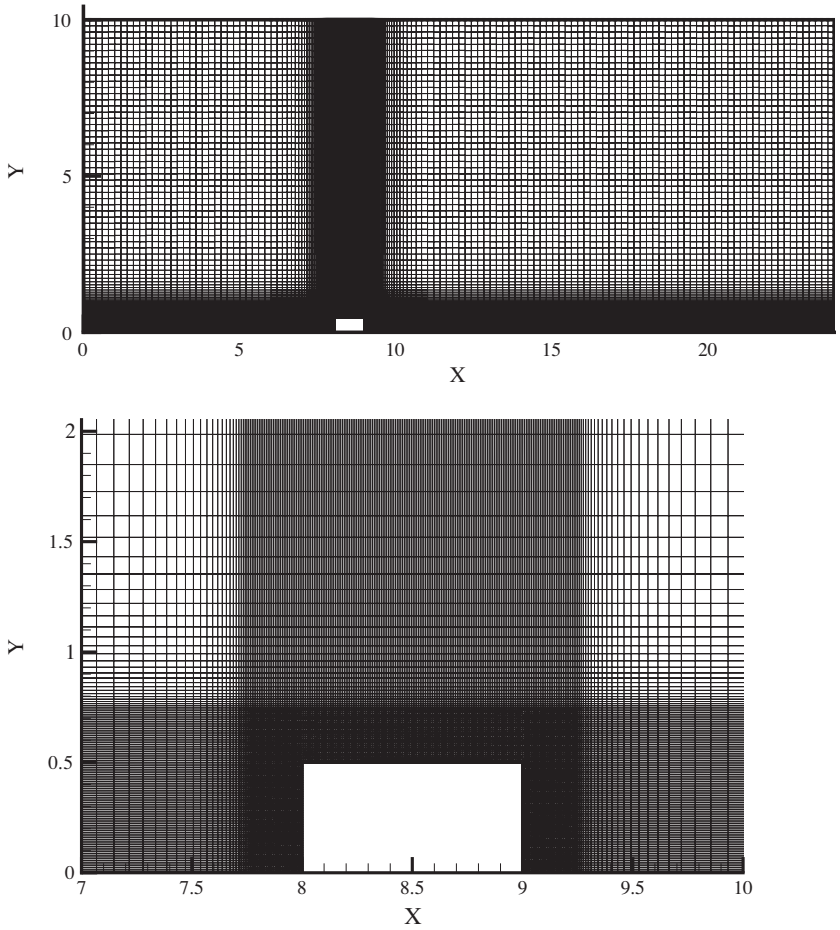

Fig. 2. Non-uniform computational grid structure.

Table 2
Curve-fit relations proposed by Vajjha and Das [32].

Type of particles	β	Concentration
Al_2O_3	$8.4407(100\phi)^{-1.07304}$	$1\% \leqslant \phi \leqslant 10\%$
CuO	$9.881(100\phi)^{-0.9446}$	$1\% \leqslant \phi \leqslant 6\%$

Table 3
Physical properties of nanoparticles.

Material	ρ (kg/m^3)	Cp (J/kg·K)	k (W/m K)
Al_2O_3	3970	765	40
CuO_2	6350	535.6	76.5

$$k_{nf} = \frac{k_{np} + 2k_{bf} - 2(k_{bf} - k_{np})\phi}{k_{np} + 2k_{bf} + (k_{bf} - k_{np})\phi} k_{bf} + 5 \times 10^4 \beta\phi\rho c_{p,bf} \times \sqrt{\frac{\kappa T}{\rho_{np} d_{np}}} f(T,\phi), \tag{6a}$$

where

$$f(T,\phi) = \left(2.8217 \times 10^{-2}\phi + 3.917 \times 10^{-3}\right)\frac{T}{T_0} + \left(-3.0669 \times 10^{-2}\phi - 3.91123 \times 10^{-3}\right). \tag{6b}$$

In the above equation, T_0 is set at 273 K and also the expressions of β for Al_2O_3 and CuO nanoparticles are given in Table 2. These relations are valid for 298 K $\leqslant T \leqslant$ 363 K.

– *Viscosity*

In a recent paper, Masoumi et al. [17] developed a theoretical model for the prediction of the effective viscosity of nanofluids based on Brownian motion. They showed that their presented model could accurately predict the effective viscosity of different nanofluids. Their model is:

$$\mu_{nf} = \mu_{bf} + \frac{\rho_{np} V_B d_{np}^2}{72C\delta}, \tag{7a}$$

in which:

$$V_B = \frac{1}{d_{np}}\sqrt{\frac{18\kappa T}{\pi\rho_{np} d_{np}}}, \tag{7b}$$

$$\delta = \sqrt[3]{\frac{\pi}{6\phi}} d_{np}, \tag{7c}$$

$$C = \mu_{bf}^{-1}\left[\left(c_1 d_{np} \times 10^9 + c_2\right)\phi + \left(c_3 d_{np} \times 10^9 + c_4\right)\right], \tag{7d}$$

where:

$$c_1 = -0.000001133,$$
$$c_2 = -0.000002771,$$
$$c_3 = 0.00000009,$$
$$c_4 = -0.000000393.$$

The thermophysical properties equations summarised in the previous sections require the values of the properties of the base fluid as well as nanoparticles. The properties of nanoparticles are taken to be constant in the present operating range of 300 K to about 320 K (Table 3).

The thermophysical properties of water and EG:W were obtained from the ASHRAE Handbook [33] were curve fitted as a function of the temperature with the following equations.

– *Thermophysical properties of water*

$$\rho_{bf} = -0.0036T^2 + 1.9159T + 748.19, \tag{8}$$
$$c_{p,nf} = -0.0001T^3 + 0.1155T^2 - 41.296T + 9017.8, \tag{9}$$
$$k_{bf} = -8 \times 10^{-6}T^2 + 0.0062T - 0.5388, \tag{10}$$
$$\mu_{bf} = 0.00002414 \times 10^{(247.8/(T-140))}, \tag{11}$$

– *Thermophysical properties of EG:W*

$$\rho_{bf} = -0.002475T^2 + 0.9998T + 1002.5, \tag{12}$$
$$C_{p,bf} = 4.248T + 1882.4, \tag{13}$$
$$k_{bf} = -3.196 \times 10^{-6}T^2 + 0.0025T - 0.1054, \tag{14}$$
$$\mu_{bf} = 0.001 \times \exp\left(3135.6 \times \frac{1}{T} - 8.9367\right). \tag{15}$$

Then they were substituted into the density, specific heat, thermal conductivity and viscosity equations, Eqs. (4)–(7), to evaluate the properties of nanofluids at different temperatures, concentrations and nanoparticle diameters. This was done by developing various User Defined Functions (UDFs) in C language which were then interpreted and incorporated into the main solver. Hence, in this study the properties of nanofluids are temperature dependent. Tables 4 and 5 show the physical properties of nanofluids based on water and EG:W at T = 300 K, respectively.

2.8. Validation of results

The results were validated using the available data in the literature which are mostly oriented to air (Pr = 0.7). Separate runs were necessary to determine the results at specific Reynolds numbers of 5, 20 and 40. Table 6 compares the drag coefficient c_d and overall Nusselt number of the cylinder $\overline{Nu}$ obtained in the present research with those from references [7,26]. It is clear that the results are in very good agreement with previous studies.

3. Results and discussion

Computations were carried out in a complete laminar and steady regime. The Peclet numbers were chosen to be 25, 50, 100 and 200 so the corresponding Reynolds numbers would not exceed 45 (for Re > 50 the flow becomes unsteady). A total number of 72 simulations were carried out for four nanofluids of water/Al_2O_3, water/

Table 4
Physical properties of nanofluids with the base fluid of water at T = 300 K.

Nanofluid	d_{np} (nm)	ϕ (%)	ρ (kg/m^3)	c_p (J/kg K)	k (W/m K)	μ (kg/m s)	Pr
Water/Al_2O_3	30	2	1056.0	3924.3	0.6857	9.942E−04	5.689
		4	1115.5	3694.8	0.7215	1.188E−03	6.086
	100	2	1056.0	3924.3	0.6679	8.715E−04	5.121
		4	1115.5	3694.8	0.7043	8.909E−04	4.674
Water/CuO	30	2	1103.6	3761.7	0.6870	1.032E−03	5.650
		4	1210.7	3416.3	0.7272	1.277E−03	6.001
	100	2	1103.6	3761.7	0.6689	8.767E−04	4.930
		4	1210.7	3416.3	0.7082	9.012E−04	4.348

Table 5
Physical properties of nanofluids with the base fluid of EG:water (60:40) at $T = 300$ K.

Nanofluid	d_{np} (nm)	φ (%)	ρ (kg/m^3)	c_p (J/kgK)	k (W/mK)	μ (kg/ms)	Pr
EG:Water/Al_2O_3	30	2	1137.5	2989.8	0.4143	5.310E−03	38.320
		4	1195.3	2839.0	0.4356	6.347E−03	41.374
	100	2	1137.5	2989.8	0.3997	4.655E−03	34.819
		4	1195.3	2839.0	0.4215	4.758E−03	32.055
EG:Water/CuO	30	2	1185.1	2875.9	0.4149	5.511E−03	38.193
		4	1290.5	2640.9	0.4394	6.823E−03	41.003
	100	2	1185.1	2875.9	0.4002	4.682E−03	33.649
		4	1290.5	2640.9	0.4238	4.813E−03	29.991

Table 6
Comparing the values of $\overline{Nu}$ and C_D with the data in the literature (air, $Pr = 0.7$).

	$Re = 5$		$Re = 20$		$Re = 40$	
	$\overline{Nu}$	c_d	$\overline{Nu}$	c_d	$\overline{Nu}$	c_d
Present study	1.27	4.83	2.07	2.43	2.72	1.83
Paliwali et al. [26]	1.22	–	2.07	–	2.71	1.98
Sharma and Eswaran [7]	1.24	4.86	2.05	2.35	2.71	1.75

CuO, EG:W/Al_2O_3, and EG:W/CuO using values of $d_{np} = 30$ and 100 as well as $\phi = 0$, 2% and 4%. Twelve extra simulations were also conducted to determine the required values for presenting Fig. 10.

Fig. 3 shows the streamlines plots in the vicinity of the square cylinder at $Pe = 25$, 50, 100 and 200 for water/CuO4% ($d_{np} = 30$ nm). It is clear from Fig. 3(a)–(d) that the flow is attached to the block until it reaches the trailing edge of the upper surface. At this point, the flow separates from the block and forms a recirculation region behind the cylinder. At $Pe = 25$ (Fig. 3(a)), this region is small but by increasing the Peclet number the recirculation region develops and at $Pe = 200$ (Fig. 3(d)) extends to less than 3 times L. In the case of

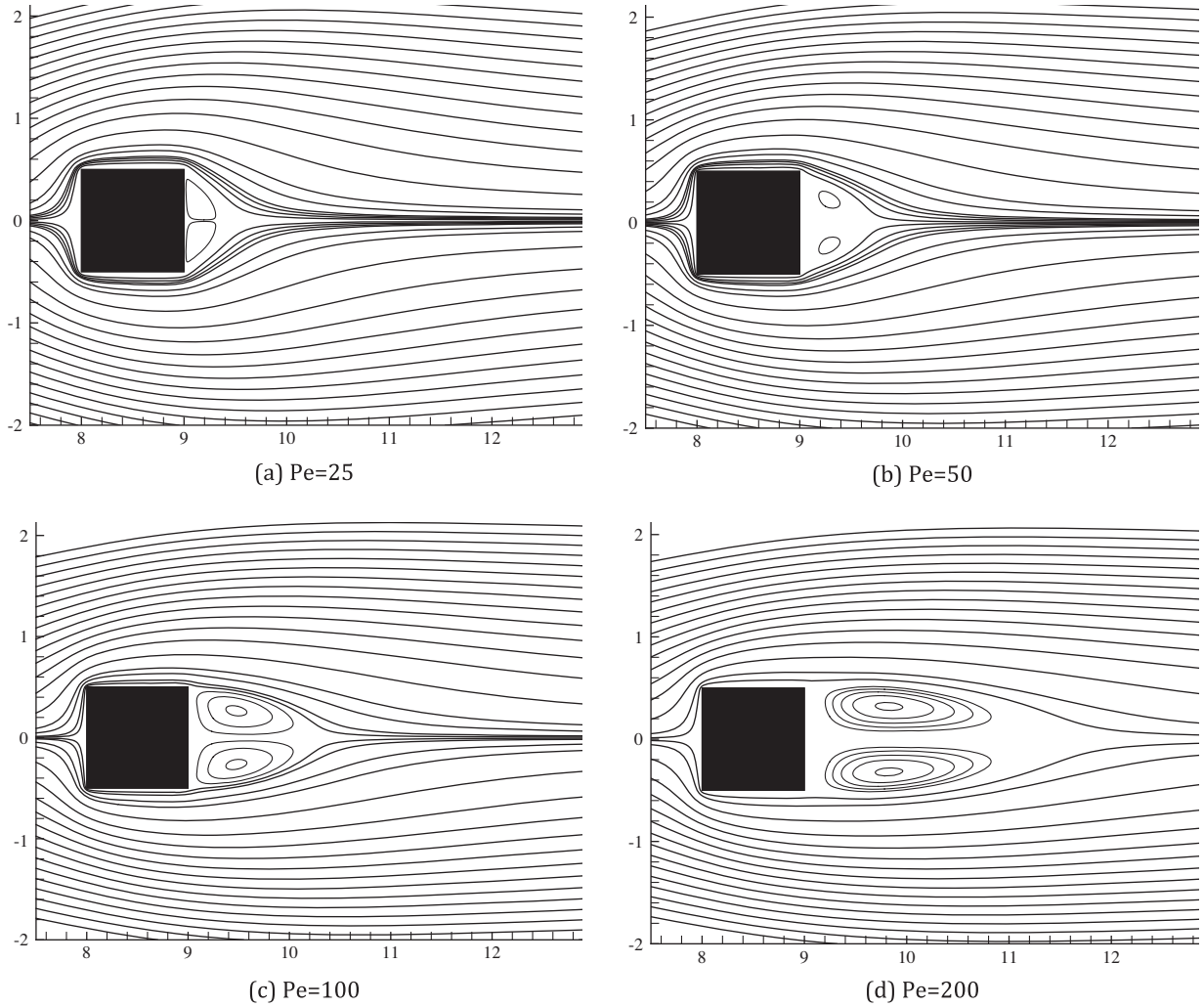

Fig. 3. Streamlines of water/CuO 4% ($d_{np} = 30$ nm) at different Peclet numbers.

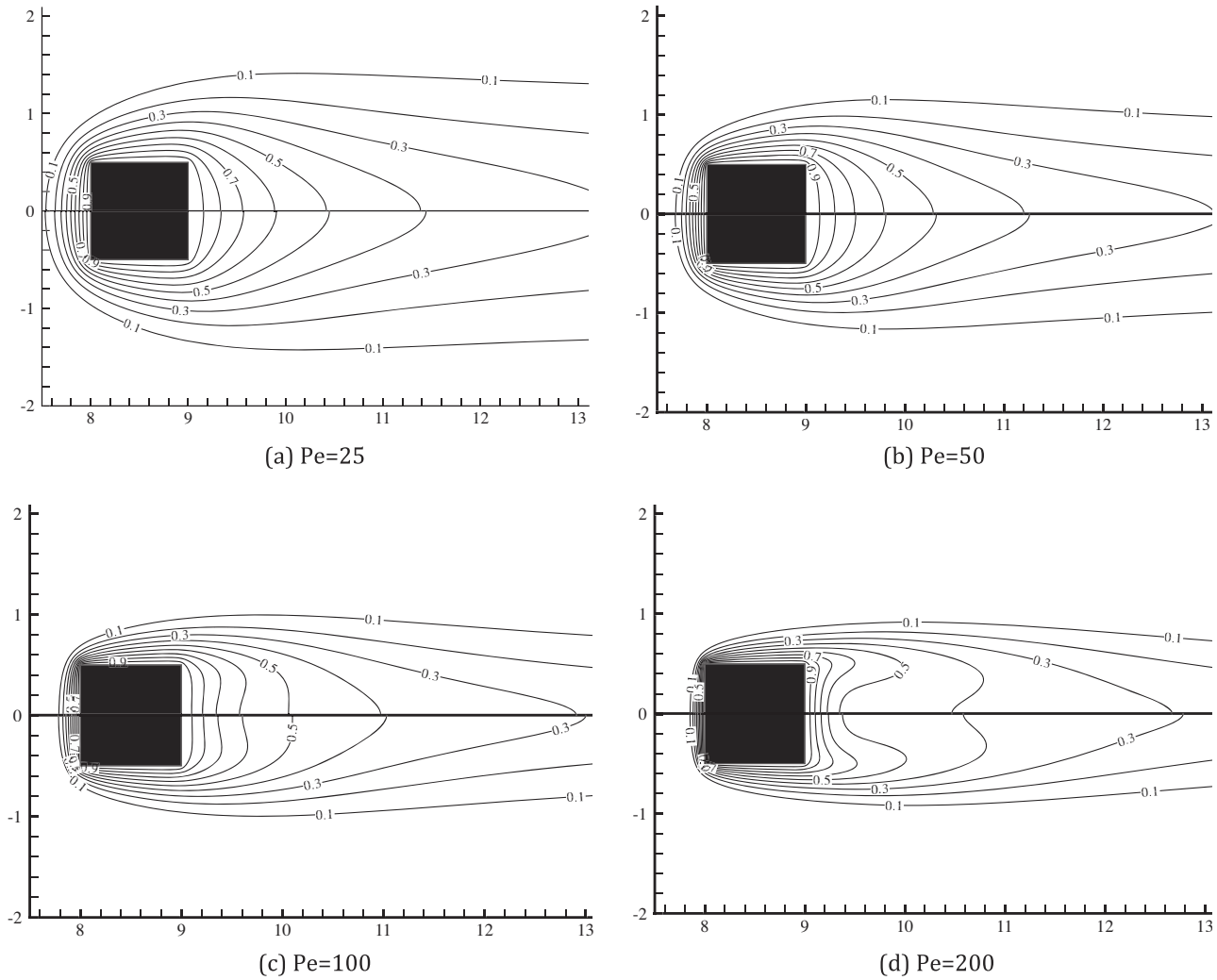

Fig. 4. Temperature contours of water (upper half) and water/CuO 4% (d_{np} = 30 nm, lower half) at different Peclet numbers.

water/CuO 4% (d_{np} = 30 nm), the Peclet numbers of 25, 50, 100 and 200 correspond to Reynolds numbers of 4.2, 8.3, 16.7 and 33.3.

Fig. 4 depicts the non-dimensional temperature contours (temperature is non-dimensionalised as $\theta = (T - T_\infty)/(T_w - T_\infty)$) around the block for different Peclet numbers. The top half and the lower half show the isotherms of water and water/CuO4% (d_{np} = 30 nm), respectively. Clearly, the contours of both fluids have the same pattern but the nanofluids show a higher capability of transferring the heat from the cylinder, particularly at higher Peclet numbers. It is evident from Fig. 4 that temperature contours are much denser near the front surface of the block. This indicates the higher temperature gradient and, subsequently, greater heat transfer coefficient. At the trailing edge of the upper surface of the cylinder, where the flow separates from the block, the temperature contours start to disperse. As the Pe increases and the recirculation region behind the cylinder grows, this dispersion reduces and the isotherms become closer to the rear side of the block.

Fig. 5 shows the local heat transfer coefficient along the cylinder surfaces for water/CuO 4% (d_{np} = 30 nm) at different Peclet numbers. The heat transfer coefficient around the block is defined as:

$$h = \frac{k_{nf}\partial T/\partial n}{T_w - T_\infty}. \tag{16}$$

As expected, the h values increase with increasing the Peclet number. Generally, the front surface has the highest heat transfer coefficient which is predictable according to Fig. 4. It is also clear that heat transfer coefficient curve reaches a peak at the corners of the block which is due to the high temperature gradients at these points. The averaged values of h over the rear surface of the cylinder is lower than the front and upper surfaces as the temperature contours are less crowded behind the block.

Fig. 6 presents the average heat transfer coefficient around the block at different Peclet numbers, nanoparticles volume fractions and diameters for the cases of Al_2O_3/water and CuO/water nanofluids. The results indicate that the average heat transfer coefficient of nanofluid rises with increasing Peclet number as well as the particle volume fraction and decreases with an increase in particle diameter.

Since the denominator of Eq. (16) is constant, the effect of nanofluids on the heat transfer coefficient can be explained based on the variation in thermal conductivity and wall temperature gradient.

In this paper the inlet velocity is adjusted to achieve a constant Peclet number ($Pe = \frac{\rho u_\infty L C_p}{k}$) for different cases of nanofluids. According to Table 4, at higher concentration levels, the values of thermal conductivity and density increase and the heat capacity reduces. However, the overall interaction of these parameters is such that the inlet velocity should increase to achieve a constant Peclet number which may lead to a higher velocity gradient and as a result, depending on the Prandtl behaviour, the temperature gradient around the block changes. On the other hand, increasing the particle concentration boosts the viscosity which may tend to decrease the velocity gradient near the block. Therefore, these

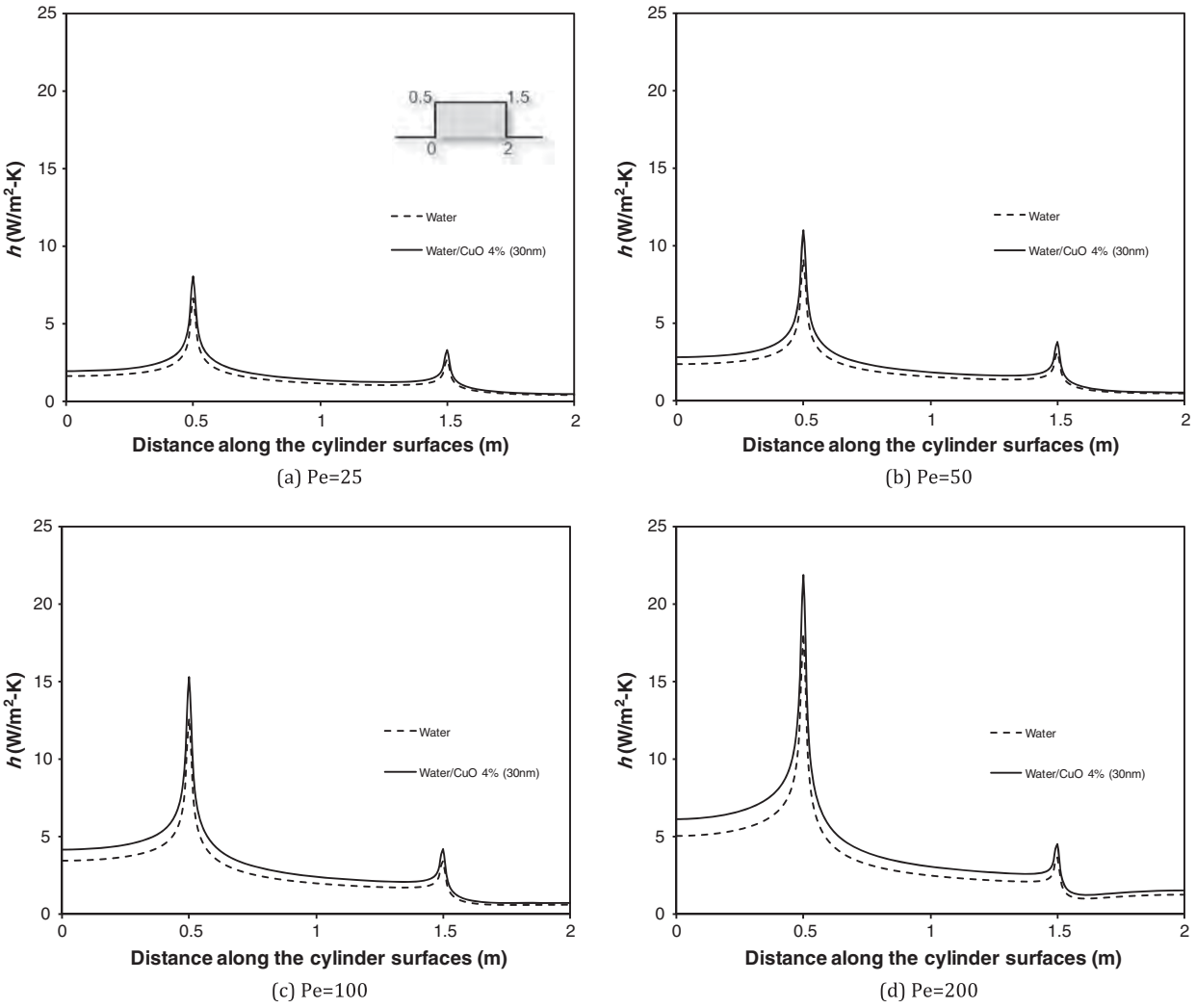

Fig. 5. Local heat transfer coefficient of water and water/CuO 4% (d_{np} = 30 nm) along the cylinder surfaces at different Peclet numbers.

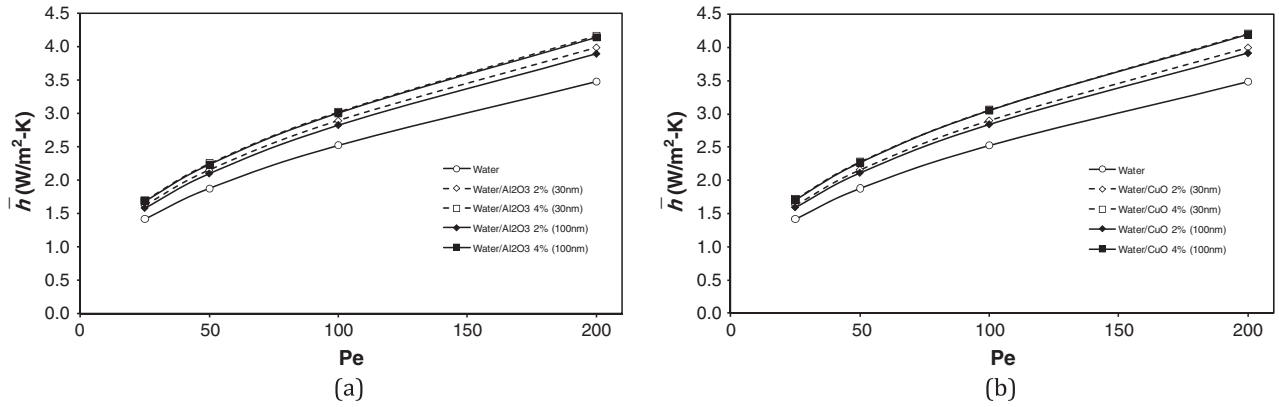

Fig. 6. Average heat transfer coefficient of the cylinder as a function of Peclet number for water and different nanofluids with base fluid of water.

opposing behaviours during particle concentration enhancement should be considered to realise the resultant heat transfer characteristics of nanofluids.

Fig. 6 shows that, at any given *Pe*, the heat transfer coefficient is enhanced as the particle concentration increases. According to Eq. (16), this manner proves that for the nanofluids shown in this figure, the upward trend of thermal conductivity dominates the heat transfer coefficient behaviour. It can also be seen that the effect of particle concentration becomes more significant at higher Peclet numbers.

Similarly, for a given particle concentration the heat transfer coefficient increases at a higher *Pe*. That is due to the fact that for constant thermophysical properties and a fixed geometry the only way to increase the Peclet number is to increase the inlet